



Characterisation of
Fluorescent Extracellular Vesicles
and their Distribution in the Prostate
Cancer Microenvironment

By

Timothea Konstantinou

Thesis submitted for the degree

DOCTOR OF PHILOSOPHY

Division of Cancer and Genetics

School of Medicine

Cardiff University

2021

Acknowledgements

First and foremost, I would like to thank Cancer Research UK for their generous funding and for entrusting me with this project, and overall support I was given throughout my studies, especially during the difficult times of the COVID-19 pandemic.

Next, I would like to express my deepest and sincerest gratitude to my primary supervisors Professor Rachel Errington and Professor Aled Clayton, who have stuck by my side through thick and thin; their precious guidance has been a beacon of hope, inspiring me and motivating me through this journey.

Throughout this project I had the opportunity to work with many excellent collaborators to whom I extend my gratitude for their advice, support, and expert knowledge which have brought this project to fruition. Special thanks to our collaborators at the BSRC Mass Spectrometry and Proteomics Facility at the University of St. Andrews, Dr Simon Powis, Dr Sally Shiran and Dr Silvia Synowsky, and our collaborators at the School of Chemical and Process Engineering at the University of Leeds Dr Andy Brown and Dr Nicole Hondow.

This PhD would not have been possible without the precious help of friends and colleagues at the Tissue MicroEnvironment Group, who have made my hectic and difficult days a bit brighter. I would like to especially thank Mrs. Marie Wiltshire, the person I mostly counted on in the lab for her everyday support and guidance in everything regarding cell culture and flow cytometry. Dr Rachel Howard-Jones also deserves my deepest gratitude as her contribution to my project has been invaluable as well as her overall support during the difficult times of COVID-19. I am eternally grateful to both for their support and friendship.

I would also like to thank Dr Dimitris Parthimos, Dr Jason Webber and Dr Stephen Mann for all of their excellent guidance on image analysis, advice on extracellular vesicles and great support throughout this long PhD journey. Special thanks are also due to Dr Andreia de Almeida and Dr Kate Milward for all their support around the lab, excellent advice on flow cytometry and microscopy and overall, making every working day in the lab more fun. I extend my gratitude to Dr Lauren Evans, Dr Sara Veiga, Muireann Ni Bhaoighill and Basmah Almagwashi; I can't begin to remember how many countless days and nights we spent at the lab working and exchanging advice, but it was our delightful banter and jokes that were the true lifesaver. Our newest lab members Dr Amr Alraies, and Mariama Mbengue also deserve my thanks, as their friendship was invaluable during the COVID-19 late shifts at the lab.

Last but not least, I would like to thank my family and friends who have always been by my side. I especially want to thank my mother Andri, who has made everything possible; she was the first person to believe in me and inspired me to go where not many people would have the courage to go. I extend my gratitude to my grandparents and especially my grandmother Tsikkina, for her encouragement and praise. Many thanks to my sister Christina, who was there for me throughout this journey, trying to cheer me up with her witty, black humour – even though she wasn't always successful in doing so. Finally, my deepest appreciation and sincerest gratitude go to my best friend Vasiliki, and my partner in life Giorgos, who have put up with me through sleepless nights and long days, through laughing and crying.

My sincerest thanks to everyone who have made this possible, it has truly been an unforgettable adventure.

I dedicate this Thesis to my dearest godfather; we lost you too early... your battle with cancer has been life changing. Through sadness and pain, losing you became a source of motivation for wanting to do the best for other people; I hope I have made you proud.

Summary

Small extracellular vesicles (sEVs) are nanovesicles secreted from cells, that elicit intercellular communication by transferring their cargo to recipient cells. This form of communication contributes towards disease-critical processes in prostate cancer (PCa), including sEV-mediated microenvironment remodelling, tumour progression, angiogenesis, and formation of the pre-metastatic niche. The fundamental mechanisms of sEV dissemination through the microenvironment, as well as distribution within tissues have not been extensively investigated. This is the topic of the current study.

To address these questions, sEVs require fluorescent labelling; we developed two PCa cell lines that generate endogenously fluorescent sEVs by expressing GFP or Tdtomato fluorescent proteins fused to CD63 or CD81, respectively. Fluorescent sEVs were used to microscopically characterise uptake kinetics (dosing), retention, and distribution in recipient PCa cell- and bone marrow-derived mesenchymal stem-cell (BM-MSC) - populations. Additionally, a vital consideration was the impact of the tetraspanin-fluorescent protein fusions on the phenotype of the parent cells, and the corresponding sEVs.

Forced overexpression of tetraspanin-fluorescent protein fusions drove significant phenotypic and proteomic changes at both the cell and sEV level. The differential impact of a two- versus three-dimensional cell culture microenvironment on the phenotype of cells and sEVs was also demonstrated, emphasising the importance of platform definition and characterisation. Nevertheless, the behaviour of fluorescent sEVs revealed conserved principles in sEV uptake kinetics, retention, and distribution in two-dimensional dynamic cell systems, highlighting recipient-cell type differences in signal uptake and retention. In addition, functional effects of sEV uptake were identified demonstrating osteogenic differentiation of BM-MSCs as a result of chronic dosing with PCa-derived sEVs.

To conclude, our study generated new optical tools allowing fundamental principles of sEV distribution in tissues or cells to be defined. The data provides the basis for understanding the dispersion of sEVs in tissue microenvironments, and new insights into their great potential for diverse clinical applications.

Publications

Konstantinou, T., Clayton, A. and Errington, R. 2021. Proteomic characterisation of fluorescent extracellular vesicle and their distribution in cell systems. *In preparation*.

Burton, C., Clayton, A., et al. 2021. EVee - “the 3D-EV”: A handheld 3D model representing an Extracellular Vesicle, as a public engagement tool. *In preparation*.

Presentations

- Oral presentation- Division of Cancer and Genetics (DCG) day, 2017, Cardiff University, United Kingdom
- Oral presentation-Postgraduate Research (PGR) day, 2018, Cardiff University, United Kingdom
- Poster presentation- Postgraduate research (PGR) day 2019, Cardiff University, United Kingdom
- Oral presentation/Seminar-DCG seminar series 2019, Cardiff University, United Kingdom
- Poster presentation- UK Society for Extracellular Vesicles (UKEV) conference 2019, London, United Kingdom
- Oral presentation- International Society for Advancement of Cytometry (ISAC) CYTO2019 conference, 2019, Vancouver, Canada
- Poster presentation- International Society for Advancement of Cytometry (ISAC) CYTO2021 conference, 2021(virtual)

Grants

- WM Thomas fund, £200 – Travel grant to attend CYTO2019 annual meeting, Vancouver, Canada, June 2019
- M Banfill Scholarship, £1000– Travel grant to attend CYTO2019 annual meeting, Vancouver, Canada, June 2019
- CYTO 2019 Award, \$1000– Travel award to attend CYTO2019 annual meeting, Vancouver, Canada, June 2019

Abbreviations

2D/3D	Two-Dimensional/Three-Dimensional
A (Fraction)	Adherent Fraction
ADAM-17	A disintegrin and metalloprotease 17
AKAP10	A-Kinase Anchoring Protein 10
Alix	ALG-2-interacting protein X
ALP	Alkaline Phosphatase
ANOVA	Analysis of variance
AR	Androgen Receptor
ARF6	ADP-ribosylation factor 6
ARHGAP1	Rho GTPase-activating protein 1
AT1B3	Sodium/potassium-transporting ATPase subunit beta-3
B2M	β 2 microglobulin
BCA	Bicinchoninic acid
BCAM	Basal cell adhesion molecule
BM-MSC	Bone Marrow-Derived Mesenchymal Stem Cell
BSA	Bovine serum albumin
CAF	Cancer-Associated Fibroblast
CAPZA1	Capping Actin Protein of Muscle Z-Line Subunit Alpha 1
Cd/Te	Cadmium/Tellurium
CFDA	Carboxyfluorescein diacetate succinimidyl ester
CFSE	Carboxyfluorescein succinimidyl ester
CHMP1B	Charged Multivesicular Body Protein 1B
CHMP2A	Charged Multivesicular Body Protein 2a
CK	Cytokeratin
Cryo-TEM	Cryogenic Transmission Electron Microscopy
CTNNB1	Catenin beta-1 / β -catenin
CV	Coefficient of Variation
CXCL12	Stromal cell-derived factor 1
DAPI	4',6-diamidino-2-phenylindole
DDA	Data-Dependent Acquisition
DIA	Data-Independent Acquisition
DiD	Dil-chlorobenzenesulfonate salt
Dil	1,1'-dioctadecyl-3,3,3',3'-tetramethylindocarbocyanine
DiO	3,3'-Dioctadecyloxycarbocyanine Perchlorate
DMEM	Dulbecco's Modified Eagle Medium
DYNEIN 1	Cytoplasmic dynein 1 heavy chain 1
ECL	Extracellular Loop
ECM	Extracellular Matrix
EEF	Eukaryotic Translation Elongation Factor
EGFR	Epidermal Growth Factor Receptor
EIF	Eukaryotic Translation Initiation Factor
EMT	Epithelial-to-Mesenchymal Transition
EPCAM	Epithelial cell adhesion molecule
ERM	Ezrin, Radixin and Moesin
ESCRT	Endosomal Sorting Complexes Required for Transport
EV	Extracellular Vesicle
ExoFBS	Foetal Bovine Serum Depleted of Bovine Extracellular Vesicles
FABP5	Fatty Acid-Binding Protein 5
FACS	Fluorescence-Activated Cell Sorting
FAM134A	Family with Sequence Similarity 134, Member A
FasL	Fas Ligand
FBS	Foetal Bovine Serum
FC	Fold Change
FDR	False Discovery Rate
FGF-2	Fibroblast Growth Factor 2
FSC-A/H	Forward scatter-area/height
FunRich	Functional Enrichment analysis Tool
FWHM	Full Width at Half Maximum

GFP	Green Fluorescent Protein
gMFI	Geometric Mean Fluorescence Intensity
GRB2	Growth factor receptor-bound protein 2
GRP94	Endoplasmic Reticulum Chaperone Glycoprotein
h	Hour(s)
HECTD1	E3 Ubiquitin-Protein Ligase HECTD1
HGF	Hepatocyte Growth Factor
HSC70	Heat shock cognate 71 kDa protein
HSP27/90	Heat shock protein 27/90
HSPG	Heparan Sulfate Proteoglycans
ICAM1	Intercellular adhesion molecule 1
ID	Identification
Ig	Immunoglobulin
ILV	Intraluminal Vesicle
IMA1	Importin subunit alpha-1
K-RAS	Kirsten rat sarcoma virus
LAT1	Large Neutral Amino-Acid Transporter Small Subunit 1
LC-MS/MS	Liquid Chromatography Tandem Mass Spectrometry
IEV	large Extracellular Vesicle
MHC	Major Histocompatibility Complex
min	Minutes
MiRNA	MicroRNA
MMP	Matrix Metalloproteinase
MVB	Multivesicular Body
NK	Natural Killer
NTA	Nanoparticle Tracking Analysis
O/N	Overnight
PCA	Principal Component Analysis
PCa	Prostate Cancer
PI(3)P	Phosphatidylinositol 3-phosphate
PI4K	Phosphatidylinositol 4-kinase
PK2M	Pyruvate Kinase 2
PP4C	Protein Phosphatase 4
PPI	Protein-Protein Interaction
PSF	Point-Spread Function
PTGR1	Prostaglandin Reductase 1
PTPN23	Protein Tyrosine Phosphatase Non-Receptor Type 23
QD705	Qtracker705™ (QD-705nm emission maxima)
QDs	Quantum Dots
RAI3	Retinoic acid-induced protein 3
RCC2	Regulator of Chromosome Condensation 2
RIPA (buffer)	Radioimmunoprecipitation assay (buffer)
RPL7/27	60S Ribosomal Protein L7/27a
RPMI	Rosewell Park Memorial Institute
RPS16	40S Ribosomal Protein S16
RT	Room Temperature
RUNX2	Runt-Related Transcription Factor 2
S(Fraction)	Suspension Fraction
S100A10	S100 Calcium Binding Protein A10
SA(Fraction)	Semi-Adherent Fraction
SD	Standard Deviation
Sec23A	Protein Transport Protein Sec23A
sEV	small Extracellular Vesicle
SSC-A/H	Side scatter-area/height
STRING	Search Tool for the Retrieval of Interacting Genes
STRIP2	Striatin Interacting Protein 2
SWATH-MS	Sequential Windows Acquisition of All Theoretical Spectra
TAP1	Antigen Peptide Transporter 1
Tdtomato	Tandem Dimer Tomato
TEM	Tetraspanin-Enriched Microdomains

TfR	Transferrin Receptor
TGF- β	Transforming Growth Factor Beta
TIGAR	TP53 Induced Glycolysis Regulatory Phosphatase
TLDC1	MTOR Associated Protein Eak-7 Homolog
TMEM184C	Transmembrane Protein 184C
TNAP2	Tumour Necrosis Factor Alpha-Induced Protein 2
TNF- α	Tumour Necrosis Factor Alpha
TNM	TNM cancer staging system: T (primary tumour), N (regional lymph nodes), M (distant metastasis)
TRAIL	TNF-Related Apoptosis-Inducing Ligand
TRF	Time-Resolved Fluorescence
TRIM47	E3 Ubiquitin-Protein Ligase TRIM47
TSG101	Tumour susceptibility gene 101
TSPAN15	Tetraspanin 15
uPA	Urokinase-type plasminogen activator
VAMP3	Vesicle-Associated Membrane Protein 3
VEGF	Vascular Endothelial Growth Factor
VPS37B	Vacuolar Protein Sorting-Associated Protein 37B
VPS4A/B	Vacuolar Protein Sorting-Associated Protein 4 Homolog A/B
WT	Wild-Type

Table of Contents

1.	CHAPTER 1: Introduction.....	1
1.1.	Extracellular Vesicle (EV) Definition and Nomenclature.....	2
1.2.	sEV Biogenesis and Composition.....	4
1.2.1.	sEV Biogenesis.....	4
1.2.2.	sEV Secretion.....	5
1.2.3.	sEV Composition.....	7
1.3.	sEV Roles in Prostate Cancer.....	9
1.3.1.	PCa Microenvironment.....	9
1.3.2.	Roles of sEVs in the PCa microenvironment.....	10
1.3.3.	Pre-Metastatic Niche and Role of PCa sEVs.....	13
1.4.	sEV Interaction, Internalisation and Fate in Cells.....	16
1.4.1.	sEV Direct Interactions at the Cell Membrane.....	16
1.4.2.	sEV Internalisation by Recipient Cells.....	17
1.4.3.	sEV Fate.....	19
1.5.	sEV Kinetics and Distribution in Cell Systems.....	21
1.5.1.	Clinical Interest.....	21
1.5.2.	Fluorescent sEV Reporters for Dosing and Distribution in Cell Systems ...	22
1.6.	Thesis Hypotheses and Aims.....	32
2.	CHAPTER 2: Materials and Methods.....	34
2.1.	Cell Culture.....	35
2.2.	Plasmid Expansion.....	35
2.3.	Cell Transfection.....	36
2.3.1.	Transient Transfection Optimisation.....	36
2.3.2.	Stable Transfection and Selection with Geneticin.....	36
2.4.	Cell Sorting and Monitoring of Fluorescence Expression.....	37
2.5.	Growth Curve Analysis.....	37
2.6.	Cell Cycle Arrest Analysis.....	38
2.7.	Live-Cell Fluorescence Imaging Analysis.....	38
2.8.	CellProfiler™: Cellular Phenotypic Image Analysis.....	38
2.9.	sEV-Associated Cell Membrane Protein Analysis.....	39

2.10.	Differential Ultracentrifugation and sEV Secretion Analysis	40
2.11.	Sucrose-Cushion Ultracentrifugation for sEV Isolation	41
2.12.	BCA Protein Assay.....	41
2.13.	Nanoparticle Tracking Analysis (NTA)	42
2.14.	Immuno-Phenotyping ELISA-like Assay	42
2.15.	sEV Detection and Point-Spread Function Analysis	43
2.16.	SWATH-MS Proteomics Analysis	44
2.16.1.	Sample Preparation and Protein Quantification (Cells and sEVs).....	44
2.16.2.	Spectral Library Generation and SWATH-MS	44
2.16.3.	SWATH-MS Data Processing	45
2.16.4.	SWATH-MS Statistical Analysis.....	46
2.16.5.	Gene Enrichment and Interaction Analysis	46
2.16.6.	Validation of Proteomics Targets	47
2.17.	Western Blot analysis.....	48
2.18.	CELLine Bioreactor Maintenance and Characterisation	50
2.18.1.	Maintenance Procedure	50
2.18.2.	Characterisation Procedure	50
2.19.	QD705 and EV-647 Dosing Experiments in DU145 and Y201	54
2.19.1.	QD705 Dosing in DU145 Cells.....	54
2.19.2.	Comparison of QD705 Dosing in DU145 vs Y201 Cells	55
2.19.3.	Comparison of QD705 Vs EV-647 Dosing in DU145 Cells.....	56
2.20.	CD81-Tdtomato sEV Delivery in cell systems	57
2.20.1.	CD81-Tdtomato sEV Dosing Optimisation in DU145.....	57
2.20.2.	CD81-Tdtomato sEV Acute Delivery in DU145 and Y201 cells.....	58
2.20.3.	CD81-Tdtomato sEV Chronic Delivery in Y201 Cells	58
2.21.	QD705 and CD81-Tdtomato sEV Dosing: Image Analysis.....	59
2.21.1.	Single-cell Image Analysis for QD705 Dosing	59
2.21.2.	Single-Cell and Field-Of-View Image Analysis for sEV Dosing	61
2.22.	Assessment of Osteogenic Differentiation by sEVs.....	63
2.22.1.	Late Osteogenic Differentiation Assessment	63
2.22.2.	Early Osteogenic Differentiation Assessment.....	64

2.23.	Data and Statistical Analysis.....	68
3.	CHAPTER 3: Cancer Cell Lines Generating Endogenously Fluorescent Extracellular Vesicles	69
3.1.	Introduction.....	70
3.2.	Aims and Objectives	72
3.3.	Results	73
3.3.1.	Generation of Stable Cell Lines Expressing Fluorescently Conjugated Tetraspanins.....	73
3.3.2.	Phenotypic Characterisation of Stable Cell Lines	76
3.3.3.	Isolation, Characterisation and Detection of sEVs.....	90
3.4.	Discussion	100
3.5.	Conclusions.....	105
4.	CHAPTER 4: Quantitative Proteomics by SWATH-MS on DU145 cells and Extracellular Vesicles Overexpressing CD63 or CD81	106
4.1.	Introduction.....	107
4.2.	Aims and Objectives	109
4.3.	Results	110
4.3.1.	Quantitative Analysis of Differentially Expressed Proteins	110
4.3.2.	Visualisation of proteins with significant differences in abundance in cells and sEVs	119
4.3.3.	Gene Enrichment and Protein-Protein Interaction Network Analysis	134
4.3.4.	Validation of selected dysregulated protein targets in sEVs.....	143
4.4.	Discussion	148
4.5.	Conclusions.....	156
5.	CHAPTER 5: Phenotypic Changes of Prostate Cancer Stable Cell Lines and Secreted Extracellular Vesicles in 3D-Emulated Bioreactor Microenvironments	157
5.1.	Introduction.....	158
5.2.	Aims and Objectives	160
5.3.	Results	161
5.3.1.	Establishing the Bioreactor Characterisation procedure.....	161
5.3.2.	Phenotypic Characteristics of Cells in Bioreactors	161
5.3.3.	Phenotypic Characteristics of Bioreactor-derived sEVs.....	174
5.4.	Discussion	194

5.5.	Conclusions.....	200
6.	CHAPTER 6: Nanoparticle and Extracellular Vesicle Uptake and Retention in Prostate Cancer and Bone Marrow- Derived Mesenchymal Stem Cells.....	201
6.1.	Introduction.....	202
6.2.	Aims and Objectives	205
6.3.	Results	206
6.3.1.	Multi-Platform Quantification of QD705 Uptake in DU145 Cells	206
6.3.2.	Quantification of QD705 Retention in DU145 Cells	212
6.3.3.	Quantification of QD705 Uptake and Retention in Y201 Mesenchymal Stem Cells vs DU145 PCa Cells.....	214
6.3.4.	QD705 vs sEV Dosing in DU145 Cells	220
6.3.5.	Acute CD81-Tdtomato sEV Uptake and Retention in DU145 Cells.....	224
6.3.6.	Quantification of CD81-Tdtomato sEV Uptake and Retention in DU145 Compared to Y201 Cells.	228
6.4.	Discussion	246
6.5.	Conclusions.....	254
7.	CHAPTER 7: Prostate Cancer Derived Extracellular Vesicle-Induced Osteogenic Differentiation of Bone Marrow-Derived Mesenchymal Stem Cells	255
7.1.	Introduction.....	256
7.2.	Aims and Objectives	257
7.3.	Results	258
7.3.1.	Effects of CD81-Tdtomato sEVs on Late Osteogenic Differentiation	258
7.3.2.	Gene Expression Analysis of the Effects of sEVs on Early Osteogenic Differentiation	260
7.4.	Discussion	265
7.5.	Conclusions.....	268
8.	CHAPTER 8: General Discussion.....	269
8.1.	Summarising Discussion.....	270
8.2.	Future Directions.....	277
9.	REFERENCES	280
10.	APPENDIX I	296
11.	APPENDIX II	337

Table of Figures

Figure 1.1. Overview of Extracellular Vesicle (EV) biogenesis and exosome composition.	3
Figure 1.2. ESCRT- dependent and ESCRT-independent mechanisms of sEV biogenesis.	6
Figure 1.3. The PCa microenvironment and role of sEVs.	12
Figure 1.4. Role of PCa sEVs in pre-metastatic bone niche formation.	15
Figure 1.5. sEV interactions, internalisation, and fate in recipient cells.	20
Figure 1.6. Common methods of sEV fluorescent labelling.	25
Figure 2.1. Single-cell image analysis with Li's Thresholding method for QD705-labelled cells.	60
Figure 2.2. Single-cell and Field-of-view image analysis schematic.	62
Figure 3.1. Timeline of GFP-CD63 and CD81-Tdtomato stable cell line FACS and fluorescence expression.	78
Figure 3.2. Scatter and Fluorescence properties of GFP-CD63, CD81-Tdtomato and WT DU145 parallel cell lines (GFP-Parallel and Tom-Parallel controls).	79
Figure 3.3. Growth curve analysis for GFP-CD63 and CD81-Tdtomato DU145 cells compared to the WT DU145 parallel control counterparts.	82
Figure 3.4. Cell cycle progression for GFP-CD63 and CD81-Tdtomato DU145 cells compared to their WT DU145 parallel control counterparts.	83
Figure 3.5. GFP-CD63 and CD81-Tdtomato live-cell localisation.	87
Figure 3.6. Cell morphology analysis for GFP-CD63 and CD81-Tdtomato compared to their WT parallel controls.	88
Figure 3.7. Cell membrane expression of EV-associated markers by GFP-CD63 and CD81-Tdtomato cells compared to their WT parallel controls.	89
Figure 3.8. Characterisation of isolated EVs for size and EV-associated protein markers.	93
Figure 3.9. sEV secretion comparison between overexpressing cell lines and WT controls.	94
Figure 3.10. Point-Spread Function measurements and fluorescence intensity analysis of GFP-CD63 and CD81-Tdtomato sEVs.	99
Figure 4.1. Schematic workflow describing the SWATH-MS process.	111
Figure 4.2. Venn Diagrams for cells and sEVs overexpressing CD63 or CD81 compared to WT parallel controls.	115
Figure 4.3. Sub-cellular localisation of common identified proteins in cells and sEVs.	118
Figure 4.4. Volcano plots for comparisons of protein abundance in sEVs and cells overexpressing CD63 or CD81 compared to controls.	120
Figure 4.5. Venn Diagrams depicting unique and overlapping upregulated and downregulated proteins between cells and sEVs overexpressing CD63 or CD81.	123
Figure 4.6. Heatmaps of the most significantly altered proteins in GFP-CD63 sEVs and cells compared to WT Parallel controls.	127
Figure 4.7. Heatmaps of the most significantly altered proteins in CD81-Tdtomato sEVs and cells compared to the WT Parallel controls.	132
Figure 4.8. Gene Enrichment Analysis comparing biological processes of dysregulated proteins between cells and sEVs.	136

Figure 4.9. Gene Enrichment Analysis comparing Molecular Functions of dysregulated proteins between cells and sEVs.	137
Figure 4.10. Protein-Protein Interaction network analysis.	141
Figure 4.11. Validation of selected SWATH-MS protein targets via Western Blot analysis. ...	146
Figure 5.1. Schematic illustration and Scanning Electron Microscopy of the CELLine Bioreactor Flask.	159
Figure 5.2. Schematic and timeline for Bioreactor Characterisation procedure.	163
Figure 5.3. Growth and adhesion characteristics of cell lines in Bioreactor Flasks.	166
Figure 5.4. Viability of GFP-CD63 and CD81-Tdtomato compared to WT DU145 parallel cell lines in Bioreactor Flasks.	167
Figure 5.5. Distribution of cells of all fractions in G ₁ , S/G ₂ /M and polyploid cell phase over time.	169
Figure 5.6. Fluorescence signal stability of GFP-CD63 cells in Bioreactor Flasks.	172
Figure 5.7. Fluorescence signal stability of CD81-Tdtomato cells in Bioreactor Flasks.	173
Figure 5.8. Western blot characterisation of Bioreactor-derived sEVs vs corresponding DU145 cells.	177
Figure 5.9. Effects of CD63 or CD81 overexpression on Bioreactor-derived sEV cargo.	180
Figure 5.10. Time-dependent effects of Bioreactors on sEV-associated protein markers.	181
Figure 5.11. Nanoscale Flow Cytometry to detect CD81-Tdtomato sEV fluorescence.	184
Figure 5.12. Nanoscale Flow Cytometry to detect GFP-CD63 sEV fluorescence.	185
Figure 5.13. Effects of overexpression of CD63 and CD81 on sEV size distribution.	187
Figure 5.14. Cryo-TEM exemplary images depicting morphology of CD81-Tdtomato and Tom-Parallel EVs.	190
Figure 5.15. CryoTEM morphology analysis of EVs.	191
Figure 5.16. Cryo-TEM size distribution analysis of EVs.	193
Figure 6.1. Uptake of QD705 nanoparticles in the DU145 cell population.	208
Figure 6.2. Uptake and Spot Count analysis of QD705 nanoparticles in DU145 cells reproduced by imaging flow cytometry.	209
Figure 6.3. Single-cell image analysis QD705- labelled DU145 cells.	211
Figure 6.4. QD705 fluorescence signal distribution and decay over time in DU145 cells.	213
Figure 6.5. QD705 nanoparticle fluorescence signal uptake and retention in DU145 and Y201 cells.	217
Figure 6.6. QD705 uptake and retention in DU145 and Y201 cells.	218
Figure 6.7. QD705 and EV-647 dosing in DU145 cells.	222
Figure 6.8. CD81-Tdtomato sEV dosing in DU145 cells by fluorescence microscopy.	227
Figure 6.9. CD81-Tdtomato sEV uptake and retention after acute sEV-delivery comparing DU145 and Y201 cells.	231
Figure 6.10. Representative images of acute CD81-Tdtomato sEV dosing in DU145 and Y201 cells.	233

Figure 6.11. Field-of-view image analysis of CD81-Tdtomato chronic sEV delivery in Y201 cells.	237
Figure 6.12. Single-cell image analysis of CD81-Tdtomato sEV uptake and retention up to 48 hours post chronic delivery in Y201 cells.	242
Figure 6.13. Representative images of chronic CD81-Tdtomato sEV dosing in Y201 cells.	243
Figure 7.1. Visualisation and quantification of Alizarin Red S Staining in differentiating Y201 cells dosed with CD81-Tdtomato sEVs in osteogenic and regular media.	263
Figure 7.2. Gene expression analysis of osteogenic differentiation genes in Y201 cells dosed with increasing concentrations of sEVs in osteogenic or regular media.	264

Table of Tables

Table 1.1. Advantages and limitations of EV fluorescence labelling methods.	31
Table 2.1 . Primary Antibodies used in Western Blot analysis.	49
Table 2.2. Particle and protein concentrations of DU145-derived sEVs.	53
Table 2.3. sEV dosing experimental conditions for Y201 osteogenic differentiation.	64
Table 2.4. Primers used for qPCR analysis.....	67
Table 3.1. Evaluation of transfection reagents effects on transfection efficiency, cell expression level and overall toxicity.	75
Table 3.2. Evaluation of DNA concentration, DNA: Lipofectamine™3000 ratio and incubation time, for transfection efficiency, cell expression level and overall toxicity.	75
Table 3.3 . Evaluation of 1:3 or 1:5 DNA: Lipofectamine™3000 Ratio on transfection efficiency, cell expression level and overall toxicity for various DNA constructs.	75
Table 4.1 . Detected and quantified proteins from SWATH-MS analysis in DU145 sEVs and cells overexpressing CD63 or CD81 compared to WT parallel controls.	114

Table of Supplementary Figures- Appendix I

Supplementary Figure 1. Detailed plasmid maps for each DNA construct.	297
Supplementary Figure 2. Fiji macro code used for image analysis..	301
Supplementary Figure 3. Gating strategy for Fluorescence-Activated Cell Sorting (FACS) of GFP-CD63 and CD81-Tdtomato DU145 cells.	304
Supplementary Figure 4. Gating strategy for cell cycle analysis of GFP-CD63, CD81-Tdtomato and WT DU145 parallel control counterparts.	305
Supplementary Figure 5. Exemplary cell cycle histogram overlays of GFP-CD63, CD81-Tdtomato and WT parallel controls.	306
Supplementary Figure 6. Live-cell localisation of GFP, Tdtomato, GFP-CD63 and CD81-Tdtomato in DU145 cells.	307
Supplementary Figure 7. Gating strategy for flow cytometry analysis of cellular membrane expression of EV-associated protein markers.	308
Supplementary Figure 8. Examples of fluorescence scatter plots and histograms for flow cytometry analysis of EV-associated markers in cells.	309
Supplementary Figure 9. FWHM distribution analysis from PSF calculations of GFP-CD63 and CD81-Tdtomato EVs.	311
Supplementary Figure 10. Principal Component analysis of cell and sEV samples.	312
Supplementary Figure 11. Venn Diagram unique protein IDs for cells and sEVs.	313
Supplementary Figure 12. Western Blot analysis developed raw membranes.	315
Supplementary Figure 13. Cell numbers recovered from Bioreactor Flasks.	316
Supplementary Figure 14. Gating strategy for cell viability analysis.	317
Supplementary Figure 15. Gating strategy for cell cycle analysis.	318
Supplementary Figure 16. Comparison of Bioreactor-derived cell numbers with sEV numbers and protein yield.	319
Supplementary Figure 17. Nanoscale flow cytometry gating strategy for beads and sEVs. .	320
Supplementary Figure 18. Test for coincidence in Nanoscale flow cytometry.	321
Supplementary Figure 19. Detection of fluorescence signal of CD81-Tdtomato and GFP-CD63 sEVs by fluorescence microscopy.	322
Supplementary Figure 20. Nanoparticle Tracking Analysis- derived EV size distributions.	323
Supplementary Figure 21. sEV size Chi Square distribution comparisons.	324
Supplementary Figure 22. Gating strategy for the QD705 uptake and distribution flow cytometry experiment.	325
Supplementary Figure 23. Gating strategy for the 24-hour QD705 uptake imaging flow cytometry experiment.	326
Supplementary Figure 24. Chi Square distribution comparisons of QD705 fluorescence signal decay.	327
Supplementary Figure 25. Chi Square distribution comparisons of QD705 fluorescence signal uptake and decay.	328

Supplementary Figure 26. Relationship of cell characteristics and QD705 fluorescence signal in DU145 and Y201 cells.	330
Supplementary Figure 27. EV-647 uptake and retention in DU145 via flow cytometry.	331
Supplementary Figure 28. CD81-Tdtomato EV uptake and correlation to DU145 cell shape.	332
Supplementary Figure 29. CD81-Tdtomato EV uptake in DU145 cells by flow cytometry. ...	333
Supplementary Figure 30. Correlation of CD81-Tdtomato EV uptake with DU145 and Y201 cell shape characteristics after acute EV delivery.	334
Supplementary Figure 31. Chi Square distribution comparisons of Tdtomato fluorescence between doses over time in Y201 cells.	335
Supplementary Figure 32. Correlations and Chi Square distribution comparisons for cell shape on uptake of CD81-Tdtomato EVs in Y201 cells.	336

Table of Supplementary Tables- Appendix II

Supplementary Table 1. Proteins significantly up/downregulated in GFP-CD63 vs GFP-Parallel control sEVs	338
Supplementary Table 2. Proteins significantly up/downregulated in CD81-Tdtomato vs Tom-Parallel control sEVs.	340
Supplementary Table 3. Proteins significantly up/downregulated in GFP-CD63 vs GFP-Parallel control cells	343
Supplementary Table 4. Proteins significantly up/downregulated in CD81-Tdtomato vs Tom-Parallel control cells.	345

CHAPTER 1: Introduction

1.1. Extracellular Vesicle (EV) Definition and Nomenclature

Extracellular Vesicles are lipid bilayer membrane vesicles secreted from cells, a process which is highly evolutionary conserved, from prokaryotic to eukaryotic organisms (1). Traditionally these vesicles were classified based on their size and modes of biogenesis, with the major classes of vesicles being: (i) “exosomes”, which are vesicles of endosomal origin, sized from 30-150nm and (ii) “microvesicles” or “ectosomes”, which are vesicles that bud directly from the plasma membrane, sized from 50-1000nm ([Figure 1.1](#)), as well as (iii) “apoptotic bodies” which are vesicles sized 100-5000nm, formed during plasma membrane blebbing of a cell undergoing apoptosis (2-5).

According to the recent guidelines published by the International Society for Extracellular Vesicles (ISEV 2018) the term Extracellular Vesicle or EV, is currently preferred as an “umbrella term” to describe all these secreted vesicles, as the field has not reached a consensus in their specific classification into EV subtypes based on their origin or composition (6). Due to these challenges, alternative classifications were proposed, for example based on their size, with EVs smaller than 200nm referred as small EVs (sEVs), whereas EVs larger than 200nm referred as large EVs (IEVs) (6). However, classification based on the physical characteristics of EVs does not account for vesicles produced by distinct mechanisms as being fundamentally different entities, e.g., small vesicles that bud directly from the plasma membrane (3, 4, 6). Furthermore, these classifications cannot be absolute, as sEVs and IEVs were reported to share common components and can even be co-isolated (6, 7). Hence, until the field gains more insight into the distinct molecular signatures of these EVs, caution must be taken when using specific terminology. In this study we follow the MISEV2018 guidelines and utilise the blanket term “EVs” when referring to vesicles, or “sEVs” when there is clear characterisation of the physical properties of these vesicles (size <200nm) (6).

In the following Sections, we will discuss details about the biogenesis, composition, and secretion of sEVs, as well as their roles in the prostate cancer microenvironment and the pre-metastatic niche. Furthermore, we will explore the interactions, internalisation, and fate of sEVs in recipient cells, as well as discuss their uptake kinetics and distribution in cell systems after their fluorescence labelling by organic dyes or genetically encoded fluorescent proteins.

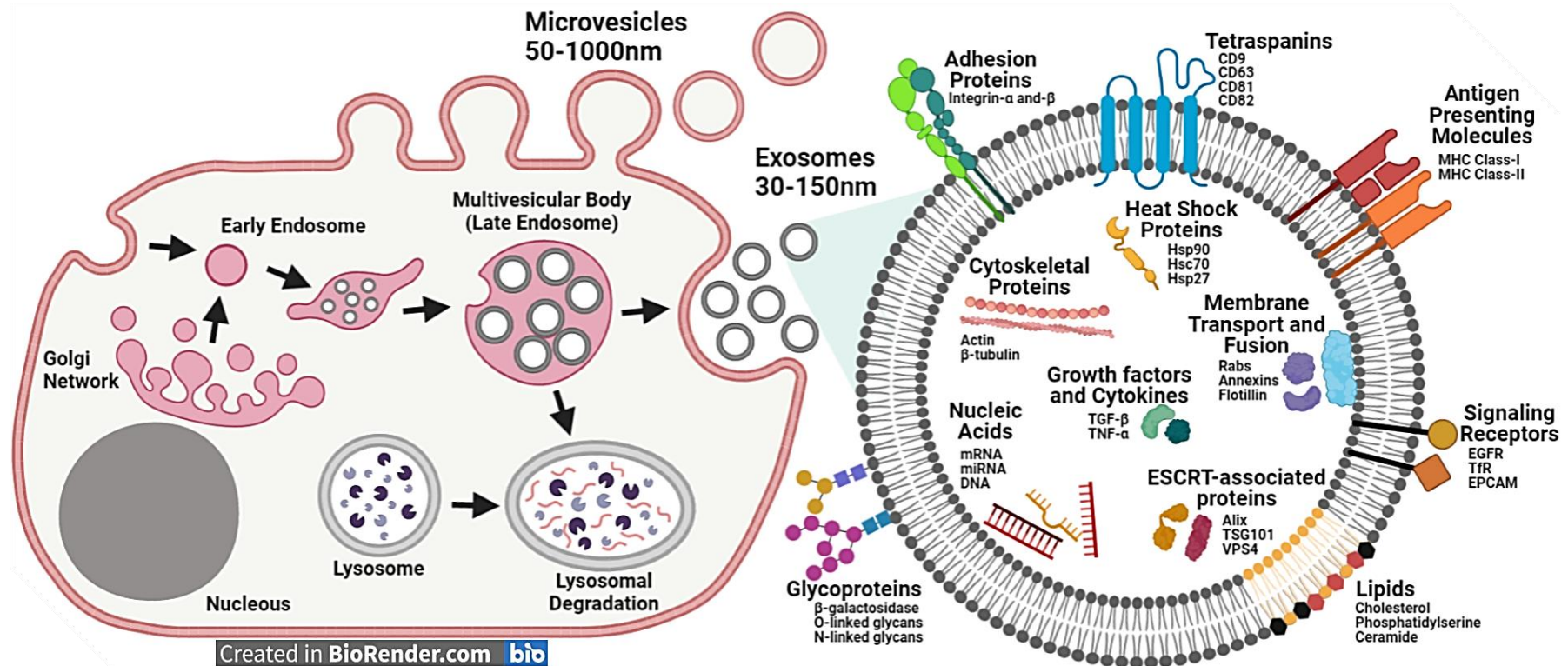


Figure 1.1. Overview of Extracellular Vesicle (EV) biogenesis and exosome composition.

EVs have been traditionally classified in two major classes: microvesicles (50nm-1 μ m) and exosomes (30-150nm). Microvesicles are generated by the outward budding and fission of the plasma membrane. Exosomes are produced in multivesicular bodies (MBVs), an intermediate during endosome maturation, and are subsequently released in the extracellular space when MBVs fuse with the plasma membrane. Typically, exosomes are lipid-bilayer vesicles containing various molecules like proteins (e.g., tetraspanins, antigen-presenting and adhesion molecules, signalling receptors, growth factors and cytokines, ESCRT(endosomal sorting complexes required for transport)-machinery, cytoskeletal and heat-shock proteins, glycoproteins, membrane fusion and transport proteins), nucleic acids (e.g., miRNAs, mRNA, DNA and other non-coding RNAs), and lipids (e.g., cholesterol, phosphatidylserine, phosphatidylcholine, ceramide etc).

Figure modified from "The exosome journey: from biogenesis to uptake and intracellular signalling" (Gurung et al., 2021)

1.2. sEV Biogenesis and Composition

1.2.1. sEV Biogenesis

sEVs (specifically “exosomes”) are intraluminal vesicles (ILV) which are generated by the inward budding of the early endosomal membrane into the lumen of the compartment, towards maturation into multivesicular bodies (MVB, late endosomes) (8). These MVBs can be either destined to lysosomes for cargo degradation, or fuse with the plasma membrane, thus secreting sEVs in the extracellular space (3, 4), as shown in [Figure 1.1](#).

The biogenesis of sEVs is rather complex, as it involves both ESCRT (Endosomal Sorting Complex Required for Transport)-dependent and ESCRT-independent machineries (9, 10). These machineries have been involved in clustering of cargo molecules (lipids and membrane-associated proteins) on the limiting membrane of MVBs, as well as in recruiting luminal molecules (luminal proteins and nucleic acids), followed by inward budding of the membrane, fission and release of the ILVs (sEVs) within the MVB lumen; these processes are presented in great depth in recent review articles (3, 4, 11).

1.2.1.1. ESCRT-Dependent Mechanisms

The main mechanism driving sEVs biogenesis is ESCRT-dependent, and includes 5 core complexes, which act sequentially namely ESCRT-0, -I, -II, -III and VPS4 (vacuolar protein sorting-associated protein 4) (9, 10). Firstly, ESCRT-0 localises on the limiting membrane of MVBs via its interaction with the endosome-enriched PI3P (phosphatidylinositol-3-phosphate), and then recognises, binds to, and clusters ubiquitinated cargo (e.g., lipids, membrane-associated and transmembrane proteins) which is present on the MVB membrane. Secondly, ESCRT-0 recruits ESCRT-I to MVBs from the cytoplasm by interacting with TSG101 (tumour susceptibility gene 101) on the ESCRT-I subunit, and promotes clustering with soluble cargo (e.g., cytosolic proteins and RNA). In turn ESCRT-I recruits ESCRT-II, and thirdly, the now three ESCRT complexes (ESCRT-0, -I, and -II) can interact with the ubiquitinated cargo and promote clustering, followed by inward budding around the clusters of these proteins (microdomains) in the MVB membrane. Finally, the ESCRT-III complex is recruited, and mediates cargo de-ubiquitination (via recruiting de-ubiquitinases), and performs budding

and fission of the microdomains into the lumen of the MVB (generating an ILV), followed by recruitment of VPS4, which then leads to the disassembly of ESCRT-III and termination of the MVB cargo sorting and ILV formation cycle ([Figure 1.2.a,b,e,f](#)). Notably, the ESCRT-III complex is required for the fission of ILVs and release into the MVB lumen, but the clustering of cargo and inward the budding of the MVB limiting membrane can also occur by ESCRT-independent mechanisms (9, 10).

1.2.1.2. ESCRT-Independent Mechanisms

Even though the ESCRT complex is the main machinery of sEV biogenesis, ESCRT-independent mechanisms were also reported, as sEVs loaded with tetraspanin CD63 (protein highly associated with sEVs, explained in greater detail in the next section), were successfully detected, despite the downregulation of subunits in the ESCRT complexes (0-III) (12). Further investigation of ESCRT-independent mechanisms demonstrated the involvement of complex lipids and other proteins interactions (3, 4, 13); examples are shown in [Figure 1.2.c-f](#). Firstly, protein–protein interactions between tetraspanins and the syndecan-syntenin complex promote the initial cargo sorting at microdomains on the limiting membrane of the MVB, followed by recruitment of Alix, which in turn associates with the ESCRT-III complex, to promote the inward budding of the MVB limiting membrane (14). This happens in conjunction with the generation of ceramide (a cone-shaped lipid) by sphingomyelinases, resulting in spontaneous negative curvature, thus contributing to the inward budding of the membrane (15).

1.2.2. sEV Secretion

Following the generation of ILVs in the MVB lumen, MVBs can either fuse with lysosomes for degradation, or be transported to the plasma membrane for fusion and secretion of ILVs to the extracellular space, which then become sEVs (i.e., “exosomes”). In both cases, MVBs are transported by the cytoskeleton (e.g., actin filaments and microtubules) via motor proteins (dynein, kinesins and myosins) and are regulated by Rab GTPases (16). Once transported to the membrane, RAB27A and RAB27B aid in the docking of the MVB to the membrane by rearranging the actin cytoskeleton (17), followed by fusion with the plasma membrane via SNARE (YKT6) proteins and synaptotagmins for release of sEVs to the extracellular space (13).

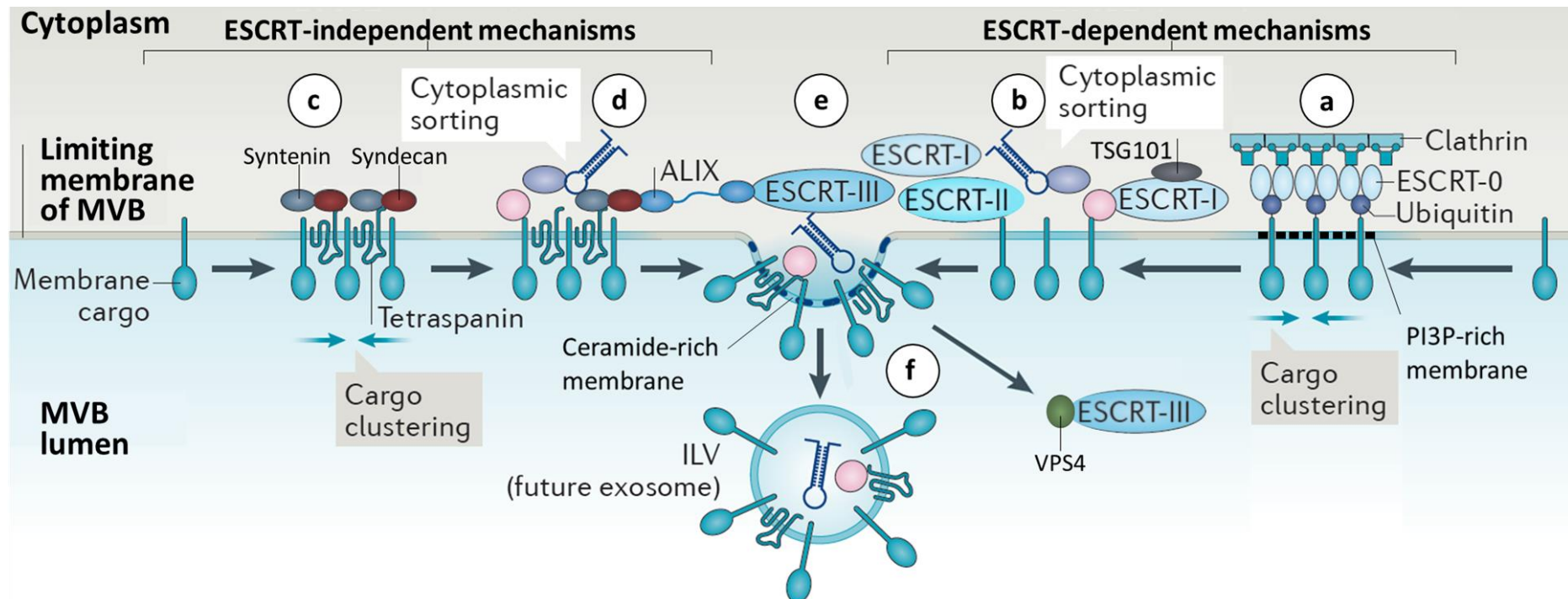


Figure 1.2. ESCRT- dependent and ESCRT-independent mechanisms of sEV biogenesis.

ESCRT- dependent mechanisms involve: **(a)** Recruitment of ESCRT-0 to PI3P microdomains in the limiting membrane of MVBs and clustering with ubiquitinated cargo (e.g., lipids, membrane-associated- and transmembrane- proteins) **(b)** Recruitment of ESCRT-I via binding to TSG101, followed by recruitment of ESCRT-II and further sequestration and clustering of soluble components (e.g., cytosolic proteins and RNA species). Alternative to this mechanism, ESCRT- independent mechanisms involve: **(c)** recruitment of syndecan and syntenin in tetraspanin-enriched microdomains followed by **(d)** recruitment of Alix which in turn associates with the ESCRT-III complex and along with ceramide (generated by sphingomyelinases) allows the inward budding of the MVB limiting membrane. The final step is common for both mechanisms and involves the **(e)** recruitment of ESCRT-III (via association with ESCRT-I-II) followed by inward budding and fission around the clusters of these proteins in the MVB membrane microdomains, leading to release of ILVs into the lumen with **(f)** VPS4 also recruited to ESCRT-III for its disassembly and termination of cargo sorting.

Figure adapted from "Shedding light on the cell biology of extracellular vesicles" (van Niel et al., 2018)

1.2.3. sEV Composition

Predictably, the composition of sEVs strongly reflects their biogenesis, as sEVs are composed of a plethora of proteins, lipids and nucleic acids, which are packaged during cargo sorting ([Figure 1.2](#)). The composition of sEVs has been thoroughly reviewed in the literature (3, 4, 8, 11, 18), and examples of cargo are shown in [Figure 1.1](#).

Briefly, sEVs contain proteins which can be transmembrane, membrane-associated, or luminal. Examples of these proteins are: (i) tetraspanins (e.g., CD9, CD63, CD37, CD81, CD82, CD53), (ii) adhesion-associated proteins (e.g., integrins- α and $-\beta$), (iii) antigen-presenting molecules like major histocompatibility complex (MHC) Class I and II (iv) signaling receptors (e.g., EGFR, EPCAM and Transferrin (TfR) receptors), (v) glycoproteins (e.g., β -galactosidase and O- and N-linked glycans), (vi) cytoskeletal proteins (e.g., actin and tubulin), (vii) ESCRT proteins (e.g., Alix and TSG101), (viii) growth factors and cytokines (e.g. TGF- β , TNF- α), (ix) heat-shock proteins (e.g., Hsp90, Hsc70), as well as (x) membrane transport and fusion- associated proteins (e.g., Rab GTPases, Annexins). Furthermore, sEVs carry a plethora of nucleic acids (e.g., DNA, mRNA, miRNA, ribosomal RNA (rRNA), transfer RNA (tRNA), long non-coding RNAs (lncRNA) etc.), as well as lipids (e.g. ceramide, sphingomyelin, cholesterol, phosphatidyl-serine and -choline) (3, 4, 8, 11, 18).

1.2.3.1. Focus on Tetraspanins: “Classic Exosome Markers”

Tetraspanins are hydrophobic proteins crossing the lipid bilayer membrane four times (hence their name) and are localised in the plasma membrane, in endosomal and lysosomal compartments (19-22). Tetraspanins form a protein superfamily with 4 subfamilies with 33 members in humans; CD63 is the sole member of the “CD63 subfamily” due to its more ancient origin, whereas the majority of other tetraspanins like CD9, CD37 CD81, CD82 and CD151 belong to the “CD subfamily” (21). Despite belonging to a protein superfamily, tetraspanins have relatively low sequence homology but exhibit highly-conserved secondary and tertiary structures, which include their four transmembrane domains (19, 20). These transmembrane domains are responsible for tetraspanin biosynthesis, function, and interactions with other tetraspanins, as well as contribute to the creation of two extracellular loops (EC1 and EC2) with conserved cysteine residues, two intra-cellular N- and C-terminal tails, and a cholesterol-binding pocket (23, 24).

Through these direct interactions of tetraspanins with themselves and other transmembrane or cytosolic proteins, as well as through indirect interactions with other proteins via common binding partners, tetraspanins have the ability to cluster with proteins at the cell membrane and become organised into the specialised tetraspanin-enriched microdomains (TEMs) (20, 22, 24). Some of these proteins include integrins (e.g., α - and β -integrins) antigen-presenting molecules (e.g., MHC-I and MHC-II), adhesion molecules (e.g., vinculin, talin, focal adhesion kinase), metalloproteinases (e.g., MT1-MMP), signalling receptors (e.g. EGFR, PI4K) and effectors (e.g. β -catenin, Cdc42, Rac etc.), as well as connect to the actin cytoskeleton through ezrin, radixin, and moesin (ERM) proteins; these and other examples have been comprehensively reviewed previously (19, 20, 22, 24).

Hence, through the TEMs, tetraspanins can exert a plethora of functions, including adhesion to extracellular matrix or other cells, cell migration, membrane fusion, regulation of signalling pathways, as well as protein and vesicle trafficking (20, 22, 24). Tetraspanins are involved in vesicle trafficking by ESCRT-independent mechanisms for sEV biogenesis and cargo sorting (as mentioned in the previous section), especially CD63 via its interactions with syntenin (22, 25), which might explain the presence of CD63-positive sEVs even in the absence of ESCRT complexes (12). Furthermore, studies reported that CD63 was essential for the biogenesis of lysosome-related organelles (25). On the other hand, knockdown of CD81 in lymphocytes did not affect sEV secretion several CD81 interacting protein partners were depleted from sEVs isolated from CD81-deficient lymphoblasts (22). Besides their involvement in sEV-biogenesis and cargo sorting, tetraspanins are also involved in sEV targeting and uptake to recipient cells, as well as antigen presentation (19, 22). Overall, tetraspanins are thought to be highly enriched in sEVs, as they exhibit a 7- to 124- fold enrichment compared to cells, with the most prevalent described as CD63 and CD81 (19, 21); these are currently considered “classical exosome markers” (26) and together with their interacting partners at the TEMs were reported to account for almost 50% of the protein cargo of sEVs (22).

1.3. sEV Roles in Prostate Cancer

Historically, one of the reasons considered behind sEV secretion, was to remove unneeded material from the cell, which was suggested by studies showing secreted vesicles (coined as “exosomes”) with transferrin receptors during reticulocyte maturation (27, 28). However, research in the next decade demonstrated that “exosomes” are actually functional and a means of cell-to-cell communication for activation of signalling pathways; a benchmark study in the field showed that exosomes derived from B lymphocytes can induce an antigen-specific MHC class II-restricted T-cell immune response (29). Further research for the next 30 years highlighted that sEVs are far from a “waste disposal” system, as they are fundamental mediators of cell-to-cell communication by delivering their cargo to recipient cells, in both physiological and pathological processes, including cancer (13). As there is a broad scope of sEV functions in a plethora of cancers, this next section will briefly explore the roles of cancer-derived sEVs in the context of prostate cancer (PCa), as our study focuses on PCa-derived sEV distribution in the PCa microenvironment.

1.3.1. PCa Microenvironment

It is currently established that PCa is not just a disease of the abnormally dividing epithelial prostate cells, but rather an imbalance in the complex interactions between the cancerous cells (including PCa stem cells) and components of the prostate microenvironment like the extracellular matrix (ECM) and various stromal cells like fibroblasts, cancer-associated fibroblasts (CAFs) or myofibroblasts, neuroendocrine cells, endothelial cells, pericytes, immune cells like T- and B- lymphocytes, dendritic cells, monocytes, natural killer (NK) cells, macrophages and mast cells, as well as bone-marrow derived mesenchymal stem cells (BM-MSCs) (30, 31); [Figure 1.3](#) shows a schematic with cell types involved in the PCa microenvironment.

Stromal cells can undergo a series of cellular changes and alterations and switch to secreting various factors such as chemokines, cytokines, matrix-degrading enzymes, and ECM, ultimately promoting cancer progression, pre-metastatic niche formation, invasion, metastasis, and drug resistance (30-32). For example, CAFs or myofibroblasts secrete various metabolites and cytokines, altering the composition of the ECM and leading to the formation of a “reactive stroma”, which promotes cancer progression, invasiveness, and angiogenesis (33, 34). In addition, endothelial cells, which, via

interactions with tumour cells, can promote an “angiogenic switch” by increasing pro-angiogenic factors such as VEGF (vascular endothelial growth factor), and lead to alterations in the ECM by formation of immature “leaky” blood vessels, as well as promote metastasis by suppression of the androgen receptor (AR) (30, 35). Furthermore, immune and inflammatory cells, can infiltrate the PCa microenvironment and produce various cytokines and chemokines to promote proliferation, inflammation and angiogenesis (36).

Finally, circulating BM-MSCs can also be recruited to the PCa tumour microenvironment (Figure 1.3); BM-MSCs are multipotent stem cells usually residing in the bone marrow, which can differentiate towards a chondrogenic, adipogenic or osteogenic lineage (37), and contribute to tissue homeostasis and wound healing (38, 39). Due to chronic inflammation in PCa tumours, BM-MSCs are recruited and can differentiate into CAFs or endothelial cells (38, 39). This differentiation to CAFs and endothelial cells promotes alterations in the ECM, leading to cancer cell migration and epithelial-to-mesenchymal transition (EMT), as well as stimulates PCa growth, angiogenesis, and metastasis (especially to the bone) (38, 39). Human PCa biopsies demonstrated that the BM-MSC population represented 0.01– 1.1% of the total tumour (37).

1.3.2. Roles of sEVs in the PCa microenvironment

Overall, PCa-derived sEVs are known to modulate the tumour microenvironment by transferring their cargo, thus promoting immune system suppression, tumour growth, stimulation of angiogenesis and metastasis, as well as drug resistance and formation of the “pre-metastatic niche” (40-43). [Figure 1.3](#) shows examples of the effects of PCa sEVs in the PCa microenvironment.

To begin with, PCa-derived sEVs were shown to perform immunosuppressive functions, thus aiding in immune evasion. For example, they were shown to express ligands that downregulate NKG2D on NK and CD8+ T-cells (NKG2D is a membrane receptor for activation of immune cells), thus impairing their activation and consequently their cytotoxic function (44). Moreover, PCa sEVs can induce apoptosis of CD8+ T-cells, by delivering the FasL (ligand) to the Fas receptor in T cells, which subsequently induces apoptosis either directly via the receptor CD95/APO1, or indirectly via dendritic cells (45).

In addition, it has been established that PCa sEVs can trigger fibroblast to myofibroblast differentiation through TGF- β (transforming growth factor beta) tethered to the vesicle membrane, which can then lead to activation of SMAD3-dependent or SMAD-

independent signalling and thus promote tumour growth (46, 47). Furthermore, this differentiation towards myofibroblasts by PCa sEVs carrying TGF- β stimulates angiogenesis by elevated secretion of pro-angiogenic factors within the tumour microenvironment, including VEGF, HGF (Hepatocyte Growth Factor), FGF-2 (Fibroblast Growth Factor), and uPA (urokinase-type Plasminogen Activator) (46, 47). Interestingly, PCa sEVs can also induce BM-MSC differentiation to myofibroblasts, with elevated secretion of VEGFA, HGF and MMP-1, MMP-3, and MMP-13 (MMP: Matrix Metalloproteinase), thus further supporting tumour progression and angiogenesis (48).

Besides TGF- β , PCa sEVs can transport miRNA (short noncoding RNAs that regulate gene expression) to stromal cells ultimately promoting angiogenesis and metastasis; for example miR-92a and miR-17-92 transfer in endothelial cells results in increased proliferation and migration, whereas transfer of miR-21, miR-100 and miR-139 in fibroblasts results in increased migration and expression of pro-metastatic factors MMP-2, MMP-9, MMP-13 and RANKL (49).

Interestingly, a “horizontal transfer” of PCa sEV cargo towards normal prostate cells or other PCa cells in the tumour microenvironment has been recently suggested, and is thought to promote cancer progression and drug resistance (50). A recent study delivered PCa sEVs derived from a DU145 cell line resistant to docetaxel to parental DU145 cells, as well as other PCa cell lines (LNCaP and 22Rv1) and observed that recipient cells ultimately developed chemoresistance to docetaxel (51). Another study also demonstrated that sEVs isolated from PCa patients promoted cell migration, proliferation, and cancer progression in the normal epithelial prostate cell lines (RWPE-1 and PNT-2), when compared to sEVs from healthy individuals, or patients with benign prostate hyperplasia (52).

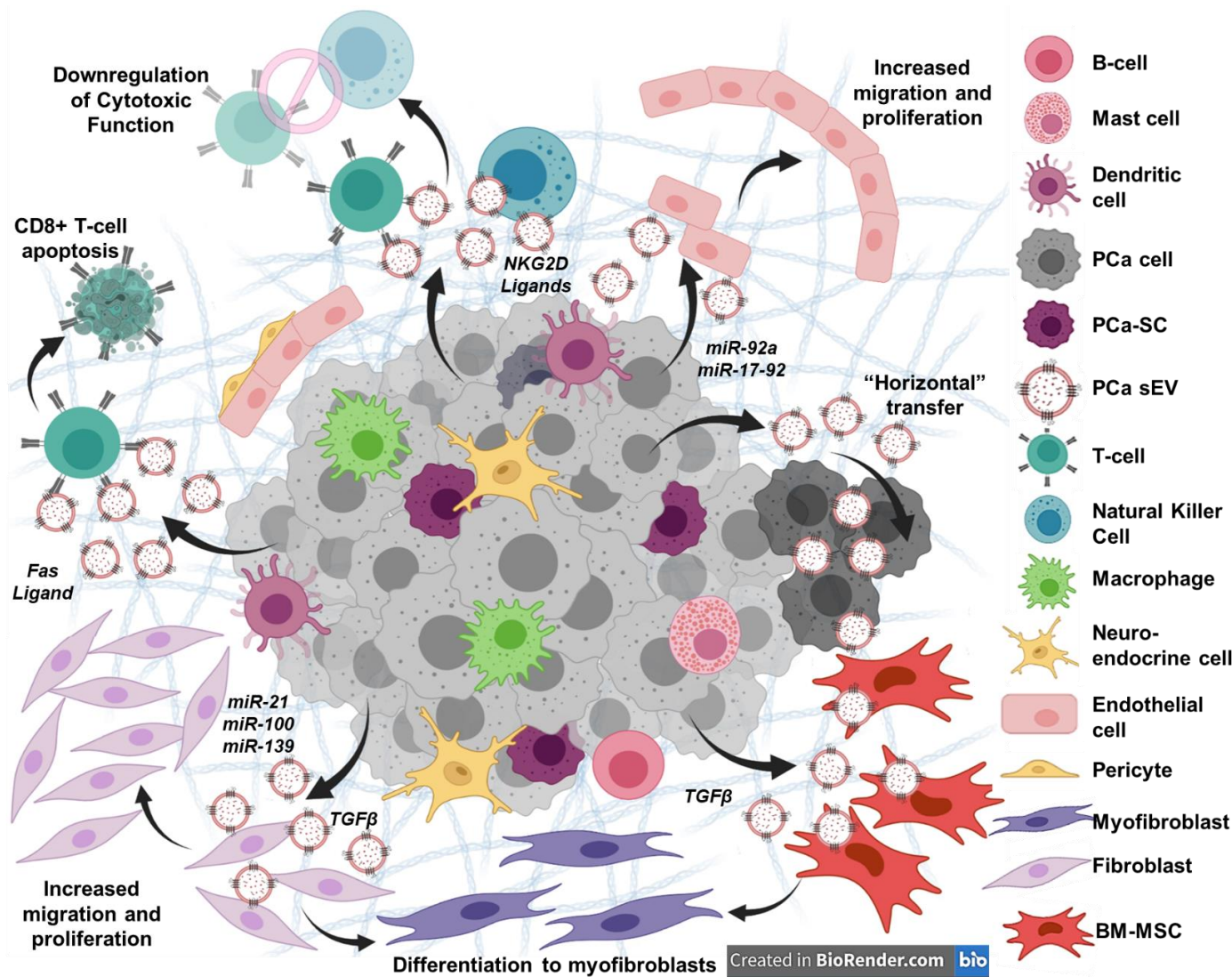


Figure 1.3. The PCa microenvironment and role of sEVs.

The PCa microenvironment encompasses PCa epithelial cells and interactions with stromal cells like fibroblasts, myfibroblasts, neuroendocrine cells, endothelial cells, pericytes, immune cells like T- and B- lymphocytes, dendritic, natural killer, mast cells, and macrophages, as well as circulating bone-marrow derived mesenchymal stem cells (BM-MSCs). PCa sEVs perform various functions in the microenvironment, contributing to the promotion of cancer progression, angiogenesis, and metastasis. PCa sEVs can suppress the immune system, by downregulating their cytotoxic function or inducing apoptosis. They can also promote fibroblast and BM-MSC differentiation to myfibroblasts via TGF-β, as well as promote endothelial cell- and fibroblast- migration/proliferation via delivery of various miRNAs. Besides effects of sEVs on tumour stroma, PCa sEVs can directly affect other PCa cells via “horizontal transfer”, a mechanism providing chemoresistance and further promoting cancer progression.

1.3.3. Pre-Metastatic Niche and Role of PCa sEVs

Beyond the primary tumour, PCa cells secrete sEVs that appear to generate a favourable and supportive environment for the survival and growth of the tumour in a secondary site; this pre-conditioned microenvironment is generated prior to establishment of metastasis and is termed the “pre-metastatic niche” (53-56). PCa exhibits metastatic tropism to the bone, as more than 90% of PCa patients develop bone metastasis (57). Metastatic PCa is characterised by alteration of the balance between the bone-resorbing osteoclasts and the bone-forming osteoblasts, to generate a favourable tumour-supportive environment, which results in the formation of predominantly osteoblastic or osteolytic lesions. Osteoblastic lesions are characterized by increased deposition of low-quality bone tissue around tumour sites, and osteolytic lesions by increased depletion and resorption of bone tissue; these lesions are associated with deregulation of osteoblast and osteoclast activities, respectively (54, 55). The dynamic between PCa cells and bone cells disrupting normal bone homeostasis and promoting cancer progression has been established as the “vicious cycle” (54, 55).

PCa sEVs participate in this “vicious cycle” by affecting resident bone cells (including osteoblasts, osteoclasts and BM-MSCs), thus promoting the formation of this pre-metastatic bone niche (53-56). For example, a study using sEVs derived from PC3 PCa cells, demonstrated an increase in osteoblast viability, as well as improved growth for PCa cells when cultured with the sEV-treated osteoblasts (58). A different study showed that transfer of the miR-141-3p non-coding RNA by sEVs isolated from MDA PCa 2b cells promoted osteoblast activity and increased osteoprotegerin expression; the underlying mechanism was the suppression of the DLC1 gene (protein involved in the regulation of Rho GTPases), thus activating the p38MAPK pathway and ultimately increasing osteoblast proliferation, calcium deposition and expression of osteoblastic differentiation markers (59).

On the other hand, the effect of PCa- derived sEVs on osteoclasts are contradicting in the literature. For example, a study using murine PCa sEVs from the TRAMP-C1 cell line, demonstrated a significant decrease in the fusion and differentiation of monocytic osteoclast precursors to mature osteoclasts in the presence of sEVs, with simultaneous decrease in expression of relevant osteoclastic markers like the transmembrane AMPAR regulatory proteins, cathepsin K and MMP-9; the authors suggested that this agreed with the osteoblastic nature of PCa bone metastases (60). Furthermore, a study using human PCa-derived PC3 sEVs showed an increase in Cavin-1 expression, which resulted in reduced uptake of these sEVs by osteoclast progenitors (RAW264.7 cells) and primary

human osteoblasts, as well as attenuated sEV-mediated osteoclastogenesis and osteoblast proliferation, potentially by affecting cargo recruitment to sEVs (61). Conversely, a study using sEVs from the same PCa cell line identified high expression of the miR-152-3p miRNA, and showed that sEV-mediated delivery of this miRNA in bone-marrow derived macrophages promoted osteoclastogenesis by silencing the osteoclastogenic regulator MAFB (V-maf musculoaponeurotic fibrosarcoma oncogene homolog B), which in turn promoted the increase of tumour burden and osteolytic progression of PCa bone metastasis (62).

Besides the direct effects of PCa sEVs on the osteoblast-osteoclast balance at the bone pre-metastatic niche, emerging evidence also suggest effects of PCa sEVs on the BM-MSCs at this site, even though this is still greatly unexplored (63, 64). BM-MSCs are considered the main progenitor for osteoblast production *in vivo*, as they become differentiated towards an osteoblastic lineage at the bone marrow (65). Previously, it has been shown that metastatic PCa promotes the differentiation of BM-MSCs towards osteoblasts at the bone, which indirectly supports the formation of the favourable osteoblastic bone metastatic niche (63). Specifically, it has been shown that PCa PC3 cells secrete “soluble factors” in their cell-conditioned media which result in an increased expression of pro-osteoblastic markers in BM-MSCs (α_5/β_1 integrins, fibronectin, and osteoprotegerin), thus committing them towards an osteoblastic lineage (63). A more recent study showed a novel direct mechanism of PCa sEVs promoting the formation of the pre-metastatic bone niche; PCa-derived C4-2B sEVs were shown to transfer pyruvate kinase M2 (PKM2) into BM-MSCs, resulting to upregulation of CXCL12 (C-X-C motif chemokine ligand 12), and ultimately promoting PCa adhesion and growth at the metastatic bone niche (64). A different study identified a highly expressed non-coding RNA (hsa-miR-940 miRNA) in sEVs derived from human PCa cell lines (C4, C4-2, and C4-2B), and then proceeded to show that delivery of these sEVs in BM-MSCs lead to downregulation of transcription and protein expression of ARHGAP1 and FAM134A, which eventually increased the expression of ALP (alkaline phosphatase), thus denoting the onset of osteoblastic differentiation of BM-MSCs (66). [Figure 1.4](#) shows a schematic summarising the role of sEVs in the formation of the pre-metastatic bone niche.

Despite the ongoing interest of the field in understanding the molecular mechanisms behind PCa-derived sEVs promoting the formation of the pre-metastatic niche, it still remains to be elucidated how sEVs disseminate through the tumour microenvironment (tumour cells, stroma, ECM, basement membranes) to reach the pre-metastatic niche and eventually be detected into the biofluids of patients (67, 68).

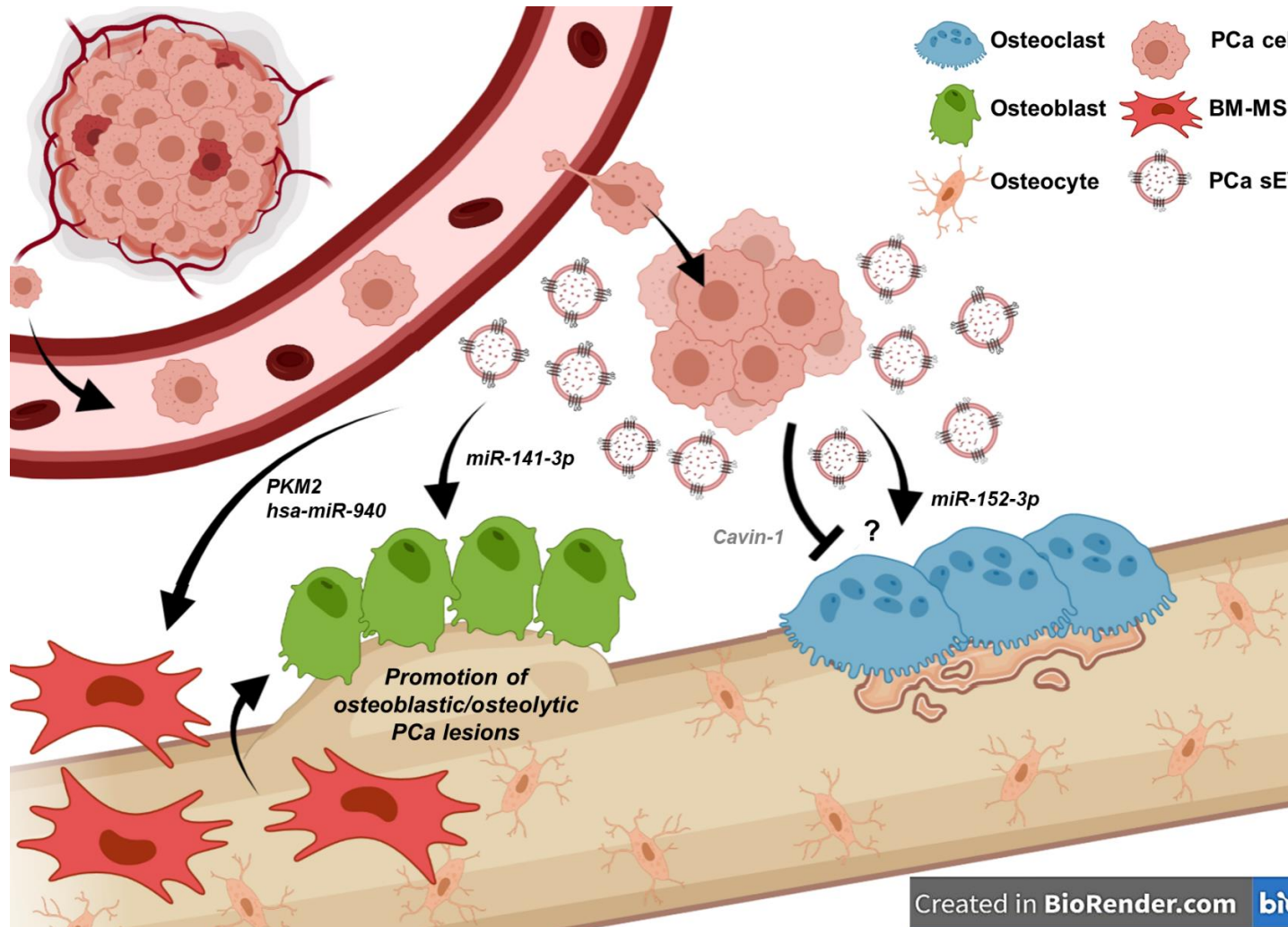


Figure 1.4. Role of PCa sEVs in pre-metastatic bone niche formation.

sEVs from circulating PCa cells support the formation of the pre-metastatic niche by promoting a supportive environment for the prostate tumour to metastasize from the primary site by disrupting the normal bone homeostasis between osteoclasts and osteoblasts. PCa-derived sEVs can deliver cargo to upregulate the function, proliferation, or differentiation of osteoblasts (e.g., via miR-141-3p), and osteoclasts (e.g., via miR-152-3p). However, PCa sEVs can also be regulated by cavin-1 to attenuate osteoclastogenesis. PCa sEVs also deliver cargo to BM-MSCs (e.g., pyruvate kinase M2 PKM2, and non-coding RNA hsa-miR-90) which promotes their differentiation into osteoblasts, further aiding the formation of a pre-metastatic supportive environment for PCa metastasis.

1.4. sEV Interaction, Internalisation and Fate in Cells

Even though research concerning biogenesis, composition, and the multitude of functions of sEVs in the tumour microenvironment has been quite extensive, studies have just started to focus on the mechanisms of sEV internalisation, and sEV fate and distribution in recipient cells within tissues. Overall, sEV-mediated communication starts by docking of sEVs at the cell surface, followed by delivery of signals or cargo either by interactions at the cell surface e.g., by directly binding to receptors or by fusing with the cell membrane, or by internalisation by the recipient cell e.g., via clathrin-dependent or-independent mechanisms (69, 70).

1.4.1. sEV Direct Interactions at the Cell Membrane

1.4.1.1. Surface Binding

After docking of sEVs at the cell surface, sEVs can bind and activate various receptors through their ligands leading to activation of downstream signalling pathways, enable antigen presentation and anchorage-independent growth, as well as modulate apoptosis, as shown in [Figure 1.5.A](#). This direct interaction of sEVs with the cell surface is proposed to be target cell- specific, depending on the repertoire of receptors or ligands on sEVs and recipient cells, including heparan sulfate proteoglycans (HSPGs), lectins, tetraspanins, integrins, and ECM components (69, 70). Tetraspanins can promote sEV binding at the cell surface and uptake via their interactions with cellular integrins (71, 72). In addition, ECM components on sEVs like fibronectin can interact with integrins at the cell surface to promote binding (73). It is also hypothesised that cancer sEVs from various tissues can preferentially bind to specific target cells at the metastatic sites via various sEV-associated integrins, thus promoting the formation of the pre-metastatic niche specifically at these sites (74), even though this is still poorly understood (75).

1.4.1.2. Cell Membrane Fusion

A second proposed mechanism of sEV interaction is by direct fusion with the plasma membrane, even though this is still poorly understood and previously reported for IEVs (e.g., glioma IEVs transferring the oncogenic receptor EGFRvIII (76)). It has been suggested that the hydrophobic lipid bilayers of sEVs can fuse with the plasma membrane and expand, thus forming an integrated structure; regulation of this process is done by various proteins like SNAREs, Rab5B, and Sec1/Munc-18 related proteins,

and it leads to release of sEV cargo in the cytosol (69, 70), as shown in [Figure 1.5.B](#). Fusion of sEVs with the membrane is thought to be promoted by acidic microenvironments, which are commonly observed in cancer (77). A study has shown that sEVs can be at least partly taken up by fusion in target cells, as when using filipin, (an inhibitor which perturbs the composition of cell membranes via associating with cholesterol) the direct fusion of sEVs was inhibited by half (77).

1.4.2. sEV Internalisation by Recipient Cells

Besides membrane interactions, sEVs are most commonly internalised in recipient cells via endocytosis, which can be mediated via various mechanisms including: (a) clathrin-mediated endocytosis, (b) caveolin-dependent endocytosis, (c) phagocytosis, (d) micropinocytosis, and (e) lipid-raft mediated endocytosis, which are not mutually exclusive (69, 70).

1.4.2.1. Clathrin- and Caveolin-Mediated Endocytosis

Clathrin-mediated endocytosis involves the progressive assembly of clathrin-coated vesicles by the complex interactions of various molecules (e.g., the adaptor protein AP2 complex and phosphatidylinositol 4,5-bisphosphate (PI(4,5)P₂), etc.) which is followed by invagination of the plasma membrane, maturation, fission, and release of the clathrin-coated vesicle into the cytosol (78). Previous studies demonstrated that chlorpromazine, (a clathrin-mediated endocytosis inhibitor) reduced the internalisation of SKOV3- derived sEVs in SKOV3 ovarian cancer cells (79), as well as of the PC12 (rat pheochromocytoma) sEVs in BM-MSCs (80), suggesting that this mechanism of endocytosis is at least partly responsible for sEV internalisation. After internalisation, the clathrin-coated vesicle coat then becomes disassembled (either by chaperones like HSC70 or by dephosphorylation of PI(4,5)P₂) and then the vesicle fuses with endosomes for cargo delivery (78), as shown in [Figure 1.5.C](#).

Internalisation of sEVs has also been suggested to be mediated by caveolin-dependent endocytosis (81). This mechanism of endocytosis involves oligomerisation of caveolin proteins (e.g., caveolin-1), followed by formation of caveolin-rich glycolipid rafts on the plasma membrane, which also encompass cholesterol and sphingolipids; this eventually leads to actin cytoskeleton remodelling and the formation of small invaginations on the membrane (caveolae) which are then endocytosed as vesicles and targeted to endosomes for cargo release (81, 82), as shown in [Figure 1.5.D](#). This aspect

of sEV endocytosis however still lacks consensus due to contradicting studies. For example, a study on sEVs derived from B-lymphocytes demonstrated that their internalisation by caveolae-dependent endocytosis was severely impaired after caveolin-1 knockdown (83). On the other hand, knockout of this protein in mouse embryonic fibroblasts lead to an increase in U87MG glioma sEV internalisation (84).

1.4.2.2. Phagocytosis, Macropinocytosis and Lipid-Raft Mediated Endocytosis

Phagocytosis is a process often executed by immune cells (e.g., macrophages or dendritic cells) and typically involves the internalisation of opsonised large particles (e.g., bacteria or cell debris) (85). It is a stepwise process dependent on the actin cytoskeleton, on Phosphatidylinositol-3-kinase (PI3K) and phospholipase C (PLC), and involves the formation of membrane deformations, leading to invagination and encirclement of particles thus forming the phagosomes, which are then internalised and targeted to endosomes or lysosomes (85). Recently, it was shown that macrophages and dendritic cells can internalise smaller vesicles like sEVs via phagocytosis (86) ([Figure 1.5.E](#)).

Alternative to phagocytosis, macropinocytosis is an endocytic pathway that involves formation of “membrane ruffles”, which are lamellipodia that can extend from the plasma membrane and engulf particles, extracellular fluid, and other components; this is followed by “ruffle closure” via membrane re-fusion, and subsequent release of the mature macropinosome in the cytosol targeting to the endo-lysosomal compartments ([Figure 1.5.F](#)). Similar to phagocytosis, macropinocytosis requires actin cytoskeleton remodelling and is dependent on PI3K and growth factors (87). Previous studies demonstrated uptake of oligodendrocyte-derived sEVs by macropinocytosis in microglia and macrophages, which was dependent on the phosphatidylserine cargo on sEVs (88). Another study using PC12-derived sEVs, demonstrated reduction in sEV internalisation by BM-MSCs when using macropinocytosis inhibitors (EIPA and LY294002) (80).

Finally, lipid raft-mediated endocytosis is another possible mechanism of sEV internalisation. Lipid rafts are microdomains within the plasma membrane enriched in phospholipids, sphingolipids, glycoproteins, as well as glycosylphosphatidylinositol (GPI)-anchored proteins (89). Lipid raft-mediated endocytosis is a cholesterol-sensitive mechanism, associated with caveolin-1 and flotillin, and involves invagination of the membrane for internalisation of particles and delivery to endosomes (89) ([Figure 1.5.G](#)). A previous study demonstrated successful internalisation of sEVs in the H4 neuroglioma cell line, despite the use of inhibitors for macropinocytosis, caveolin-dependent and clathrin-dependent endocytosis, suggesting endocytosis via lipid rafts (90).

1.4.3. sEV Fate

Despite some advances in sEV internalisation, knowledge on sEV fate in recipient cells is still lacking. It has been proposed that after uptake of sEVs via all these different mechanisms, sEVs can be then trafficked to early endosomes and then can be targeted to lysosomes presumably for degradation (91). Another proposed mechanism, is that sEVs can persist in early endosomes and be secreted back to the membrane directly, or remain until they mature to late endosomes (MVBs) and then trafficked back to the plasma membrane for re-secretion (92). Other proposed mechanisms, which are albeit less understood, are sEVs exhibiting “back-fusion” i.e., fusion directly with the limiting membrane of MVBs, followed by secretion of their cargo into the cytosol (93), or sEVs being targeted to the nucleoplasmic reticulum, incorporated in late endosomes (94). [Figure 1.5.H](#) summarises the various proposed mechanisms for fate of sEVs in recipient cells after internalisation.

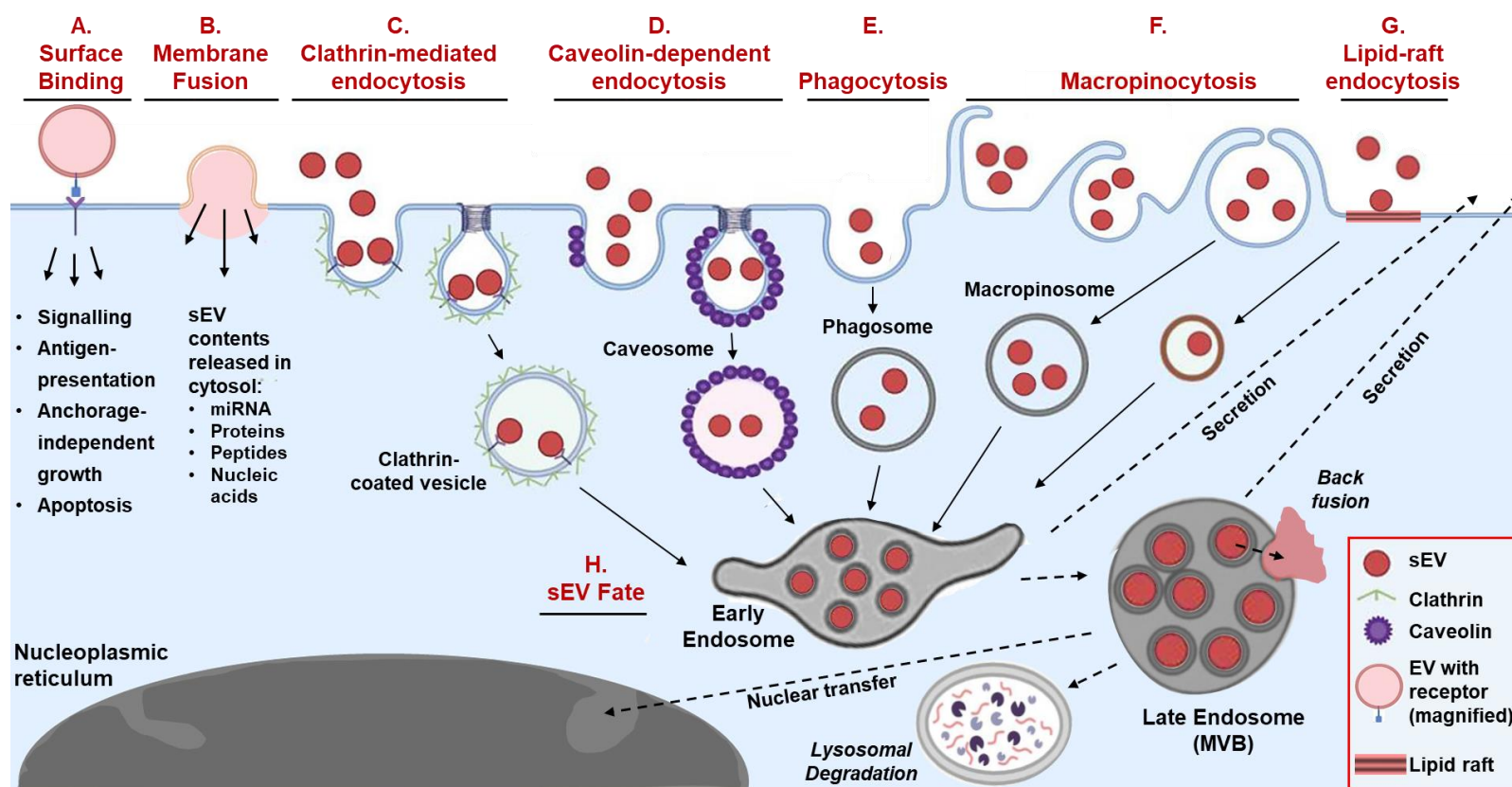


Figure 1.5. sEV interactions, internalisation, and fate in recipient cells.

sEVs interact with cells directly either by **A.** Surface binding (e.g., with integrins or tetraspanins), or by **B.** Membrane fusion (e.g., with SNAREs), resulting to activation of signalling cascades or secretion of sEV content into the cytosol, respectively. sEVs may also be internalised by **C.** clathrin-mediated endocytosis, **D.** caveolin-dependent endocytosis, **E.** phagocytosis, **F.** macropinocytosis or **G.** lipid raft-mediated endocytosis, which result in specialised vesicles transporting internalised sEVs to the endosomal pathway. **H.** Internalised sEVs are delivered to early endosomes, and then can either be secreted directly to the plasma membrane, or reach late endosomes (MVBs), which can then be fused with lysosomes for degradation, or secreted to the plasma membrane mixed with ILVs. Recent studies also suggested that in MVBs, internalised sEVs can exhibit back-fusion with the membrane of the MVB and secrete their contents in the cytosol, or that MVBs with internalised sEVs can even be transferred to the nucleoplasmic reticulum in the nucleus.

Figure adapted from "The exosome journey: from biogenesis to uptake and intracellular signalling" (Gurung et al., 2021)

1.5. sEV Kinetics and Distribution in Cell Systems

Even though the important functions of sEVs in cancer have been extensively studied, and the precise mechanisms of interaction, internalisation, and fate of sEVs in cells have just now started to be investigated (as discussed above), the kinetics of sEV uptake (dosing) and distribution at the cell population- or tissue-level, either at the tumour microenvironment or at the pre-metastatic niche, have been unexplored. Moving from single-cell to cell-population level for investigation of sEV uptake, distribution and dissemination in tissue microenvironments is essential however, especially due to the rising clinical interest in sEVs as diagnostic, prognostic, and therapeutic tools (95, 96).

1.5.1. Clinical Interest

The presence of cancer-derived sEVs in the biofluids of patients supports their dissemination in tissue microenvironments and highlights their potential as disease biomarkers; their repertoire of cargo including RNAs (e.g., mRNAs and miRNAs), DNA, proteins and lipids, have been extensively studied for their potential as biomarkers in various cancers (95, 96), including PCa (97). Notable examples include the identification of sEVs carrying a mutated EGF-receptor in the urine of patients with glioblastoma (98) and sEVs highly enriched in TM256 and LAMTOR1 in the urine of PCa patients (99). These studies underline that sEVs can migrate from the primary tumour site like the brain, through the blood-brain barrier (BBB) and into the circulation, or through the renal filtration barrier to enter the urinary compartment; however, the mechanisms behind their dissemination through cells, tissues and ECM still remains largely unexplored. Besides their use as biomarkers, sEVs have therapeutic potential as gene and drug delivery vectors (95, 96). sEVs are desirable drug delivery vehicles due to their biocompatibility, high stability, low immunogenicity, their capability to be loaded endogenously or exogenously with selected cargo, and most importantly due to their inherent ability to disseminate through tissue microenvironments, even across biological barriers like the BBB, and transfer their cargo into target cells, which can also be highly specific (95, 96).

Thus, elucidating the mechanisms behind sEV dosing and dispersion in cell populations, tissues, and the ECM, is of vital importance for the development of biomarkers, as well as for the design of superior sEV-based therapeutics with selective targeting and dissemination in the tissues of interest.

1.5.2. Fluorescent sEV Reporters for Dosing and Distribution in Cell Systems

To begin to address sEV dissemination in complex three-dimensional tissues, the kinetics of uptake (dosing) and behaviour of sEVs must be first investigated in simpler, two-dimensional dynamic cell systems. Thus, for the visualisation, tracking and spatiotemporal analysis of sEVs *in situ*, high-resolution microscopy is necessary. However, due to the small diffraction-limited sub-resolution size of sEVs, direct imaging with optical microscopy is restricted, hence several labelling methods have been developed to enable for the detection and tracking of sEVs *in vitro* and *in vivo*, including fluorescence labelling for conventional fluorescence microscopy (100).

sEV fluorescence labelling methods can be broadly categorised into exogenous, for labelling with organic dyes like lipophilic dyes, membrane-permeable compounds, and thiol-based dyes, as well as endogenous, for labelling with genetically encoded fluorescent reporters; examples will be discussed below and are outlined in [Figure 1.6](#). Furthermore, relevant studies addressing sEV kinetics, dosing, retention, and distribution in cell systems will be also briefly discussed for each labelling method, followed by a summary of advantages and limitations for each approach ([Table 1.1](#)).

1.5.2.1. Exogenous labelling: Organic Dyes

Lipophilic Dyes

By far the most common method to label sEVs is fluorescent lipophilic membrane dyes which incorporate non-covalently into the sEV lipid-bilayer membrane ([Figure 1.6.A](#)). Examples of lipophilic dyes used for sEV labelling include PKH26, PKH67, the carbocyanine dyes Dil, DiD, DiO and CellMask (100-103).

Unfortunately, despite their commercial availability, long-lasting fluorescence and ease of use, there are many limitations to using lipophilic dyes, due to their inherent ability to incorporate into lipid bilayers ([Table 1.1](#)) (100). These dyes are not specific to sEV membranes, as they have been found to label other EV co-isolates like lipoproteins, including very low-density-, low-density-, and high-density lipoproteins (102, 103). Furthermore, it has been postulated that binding of these dyes can induce structural modifications to sEVs, for example labelling with PKH26, Dil or DiD resulted in an increase in sEV size (104, 105); this might lead to changes in their uptake dynamics or function, as it was previously shown that uptake of larger EVs is decreased compared to

smaller EVs (106). In addition, these dyes have been found to form aggregates or micelles of similar size to sEVs, resulting in misleading false positive signals and a gross overestimation of sEV entry (101, 107). Furthermore, they were shown to persist for long periods of time (longer half-life than sEVs *in vivo*), resulting in artefacts and leading to misinterpretation of sEV kinetics (100, 108).

In a relevant sEV kinetics study, the authors labelled PC12 sEVs with DiD and showed a time-dependent uptake in parental cells (increase of DiD signal), detected as early as 5 minutes for ~5% of cells, whereas by 3 hours the signal was perinuclear and co-localised with endosomes. The authors also investigated sEV retention, and showed progressive loss of signal from the cell population, even though at 6 hours post-uptake they observed DiD signal recycling back to the plasma membrane, which was unclear whether it was due to lipid recycling (lipid-dye separation from sEVs), or sEVs transporting back for secretion (91).

A different study using LNCaP and PC-3 PCa cell lines, RC92a/hTERT telomerase immortalised malignant primary prostate cells and benign immortalised prostate epithelial PNT2 cells, also showed a time-dependent increase in the uptake of DiI-labelled sEVs in each cell population. Furthermore, after 16 hours of continuous exposure to sEVs, the majority of DiI signal was endo-lysosomal even though ~5% of the fluorescent signal co-localised with the plasma membrane. Due to the nature of the dye however, it was uncertain whether after 16 hours that signal was still sEV-associated (i.e., representing sEVs or sEV cargo), or represented artefacts from “leakiness” of the dye to these compartments (109).

Membrane-Permeable Compounds

Membrane-permeable compounds are also used for labelling of sEVs and include carboxyfluorescein succinimidyl ester (CFSE), carboxyfluorescein succinimidyl diacetate (CFDA) (79, 107) and calcein AM (acetoxymethyl) (110) ([Figure 1.6.B](#)). These molecules are membrane-permeant and non-fluorescent until they become activated upon hydrolysis of their acetoxymethyl ester moieties by intra-vesicular esterases, at which point they become fluorescent and relatively membrane-impermeant (110). Even though these compounds are less “problematic” than the lipophilic dyes, there are still limitations for their use, which include a higher fluorescence background resulting from free compounds that spontaneously hydrolyse (CFSE and CFDA) ([Table 1.1](#)). These free compounds can then bind/incorporate into other non-specific compartments such as cell membranes, unless carefully removed by size-exclusion chromatography (107). A previous study utilising these dyes has shown a time-dependent uptake of SKOV3-

derived sEVs labelled with CFSE in parental cells, with detectable fluorescence signal as early as 30 minutes, which then increased up to 4 hours (79). Two other studies on PC12- derived sEVs utilised CFSE staining as a control for the potential diffusion of DiD lipophilic dyes and demonstrated the uptake of sEVs in parental cells after 3 and 6 hours, respectively, with localisation of the fluorescent signal at the endo-lysosomal compartment (80, 111). Another type of membrane-permeable compound is the SYTO™ RNASelect™ dye, which selectively binds to RNA, and has been previously utilised to quantify the uptake of sEVs in various cell types, including monocytes and dendritic cells (112, 113). However, a previous study labelling DU145 PCa-derived sEVs with the SYTO™ RNASelect™ dye, showed dye “escape” within one hour of sEV uptake in lung fibroblasts (114).

Thiol-Based Dyes

A novel method of sEV labelling established in the Tissue MicroEnvironment Group, involves the thiol-based Alexa Fluor-conjugated maleimide dyes (e.g., Alexa Fluor647-C₂ maleimide, Alexa Fluor594-C₅ maleimide). These dyes covalently bind through their thiol (sulph-hydryl, -S-H) groups to cysteines of sEV-associated transmembrane proteins, forming a stable, non-reversible, thio-ether linkage ([Figure 1.6.C](#)). The maleimide-dye labelling reportedly does not influence sEV size or functionality (ability of sEVs to induce differentiation of lung fibroblasts to myofibroblasts) and is free of artefacts (no free dye or dye aggregates detectable by Nanoparticle Tracking Analysis) (115). A study on DU145 sEVs labelled with the Alexa Fluor488-maleimide dye showed a time-dependent uptake of sEVs in the HeLa cell population (increase in fluorescence from 30 minutes to 2 hours), and a noticeable shift from cytosolic to perinuclear punctate fluorescent signal, indicative of endosomes/lysosomes (115). Another study from our laboratory also demonstrated a time-dependent and dose-dependent uptake of DU145 sEVs labelled with the Alexa Fluor488-maleimide dye in lung fibroblasts, with detectable fluorescent signal as early as 15 minutes, and punctate perinuclear endo-lysosomal localisation after 1 hour (114). Despite the advantages and practical uses of this dye, its limitation is the potential “bleeding” into other non-specific compartments after long incubation periods ([Table 1.1](#)). For example, in this previous study, 72 hours post- sEV uptake in lung fibroblasts, the distinct punctate fluorescent perinuclear signal was lost and replaced by a cytosolic diffused staining pattern, potentially suggesting decoupling of dye from sEVs and loss of signal specificity (114).

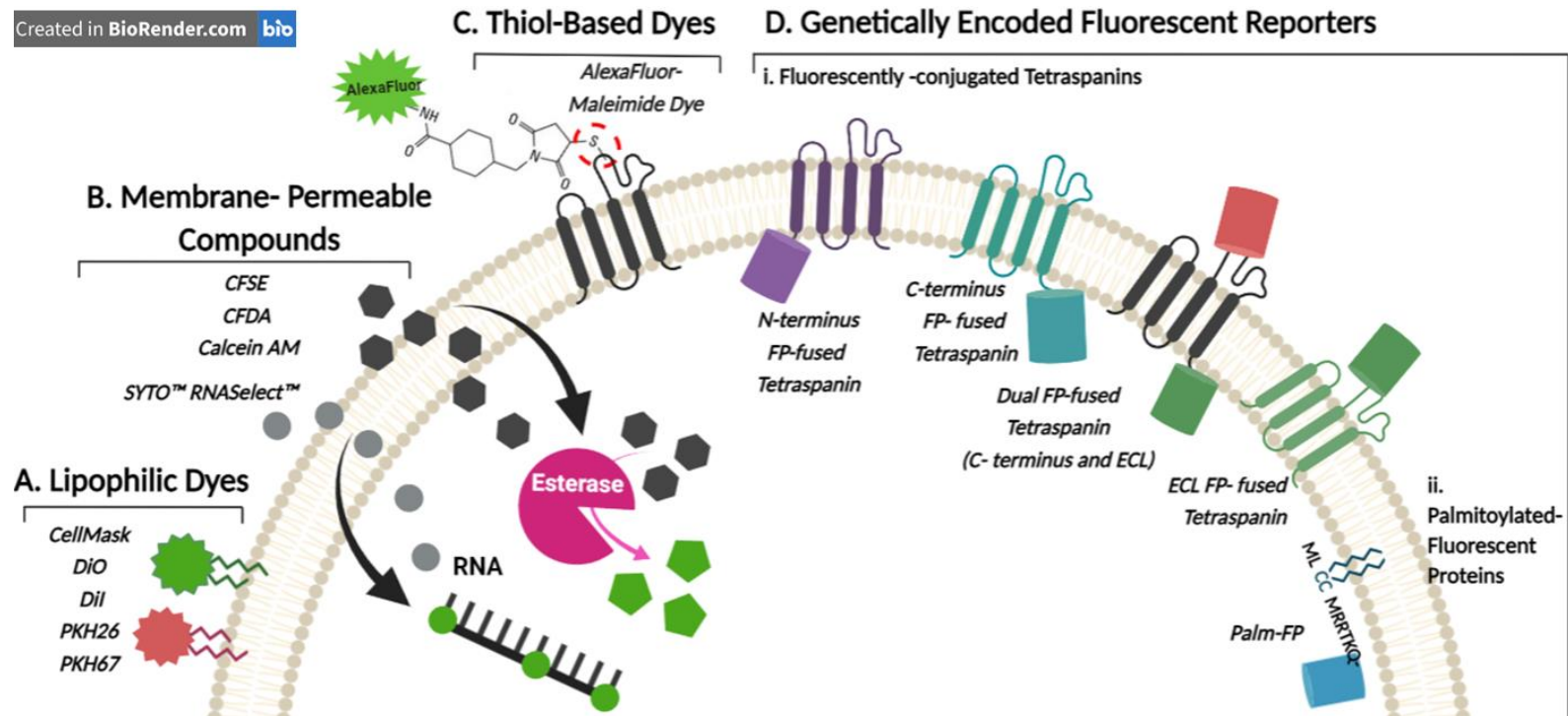


Figure 1.6. Common methods of sEV fluorescent labelling.

A-C. Purified sEVs can be labelled exogenously with fluorescent organic dyes: **A.** Lipophilic dyes (e.g., CellMask, DiO, DiI, PKH26, PKH67) comprise of an organic fluorescent "head group" and long aliphatic "tail" that incorporates non-covalently into the sEV lipid bilayer. **B.** Membrane-permeable compounds can passively enter sEVs, like CFSE, CFDA and Calcein AM, where esterase enzymes hydrolyze and remove the acetate groups, converting the molecule to a fluorescent membrane-impermeant ester; SYTO™ RNaselect™ also passively enters sEVs and binds to RNA (not DNA) resulting to fluorescence emission. **C.** Thiol-based dyes (e.g., maleimide group conjugated with the AlexaFluor organic fluorophores) can covalently bind to cysteines of proteins on the sEV surface, forming a sulfhydryl bond (red circle). **D.** Genetically encoded endogenously fluorescent sEV reporters can be generated by stable cell lines expressing: **(i)** tetraspanins (CD63, CD81, CD9) -conjugated with fluorescent proteins (GFP, RFP, pHluorin etc.) at the N-terminus, C-terminus or Extracellular Loop (ECL), or by dual labelling with two fluorescent proteins at both the C-terminus and ECL, and **(ii)** fluorescent proteins fused with a palmitoylation signal (PalmGFP or PalmTdtomato, signal: MLCCMRRTKQ). Note FP=fluorescent protein.

1.5.2.2. Endogenous Labelling: Genetically Encoded Fluorescent Reporters

Whereas organic dye-based methods have many advantages, including commercial availability, variety in fluorescence colours, as well as emission signal stability and brightness of fluorescence signal, their greatest limitation is that they can only be used to exogenously label purified sEVs. However, in order to also investigate sEV biogenesis, tracking from cell-to-cell, endocytosis and exocytosis processes, a different strategy must be followed; that is, the generation of stable cell lines expressing endogenously-fluorescent sEVs, i.e., “fluorescent sEV reporters” (100). [Figure 1.6.D](#) demonstrates different examples of genetically encoded fluorescent sEV reporters.

sEV-Associated Proteins Conjugated to Fluorescent Proteins

Fluorescent sEV reporters mainly involve the fusion of fluorescent proteins to sEV-associated protein markers like tetraspanins. Tetraspanins are usually selected for these studies as they are highly enriched in sEVs and are considered “exosome markers”, especially CD9, CD63 and CD81 as discussed in previous Sections (19, 21). The majority of these studies use the tetraspanin CD63 conjugated with fluorescent proteins to provide a specific method of sEV visualisation for the investigation of sEV kinetics in a plethora of *in vitro* and *in vivo* studies (116-123), some of which discussed below. [Figure 1.6.D.i](#) demonstrates the variety of fusion methods for the fluorescent proteins mentioned in these studies, including fusion at the N- terminus, C-terminus, or extra-cellular loop (ECL) of tetraspanins, as well as dual fusion (usually C-terminus and ECL fusions).

CD63 Conjugated with Fluorescent Proteins

Most commonly, studies encode GFP (Green Fluorescent Protein) fused to CD63 (GFP-CD63) to generate endogenous fluorescent sEVs and investigate uptake kinetics and retention in cell systems. A study utilising the GFP-CD63 reporter system in HEK293T (human embryonic kidney cells)- derived sEVs, investigated their kinetics of internalisation and retention in parental cells by imaging flow cytometry (116). This study showed that sEVs were internalised in a time- and dose-dependent manner for up to 12 hours, at which point the fluorescence signal was saturated, followed by concomitant decrease of signal by 24 hours, indicating degradation/processing of sEVs (116).

Similarly, a study addressed HEK293T sEV uptake, internalisation and shuttling to endosomes of HEK293 cells, by individually tracking sEVs entering cells via the filopodia,

using the GFP(emerald)-CD63 and mCherry-CD63 fluorescent reporters (92). They showed that sEVs were taken up in a dose- and time-dependent manner, which reached saturation after 8 hours of dosing, with more than 95% of the cell population saturated with fluorescence signal (even at the lowest dose tested). Analysis of the fluorescence signal showed the typical perinuclear localisation and co-localisation with endosomal and lysosomal markers (92). Furthermore, another study using the GFP-CD63 fluorescent sEV reporter system in the PC3 PCa cell line (which is to our knowledge the only study currently on PCa), developed a 3D (three-dimensional) heterotypic spheroid model comprised of these cells and human peripheral blood mononuclear cells (PBMCs) and visualised the transfer of GFP-CD63 sEVs to PBMCs, even though sEV kinetics were not addressed (117).

These fluorescent reporters have also been explored *in vivo*, for example a study generated a transgenic rat model using GFP-CD63 (human) to elucidate the intercellular transfer fate of sEVs *in vivo* (123). This transgenic rat model exhibited high expression of GFP in various tissues which allowed the detection of exogenous human GFP-CD63 on rat sEVs isolated from bodily fluids (blood serum, breast milk and amniotic fluid). The isolated serum-derived GFP-CD63 sEVs were also successfully incorporated into the endosomal compartment of recipient rat embryonic fibroblasts (123).

Studies also explored a variant of GFP (pHluorin) which is a pH-sensitive green fluorescent protein that acts as a reversible pH-sensor which is nearly non-fluorescent at pH 5.5 (the pH of MVBs) but is brightly fluorescent at pH 7.4 (extracellular pH) (124). An *in vitro* study generated a cervical cancer HeLa cell line expressing CD63-pHluorin, by fusing pHluorin to the first extra-vesicular loop of CD63, which enabled the detection of MVB fusion events at the plasma membrane and the subsequent secretion of fluorescent sEVs (118). A more recent study further developed the CD63-pHluorin system, by incorporating a mutation in the pHluorin moiety (M153R), which ultimately improved and stabilised its fluorescence signal (119). Based on the CD63-pHluorin systems, the authors further developed an *in vivo* model by expressing CD63-pHluorin in zebrafish, thus enabling the study of biogenesis, composition, transfer, uptake, and fate of endogenous sEVs in the developing embryo, using live-cell fluorescence microscopy (120).

Other sEV-Markers Conjugated with Fluorescent Proteins

Aside from CD63, other studies expanded to fluorescent sEV reporters utilizing other tetraspanins (like CD9 and CD81) and other “exosome” markers (like Alix), fused with fluorescent proteins. For example, an *in vitro* study constructed seven different HEK293

stable cell lines expressing CD63, CD9 or CD81 fused with either GFP or RFP (conjugated at the intra-vesicular C-terminus of tetraspanins). Furthermore, they developed a dual reporter by expressing CD63 fused with both RFP and GFP (fused to the second extra-vesicular loop and the intra-vesicular C-terminus of CD63, respectively) (121). These reporter proteins enabled monitoring of the secretion and uptake of endogenously-fluorescent sEVs via live-cell fluorescence microscopy, and enabled investigation of the surface engineering of sEVs *in vitro* (121).

A recent study also generated and characterized multiple fluorescent sEV reporters by fusing sEV-associated proteins with fluorescent proteins, including: (i) transmembrane proteins like CD9, CD63, CD81, LAMP-2B and Syndecan, (ii) membrane-associated proteins like Flotillin-2, as well as (iii) luminal proteins like Alix and Syntenin in HEK293T sEVs. The authors demonstrated that fluorescent protein- fusions with transmembrane proteins were of higher efficiency than fusions with membrane-associated or luminal proteins, as shown by fluorescence microscopy, even though they did not conduct any functional studies for sEV kinetics, uptake or retention (122).

“Universal” Fluorescent Protein Reporters

Aside from the fusion of fluorescent proteins to sEV-associated proteins, studies have adopted other approaches in an attempt to generate “universal” fluorescent sEV reporters, thus avoiding the limitation of labelling only a specific sub-population of EVs. For example, a study genetically encoded fluorescent proteins (GFP and Tdtomato) fused to a palmitoylation signal (PalmGFP and PalmTdtomato) in HEK293T cells, which targets these constructs to lipid-bilayer membranes, thus including cells and all subpopulations of EVs (108). [Figure 1.6.D.ii](#) shows the localisation of the Palm-fluorescent protein reporters, which are incorporated at the internal sEV membrane (the palmitoylation signal sequence is also shown). The limitation of this approach is that targeting all lipid bilayer membranes will inadvertently label all types of secreted vesicles including apoptotic bodies, large EVs or EVs that directly bud from the plasma membrane etc., and results must be interpreted with caution. Another potential complication is “lipid recycling” which might result in re-purposing of lipid-fluorescent protein components, thus resulting to residual non-specific signal to other non-EV compartments.

The previous study that generated these reporters demonstrated that PalmGFP and PalmTdtomato EVs were directly secreted from the membrane of each cell line and were bi-directionally exchanged between cells by tracking via confocal fluorescence microscopy (108). Furthermore, they showed that exposure of glioma cells to PalmGFP

EVs for 90 minutes lead to their active internalisation, which appeared to be time-dependent as the percentage of fluorescently-labelled cells increased over time (up to 3 hours), but then subsequently started to decrease until 12 hours post-dosing. From 12 to 24 hours post-dosing, the fluorescent signal plateaued and did not reach the baseline suggesting that either a percentage of EVs remained intact in the recipient cells, or EVs were not fully degraded and some EV membrane (with the PalmGFP reporter) remained in the cells, or that the EV membrane with the reporter was “recycled” in the cell, thus emitting non-specific fluorescent signal (108).

Another interesting, albeit more complex, method for generating “universal” fluorescent protein sEV reporters is the Cre-*loxP* method, which enables investigation of sEV transfer *in vitro* and *in vivo* (125). This Cre-*loxP* system was designed to include a fluorescent Cre-reporter cell (DsRed) acting as the EV-recipient, and a fluorescent Cre-recombinase cell (CFP) acting as an sEV donor. When the Cre-reporter cells internalise sEVs from the Cre-recombinase cells, the Cre-reporter cells switch from DsRed to GFP, due to Cre-mediated removal of DsRed by the sEV cargo (carrying Cre recombinase). Collectively, this method enables the visualisation of sEV uptake by recipient cells (GFP fluorescent) and the ability to distinguish them from donor cells (CFP fluorescent), or cells that have not taken up EVs yet (still DsRed fluorescent), and can thus be adapted to study sEV kinetics and retention in various cell populations *in vitro* and *in vivo* (125).

Advantages, Limitations and Gaps in the Literature

Overall, fluorescent reporters fused to sEV-associated proteins (usually tetraspanins) provide a direct versatile method of sEV visualization, as they enable both the detection and tracking of endogenously produced sEVs *in situ* e.g., for biogenesis, or secretion studies, but also enable the detection of these sEVs when they are exogenously added to any other cell system, e.g., for uptake kinetics studies in recipient cell systems. Furthermore, this labelling strategy avoids false positive signals and artefacts observed with organic dyes (100, 102, 103).

However, the major limitations of this approach are that genetically encoding fluorescent proteins fused to specific sEV markers inadvertently result in fluorescent labelling of only a subpopulation of sEVs depending on the loading of that marker on sEVs, thus limiting the observation of multiple sEV types and introducing bias. These genetically encoded fluorescent reporters can also be of dimmer fluorescence than organic dyes, partly because their fluorescence depends on the expression of the conjugated protein marker on the sEV membrane. Furthermore, genetically encoding tetraspanins fused with fluorescent proteins can induce their overexpression at the cellular level, and as they are vital players in sEV biogenesis and structure at the TEMs via interacting with a plethora of other proteins, the composition and function of secreted sEVs might become altered (Table 1.1). Unfortunately, beyond basic sEV characterisation (e.g., sEV size and expression of selected few sEV markers like Alix, TSG101 and tetraspanins) most studies do not thoroughly investigate potential changes in the phenotype or proteome of engineered sEVs (116-121). On the other hand, universal reporters might be a better choice to avoid labelling only a subpopulation of sEVs, but careful characterisation must take place to distinguish between sEVs, IEVs, apoptotic bodies etc. to avoid misinterpretation of results.

Table 1.1. Advantages and limitations of EV fluorescence labelling methods.

Extracellular Vesicle Fluorescent Labelling Methods			
Lipophilic Dyes		Membrane-permeable Compounds	
<ul style="list-style-type: none"> + Simple method + Most common method + Commercially available + Multiple fluorescent moieties available + Bright fluorescence 	<ul style="list-style-type: none"> - Not EV specific - Form aggregates or micelles indistinguishable from sEVs - Artefacts due to longer half-life than sEVs - Dye “leakiness” to other compartments - Exogenous sEV labelling only - Structural alterations to sEVs 	<ul style="list-style-type: none"> + Simple method + Commercially available + Multiple fluorescent moieties + Bright fluorescence + More EV specific than lipophilic dyes 	<ul style="list-style-type: none"> - Higher fluorescence background due to spontaneous hydrolysis - “Leakiness” to other compartments after hydrolysis leading to artefacts - Exogenous sEV labelling only
Thiol-based Compounds		Genetically Encoded Fluorescent Reporters fused to EV-associated proteins	
<ul style="list-style-type: none"> + Simple method + Commercially available + Multiple fluorescent moieties available + Bright fluorescence 	<ul style="list-style-type: none"> - Not EV specific - Dye “leakiness” to other compartments leading to artefacts - Newer method requiring further characterisation - Exogenous sEV labelling only 	<ul style="list-style-type: none"> + Highly sEV- specific labelling method + Endogenously produced fluorescent sEVs + Use of fluorescent sEVs exogenously in models + Free of artefacts + Common method used in the literature 	<ul style="list-style-type: none"> - Complex method - Labelling of sEV subpopulations - Potential phenotypic alterations of sEVs - Dimmer fluorescence

1.6. Thesis Hypotheses and Aims

The hypothesis addressed in this thesis is that the endogenous labelling of sEVs provides a unique tool for understanding the kinetics of sEV uptake, retention, and distribution in different two-dimensional (2D) dynamic cell systems, by utilising genetically encoded fluorescent sEV reporters overexpressing fluorescent proteins tagged to tetraspanins CD63 or CD81. However, due to the fact that tetraspanins play a major role in sEV biogenesis and cargo sorting, it is hypothesised that overexpression of these tetraspanin-fused fluorescent proteins would induce phenotypic and proteomic alterations on both the engineered stable cell lines overexpressing CD63/CD81 and the generated sEVs. Therefore, this project aimed to:

- Generate two fluorescent sEV reporters by establishing stable PCa cell lines (DU145) overexpressing tetraspanins CD63 or CD81 fused with fluorescent proteins GFP or Tdtomato, respectively.
- Characterise the phenotype and proteome of the fluorescent CD63/CD81 overexpressing cell lines and sEVs in 2D and 3D-like microenvironments.
- Investigate sEV kinetics of uptake (dosing), retention, and distribution in 2D propagating cell populations, including both the parental PCa cell line and a bone-marrow derived mesenchymal stem cell line (BM-MSCs), aiming to represent the primary tumour microenvironment and the bone pre-metastatic niche, respectively.
- Undertake a proof-of-principle experiment to detect early markers of osteogenic differentiation as a result of dosing BM-MSCs with PCa sEVs overexpressing CD63 or CD81.

CHAPTER 2:

Materials and Methods

2.1. Cell Culture

DU145 PCa cells were purchased from ATCC (HTB-81™) and the Y201 BM-MSCs (hTERT-BMSC clone Y201, generated by the Genever group (126)) were provided by the Tissue MicroEnvironment Group. Cell lines were cultured with reagents from ThermoFisher Scientific: RPMI-1640 medium (Cat. No.11544446) was used for DU145 cells and DMEM (Dulbecco's Modified Eagle Medium, Cat. No.11995065) was used for Y201 cells, which were supplemented with 2mM L-Glutamine (Cat. No.25030081), 100 units/ml Penicillin/Streptomycin (Cat. No.15140122) and 10% exoFBS (Foetal Bovine Serum depleted of bovine EVs). ExoFBS was prepared according to a published protocol (127). Briefly, FBS (Cat. No. 26140079) was transferred in Quick-Seal polyallomer bell top centrifuge tubes (Beckman Coulter, Cat. No.344623), which were then placed in a 70-Ti fixed angle rotor and ultracentrifuged at 100000g, for 18h (hours) at 4°C in the Beckman Coulter Optima™ LE-80K ultracentrifuge. After ultracentrifugation, the FBS supernatant was vacuum-filtered sequentially through a 0.22µm filter (Cat. No.10176660) and then a 0.1µm filter (Cat. No.10182431); the resultant exoFBS was aliquoted and stored at -20°C. DU145 stable cell lines were also supplemented with 500µg/ml Geneticin (G418, Sigma Aldrich, Cat. No. 8168). Cell lines were passaged by washing with 1XPBS pH 7.4 (Phosphate Buffered Saline, Sigma Aldrich, Cat. No. 10010023) followed by trypsinisation with 0.05% trypsin/0.53 mM EDTA (Sigma Aldrich, Cat. No. 11590626) for 5min (minutes), and neutralisation with complete media.

2.2. Plasmid Expansion

CD63-EGFP C2 (“GFP-CD63”) was generated by Dr. Paul Luzio (purchased from Addgene: plasmid #62964), while tdTomato-CD81-10 (“CD81-Tdtomato”), EGFP-C1 (“GFP”) and tdTomato-C1 (“Tdtomato”) were generated by Dr. Michael Davidson (purchased from Addgene: plasmids #58078, #54759 and #54653, respectively). Plasmid maps are shown in detail in Supplementary Figure 1. To expand the plasmids, *E. coli* HST08 strain Stellar™ Competent Cells (Takara, Cat.No 636763) were transformed with DNA via heat shock (42°C for 45 seconds) after a 30min incubation with the DNA on ice. Following heat shock, the competent bacteria were transferred on ice (for 5 min) and SOC medium was added (Takara, Cat. No 636763), followed by a 1-h incubation at 37°C in an orbital shaker at 500 rpm. Next, the bacterial culture was plated in agar plates prepared with Luria low salt LB agar (Sigma Aldrich, Cat. No L3272) supplied with 10mg/ml Kanamycin (Sigma Aldrich, Cat. No K0879). The inoculated agar

plates were left to grow overnight (O/N) at 37°C, and the next day single colonies were isolated and transferred in tubes with Luria low salt LB broth (Sigma Aldrich, Cat. No L3397) supplied with 10mg/ml Kanamycin. The bacterial cultures were left to expand O/N at 37°C in an orbital shaker at 500rpm, followed by plasmid DNA extraction via the GenElute™ HP Plasmid Miniprep (Sigma Aldrich, Cat.No NA0160) according to the manufacturer's protocol. The isolated plasmid DNA concentration was measured via the NanoDrop2000™ Spectrophotometer (ThermoFisher Scientific).

2.3. Cell Transfection

2.3.1. Transient Transfection Optimisation

12000 DU145 cells (40000 cells/ml) were seeded in a polymer-treated μ -Slide (8-chamber well slide) (ibidi, Cat. No 80826) and were left to grow for 48h until reaching 70% confluency. Optimisation of transfections was done using various reagents: FuGENE® HD (Promega, Cat. No E2311), Lipofectamine™2000 (ThermoFisher Scientific, Cat. No 11668019), Lipofectamine™3000 (ThermoFisher Scientific, Cat. No L3000015) and Lipofectamine™ LTX Reagent with PLUS™ Reagent (ThermoFisher Scientific, Cat. No 15338100), according to each manufacturer's protocol. Various DNA concentrations, DNA: Transfection reagent ratios and incubation times were also tested to achieve optimal transfection efficiency and minimal toxicity. Briefly, 25ng, 50ng or 100ng of DNA were tested for transfection, in 1:3 or 1:5 ratio of DNA: Transfection Reagent, with various incubation durations for the DNA: Transfection Reagent within the cells (4h, 6h, 8h or O/N).

2.3.2. Stable Transfection and Selection with Geneticin

200000 DU145 cells (100000 cells/ml) were seeded in cell culture-treated 6-well plates and were left to grow for 24h until reaching 70% confluency. 500ng of GFP-CD63 or CD81-Tdtomato DNA were transfected with Lipofectamine™3000 (ratio of 1:5 of DNA: Lipofectamine™3000) and left to incubate within cells for 4h, followed by washing with warm media. After 24h, the cell media was replenished, and 48h post-transfection the cells were transferred to T25 cell culture flasks. Lastly, 72h post transfection, the cells were put under continuous selection with 500 μ g/ml Geneticin (G418) (Sigma Aldrich, Cat. No. 8168) to establish the stably-transfected cells. The concentration of G418 was

determined after conducting an antibiotic kill curve which showed that 500µg/ml of G418 killed all non-transfected wild-type (WT) DU145 cells in 7 days (data not shown).

2.4. Cell Sorting and Monitoring of Fluorescence Expression

Fluorescence expression of stable transfected cells was monitored via flow cytometry using the FACSCalibur (Beckton Dickinson) cytometer starting 7 days post-selection with G418. Fluorescence-Activated Cell Sorting (FACS) was performed to enrich the stable cell population using the BD FACSAriaIII cell sorter, starting four weeks post-selection with G418. For the FACSCalibur, fluorescence excitation was conducted using a 488nm laser, while detection was conducted using bandpass emission filters 530±15nm (for GFP) and 585±21nm (for Tdtomato). For the FACSAriaIII, excitation was conducted using a 488nm laser and detection using the bandpass emission filters 530±15nm (for GFP), while for Tdtomato, excitation was conducted using the 532nm laser and detection using the bandpass emission filters 585±21nm.

2.5. Growth Curve Analysis

7500 GFP-CD63, CD81-Tdtomato, GFP-Parallel and Tom-Parallel control cells were seeded in complete media (in triplicate) in 12-well plates (3750 cells/ml), so that in every timepoint one triplicate was processed and measured. GFP-Parallel and Tom-Parallel control cells are WT DU145 cells of the same cell passage as GFP-CD63 or CD81-Tdtomato cells, respectively. 24, 48, 72, 96 and 168h after seeding, the media from the triplicate wells was collected, followed by a 1xPBS wash of the cells (which was also collected) and then trypsinisation of the cells (also collected). For every sample, the total amount of cells in the media, wash and trypsin were counted thrice through the Z1 Coulter® Particle Counter (Beckman Coulter). All the different measurements and timepoints were used to plot a growth curve for every cell line. These measurements were also used to calculate the population doubling time based on the following formula: $DT = T \ln 2 / \ln (X_e / X_b)$, where T is the incubation time in hours, X_b is the cell number at the beginning of the incubation time and X_e is the cell number at the end of the incubation time (formula applied to exponential phase of cell growth).

2.6. Cell Cycle Arrest Analysis

50000 GFP-CD63, CD81-Tdtomato, GFP-Parallel and Tom-Parallel control cells were seeded in 12-well plates (25000 cells/ml) in complete media and were left for 24h to grow. The following days, actively dividing cells were treated with 60ng/ml KaryoMAX™ Colcemid™ Solution (ThermoFisher Scientific, Cat. No 15212012) for 8, 16, 24 and 32h to block microtubular formation (128). After mitotic arrest, cells were harvested via trypsinization and after centrifugation (900rpm for 7 min, CENTAUR 2 MSE centrifuge) were resuspended in complete media supplemented with 20mM HEPES (Sigma Aldrich, Cat. No H3537). After harvest, the cells were incubated with 20µM DRAQ5™ for 15min at 37°C to label nuclear DNA. Cell cycle analysis (129) was done using the BD FACSCalibur Flow cytometer (excitation with 488nm laser, detection with 670nm long-pass emission filter) and the FlowJo software (v10)(130).

2.7. Live-Cell Fluorescence Imaging Analysis

20000 GFP-CD63, CD81-Tdtomato, GFP-Parallel and Tom-Parallel control cells were seeded in polymer-treated 8-chamber µ-Slides (~66700 cells/ml) and were left to grow O/N in complete media. The following day, the media was replaced with phenol-red free FluoroBrite™ DMEM media (ThermoFisher, Cat. No. A1896701) and the cells were either imaged live as is, or after incubation with 4µM DRAQ5™ (Biostatus, Cat. No. DR50200) for 10min at 37°C, to label nuclear DNA (129). Imaging was performed using the Zeiss Axiovert 100 widefield fluorescence microscope (x63 magnification, 1.4 NA oil lens), for GFP: 489/515nm (70% attenuation- 750ms), for Tdtomato: 585/602nm (20% attenuation- for 100ms) and for DRAQ5: 650/669nm for 250ms.

2.8. CellProfiler™: Cellular Phenotypic Image Analysis

20000 cells/ml GFP-CD63, CD81-Tdtomato, GFP-Parallel and Tom-Parallel control cells were seeded in polymer-treated µ-24-well plates (ibidi, Cat. No 82406) and were left to grow for 48h in complete media. After 48h, the cells were washed once with 1xPBS and fixed with 2% PFA (Paraformaldehyde, ThermoFisher Scientific Cat. No 28908) for 20min at RT (room temperature). After fixation, the cells were washed twice with 1xPBS and then were permeabilised with 0.1% Triton-X100 (Sigma Aldrich, Cat. No T8787) for 10min at RT. After washing twice with 1xPBS, the cells were labelled with ActinGreen™

(ThermoFisher Scientific, Cat. No. R37110) for 30min (at RT) to label the actin cytoskeleton. After two 1xPBS washes, the NucBlue™-DAPI reagent (ThermoFisher Scientific, Cat. No. R37606) was added to the cells to label nuclear DNA, following by imaging of cells using the Zeiss Axio Observer Z1 inverted fluorescence microscope. For each cell line, at least 30 fields of view were collected using the 20x objective 0.8 NA air lens; for AlexaFluor488: max excitation 493nm -max emission 517nm and for DAPI: max excitation 353nm-max emission 465nm.

Phenotypic image analysis was conducted on these fixed-cell images using the freely available CellProfiler™ software (v.3.1.8) (131) and two customised pipelines comparing GFP-CD63 vs GFP-Parallel cells and CD81-Tdtomato vs Tom-Parallel cells, respectively. Firstly, both customised pipelines identified and segment cell nuclei using the DAPI stain, via a global Otsu thresholding algorithm with 2-classes (background and foreground) and a thresholding Gaussian filter (threshold smoothing scale 1.3488 and threshold correction factor 1.0). Next, the pipelines can determine and segment the cell boundaries using the Actin488 cytoskeleton dye, starting at the previously- identified nuclei via a propagation method again using the global Otsu algorithm. Finally, after segmentation of cell outlines, the CellProfiler™ pipelines were used to measure cell shape characteristics; specifically, cell area and form factor (circularity) using the module "MeasureObjectSizeShape". Output data were analysed using the FlowJo™ software (v10)(130).

2.9. sEV-Associated Cell Membrane Protein Analysis

50000 GFP-CD63, CD81-Tdtomato, GFP-Parallel and Tom-Parallel control cells were seeded in 12-well plates in complete media (25000 cells/ml) and were left to grow for 48h. At this point, cells were harvested via trypsinization and after centrifugation (900rpm for 7min) were resuspended in complete media supplemented with 20mM HEPES. Next, the cell suspensions were incubated live with the following antibodies (Biolegend) directly-conjugated to PERCP/Cy5.5 (concentration: 2µl antibody for 200000 cells): anti-human CD63, (Cat.No 353020), CD81 (Cat.No 349508), CD9 (Cat.No 312110), MHC-1 (Cat.No 311419) and IgG-Fc (isotype control, Cat.No 409311). Incubation with antibodies was 1h at 4°C in the dark. After incubation, cells were washed with 1XPBS and pelleted via centrifugation, followed by resuspension in cold complete media (supplemented with 20mM HEPES) and analysis of PERCP/Cy5.5 fluorescence using the BD FACSCalibur Flow cytometer (excitation at 488nm, detection with 670nm long-pass emission filter). Analysis was done in the FlowJo software (v10) (130).

2.10. Differential Ultracentrifugation and sEV Secretion Analysis

130000 GFP-CD63, CD81-Tdtomato, GFP-Parallel and Tom-Parallel control cells were seeded in T75 tissue-culture flasks in 10ml complete media (fifteen T75 flasks were used for every cell line). Cells were left to grow for 7 days, at which point the cells and conditioned media was collected and further processed.

The cell conditioned media was centrifuged twice at 400g (in Heraeus Megafuge 1.0R) for 6min (at 4°C) to pellet and remove dead cells. Next, the supernatant was centrifuged at 2000g for 15min (at 4°C), to remove cell debris. After serial centrifugation, the supernatant was transferred in Quick-Seal polyallomer centrifuge tubes for EV isolation via differential ultracentrifugation. Specifically, the Quick-Seal tubes were placed in a fixed angle rotor (Beckman Coulter, 70-Ti) and centrifuged at 10000g, for 90min (4°C) in the Optima™ LE-80K ultracentrifuge. The supernatants were then transferred into new Quick-Seal tubes and ultracentrifuged at 100000g in the fixed angle rotor (70-Ti) for 90min (4°C). This resulted in pelleting of sEVs, which were then resuspended in a total volume of 5ml 1XPBS and transferred in OptiSeal centrifuge tubes (Beckman Coulter, Cat. No.361621). The OptiSeal tubes were then placed in a fixed angle rotor (Beckman Coulter, TLA110) and ultracentrifuged again at 100000g, for 60min (4°C) in the Optima™ MAX-XP Ultracentrifuge to wash and pellet sEVs. Lastly, the isolated sEVs were resuspended in 185µl 1xPBS and stored in -80°C until required for experiments.

To evaluate the number of vesicles secreted per cell (Vesicle Secretion Analysis), the cells grown in T75 flasks (mentioned above) were trypsinised and counted in triplicate with the Z1 Coulter® Particle Counter (Beckman Coulter), alongside EV-processing. After cell counting and EV isolation via differential ultracentrifugation, EVs were analysed via Nanoparticle Tracking Analysis (see [Section 2.13](#)) to calculate their particle concentration (particles/ml). The sEV particle concentration (particle/ml) and the total volume of sEV isolate (185µl), were used to calculate the total sEV particle number secreted by each cell line, which was then normalised to the total cell number, thus estimating the normalised sEV number secreted per cell.

2.11. Sucrose-Cushion Ultracentrifugation for sEV

Isolation

EV-rich conditioned media, collected from either conventional T75 flasks ([Section 2.16.1](#)), or CELLLine Bioreactor Flasks ([Section 2.18.2.2](#)) was pre-cleared by being subjected to serial centrifugation steps to pellet and remove cells and debris (twice at 400g for 6min and once at 2000g for 15min at 4°C in the Heraeus Megafuge 1.0R). Next, the EV-rich conditioned media was filtered through a 0.22µm syringe filter (ThermoFisher, Cat.No 10268401) and was stored in -80°C until EV isolation by the 30% sucrose/D₂O cushion ultracentrifugation method (132). Specifically, after thawing, the pre-cleared media was transferred in Quick-Seal polyallomer centrifuge tubes and was underlain with 4ml of 30% sucrose/D₂O at a density of 1.2g/ml (flotation density of sEVs: 1.13–1.19g/ml (40)). The polyallomer tubes were then ultracentrifuged at 100000g using the SW-32 rotor (Beckman Coulter) for 90min at 4°C in the Optima™ LE-80K ultracentrifuge. Next, 2-3ml of the central base of the sucrose cushion solution was collected and diluted in excess 1xPBS, followed by transfer in Quick-Seal tubes and placement in the fixed angle rotor 70-Ti (Beckman Coulter) for ultracentrifugation at 100000g, for 90min (4°C) in the Optima™ LE-80K ultracentrifuge. After ultracentrifugation, the sEV pellets were resuspended in 1xPBS and stored at -80°C, until required for further experimental use.

2.12. BCA Protein Assay

10µl of isolated sEV samples, or sEV lysates or cell lysates were used for protein estimation using a micro-BCA kit (Thermo Fisher Scientific, Cat. No. 23235), according to the manufacturer's protocol. Samples were diluted (1:8) and then compared in triplicates against serially diluted BSA (Bovine Serum Albumin) as standard (concentration range 0-2000µg/ml). Absorbance values of BSA standards were used to generate a standard curve for concentration, of which values for samples were extrapolated (using a third-order polynomial equation, with $R^2 > 0.98$ for each assay). Absorbance measurements (570nm) were conducted on a PHERAstar FS Microplate Reader (BMG Labtech). The protein concentrations of sEVs isolated from conventional 2D tissue-culture flasks or CELLLine Bioreactor Flasks are shown in [Table 2.2](#).

2.13. Nanoparticle Tracking Analysis (NTA)

Isolated sEVs were analysed by nanoparticle tracking to determine their size distribution profile and particle concentration, using the NanoSight™ NS300 system (Malvern Panalytical), configured with a 405 nm laser and a high sensitivity sCMOS Camera System (OrcaFlash2.8, Hamamatsu C11440). Each sEV sample was diluted in MilliQ purified water as necessary, so that number of particles per frame was approximately 50. Samples were administered at set temperatures (25°C) and recorded under controlled flow, using the NanoSight syringe pump (set to 50) and script control system. For each sample, three videos of 60-second duration were recorded, with a 10-second delay between recordings, generating three replicate histograms that were averaged. Videos were batch analysed using NTA 3.1 software (version 3.1) with the camera's sensitivity and detection threshold set at 14-16. 100nm polystyrene beads (Malvern Panalytical, Cat. NTA 4088) were also used as a standard to confirm that NTA measurements were accurate. The particle concentrations (particles/ml) of sEVs isolated from conventional 2D tissue-culture flasks or CELLLine Bioreactor Flasks are shown in [Table 2.2](#).

2.14. Immuno-Phenotyping ELISA-like Assay

sEVs were diluted in 1xPBS and bound onto high protein binding ELISA strip 96-well plates (Greiner Bio-One, Cat. No. 756071), at a dose of 10µg/ml and incubated O/N at 4°C. Then, the wells were washed 3 times using a Tris-based wash buffer (Perkin Elmer, Cat. No. 4010-0010), in the Wellwash™ Microplate Washer (ThermoScientific) to remove unbound sEVs. Blocking solution of 1% BSA/PBS w/v (R&D Systems, Cat. No. DY995) was added for 2h, before being washed 3 times. Primary antibodies were then added at 1µg/ml for 2h at RT (diluted in 0.1% BSA/PBS w/v). Antibodies used were mouse anti-human CD9 (R&D Systems, Cat. No. MAB1880), CD63 (Serotec, Cat. No. MCA2142), CD81 (Biorad, Cat. No. MCA1847EL) and MHC-1 (eBioscience™, Cat. No. 16-9983-85). Isotype control antibodies were also used: IgG2_b (Cat. No. 14-4732-82) for CD9, IgG₁ (Cat. No. 14-4714-82) for CD63 and CD81, as well as IgG2_a (Cat. No. 16-4724-82) for MHC-1, all purchased from eBioscience™. After antibody incubation, the wells were washed 3 times, followed by addition of the secondary antibody; this goat anti-mouse biotinylated antibody (Perkin Elmer, Cat. No. NEF823001EA) was diluted in 0.1% BSA/PBS w/v, at a 200ng/ml working concentration and was left to incubate in the wells for 1h at RT. Next, the wells were washed 3 times, before adding the Europium-

Streptavidin conjugate (Perkin Elmer, Cat. No. 1244-360), diluted in Assay Buffer (Perkin Elmer, Cat. No. 1244-111), for 45min at RT. The wells were then washed 6 times, followed by addition of Enhancement Intensifier solution (Perkin Elmer, Cat. No. 1244-105), for 5min at RT. Lastly, the Europium fluorescent signal was assessed by time-resolved fluorescence (TRF) on the PHERAstar FS Microplate Reader.

2.15. sEV Detection and Point-Spread Function

Analysis

Tetraspeck™ fluorescent 100nm microspheres (ThermoFisher Scientific, Cat. No. T7279), as well as GFP-CD63 and CD81-Tdtomato sEVs were diluted in a three-dimensional (3D) thermo-reversible hydrogel CyGEL™ (Biostatus, Cat. No. CY10500), followed by imaging and Point-Spread Function (PSF) analysis. A Nunc™ Lab-Tek™ chambered coverglass (ThermoFisher Scientific, Cat. No. 155380) was placed on ice, containing small circular PVC inserts. After vortexing, microspheres and sEVs were spread evenly within the inserts and then CyGEL™ (which is liquid at 4°C) was added directly on top (dilution 1:20). The chambered coverglass was then removed from ice, enabling the CyGEL™ to solidify, followed by imaging using the confocal microscope Zeiss LSM 880. Imaging parameters were the following: Objective: 63X, Laser: 488 or 543nm, Numerical Aperture (NA): 1.4, Pinhole: 1.0 Airy Units, Frame Size: 2048x2048. 3D images were collected as a collection of Z-stacks, followed by determination of PSF and FWHM (Full Width at Half Maximum) using the MetroloJ plugin (Fiji Software (133)) according to a published protocol (134), as well as projected into a 2D average intensity image.

2.16. SWATH-MS Proteomics Analysis

2.16.1. Sample Preparation and Protein Quantification (Cells and sEVs)

130000 GFP-CD63, GFP-Parallel control, CD81-Tdtomato and Tom-Parallel control DU145 cells were cultured in conventional T75 flasks (10 flasks per cell line) for 7 days in RPMI complete media supplemented with 10% exoFBS. After 7 days the cell-conditioned media was collected followed by pre-clearing and then pelleting sEVs by sucrose cushion ultracentrifugation ([Section 2.11](#)). After formation of the sEV pellet, sEVs were resuspended directly in 1% SDC lysis buffer (sodium deoxycholate diluted in 50mM ammonium bicarbonate, Sigma Aldrich Cat. No. D6750 and A6141, respectively) and were stored in -80°C until protein quantification. Simultaneously, upon removal of cell-conditioned media after 7 days of culture, cells were washed twice with 1xPBS, followed by trypsinisation with 0.05% trypsin/0.53 mM EDTA, neutralisation with complete RPMI and centrifugation (400g for 6min, RT) to pellet the cells. Next, the cell pellet was washed twice with 1XPBS and centrifuged again, following by resuspension in the 1% SDC lysis buffer. Cells resuspended in lysis buffer were then spread in a 6-well plate and placed on ice for 10min to enable cell lysis, following by addition of Benzonase® Nuclease (Sigma Aldrich, Cat. No. E1014) to degrade nucleic acids, and storage in -80°C until protein quantification. Protein quantification of cell and sEV lysates was done using the BCA protein assay ([Section 2.12](#)).

2.16.2. Spectral Library Generation and SWATH-MS

After protein quantification, cell and sEV lysates were sent to our collaborators at the BSRC Mass Spectrometry and Proteomics Facility at the University of St. Andrews (Dr Simon Powis, Dr. Sally Shiran and Dr. Silvia Synowsky) to conduct SWATH-MS analysis (Sequential Windows Acquisition of All Theoretical Mass Spectra) according to their protocol (135). The rationale for this experiment was to compare the GFP-CD63 with the GFP-Parallel control cells and sEVs, and the CD81-Tdtomato with the Tom-Parallel control cells and sEVs; both GFP- and Tom- Parallel controls were used to establish the basal protein expression levels of DU145 cells and sEVs before overexpression of CD63 or CD81, respectively (see [Figure 4.1](#)).

Briefly, cell lysates were digested to generate spectral libraries, as follows: (i) Set 1 (Library 1) consisted of GFP-CD63 and GFP-Parallel control cell protein samples combined and (ii) Set 2 (Library 2) consisted of CD81-Tdtomato and Tom-Parallel control cell protein samples combined; these were further fractionated by strong cation exchange (SCX) chromatography and high pH reversed phase chromatography (135).

Furthermore, digestions of cell and sEV lysates were prepared for SWATH-MS proteomics analysis, as follows: (i) Set 3 consisted of GFP-CD63 and GFP-Parallel control cell samples, (ii) Set 4 consisted of CD81-Tdtomato and Tom-Parallel control cell samples (iii) Set 5 consisted of GFP-CD63 and GFP-Parallel control sEV samples, and (iv) Set 6 consisted of CD81-Tdtomato and Tom-Parallel control sEV samples. Note that in each set every sample was digested separately.

After digestion, Sets 1-2 were used for spectral library generation via LC-MS/MS analysis using the Sciex TripleTOF 5600+ system mass spectrometer (Sciex) on DDA mode (Data-Dependent Acquisition). Furthermore, Sets 3-6 were used for SWATH-MS data acquisition with the same mass spectrometer run on DIA mode (Data-Independent Acquisition). To account for sample variability due to multiple sample processing steps, each sample was ran as a technical replicate (triplicate). Reference iRT peptides (Biognosys) were also added to each sample according to the manufacturer's instructions to enable correction of retention times.

2.16.3. SWATH-MS Data Processing

The Skyline v20.1.0.155 software (136) was used for spectral library generation (against the UniProt/Swiss-Prot human database) using a global false discovery rate (FDR) of 1% as a threshold for the imported proteins. The SWATH-MS results were mapped against their corresponding spectral libraries (Library 1 or 2) to extract chromatographic peaks. Specifically, Library 1 was used for GFP-CD63 and GFP-Parallel control samples (cells and sEVs, Sets 3 and 5 respectively), whereas Library 2 was used for CD81-Tdtomato and Tom-Parallel control samples (cells and sEVs, Sets 4 and 6 respectively). The Skyline parameters were chosen as follows: (i) Peptide settings (trypsin digestion with 0 missed cleavage, human as background proteome, carbamidomethylation (C) and oxidation (M) as modifications) and (ii) Transition settings (2+ and 3+ precursor charges, 1+ and 2+ ion charges, b and y ions and precursor, and six transitions were selected per peptide).

Final chromatogram peak area was normalized based on the median value, and accepted proteins were identified with at least two unique peptides, only when fragment

ions exhibited more than 75% matching of the chromatogram peak intensity to the corresponding spectral library (1 or 2) and when they aligned exactly over the expected elution time of the spectral library. In addition, only proteins with a peak area variability of less than 50% for two technical replicates were considered in the subsequent analysis (coefficient of variation (CV) cut-off <50%). Note that Skyline import of proteins and set of parameters were performed by our collaborators at the University of St. Andrews and were based on their previous study on SWATH-MS proteomic analysis (135), whereas the following statistical analysis, Gene Enrichment and Interaction analysis were conducted by myself.

2.16.4. SWATH-MS Statistical Analysis

Normalised data were exported from Skyline to the Perseus software (MaxQuant) (137) where they were \log_2 transformed, followed by statistical analysis (Student's t-test for adjusted p-value) and generation of Volcano Plots to visualise the differences of protein expression between cells and sEVs overexpressing CD63 or CD81, compared to their respective parallel controls. Furthermore, the normalised protein expression data were analysed by Principal Component Analysis (PCA) to investigate clustering of technical replicates and potential differences between other samples. In addition, Heat Maps with hierarchical row and column clustering were constructed after the filtered normalised data were Z-scored (calculated by subtracting the protein abundance from its mean value for that protein across all samples in the row/column, then divided by the standard deviation (SD) of said row/column), followed by clustering using the following parameters: Euclidean distance, linkage method average and k-means pre-processing.

2.16.5. Gene Enrichment and Interaction Analysis

Gene Enrichment analysis was done in the FunRich functional enrichment and network analysis tool (v3.1.3, released March 2017) which incorporates many databases i.e., Exocarta, UniProt, KEGG, Reactome etc. (138, 139). FunRich was used to determine the enriched cellular components, biological processes, and molecular functions of protein identifications in cell and sEV samples overexpressing CD63 or CD81, compared to their respective parallel controls (enriched when p-value <0.05 of a hypergeometric test against the whole genome/proteome). Venn diagrams were also generated (after conversion from UniProt identifier to GeneEntrez IDs) to reveal the number of unique

and overlapping identifications between samples and the Vesiclepedia compendium of EV molecular data (140). Finally, to generate a protein-protein interaction (PPI) network the Search Tool for the Retrieval of Interacting Genes (STRING) database (141) was utilised, with the following parameters: FDR stringency medium (5%), initial sort order by enrichment score and Markov Clustering inflation parameter equal to 1.7 (142).

2.16.6. Validation of Proteomics Targets

In order to validate some of the targets discovered in the SWATH-MS proteomics analysis in cells and sEVs, Western Blot analysis was conducted. To mirror the previous SWATH-MS experiment, cells of the same passage (GFP-CD63, CD81-Tdtomato and parallel controls) were cultured in the same way in conventional T75 flasks (10 flasks per cell line) for 7 days (in RPMI complete media supplemented with 10% exoFBS), after which cells and EV-rich cell-conditioned media were extracted. Cells lysates were prepared as explained below ([Section 2.17](#)) and sEVs were isolated by firstly pre-clearing the cell-conditioned media and then conducting sucrose cushion ultracentrifugation ([Section 2.11](#)). Prior to Western Blotting, protein quantification of cell lysates and sEVs was done using the BCA assay ([Section 2.12](#) and [Table 2.2](#) for sEV concentrations, isolation #3). Description of Western Blot analysis and primary antibodies used for SWATH-MS target validation are shown in [Section 2.17](#) and [Table 2.1](#).

2.17. Western Blot analysis

GFP-CD63, GFP-Parallel controls, CD81-Tdtomato and Tom-Parallel control cells grown in tissue-culture flasks were harvested with the same method as mentioned previously ([Section 2.16.1](#)) but using a different lysis buffer at the final step, the RIPA lysis buffer system (Santa Cruz Biotechnology, Cat. No. SC-24948) which was used to lyse cells for 10min on ice and was prepared by addition of 1X Protease Inhibitor cocktail, 100mM Sodium orthovanadate and 200nM phenylmethane sulfonyl fluoride (PMSF). Then, cell lysates were centrifuged at 10000g for 10min (at 4°C), after which the supernatant was collected and stored at -80°C for later use. Prior to Western Blotting, cell lysates and sEVs isolated by sucrose cushion ultracentrifugation from tissue-culture flasks ([Section 2.16.6](#)), or CELLline Bioreactor Flasks ([Section 2.18.2.2](#)) were used for protein quantification using the BCA protein assay ([Section 2.12](#)).

After protein quantification, the NuPAGE™ LDS Sample Buffer (1X) (Invitrogen, Cat. No. NP0007) was added to 10µg protein from cell lysates and isolated sEVs (ratio 1:2) along with 20mM dithiothreitol (DTT; Sigma Aldrich, Cat. No. D0632) for reducing conditions (or DTT was not added for non-reducing conditions), following by heating of the samples for denaturation at 70°C for 10min (according to manufacturer's instructions). Next, samples and the molecular weight marker SeeBlue® Plus 2 Precision Stain (ThermoFisher Scientific, Cat. No. LC5925) were loaded on the NuPAGE™ precast 4-12% Bis-Tris gradient gels (ThermoFisher Scientific, Cat. No. NP0321PK2) and subjected to electrophoresis in the XCell SureLock Mini-Cell Electrophoresis System (Invitrogen). The conditions for electrophoresis varied depending on the molecular weight (MW) of the proteins under investigation but ranged from 120-150V and 1-2h of running time in NuPAGE™ MOPS SDS Running Buffer (ThermoFisher Scientific, Cat. No. NP000102).

After electrophoresis, the NuPAGE™ gels were transferred on a methanol-activated polyvinylidene fluoride (PVDF) membrane (GE Life Sciences, Cat. No. 10600023) and were placed in the Mini Trans-Blot® Cell (BioRad) with 25mM Trizma Base® and 192mM glycine (Sigma Aldrich, Cat. No. T1503 and G8898, respectively); transferring of proteins to the PVDF membrane was done at 80V for 90min (at ice-cold conditions).

After protein transfer, the PVDF membranes were blocked in 5% (w/v) non-fat milk powder (Marvel), diluted in 1xPBS-T (1xPBS with 0.1% (w/v) Tween20®) O/N at 4°C on orbital shaker. After blocking and three 5-min washes with 1xPBS-T, membranes were incubated with primary antibodies (see [Table 2.1](#)) for 2h at RT (or O/N at 4°C on orbital shaker). Next, membranes were again washed 3 times with 1xPBS-T, followed by a 1-h

incubation (at RT) with the goat anti-mouse horseradish peroxidase (HRP)-conjugated secondary antibody (Santa Cruz Biotechnology, Cat. No. SC-2005, 1:10000 dilution). After incubation with the secondary antibody, membranes were again washed three times with 1xPBS-T (5-min washes), followed by a 5-min incubation with the WesternSure® Chemiluminescent Substrate (Li-Cor, Cat. No. 926-95000) and detection of protein bands using the C-Digit blot scanner (Li-Cor). In some cases when the membrane had to be re-probed with a different primary antibody, after detection of protein bands via chemiluminescence, the membrane was washed three times with 1xPBS-T (5-min washes), followed by a 1-h blocking at RT (5% w/v non-fat milk powder diluted in 1xPBS-T), or by an O/N blocking at 4°C on orbital shaker. After blocking, the procedures for primary and secondary antibody incubations, as well as the detection of bands, were followed like mentioned previously.

Table 2.1. Primary Antibodies used in Western Blot analysis.

PRIMARY ANTIBODY	DILUTION	CATALOGUE NUMBER	COMPANY
Alix	1:200	sc-166952	Santa Cruz Biotechnology
Annexin III	1:200	sc-390700	
EGFR	1:200	sc-373746	
Ezrin	1:200	sc-58758	
GRP94	1:200	sc-393402	
Integrin α_2	1:100	sc-74466	
Integrin β_5	1:100	sc-390186	
TSG101	1:200	sc-7964	
VPS4A/B	1:100	sc-133122	
β-catenin	1:200	sc-7963	
CD81	1:100	sc-166029	
CD63	1:1000 (non-reducing conditions)	sc-5275	
GAPDH	1:10000	NBP1-47339	Novus biologicals

2.18. CELLine Bioreactor Maintenance and Characterisation

2.18.1. Maintenance Procedure

DU145 cells were cultured long-term in the inner cell compartment of the CELLine adherent Bioreactor Flasks (Sigma Aldrich, Cat.No 688045-3EA) according to a published protocol (127). The cell-free outer compartment contained complete RPMI-1640 media plus 5% regular FBS, and maintenance involved weekly replenishment of the outer compartment with fresh complete media. The inner cell compartment maintained the DU145 cell lines which were cultured in RPMI-1640 complete media supplemented with 5% exoFBS. The CD81-Tdtomato and GFP-CD63 cells were also supplemented with 500µg/ml G418 in both the outer and inner compartment media. During the weekly maintenance, the EV-rich conditioned media was collected from the inner cell compartment, followed by washing of the compartment with media (three times) and subsequent replenishment with fresh complete media. The collected EV-rich conditioned media was then pre-cleared and stored in -80°C (see [Section 2.11](#)).

2.18.2. Characterisation Procedure

2.18.2.1. Cell-Associated Processes

25x10⁶ CD81-Tdtomato, Tom-Parallel control, GFP-CD63 and GFP-Parallel control cells were seeded in the inner cell compartment of Bioreactor Flasks for long-term culture as mentioned above. At weeks 4,8 and 11 the Characterisation Procedure took place, where the contents of the inner cell compartment were collected and processed.

Briefly, the supernatant of the inner cell compartment was collected to isolate the cells in suspension (Suspension Fraction), followed by three media washes which were also collected to isolate the semi-adherent cells (Semi-Adherent Fraction). The cells left adhering to the inner cell compartment (Adherent Fraction) were isolated after a 15-min trypsinisation. The three cell fractions were then pelleted via centrifugation (400g for 6min, RT), and the EV-rich supernatant of the Suspension Fraction was kept for further processing. Cells were then counted (in triplicate) using the Z1 Coulter® Particle Counter, followed by re-seeding of 3.9x10⁶ cells back (of Adherent Fraction) back into the Bioreactors. Cells from all fractions were then resuspended in complete RPMI-60

media supplemented with 20mM HEPES (final concentration 5×10^5 cells/ml), followed by addition of 3 μ M DRAQ7™ to monitor cell viability (143, 144), or 20 μ M DRAQ5™ to assess cell cycle (129), according to the manufacturer's protocols. Analysis was conducted using the FACSCalibur flow cytometer, with the following parameters: excitation laser 488nm, emission filters FL1: 530/30nm for GFP, FL2: 585/42nm for Tdtomato, FL3: 670nm long-pass emission filter for DRAQ5™ and FL4: 661/16nm for DRAQ7™. Compensation was used for Tdtomato and DRAQ5™ cell cycle analysis (FL3-FL2 =51%).

2.18.2.2. sEV-Associated Processes

Parallel to processing of the cell Fractions, the supernatants of the Suspension Fractions (EV-rich conditioned media) were also processed with the same protocol as the weekly Bioreactor Maintenance procedure (see [Section 2.18.1](#)). To clarify, the EV-rich conditioned media processing occurred weekly and not just during the characterisation procedure, i.e., collected from Weeks 2 to 4, Weeks 6 to 8 and Weeks 10 to 11. Then the conditioned media was pre-cleared and stored at -80°C, until sEV isolation by sucrose-cushion ultracentrifugation (see [Section 2.11](#)). It is important to note that prior to sEV isolation, the pre-cleared media was batched together: Weeks 2 to 4 (Batch 1), Weeks 6 to 8 (Batch 2) and Weeks 10-11 (Batch 3), as shown in [Figure 5.1](#).

Nanoscale Flow Cytometry

Fluorescence signal of isolated sEVs was assessed using the Apogee A50 microparticle flow cytometer (Apogee Flow Systems). For optimisation and comparison to sEVs, the following reference polystyrene beads were used as non-fluorescent standards: (a) 100nm NIST (Thermo Fisher, Cat. No. 3100A) and (b) 200nm NTA (Malvern Panalytical, Cat. No. NTA4089), as well as fluorescent standards: Tetraspeck™ microspheres (a) 100nm and (b) 200nm (ThermoFisher, Cat. No. T7279 and T7280) which emit blue/green/orange/dark red fluorescence. Furthermore, a manufacturer-supplied mixture of silica and polystyrene standards were also used to calibrate and perform quality control on the instrument (Apogee Standards, Apogee Flow Systems, Cat. No. 1493). The instrument was run at a steady flow speed of 1.5 μ l/min and light scatter was provided using the 405nm laser (50mW); green fluorescence signal was generated using the

488nm laser (50mW, emission 535/35nm) and orange fluorescence signal was generated using the 532nm laser (emission 580/30nm).

Each sEV sample was run in triplicate, and after calibration with the Apogee #1493 beads, a serial dilution test for coincidence and swarm effect was conducted. For this experiment, EV batches were pooled together in volume ratio of 1:1:1 (Batch 1-3, Weeks 2-11) to represent the entire sEV population and avoid batch-to-batch variability, and a serial dilution was done (1:1000, 1:2000, 1:5000, 1:10000, 1:20000, 1:50000 and 1:1000000) to estimate particle concentration (particle/ml), followed by linear regression to determine optimal sEV dilutions (see [Supplementary Figure 18](#)). The selected optimal sEV dilutions (1:20000 for GFP-CD63 and GFP-Parallel sEVs and 1:10000 for CD81-Tdtomato and Tom-parallel control sEVs) ensured that the number of particle events/sec detected by the Apogee microparticle flow cytometer remained stable and lower (~1000 events/sec) than the swarm threshold (>5000 events/sec).

Cryogenic Transmission Electron Microscopy (Cryo-TEM)

Cryogenic transmission electron microscopy (Cryo-TEM) experiments were performed by our collaborators Dr. Nicole Hondow and Dr. Andy Brown at the School of Chemical and Process Engineering at University of Leeds. Briefly, Cryo-TEM was conducted on a FEI Titan³ Themis G2 operating at 300kV fitted with 4 EDX silicon drift detectors and a Gatan One-View CCD. sEV samples were prepared for Cryo-TEM using a FEI Vitrobot mark IV plunge freezer. A 3.5 μ l drop of suspension was placed on a lacey carbon coated copper TEM grid (EM Resolutions), blotted at blot force 6 and then rapidly plunged into liquid ethane. A Gatan 914 cryo-holder was used for TEM, and the temperature maintained below -160°C to prevent devitrification. Cryo-TEM images were recorded at a total electron fluence of 5e⁻/Å² to limit devitrification of the sample during imaging. Cryo-TEM image analysis was conducted using the Fiji Software (v1.52c) (133), and involved maximum diameter measurements of EVs (n= 1000 vesicles counted for each EV type). CD81-Tdtomato and Tom-Parallel control EVs were selected for Cryo-TEM analysis and to exclude week-to-week variability, the three Bioreactor-derived EV batches (Batch 1 to 3) were all pooled together for each EV type in a 1:1:1 ratio, thus generating a pooled Batch 1-3 (Weeks 2-11) EV sample.

EV Isolation Method	Platform	Parental Cell line	Isolation/ Batch Number	BCA concentration (µg/ml)	NTA (Particles/ml)
Differential Ultracentrifugation	T75 tissue culture flask	CD81-Tdtomato	Isolation #1	125.62	1.11E+12
		Tom-Parallel control		123.52	1.28E+12
		GFP-CD63		115.26	6.97E+11
		GFP Parallel control		165.46	7.78E+11
Sucrose Cushion Ultracentrifugation	T175 tissue culture flask	CD81-Tdtomato	Isolation #2	747.02	N/A
		Tom-Parallel control		768.47	N/A
		GFP-CD63		253.06	N/A
		GFP Parallel control		513.94	N/A
Sucrose Cushion Ultracentrifugation	T175 tissue culture flask	CD81-Tdtomato	Isolation #3	924.03	N/A
		Tom-Parallel control		921.11	N/A
		GFP-CD63		1573.18	N/A
		GFP Parallel control		915.27	N/A
Sucrose Cushion Ultracentrifugation	CeLLine Bioreactor 1	CD81-Tdtomato	Isolation #4 Batch 1, Weeks 2-4	817.81	1.52E+13
	CeLLine Bioreactor 2	Tom-Parallel control		1607.74	2.45E+13
	CeLLine Bioreactor 3	GFP-CD63		874.56	2.39E+13
	CeLLine Bioreactor 4	GFP Parallel control		1240.31	1.93E+13
Sucrose Cushion Ultracentrifugation	CeLLine Bioreactor 1	CD81-Tdtomato	Isolation #5 Batch 2, Weeks 6-8	2457.71	4.21E+13
	CeLLine Bioreactor 2	Tom-Parallel control		3479.15	7.89E+13
	CeLLine Bioreactor 3	GFP-CD63		2995.68	4.49E+13
	CeLLine Bioreactor 4	GFP Parallel control		2035.34	3.19E+13
Sucrose Cushion Ultracentrifugation	CeLLine Bioreactor 1	CD81-Tdtomato	Isolation #6 Batch 3, Weeks 10-11	2424.18	2.64E+13
	CeLLine Bioreactor 2	Tom-Parallel control		2847.70	2.86E+13
	CeLLine Bioreactor 3	GFP-CD63		2326.68	2.91E+13
	CeLLine Bioreactor 4	GFP Parallel control		3018.66	2.6E+13
Sucrose Cushion Ultracentrifugation	CeLLine Bioreactor 1	CD81-Tdtomato	Batch 1-3, Weeks 2-11 * pooled Batches volume ratio 1:1:1	2059.31	N/A
	CeLLine Bioreactor 2	Tom-Parallel control		2199.87	N/A
	CeLLine Bioreactor 3	GFP-CD63		2005.10	N/A
	CeLLine Bioreactor 4	GFP Parallel control		2322.20	N/A
Sucrose Cushion Ultracentrifugation	CeLLine Bioreactors 5-8	CD81-Tdtomato	Isolation #7 Weeks 1-12	3033.50	2.84E+13
Sucrose Cushion Ultracentrifugation	CeLLine Bioreactor 9	GFP-CD63	Isolation #8 Weeks 1-12	1647.90	1.74E+13
Sucrose Cushion Ultracentrifugation	CeLLine Bioreactor 10	DU145	Isolation #9 Weeks 1-12	1473.71	2.16E+13

Table 2.2. Particle and protein concentrations of DU145-derived sEVs.

Particle and protein concentrations of DU145-derived sEVs calculated by BCA protein assay and NTA (respectively) of 9 separate sEV preparations isolated by either differential ultracentrifugation or sucrose cushion ultracentrifugation from 2D tissue culture flasks or CeLLine Bioreactors.

2.19. QD705 and EV-647 Dosing Experiments in DU145 and Y201

2.19.1. QD705 Dosing in DU145 Cells

30000 DU145 cells were seeded into 12-well plates in complete RPMI supplemented with 10% exoFBS and incubated at 37°C and 5% CO₂ for 24h. Next, cells were dosed with 3nM QD705 using the Qtracker®705 Cell Labelling Kit (ThermoFisher Scientific, Cat. No. Q25061MP) in serum-free media as previously described (145, 146). Briefly, the Qtracker™ carrier and Qtracker™ 705 were vortexed for 5sec, followed by addition of the Qtracker™ carrier in a falcon tube as a droplet; then Qtracker™ 705 was pipetted directly into the carrier droplet at a ratio of 1:1, to reach a final concentration of 3nM. The mixture was then incubated for 5min at RT, followed by addition of serum-free RPMI and a 10-sec vortex. Finally, 500µl of QD705 mixture was added per well and was left to incubate for 1h at 37°C (and 5% CO₂) with intermittent stirring every 15min. For control wells, Qtracker™ carrier was used alone. After incubation, cells were washed twice with media, followed by replacement with complete media. The QD705 cell uptake and retention was assessed for the next 4 days of the experiment (24-, 48-, 72- and 96-h post-labelling) by measuring the QD705 fluorescence intensity via flow cytometry using the BD FACSCalibur flow cytometer (excitation 488nm and emission FL3 (670nm long-pass filter)), which was calibrated using Dako FluoroSpheres (Agilent Technologies, Cat. No. K011011-2). This experiment was repeated 3 times (N=3) with triplicates for each control and 3nM QD705 –treated cell sample. Furthermore, the QD705 cell uptake was imaged using the ImagestreamX flow cytometer (Amnis) with 30.000 events collected for QD705-treated and control cells using the 488 nm excitation laser, 60X objective lens and 642–740 nm spectral channel for detection (pixel size 0.33µm, 2.5µm depth-of-field, 0.9 NA). Analysis for flow and imaging flow cytometry experiments was conducted in GraphPad Prism (v5), FlowJo™ (v10) and IDEAS® (Amnis).

2.19.2. Comparison of QD705 Dosing in DU145 vs Y201 Cells

7500 DU145 cells/well and 4000 Y201 cells/well were seeded in 8-well μ -Slides in a final volume of 300 μ l in complete RPMI or DMEM respectively, supplemented with 10% exoFBS and incubated for 24h at 37°C (and 5% CO₂). Cells were then dosed with QD705 as in [Section 2.19.1](#), except that the final volume of QD705 mixture added per well was 125 μ l (in duplicate for each condition). After dosing, cells were washed twice with media, followed by replacement with complete media (RPMI or DMEM depending on cell line). 24h and 72h post labelling, cells were fixed with 1X CellFIX and labelled with ActinGreen™ and NucBlue™ as mentioned previously, to label actin and nuclear DNA, respectively ([Section 2.8](#)). Multi-dimensional image acquisition was conducted on the Zeiss Axiovert 100 widefield microscope (x20 objective, 0.8 NA lens), for ActinGreen™ (Actin-488, Ex:489nm/Em:515nm), for NucBlue™ (DAPI, Ex:353nm/Em:465nm) and for QD705 (Ex:405nm/Em:669nm) and using the MetaMorph software (Z-step=0.2 μ m, 100 slices). Single-cell image analysis was done in the Fiji software (133) and is explained in [Section 2.21.1](#) and graphically shown in [Figure 2.1](#).

2.19.3. Comparison of QD705 Vs EV-647 Dosing in DU145 Cells

2.19.3.1. sEV Labelling with Alexa Fluor647 C₂ Maleimide Dye

Bioreactor-derived WT DU145 sEVs (Bioreactor No. 10, Weeks 1-12 isolation #10, see [Table 2.2](#)) were labelled with the AlexaFluor647 C₂ Maleimide dye, as reported previously (115) to generate the EV-647 population. Firstly, 200µg/ml AlexaFluor647 C₂ Maleimide dye (ThermoFisher Scientific, Cat. No. A20347) was added to a 30µl of sEV sample and diluted with 1XPBS up to final volume of 50µl, followed by incubation of the mixture for 1h (at RT) under continuous orbital shaking in the dark. Then, EV Spin Columns MW3000 (ThermoFisher Scientific, Cat. No. 4484449) were prepared according to manufacturer's instructions; specifically, 650µl 1xPBS was used to rehydrate the spin column for 15min at RT, followed by centrifugation (750g for 2min in RT) to remove the interstitial fluid. Then, the sEV-dye mixture was added to the top of the column, followed by another centrifugation (750g for 3min in RT) to finally elute the Maleimide-labelled sEVs (EV-647), whereas lower molecular weight contaminants like the free AlexaFluor647 C₂ Maleimide dye is being retained by the spin column. This process was repeated with a final mixture of dye and 1xPBS only (without sEVs), and the eluted solution was collected and used as a negative control to demonstrate the retention of free dye by the spin columns (used as controls in flow cytometry). Concentration of EV-647 after the labelling process was estimated by measuring 1µl on the Nanodrop™ 2000 Spectrometer.

2.19.3.2. Dosing with QD705 Vs EV-647

7500 DU145 cells were seeded in 8-well µ-Slides and incubated for 24h at 37°C (and 5% CO₂) prior to dosing. The next day, DU145 cells were dosed for 1h at 37°C with EV-647 (50µg/ml) or 3nM QD705 with intermittent stirring every 15min (see [Section 2.19.2](#)). After dosing, cells were washed with 1xPBS, fixed with 1X CellFIX, permeabilised with 0.1% Triton-X100 and labelled with ActinGreen™ and NucBlue™. Image acquisition was conducted on the Zeiss Axiovert 100 microscope (x63 objective, 1.6 NA oil lens) for ActinGreen™ (Ex:489nm/Em:515nm), for NucBlue™ (DAPI, Ex:353nm/Em:465nm), for QD705 (Ex:405nm/Em:669nm) and for EV-647 (Ex:650nm/Em:669nm) and using the MetaMorph software.

2.20. CD81-Tdtomato sEV Delivery in cell systems

2.20.1. CD81-Tdtomato sEV Dosing Optimisation in DU145

7500 DU145 cells/well were seeded in 8-well μ -Slides 24h prior to dosing (final volume 300 μ l) in complete RPMI supplemented with 10% exoFBS respectively. CD81-Tdtomato sEVs used for dosing derived from Bioreactors No.5-8 (Weeks 1-12, see [Table 2.2](#)). Specifically, CD81-Tdtomato sEVs were batched by pooling EV batches for Weeks 1-3, 4-6, 7-9 and 10-12 in a ratio 1:1:1:1 after a short vortex (10sec). Then, the pooled CD81-Tdtomato sEVs (Weeks 1-12) were vortexed again for 10sec and after a short spin were diluted in complete RPMI to reach concentration of 100 μ g/ml, after which 100 μ l were added in every well in duplicate (complete media used in separate wells as negative control). Then, the μ -Slides were manually mixed for 10sec and were placed in a humidifying chamber in the incubator (100cm dish with 35mm dish filled with 1XPBS).

Cells were then dosed with the EV-rich media for 1, 2 or 3h, followed by two media washes and addition of 300 μ l fresh complete media supplemented with 10%exoFBS and 20mM HEPES. Finally, the μ -Slides were imaged live using multi-dimensional image acquisition of Brightfield and Tdtomato fluorescence (Ex:554nm/Em:581nm) using the Zeiss Axio Observer Z1 microscope (x63 1.4 NA oil M27 lens and AxioCam506 detection camera) which generated Z-stacks that encompassed the entire cell (Z-stack interval= 0.5 μ m, 5 to 7 fields of view per condition). Single-cell image analysis was done in the Fiji software (133) as explained in [Section 2.21.2](#) and shown in [Figure 2.2](#). This experiment was repeated twice (N=2).

2.20.2. CD81-Tdtomato sEV Acute Delivery in DU145 and Y201 cells.

7500 DU145 cells/well and 4000 Y201 cells/well were seeded in 8-well μ -Slides 24h prior to dosing (final volume 300 μ l) in complete RPMI or DMEM supplemented with 10% exoFBS respectively. The batch of sEVs for dosing (Bioreactors No.5-8, CD81-Tdtomato sEVs Weeks 1-12) was generated as above ([Section 2.20.1](#)) and diluted accordingly in complete DMEM (with 10% exoFBS) to reach concentrations of 50 μ g/ml, 100 μ g/ml or 200 μ g/ml. Next, 125 μ l of each sEV concentration was added in each well in duplicate (complete media was also added in separate wells as negative control), followed by incubation for 1h (acute exposure) at 37°C, 5% CO₂.

After incubation, the EV-rich media was replaced by fresh complete media (DMEM for Y201 and RPMI for DU145 cells) supplemented with 10%exoFBS and 20mM HEPES. Finally, the μ -Slides were imaged live as detailed above ([Section 2.20.1](#)) directly after the 1h incubation, as well as 24- and 48-h post-incubation without any further media changes; the slides were kept in the humidifying chamber in-between imaging sessions. Single-cell image analysis was done as explained in [Section 2.21.2](#) and shown in [Figure 2.2](#).

2.20.3. CD81-Tdtomato sEV Chronic Delivery in Y201 Cells

For this experiment we repeated the above method ([Sections 2.20.2](#)), with Y201 cells dosed with 50 μ g/ml, 100 μ g/ml or 200 μ g/ml CD81-Tdtomato sEVs (Weeks 1-12) for 72h (chronic sEV delivery) in duplicate wells, with slides intermittently mixed twice every 24h. After incubation, the EV-rich media was replenished with fresh media and the μ -Slides were imaged live directly after the 72h incubation, as well as 24-, 48-, 72- and 96-h post-incubation. Live-cell imaging was done as previously explained ([Section 2.20.1](#)), with the following multi-image acquisition parameters: Z interval= 0.5 μ m, 20 slices and 16 fields of view per condition. Image analysis was done in the Fiji software (133) and involved Single-cell as well as Field-of-view analysis; these are explained in [Section 2.21.2](#) and shown in [Figure 2.2](#).

2.21. QD705 and CD81-Tdtomato sEV Dosing: Image Analysis

2.21.1. Single-cell Image Analysis for QD705 Dosing

Single-cell image analysis was done in the Fiji Software (v1.52c) (133) and firstly involved maximum intensity projection of the Z-stack QD705 fluorescence channel to generate single 2D images (i.e., QD705 channel max-projected image). Next, background was subtracted from each condition by removing the background fluorescence using the negative controls (different for each timepoint). For this action the Calculator Plus plugin was used with the following parameters: $i1$ =QD705 channel max-projected image, $i2$ = Background max-projected image, $operation$ = [Subtract: $i2 = (i1-i2) \times k1 + k2$]; ($k1=2.5$ $k2=-2.5$). Next, manual segmentation was done for every cell using the Actin-488 (cytoskeleton) image; each segmented ROI (Region of Interest) was saved and then used to extract single-cell images from the QD705 channel, followed by extraction of cell shape information (cell area, convexity, roundness, circularity). Next, the single-cell QD705 max-projected (and background-subtracted images) were duplicated followed by contrast enhancement (histogram normalisation with 0.2% saturation) and conversion to 8-bit using the "ScaleConversions" function to enable for automatic thresholding. Specifically, Li's automatic thresholding method (Minimum Cross Entropy thresholding method based on the iterative version of Li's algorithm (147)) was applied by firstly generating a mask based on the 8-bit converted and contrast enhanced image, which was then finally applied to the original maximally projected (and background subtracted) image to extrapolate fluorescence QD705 intensity measurements. Graphic representation of this method is shown in [Figure 2.1](#) and macro code is shown in [Supplementary Figure 2.A-D](#).

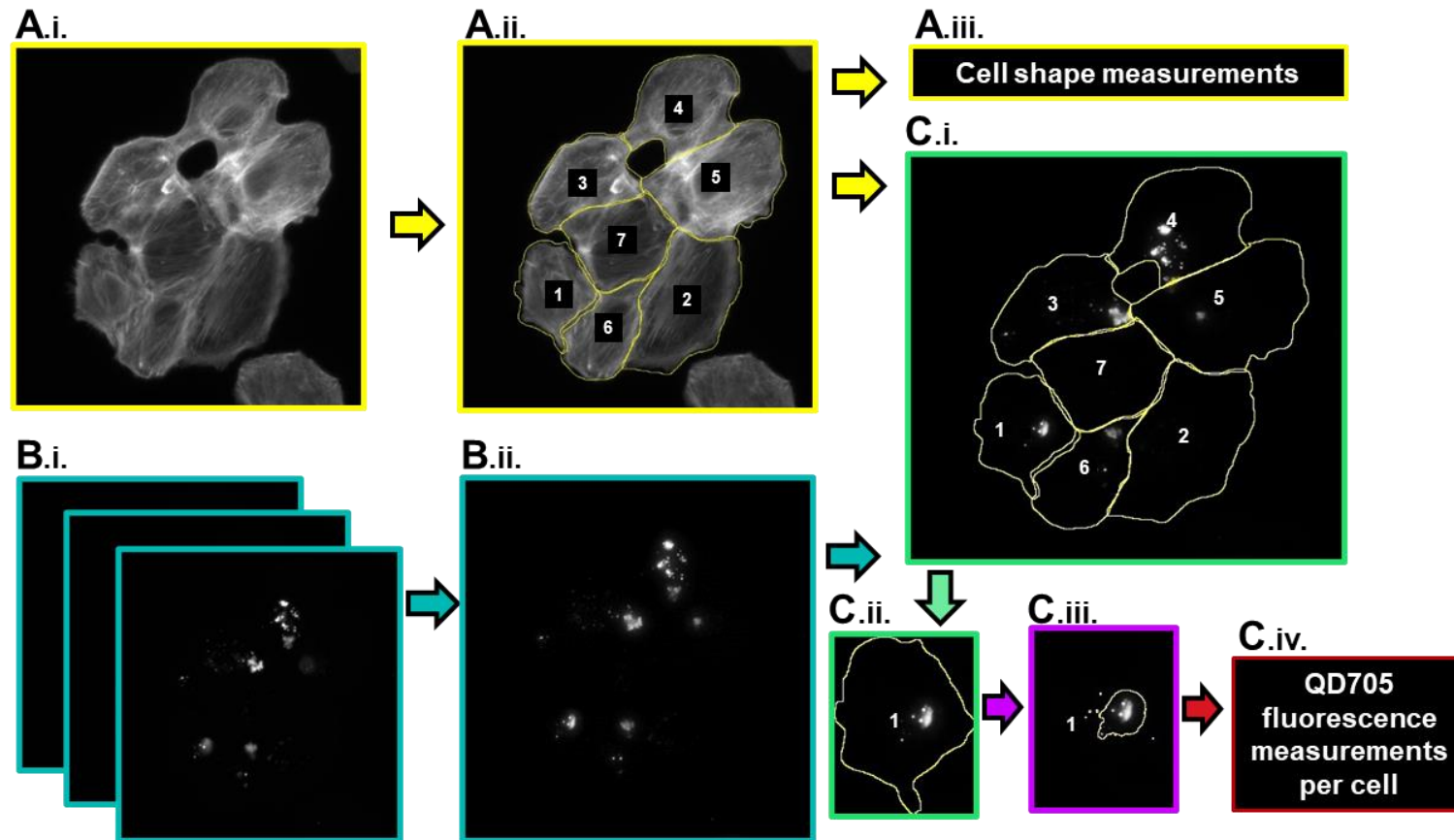


Figure 2.1. Single-cell image analysis with Li's Thresholding method for QD705-labelled cells.

A. Actin-488 images (cytoskeleton labelling) (i), were used to manually segment every cell and generated ROIs for every cell (ii), followed by cell shape measurements (area, convexity, roundness, and circularity) based on segmentation (iii). **B.** Fluorescence Z-stack images (QD705-labelled cells) (i), were Z-projected using maximum intensity projection (ii), followed by background subtraction (auto-fluorescence of control cells). **C.** Maximally projected and background-subtracted fluorescence images were segmented based on the previously generated ROIs (i) with every cell being duplicated (ii) followed by contrast enhancement (histogram normalisation with 0.2% saturation), conversion to 8-bit image and generation of a mask using Li's automatic Thresholding Method (iii), thus enabling mean or integrated QD705 fluorescence intensity measurements (iv).

2.21.2. Single-Cell and Field-Of-View Image Analysis for sEV Dosing

Image analysis of CD81-Tdtomato sEV dosing experiments was done in the Fiji Software (v1.52c) (133) and firstly involved maximum intensity projection of Z-stack Tdtomato fluorescence channel to generate single 2D images and subtraction of background from each condition by removing background fluorescence using the negative controls (different for each timepoint). For this action the Calculator Plus plugin was used with the following parameters: $i1$ =Tdtomato channel max-projected image, $i2$ = Background max-projected image, $operation$ = [Subtract: $i2 = (i1-i2) \times k1 + k2$]; ($k1=2.5$ $k2=-2.5$).

Next for Single-cell image analysis every cell was manually segmented using the Brightfield image; each segmented cell ROI was saved and then used to extract single-cell images from the Tdtomato channel, followed by extraction of cell shape information (cell area, convexity, roundness, circularity). Then, every single-cell Tdtomato max-projected (and background subtracted image) was duplicated followed by contrast enhancement (histogram normalisation with 0.2% saturation) and conversion to 8-bit using the "ScaleConversions" function to enable for automatic thresholding. Finally, Li's automatic thresholding method (147) was applied by firstly generating a mask based on the 8-bit converted and contrast enhanced image, which was then applied to the original maximally projected (and background subtracted) image to extrapolate fluorescence Tdtomato intensity measurements. Graphic representation of this method is shown in [Figure 2.2.A](#) and macro code is shown in [Supplementary Figure 2.A-D](#).

Alternatively, for the Field-of-view image analysis, after background subtraction, the mean fluorescence intensity per field-of-view (for 0- to 96-h timepoints) was directly calculated using Li's automatic thresholding method (as explained above). Specifically, entire field-of-view max-projected and background subtracted Tdtomato channel images were duplicated followed by contrast enhancement (histogram normalisation with 0.2% saturation) and conversion to 8-bit using the "ScaleConversions" function to enable for automatic thresholding. Next, Li's automatic thresholding method was used by firstly generating an entire field-of-view mask that was then applied to the original maximally projected (and background-subtracted) Tdtomato image to extrapolate fluorescence intensity measurements. Finally, after manual counting of fluorescent cells in each field of view, the mean fluorescence per field-of-view was divided by the number of cells in each field to estimate the Tdtomato fluorescence per image and per cell. Graphic representation of this method is shown in [Figure 2.2.B](#) and macro code shown in [Supplementary Figure 2. A,B,E](#).

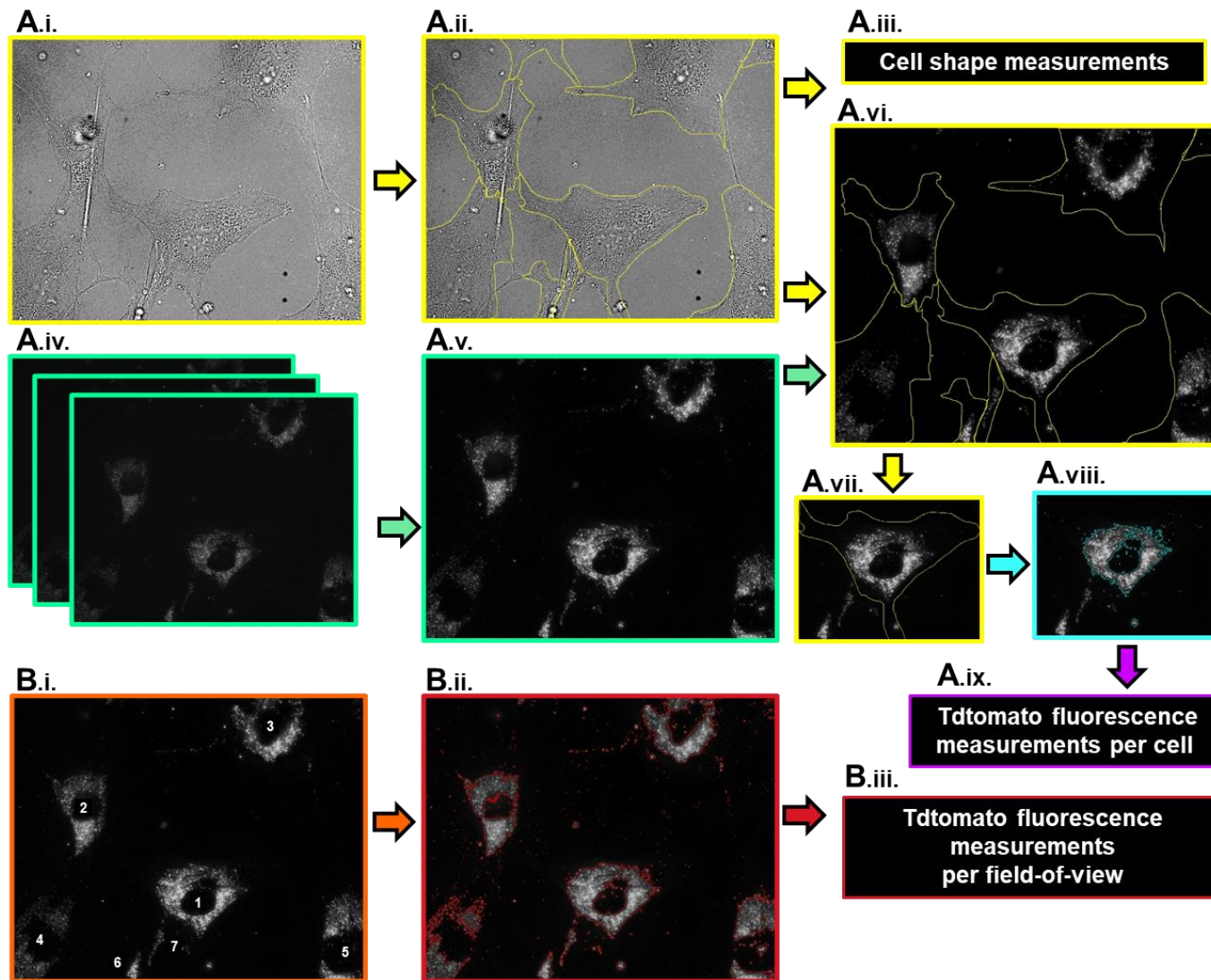


Figure 2.2. Single-cell and Field-of-view image analysis schematic.

A. Single-cell image analysis: Brightfield images (i), were used to manually segment every cell and generated ROIs for every cell (ii), followed by cell shape measurements (area, convexity, roundness, and circularity) based on segmentation (iii). Fluorescence Z-stack images of Tdtomato-labelled cells (iv), were Z-projected using maximum intensity projection, followed by background subtraction (auto-fluorescence of control cells) (v). The maximally projected and background-subtracted fluorescence images were then segmented based on the previously generated ROIs (vi) with every cell being duplicated (vii) followed by contrast enhancement (histogram normalisation with 0.2% saturation), conversion to 8-bit image and by generation of a mask using Li's automatic Thresholding Method (viii), to measure Tdtomato fluorescence intensity per cell (ix).

B. Field-of-view image analysis: maximally projected and background subtracted fluorescence images (from A.v) were used to count fluorescent cells B(i) followed by contrast enhancement (histogram normalisation with 0.2% saturation), conversion to 8-bit image and by generation of a mask using Li's automatic Thresholding Method (ii), to measure Tdtomato fluorescence intensity per field-of-view (iv).

2.22. Assessment of Osteogenic Differentiation by sEVs

2.22.1. Late Osteogenic Differentiation Assessment

Chronic Dosing with CD81-Tdtomato sEVs: Y201 cells were cultured in 8-well Ibidi μ -Slides (4000 cells/well) in complete DMEM media supplemented with 10% exoFBS (regular media). Osteogenic media was also prepared as complete DMEM was supplemented with β -glycerophosphate (5mM), dexamethasone (10nM) and 50 μ g/mL ascorbic acid. CD81-Tdtomato sEVs (Bioreactors No.5-8, Weeks 1-12) were prepared as explained in [Section 2.20.1](#) and were diluted in regular or osteogenic media to reach concentrations of 50 μ g/ml, 100 μ g/ml and 200 μ g/ml (6 different preparations). For dosing, 125 μ l of each sEV concentration (in regular or osteogenic media) was added in every μ -Slide well, along with negative control wells (regular or osteogenic media only). Then, the μ -Slide was manually mixed for 10sec and was placed in a humidifying chamber at 37°C (5%CO₂) for 72h (chronic sEV delivery), with the slide intermittently mixed twice every 24h. After incubation, the EV-rich media was removed from cells, followed by a media wash (with regular or osteogenic media respectively) and then replenishment with fresh media (regular or osteogenic). This media was changed every 3 days up to day 21 (i.e., 18 days after the end of the 72-h sEV dosing).

At day 21, the Alizarin Red S calcium stain was used to visualise and measure the potential mineralised matrix depositions that form due to osteoblast mineralisation (148). Specifically, the media was carefully removed from the wells, followed by three gentle 1xPBS washes. Cells were then fixed with 4 % PFA (250 μ l per well) for 15 min at RT, followed by a wash with dH₂O and staining with 250 μ l Alizarin Red S solution (40mM, Sigma Aldrich, Cat. No. A5533) for 30min in the dark (with gentle agitation, at RT). After staining, the dye was carefully removed and the μ -Slide was washed 6 times with 50% Ethanol in dH₂O, by placing in a shaking platform for 15 min. After washing, the μ -Slide was left for 2 min to air dry and was imaged in the Zeiss Axio Observer Z1 microscope to visualise the calcium deposits and potential osteogenic nodules (x5 lens, AxioCam506 coloured detection camera, 5X5 Tile). Then, to quantify calcium deposits a 10%w/v solution of Cetylpyridinium Chloride (CPC, Sigma Aldrich, Cat. No. C0732) was used. Specifically, 250 μ l CPC was added to every well, and then the μ -Slide was placed on a shaking platform for 16h until the red colour (from Alizarin Red S stain) was removed. Then, the supernatant was transferred to opaque-walled, transparent-bottomed plates and absorbance was read at 562nm in the PHERAStar plate reader.

2.22.2. Early Osteogenic Differentiation Assessment

Chronic Dosing with GFP-CD63, CD81-Tdtomato and WT DU145 sEVs: Y201 cells were cultured in 24-well plates (8,000 cells/well) in complete DMEM supplemented with 10% exoFBS (regular media) 24h prior to dosing. The following day three type of sEVs were prepared for dosing: CD81-Tdtomato, GFP-CD63 and WT DU145 sEVs. These sEVs were all generated in CELLine Bioreactor Flasks (Bioreactors No.5-8, 9 and 10 respectively, see [Table 2.2](#)) and were isolated in time-dependent batches i.e., Batch 1: Weeks 1-3, Batch 2: Weeks 4-6, Batch 3: Weeks 7-9 and Batch 4: Weeks 10-12; these batches were pooled together in a ratio of 1:1:1:1 after a short vortex (10 sec) and spin. This generated the following pooled sEV samples: (i) CD81-Tdtomato (Weeks 1-12, used previously for dosing), (ii)GFP-CD63 (Weeks 1-12) and (iii) WT DU145 sEVs (Weeks 1-12). These pooled sEV samples were again vortexed for 10 sec and after a short spin were further diluted in media (control or osteogenic) to reach concentrations of 50µg/ml, 100µg/ml and 200µg/ml as shown in [Table 2.3](#).

Next, media was discarded from the 24-well plates and 250µl of each sEV concentration (in regular or osteogenic media) was added in every well, along with negative control wells (regular or osteogenic media only). Next, PBS was added in-between wells to avoid evaporation and the plates were manually mixed for 10sec, after which they were placed in the incubator (37°C, 5%CO₂). Then, at set time-points, plates were sacrificed for RNA extraction, specifically: (i) at 24h of continuous sEV dosing, (ii) at 72h of continuous sEV dosing, (iii) at 24h after the 72- h sEV dosing (96h) and finally (iv) at 72h after the 72-h sEV dosing (144h). Note that the plates were intermittently mixed (twice) every 24h for the first 72h of the assay.

Table 2.3. sEV dosing experimental conditions for Y201 osteogenic differentiation.				
	WT DU145 sEVs (Weeks 1-12)	CD81-Tdtomato sEVs (Weeks 1-12)	GFP-CD63 sEVs (Weeks 1-12)	Negative Control
Regular Media	50µg/ml 100µg/ml 200µg/ml	50µg/ml 100µg/ml 200µg/ml	50µg/ml, 100µg/ml*	0µg/ml
Osteogenic media	50µg/ml 100µg/ml 200µg/ml	50µg/ml 100µg/ml 200µg/ml	50µg/ml, 100µg/ml*	0µg/ml
*GFP-CD63 sEVs were not dosed at the highest concentration (200µg/ml) due to insufficient sample.				

2.22.2.1. RNA Extraction and cDNA Synthesis

RNA Extraction, Cleanup and Concentration

To prepare for RNA isolation, the conditioned media from the plates was removed at the time-points mentioned above, followed by washing with 1XPBS and RNA extraction using the RNeasy Mini Kit (Qiagen, Cat. No. 74106). Briefly, the plate was placed on ice and 350µl lysis buffer (Buffer RLT supplemented with 1%v/v β-mercaptoethanol) was added, followed by disruption and homogenisation of the lysate, short vortex (10-20sec) and then storage at -80°C (long-term storage). When all plates were lysed at the end of the experimental timeline, the lysates were simultaneously processed for RNA extraction. After a 3-min centrifugation (max speed), the supernatant was removed, followed by addition of 70% ethanol (350µl) and resuspension. Then the sample was transferred to a RNeasy Mini spin column, placed in a collection tube, and was centrifuged at 10000g for 15sec, after which the flow-through was discarded. Next, 700µl of Buffer RW1 was added to the column, centrifuged and flow-through was disposed. Next 500µl of Buffer RPE were added to the column, followed by centrifugation (10000g for 15 sec) and removal of the flow-through; this step was repeated with a longer centrifugation step (2min at 10000g). Finally, the RNeasy spin column was transferred in a new collection tube and 30µl of RNase-free water were added directly to the spin column membrane, followed by centrifugation (1min at 10000g) to elute RNA.

After RNA extraction, the RNA samples were further purified and concentrated using the GeneJET RNA Cleanup and Concentration Micro Kit (ThermoFisher, Cat. No. K0841) according to the manufacturer's instructions. Briefly RNA samples were adjusted to 200µl of RNase-free water, followed by addition of 100µl of binding buffer and resuspension. Then, 300µl of 100% ethanol was added, followed by transfer to the purification column and centrifugation at 14000g for 1min (flow-through was discarded). 700µl of Wash Buffer 1 was then added to the column, followed by centrifugation (14000g, 1min) and disposal of the flow-through. The next step was repeated twice and involved addition of 700µl of Wash Buffer 2 to the column, followed by centrifugation (14000g, 1min), and disposal of the flow-through. Then, the empty column was again centrifuged (14000g, 1min), to completely remove any residual wash buffer, followed by its transfer to a new collection tube. Finally, RNase-free water (10µl) was added to the column followed by centrifugation for 1min at 14000g to elute the concentrated RNA, which was then stored at -80°C. The concentration and purity of RNA was measured using the Nanodrop™ Spectrometer (absorbance ratio 260:280nm >1.7 for high quality RNA sample).

cDNA Synthesis by Reverse Transcription

After determination of RNA concentration, 0.5µg of RNA was mixed with 0.5µl of random hexamer primers (Promega, Cat. No. C1181) and made up to 6.5µl with RNase/DNase-free water (Invitrogen, Cat. No. AM9938). This was mixed and heated to 70°C (5 min), followed by cooling on ice (5min). Then a master mix of 2.5µl mmLV 5xbuffer (Cat. No. M531A), 0.5µl RNasin (20u, Cat. No. N2611), 2.5µl deoxynucleotide triphosphate mix - dNTPs (10mM, Cat. No. U1330) and 0.5µl mmLV reverse transcriptase-RT (100u, Cat. No. M1701) was added to each sample; these were all purchased from Promega. This master-mix was then incubated at 25°C for 10min (primer annealing), 42°C for 1h (extension) and finally at 95°C for 5min (enzyme deactivation) in the S1000 thermal cycler (BioRad). Synthesised cDNA was stored at -20°C until required. Note that RNA was reverse transcribed and matched to the sample with the lowest RNA concentration to control for RT bias.

2.22.2.2. Quantitative polymerase chain reaction (qPCR)

To evaluate the effect of sEVs on expression of osteogenic-associated genes (ALP, RUNX2) by Y201 cells, the isolated RNA from treated cells was assessed by quantitative polymerase chain reaction (qPCR). In a 25µl PCR reaction, 2.5µl cDNA (8ng) was mixed with 12.5µl SYBR™ Green PCR Master Mix (Thermo Fisher, Cat. No. 4309155, contains: AmpliTaq Gold® DNA Polymerase, dNTPs with dUTP, Passive Reference Dye (ROX) and optimized buffer), 2µl forward primer (200nM), 2µl reverse primer (200nM) and 6µl of water for the following genes (every sample was assessed in triplicate for each gene), as shown in [Table 2.4](#).

Gene	Primer Sequence
GAPDH (selected reference gene)	F 5'-GCCTCTTTACTACCACTCACC-3' R 5'-AGATGGCAGTGACCGTGGGAAT-3'
ALP (Alkaline Phosphatase)	F 5'-GTACGAGCTGAACAGGAACAACG-3' R 5'-CTTGGCTTTTCTTCATGGTG-3'
RUNX2 (Runt-related transcription factor 2)	F 5'-GTGGACGACGCAAGAGTT-3' R 5'-TTCCCGAGGTCCATCTAC-3'
***Due to large sample size only 3 genes could be tested in each plate. GAPDH (reference gene), ALP and RUNX2 were selected from an optimization of gene expression comparison between day 7 (earliest time point RNA available) and day 21 of osteogenic differentiation.	

Then samples (in 96-well plate) were loaded into the StepOnePlus™ real time PCR thermocycler (Thermofisher). Due to large sample number, each qPCR plate contained samples of cells treated with sEVs at one concentration (i.e., 0µg/ml, 50µg/ml, 100µg/ml or 200µg/ml, in both regular and osteogenic media) and one time-point (24h, 72h, 96h or 144h) for comparison of gene expression (GAPDH, ALP, RUNX2). Reaction steps: initial denaturation at 95°C for 10min, then amplification for 40 cycles, with each cycle consisting of a 95°C denaturation step for 15sec and then an annealing step at 60°C for 30sec. After completion of the reaction, the cycle threshold (CT) value (number of cycles required to detect a fluorescent signal) was calculated to determine relative RNA expression, with GAPDH being the selected reference gene. The established $2^{-\Delta\Delta Ct}$ method was adopted to analyse the relative quantities of gene expression (149).

Note that RNA extraction, cDNA synthesis and qPCR analysis was conducted by Dr Rachel-Howard Jones as part of a collaboration for this experiment.

2.23. Data and Statistical Analysis

Data analysis for flow cytometry and imaging experiments was conducted in FlowJo (v10)(130) as well as the freely available Fiji Software (v1.52c) (133) or CellProfiler™ (v.3.1.8) (131), where appropriate. Statistical analysis was performed using GraphPad Prism (v5) which included one-way or two-way ANOVA with Tukey's or Bonferroni's multiple comparisons post-test (respectively) or Student's T-test with Welch's correction. These tests were performed where appropriate (stated in figure legends), to assess the significance of means differences. Significant differences were denoted as either * $p < 0.05$, ** $p < 0.01$, *** $p < 0.0001$ or **** $p < 0.00001$. Error bars denoted standard deviation or standard error of the mean.

Statistical analysis was also conducted in FlowJo (v10) and involved the Chi Square distribution comparisons test (130, 150, 151). This algorithm can detect differences between populations by binning the "control" and "test" sample (using the same number of bins) so that their variance in standard deviations (SD) can be measured by the Chi Square statistical test. The Chi Square value is then converted into a T(X) metric value that can be used to estimate the probability that a test population is different from a control population. In this study the baseline variance was determined by calculation of the variance between control populations; this provided the minimum value of T(X) (baseline T(x) value). The test populations in comparison were considered significantly different when the estimated T(X) values were larger than the baseline T(x) values. FlowJo statistical analysis also involved the comparison algorithms Overton and SE (Super-Enhanced) Dymax % Positive algorithms (152). The Overton % Positive algorithm was used to calculate the percentage of different events between two distributions by subtracting one from the other. The SE Dymax % Positive algorithm was also used as a comparison and calculated the percentage of different events between two distributions by normalizing the data to a unit scale to protect against outliers, and by factoring in the distribution of the data.

CHAPTER 3:
Characterisation of Prostate
Cancer Cell Lines Generating
Endogenously Fluorescent
Extracellular Vesicles

3.1. Introduction

The understanding of sEV biogenesis, dissemination through the tissue microenvironment, cell uptake and distribution through the propagating cell population, is of particular importance for investigating the roles of these vesicles in pathological conditions. This would include understanding sEV-mediated processes in cancer (41, 42), as well as their use as potential biomarkers (153) and as therapeutic drug delivery systems (154, 155). Current sEV analysis methods like Electron Microscopy, Nanoparticle Tracking Analysis (NTA), and Nanoscale Flow Cytometry are useful to characterise their physical properties, size, concentration, and cargo. However, to visualise and track spatiotemporal behaviour of sEVs *in situ*, high-resolution imaging is essential (100, 108).

Currently, there are technical limitations for detection and tracking of endogenous sEVs, as well as restrictions for using suitable *in vitro* and *in vivo* models for direct imaging (100, 102, 120). Especially due to the diffraction-limited sub-resolution size of sEVs, several methods have been developed to fluorescently-label sEVs, thus enabling their detection and tracking *in vitro* and *in vivo* using Fluorescence Microscopy (explained in detail in the Introduction).

One of the most common methods of sEV labelling is organic dyes, usually lipophilic (e.g., PKH26, PKH67, Dil, DiD) or membrane-permeable compounds (e.g., CFSE and CFDA). However, these dyes have various disadvantages; for example, lipophilic dyes have the propensity to “leak” from sEVs to other cell compartments or EV co-isolates like lipoproteins, or form micelles resulting to artefacts, or even induce structural modifications to sEV membranes resulting to increase of their size, leading to changes in their uptake dynamics or function (102-105). It was previously shown that uptake of larger EVs is less efficient than smaller EVs (106). Membrane-permeable compounds also have limitations, like their spontaneous hydrolysis, which results to higher fluorescence background that can ultimately reduce signal-to-noise ratio and make their detection by microscopy challenging (107). Finally, a common limitation of all organic dyes is that they can only be used to exogenously label sEVs; thus, they are not suitable for studies of sEV biogenesis or cell-to-cell transfer (102, 103).

In order to study sEV biogenesis, tracking from cell-to-cell, and cell uptake, many studies design “fluorescent sEV reporters” by generating stable cell lines expressing fluorescent proteins fused with sEV-associated proteins, which ultimately produce endogenously fluorescent sEVs; this allows for sEV studies without their prior isolation, thus avoiding potential bias due to choice of isolation method (100). Usually, tetraspanins

(CD9, CD63 and CD81) are chosen to be fused with fluorescent proteins, as they are highly conserved, structurally well-characterised, and highly enriched in sEVs (4, 19, 21, 156); hence they provide a specific method of sEV visualisation, shown in a plethora of *in vitro* and *in vivo* studies (116-123). Advantageously, as the fluorescent proteins are specifically conjugated into sEV-associated proteins, this labelling strategy also avoids false positive signals and artefacts observed with organic dyes (100).

However, there are also some limitations to this approach, for example, genetically encoding fluorescent proteins fused to specific sEV markers may result in labelling of specific subpopulations of sEVs, and not the entire sEV population, thus introducing bias. Furthermore, this approach may induce overexpression of sEV-associated proteins like tetraspanins, which might inadvertently cause changes in the phenotype and function of generated sEVs, as these proteins are central players in sEV biogenesis (19, 21). Despite this established role of tetraspanins, most studies using these fluorescent sEV reporters fail to acknowledge this issue and do not thoroughly investigate changes in the phenotype of engineered cells or EVs (116-121).

Our study focused on generating stable DU145 prostate cancer (PCa) cell lines, secreting endogenously-fluorescent sEVs by conjugating tetraspanins (CD63 or CD81) with fluorescent proteins (GFP or Tdtomato, respectively). However, acknowledging that this might induce overexpression of tetraspanins at the cellular level (and potentially the sEV level), we also investigated any potential phenotypic changes that might have occurred both in the engineered cells and the generated EVs due to these manipulations.

3.2. Aims and Objectives

In order to facilitate fluorescence detection of sEVs for cell uptake, retention, and distribution studies, we aimed to establish “fluorescent sEV reporters”. Opting for the tetraspanin- fluorescent protein fusion approach, we hypothesised that there would be some degree of tetraspanin overexpression in the engineered stable cell lines, which might have significant impact on the general properties of the cells and generated EVs. Hence, once these cell lines were established, we aimed to characterise both the phenotype of engineered cells and the EVs they produce, in order to determine the suitability of these research tools for these intended purposes. To attend to these aims we identified the following main objectives:

- To transfect DU145 PCa cells with plasmids genetically encoding tetraspanin-fluorescent protein fusions; specifically, GFP-CD63 or CD81-Tdtomato.
- To undertake serial fluorescence-activated cell sorts to enrich for fluorescently positive cells, and to establish the stability of each transfected cell line.
- To assess cell cycle, growth, morphology and membrane expression of sEV-associated protein markers for stable cell lines expressing GFP-CD63 or CD81-Tdtomato.
- To utilise stable cell lines expressing GFP-CD63 or CD81-Tdtomato for EV isolation.
- To determine EV size distribution and expression of sEV-associated protein markers.
- To detect and characterise fluorescent sEVs via confocal fluorescence microscopy.

3.3. Results

Fluorescent labelling of sEVs is essential to allow for their detection using an optical detection platform, such as flow cytometry or microscopy. Thus, the DU145 PCa cell line was used as the parent cell line for generating stable cell lines expressing fluorescently labelled EV-associated tetraspanins (GFP-CD63 or CD81-Tdtomato). The GFP-CD63 plasmid was generated by Dr. Paul Luzio and involved fusion of GFP to the N-terminus of CD63, and the CD81-Tdtomato plasmid was generated by Dr. Michael Davidson and involved fusion of Tdtomato to the C-terminus of CD81 (see Introduction, [Figure 1.6.D.i](#)); both plasmids were purchased from Addgene (GFP-CD63: #62964 and CD81-Tdtomato: #58078). Detailed plasmid maps are shown in Supplementary Figure 1. The GFP-CD63 and CD81-Tdtomato DU145 stable cell lines were generated to enable studies such as EV delivery, cell uptake and retention in dynamic cell systems; these will be discussed in subsequent chapters.

3.3.1. **Generation of Stable Cell Lines Expressing Fluorescently Conjugated Tetraspanins.**

3.3.1.1. **Transfection Optimisation**

Firstly, selection and optimisation of the most appropriate transfection method was conducted for DU145 cells. Initial transfection optimisations were performed using 25ng of GFP-CD63 DNA and the transfection reagents tested were FuGENE® HD, Lipofectamine™2000, Lipofectamine™3000 and Lipofectamine™ LTX Reagent with PLUS™ Reagent. [Tables 3.1-3](#) summarise our observations by widefield fluorescence microscopy (with a simple scoring system) for transiently transfected cells regarding transfection efficiency, expression level and overall toxicity (apparent by number of detached and/or dead cells). We observed that Lipofectamine™3000 resulted in the highest transfection efficiency and moderate toxicity, with a range of fluorescence expression, and we thus selected it for further optimisation ([Table 3.1](#)).

Secondly, following selection of the optimal transfection reagent (Lipofectamine™3000), we conducted further optimisation regarding DNA concentration, DNA: Lipofectamine™3000 ratio and incubation time, in order to increase transfection efficiency while simultaneously minimising toxicity. 25, 50 or 100ng of GFP-CD63 DNA were used for transfection in 1:3 or 1:5 DNA: Lipofectamine™3000, followed by incubation within cells for 4, 6 or 8h. We observed that 50ng of DNA in ratio of either 1:3

or 1:5 DNA: Lipofectamine™3000 incubated within cells for 4h, resulted in the highest transfection efficiency and the minimum toxicity (Table 3.2).

Thirdly, a final optimisation experiment was conducted for transfecting GFP (untagged), GFP-CD63, Tdtomato (untagged) and CD81-Tdtomato DNA in DU145 cells using 50ng of DNA in 1:3 or 1:5 DNA: Lipofectamine™3000 ratio incubated within cells for 4h (Table 3.3). It was determined that the optimal transfection combination is 50ng of DNA transfected in a ratio of 1:5 DNA: Lipofectamine™3000 and incubated within cells for 4h, which gave the highest transfection efficiency and moderate toxicity for all the different DNA constructs tested. These transfection parameters were used further in a larger scale, to transfect a higher number of cells for the generation of stable cell lines.

Table 3.1. Evaluation of transfection reagents effects on transfection efficiency, cell expression level and overall toxicity.

Transfection Reagent	Time post-transfection	Transfection Efficiency	Expression Level	Toxicity
FuGENE® HD	24h	+	+	-
Lipofectamine™2000		++	++ to +++	+++
Lipofectamine™3000		+++	++ to ++++	++
Lipofectamine™ LTX Reagent with PLUS™ Reagent		++	++	+
FuGENE® HD	48h	+	+	-
Lipofectamine™2000		+	+ to ++	+++
Lipofectamine™3000		++++	+ to ++++	+++
Lipofectamine™ LTX Reagent with PLUS™ Reagent		++	+ to ++++	++
FuGENE® HD	72h	+	+ to ++	+
Lipofectamine™2000		+++	+ to +++	+++
Lipofectamine™3000		++++	+ to ++++	+++
Lipofectamine™ LTX Reagent with PLUS™ Reagent		++	+ to ++	++

**Note:
Transfected DNA: 25ng GFP-CD63, DNA:Transfection Reagent Ratio 1:3, incubation within cells: overnight (O/N)*

Table 3.2. Evaluation of DNA concentration, DNA: Lipofectamine™3000 ratio and incubation time, for transfection efficiency, cell expression level and overall toxicity.

GFP-CD63 DNA Concentration	DNA:Lipofectamine™3000 Ratio	Incubation Duration	Transfection Efficiency*	Expression Level*	Toxicity*
25ng	1:3	8h	-	-	-
25ng	1:5	6h	-	-	-
25ng	1:5	8h	+	+	+
50ng	1:3	4h	++	+ to ++	-
50ng	1:3	6h	++	+ to ++	+
50ng	1:3	8h	++	+ to ++	++
50ng	1:5	4h	+++	+ to +++	++
50ng	1:5	6h	++	+ to ++++	+++
50ng	1:5	8h	++	+ to ++++	++++
100ng	1:3	4h	+++	++ to ++++	++++
100ng	1:3	6h	++	++ to +++++	+++++
100ng	1:3	8h	++	++ to +++++	+++++

**Assessed 24 hours post-transfection via widefield fluorescence microscopy*

Table 3.3. Evaluation of 1:3 or 1:5 DNA: Lipofectamine™3000 Ratio on transfection efficiency, cell expression level and overall toxicity for various DNA constructs.

DNA Construct	DNA Concentration	Incubation Duration	DNA:Lipofectamine™3000 Ratio	Transfection Efficiency*	Expression Level*	Toxicity*
GFP-CD63	50ng	4h	1:3	+	+to +++	+
			1:5	++	+to ++++	++
GFP			1:3	+	+to +++++	+
			1:5	++	+to +++++	++
CD81-Tdtomato			1:3	+	+to +++++	++
			1:5	++	+to +++++	+++
Tdtomato			1:3	+	+	-
			1:5	+++	+++to +++++	++

**Assessed 24 hours post-transfection via widefield fluorescence microscopy*

3.3.1.2. Transfection and Sequential Sorting

After transfection optimisation, we conducted a larger-scale transfection of GFP-CD63 and CD81-Tdtomato in order to generate stable cell lines; 72h post-transfection, the cells were put under continuous selection with the antibiotic Geneticin (G418, 500µg/ml). Starting one week after G418 selection, fluorescence expression of the GFP-CD63 and CD81-Tdtomato DU145 cells was assessed via flow cytometry, and four weeks after G418 selection, the stable cells were sorted sequentially via FACS (Fluorescence-Activated Cell Sorting) to enrich the fluorescent cells. [Figure 3.1](#) presents the timeline of FACS (via the FACSAria III cell sorter) and monitoring of fluorescence expression (via the FACSCalibur flow cytometer). Of note, the FACSCalibur flow cytometer excitation laser (488nm) is not optimal for the Tdtomato orange fluorescent protein (excitation maxima 554nm), thus cells with low fluorescence might be under-represented in the total percentage of fluorescent cells.

We observed that the GFP-CD63 cell line was enriched to more than 90% positive cells after 3 sorts ([Figure 3.1](#), Day 89 post-transfection) and fluorescence expression was stable for at least 80 days (Day 175 post-transfection). The CD81-Tdtomato cell line was enriched to about 80% fluorescence expression after 9 sorts ([Figure 3.1](#), Day 139 post-transfection). For 3 of those FACS cycles, a sub-population of cells with intermediate fluorescence expression was sorted ([Figure 3.1](#), Days 79, 89 and 106 post-transfection). [Supplementary Figure 3](#) describes the FACS gating strategy for sorting GFP-CD63 and CD81-Tdtomato cells.

3.3.2. Phenotypic Characterisation of Stable Cell Lines

3.3.2.1. Fluorescence Profile of GFP-CD63 and CD81-Tdtomato Cells

The fluorescence expression of GFP-CD63 and CD81-Tdtomato cells was monitored long-term via flow cytometry, as we mentioned above ([Figure 3.1](#)). Wild-Type (WT) non-transfected DU145 cells of the same cell passage were monitored in parallel to this timeline and were used as controls; namely “GFP-Parallel” and “Tom-Parallel” controls, respectively. These WT parallel cell lines were used to control for any potential phenotypic changes due to an aging cell line; the CD81-Tdtomato cells were 20 cell

passages older than GFP-CD63 cells due to the longer duration of FACS (9 cycles for CD81-Tdtomato vs 3 cycles for GFP-CD63 DU145 cells).

After the final sorting cycles and enrichment of the GFP-CD63 and CD81-Tdtomato cells, we investigated their stability, scatter, and fluorescent properties at 80- and 30-days post-enrichment, respectively, in comparison to GFP-Parallel and Tom-Parallel controls via flow cytometry. We observed that GFP-CD63, and GFP-Parallel control cells had similar scatter properties (size and granularity). This was evident from the Forward Scatter (FSC-H) Vs Side Scatter (SSC-H) plots of GFP-CD63 (Mean FSC-H=421, Mean SSC-H=176) and GFP-Parallel controls (Mean FSC-H=423, Mean SSC-H=169) ([Figure 3.2.A.i,ii](#)).

On the other hand, we observed that CD81-Tdtomato cells exhibited some differences to Tom-Parallel controls, as they were of smaller size and lower granularity; the FSC-H Vs SSC-H scatter plots for CD81-Tdtomato (Mean FSC-H=414, Mean SSC-H=198) and Tom-Parallel controls (Mean FSC-H=465, Mean SSC-H=225) are shown in [Figure 3.2.A.iii,iv](#). These results suggested that expression of CD81 in DU145 might have induced changes in cell morphology, but further investigation is needed to confirm this, especially when cells are attached to a substrate.

Regarding their fluorescence properties, this experiment demonstrated that GFP-CD63 and CD81-Tdtomato cells retained their fluorescence for at least 30-days post-stabilisation, as ~95% and ~78% of cells (respectively) were still fluorescent at that time ([Figure 3.2.B.i,iii](#)). In addition, this experiment showed that the GFP-CD63 cells exhibited a constrained range of fluorescence intensity, suggesting that GFP expression is homogeneous within the cell population (SD=26.1) ([Figure 3.2.C.i](#)). On the other hand, the CD81-Tdtomato cells had a wider range of fluorescence (SD=244), as shown by the wide fluorescence histogram distribution ([Figure 3.2.C.iii](#)), thus suggesting a rather heterogeneous fluorescent cell population.

As expected, the GFP-Parallel and Tom-Parallel control DU145 cells showed no fluorescence expression, except low signal resulting from a minor percentage of auto-fluorescent cells, as shown in the fluorescence histogram distributions in [Figure 3.2.C.ii,iv](#) (geometric mean fluorescence intensity (gMFI) =2.04 or 3.57 respectively).

To conclude, expression of GFP-CD63 and CD81-Tdtomato in DU145 cells appeared stable for at least 30-days post-enrichment. Furthermore, the expression of GFP-CD63 resulted in a homogeneous fluorescent cell population, whereas expression of CD81-Tdtomato resulted in a more heterogeneous fluorescent population that also showed potential morphological differences to Tom-Parallel control cells.

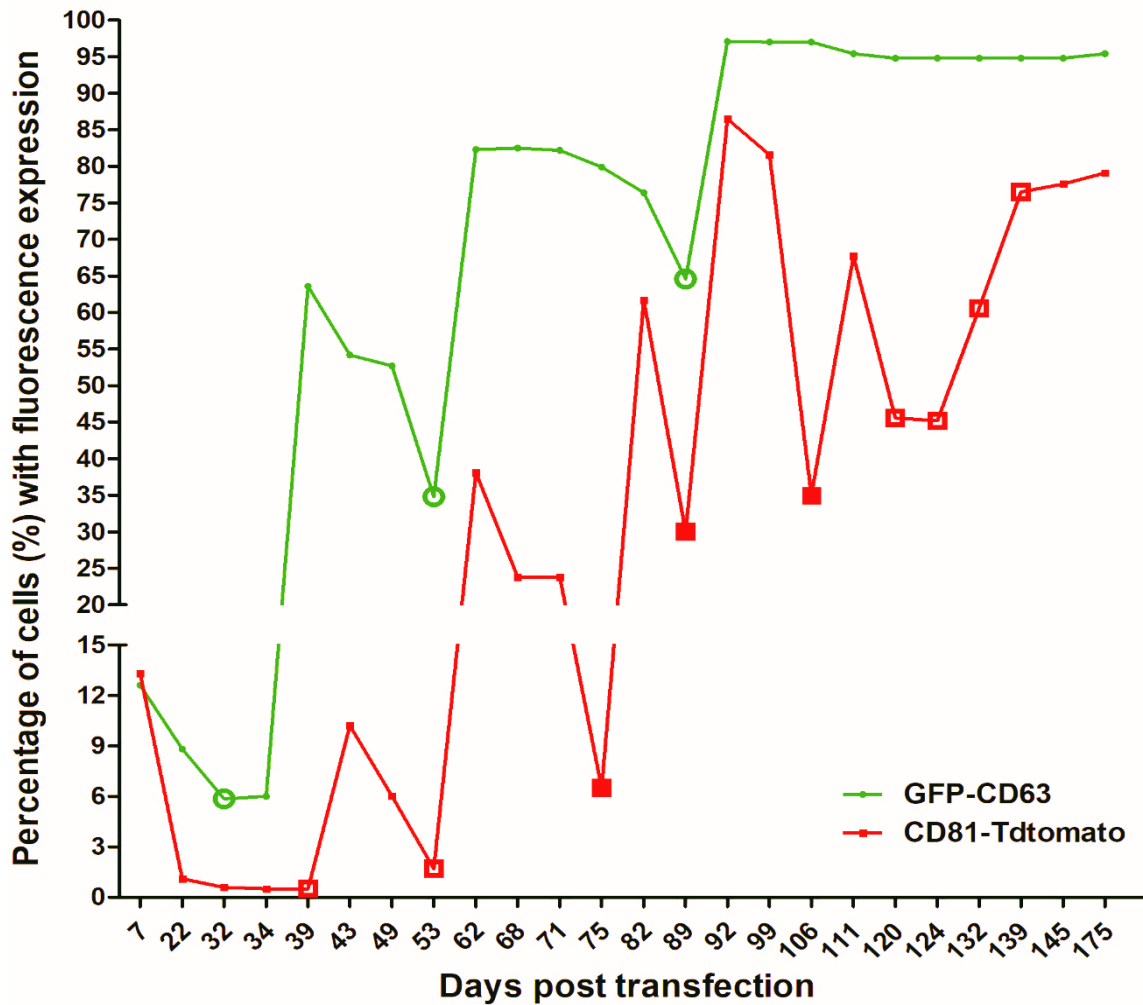


Figure 3.1. Timeline of GFP-CD63 and CD81-Tdtomato stable cell line FACS and fluorescence expression.

Line chart depicting the progression of the fluorescent cell population enrichment for GFP-CD63 (green line) or CD81-Tdtomato (red line) cells, over time (days post-transfection). The small circle or square points depict the percentage of fluorescent GFP-CD63 or CD81-Tdtomato cells respectively, as determined by flow cytometry.

Note that the large circle or square points denote FACS events for GFP-CD63 or CD81-Tdtomato cells respectively. The large, filled squares depict FACS of a sub-population of CD81-Tdtomato cells with intermediate fluorescence expression.

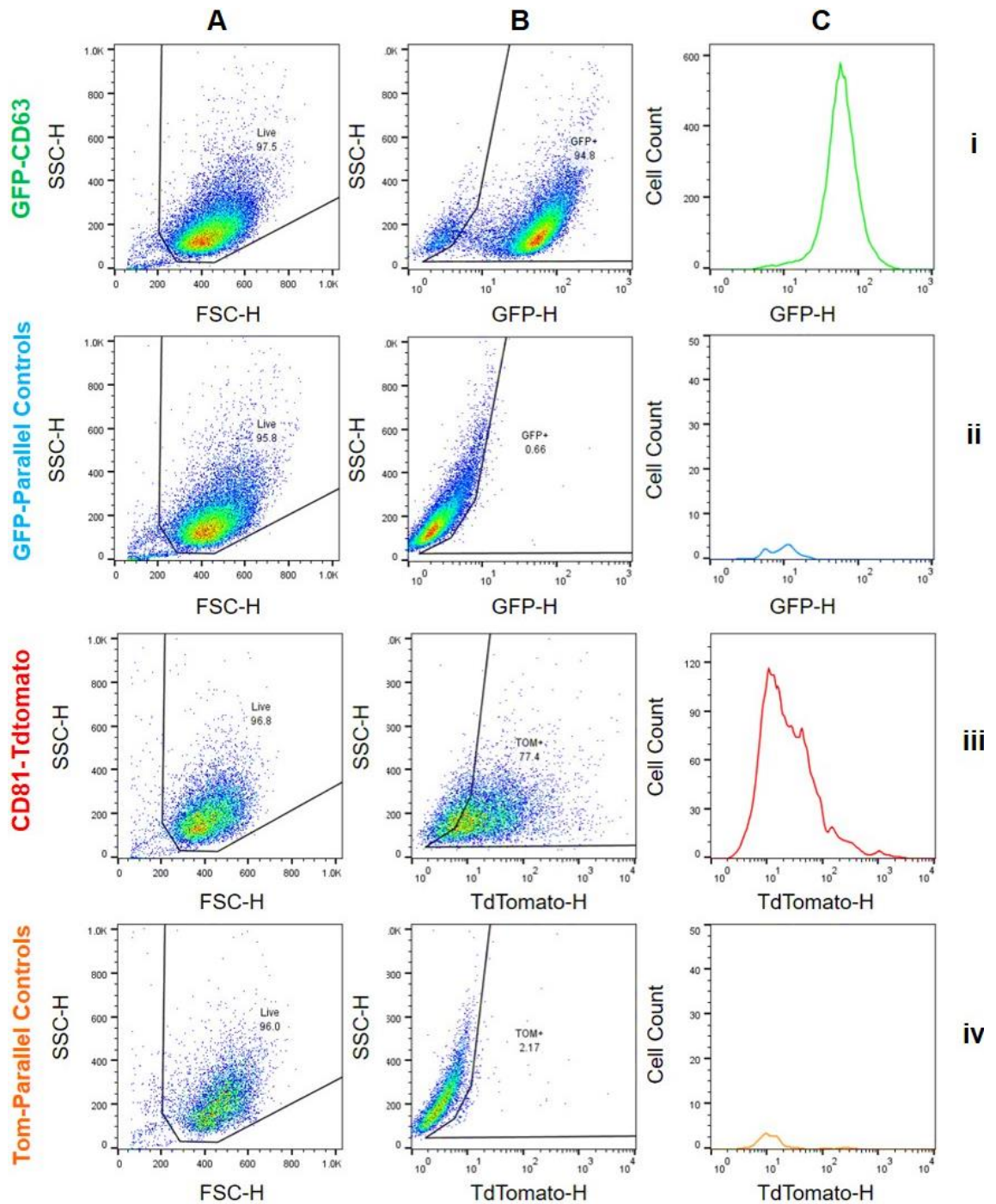


Figure 3.2. Scatter and Fluorescence properties of GFP-CD63, CD81-Tdtomato and WT DU145 parallel cell lines (GFP-Parallel and Tom-Parallel controls).

A. Forward scatter FSC-H(eight) Vs Side Scatter SSC-H(eight) plot demonstrating the gate used (“Live”) to sort viable **(i)** GFP-CD63, **(ii)** GFP-Parallel controls, **(iii)** CD81-Tdtomato and **(iv)** Tom-Parallel controls. **B.** SSC-H vs Fluorescence-H plots of viable cells showing percentage of fluorescent cells for **(i)** GFP-CD63 and **(ii)** GFP-Parallel controls (gate “GFP+”), as well as for **(iii)** CD81-Tdtomato and **(iv)** Tom-Parallel controls (gate “TOM+”). **C.** Fluorescence intensity histograms of viable GFP+ cells for **(i)** GFP-CD63 and **(ii)** GFP-Parallel controls, as well as viable TOM+ cells for **(iii)** CD81-Tdtomato and **(iv)** Tom-Parallel controls.

3.3.2.2. Growth Curve Analysis

Further phenotypic analysis involved investigation of the growth rates for the GFP-CD63 and CD81-Tdtomato stable cell lines, which were compared alongside the non-transfected WT DU145 cells of the same cell passage (GFP-Parallel and Tom-Parallel controls). Thus, we conducted a growth curve analysis, where we seeded the same numbers of cells for every cell line (in triplicate) and 24, 48, 72, 96 and 168h after seeding cells were counted with the automated Z1 Beckman Coulter® Particle Counter. Next, we generated the growth curves for every cell line as shown in [Figure 3.3](#). We observed that GFP-CD63 cells exhibited a similar growth rate as their control counterparts (GFP-Parallel cells) as no statistically significant differences were observed, with the cell population doubling times being 29.40h and 29.77h respectively ([Figure 3.3.A](#)). Conversely, the CD81-Tdtomato cells showed a significantly lower growth rate (from 96h onwards) than their control counterparts (Tom-Parallel cells) with the cell population doubling times being 28.28 and 27.14h respectively ([Figure 3.3.B](#)). Doubling times were calculated based on the formula $DT = T \ln 2 / \ln(Xe/Xb)$, where T equals to incubation time in hours, Xb equals to the cell number at the beginning of the incubation time and Xe equals to the cell number at the end of the incubation time.

3.3.2.3. Cell Cycle Analysis

Due to the significant differences in growth rate between the CD81-Tdtomato and Tom-Parallel controls, we further investigated their capacity for cell cycle progression. Cell cycle progression studies were conducted using Colcemid; a mitotic spindle poison (microtubule-depolymerizing agent) which induces mitotic arrest and is useful for studying cell cycle dynamics based on the rate of accumulation of cells to S/G₂/M phase (128).

Briefly, GFP-CD63 and CD81-Tdtomato cells, as well as GFP- and Tom-Parallel control cells were treated with Colcemid for 8, 16, 24, 32h or were left untreated (0h), followed by DRAQ5™ incubation to label nuclear DNA, and finally cell cycle analysis via flow cytometry. The gating strategy for cell cycle analysis, including gates for cell phases: G₁, S/G₂/M and polyploid (>2n), is described in [Supplementary Figure 4](#). Examples of cell cycle distribution histograms (DRAQ5™) are depicted in [Supplementary Figure 5](#) as overlays of GFP-CD63 and CD81-Tdtomato with GFP- and Tom-Parallel control cells respectively; these exemplary histograms showed the effects of Colcemid treatment (0, 8, 16, 24, 32h) on cell cycle progression.

Cell cycle analysis demonstrated that Colcemid treatment caused similar arrest of GFP-CD63 and GFP-Parallel control cells at S/G₂/M phase proportionally to the duration of treatment, with cells plateauing at S/G₂/M phase after 16h of treatment ([Figure 3.4.A](#), green lines). Interestingly, it was observed that a lesser population of GFP-CD63 cells participated in cell cycle, as a ~5% higher percentage of cells still remained in G₁ phase even after 32h of Colcemid treatment ([Figure 3.4.A](#), blue lines). On the other hand, no significant differences were observed between GFP-CD63 and GFP-Parallel control cells regarding progression to a polyploid cell phase (>2n) even after 32h of Colcemid treatment ([Figure 3.4.A](#), black lines).

Conversely, CD81-Tdtomato and Tom-Parallel control cells showed differential progression to S/G₂/M phase after Colcemid treatment. Specifically, while Tom-Parallel control cells plateaued at S/G₂/M phase after 16h of Colcemid treatment, CD81-Tdtomato cells plateaued at 24h after treatment, suggesting slower S/G₂/M phase arrest for the latter ([Figure 3.4.B](#), red lines). In addition, a significantly higher percentage of CD81-Tdtomato cells was observed at G₁ cell phase (~10%), thus not participating in cell cycle, which persisted until 16h after Colcemid treatment ([Figure 3.4.B](#), blue lines). After 16h of Colcemid treatment CD81-Tdtomato and Tom-Parallel control cells showed similar accumulation at G₁ cell phase. However, significant differences were observed regarding progression to polyploidy, with a higher percentage of Tom-Parallel control cells progressing to a polyploid cell phase (>2n) over the first 24h of Colcemid treatment, compared to CD81-Tdtomato cells ([Figure 3.4.B](#), black lines).

To conclude, cell cycle analysis demonstrated that GFP-CD63 and GFP-Parallel DU145 cells show similar cell cycle progression; however, CD81-Tdtomato cells exhibit slower cell cycle progression compared to the Tom-Parallel DU145 control cells.

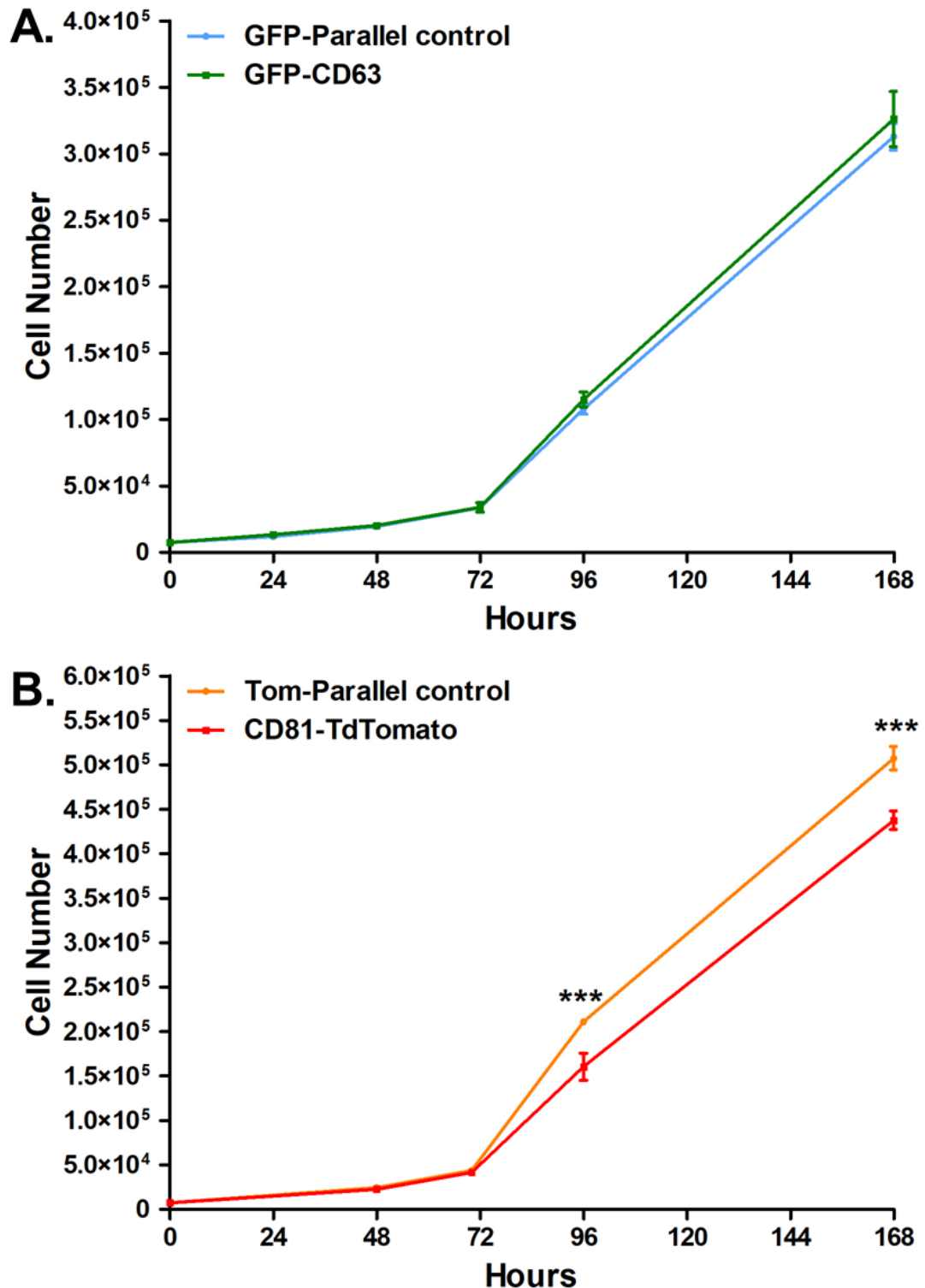


Figure 3.3. Growth curve analysis for GFP-CD63 and CD81-Tdtomato DU145 cells compared to the WT DU145 parallel control counterparts.

A. Growth curve for GFP-CD63 (green) and GFP-Parallel WT control (blue) cells demonstrating cell numbers 24, 48, 72, 96 and 168h post-seeding. **B.** Growth curve CD81-Tdtomato (red) and Tom-Parallel WT control (orange) cells demonstrating cell numbers 48, 72, 96 and 168h post-seeding. This experiment was conducted with triplicate samples (N=3); error bars denote standard deviation and statistical analysis was done using two-way ANOVA and Bonferroni's post-hoc multiple comparisons denoting significant differences with *** $p < 0.0001$.

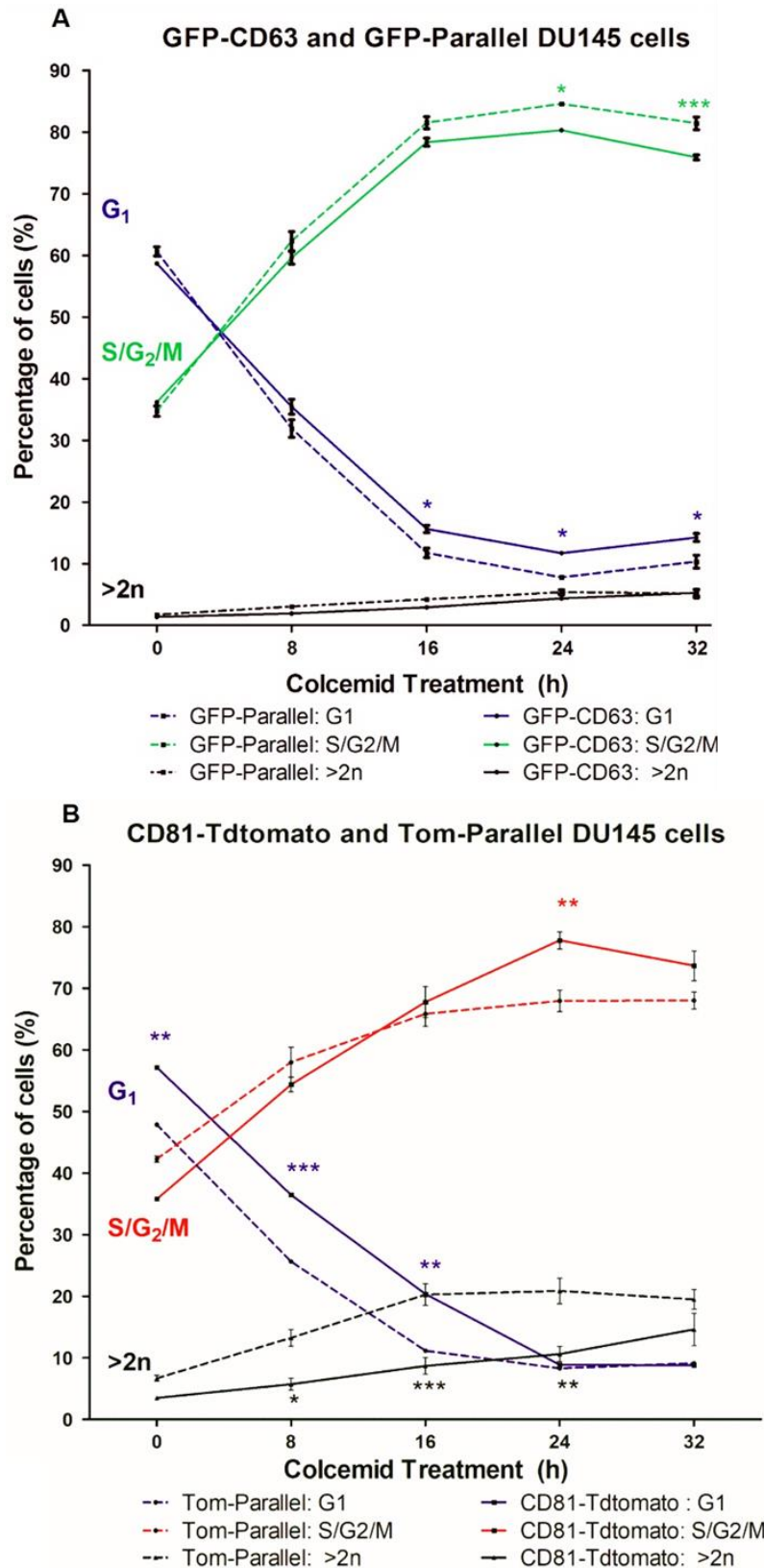


Figure 3.4. Cell cycle progression for GFP-CD63 and CD81-Tdtomato DU145 cells compared to their WT DU145 parallel control counterparts.

A. Percentages of GFP-CD63 cells (solid lines) or GFP-Parallel control cells (dashed lines) distributed in G₁ cell phase (blue), S/G₂/M cell phase (green) and polyploid cell phase (>2n, black) after 0,8,16,24 and 32h of Colcemid treatment. **B.** Percentages of CD81-Tdtomato cells (solid lines) or Tom-Parallel DU145 control cells (dashed lines) distributed in G₁ cell phase (blue), S/G₂/M cell phases (red) and polyploid cell phase (>2n, black) after 0,8,16,24 and 32h of Colcemid treatment. This experiment was conducted three times (N=3); error bars denote standard error and statistical analysis was done using two-way ANOVA and Bonferroni's post-hoc multiple comparisons test denoting significant statistical differences with *p<0.05, **p<0.001 and ***p<0.0001.

3.3.2.4. Localisation and Effects on Cell Morphology

Live-cell and fixed-cell imaging ([Figures 3.5-3.6](#)) were also conducted to investigate the localisation of GFP-CD63 and CD81-Tdtomato and assess their potential effects on cell morphology. Live-cell imaging involved direct imaging of GFP-CD63, CD81-Tdtomato, GFP-Parallel and Tom-Parallel controls after nuclear staining with 20µM DRAQ5™ (129), whereas fixed-cell imaging involved cytoskeletal labelling with ActinGreen488 and nuclear labelling with NucBlue (“DAPI”).

To begin with, live-cell imaging showed that GFP-CD63 (green fluorescence) and CD81-Tdtomato (orange fluorescence) constructs were predominantly localised at the cell membrane, cell protrusions and in some cases appeared with punctate perinuclear staining ([Figure 3.5.A,C](#) and [Supplementary Figure 6. B,D](#)). In contrast to the localisation of GFP-CD63 and CD81-Tdtomato, untagged GFP and Tdtomato exhibited diffused cytosolic green or orange fluorescence signal, respectively ([Supplementary Figure 6. A,C](#)). The GFP-Parallel and Tom-Parallel control DU145 cells showed no fluorescence expression (no autofluorescence) in the GFP ([Figure 3.5.B](#)) or Tdtomato ([Figure 3.5.D](#)) fluorescence emission channels.

Furthermore, fixed-cell imaging demonstrated that GFP-CD63 cells exhibited a more typical DU145 epithelial cell morphology, similar to GFP-Parallel controls ([Figure 3.6.A,B](#)). In addition, live-cell imaging showed homogeneous GFP expression for GFP-CD63 cells ([Figure 3.5.A](#)), thus agreeing with the previous flow cytometry results ([Figure 3.2.C.i](#)). Conversely, live-cell imaging showed that CD81-Tdtomato cells exhibited a range of fluorescence expression ([Figure 3.5.C](#)) which also agreed with the flow cytometry results ([Figure 3.2.C.iii](#)). This heterogeneous fluorescence reflected a morphologically heterogeneous CD81-Tdtomato cell population ([Figure 3.6.C](#)), which was also observed for the Tom-Parallel controls ([Figure 3.6.D](#)).

CellProfiler™ Automated Morphology Analysis

Next, we followed a quantitative approach to investigate the effects of GFP-CD63 and CD81-Tdtomato expression on cell morphology. To achieve this, the fixed-cell images of GFP-CD63, CD81-Tdtomato, GFP-Parallel and Tom-Parallel control cells ([Figure 3.6](#)) were processed using the CellProfiler™ software (v.3.1.8) (131). Specifically, two customised pipelines were used to compare GFP-CD63 vs GFP-Parallel and CD81-Tdtomato vs Tom-Parallel controls. These customised pipelines were used to perform automated cell identification by: **(i)** detecting the nucleus (using the NucBlue™- DAPI

stain), **(ii)** detecting the cytoskeleton (i.e., the cell outline, via the ActinGreen488 dye), followed by **(iii)** measurement of various cell features, including cell area and form factor (circularity) ([Figure 3.6.E](#)).

Then, these measurements were imported into FlowJo™ to generate the histogram distributions of cell area and form factor, followed by a Chi Squared statistical test (130, 150); this test was used to calculate the variance in SD between cells expressing GFP-CD63 and CD81-Tdtomato, compared with their relevant WT parallel controls ([Figure 3.6.F,G](#)). CellProfiler™ and statistical analysis demonstrated that expression of GFP-CD63 lead to generation of cells with a significantly larger cell area (> 65 SD variance), and with a more circular shape (larger form factor >13 SD variance) than GFP-Parallel control cells ([Figure 3.6.F,G.i](#)). Conversely, expression of CD81-Tdtomato lead to the development of cells with significantly smaller cell area than Tom-Parallel control cells (>19 SD variance, [Figure 3.6.F.ii](#)); however, no significant differences were observed regarding circularity (form factor, <1 SD variance) as shown in [Figure 3.6.G.ii](#).

Interestingly, the smaller size of CD81-Tdtomato cells was also reflected in the flow cytometry experiments, but not the larger size of GFP-CD63 cells ([Figure 3.2.A.iii.i](#)). To conclude, our results suggested that expression of GFP-CD63 or CD81-Tdtomato resulted in differential morphological changes of DU145 cells, when compared to GFP-Parallel and Tom-Parallel controls, respectively.

3.3.2.5. Cell Membrane Expression of sEV-Associated Protein Markers

Besides cell morphology, further characterisation was essential to measure the protein levels of the tetraspanins CD9, CD63 and CD81, as well as other proteins like the MHC Class I receptor (MHC-1), especially since they are highly associated with sEVs (19). To achieve this, the cell membranes of GFP-CD63, CD81-Tdtomato and respective WT parallel control cells were labelled live with antibodies against CD63, CD81, CD9 and MHC-1 (directly conjugated to PERCP/Cy5.5). These samples were then analysed via flow cytometry to evaluate cellular membrane expression of these proteins. The gating strategy for these experiments is described in [Supplementary Figure 7](#), and examples of raw data (fluorescence intensity scatter plots and histograms) are shown in [Supplementary Figure 8](#).

Firstly, we observed overexpression of CD63 in the membrane of GFP-CD63 cells, compared to other cell types (3- to 4-fold increase in gMFI of PERCP/Cy5.5 signal), which was expected. Furthermore, we observed a slight increase of the other

tetraspanins (CD9 and CD81) compared to GFP-Parallel controls. Interestingly, we also observed that GFP-CD63 cells exhibited a 2-fold higher expression of MHC-1, something that was not observed in any of the other cell lines ([Figure 3.7](#)).

On the other hand, the CD81-Tdtomato cells only showed significant increase in the membrane expression of CD81 compared to the other cell lines, whereas no significant differences were observed for CD9, CD63 or MHC-1 ([Figure 3.7](#)). Interestingly, some minor differences in membrane expression of CD9 and CD63 were observed between the WT parallel control cells, which might suggest phenotypic changes in cells after a certain period of cell passaging.

These results suggested that overexpression of CD63 resulted in differential expression of tetraspanins and MHC-1 at the cell membrane, compared to overexpression of CD81, which only appeared to increase the levels of CD81 at the cell membrane.

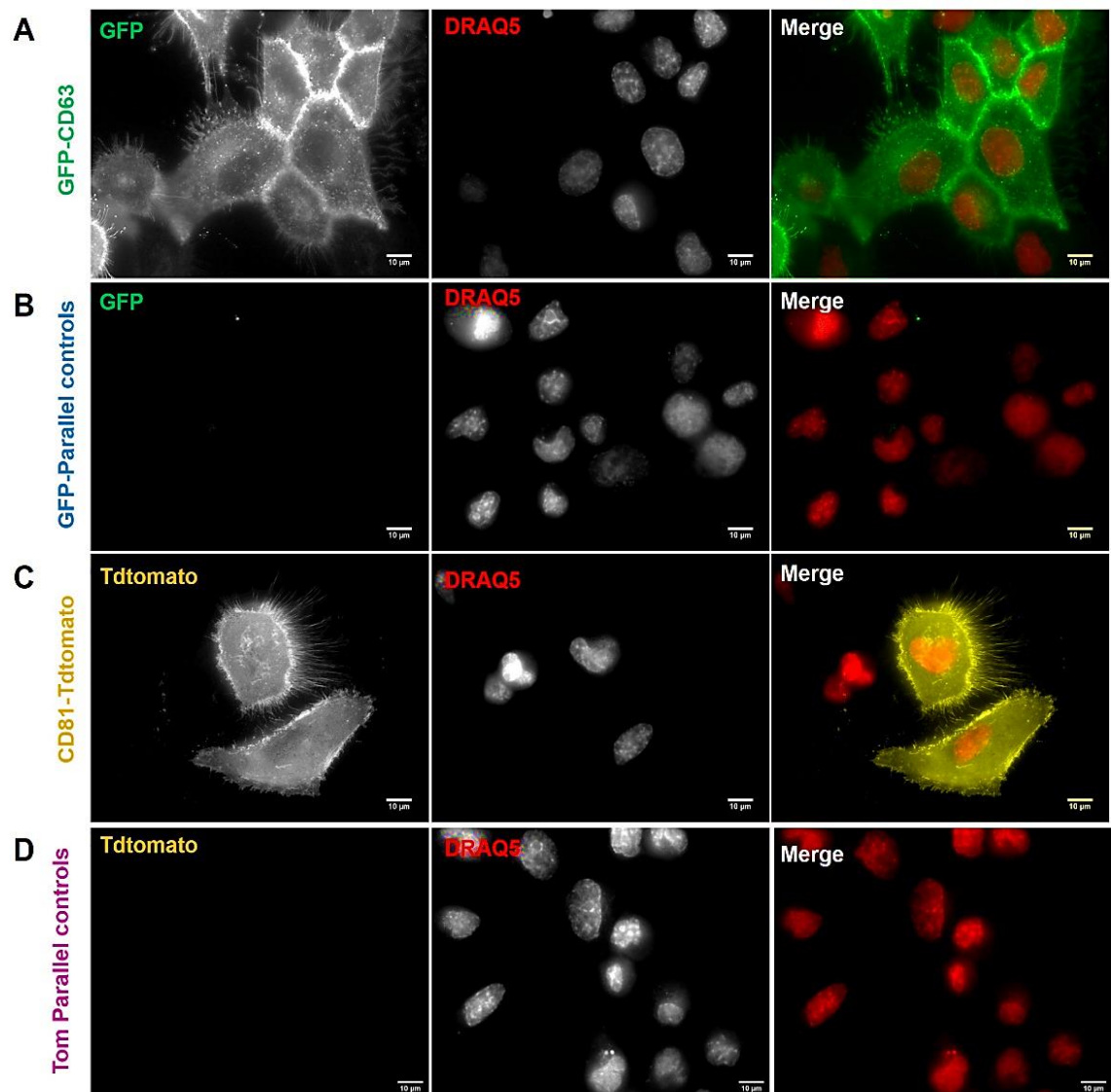


Figure 3.5. GFP-CD63 and CD81-Tdtomato live-cell localisation.

Live-cell fluorescence images for: **A.** GFP-CD63 cells, **B.** GFP-Parallel control cells, **C.** CD81-Tdtomato cells and **D.** Tom-Parallel control cells. The left column depicts GFP fluorescence (green) or Tdtomato fluorescence (yellow/orange). Middle column depicts cell nuclei (DRAQ5™ was used to label nuclear DNA red). Right column consists of the merged channel images. *Scale bars represent 10µm (63x magnification, widefield fluorescence microscope).*

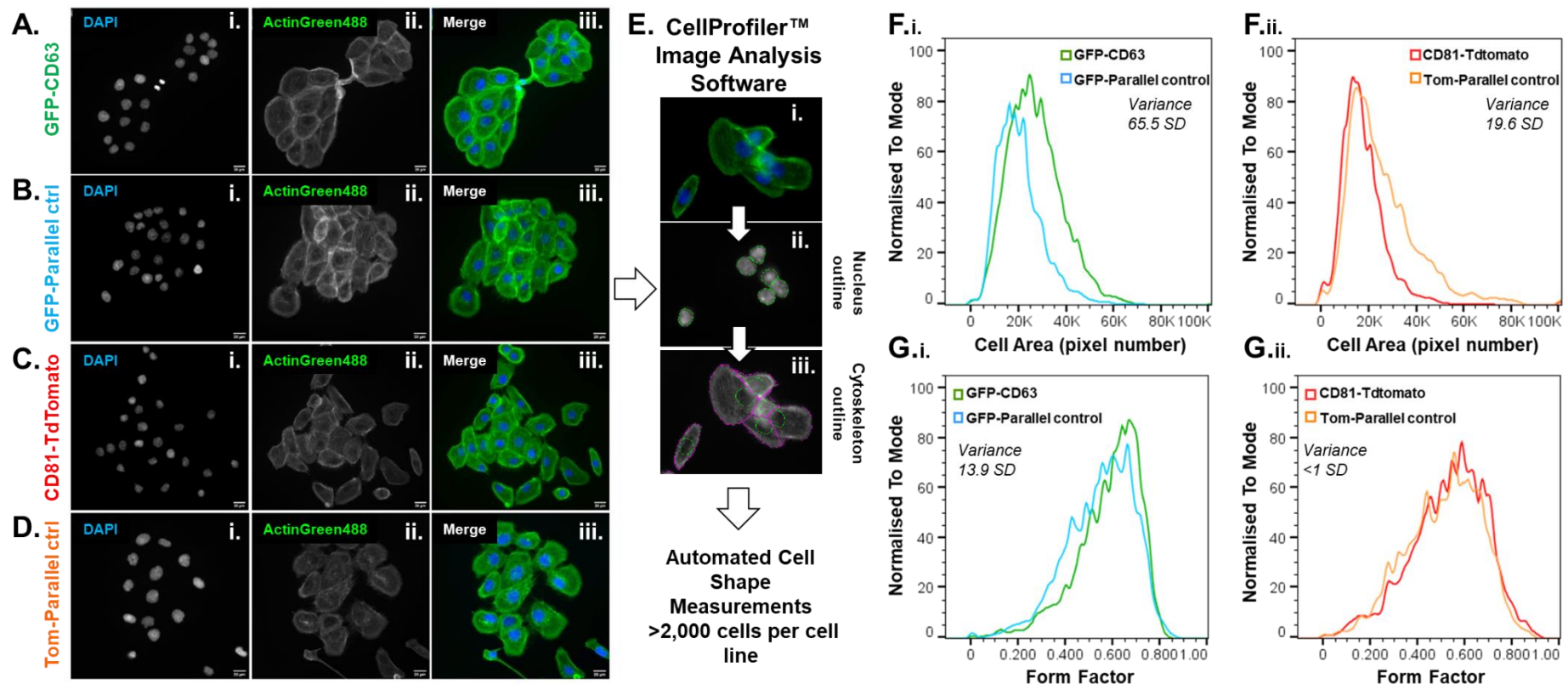


Figure 3.6. Cell morphology analysis for GFP-CD63 and CD81-Tdtomato compared to their WT parallel controls.

Fixed-cell images of **A.** GFP-CD63, **B.** GFP-Parallel control, **C.** CD81-Tdtomato and **D.** Tom-Parallel control cells labelled with (i) NuncBlue (DAPI) to stain cell nuclei, (ii) ActinGreen488 to label actin cytoskeleton and (iii) the merged image. Scale bars represent 20µm (20x magnification, widefield fluorescence microscope). **E.** Schematic describing the CellProfiler™ pipeline used for image analysis: (i) separate channels of fixed-cell images were used to firstly (ii) outline the nuclei (using DAPI) and then to detect the (iii) cytoskeleton outline using ActinGreen488. The CellProfiler™ software was used for automated cell identification and measurements **F.** Cell area and **G.** Form Factor (circularity) for: (i) GFP-CD63 (green) vs GFP-Parallel controls (blue) and (ii) CD81-Tdtomato (red) vs Tom-Parallel controls (orange). CellProfiler automated analysis was conducted for more than 2,000 cells per cell line and further statistical analysis was done in FlowJo™ using the Chi Squared statistical test to calculate the variance (in SD) between overexpressing cells and controls.

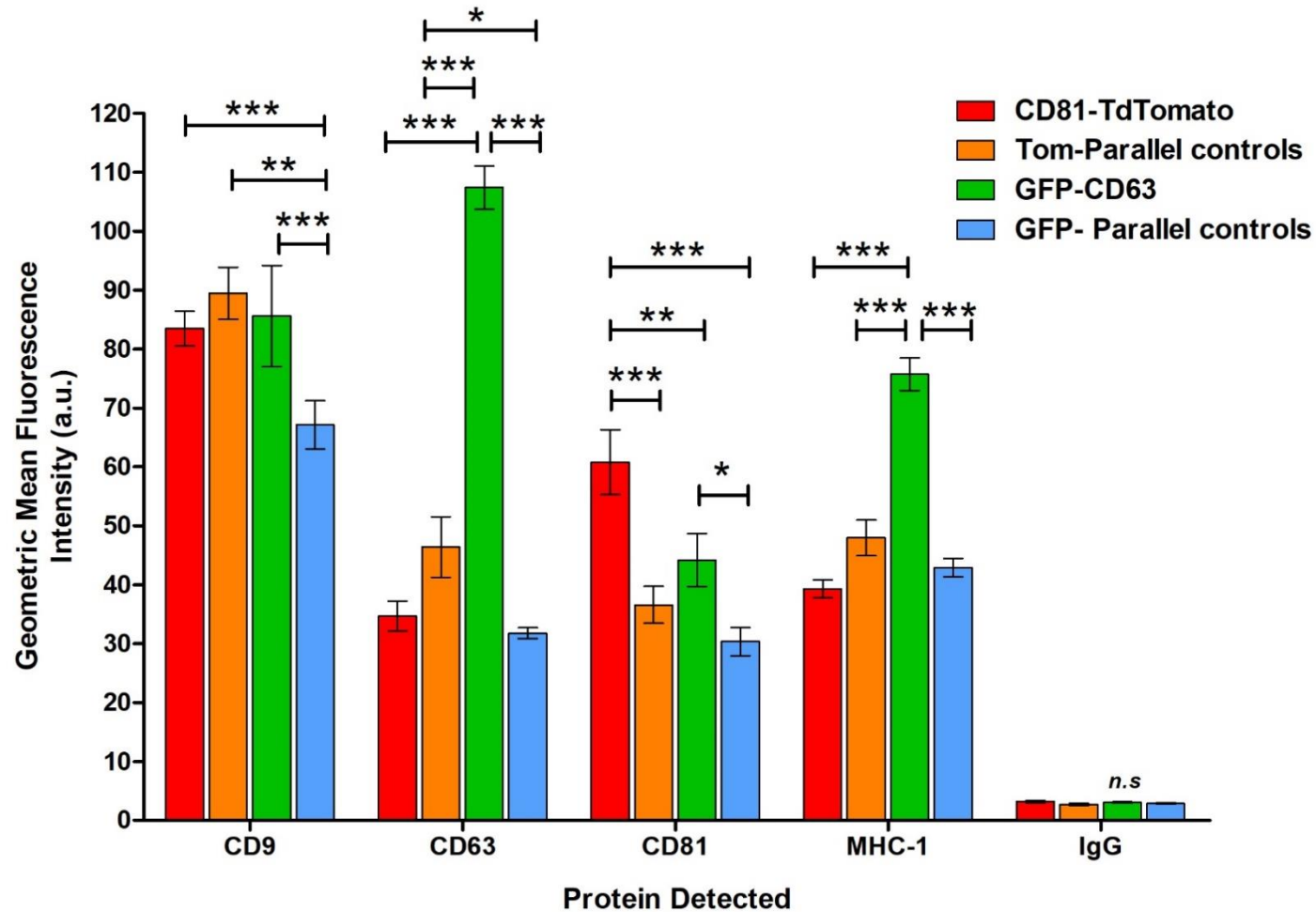


Figure 3.7. Cell membrane expression of EV-associated markers by GFP-CD63 and CD81-Tdtomato cells compared to their WT parallel controls.

Geometric mean PERCP/Cy5.5 fluorescence intensity denoting membrane protein levels of CD9, CD63, CD81, MHC-1 and IgG (isotype control) in GFP-CD63 (green), GFP-Parallel controls (blue), CD81-Tdtomato (red) and Tom-Parallel control cells (orange). These column graphs represent three independent experiments (N=3 and technical triplicates); error bars denote standard error and statistical analysis was done using 2-way ANOVA with Bonferroni's post-test multiple comparisons. Significant differences are shown in the graphs, denoted with * $p < 0.05$, ** $p < 0.01$ or *** $p < 0.0001$, whereas ns denotes non-significance.

3.3.3. Isolation, Characterisation and Detection of sEVs

The characterisation of GFP-CD63 and CD81-Tdtomato DU145 stable cell lines described above, suggested that overexpression of these proteins differentially affected the phenotype of the resulted cell lines. Thus, it was essential to characterise generated EVs from these cell lines as their phenotype and secretion may also be impacted by the cell manipulations.

To address this, GFP-CD63, CD81-Tdtomato and WT parallel cell lines were grown in conventional 2D (two-dimensional) tissue culture flasks for 7 days, after which the conditioned media was used for EV isolation by differential ultracentrifugation (see Materials and Methods, [Section 2.10](#)). The use of the differential ultracentrifugation method was necessary due to the large volume of cell-conditioned media, but it was albeit a fast method, with intermediate recovery and specificity according to MISEV2018 guidelines (6), which was used to preliminary assess the size distribution, loading of EV-associated markers and fluorescence signal of isolated EVs. Of note, as vesicles were isolated from the 100000g ultracentrifugation pelleting step (after removal of the larger vesicles at the previous 10000g ultracentrifugation step), they can be considered as small EVs, which will be referred to from now on as “sEVs” based on the MISEV2018 guidelines (6). In Chapter 4 we explore thoroughly the phenotype of sEVs (and parental cells) by proteomics analysis, using sEVs isolated by the 30% sucrose/D₂O cushion ultracentrifugation method, which is a high-specificity and high-purity method for sEV isolation (6, 157) (see Materials and Methods, [Section 2.11](#)).

3.3.3.1. Comparison of EV size and sEV-associated proteins

To confirm successful isolation of EVs, the protein and particle concentrations of the isolates were determined using the BCA protein assay and Nanoparticle Tracking Analysis (NTA), respectively. NTA is a method of visualisation and analysis of nanometre-sized vesicles (50 – 1000 nm), and is used to determine their size distribution and particle concentration (158). [Table 2.2](#) shows the protein and particle concentrations for all EV isolations for each cell line (isolation #1).

To begin with, representative NTA size distributions for isolated vesicles (from all cell lines) are shown in [Figure 3.8.A](#), which demonstrated relatively monodispersed populations of vesicles mostly sized between 50-150nm (diameter), which are indicative of small EVs (157, 159, 160). The NTA size distributions between GFP-CD63 vs GFP-

Parallel ([Figure 3.8.A.i](#)) and CD81-Tdtomato vs Tom-Parallel sEVs ([Figure 3.8.A.ii](#)) exhibited similar size distributions, suggesting that overexpression of GFP-CD63 or CD81-Tdtomato did not apparently alter the size of secreted sEVs, when isolated by the differential ultracentrifugation method.

An immuno-phenotyping ELISA-like assay was also performed to determine the presence and protein levels of CD9, CD63, CD81 and MHC-1 in isolated sEVs. This immuno-phenotyping assay involved immobilisation of sEVs in high-affinity protein-binding microplates, followed by blocking and then addition of primary antibody (anti-CD9, CD63, CD81, MHC-1 and isotype controls) and subsequent recognition by a secondary-biotinylated antibody; lastly, a streptavidin-europium conjugate was used to amplify the signal which was detected using time-resolved fluorescence (TRF).

Results from this assay confirmed that isolated sEVs from all four parental cell lines carried these typical highly sEV-associated protein markers ([Figure 3.8.B](#)). Interestingly, we observed that GFP-CD63 sEVs carried significantly higher sEV-associated proteins compared to GFP-Parallel controls, CD81-Tdtomato and Tom-Parallel sEVs (approximately 2-fold increase of CD9, CD63, CD81 and MHC-1 levels). Conversely, CD81-Tdtomato sEVs showed no significant phenotypic differences compared to Tom-Parallel control sEVs (except the levels of CD9 which were 1.2-fold lower), as shown in [Figure 3.8.B](#). Surprisingly, there was no evidence for heightened CD81 expression on these sEVs as we might have expected from overexpression of CD81, as previously seen in parental cells ([Figure 3.7](#)).

3.3.3.2. Comparison of sEV Secretion

Finally, we investigated whether GFP-CD63 and CD81-Tdtomato DU145 cell lines exhibited differences in sEV secretion, as CD63 and CD81 have central roles in sEV biogenesis and secretion (22, 24). For this preliminary experiment, we utilised the cells previously cultured in the conventional tissue-culture flasks for EV production (see above and [Section 2.10](#)). Specifically, simultaneously to sEV isolation by differential ultracentrifugation, cells grown in the conventional 2D tissue-culture flasks were trypsinised and counted to calculate the total cell number for each cell line. Then, in conjunction with the particle concentration of isolated sEVs (particle/ml via NTA) and the total volume of sEV isolate, we calculated the total sEV particle number secreted by each cell line and normalised that to total cell number, thus estimating the normalised sEV number secreted per cell.

We observed that CD81-Tdtomato cells secreted the highest sEV number per cell (~9100 sEVs/cell), followed by Tom-Parallel control (~6700 sEVs/cell), GFP-CD63 (~3900 sEVs/cell) and GFP-Parallel control cells (~3100 sEVs/cell), as shown in [Figure 3.9](#). This suggested that overexpression of CD81 or CD63 lead to alterations in sEV biogenesis and/or secretion, as demonstrated by the 1.4-fold increase in secreted sEVs by CD81-Tdtomato cells (compared to Tom-Parallel controls) and the 1.25-fold increase by GFP-CD63 cells (compared to GFP-Parallel controls). More prominent differences became apparent when directly comparing CD81-Tdtomato to GFP-CD63 cells, as overexpressing CD81 lead to a 2.3-fold increase in sEV secretion compared to overexpression of CD63.

Surprisingly, we also observed differences in sEV secretion by the WT parallel control cells, as Tom-Parallel controls demonstrated a 2.2-fold increase in sEV secretion compared to GFP-Parallel controls. It remains to be elucidated if the aging of the DU145 cell line (Tom-Parallel controls are 20 cell passages older than GFP-Parallel controls) may also be a contributor to changes in sEV secretion. As this is a preliminary experiment, further investigation is necessary to validate our results, however they suggested that overexpressing CD63 or CD81 in DU145 cells resulted to increased sEV biogenesis/secretion, which is probably attributed to the essential roles of these tetraspanins in these processes (22, 24).

Collectively, the above observations suggested that overexpression of CD63 or CD81 in DU145 cells did not have apparent effects on the size distribution of secreted sEVs when isolated by differential ultracentrifugation. On the other hand, overexpression of CD63 in DU145 cells induced phenotypic changes in sEVs, which were evident by elevation of various sEV-associated proteins at the EV membrane (CD63, CD81, CD9, MHC-1), even though overexpression of CD81 did not cause any analogous changes in these proteins. Despite this, we also demonstrated that overexpression of CD63 or CD81 lead to significant changes in the quantity of secreted sEVs per cell (increased secretion compared to controls), thus demonstrating how these fluorescent sEV reporter cell lines overexpressing tetraspanins can induce significant changes to sEV biogenesis and secretion.

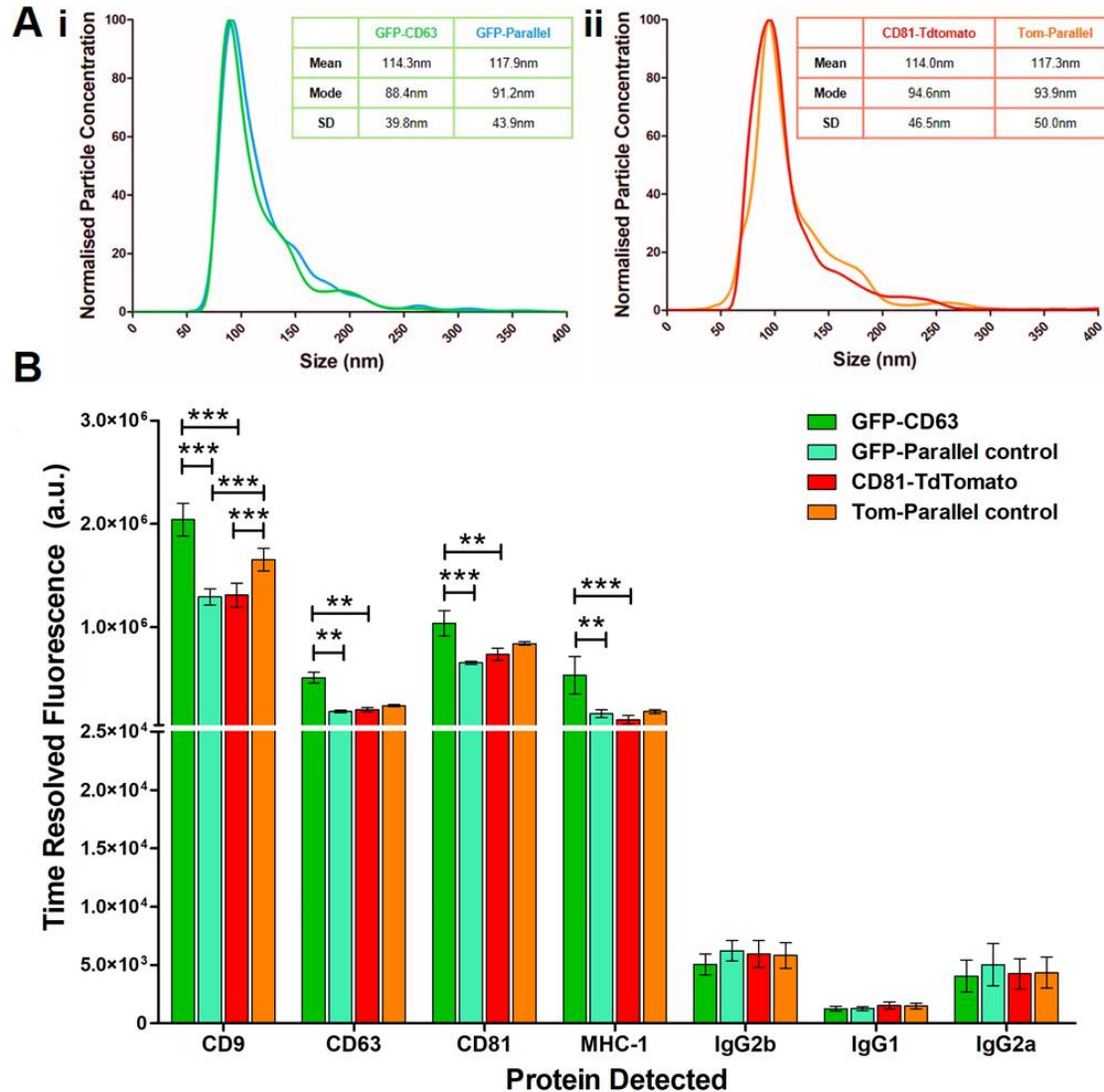


Figure 3.8. Characterisation of isolated EVs for size and EV-associated protein markers.

A. Nanoparticle Tracking Analysis (NTA) showing size distributions of **i.** GFP-CD63 (green) versus GFP-Parallel (blue) and **ii.** CD81-Tdtomato (red) versus Tom-Parallel (orange) isolated sEVs. The NTA histograms represent the average of three NTA acquisitions which were acquired in a single experiment (N=1). The mean, mode and standard deviation (SD) for size (nm) are indicated for each sEV population and were calculated based on the three NTA acquisitions. **B.** An immunophenotyping ELISA-like assay on isolated sEVs showing the levels of typical sEV-associated markers tetraspanins CD9, CD63, CD81 and the sEV-associated MHC-1 receptor (with isotype controls IgG_{2b} for CD9, IgG₁ for CD63 and CD81 and IgG_{2a} for MHC-1). The column graphs represent three independent experiments (N=3); error bars denote standard error and statistical analysis was done using two-way ANOVA and Bonferroni's post-test multiple comparisons. Significant differences only are shown in the graphs, denoted with *p<0.05 or **p<0.001 or ***p<0.0001.

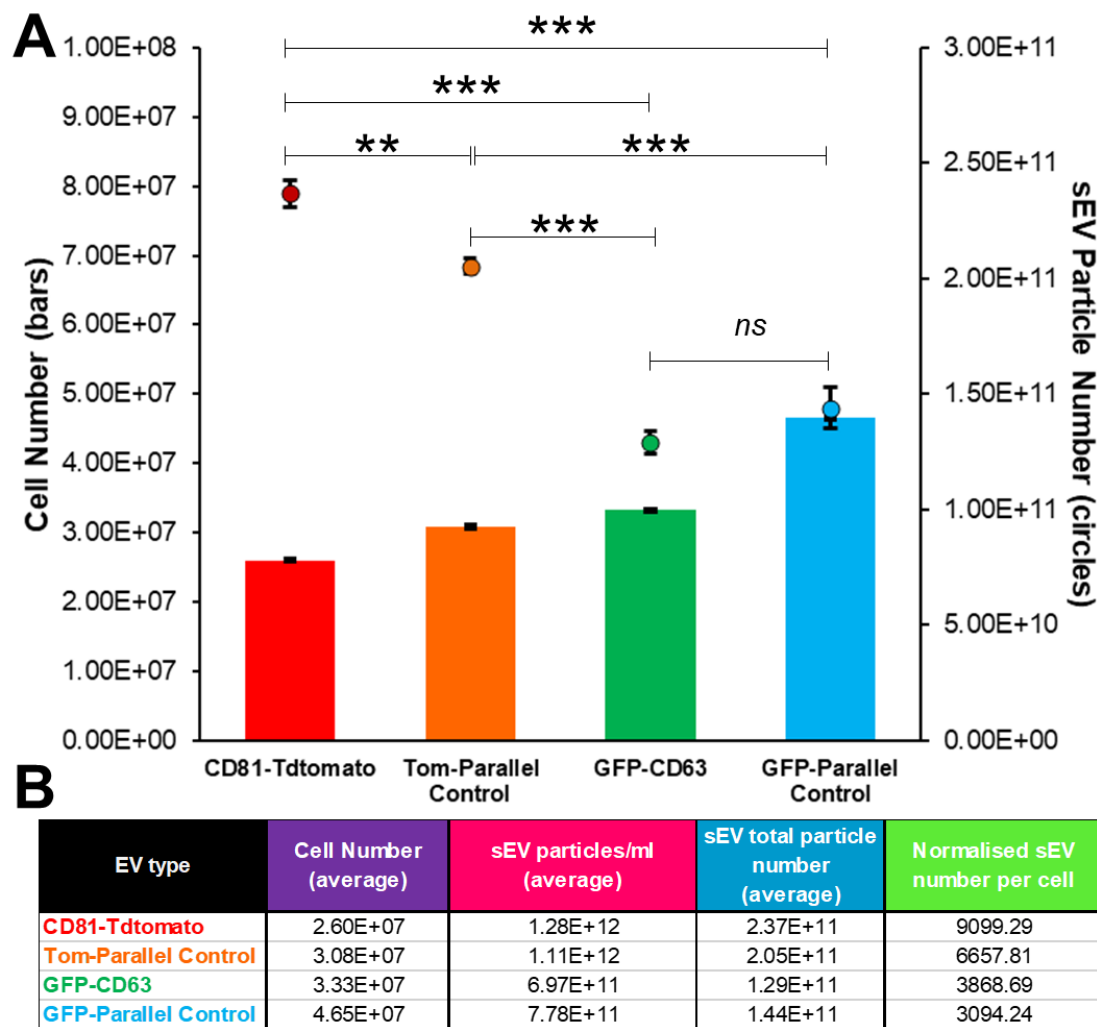


Figure 3.9. sEV secretion comparison between overexpressing cell lines and WT parallel controls.

A. Combination plot of CD81-Tdtomato (red), Tom-Parallel control (orange), GFP-CD63 (green) and GFP-Parallel control (blue) cell numbers indicated with bars (left y-axis), whereas respective sEV particle numbers are shown with points (right y-axis). **B.** Table showing the average cell number, sEV concentration (particles/ml), estimated total sEV particle number for all cells (based on volume of isolate), as well as the calculated normalised sEV number per cell for each cell line.

This preliminary experiment was conducted once (N=1), with three technical measurements of cell and particle numbers. Error bars denote standard deviation and statistical analysis was done using two-way ANOVA and Bonferroni's post-test multiple comparisons. Significant differences only are shown in the graphs, denoted with **p<0.001 and ***p<0.0001, or with ns for non-significance. Note that asterisks (*) refer to sEV particle numbers as no statistically significant differences were found between cell numbers of each cell line.

3.3.3.3. Detection of Fluorescent sEVs

Due to their nanoparticulate size, sEVs are diffraction-limited (<200nm) and their detection will be restricted by their total fluorescence intensity, whereas their resolution will be dependent on their size; thus, imaging sEVs in cells is limited by their spatiotemporal parameters and their low signal-to-noise ratio. Even though the GFP-CD63 and CD81-Tdtomato cell lines were successfully generated and are inherently fluorescent, the fluorescence properties of sEVs needed to be assessed to determine if their signal is detectable by confocal microscopy. It was also essential to optimise and improve the detectability of sEVs by using different acquisition parameters and studying their effects on spatial resolution using Point-Spread Function (PSF) measurements (134).

PSF, Optical System Resolution and Theoretical Resolution

PSF is the three-dimensional resulting image of a sub-resolution point source and originates from diffracted light passing through the microscope (134). PSF depends on the wavelength of emitted light from the point source, the numerical aperture of the objective and the size of the object. The generated axial and lateral 3D PSF, provide the respective Full Width at Half Maximum (FWHM), which is the estimated resolution of the optical system; thus, the FWHM can be compared to the Theoretical resolution (134). The Theoretical resolution represents the “optimal ability” of an optical system to discriminate between two objects in close proximity, and is based on the Rayleigh criterion (161). Generally, Theoretical resolution depends on the excitation wavelength of the laser, the refractive index of the immersion medium the numerical aperture of the objective lens, and is affected by the emission wavelength, sample thickness and pinhole size of the confocal microscope (134).

Hence, in these initial imaging studies, the GFP-CD63 sEVs, CD81-Tdtomato sEVs, and the commercially available Tetraspeck microspheres™ (100nm diameter) were detected via confocal fluorescence microscopy, followed by generation of their respective PSFs and FWHM which were then compared to the Theoretical resolution. As the fluorescent properties (fluorescence intensity and signal-to-noise ratio) of sEVs were still unknown, the Tetraspeck™ fluorescent microspheres served as standards for detection using confocal microscopy. These 100nm-sized microspheres are used as sub-resolution fluorescent sources for calibrating fluorescence microscope optics for high-precision multi-colour imaging, especially in 3D applications. In addition, these

microspheres are brightly fluorescent (high signal-to-noise ratio) and they are stained throughout with four different fluorescent dyes; displaying four well-separated excitation/emission peaks - 360/430 nm (blue), 505/515 nm (green), 560/580 nm (orange) and 660/680 nm (dark red). Hence, they could be compared to both the green GFP and orange Tdtomato sEVs and, advantageously, their 100nm- size was also comparable to the average size of sEVs. Therefore, the Tetraspeck™ microspheres were used as a standard for detecting a diffraction-limited fluorescent nanoparticle using confocal microscopy (162). In extent, detection of the Tetraspeck™ fluorescent microspheres alongside sEVs enabled the direct comparison of their generated PSFs and FWHM (optical resolution). Of note, Tetraspeck™ microspheres and sEVs, like other vesicles and small particles, exhibited a Brownian-like motion in liquids, which rendered their detection inherently difficult, lowering the spatial resolution (163). Thus, to minimise Brownian motion, the microspheres and sEVs were immobilised in a 3D thermo-reversible hydrogel (CyGEL), followed by their detection using confocal microscopy.

PSF Analysis of Microspheres and sEVs

Confocal imaging analysis revealed the fluorescence signal of GFP-CD63 and CD81-Tdtomato sEVs compared to the Tetraspeck™ microspheres. [Figure 3.10](#) shows representative fluorescence images (Z-stacks projected based on average fluorescence intensity to form a 2D image), generated PSFs images, the Theoretical resolution and the estimated FWHM (optical resolution of the system). In addition, [Supplementary Figure 9](#), shows the FWHM (axial and lateral) resolution analysis of all the manually counted Tetraspeck™ microspheres and sEVs (Tetraspeck™ (n=100), GFP-CD63 sEVs (n=176) and CD81-Tdtomato sEVs (n=199)) and the percentage of spheres and sEVs that are optically characterizable, based on Theoretical resolution. Firstly, we observed that the Tetraspeck™ microspheres were relatively monodispersed with homogeneous size and fluorescence intensity ([Figure 3.10.A.i,iii](#)). Secondly, whereas the GFP-CD63 and CD81-Tdtomato sEVs had detectable fluorescence signal, they presented with colloidal-like structures and clusters, as well as relative heterogeneity in size and fluorescence intensity ([Figure 3.10.A.ii,iv](#)).

The Theoretical resolution for our optical system was calculated as 0.139µm for the 488nm excitation laser, and 0.155µm for the 543nm excitation laser (lateral resolution, XY-axes), suggesting that objects distanced closer than 0.139µm or 0.155µm respectively, cannot be optically resolved ([Figure 3.10.A,B](#)). Differences in resolution are expected as longer wavelengths of excitation light lower the lateral and axial resolution

of the optical system (134). Similarly, the Theoretical axial Resolution (Z-axis) was 0.349 μm or 0.388 μm , for each excitation laser (488 or 543nm) respectively ([Figure 3.10.A,B](#)); the axial FWHM was larger compared to lateral FWHM, as expected from the literature (134).

To calculate and compare the size of the Tetraspeck™ microspheres according to the resolution of our optical system, generated PSFs lead to calculation of FWHM and distribution analysis ([Supplementary Figure 9](#)). This demonstrated that the average FWHM of lateral resolution (xy-axes) for the microspheres was estimated at 0.210 μm and 0.240 μm , when excited by the 488 or 543nm laser respectively ([Figure 3.10.B: xy-axes](#)). Similarly, the average FWHM for axial resolution (Z axis) was estimated at 0.440 μm and 0.530 μm (Ex:488nm or 543nm, respectively, [Figure 3.10.B: z-axis](#)). Therefore, even though the Tetraspeck™ microspheres are 100nm in diameter, the optical system resolved them as 210nm or 240nm laterally, and 440 or 530nm axially, when excited by the 488nm and 543nm lasers, respectively.

Regarding GFP-CD63 sEVs, we observed that the mean lateral resolution of the sEV population was 0.250 μm , and the axial resolution was 0.43 μm , which is a slightly lower than the Tetraspeck microspheres (excited at 488nm) ([Supplementary Figure 9](#) and [Figure 3.10.B](#)). On the other hand, the mean lateral resolution of the CD81-Tdtomato sEV population was 0.230 μm , and the axial resolution was 0.46 μm , which is a slightly higher resolution than the Tetraspeck microspheres (excited at 543nm) ([Supplementary Figure 9](#) and [Figure 3.10.B](#)). Despite these small differences, our results overall suggested that the FWHM between the Tetraspeck™ microspheres was comparable to GFP-CD63 and CD81-Tdtomato sEVs, as no statistically significant differences were notable ([Figure 3.10.B](#)).

Fluorescence Intensity Analysis of Microspheres and sEVs

Finally, image analysis involved the comparison of the fluorescence intensity of Tetraspeck™ microspheres and sEVs. Specifically, the gMFI of objects (sEVs or microspheres) was measured manually after subtracting the background, using the Fiji software. As expected, the Tetraspeck™ microspheres exhibited a constrained range of fluorescence intensity at both the *green* and *orange* emission channels (SD=33.17 and 45.84, respectively), demonstrating high signal-to-noise ratio ([Figure 3.10.C](#)).

Conversely, GFP-CD63, and especially CD81-Tdtomato sEVs, had wider fluorescence intensity distributions (SD=62.64 or 691.0, respectively), suggesting that sEVs are of lower signal-to-noise ratio. Despite this, the mean fluorescence intensity of

CD81-Tdtomato sEVs (gMFI=418.7) was significantly higher than the Tetraspeck™ microspheres (gMFI=142.3, orange emission channel). On the other hand, the mean fluorescence intensity of GFP-CD63 (gMFI=54) was significantly lower than the Tetraspeck™ microspheres (gMFI=84.86, green emission channel), as shown in [Figure 3.10.C](#).

Collectively, these initial experiments confirmed that the GFP-CD63 and CD81-Tdtomato sEVs have detectable fluorescent signal, suggesting they can be used for further imaging studies. It also became evident that, as sEVs are biologically complex and heterogeneous (heterogeneous size, dispersion, and fluorescence intensity), they pose significant challenges for high-resolution imaging, e.g., due to their low signal-to-noise ratio and refractive index; thus, all these parameters need to be taken into consideration for future imaging studies.

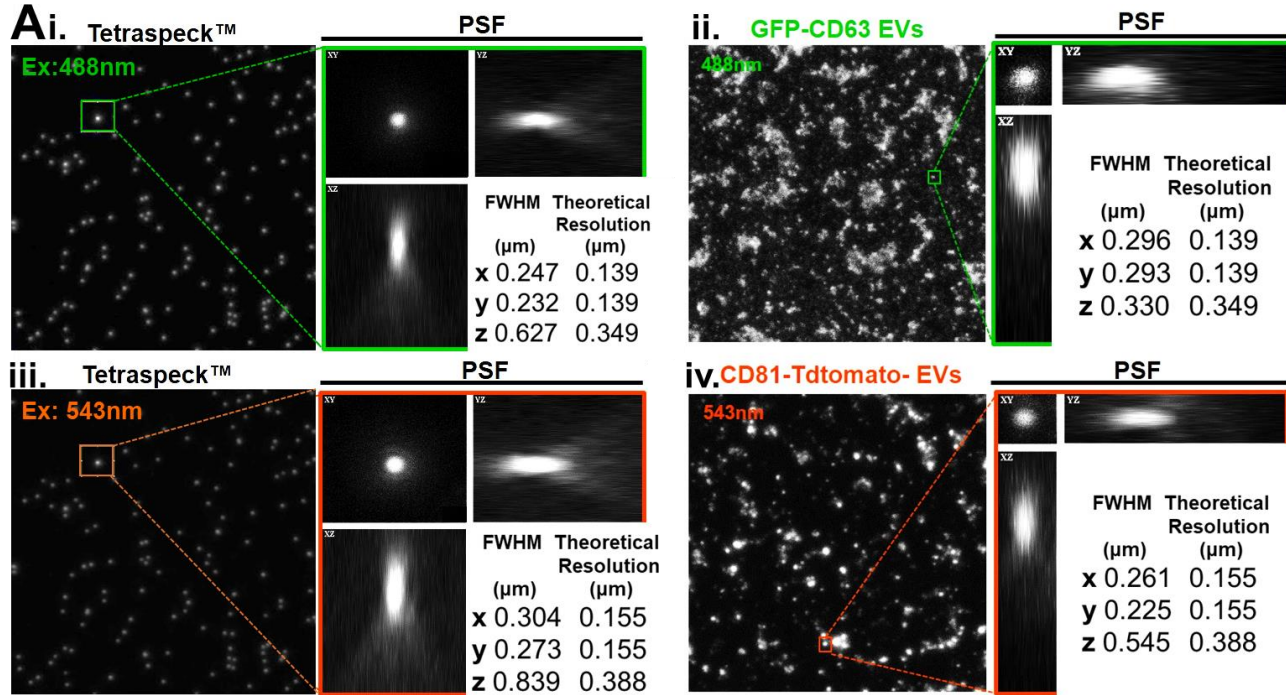
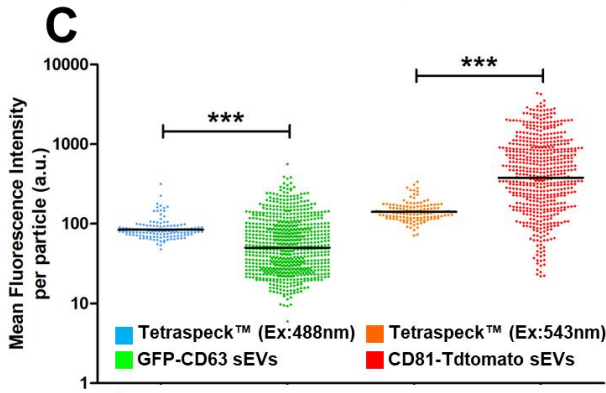
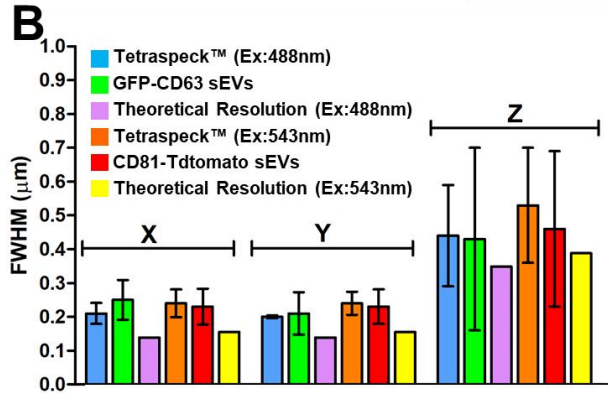


Figure 3.10. Point-Spread Function measurements and fluorescence intensity analysis of GFP-CD63 and CD81-Tdtomato sEVs.

A. Average intensity projected images (from Z-stacks) were used to calculate the PSF (lateral and axial views of the object) and the estimated resolution of the optical system (FWHM-Full Width at Half Maximum) compared to the Theoretical resolution for: **(i)** Tetraspeck™ microspheres (excitation 488nm), **(ii)** GFP-CD63 sEVs, **(iii)** Tetraspeck™ microspheres (excitation 543nm) and **(iv)** CD81-Tdtomato sEVs. Calculation of PSF and FWHM (x-y-z axes) was done using the MetroloJ plugin (Fiji Software) after manual selection of particles: Tetraspeck™ (n=100), GFP-CD63 sEVs (n=176) and CD81-Tdtomato sEVs (n=199). **B.** Graph showing the mean lateral and axial FWHM of microspheres and sEVs (calculated from PSF analysis generating FWHM distributions, see Supplementary Figure 9.) Graph also includes the Theoretical resolution (excitation 488 or 543nm) for comparison. Statistical analysis was done using two-way ANOVA and Bonferroni's post-test multiple comparisons, but no significant differences were apparent. **C.** Fluorescence intensity distribution of microspheres and sEVs. Statistical analysis was done using a Student's T-test with Welch's correction (for each fluorescence channel, separately) denoting significance with ***p<0.0001; geometric mean (horizontal line) is also shown.



3.4. Discussion

In summary, the aims for this chapter included the generation and phenotypic characterisation of DU145 cell lines stably expressing fluorescently conjugated sEV-associated tetraspanin proteins (GFP-CD63 and CD81-Tdtomato). Our aim was to characterise sEVs from such cells and detect endogenous fluorescent sEVs. The GFP-CD63 and CD81-Tdtomato were selected based on many studies using similar reporters *in vitro* and *in vivo* (116-123), especially on a previous study expressing CD63-, CD81- and CD9- pHluorin (GFP variants) on HEK293 and HeLa cells, which determined that CD63 and CD81-pHluorin vesicles exhibited similar MVB to plasma membrane fusion characteristics typically associated with sEVs, whereas CD9-pHluorin exhibited shorter fusion events typically associated with small EVs that bud from the plasma membrane (118, 164).

As an important consideration of this, it was essential to investigate potential effects of overexpression of these tetraspanins on both the parental cell and secreted sEV phenotype; especially since CD63 and CD81 play such vital roles in sEV biogenesis (19, 21) as well as cell adhesion, motility, invasion, membrane fusion, signalling and protein trafficking (165, 166). Potential phenotypic changes due to tetraspanin overexpression is a well-known limitation of genetically-encoded fluorescent tetraspanin cell lines; albeit it is vastly underexplored by previous studies which relied on these approaches (116, 117, 119-121, 123).

To begin with, we observed that overexpression of CD81 (but not CD63), led to changes in cell cycle progression and cell growth compared to the WT control counterparts. Further investigation is needed to elucidate the mechanism behind the slower growth and cell cycle of CD81-Tdtomato DU145 cells; however, previous studies have shown that CD81 overexpression induces cytostasis (inhibition of cell growth and multiplication) in various cell types including glioma cells, hematopoietic stem cells and astrocytes (167-169).

Furthermore, we demonstrated that overexpression of CD63 leads to the upregulation of all sEV-associated markers tested (CD63, CD81, CD9 and MHC-1) at the cell membrane, whereas overexpression of CD81 only led to upregulation of CD81. These differential roles of CD63 and CD81 may be attributed to the different roles of these tetraspanins or the different basal expression level (caused by the overexpression system) which may subsequently affect other proteins in a different, greater or lesser extent, through interactions in the TEMs at the plasma membrane (19, 21). These observations, however, only concern the cell membrane levels of CD63, CD81, CD9 and

MHC-1 as the endocytic pool of these factors has not been investigated yet; thus, Western Blot and immunofluorescence analysis with antibodies against these elements may be more informative on their total protein levels as well as their potential changes arising in their subcellular localisation.

Indeed, fluorescence microscopy analysis showed that the cellular localisation of GFP-CD63 and CD81-Tdtomato was predominantly in the plasma membrane, cell protrusions and in the perinuclear compartment, in agreement with previous studies (117, 118, 121, 123); this was expected due to the transmembrane structure of CD63 and CD81, which can be localised in membranes and endosomes (19, 21). Fluorescence microscopy analysis also demonstrated that overexpression of CD63 or CD81 led to changes in cell morphology as resulting cells were significantly larger or smaller, respectively, to WT parallel controls. Overall, it remains to be elucidated why a rather modest overexpression of CD63 or CD81 resulted in such differential phenotypic changes at the cellular level (changes in growth, cell cycle, morphology, expression of sEV-associated markers). To our knowledge, the effects of CD63 or CD81 overexpression have not been greatly addressed in PCa cell lines.

Limited studies suggested that CD63 overexpression effects may potentially depend on the cell type. For example, a study in melanoma demonstrated that CD63 overexpression inhibited invasiveness and epithelial-to-mesenchymal transition (EMT) (170), whereas a study in ovarian and gastric cancer cell lines showed that CD63 downregulation inhibited EMT (171). Regarding CD81, studies from various cancers overall support that CD81 promotes cancer progression (172-174). For example, a study in melanoma demonstrated that ectopic CD81 expression results in increased cell migration and invasion, and promotes acquisition of a mesenchymal spindle-like cell shape (172), while a study in breast cancer also demonstrated increased cell proliferation and migration after CD81 overexpression (173). Furthermore, one study in PCa showed that increased expression of CD81 is a poor prognostic marker of PCa as it is significantly associated with lymph node metastasis, TNM cancer stage (T: primary tumour, N: regional lymph nodes, M: distant metastasis) and poor survival (174). This study also demonstrated that knockdown of CD81 in DU145 and PC3 PCa cell lines resulted to inhibition of cancer cell proliferation, migration, and invasion (174). This study however has not conducted any CD81 overexpression studies on PCa cell lines; thus, further investigation is necessary to address the effects of CD63 or CD81 overexpression on the phenotype of DU145 PCa cells.

In conclusion, basic morphological and phenotypical characterisation of the GFP-CD63 and CD81-Tdtomato DU145 cell lines demonstrated significant changes in the phenotype of these cell lines. Previous studies using these fluorescent tetraspanin

reporter overexpression systems, have not done any similar investigations (116, 117, 119-121, 123), and have wrongly assumed that overexpression of tetraspanins does not alter their cell systems. However, this Chapter highlighted the importance of phenotypic characterisation of the parental cells, as these changes would inadvertently affect the secreted sEVs, in terms of the sub-population distributions, their molecular content and ultimately their functions. Further insights into the molecular changes that arise in GFP-CD63 and CD81-Tdtomato DU145 cell lines will be gained from proteomics analysis, described in detail in Chapter 4.

After basic phenotypic characterisation of the GFP-CD63 and CD81-Tdtomato DU145 cell lines, isolation of sEVs was performed followed by NTA which determined the distribution of their size (diameter approx. 50-150nm). This agreed with the typical size for WT PCa-derived sEVs, also observed from other studies (157, 159, 160). Further analysis suggested that whereas overexpression of CD63 or CD81 did not affect the size distribution of sEVs, overexpression of CD63 (but not CD81) induced the elevation of sEV-associated markers on the EV membrane, thus reflecting the changes observed at the cell membrane. In contrast to our observations, a previous study showed that overexpression of CD63-pHluorin (GFP variant) in HeLa cells, did not significantly affect the levels of tetraspanins in isolated sEVs compared to WT cells (determined by Western Blot analysis) (164).

We also observed that overexpression of CD63 in DU145 cells increased the quantity of secreted sEVs compared to WT control cells, even though this previous study supported that overexpression of CD63-pHluorin did not result in significant increase in sEV secretion (164). However, a follow-up study overexpressing pHluorin_M153R-CD63 (M153R is a stabilising mutation in the pHluorin moiety) in HT1080 fibrosarcoma cells, demonstrated increased secretion rate of sEVs (119).

It is still unknown why CD63 expression induced this significant phenotypic change in sEVs. It may be attributed to the generally higher levels of tetraspanins (CD9, CD63 and CD81) present within the cell and/or the cell membrane, which subsequently resulted in higher levels of these tetraspanins being sorted into sEVs. However, it was surprising that CD81 overexpression on the cell membrane did not result to changes in the repertoire of EV-associated markers on the sEV membrane but did significantly increase the quantity of sEV secretion in these cells. These differences between the fluorescent EV reporter systems might be attributed to the different functions and protein interactions of CD63 and CD81 (e.g., with other proteins and tetraspanins at the TEMs) (19, 21). For example, CD63 participates in cargo sorting for sEVs via ESCRT-dependent and ESCRT-independent mechanisms (12); CD81 also participates in cargo sorting and may induce inward budding of the TEM due to clustering with other proteins and cholesterol

(23, 156). Furthermore, it has been shown that CD63 is absolutely vital for the biogenesis of lysosome-related organelles in melanoma cells (25); however, CD81 is not as essential in lymphocytes, as its absence did not have any effects on sEV secretion (22). Another aspect is that perhaps overexpressing CD63 or CD81 causes a shift in the subpopulations of sEVs secreted from CD81-Tdtomato or GFP-CD63 cells, which might collectively be responsible for different effects on sEV phenotype and secretion (7, 175).

Lastly, the stable cell-line derived fluorescent sEVs were successfully detected via confocal fluorescence microscopy and were further analysed to determine the distribution of their fluorescence intensity and to measure their response (degree of blurring and detectability) in a biological mimic environment – this is termed the point-spread function (PSF). Both the microsphere standard and the sEVs were placed in a 3D hydrogel designed with specific biophysical properties, such that the optical path was tightly defined. Whereas the Tetraspeck™ microspheres are 100nm, their FWHM was larger than the Theoretical resolution, thus demonstrating the actual limits of the optical system to resolve a diffraction-limited fluorescent standard microsphere. According to the literature, the PSF of a sub-resolution fluorescent microsphere should ideally be within 10–40% of the Theoretical resolution which was indeed observed for the Tetraspeck™ microspheres, the GFP-CD63 and the CD81-Tdtomato sEVs (134). The PSF measurements also showed that the axial PSF was larger than the lateral PSF (estimated 3 times larger), thus corresponding to the literature (134).

A lower resolving ability of sEVs was expected due to their range in sizes (50-150nm), varying fluorescence intensity, lower signal-to-noise ratio and lower refractive index compared to the Tetraspeck™ microspheres (sEV RI range 1.36-1.398 and polystyrene microsphere RI is 1.633) (176); the latter being uniformly shaped with high fluorescence yield and high signal-to-noise ratio. One relevant study successfully detected CellTracker™-Dil-labelled sEVs, as well as sEVs co-labelled with CellTracker™-Dil and anti-CD63 antibodies-fused to AlexaFluor647, using super-resolution fluorescence microscopy, TIRF, PALM and STORM (TIRF: Total Internal Reflection Microscopy, PALM: Photo-Activated Localisation Microscopy and STORM: Stochastic Optical Reconstruction Microscopy) (177). This study subsequently generated PSFs for sEVs and estimated the FWHM at 650nm for TIRF, and 70nm for PALM/STORM (177). However, this study generated PSFs with exogenously-labelled sEVs and/or conjugated with antibodies, whereas in our study we were able to detect and optically characterise single endogenously fluorescent sEVs in live-cell imaging conditions. A recent study also generated PSFs of endogenously fluorescent sEVs (CD63-GFP-mCherry) immobilised on glass slides and compared them to PSFs of 100nm Tetraspeck microspheres (122). Specifically, they detected and optically

characterised sEVs and Tetraspeck microspheres by widefield fluorescence microscopy, followed by deconvolution, and reported similar Theoretical and optical resolution to our study (122).

Some issues that occurred with detecting endogenously fluorescent sEVs were the colloid-like structures and clustering that were especially prominent with GFP-CD63 sEVs; these may be partly attributed to the isolation method that was used. While ultracentrifugation-based methods are common for vesicle purification, this approach can result in co-isolation of non-vesicular materials; thus, future isolations will be conducted with ultracentrifugation on a 30% sucrose/D₂O cushion which results in higher purity preparations, as it focusses on collecting vesicles of a certain density of 1.2g/ml, and is effective at eliminating a large proportion of non-vesicular matter (157).

Collectively, this study generated PSFs of stable-cell line derived fluorescent sEVs and compared them with commercially available microspheres of relevant size (Tetraspeck™) using conventional confocal fluorescence microscopy. Furthermore, detection and PSF analysis was conducted for the first time on a 3D hydrogel (CyGEL) which emulated a simple 3D tissue-mimic model; thus, it provided valuable information on the ability of the optical system to resolve the GFP-CD63 and CD81-Tdtomato sEVs and established the baseline for future high-resolution imaging studies on more complex models.

3.5. Conclusions

To summarise, this was the first study that has generated and attempted to phenotypically characterise DU145 PCa cell lines expressing the GFP-CD63 and CD81-Tdtomato fluorescent sEV reporter proteins. Collectively, GFP-CD63 expression increased the protein levels of sEV-associated proteins (CD9, CD63, CD81 and MHC-1) in both the cell and sEV membrane. Conversely, CD81-Tdtomato expression did not significantly affect the levels of these proteins at the cell or sEV membrane (except upregulation of CD81 in parental cells). Interestingly, whereas GFP-CD63 expression induced significant phenotypic changes to sEVs and EV-associated proteins at the cell membrane, it did not cause significant effects on cell growth or cell cycle but did alter cell morphology (larger cell area and more cobblestone-like shape) and increased sEV secretion. On the other hand, CD81-Tdtomato expression did not induce significant phenotypic changes to sEVs and or EV-associated protein expression at the cell membrane expression, however, it did cause significant phenotypic changes to the cells including slower growth rate, slower cell cycle progression, morphological changes (smaller cell area compared to controls) and increased sEV secretion. Further investigation is thus necessary to elucidate the mechanisms behind these differential results for GFP-CD63 and CD81-Tdtomato DU145 cells and sEVs. Despite these observations, the GFP-CD63 and CD81-Tdtomato stable DU145 cell lines were used to isolate fluorescent sEVs, which were then successfully detected and optically characterised via confocal fluorescence microscopy. These initial imaging studies confirmed the detectability of the GFP-CD63 and CD81-Tdtomato sEV fluorescence signal and underlined their biological complexity in terms of size, dispersion, and fluorescence heterogeneity, which needs to be taken into consideration for future imaging studies.

CHAPTER 4:
Quantitative Proteomics by
SWATH-MS on DU145 cells and
Extracellular Vesicles
Overexpressing CD63 or CD81

4.1. Introduction

In the previous chapter (Chapter 3), we demonstrated that overexpression of CD63 or CD81 fused with fluorescent proteins (GFP and Tdtomato respectively) induces various phenotypic changes in DU145 cells (changes in cell morphology, cell growth, cell cycle and expression of tetraspanins at the cell membrane), as well as in generated sEVs (differences in tetraspanins levels or secretion levels). Further investigation of changes in the proteome of CD81-Tdtomato and GFP-CD63 sEVs was essential however, especially since they would be further used for dosing and functional studies, which might be influenced by altered protein composition of these sEVs. As mentioned previously, many studies have generated stable cell lines expressing fluorescent proteins fused with tetraspanins for use as fluorescent sEV reporter systems *in vitro* and *in vivo* (117, 118, 121-123, 178); however, the majority of them have not investigated whether overexpression of these tetraspanins altered the phenotype or proteome of engineered cells or sEVs.

Conventionally, DDA-MS (Data-Dependent Acquisition tandem Mass Spectrometry) approaches have been utilised for proteomics analysis of sEVs, and allow the phenotypic determination and identification of biomarkers in the proteome of various cancer-derived sEVs, e.g., PCa (179-182), bladder cancer (183), colorectal cancer (184), ovarian cancer-derived sEVs (185), and even sEVs generated from the 60 types of cancer cell lines deriving from the National Cancer Institute (NCI-60) (186). Other studies have utilised DDA-MS analysis to investigate potential changes of the sEV proteome after exposure of cancer cells to therapeutics e.g., treatment of PCa cell lines with docetaxel (187) and dihydrotestosterone (188), or exposure to hypoxia (PCa- and glioma cell-derived sEVs) (189-191). In addition, a few studies investigated the changes in the proteomic profile of sEVs after genetic manipulation of the cells of origin i.e., overexpression of CD151 and knockdown of CD9 in the RWPE1 prostate cells (192), or overexpression of GFP-CD63 in HEK293T (human embryonic kidney) cells (122).

Following the same rationale as these studies, our aim was to investigate whether overexpression of CD63 or CD81 (fused with GFP and Tdtomato, respectively) would alter the proteome of the DU145 cells of origin, and the generated sEVs. However, instead of conducting a conventional DDA-MS analysis, we utilised a next generation DIA (Data-Independent Acquisition) approach, named SWATH-MS which stands for Sequential Windows Acquisition of All Theoretical Spectra (193).

DDA-MS is the classic form of tandem mass spectrometry (MS/MS), which involves scanning of all precursor peptide ions during the survey scan (MS1), and selection of a

specific number of predefined precursor ions (usually the most abundant), which are then subjected to fragmentation (MS2) and then analysed with a database search algorithm (194, 195). On the other hand, the DIA SWATH-MS approach starts by scanning all precursor ions at MS1 (similarly to DDA-MS), but the second step involves fragmentation of all these precursor ions within a specific mass-to-charge ratio (m/z) region, by fragmenting sequentially in a fixed number of windows that cover the entire m/z range, thus leading to increased proteomic coverage (193-195). Furthermore, the SWATH-MS DIA analysis requires a reference library of spectra (Spectral Library) generated in DDA mode, in order to extract fragment ion chromatograms based on this library (193-195). Recently, SWATH-MS has started being utilised in quantitative proteomics analysis of sEVs; one example is a comprehensive study profiling glioma sEVs as a method of tumour surveillance (196), and another example is an exploratory study screening for biomarkers in urinary sEVs (197).

Collectively, due to the design of the DDA-MS method, its major limitations are the lack of reproducibility between technical replicate experiments and low sensitivity, as low abundant peptides are missed and cannot be measured by this analysis; on the other hand, the DIA SWATH-MS approach that sequentially scans the whole m/z range in predefined windows increases the sensitivity for detection and has been reported to be highly reproducible between runs (194, 195). [Figure 4.1](#) shows a schematic workflow describing the SWATH-MS process.

4.2. Aims and Objectives

In this Chapter we selected the SWATH-MS method as it is a sensitive, quantitative, and unbiased approach, in order to determine the global proteomic changes in DU145 cells and generated sEVs after overexpression of CD63 or CD81, compared to their respective WT parallel controls. Ultimately, we aimed to conduct dosing and functional experiments with these sEVs; thus, it was imperative to fully understand the biological consequences of overexpressing CD63 or CD81 on this system. Therefore, this chapter aimed:

- To utilise a DIA-MS approach for global proteomic profiling of cells and sEVs.
- To identify and compare differentially expressed proteins in cells and sEVs.
- To explore potential biological implications of these predicted proteomic alterations *in silico*, in order to determine the likely severity of these changes on sEV functions.
- To validate the MS-based protein identifications as differentially expressed using other methods such as Western Blot.

4.3. Results

4.3.1. Quantitative Analysis of Differentially Expressed Proteins

4.3.1.1. SWATH-MS Rationale and Workflow

As CD63 and CD81 are major players in sEV biogenesis (19, 24, 156, 198), and CD81-Tdtomato and GFP-CD63 sEVs were to be used for further dosing and functional studies, it was essential to investigate potential phenotypic differences of both the cells of origin and generated sEVs. For this Chapter we conducted a comprehensive quantitative proteomics analysis for the generated CD81-Tdtomato and GFP-CD63 sEVs (and the parental cells) to profile any potential proteomic variations after overexpression of CD63 or CD81 compared to their respective WT DU145 parallel controls.

For this analysis, the cell-culture conditions of Chapter 3 were reproduced with GFP-CD63, CD81-Tdtomato and WT parallel control DU145 cells grown in conventional 2D tissue-culture flasks, followed by extraction of the EV-rich cell-conditioned media after 7 days, pre-clearing to remove dead cells and debris, and then pelleting and isolating vesicles by the 30% sucrose/D₂O cushion ultracentrifugation method (see Chapter 2, Materials and Methods, [Section 2.11](#)). The sucrose cushion ultracentrifugation method is a high-specificity and high-purity approach that enables the isolation of sEVs (small EVs, size $\leq 200\text{nm}$) by flotation at a certain density (1.2g/ml) and eliminates the majority of non-vesicular constituents (6, 157). In parallel to sEV isolation, cells grown in the tissue-culture flasks were extracted, and together with isolated sEVs, were lysed followed by protein quantification ([Table 2.2](#), isolation #2).

After protein quantification, the cell and sEV lysates were used for SWATH-MS analysis, which is a DIA method used in conjunction with a targeted data extraction strategy to comprehensively profile these cells and sEVs and determine global proteomic changes (193). This strategy involved the generation of custom spectral libraries by DDA analysis of the combined proteomes of: (i) GFP-CD63 and GFP-Parallel cells (Spectral Library 1) and (ii) CD81-Tdtomato and Tom-Parallel cells (Spectral Library 2). These spectral libraries were then used as reference libraries to match peptide fragmentation spectra (generated in SWATH-MS DIA runs) and extract the identities (IDs) and quantities of the proteins in the Skyline software (136). A schematic workflow describing the preparation of cell and sEV lysates, generation of spectral libraries, SWATH MS runs, data extraction and comparisons in the Skyline Software is shown in [Figure 4.1](#).

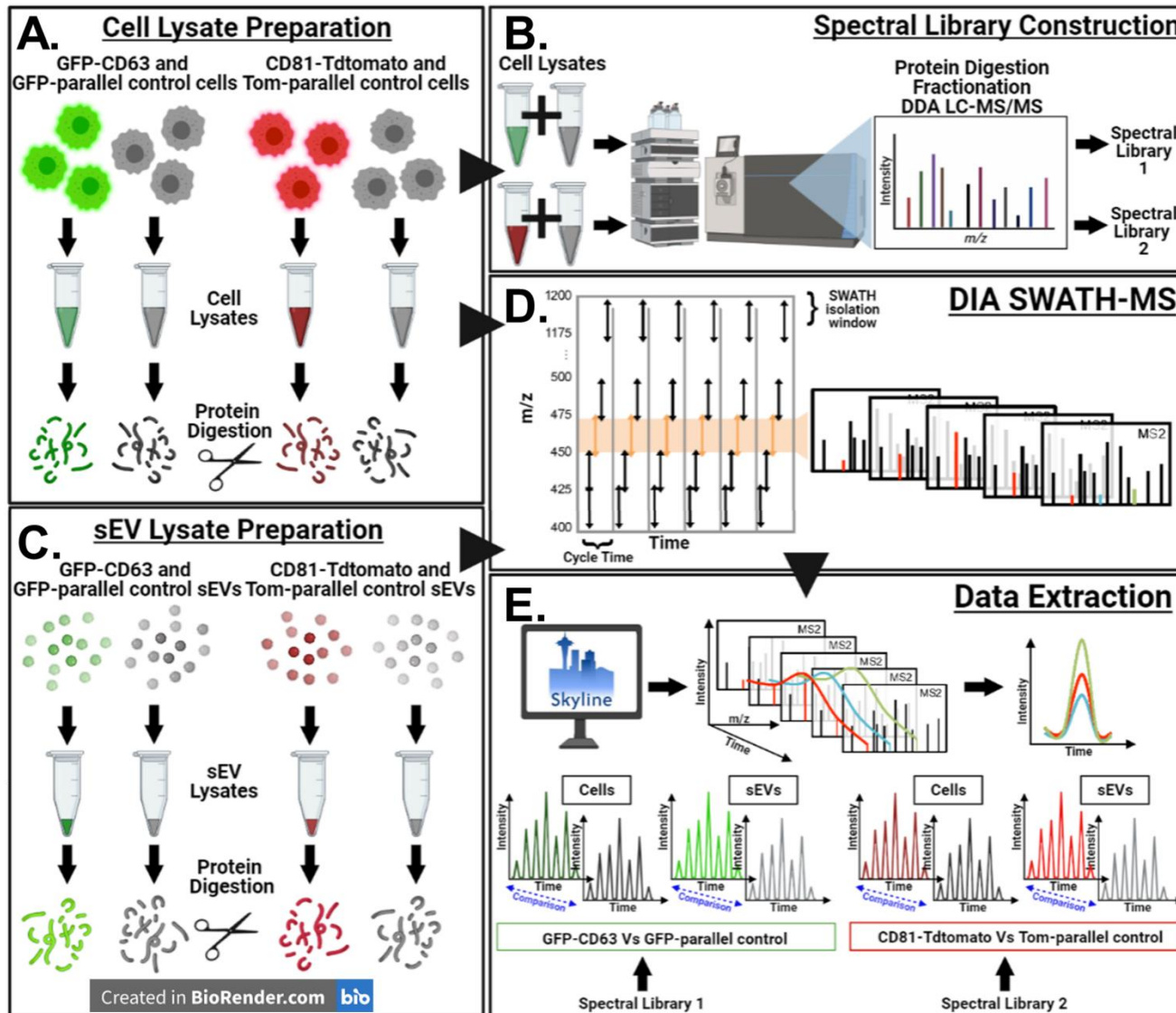


Figure 4.1. Schematic workflow describing the SWATH-MS process.

A. GFP-CD63 (green), CD81-Tdtomato (red) and GFP- and Tom-Parallel control cells (grey) were cultured in 2D culture flasks, with the cell-conditioned media being extracted to isolate sEVs, followed by lysis of the cells, protein quantification and tryptic digestion. **B.** Spectral Library generation was done after fractionation of digested cell samples, based on all identified fragment ions, peptides, and proteins from DDA LC-MS/MS (GFP-CD63 with GFP-Parallel for Spectral Library 1 and CD81-Tdtomato with Tom-Parallel for Spectral Library 2). **C.** sEVs were isolated from the EV-rich conditioned media (from **A.**) by 30%/D₂O sucrose cushion ultracentrifugation, followed by sEV lysis, protein quantification and tryptic digestion. **D.** DIA SWATH-MS analysis was done using digested cell and sEV samples. **E.** The Skyline software was used for targeted data extraction and peptide quantification based on the predefined targets found in the spectral libraries. Further data processing was done to compare GFP-CD63 with GFP-Parallel and CD81-Tdtomato with Tom-Parallel controls (cells and sEVs).

*LC-MS/MS: *Liquid Chromatography Tandem Mass Spectrometry*

4.3.1.2. Detection of proteins in cells and sEVs by SWATH-MS analysis

As shown in the previous workflow schematic [Figure 4.1](#) after preparation of cell lysates, tryptic digestion and fractionation, a LC-MS/MS (Liquid Chromatography Tandem Mass Spectrometry) DDA analysis was conducted to generate spectral libraries, which consisted of 3470 proteins (Spectral Library 1, GFP-CD63 and GFP-Parallel control cells) and 3364 proteins (Spectral Library 2, CD81-Tdtomato and Tom-Parallel control cells) with a 1% false discovery rate (FDR).

Next, DIA SWATH-MS runs were conducted comparing: (i) GFP-CD63 with GFP-Parallel control cells, (ii) GFP-CD63 with GFP-Parallel control sEVs, (iii) CD81-Tdtomato with Tom-Parallel control cells and (iv) CD81-Tdtomato with Tom-Parallel control sEVs, for protein identifications, followed by chromatogram peak alignment to the corresponding Spectral Library (1 or 2). Of note, each cell and sEV sample was run as a technical replicate (triplicate) to account for potential sample variability due to complex sample processing.

Principal Component Analysis (PCA) of the technical replicates was performed and demonstrated the variability between different samples, but effective clustering of the three technical replicates for each sample, as shown in [Supplementary Figure 10](#). Of these detected proteins, only proteins with chromatogram peak area variability of less than 50% between two technical replicates were included in the subsequent analysis (CV <50%). The number of detected proteins for each sEV and cell sample are shown in detail in [Table 4.1](#). Briefly, DIA SWATH-MS led to the detection of 346 and 347 proteins for GFP-CD63 and GFP-Parallel control sEVs, as well as 280 and 279 proteins for CD81-Tdtomato and Tom-Parallel control sEVs (respectively). On the other hand, a higher number of proteins were detected for cell samples i.e., 1028 and 1030 proteins for GFP-CD63 and GFP-Parallel control cells, as well as 1079 and 1077 proteins for CD81-Tdtomato and Tom-Parallel control sEVs (respectively); all shown in [Table 4.1](#).

To begin illustrating the differences between cells and sEVs, we generated Venn Diagrams to determine the common and unique MS-protein identifications between them, comparing sEVs and cells overexpressing CD63 or CD81 with the respective WT Parallel controls ([Figure 4.2.A](#)). This analysis was done to emphasise the extreme differences in the proteome between cells and sEVs, by looking at the presence or absence of protein identifications; subsequent analysis will explore the differences arising in protein abundance.

Our analysis showed that 136 protein identifications (~40%) were unique in GFP-CD63 and GFP-Parallel control sEVs, whereas 818 protein identifications (~80%) were unique in the parental cells ([Figure 4.2.A.i](#)). Furthermore, 210 protein IDs were common in both cells and sEVs suggesting that ~60% of detected proteins in sEVs reflected the cells of origin. Interestingly, we identified 1 protein ID that was absent from GFP-CD63 sEVs, and 2 protein IDs absent from GFP-CD63 cells compared to WT Parallel controls.

Similarly, we observed 91 protein identifications (~33%) unique in CD81-Tdtomato and Tom-Parallel control sEVs, while 888 protein IDs (~83%) were unique in the parental cells. In addition, 187 proteins were common between CD81-Tdtomato and Tom-Parallel control sEVs and parental cells, suggesting that ~67% of detected proteins in sEVs reflected the cells of origin ([Figure 4.2.A.ii](#)). Finally, we detected 2 unique protein IDs in CD81-Tdtomato sEVs and 4 IDs in CD81-Tdtomato cells, which were absent from Tom-Parallel control sEVs and cells, respectively. The detailed UniProt Accession numbers and Gene Names for these common and unique proteins are shown in [Supplementary Figure 11](#).

Next, we transformed the UniProt Protein IDs of the common identified proteins of our sEV datasets into Gene Symbol IDs, and then cross-referenced them with the publicly available EV proteome database Vesiclepedia (140), using the FunRich software (139) ([Figure 4.2.B](#)). This analysis showed that >95% of detected proteins in GFP-CD63, CD81-Tdtomato and WT Parallel control sEVs have been documented previously in Vesiclepedia in PCa and other cancer types. However, we additionally identified 11 proteins not previously documented in sEVs, including: (i) TMEM184C (Transmembrane Protein 184C), (ii) STRIP2 (Striatin Interacting Protein 2), (iii) TLDC1 (MTOR Associated Protein Eak-7 Homolog), (iv) AKAP10 (A-Kinase Anchoring Protein 10) and (v) TIGAR (TP53 Induced Glycolysis Regulatory Phosphatase); AKAP10 and TIGAR were detected in all four sEV types analysed by SWATH-MS. Further investigation and validation of these targets will be necessary to establish their presence and significance on sEVs.

To conclude, our analysis so far demonstrated a partial overlap of the proteome of sEVs with the parental cells (60-67%), which is expected due to their biogenesis. However, a plethora of unique protein identifications were also detected for both the parental cells and the sEVs, highlighting their differences in composition. Finally, comparison of the proteins identified in the sEV datasets with Vesiclepedia, revealed a few novel identifications, despite the fact that the majority of IDs were previously reported.

Table 4.1. Detected and quantified proteins from SWATH-MS analysis in DU145 sEVs and cells overexpressing CD63 or CD81 compared to WT parallel controls.

SWATH-MS (DIA analysis) Sample	Detected Proteins CV 50%*	SWATH-MS (DIA analysis) Sample Comparisons	Common Proteins CV 50%*	Common Proteins CV 50%*	
				p-value<0.05	p-value<0.05 Fold Change > 1.4
GFP-CD63 sEVs	346	GFP-CD63 Vs GFP- Parallel control sEVs	346	133	78
GFP-Parallel control sEVs	347				
CD81-Tdtomato sEVs	280	CD81-Tdtomato Vs Tom-Parallel control sEVs	279	180	123
Tom-Parallel control sEVs	279				
GFP-CD63 cells	1,028	GFP-CD63 Vs GFP- Parallel control cells	1,028	483	95
GFP-Parallel control cells	1,030				
CD81-Tdtomato cells	1,079	CD81-Tdtomato Vs Tom-Parallel control cells	1,075	456	73
Tom-Parallel control cells	1,077				

***Note:** SWATH-MS detected proteins shown here were extracted after a Q value cut-off 0.01 based on decoy peptides; decoy peptides are generated *in silico* in the Skyline software by shuffling the amino acid sequences of target peptides. These decoys closely resemble the chromatographic and spectrometric properties of the target peptides and are used to determine the error rate of random co-elution fragment ions and protein inference in SWATH-MS data; thus, a threshold for false discovery rate (Q cutoff: 0.01) is applied which distinguishes detected target peptides from decoy peptides based on a scoring algorithm in the Skyline software (199).

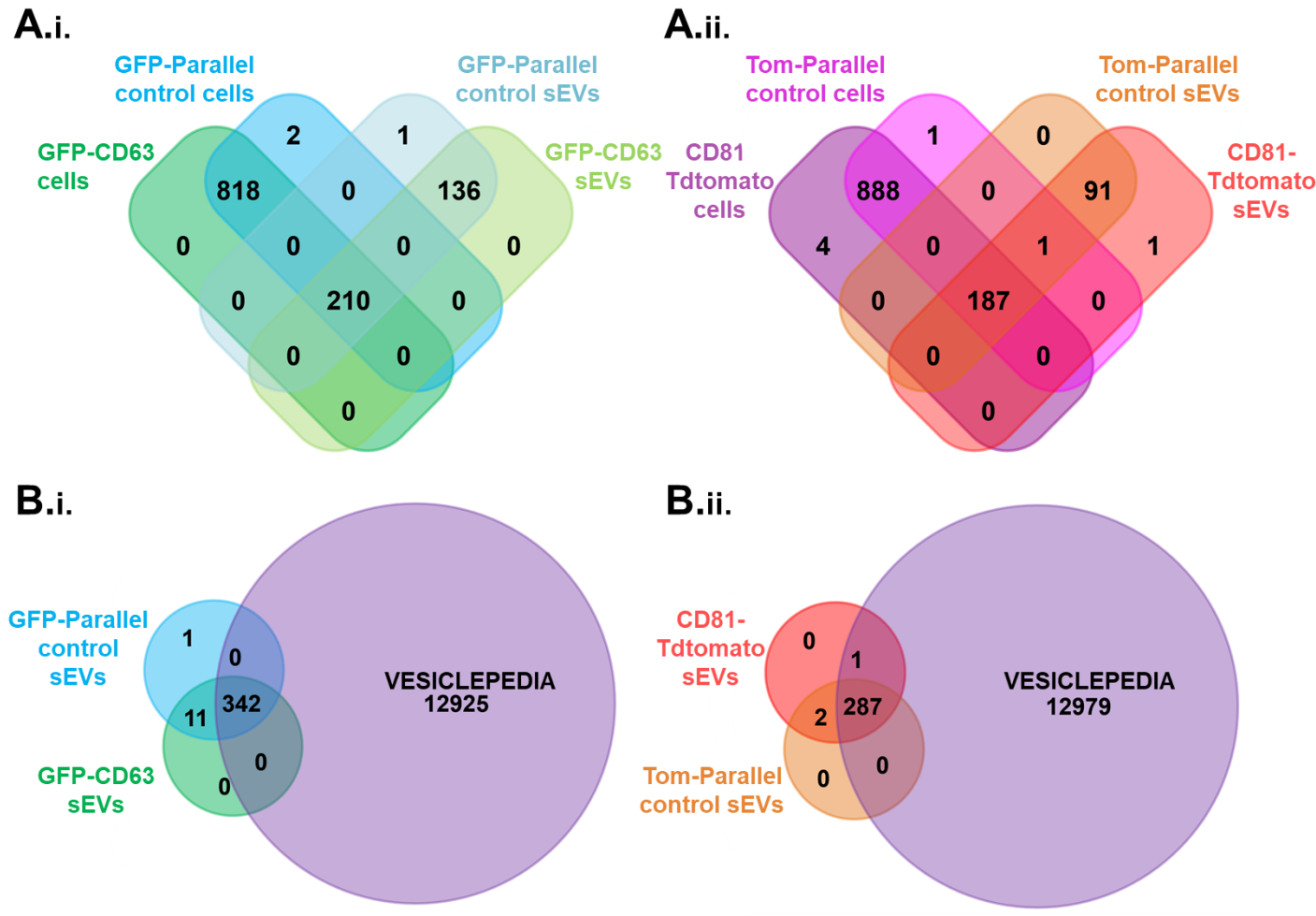


Figure 4.2. Venn Diagrams for cells and sEVs overexpressing CD63 or CD81 compared to WT parallel controls.

A. Venn Diagrams depicting unique and overlapping proteins for (i) GFP-CD63 and GFP-Parallel cells versus sEVs and (ii) CD81-Tdtomato and Tom-Parallel cells versus sEVs. For generation of these Venn diagrams the UniProt Accession numbers of proteins with peak area variability of less than 50% between two technical replicates were included for analysis (CV<50%). Details for unique IDs of each Venn diagram are shown in [Supplementary Figure 11](#). **B.** Venn Diagrams depicting unique and overlapping proteins after IDs were transformed to Gene Symbol IDs, which were detected in sEV samples compared with the Vesiclepedia database (included in the FunRich software). **B(i):** 11 unique IDs were detected for GFP-CD63 and GFP-Parallel sEVs (AKAP10, CLUH, YEATS4, TLDC1, MRPL24, ARL5B, TIGAR, DCAF13, TMEM184C, UTP6, STRIP2), as well as 1 unique ID (CD033) for GFP-Parallel sEVs only and **B(ii):** 2 unique IDs were detected for CD81-Tdtomato and Tom-Parallel sEVs (AKAP10, TIGAR).

4.3.1.3. Protein expression comparison of common proteins in cells and sEVs

Sub-cellular localisation

To determine potential changes to the cell and sEV proteome after overexpression of CD63 or CD81, only the common proteins were selected for subsequent relative expression analysis i.e., the common proteins between (i) GFP-CD63 with GFP-Parallel control cells, (ii) GFP-CD63 with GFP-Parallel control sEVs, (iii) CD81-Tdtomato with Tom-Parallel control cells and (iv) CD81-Tdtomato with Tom-Parallel control sEVs.

This led to the selection of the following common protein IDs for sEV samples: (i) 346 proteins for GFP-CD63 and GFP Parallel control sEVs, and (ii) 279 proteins for CD81-Tdtomato and Tom Parallel control sEVs. In addition, the following common protein IDs were selected for the cell samples: (i) 1028 proteins for GFP-CD63 and GFP Parallel control cells, and (ii) 1075 proteins for CD81-Tdtomato and Tom Parallel control cells. Details for these identifications are shown in [Table 4.1](#).

To begin with, these common proteins were analysed to determine their localisation in 10 sub-cellular compartments of interest, using the FunRich (Functional Enrichment analysis) software, after conversion of their UniProt IDs (proteins) into Gene symbols (genes), followed by Gene Enrichment Analysis ([Figure 4.3](#)). We observed that a higher percentage of genes in the cell samples were assigned (in order of prevalence) to the mitochondrial, cytosolic and ribosomal compartments, whereas a significantly higher percentage of genes in the respective sEV samples were assigned to the exosomal, cytoplasmic, lysosomal, plasma membrane and Golgi compartments. These general observations are expected from the known differences in the proteome of cells and sEVs, with a clear bias towards membrane and endo-lysosomal features for sEVs. Interestingly, sEVs and cells exhibited similarities in the percentage of genes localising to the nuclear and ER (endoplasmic reticulum) compartments, potentially due to “house-keeping” proteins that are equally reflected in cells and sEVs ([Figure 4.3](#)).

Relative abundance of common proteins between cells or sEVs overexpressing CD63 or CD81

After Gene Enrichment analysis was done, these common proteins were further analysed to determine any proteins with significantly differential expression (dysregulation). Firstly, from the 346 common protein identifications ([Table 4.1](#)) quantified for GFP-CD63 and GFP-Parallel control sEVs, the relative abundance of 133 proteins (38.4%) was significantly altered (p-value <0.05), with 78 of these proteins (22.5% of total) displaying higher than 1.4-fold change (FC) in relative abundance (FC > |1.4|, i.e., FC > 1.4 or FC > -1.4). Secondly, from the 279 quantified common protein identifications for CD81-Tdtomato and Tom-Parallel control sEVs, the relative abundance of 180 proteins (64.5%) was significantly altered (p-value <0.05), with 123 of these proteins (44.1% of total) displaying higher than 1.4-FC difference ([Table 4.1](#)).

Similarly, from the 1028 common protein IDs quantified for GFP-CD63 and GFP-Parallel control cells ([Table 4.1](#)), the relative abundance of 483 proteins (46.98%) was significantly altered (p-value <0.05), with just 95 of these proteins (9.24% of total) displaying higher than 1.4-FC difference. Finally, from the 1075 common protein IDs quantified for CD81-Tdtomato and Tom-Parallel control cells, the relative abundance of 456 proteins (42.42%) was significantly altered (p-value <0.05), with just 73 of these proteins (6.79% of total) displaying higher than 1.4-FC abundance ([Table 4.1](#)).

Detailed quantification and statistical analysis of the significantly altered proteins (p-value < 0.05) exhibiting higher than 1.4-FC difference (FC > |1.4|) in relative abundance are shown in [Supplementary Tables 1-4 in APPENDIX II](#): Supplementary Table 1 for GFP-CD63 and GFP-Parallel control sEVs, Supplementary Table 2 for CD81-Tdtomato and Tom-Parallel control sEVs, Supplementary Table 3 for GFP-CD63 and GFP-Parallel control cells and Supplementary Table 4 for CD81-Tdtomato and Tom-Parallel control cells. These tables include: (A) UniProt protein accession and Gene names, (B) peptide counts for each protein ID, (C) quantification of protein abundance indicated by: (i) the raw chromatogram area under the peak (Log₂ transformed), and (ii) the normalised to median chromatogram area (log₂ transformed) for all three technical replicates per sample, as well as (D) Student's T-test statistical analysis (done in the Perseus Software) comparing GFP-CD63 to GFP-Parallel controls and CD81-Tdtomato to Tom-Parallel controls, showing the statistically significant proteins with p-value < 0.05 (-Log₁₀(p) > 1.3, and calculated adjusted q-values) and with higher than 1.4-FC differences (FC > |1.4|, or log-transformed -0.5 < log₂(FC) > +0.5), as well as the calculated T-test Statistic values.

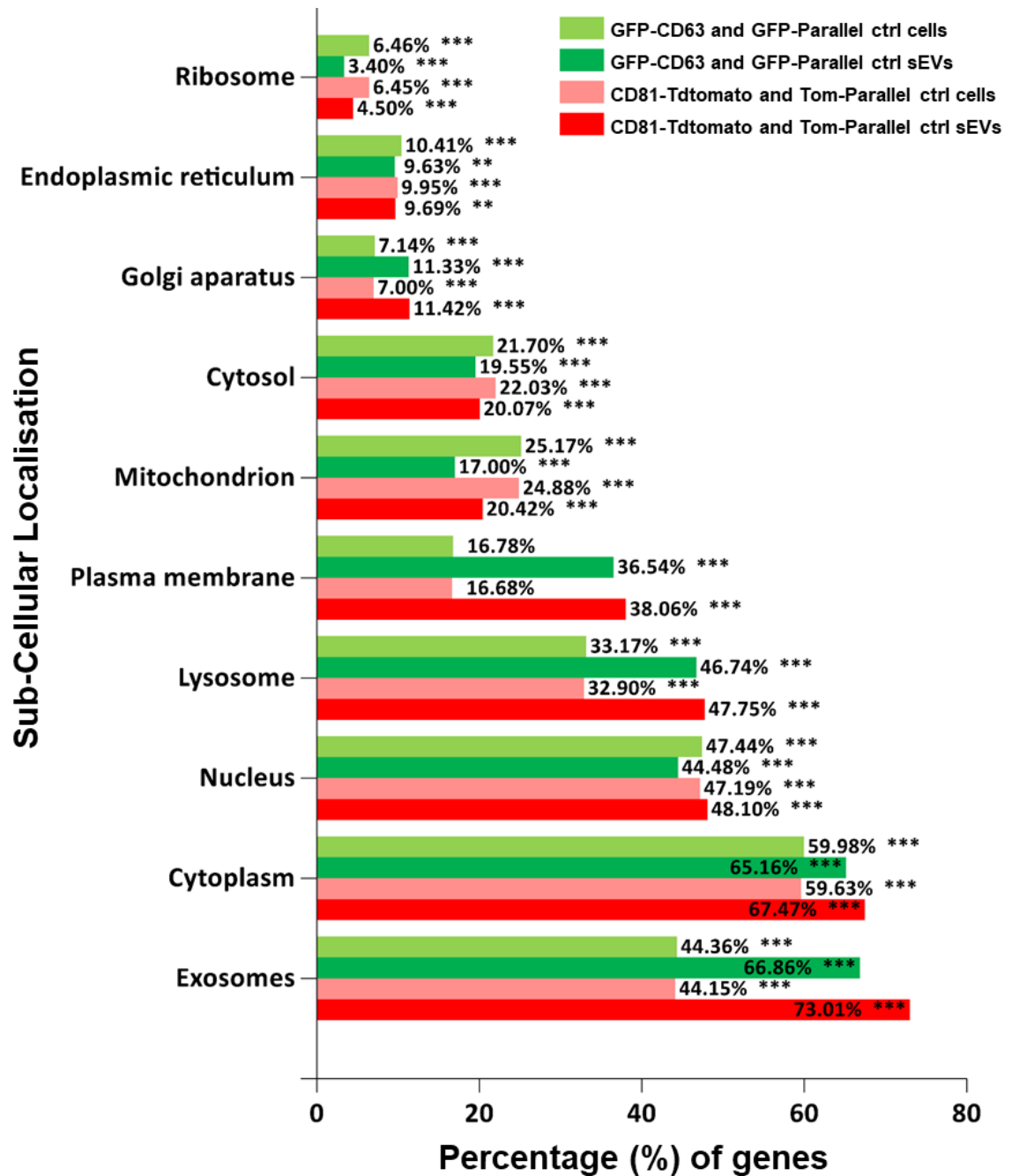


Figure 4.3. Sub-cellular localisation of common identified proteins in cells and sEVs.

Graphical representation showing the assignment of common identified proteins by SWATH-MS analysis into ten (10) sub-cellular compartments of interest. The number of common identified proteins for GFP-CD63 and GFP-Parallel cells (light green) and respective sEVs (dark green), as well as CD81-Tdtomato and Tom-Parallel cells (pink) and respective sEVs (red) are shown in [Table 4.1](#). Comparison of sub-cellular localisation was done in the FunRich (Functional Enrichment analysis) software, after conversion of UniProt IDs (proteins) into Gene symbols (genes), followed by Gene Enrichment Analysis using a hypergeometric test against all the genomes in the FunRich data base (20,515 genes); hypergeometric uncorrected p-values are shown on the graph with: **p<0.01, and ***p<0.001.

4.3.2. Visualisation of proteins with significant differences in abundance in cells and sEVs

4.3.2.1. Volcano Plots

The next step in our analysis was to generate Volcano plots to visualise the differences in protein abundance as well as highlight proteins of biological interest for cells and sEVs (Figure 4.4). In accordance with Table 4.1, from the 78 altered proteins identified in GFP-CD63 sEVs (Figure 4.4.A.i) the majority (74.4%) were upregulated with up to 2.5-fold higher abundance compared to GFP-Parallel control sEVs, whereas the rest were downregulated, with up to 5-fold lower abundance compared to control sEVs (Figure 4.4.A.i). Conversely, we detected a higher number of altered proteins (123) in CD81-Tdtomato sEVs (Figure 4.4.B.i); 56.9% of these proteins were downregulated with up to 5-fold lower abundance, whereas the rest were upregulated with up to 5-fold higher abundance compared to Tom-Parallel control sEVs (Figure 4.4.B.i).

Regarding changes in the proteome of GFP-CD63 and CD81-Tdtomato cells, we detected 95 and 73 altered proteins compared to controls, respectively (Figure 4.4.A,B.ii). 49.5% of proteins were upregulated in GFP-CD63 cells (up to 2.5-fold higher abundance) and 50.5% were downregulated (up to 8-fold lower abundance, Figure 4.4.A.ii). On the other hand, the majority of altered proteins (61.6%) in CD81-Tdtomato cells were upregulated (with up to 2.5-fold higher abundance) compared to controls, whereas the rest were downregulated (up to 11-fold lower abundance, Figure 4.4.B.ii).

Interestingly, these Volcano plots indicated that overexpression of CD81 resulted to higher dysregulation in sEVs compared to overexpression of CD63 (Figure 4.4.A), however, direct quantitative comparisons are not possible as these datasets derived from separate SWATH-MS runs and different spectral libraries. Another interesting observation is that proteomic changes of CD81-Tdtomato and GFP-CD63 cells were not exactly reflected in sEVs. Besides dysregulation of different numbers of proteins, a different relationship of upregulated versus downregulated proteins was observed in cells versus sEVs; for example, the majority of altered proteins in CD81-Tdtomato cells were upregulated, but most altered proteins in generated sEVs were downregulated compared to controls. Similarly, a higher number of downregulated proteins was found in GFP-CD63 cells, which was not reflected in the sEVs. Therefore, it became apparent that the relationship between cellular changes and sEV changes were not straightforward, as sEVs did not entirely reflect the cellular response to overexpression of CD63 or CD81.

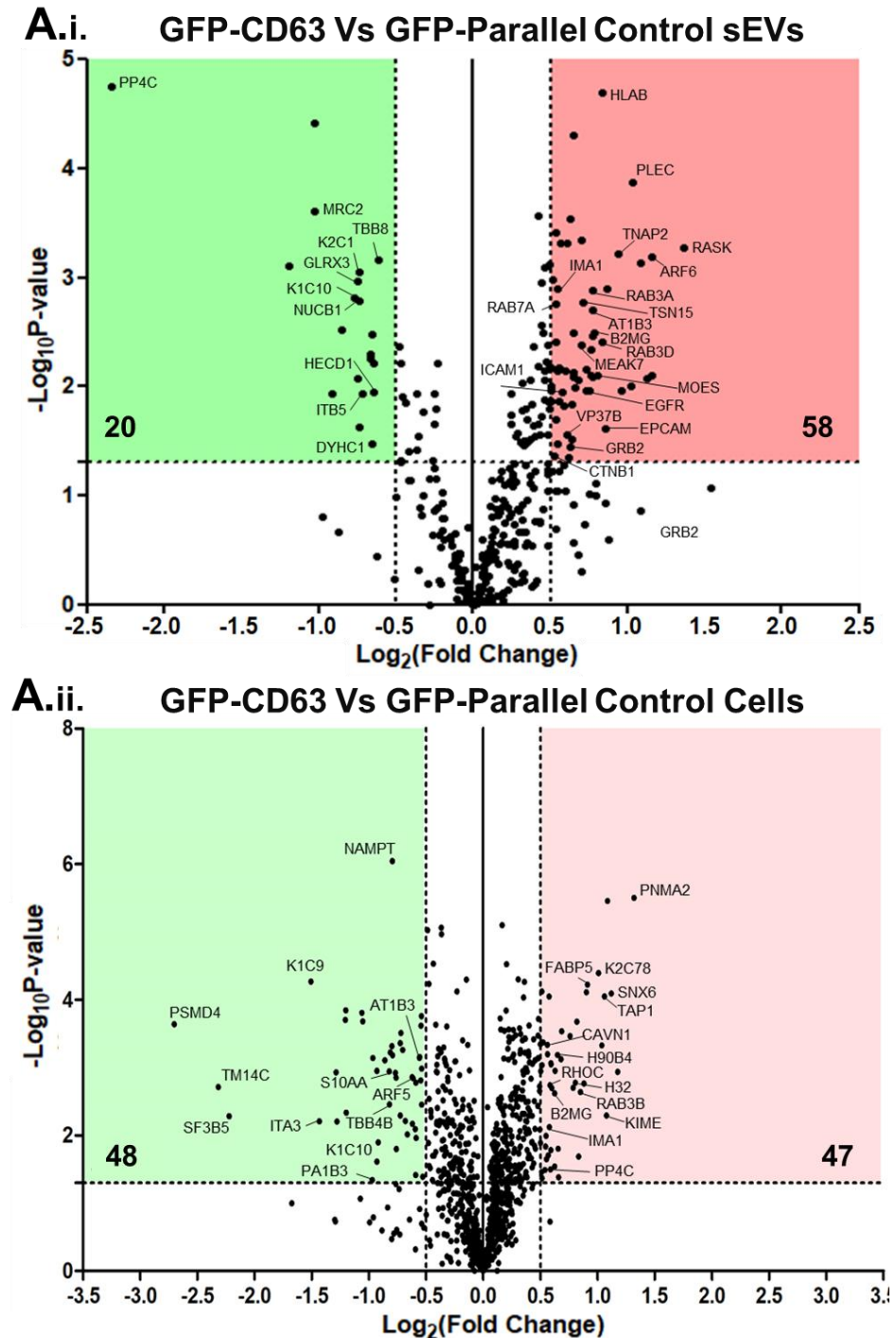


Figure 4.4. Volcano plots for comparisons of protein abundance in sEVs and cells overexpressing CD63 or CD81 compared to controls.

Volcano plots showing differences in protein abundance between: **A)** GFP-CD63 compared to WT GFP-parallel control **(i)** sEVs and **(ii)** cells, to determine upregulated and/or downregulated proteins after overexpression of CD63. Examples of dysregulated proteins (gene names) are also shown. Horizontal dashed line: cut-off for significantly altered proteins ($p < 0.05$, $-\text{Log}_{10}(p\text{-value}) > 1.3$). Vertical dashed lines: cut-off for high differences in relative abundance ($\text{FC} > |1.4|$) i.e., $\text{Log}_2(\text{Fold change}) > |0.5|$). Points in the red highlighted area indicate proteins with higher abundance, whereas points in the green highlighted area indicate proteins with lower abundance for cells and sEVs overexpressing tetraspanins compared to controls. Number of upregulated/downregulated proteins are also shown.

Figure and Figure Legend continued on next page ►

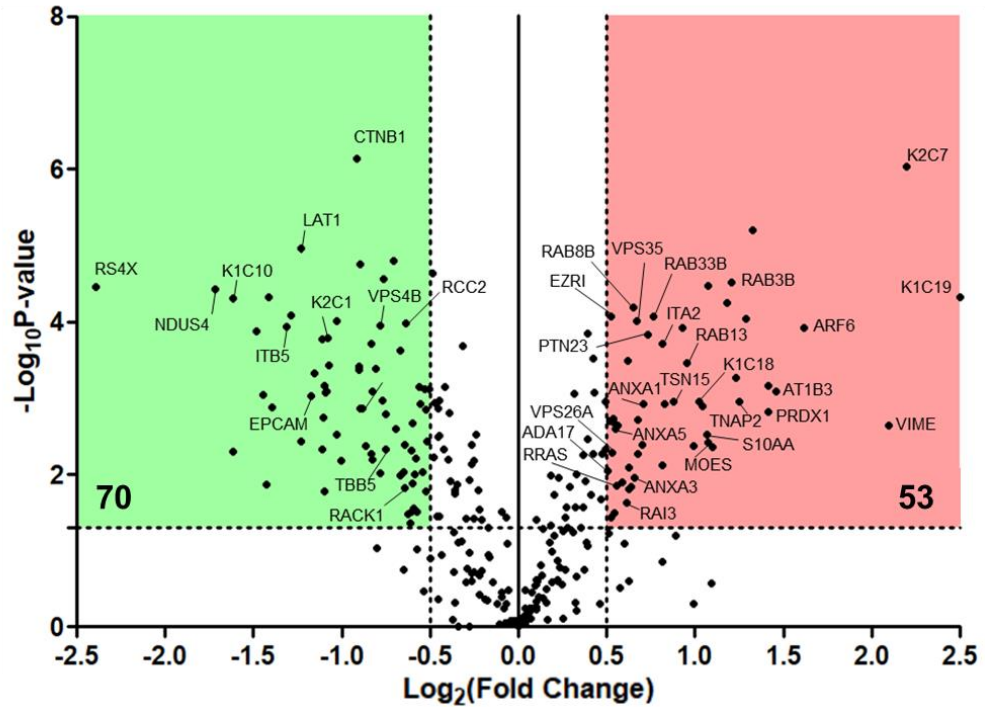
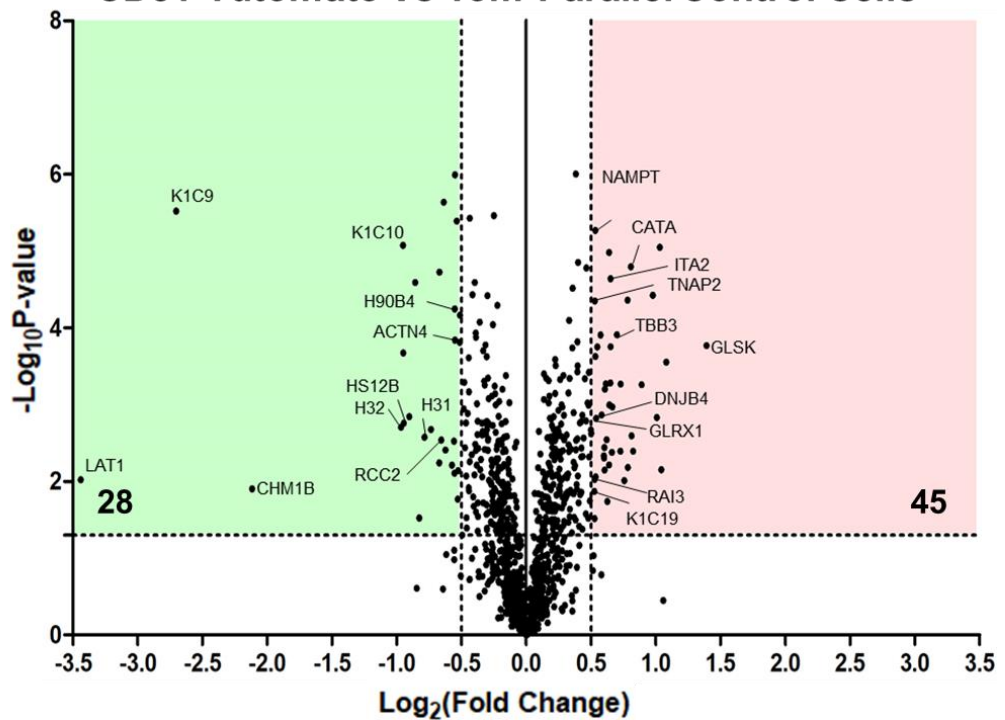
B.i. CD81-Tdtomato Vs Tom-Parallel Control sEVs**B.ii. CD81-Tdtomato Vs Tom-Parallel Control Cells**

Figure 4.4. Volcano plots for comparisons of protein abundance in sEVs and cells overexpressing CD63 or CD81 compared to controls.

► *Figure Legend continued from previous page*

Volcano plots showing differences in protein abundance between: **B**) CD81-Tdtomato compared to WT DU145 Tom-Parallel control (i) sEVs and (ii) cells to determine upregulated and/or downregulated proteins after overexpression of CD81. Examples of dysregulated proteins (gene names) are shown.

4.3.2.2. Venn Diagrams of unique and overlapping dysregulated proteins between cells and sEVs

As the previous Volcano plots demonstrated that the number of dysregulated proteins in CD81-Tdtomato and GFP-CD63 cells was not exactly reflected in the corresponding sEVs, Venn diagrams were generated to investigate the unique and/or overlapping dysregulated proteins between cells and sEVs ([Figure 4.5](#)).

To begin with, comparing the upregulated and downregulated proteins in GFP-CD63 cells versus GFP-CD63 sEVs, we observed that the majority of dysregulated proteins were not overlapping, with only 2 proteins found to be upregulated in both GFP-CD63 cells and sEVs; β -2-macroglobulin (B2MG), a component of MHC-1, and importin subunit alpha-1 (IMA1), an adapter protein for nuclear receptor KPNB. In addition, only 1 overlapping protein was found to be downregulated in both GFP-CD63 cells and sEVs, which was cytokeratin 10 (K1C10). We also detected 2 proteins that were differentially regulated between GFP-CD63 cells and sEVs; specifically, protein phosphatase 4 (PP4C, a serine/threonine-protein phosphatase) was upregulated in GFP-CD63 cells, but downregulated in GFP-CD63 sEVs, whereas the sodium/potassium-transporting ATPase subunit beta-3 (AT1B3) was downregulated in GFP-CD63 cells but upregulated in sEVs ([Figure 4.5.A](#)). These proteins were also noted in the Volcano Plots, where one can easily compare their similar or differential expression ([Figure 4.4.A](#)).

Similarly, by comparing the dysregulated proteins in CD81-Tdtomato cells versus CD81-Tdtomato sEVs, we observed that the majority were not overlapping, with only 4 proteins found to be upregulated in both CD81-Tdtomato cells and sEVs; specifically, integrin α_2 (ITA2), tumor necrosis factor alpha-induced protein 2 (TNAP2), retinoic acid-induced protein 3 (RAI3) and cytokeratin 19 (K1C19). In addition, only 3 overlapping proteins were downregulated in both CD81-Tdtomato cells and sEVs: cytokeratin 10 (K1C10), RCC2 protein (Regulator of Chromosome Condensation 2) and the large neutral amino-acid transporter small subunit 1 (LAT1). No differentially regulated proteins were detected between CD81-Tdtomato cells and sEVs ([Figure 4.5.B](#)). As mentioned above, these common dysregulated proteins are shown in the Volcano Plots (among other proteins of biological interest), for ease of comparison ([Figure 4.4.B](#)). Overall, these observations further support the previous hypothesis, as the majority of dysregulated proteins detected in cells and sEVs were not overlapping, which might be due to the differential composition of cells and sEVs, or the differential regulation/shuttling of proteins from cells to sEVs depending on the overexpression of CD63 or CD81 i.e., different sEV biogenesis and cargo loading functions of CD63 and CD81 (19, 156, 198).

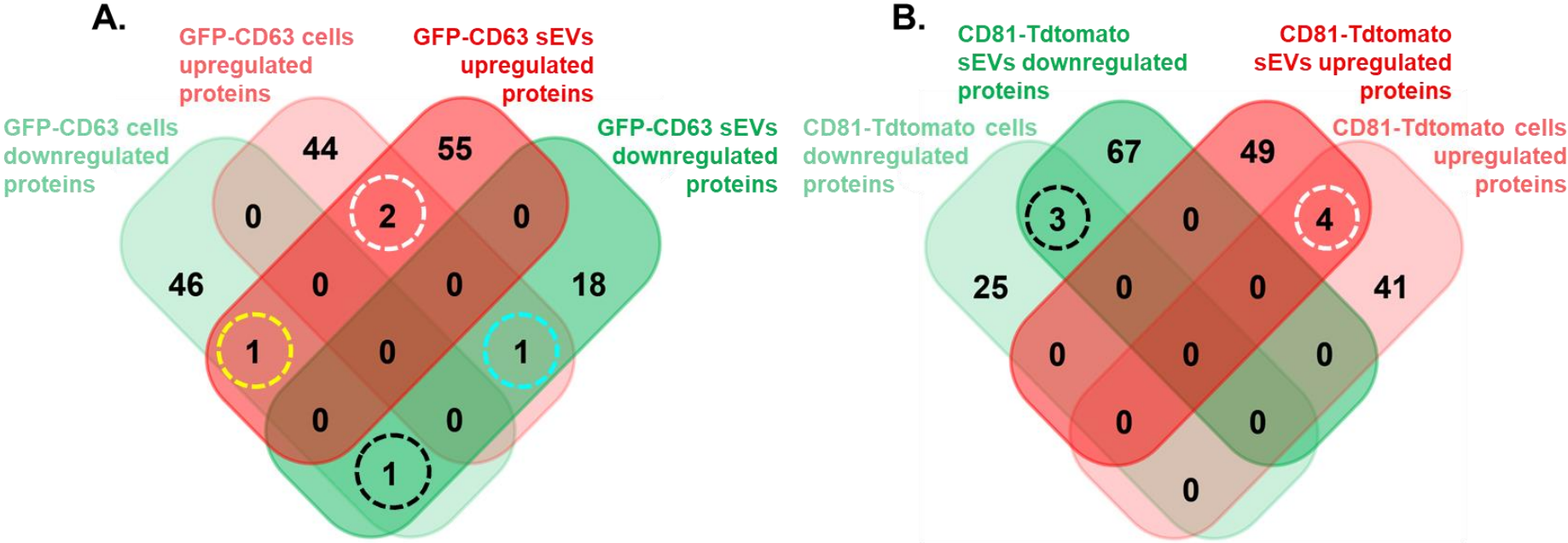


Figure 4.5. Venn Diagrams depicting unique and overlapping upregulated and downregulated proteins between cells and sEVs overexpressing CD63 or CD81.

A. Venn Diagram depicting the unique and overlapping proteins for the significantly upregulated and downregulated proteins in GFP-CD63 cells versus GFP-CD63 sEVs. This diagram depicts 2 overlapping upregulated proteins (B2MG and IMA1, white circle), 1 overlapping downregulated protein (K1C10, black circle) and 1 overlapping protein that appears upregulated in GFP-CD63 cells but downregulated in sEVs (PP4C, blue circle) and vice versa, with 1 overlapping protein that appears downregulated in GFP-CD63 cells but upregulated in sEVs (AT1B3, yellow circle). **B.** Venn Diagrams depicting unique and overlapping proteins for significantly upregulated and downregulated proteins in CD81-Tdtomato cells versus sEVs. This diagram depicts 4 overlapping upregulated proteins (ITA2, TNAP2, RAI3 and K1C19, white circle) and 3 overlapping downregulated proteins (RCC2, K1C10 and LAT1, black circle). Note: for generation of these Venn diagrams in the FunRich software, the UniProt Accession numbers were used for the significantly upregulated/downregulated proteins ($p\text{-value} \leq 0.05$ and Fold Change $> |1.4|$) as shown in Volcano Plots.

4.3.2.3. Heatmaps

To graphically present abundance differences between proteins and samples, we generated Heatmaps using only the significantly altered proteins (shown above by the Volcano Plots) which were up- or down-regulated by at least 1.4-FC (p-value <0.05 and $FC > |1.4|$). These Heatmaps were constructed in the Perseus Software after Z-score normalisation (scaling) per protein identification, with hierarchical row and column clustering (137). Z-score normalisation was done by subtracting the mean abundance of each row/column from the relative protein abundance of each sample, and then dividing the result by the standard deviation of the row/column. Note that this Z-score normalisation allows for quantitative comparison of protein abundance within a row only (i.e., between technical replicates of the two samples in comparison) and not with other protein identifications in other rows. Overall, these Heatmaps demonstrate: (i) column clustering for technical replicates exhibiting similar protein profiles and (ii) row clustering for protein identifications with similar expression profile using Euclidean Distance as a metric. Thus, Heatmaps were generated for GFP-CD63 vs GFP-Parallel control (i) sEVs and (ii) cells, both of which are shown in [Figure 4.6](#), as well as CD81-Tdtomato vs Tom-Parallel control (iii) sEVs and (iv) cells, which are shown in [Figure 4.7](#).

Heatmaps: GFP-CD63 vs GFP-Parallel control sEVs

The Heatmap of GFP-CD63 vs GFP-Parallel control sEVs demonstrated that the technical replicates 2 and 3 were clustered together compared to replicate 1, for both samples ([Figure 4.6.A](#)). The first 20 proteins depict identifications that were downregulated in GFP-CD63 sEVs (green) compared to control sEVs. Note that the corresponding UniProt Accession Number for each protein identification will be shown in the adjacent parenthesis. Some examples of downregulated proteins are the cytoskeleton-associated proteins cytokeratins 1 and 10 (P04264 and P13645) as well as β -tubulin (Q3ZCM7) and PPP4C (serine/threonine-protein phosphatase 4, P60510) which formed two distinct clusters, denoting similar expression profiles in each cluster. Other downregulated proteins were involved in adhesion like integrin β 5 (P18084), and ubiquitin-processes like the E3 ubiquitin ligase HECTD1 (Q9ULT8); however, these proteins exhibited variation between technical replicates, thus they might be targets of lower confidence. Finally, some downregulated proteins in GFP-CD63 sEVs were involved in calcium regulation/homeostasis like nucleobindin-1 (Q02818) and the c-type mannose receptor 2 (Q9UBG0); even though these proteins were not clustered together,

their expression between technical replicates was quite consistent, thus suggesting higher confidence of detection ([Figure 4.6.A](#)).

The bottom 58 proteins of the Heatmap depict those elevated in GFP-CD63 sEVs (red). Some of these are involved in major signalling pathways (growth, proliferation, and survival), in the cytoskeleton/adhesion or the immune response, and are high confidence identifications as they either belonged in the same, or adjacent clusters, with similar protein expression profiles. Examples are EPCAM (Epithelial Cell Adhesion Molecule, P16422), β -catenin (P35222), KRas (P01116), Arf6 (P62330), ICAM-1 (Intercellular Adhesion Molecule, P05362), EGFR (Epidermal Growth Factor Receptor, P00533), ezrin (P15311), moesin (P26038), HLAH (P01893), HLAB-7 (P01889) and β -2-microglobulin (P61769). High confidence identifications in adjacent clusters of expression were also proteins involved in membrane trafficking and the endosomal-MVB pathway like the vacuolar protein sorting-associated proteins VPS4A (Q9UN37) and VPS37B (Q9H9H4), as well as annexin A3 (P12429), and the GTPases Rab-3A, Rab-3D and Rab-7A (P20336, O95716 and P51149) ([Figure 4.6.A](#)).

Heatmaps: GFP-CD63 vs GFP-Parallel control cells

Regarding the Heatmap of GFP-CD63 vs GFP-Parallel control cells, we observed that the technical replicates 2 and 3 of GFP-CD63 cells were clustered together compared to replicate 1, whereas all the replicate samples for control cells clustered well with each other ([Figure 4.6.B](#)). The top 48 proteins exhibited lower abundance in GFP-CD63 cells (green) compared to controls, with the majority of these proteins having a consistent expression profile. Similar to GFP-CD63 sEVs, proteins associated with the cytoskeleton like cytokeratins 9, 10 (P35527 and P13645), β -tubulin (P68371), as well as adhesion proteins like integrin α_3 (P26006) were also downregulated in the parental cells. Interestingly, cytokeratin 10 and integrin α_3 clustered together, and β -tubulin was placed in an adjacent cluster, suggesting similar expression profiles. On the other hand, cytokeratin 9 was placed in a distant cluster, even though expression across technical replicates was similar; all these suggested that these proteins were high confidence identifications. GFP-CD63 cells also exhibited downregulation in ribosomal proteins like the 60S ribosomal proteins L15 and L27 (P61313 and P61353) and transport /signalling proteins like S100A10 (P60903), Sec23A (Q15436), and the GTPase Arf5 (P84085) which were organised in the same or adjacent clusters respectively, suggesting comparable expression profiles ([Figure 4.6.B](#)).

The bottom 47 proteins represented upregulated proteins in GFP-CD63 cells (red). Examples are proteins involved in metabolism like FABP5 (Fatty acid-binding protein 5, Q01469) and mevalonate kinase (Q03426), with mevalonate kinase exhibiting variation in its expression profile, suggesting that it is a lower confidence target. Other examples are DNA-binding proteins like histone H3 isoforms (P68431, Q71DI3, P84243) and histone 1 (P16401); these proteins were all placed in the same cluster indicating similar expression profile. Furthermore, similarly to GFP-CD63 sEVs, proteins were involved in the immune response like β -2-microglobulin (P61769) and TAP1 (Antigen peptide transporter 1, Q03518), which exhibited consistency between technical replicates in their protein expression profile ([Figure 4.6.B](#)).

Finally, other upregulated proteins were involved in protein/membrane trafficking and major pathways (similar to corresponding sEVs), like sorting nexin-6 (Q9UNH7) and caveolae-associated protein 1 (Q6NZI2), which were actually clustered together, as well as Rab-3B (P20337) and Rho-related GTP-binding protein RhoC (P08134), which were also organised in an adjacent cluster suggesting comparable expression profiles and potentially high confidence in identification ([Figure 4.6.B](#)).

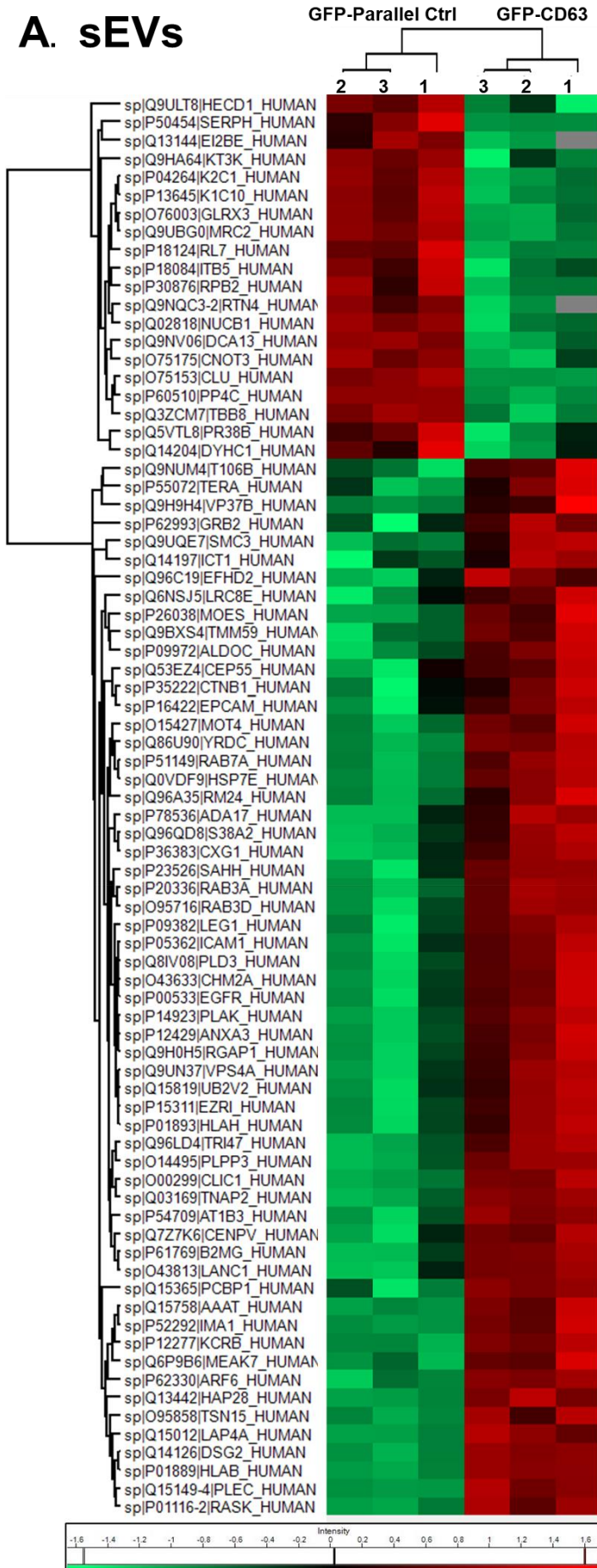


Figure 4.6. Heatmaps of the most significantly altered proteins in GFP-CD63 sEVs and cells compared to WT Parallel controls.

A. GFP-CD63 vs GFP-Parallel control sEV heatmaps with hierarchical row and column clustering based on Euclidean distance after Z-score normalisation of \log_2 relative protein abundance for significantly altered proteins (p -value < 0.05) which are up- or down-regulated by at least a 1.4-fold difference.

Up- or down-regulated proteins are indicated with their UniProt Accession number and Gene name. Scales indicate intensity for each Heat Map with relative protein abundance colour-coded either **red** to correspond to relatively high abundance (upregulation), **green** to correspond to relatively low abundance (downregulation), or **grey** to indicate missing abundance values.

► **Figure and Legend continued to next page**

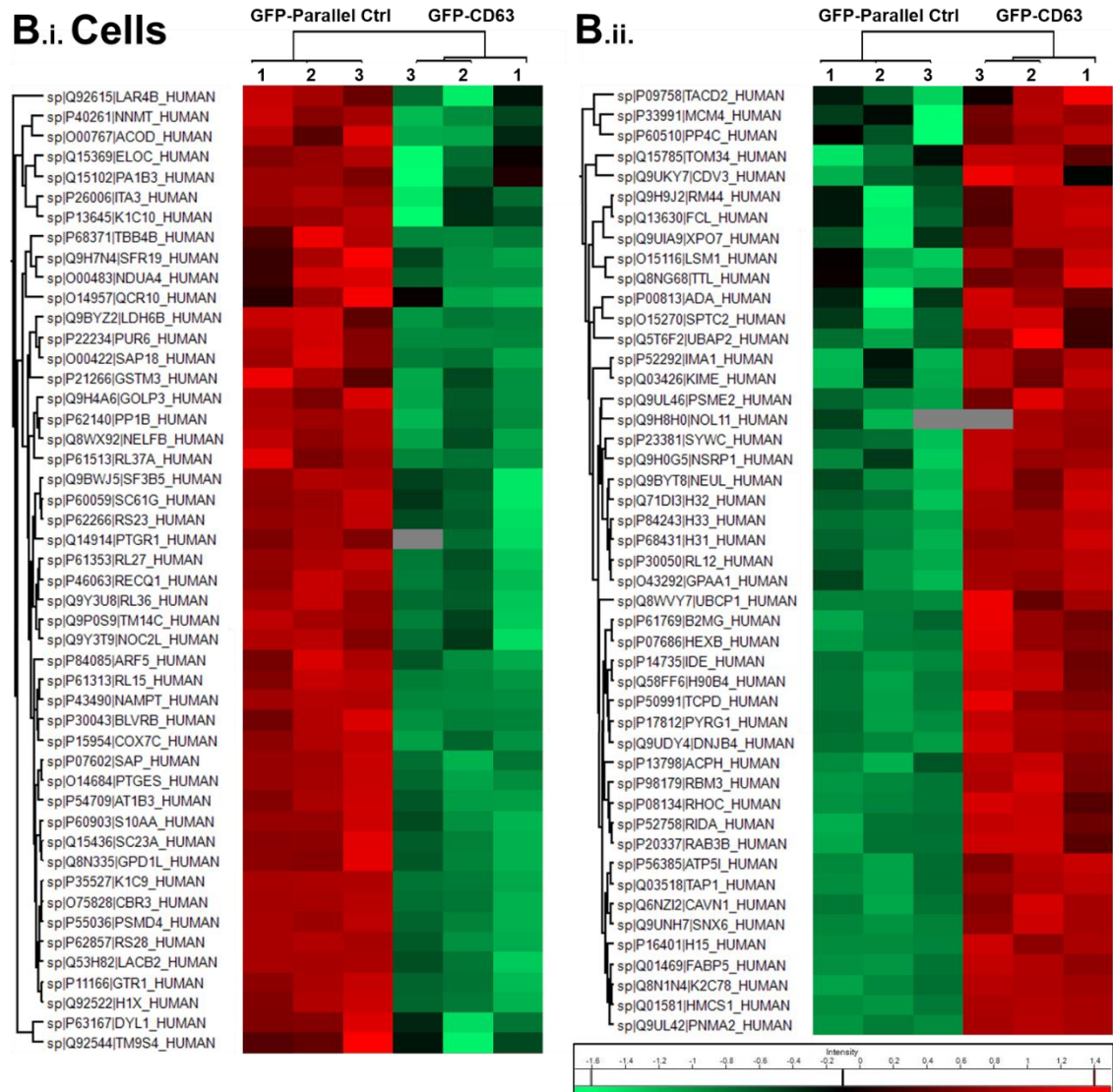


Figure 4.6. Heatmaps of the most significantly altered proteins in GFP-CD63 sEVs and cells compared to WT Parallel controls.

► **Figure and Legend continued from previous page**

B. GFP-CD63 vs GFP-Parallel control cell heatmaps with hierarchical row and column clustering based on Euclidean distance after Z-score normalisation of \log_2 relative protein abundance for significantly altered proteins (p -value < 0.05) which are (i) down-regulated or (ii) up-regulated by at least a 1.4-fold difference in GFP-CD63 cells compared to GFP-Parallel control cells.

Up- or down-regulated proteins are indicated with their UniProt Accession number and Gene name. Scales indicate intensity for each Heat Map with relative protein abundance colour-coded either **red** to correspond to relatively high abundance (upregulation), **green** to correspond to relatively low abundance (downregulation), or **grey** to indicate missing abundance values.

Heatmaps: CD81-Tdtomato vs Tom-Parallel control sEVs

Next, Heatmaps were generated for the CD81-Tdtomato and Tom-Parallel control cells and EVs. Firstly, we observed that the Heatmap comparing sEVs showed that the technical replicates 1 and 2 were clustered together compared to replicate 3, for both CD81-Tdtomato and Tom-Parallel control sEVs ([Figure 4.7.A](#)). The top 70 proteins on the Heatmap represent downregulated elements in CD81-Tdtomato sEVs (green) compared to control sEVs. As seen previously with GFP-CD63 sEVs, various cytoskeleton-associated proteins were downregulated like α - and β - tubulin (Q9BQE3 and P07437), as well as cytokeratins 1, 2, 10 and 22 (P04264, P35908, P13645 and P35908) which were placed in adjacent clusters and showed similar protein expression profiles. Other downregulated proteins were also involved in major signalling pathways (adhesion, growth, proliferation, and survival) like EPCAM (P16422), integrin β_5 (P18084) and β -catenin (P35222), which were all organised in the same cluster. Furthermore, ribosomal proteins like the 60S ribosomal protein L7 (P18124) and EIF3 (eukaryotic translation initiation factor 3, P60228) were also downregulated and exhibited consistent expression between replicates for each sample. Finally, some of these downregulated proteins were involved in endosomal-MVB pathways like VPS4B (O75351) and VAMP3 (vesicle-associated membrane protein 3, Q15836); even though VPS4B exhibited consistent expression between technical replicates, VAMP3 showed slight variation in expression.

Conversely, 53 proteins represented upregulated proteins in CD81-Tdtomato sEVs (red) ([Figure 4.7.A](#)). Some of these proteins were metabolic proteins like aldolase (P09972) and phospholipid phosphatase 3 (O14495), whereas others were involved in the cytoskeleton and/or cell adhesion and migration. Examples of these were cytokeratins 18 and 19 (P05783 and P08727), ezrin (P15311), moesin (P26038) and integrin α_2 (P17301). Other upregulated proteins were involved in major signalling pathways (growth, proliferation, survival) like Arf6 (P62330), TNAP2 (Q03169) and tyrosine-protein kinase JAK1 (P23458). Even though all the above-mentioned proteins were placed in different clusters, their protein expression was similar between technical replicates of each sample, thus establishing them as high confidence targets.

Finally, various upregulated proteins in CD81-Tdtomato sEVs were involved in membrane trafficking and the endosomal-MVB pathway like Rab-3A, Rab-3D, Rab-8B, Rab-13 (P20336, O95716, Q92930 and P51153), as well as VPS35 (Q96QK1), which actually organised in one cluster, thus exhibiting similar expression profiles and overall consistencies between technical replicates. Other proteins involved in these sEV-associated pathways, were annexins A1,3 and 5 (P04083, P12429 and P08758), which

also showed similar protein profiles, except annexin A3 which showed greater variation in protein expression ([Figure 4.7.A](#)).

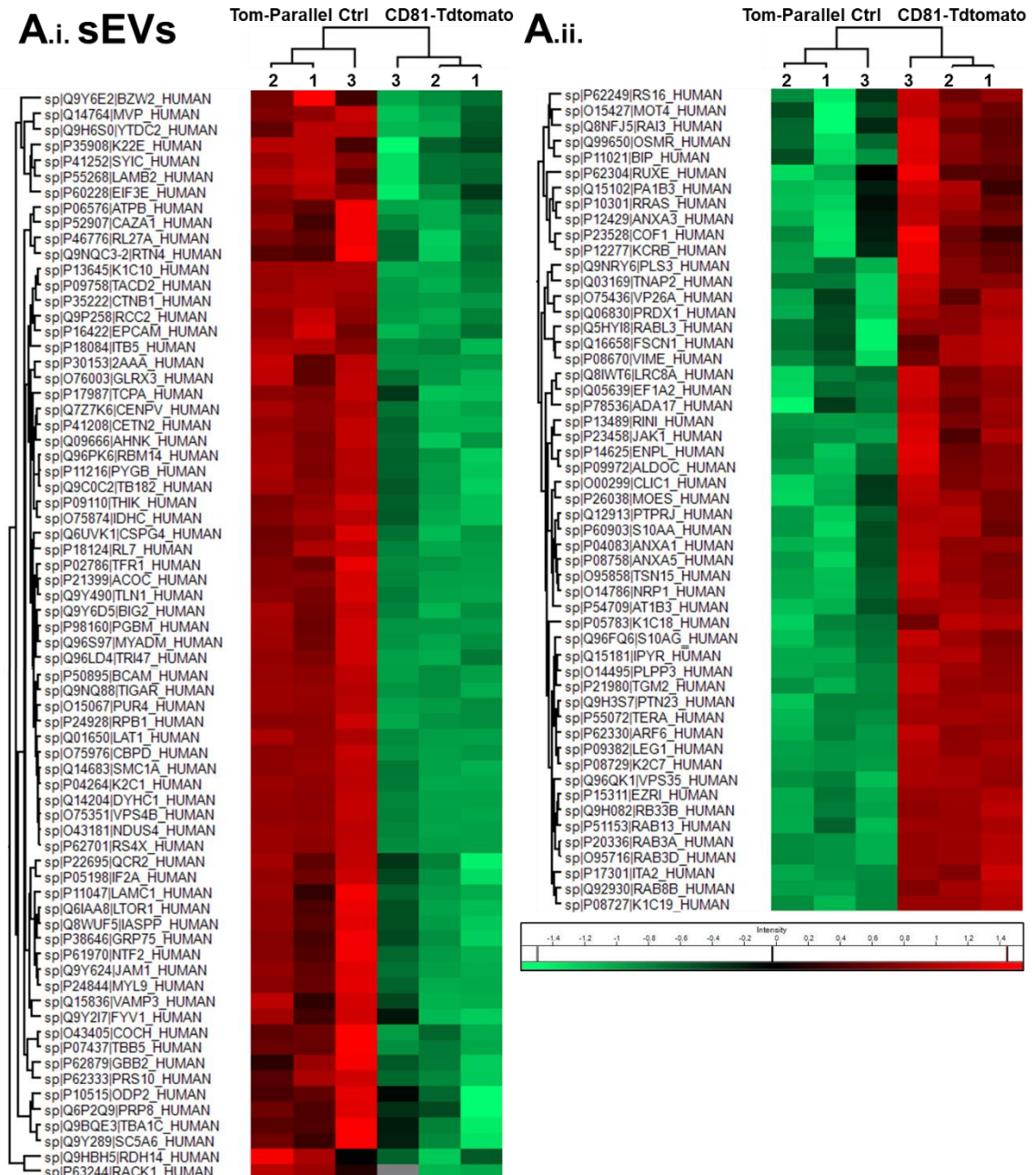
Heatmaps: CD81-Tdtomato vs Tom-Parallel control cells

The final Heatmap compared the abundance of dysregulated proteins between CD81-Tdtomato and control cells, shown in [Figure 4.7.B](#). The top 28 proteins in the Heatmap represent downregulated proteins (green), which included cytoskeleton-associated proteins like cytokeratins 9 and 10 (P35527 and P13645), as well as DNA-binding proteins like histone H3 isoforms 1,2,3 (P68431, Q71DI3, P84243); interestingly, these proteins were organised in two different clusters, thus depicting 2 distinct expression profiles. Other downregulated proteins were involved in adhesion like alpha-actinin-4 (O43707), in heat shock response like HSPA12B (heat shock 70kDa protein 12B, Q96MM6) as well as vesicle transport like CHMP1B (charged multivesicular body protein 1b, Q7LBR); expression for these proteins was consistent between sample replicates, even though CHMP1B exhibited greater variation.

The bottom 45 proteins of the Heatmap represent upregulated proteins in CD81-Tdtomato cells (red) ([Figure 4.7.B](#)) and included cytoskeleton-associated proteins like cytokeratin 19 (P08727) and metabolism-associated proteins like NAMPT (nicotinamide phosphoribosyl-transferase, P43490). Other upregulated proteins were involved in adhesion, like β -tubulin (Q13509), integrin α_2 (P17301) and integrin β_1 (P05556) which exhibited similar expression profiles, thus making them high confidence identifications. Some other high confidence targets were proteins involved in stress responses like catalase (P04040), sulfiredoxin-1 (Q9BYN0) and glutaredoxin (P35754), as well as other major signalling pathways like RhoC (P08134) and TNAP2 (Q03169). Finally, some upregulated proteins were involved in the proteasome degradation pathway like proteasome 20S subunits beta 1 and 4 (P20618 and P28070) which were clustered together depicting similar protein profiles.

Concluding remarks for Heatmap analysis

These Heatmaps enabled the visualisation of dysregulated proteins in clusters of abundance, based on the Z-scored normalised expression profile of each of the technical replicates in every sample. Interestingly, we observed that the protein profiles in the CD81-Tdtomato Heatmaps were overall more consistent between replicates (columns) and between protein IDs (rows) compared to GFP-CD63. This might be attributed to differences between these datasets during the initial normalisation in the Skyline software, prior to Z-normalisation (data not shown). Despite this, these Heatmaps demonstrated high consistency between technical replicates for expression of the majority of protein identifications, even though instances of variation, or in some rare cases complete absence of protein expression from a replicate, were also noted. Thus, these Heatmaps provided with information for high and low confidence protein identifications, which were valuable for further validation of targets by Western Blot analysis.



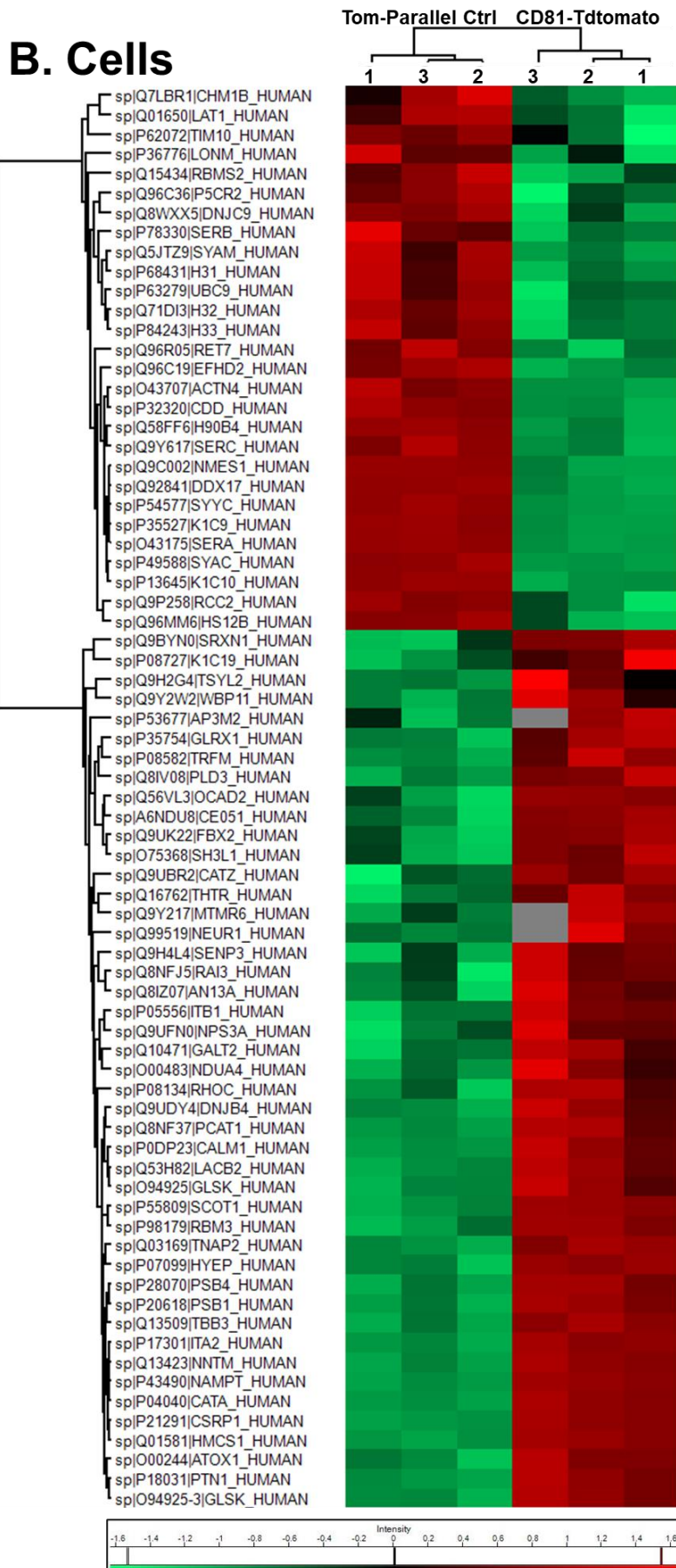


Figure 4.7. Heatmaps of the most significantly altered proteins in CD81-Tdtomato sEVs and cells compared to the WT Parallel controls.

► *Figure and Legend continued from previous page*

B. CD81-Tdtomato vs Tom-Parallel control cell heatmaps with hierarchical row and column clustering based on Euclidean distance after Z-score normalisation of log₂ relative protein abundance for significantly altered proteins (p-value <0.05) which are up- or down-regulated by at least a 1.4-fold difference.

Up- or down-regulated proteins are indicated with their UniProt Accession number and Gene name. Scales indicate intensity for each Heat Map with relative protein abundance colour-coded either **red** to correspond to relatively high abundance (upregulation), **green** to correspond to relatively low abundance (downregulation), or **grey** to indicate missing abundance values.

4.3.3. Gene Enrichment and Protein-Protein Interaction Network Analysis

Besides visualising the common/unique dysregulated proteins using Venn Diagrams and comparing their relative abundance using Heatmaps, we proceeded to perform Gene Enrichment analysis using the FunRich software, and to construct Protein-Protein interaction (PPI) networks, using STRING (Search Tool for the Retrieval of Interacting Genes). These analyses were performed to be able to predict any potential functional implications of these changes in sEVs, on their subsequent biological effects with recipient cells.

4.3.3.1. Gene Enrichment Analysis

For Gene Enrichment Analysis, dysregulated proteins shown in the Heatmaps above were imported into the FunRich software (v3.1.3) for all cell and sEV datasets. As mentioned previously, proteins were considered dysregulated when they exhibited statistically significant changes in abundance compared to controls ($p < 0.05$ and $FC > |1.4|$). In FunRich, the UniProt protein IDs were transformed into EntrezGene IDs, which were subsequently used for Gene Enrichment Analysis. As above, we compared cells or sEVs overexpressing tetraspanins vs their corresponding parallel controls.

Biological Process Comparisons

To begin with, we compared the dysregulated proteins identified in GFP-CD63 cells to sEVs ([Figure 4.8.A](#)), as well as in CD81-Tdtomato cells to sEVs ([Figure 4.8.B](#)). This was done to determine the biological processes that these dysregulated proteins were involved, and the potential similarities or differences between cells and sEVs.

Firstly, we observed that dysregulated proteins in GFP-CD63 cells were mostly involved in “house-keeping” biological processes like regulation of nucleic acid metabolism (23.58%), energy pathways and overall metabolism (19.81%). On the other hand, dysregulated proteins in GFP-CD63 sEVs were mostly involved in signal transduction (23.38%), cell communication (20.78%) and transport (12.80%), which are more indicative of sEV-associated biological processes. Processes such as metabolism (9.09%) and immune responses (6.49%) were less prominent features of altered sEVs ([Figure 4.8.A](#)). Secondly, we observed that the dysregulated proteins identified in CD81-Tdtomato cells, were involved in similar biological processes as those identified for GFP-

CD63 cells, like energy pathways (21.95%), regulation of nucleic acid metabolism (20.73%) and overall metabolism (20.73%).

Interestingly, the dysregulated proteins identified in CD81-Tdtomato sEVs, were also involved in similar processes as GFP-CD63 sEVs; for example, signal transduction (26.02%), cell communication (25.20%), cell growth/maintenance (16.26%), metabolism (14.63%) and transport (12.20%) ([Figure 4.8.B](#)).

Overall, Gene Enrichment Analysis demonstrated some distinction in biological processes in the dysregulated proteins of cells compared to their respective sEVs. Despite the use of two different spectral libraries in SWATH-MS analysis, similarities in biological processes of identified dysregulated proteins were observed both between GFP-CD63 and CD81-Tdtomato cells, as well as between GFP-CD63 and CD81-Tdtomato sEVs.

Molecular Function Comparisons

Gene Enrichment Analysis was also performed to investigate the molecular functions of altered cells or sEVs. The dysregulated proteins identified in GFP-CD63 cells exhibited mostly DNA binding functions (15.09%), transporter activity functions (9.43%), ribosomal structural functions (7.55%), oxidoreductase activity (5.66%) and ligase activity (3.77%). Conversely, dysregulated proteins in GFP-CD63 sEVs exhibited mostly cell adhesion activity (7.79%), transporter activity (6.49%), ATPase and GTPase activity (5.19%), as well as MHC-1 receptor and cytoskeletal anchoring activity (2.60%) ([Figure 4.9.A](#)).

Regarding CD81-Tdtomato cells, dysregulated proteins also exhibited mainly DNA binding functions (15.85%), transporter activity functions (6.10%) and oxidoreductase activity (4.88%) similar to GFP-CD63 cells, but they also exhibited ubiquitin-specific protease activity (4.88%) and heat-shock protein and deaminase functions (2.44%). Conversely, CD81-Tdtomato sEVs had some similarities to GFP-CD63 sEVs, like exhibiting transporter activity (7.32%) and GTPase activity (6.50%), but also exhibited distinct functions like cytoskeletal structural functions (5.69%), translation regulator activity (4.88%) and calcium ion binding functions (4.88%).

Overall, Gene Enrichment Analysis demonstrated some overlap in molecular functions of dysregulated proteins identified between GFP-CD63 and CD81-Tdtomato cells and their respective sEVs, but also highlighted some distinct functions that are associated to sEVs (e.g., GTPase activity, calcium ion binding activity and cell adhesion molecule activity). Again, despite the usage of two different spectral libraries by SWATH-MS analysis, similarities in molecular functions between GFP-CD63 and CD81-Tdtomato cells and sEVs were apparent.

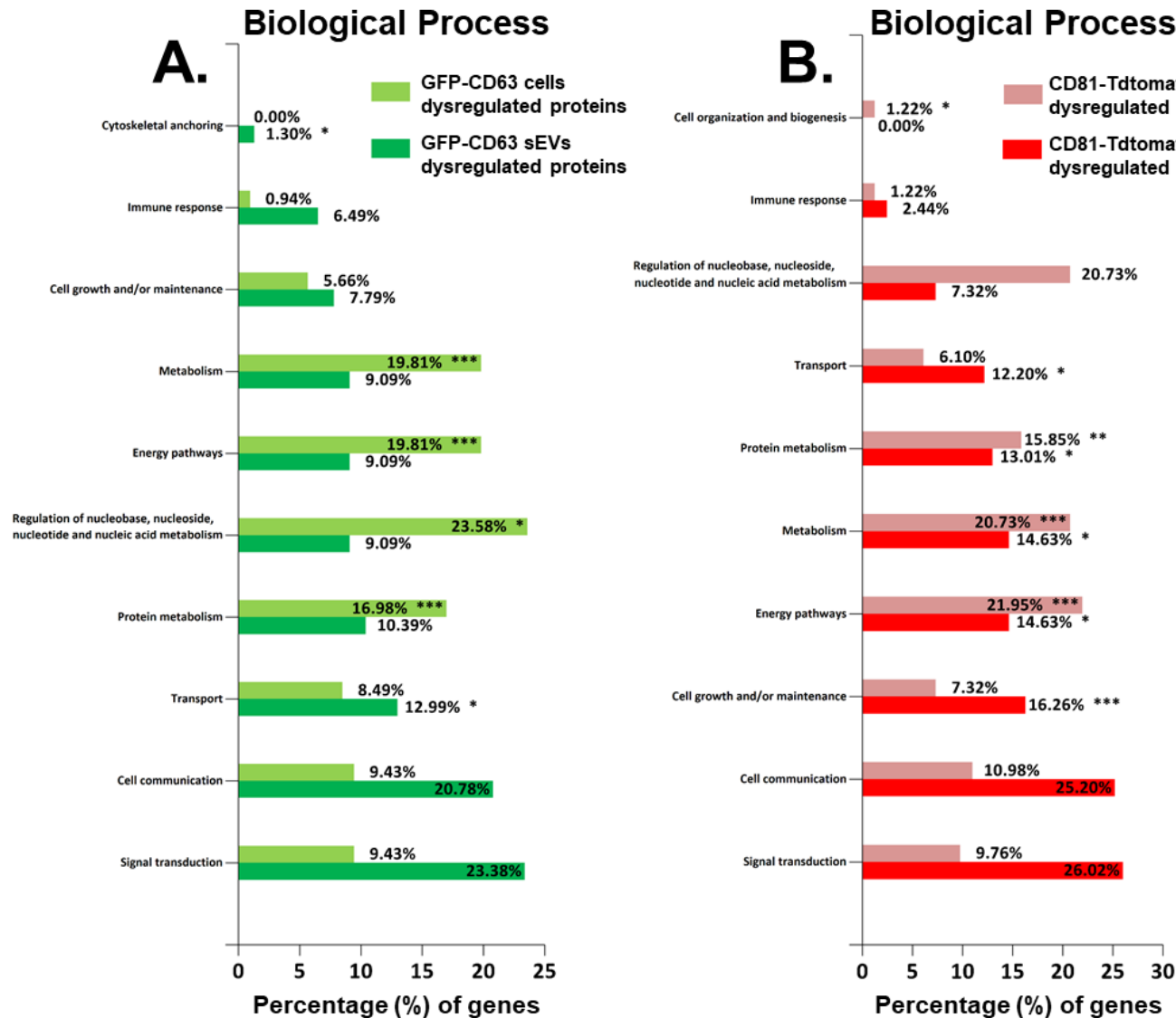


Figure 4.8. Gene Enrichment Analysis comparing biological processes of dysregulated proteins between cells and sEVs.

A. Percentage of dysregulated genes detected in GFP-CD63 cells compared to GFP-CD63 sEVs, that are involved in various biological processes.

B. Percentage of dysregulated genes detected in CD81-Tdtomato cells compared to CD81-Tdtomato sEVs, that are involved in various biological processes.

Note that Gene Enrichment Analysis was done with the FunRich software, after dysregulated protein UniProt IDs were transformed into gene names (dysregulated proteins deemed proteins with p -value < 0.05 and $FC > |1.4|$ compared to the respective parallel control). Gene Enrichment Analysis was done using a hypergeometric test against all the genomes in the FunRich database (20,515 genes); hypergeometric uncorrected p -values are shown on the graph with: * $p < 0.05$, ** $p < 0.01$, and *** $p < 0.001$. Graphs show the top 10 enriched biological processes.

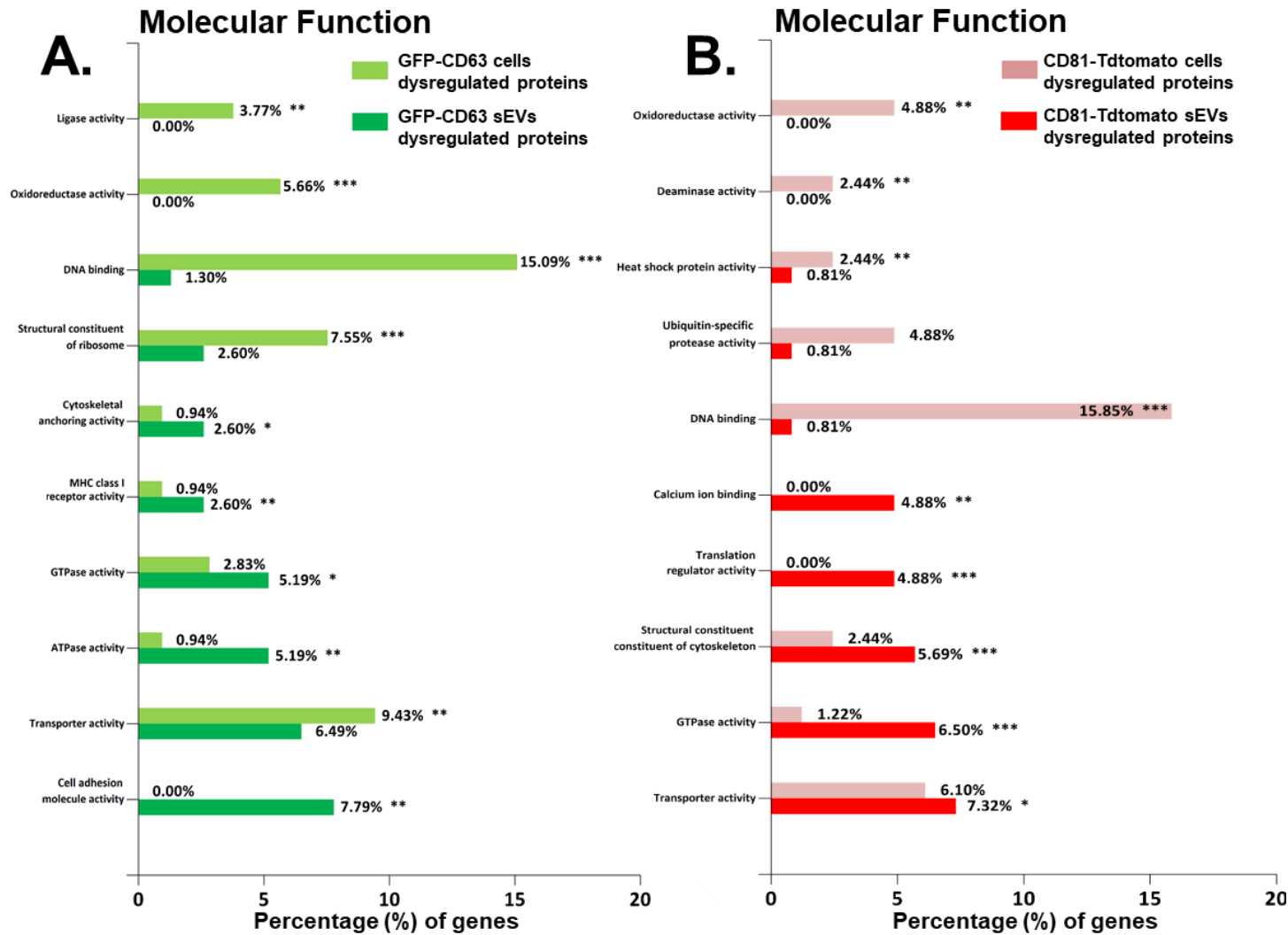


Figure 4.9. Gene Enrichment Analysis comparing Molecular Functions of dysregulated proteins between cells and sEVs.

A. Percentage of dysregulated genes detected in GFP-CD63 cells compared to GFP-CD63 sEVs, allocated to various molecular functions. **B.** Percentage of dysregulated genes detected in CD81-Tdtomato cells compared to CD81-Tdtomato sEVs, allocated to various molecular functions. Gene Enrichment Analysis was done with the FunRich software, after dysregulated protein UniProt IDs were transformed into gene names (dysregulated proteins when p -value < 0.05 and $FC > |1.4|$ compared to respective parallel control). Gene Enrichment Analysis was done using a hypergeometric test against all the genomes in the FunRich database (20,515 genes); hypergeometric uncorrected p -values are shown on the graph with: * $p < 0.05$, ** $p < 0.01$, and *** $p < 0.001$. Graphs show the top 10 enriched molecular functions.

4.3.3.2. Protein-Protein Interaction analysis in the STRING software

We proceeded to construct a network of PPI using the STRING tool (v.11, publicly available at <https://string-db.org/>) to investigate the dysregulated proteins identified in sEVs, and the potential implications of these changes in biological networks in sEVs (and potentially recipient cells). The GFP-CD63 and CD81-Tdtomato sEV networks were generated to visualise the interactions of up- and downregulated proteins and organise these proteins in clusters of function, based on confidence of interaction ([Figure 4.10](#)).

GFP-CD63 sEV STRING network

To begin with, as shown in [Figure 4.10.A](#), the 78 dysregulated proteins found in GFP-CD63 sEVs were organised in a network of 10 clusters based on Markov Clustering (142), with related proteins interconnected based on confidence (from low to highest). Cluster 1 had the highest number of dysregulated proteins (19 IDs), which were mostly interconnected with above medium confidence of interaction (0.4-0.9); 18 proteins of this cluster were significantly upregulated (shown with black halo). Interestingly, some of these upregulated proteins are involved in major growth/survival signalling pathways like receptors, adaptors, and transcription factors e.g., EGFR, EPCAM, I-CAM, ADAM-17, KRas, Grb2, Arf6 and CTNNB1 (β -catenin), and further investigation is necessary to determine if delivery of this cargo potentially “activates” relevant biological pathways in recipient cells ([Figure 4.10.A](#)).

Other examples are Clusters 2 and 6 which included 10 and 3 dysregulated proteins (respectively), mostly interconnected with high confidence of interaction (0.7-0.9). The majority of these proteins (8/10 for Cluster 2 and 3/3 for Cluster 6) were upregulated, and involved EV-associated proteins like GTPases Rab3A, Rab3D and Rab7 (Cluster 2), as well as VPS4A, VPS37B and CHMP2A (Cluster 6). As CD63 is a key player in sEV biogenesis and cargo sorting, one could expect that overexpression of this protein might alter the levels of these vacuolar regulatory proteins. Interestingly, some proteins did not appear to cluster with any other proteins, suggesting either absence of interaction or absence of any evidence for interaction e.g., integrin β_5 (ITB5) and annexin A3 (ANXA3) ([Figure 4.10.A](#)).

CD81-Tdtomato sEV STRING network

Regarding CD81-Tdtomato sEVs, as shown in [Figure 4.10.B](#), the 123 dysregulated proteins were organised in a more complex network than GFP-CD63 sEVs, forming 15 protein clusters. Cluster 1 had the higher number of dysregulated proteins (17), 5 of which were upregulated (outlined with black halo) and 12 were downregulated (outlined with gray halo); the majority of these proteins were interconnected with above medium confidence (0.4-0.9). Some of these were ribosomal-associated proteins and initiation/elongation factors e.g., RPL27A, RPL7, RPS16, EIF2S1, EIF3E and EEF1A2, as well as heat shock-related proteins e.g., HSPA5 and HSPA9.

Other clusters of interest are Clusters 2,3 and 4 which consisted of 12,11 and 10 proteins (respectively); even though the majority of Clusters 2 and 4 proteins were downregulated (10/12 and 7/10), most proteins of Cluster 3 were upregulated (8/11). Proteins in both clusters were involved in the cytoskeleton, signalling and adhesion. Examples are α - and β -tubulin (TUBA1C and TUBB), CAPZA1 (actin filament capping protein) and dynein 1 (DYNC1H1) which were found in Cluster 2, whereas ezrin (EZR), moesin (MSN), cofilin-1(CFL1) and CTNNB1 (β -catenin) were found in Cluster 3, and HSP90B1 chaperone, HSPG2, integrin α_2 and β_5 (ITGA2 and ITGB5) and talin-1 (TLN1) were found in Cluster 4 ([Figure 4.10.B](#)). As some of these proteins are major signalling proteins, further investigation is essential to determine potential biological effects of these proteins when delivered to recipient cells.

In addition, similarly to GFP-CD63 sEVs, three clusters (Clusters 7, 10 and 11) were formed with proteins highly associated with sEVs/MVBs, the majority of which were upregulated (5/7 in Cluster 7, 5/5 in Cluster 10 and 3/4 proteins in Cluster 11). Cluster 7 included annexins 1,3 and 5 (ANXA1, ANXA3, ANXA5) and annexin-associated proteins like S100A10. Cluster 10 was formed by the GTPases Rab3A, Rab3D, Rab8B, Rab13 and Rab33B, whereas Cluster 11 included VPS4B, VPS26A, VPS35 as well as PTPN23 (Tyrosine-protein phosphatase type 23, sorting protein in MVBs) ([Figure 4.10.B](#)). As mentioned above for CD63, the tetraspanin CD81 is also a major player in sEV biogenesis and cargo sorting, thus changes in vacuolar-associated proteins are expected after overexpression of CD81; the implications of these changes in recipient cells however need to be further investigated. Interestingly, as seen with GFP-CD63 sEVs, some proteins did not appear to cluster with any other proteins, e.g., proteins also found on sEVs like tetraspanin 15 (TSPAN15) and basal cell adhesion molecule (BCAM) ([Figure 4.10.B](#)).

Concluding remarks on sEV STRING networks

Overall, the GFP-CD63 and CD81-Tdtomato sEV dysregulated protein STRING networks showed differences in terms of complexity, thus reflecting the different number of dysregulated proteins found between sEV types. However, these protein-protein interaction networks also showed similarities in protein clustering (e.g., presence of vacuolar-, adhesion- or growth/survival- associated protein clusters), and protein identification, especially in sEV-associated proteins (e.g., β -catenin, vacuolar proteins VPS4, integrin β_5 , annexin A3, Rab proteins etc.). Hence, even though some of these proteins were differentially regulated between GFP-CD63 and CD81-Tdtomato sEVs, the overall protein interactome was quite similar.

A. GFP-CD63 sEVs

- Cluster 1
- Cluster 2
- Cluster 3
- Cluster 4
- Cluster 5
- Cluster 6
- Cluster 7
- Cluster 8
- Cluster 9
- Cluster 10
- Upregulated
- Downregulated



- Confidence**
- Low (0.15)
 - Medium (0.40)
 - High (0.70)
 - Highest (0.90)

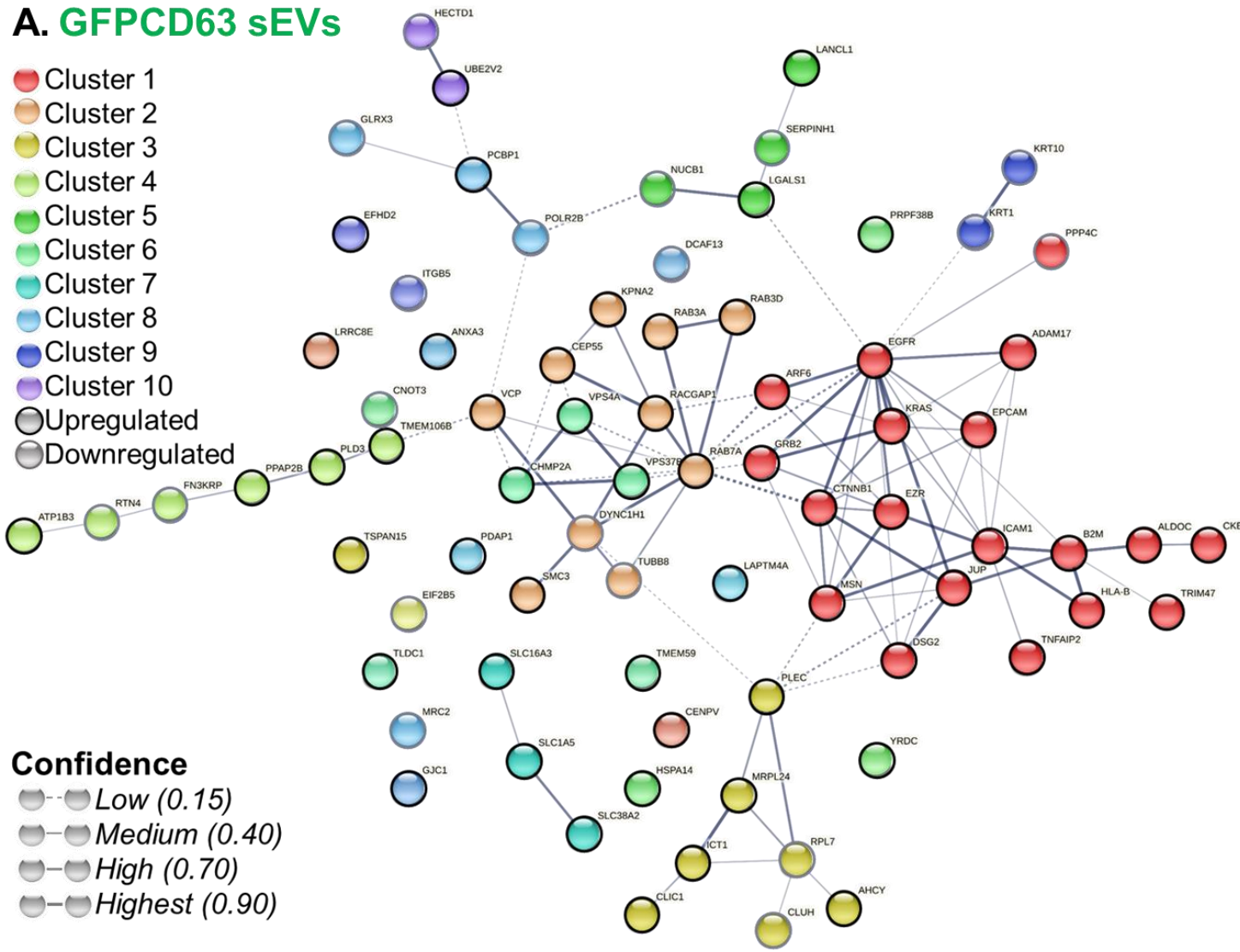


Figure 4.10. Protein-Protein Interaction network analysis.

A. Network of protein interactions using the STRING software for the **78** dysregulated proteins detected in GFP-CD63 sEVs compared to WT GFP-Parallel control sEVs. The full STRING network was generated with FDR<0.05 and with minimum confidence score of 0.4.

Dysregulated proteins were organised in **10 clusters** based on Markov Clustering (inflation parameter = 1.7). These clusters are shown in different colours and are interconnected based on **confidence** of interaction (from Low 0.15 to Highest 0.90) with gray lines.

Upregulated proteins are shown with **black** halo and downregulated proteins with **gray** halo.

Figure and Legend continued to next page ►

B. CD81-Tdtomato sEVs

- Cluster 1
- Cluster 2
- Cluster 3
- Cluster 4
- Cluster 5
- Cluster 6
- Cluster 7
- Cluster 8
- Cluster 9
- Cluster 10
- Cluster 11
- Cluster 12
- Cluster 13
- Cluster 14
- Cluster 15
- Upregulated
- Downregulated

- Confidence**
- Low (0.15)
 - Medium (0.40)
 - High (0.70)
 - Highest (0.90)

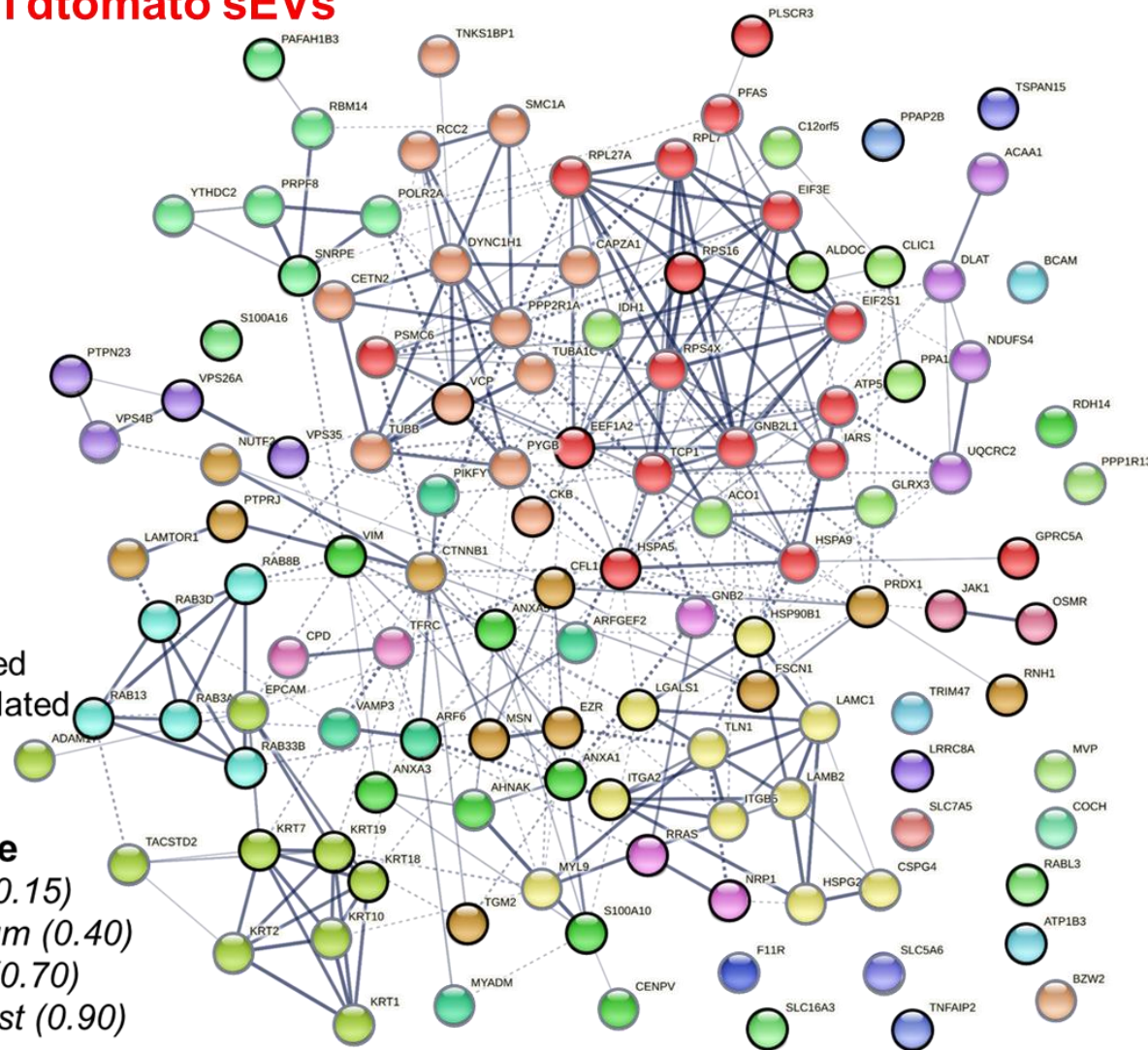


Figure 4.10. Protein-Protein Interaction network analysis.

► *Figure and Legend continued from previous page:*

B. Network of protein interactions using the STRING software for the 123 dysregulated proteins detected in CD81-Tdtomato and WT Tom-Parallel control sEVs. The full STRING network was generated with FDR<0.05 and with minimum confidence score of 0.4.

Dysregulated proteins were organised in **15 clusters** based on Markov Clustering (inflation parameter = 1.7). These clusters are shown in different colours and are interconnected based on **confidence** of interaction (from Low 0.15 to Highest 0.90) with gray lines.

Upregulated proteins are shown with **black** halo and downregulated proteins with **gray** halo.

4.3.4. Validation of selected dysregulated protein targets in sEVs

For the final section of this Chapter, we selected a number of dysregulated proteins targets identified by SWATH-MS in GFP-CD63 and CD81-Tdtomato sEVs, to validate by another technique (Western Blot). As mentioned previously, GFP-CD63 and CD81-Tdtomato sEVs will be used for dosing studies, so it was essential to determine whether these identified proteins were also shown to be dysregulated by Western Blot. Besides sEVs, the corresponding cell lysates were also prepared and were used as positive controls to confirm antibody-based detection of protein on membranes. Of note, for Western Blot analysis, all cell lines (GFP-CD63, CD81-Tdtomato and WT Parallel controls) were cultured to reflect the SWATH-MS experiment (same seeding density and cell passage), albeit in a larger scale to isolate a higher yield of cells and sEVs. Hence, cell lysates and isolated sEVs (by sucrose-cushion ultracentrifugation) underwent protein quantification by the BCA assay ([Table 2.2](#), isolation #3), followed by Western Blot analysis to validate selected protein targets ([Section 2.16.6](#)).

As the list of dysregulated proteins is rather large (78 and 123 proteins for GFP-CD63 and CD81-Tdtomato sEVs, respectively), we restricted the validation to a set of proteins that may be of biological interest and of higher confidence for detection as demonstrated by the Heatmaps. Hence, we selected proteins with different functions, vacuolar proteins, proteins from different clusters of protein-protein interaction (depicted by the STRING networks) and/or proteins that were differentially regulated in GFP-CD63 vs CD81-Tdtomato sEVs, to validate the findings of the SWATH-MS proteomics analysis. The selected identifications included: vacuolar proteins VPS4A/B and annexin A3, the adhesion proteins integrins α_2 and β_5 , the adhesion/cytoskeleton-associated protein ezrin, the growth factor receptor EGFR and the signaling molecule/transcription factor β -catenin.

4.3.4.1. GFP-CD63 and GFP-Parallel control Western Blot analysis

To begin with, GFP-CD63 and GFP-Parallel control cell lysates and sEV samples of equal protein (10 μ g) were loaded for Western Blot analysis to detect EGFR, integrin β_5 , ezrin, VPS4, β -catenin and annexin A3 by Western Blot analysis ([Figure 4.11.A](#)). GAPDH was also included in the panel as a positive control for the Western Blot transfer, labelling and detection method, and together with TSG101 were used as loading controls ([Figure 4.11.A](#)). EGFR (170kDa), ezrin (70kDa) and VPS4A/B (50kDa) were confirmed as

overexpressed in GFP-CD63 sEVs compared to GFP-Parallel controls, in agreement with the SWATH-MS proteomics results ([Figure 4.11.A.i](#)). Densitometry analysis, normalising EGFR, ezrin and VPS4A/B to GAPDH also demonstrated their higher expression in GFP-CD63 sEVs compared to control sEVs ([Figure 4.11.A.ii](#)). Interestingly, very low levels of VPS4A/B and EGFR were detected in GFP-CD63 and GFP-Parallel control cell lysates ([Figure 4.11.A.i](#)), indicating that these elements are relatively enriched in sEVs, as a proportion of the total protein present. Furthermore, higher levels of β -catenin (92kDa) were detected in GFP-CD63 and GFP-Parallel control sEVs, which also agreed with the SWATH-MS proteomics analysis ([Figure 4.11.A.i](#)). Densitometry analysis normalising β -catenin to TSG101, also demonstrated higher expression in GFP-CD63 sEVs ([Figure 4.11.A.ii](#)).

In contrast to SWATH-MS results however, integrin β_5 (100kDa) appeared overexpressed in GFP-CD63 sEVs. As the Western Blot membranes were used in a probe, and re-probe configuration, the bands for EGFR (including a truncated product) might have become heightened and overlapped with the integrin β_5 protein band. Description of the serial re-probing is explained in [Supplementary Figure 12.A.i](#). Finally, annexin A3 (36kDa) was downregulated in GFP-CD63 sEVs, which contradicts the SWATH-MS proteomics results ([Figure 4.11.A.i](#)). Densitometry analysis normalising annexin A3 to TSG101 also demonstrated this, and hence it is unlikely due to sample loading anomalies ([Figure 4.11.A.ii](#)). Of note, the raw data from the developed Western Blot membrane is shown in [Supplementary Figure 12.A](#).

4.3.4.2. CD81-Tdtomato and Tom-Parallel control Western Blot analysis

Next the same approach was employed for the CD81 overexpressing samples ([Figure 4.11.B](#)). Firstly, Integrin α_2 (138kDa) and ezrin (70kDa) was overexpressed in CD81-Tdtomato sEVs compared to Tom-Parallel controls, thus confirming the SWATH-MS proteomics analysis results ([Figure 4.11.B.i](#)). Densitometry analysis normalising Integrin α_2 and ezrin to GAPDH also demonstrated their higher expression in CD81-Tdtomato sEVs ([Figure 4.11.B.ii](#)). Interestingly, whereas integrin α_2 was also overexpressed in CD81-Tdtomato cells, ezrin was relatively under-expressed. Conversely, lower levels of integrin β_5 (100kDa), β -catenin (92kDa), VPS4A/B (50kDa) were detected in CD81-Tdtomato sEVs, again agreeing with the SWATH-MS proteomics results ([Figure 4.11.B.i](#)). Densitometry analysis also demonstrated this, with integrin β_5 normalised to TSG101, and β -catenin and VPS4A/B normalized to GAPDH ([Figure 4.11.B.ii](#)). Finally,

in contrast to SWATH-MS results, annexin A3 (36kDa) was downregulated in CD81-Tdtomato sEVs, ([Figure 4.11.B.i](#)), and this is also shown by densitometry analysis (normalized to TSG101) in [Figure 4.11.B.ii](#). The raw data from the developed Western Blot membrane is shown in [Supplementary Figure 12.B](#).

In conclusion, Western Blot analysis verified some of protein targets deriving from SWATH-MS analysis, for example, it confirmed that overexpression of CD63 in DU145 cells lead to upregulation of β -catenin and VPS4A/B in generated sEVs, whereas overexpression of CD81 lead to downregulation of these proteins. Furthermore, it was confirmed that overexpression of CD63 or CD81 in DU145 cells both resulted in overexpression of ezrin in sEVs. The Western Blot results however showed downregulation of annexin A3 in sEVs, which contradicted the proteomics analysis for unknown reasons. Overall, most protein targets selected for testing by Western Blot analysis verified the SWATH-MS results; however, future work should focus on investigation of a larger selection of protein targets from these datasets, ensuring more technical and biological replicate experiments.

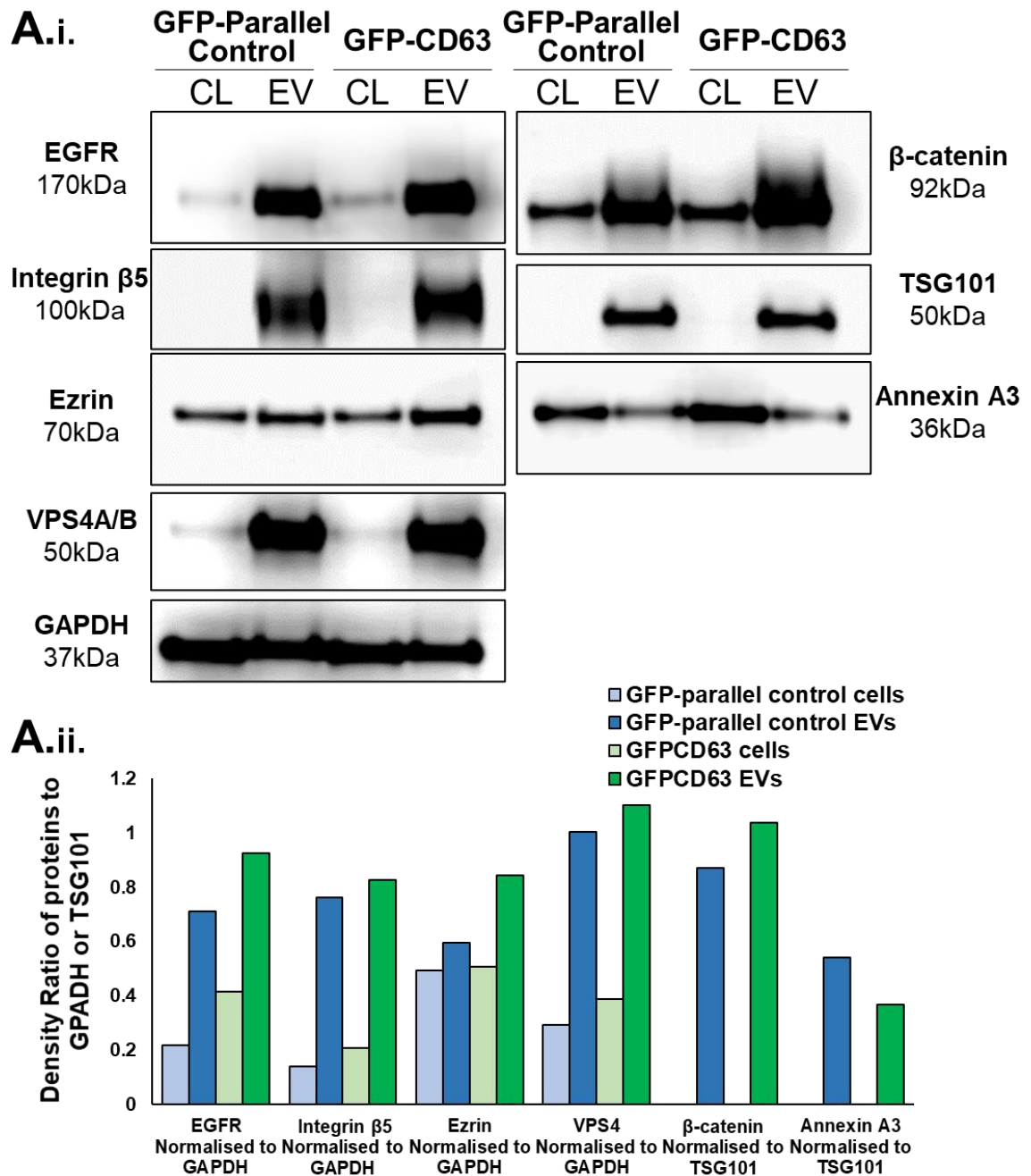


Figure 4.11. Validation of selected SWATH-MS protein targets via Western Blot analysis.

A.(i) Western Blot analysis for selected dysregulated protein targets identified by SWATH-MS analysis for GFP-CD63 sEVs compared to GFP-Parallel controls (and corresponding cell lysates) included: vacuolar proteins VPS4 and annexin A3, adhesion protein integrin β_5 , cytoskeleton protein ezrin, growth factor receptor EGFR and gene transcription regulator β -catenin with GAPDH and TSG101 used as loading controls; **(ii)** Densitometry analysis for all proteins normalized either to GAPDH or TSG101.

For raw Western Blot developed membranes see [Supplementary Figure 12.A](#).

Note that this experiment was conducted once ($n=1$).

► **Figure and Legend continued to next page:**

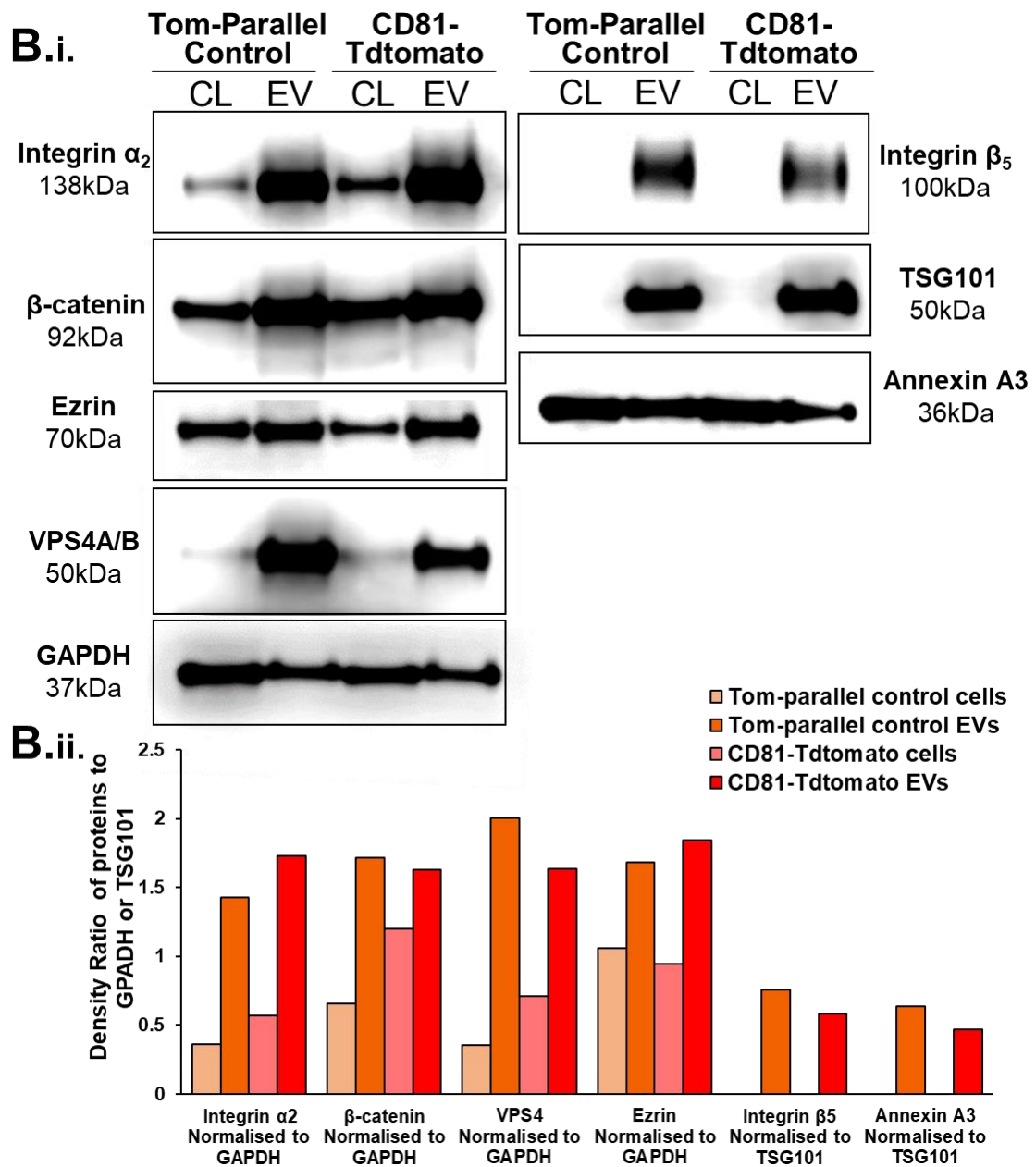


Figure 4.11. Validation of selected SWATH-MS protein targets via Western Blot analysis.

► *Figure and Legend continued from previous page*

B.(i) Western Blot analysis for selected dysregulated protein targets identified by SWATH-MS analysis for CD81-Tdtomato sEVs compared to Tom-Parallel controls (and corresponding cell lysates) included: vacuolar proteins VPS4 and annexin A3, adhesion proteins integrins α_2 and β_5 , cytoskeleton protein ezrin and gene transcription regulator β -catenin, with GAPDH and TSG101 used as loading controls; **(ii)** Densitometry analysis for all proteins normalized either to GAPDH or TSG101.

For raw Western Blot developed membranes see [Supplementary Figure 12.B](#).

Note that this experiment was conducted once (n=1).

Abbreviations on Figure: CL=cell lysate and EV= sEV lysate

4.4. Discussion

SWATH-MS design and protein detection

This Chapter focused on identifying the differences in the proteome of DU145 cells overexpressing CD63 or CD81 (fused with the fluorescent proteins GFP or Tdtomato, respectively) and their resulting sEVs. We carefully compared these with age-matched WT DU145 cells and sEVs, utilising the novel SWATH-MS technique (193-195); this method provides a wide coverage of the sample proteome, and it was hence ideal for our exploratory proteomic investigations. For this study we directly compared the proteome of GFP-CD63 cells and sEVs with the WT GFP-Parallel cells and sEVs, as well as the proteome of CD81-Tdtomato cells and sEVs with the WT Tom-Parallel cells and sEVs, to identify potential proteomic changes. In addition, proteomic changes in the GFP-CD63 cells were indirectly compared with changes in the GFP-CD63 sEVs, as the same Spectral Library (Spectral Library 1) was used for protein detection in the SWATH-MS analysis. This was also done for the CD81-Tdtomato cells compared to the CD81-Tdtomato sEVs (Spectral Library 2). Ideally in future work, a global Spectral Library would be more suitable to qualitatively and quantitatively compare the WT, and overexpressing cell lines and sEVs, even though this might prove challenging due to their fundamentally different composition, which may inadvertently bias the Spectral Library. Nevertheless, our chosen approach was a reasonable compromise that provided routes for cross-specimen comparisons in a quantitative fashion.

After the SWATH-MS runs and setting of the appropriate thresholds (FDR<1% and CV<50% between replicates), we identified ~300 proteins in GFP-CD63, CD81-Tdtomato and their respective WT Parallel sEVs, as well as ~1000 proteins in the corresponding cell samples. These numbers of identified proteins were similar to the numbers reported in the literature by studies utilising traditional DDA-MS (179, 183, 186-188, 200) and SWATH-DIA MS methods (196, 197). Using less-conservative thresholds would undoubtedly increase the number of protein identifications, however many of these would be false IDs, and would add to “data noise” that may distract from biologically relevant identifications.

Comparison of the proteins detected in our EV datasets with Vesiclepedia (compendium of proteins detected in EVs by MS-studies (201)) revealed more than 95% overlap, agreeing with other similar proteomics analysis typically reporting >90% overlap (182, 186, 196, 202). One might support that this is disappointing, as the SWATH-MS method has not revealed many highly novel sEV-associated identifications; it does

however suggest that the protein IDs we identified are actually correct and typical of other sEV datasets. Despite this, we did identify 11 proteins not previously documented in sEVs including transmembrane-, cytoskeleton-, metabolism- and proliferation-associated proteins like transmembrane protein 184C (TMEM184C), striatin-interacting protein 2 (STRIP2), TP53-Induced Glycolysis Regulatory Phosphatase (TIGAR) and mTOR-associated protein MEAK7 (respectively); future investigation of these proteins might shed some more light about their presence and potential role in sEVs.

In addition, comparison of proteins between cells and sEVs revealed more than 60% overlap, thus confirming that sEVs do not entirely reflect the parent cell proteome and carry a sub-proteome of the cell. A previous MS- proteomics study on sEVs from the NCI-60 cancer cell lines, compared the expression levels on detected proteins between cells and sEVs, and revealed both common and unique proteins, thus supporting our observations; for example they observed that actin was found in both cells and sEVs, whereas Galectin-3 was enriched in sEVs only (186). Therefore, the enrichment of elements in sEVs to an extent where they are barely, or not at all, detected in the parent cell has been reported for many sEV types and is also a feature of our datasets.

Further analysis of these identified targets involved determination of the dysregulated proteins in the CD63 or CD81 system. Interestingly, the number of dysregulated proteins was higher in sEVs rather than cells, which might be attributed to CD63 and CD81 being highly sEV-specific (up to 100-fold compared to parental cells) (19, 156, 198). Furthermore, we detected more dysregulated proteins in the CD81-Tdtomato rather than the GFP-CD63 sEV populations, which might be due to the different sEV biogenesis, cargo loading functions and protein interactions of CD63 and CD81 at the TEMs (tetraspanin-enriched microdomains) (19, 156, 198). Interestingly, even though >60% of all detected proteins were common between cells and sEVs, the majority of dysregulated proteins were not actually overlapping, suggesting differential regulation at the cellular and EV-level. Obviously, it is important to consider that overexpression of CD63 or CD81 does not result in homogeneous sEV populations, but rather more CD63+ or CD81+ or even double-positive populations; this gives another dimension of complexity between the reflection of cell to sEV proteome.

Dysregulated proteins in cell datasets

Focusing on the GFP-CD63, CD81-Tdtomato and their respective WT Parallel cells, we overall observed a similar repertoire of dysregulated proteins in the cell datasets, even though we used two separate Spectral Libraries for the SWATH-MS runs. For example, both datasets revealed dysregulated proteins associated with protein/membrane trafficking and MVB-associated pathways (e.g., sorting nexin-6, caveolae-associated protein 1, CHMP1B and GTPases like Rab-3B), proteins associated with the cytoskeleton, adhesion and migration (e.g., β -tubulin, dynein, cytokeratins (9, 10, 19 and 78) and integrins (integrin α_2, α_3 and β_1)), various 40S and 60S ribosomal proteins, proteins in other major signalling pathways like growth, proliferation and survival (e.g. Arf5, RhoC and TNFAIP2), as well as proteins involved in metabolism and protein degradation pathways (e.g., mevalonate kinase, NAMPT, ubiquitin-associated proteins, proteasome 20S and proteasome activator complex subunits). Gene enrichment analysis revealed that these dysregulated proteins exhibited similar biological processes and molecular functions in the cells, as well as localised to similar cell compartments; for example, they were mostly involved in the regulation of nucleic acid metabolism, protein metabolism, energy pathways and cell growth/maintenance, as well as exhibited similar molecular functions like DNA-binding-, transporter-, and oxidoreductase activity, and were mostly localised in the cytoplasmic, cytosolic, lysosomal, nuclear, mitochondrial and ER compartments. A plethora of these protein targets, biological processes and molecular functions were reported in a recent DDA-MS study investigating the proteome of PCa cell lines (including DU145 cells) and thus validated our observations by SWATH-MS (200).

Dysregulated proteins in sEV datasets

Next, we focused on investigating the proteome of generated sEVs (after overexpression of CD63 or CD81), especially since these sEVs are going to be used for uptake and distribution studies in various cell systems. Interestingly, whereas there is a plethora of MS-proteomics studies on various cancer-derived EV types for biomarker research (179-186), the majority of studies using tetraspanins-fused fluorescent EV reporters, do not characterise the proteome of the sEVs (or cells) (117, 118, 121, 123, 178), even though the crucial roles of tetraspanins in EV biogenesis and cargo sorting are established in the literature (19, 156, 198).

Only a very limited number of studies have investigated changes in the sEV proteome after overexpression of GFP-CD63 in HEK293T cells (122), and after overexpression of

CD151 or downregulation of CD9 in RWPE1 prostate cells (192). Surprisingly, the first study claimed that overexpression of GFP-CD63 in HEK293T cells did not induce any changes in the resulting GFP-CD63 sEV proteome besides GFP expression. Notably in this study the authors reported that there were not substantial changes in CD63 expression either. However, manual inspection of their protein targets did show differences in spectral counts, but as their study was only qualitative no quantification or statistical analysis was possible (122). The second study demonstrated that overexpression of CD151 and/or downregulation of CD9 in the RWPE1 prostate cells induced significant phenotypic changes in sEVs and differential enrichment in biological pathways depending on which tetraspanin was altered e.g., upregulated metabolism pathways for CD9-downregulated sEVs, whereas protein degradation pathways were upregulated for CD151-upregulated sEVs (192). Hence significant alterations in the composition of sEVs after overexpression of tetraspanins are likely to occur, and the assumptions that these fluorescence-tagging methods do not induce any phenotypic change in the biological system of sEVs are unwise. Thus, the danger here is that reported findings of such tetraspanin-based fluorescent EV reporters might be inaccurate and with artefacts due to an unintended modified EV proteome.

Dysregulated proteins- Gene Enrichment Analysis

Overall, the EV proteomes identified in our study were broadly consistent with that expected for sEVs, as the localisation of identified proteins in GFP-CD63 and CD81-Tdtomato sEVs demonstrated a high percentage of genes in the exosomal, cytoplasmic, lysosomal, plasma membrane, nuclear and ER compartments; previous MS-proteomics studies on PCa-derived sEVs (LNCaP, PC3, DUCaP and VCaP) (179, 188-190) and sEVs derived from the NCI-60 cancer cell lines (186) also reported similar localisation of identified proteins in all the aforementioned sub-cellular compartments. The dysregulated proteins in GFP-CD63 and CD81-Tdtomato sEVs were mostly involved in signal transduction, cell communication, cell growth/maintenance, metabolism and transport; previous MS- studies on PCa-derived sEVs (including DU145-derived sEVs) also showed their involvement in cell growth/proliferation, cell death, metabolism, endocytosis, adhesion and cytoskeleton signalling (179, 181, 187-189). Comparative studies of sEVs from 12 different cancer types (colorectal, bladder, prostate, pancreatic, breast, gastric, lung, ovarian cancer, cholangiocarcinoma, hepatocellular carcinoma, and oral squamous cell carcinoma) and the NCI-60 cancer cell lines, revealed that some detected proteins from MS-proteomics analysis were common in all sEV types and were

implicated in similar biological processes, such as cell adhesion, migration, growth/proliferation and vesicle/protein transport (186, 203). Finally, the dysregulated proteins in our sEV datasets exhibited various molecular functions like cell adhesion activity, transporter activity, ATPase and GTPase activity, cytoskeletal anchoring, MHC-1 receptor activity and calcium ion binding activity; similar functions were also reported by previous MS-proteomics studies on prostate-cancer derived sEVs (including DU145-derived sEVs) (181, 187, 188).

EV-associated dysregulated proteins

In our study, the GFP-CD63, CD81-Tdtomato and their respective WT Parallel sEV datasets showed both commonalities and differences in identified proteins. Focusing on the dysregulated proteins in sEVs after overexpression of CD63 or CD81, both datasets included proteins highly-associated with sEVs, membrane trafficking, endosomal/MVB pathways and the ubiquitin-dependent ESCRT complexes like: VPS4A/B, VPS26A, VPS35, VP37B, VAMP3, CHM2A, the ubiquitin-protein ligases HECTD1 and TRIM47, as well as the highly sEV-associated GTPases Rab-3A, Rab-3D, Rab-7A etc. and the annexins A1,3 and 5. These detected proteins further supported the putative MVB of origin for these sEV samples analysed by SWATH-MS, and agreed with reports from a previous DIA SWATH-MS study in urinary sEVs (197), as well as DDA MS-studies investigating prostate- cancer and bladder cancer derived sEVs (181, 183), sEVs derived from 12 common cancers (203) and from the NCI-60 cancer cell lines (186).

Obviously, due to the pivotal role of tetraspanins in sEV biogenesis and cargo sorting (12, 156) we expected direct or indirect changes in the loading of various proteins in sEVs after overexpression of CD63 or CD81. Examples of this phenomena include CD63 regulation of cargo sorting via ESCRT-dependent and ESCRT-independent mechanisms (12), and CD81-mediated induction of inward budding of the TEM by clustering with other proteins and cholesterol (156). Hence, some of these aforementioned proteins were similarly regulated in our sEVs after overexpression of CD63 or CD81 (e.g., Rab-GTPases and annexins were upregulated in both GFP-CD63 and CD81-Tdtomato sEVs), whereas others were differentially regulated (e.g., VPS4 and E3 ubiquitin-protein ligase TRIM47 were upregulated in GFP-CD63 but downregulated in CD81-Tdtomato sEVs). These are important observations that identify the different, and non-identical functions of these tetraspanins in the biogenesis of sEVs, that inadvertently lead to alterations in the released vesicle composition with potential consequences for their biological functions.

Western Blot analysis successfully validated the differential expression of VPS4 between GFP-CD63 and CD81-Tdtomato sEVs (and compared to their WT parallel control sEVs). A previous study demonstrated that inhibition of VPS4 decreased the levels of CD63 (decreased release of CD63+ EVs) by downregulation of ESCRT-III-dependent sEV biogenesis, however any potential effects of CD63 expression on the levels of VPS4 were not addressed (204). Our findings support that VPS4 and CD63 are linked, at least indirectly, in the biogenesis of sEVs.

It is also important to note that some highly associated sEV markers were absent from our proteomics dataset e.g., tetraspanins CD9, CD63 and CD81, Alix and TSG101, potentially since our generated spectral libraries were of cellular origin. One might hypothesise that these highly sEV-specific markers are of such low abundance in the parental cells, that they might have been missed in the generation of the spectral libraries; thus, proteins that are not included in the spectral libraries during the DDA-MS run will not be detected in the SWATH-MS DIA run (193-195). Future considerations for DIA experiments should incorporate a vesicle pool within the Spectral Library, to facilitate the identification of such elements that are relatively underrepresented in cells; hence, this is an important outcome to improve future iterations of this profiling approach.

Overall, our study detected various highly sEV-associated proteins with established functions in vesicle trafficking from the MVB/ endosomal pathway, in all our sEV samples, thus supporting their distinctive vesicular (and not cellular) nature, and the success of the technology in revealing this.

Cytoskeleton-, migration- and adhesion- associated proteins

Common proteins detected in GFP-CD63, CD81-Tdtomato and their respective WT Parallel sEVs, were those involved in the cytoskeleton, migration and adhesion e.g., α - and β - tubulin, myosin and dynein, talin-1, ezrin, moesin, EPCAM, heparan sulfate proteoglycan 2, integrins β_5 and α_2 and cytokeratins. A previous MS-study has considered the presence of cytokeratins as “inevitable contamination” from EV sample preparation (122), whereas others supported their biological significance in the context of cancer e.g. cytokeratins 18 and 19 were previously detected in breast- (205) and bladder- cancer (183) derived sEVs and have been proposed as potential biomarkers for disease progression. In addition, the presence of the cytoskeletal- and adhesion-associated proteins and receptors, were similarly reported in MS-proteomic sEV studies in the literature, like in PCa-derived sEVs from LNCaP (188, 189), DUCaP (188), PC-346C (179) and VCaP (179) cell lines, bladder cancer-derived sEVs (183), as well as in sEVs derived from 12 common cancers (203) and the NCI-60 cancer cell lines (186).

These studies hypothesised that the presence of proteins associated with the cytoskeleton, adhesion and other signalling receptors are expected in sEVs, and likely play roles in sEV biogenesis and in facilitating cell-to-cell communication (203); furthermore, a review article has summarised the presence of these proteins associated with the cytoskeleton, adhesion and migration in sEVs (198). Whether or not such constituents exist as a “mini” cytoskeletal network or pool within the sEV lumen is rarely considered, and never been demonstrated. Given the technology relies on proteolytically cleaved proteins, it is not yet determined if cytokeratins are encapsulated as functional proteins, or as partly degraded fragments.

In our study, some of these proteins were similarly regulated after overexpression of CD63 or CD81, e.g., ezrin and moesin (upregulated) and β -tubulin, dynein, integrin β_5 , cytokeratin proteins 1 and 10 (downregulated), whereas other proteins were differentially regulated e.g., EPCAM (upregulated after overexpression of CD63, but downregulated after overexpression of CD81). Western Blot analysis demonstrated the upregulated expression of ezrin for GFP-CD63 and CD81-Tdtomato sEVs, as well as the upregulation of integrin α_2 and downregulation of integrin β_5 in CD81-Tdtomato sEVs. A previous study has demonstrated that the C-terminal of CD81 directly associated with ezrin (206), which might suggest that overexpression of CD81 can sequester higher levels of ezrin to sEVs, however its association with CD63 is still unknown.

Dysregulated proteins: ribosomal constituents

Other proteins that might be considered “contamination” are proteins of ribosomal origin like 60S and 40S ribosomal proteins, translation initiation and elongation factors eIF-2BE EIF3E and EF1A. The number of these proteins was relatively low in our sEV datasets, but previous MS-proteomic studies have reported their presence in PCa-derived sEVs from LNCaP (189), PC346C (179) and VCaP (179) cell lines, as well as in sEVs derived from the NCI-60 cancer cell lines (186), and hypothesised that delivery of these ribosomal components might enable direct translation of mRNAs carried by sEVs, after their uptake by recipient cells. It is important to note that in our study, sEVs were isolated via sucrose-cushion ultracentrifugation which is considered one of the more superior methods for high purity sEV isolations for use in MS-studies (i.e., largely absent cell-derived secreted components, protein aggregates, cell fragments etc.) (207); thus, we can safely hypothesise that our sEV samples were mostly devoid of cellular contaminants. However, the incorporation of ribosomal and some other constituents into the MVB-derived sEVs is currently not well understood, and hence the possibility of co-

isolation of some of these elements during the EV isolation process is difficult to fully discount.

Dysregulated proteins in metabolism and major signalling pathways

Finally, some common proteins detected in GFP-CD63, CD81-Tdtomato and their respective WT Parallel sEVs, were involved in metabolism and other major signalling pathways (growth, proliferation, and survival); examples were the enzyme Aldolase, GTPases like Arf6, as well as receptors and signalling molecules like TNAP2, Grb2, EGFR and β -catenin. A comparison with previous MS-studies has demonstrated the presence of these and similar cytosolic proteins in EVs, including LNCaP and DUCaP PCa-derived sEVs (188), bladder cancer sEVs (183) as well as in sEVs derived from 12 common cancers (including PCa) (203). In addition, a recent review article has summarised the presence of these signalling proteins/receptors, and metabolic enzymes in sEVs (198).

Interestingly, in our study whereas proteins like Aldolase, Arf6 and TNAP2 were similarly upregulated after overexpression of CD63 or CD81, we observed that β -catenin was upregulated after overexpression of CD63 but downregulated after overexpression of CD81. Western Blot analysis did verify the upregulation of EGFR in GFP-CD63 sEVs and the differential expression of β -catenin in GFP-CD63 vs CD81-Tdtomato sEVs. Currently, there is no direct evidence that CD63 regulates EGFR in sEVs, however CD63+ EVs have been associated with EGFR, potentially through the role of CD63 in sEV biogenesis and cargo sorting via ESCRT-dependent and ESCRT-independent mechanisms (208). In addition, CD63 was shown to stabilize β -catenin signalling, as knockdown of CD63 decreased the expression levels of β -catenin, whereas no direct association is currently found for CD81 (24). An interesting hypothesis that needs further investigation is that β -catenin is downregulated in CD81-Tdtomato sEVs, as perhaps overexpression of CD81 reduces the loading of CD63 in these sEVs i.e., there is a shift of the sEV population to more CD81+ sEVs than CD63+ sEVs, thus indirectly, the total levels of β -catenin might appear downregulated.

4.5. Conclusions

This chapter was an exploratory study focused on describing protein changes on parental DU145 cells and generated sEVs, after overexpression of the tetraspanins CD63 and CD81. This proteomic study was performed using the relatively novel SWATH-MS DIA method, which revealed a wide proteome coverage for each sample and enabled the quantitative detection of a plethora of proteins, some of which were dysregulated after overexpression of CD63 or CD81. Our results demonstrated relatively similar proteomic changes in the DU145 cells after overexpression of either CD63 or CD81, which mostly involved “house-keeping” pathways like metabolism of proteins and nucleic acid related proteins. On the other hand, proteomic changes in sEVs were more varied, with some dysregulated proteins being similarly regulated, and others differentially regulated between GFP-CD63 and CD81-Tdtomato sEVs; however, we observed that collectively these dysregulated proteins were involved in MVB/sEV-, growth-, cytoskeleton, adhesion-, migration- and survival- associated pathways. Furthermore, validation of some of these dysregulated proteins by Western Blot analysis also confirmed our observations by SWATH-MS analysis, even though validation of more targets covering more protein-protein networks would be advantageous for future work. This is the first study to date (to our knowledge) that explored the proteomic changes of the genetically manipulated parental DU145 PCa cells and compared them with the proteomic changes of the secreted GFP-CD63 and CD81-Tdtomato sEVs. The majority of studies in the literature did not thoroughly investigate the proteome of their engineered sEVs; however, our exploratory study demonstrated that investigation of changes in both the cells and sEVs was essential after overexpressing tetraspanins, as we reported various dysregulated proteins involved in many biological pathways. To conclude, this Chapter has now defined in detail the emergent proteomic consequences of overexpressing these tetraspanins, and this essential understanding will be used to inform the design, and most importantly the interpretation, of studies using such engineered cell lines and fluorescent sEV reporters.

**CHAPTER 5:
Phenotypic Changes of
Prostate Cancer Stable Cell
Lines and Secreted
Extracellular Vesicles in 3D-
Emulated Bioreactor
Microenvironments**

5.1. Introduction

sEVs are produced extensively by tumours *in vivo* and have been long since detected in the biofluids of patients (e.g., plasma, urine) (99, 181, 209). Even though it is feasible to utilise these sEVs as a means of assessing disease status, the inherent low yield and low purity of these isolations, as well as patient heterogeneity, still remain some of the greatest challenges for reproducible and reliable EV studies (127). To ameliorate some of these issues, many researchers have switched to *in vitro* models for production of sEVs (95% of the MISEV2018 guidelines authors (6)). Even though the use of cell lines provides a more consistent and reproducible way to isolate higher purity sEVs, this option is not efficient or cost-effective in the long-term, as well as it is labour-intensive and produces large volumes of EV-containing media that cannot be easily processed e.g. limits in the media volume that can be loaded on ultracentrifuges, which are commonly involved in the isolation of sEVs (127).

To counteract this and further increase the yield and purity of sEV preparations, the Tissue MicroEnvironment Group have developed, adapted and adopted the CELLline Bioreactor culture system, originally designed for hybridoma culture (210), as an sEV production pipeline which has since been established in the literature (115, 127, 157, 211-214). Various studies utilised these Bioreactor Flasks to support the production of sEVs from a variety of cell lines, including the PCa cell lines LNCaP, PC3, VCaP and DU145 (115, 157, 214), patient-derived pleural malignant mesothelioma and patient-derived large granular lymphocytic leukaemia NK cells (127), colorectal cancer cell lines (SW480 and SW620) (213), leukaemia cell lines (MEC-1) (212), oral squamous cell carcinoma (PE/CA-PJ49/E10), pancreatic adenocarcinoma (BxPC3) and melanoma (H3) (211), as well as BHK (Baby Hamster Kidney) fibroblastic cell lines (215).

The CELLline Bioreactor culture system is essentially a culture flask comprising two compartments; the outer media compartment and the inner cell compartment, which are separated with a semi-permeable membrane that allows inflow of a constant source of nutrients, whereas gas exchange is achieved through a silicone membrane at the base (Figure 5.1.A). Due to the nature of its design, the CELLline Bioreactor enables high cell densities with a concomitant increase in sEV concentration in the cell conditioned medium (10- to 100-fold) and if isolation methods employ a 30% sucrose/D₂O flotation step, the resultant sEV purity can also be excellent (as assessed by a high Particle to Protein ratio) compared to conventional 2D flasks (127, 157, 211-214, 216). The CELLline Bioreactor Flask also supports the physiological 3D growth of cells and can thus emulate a 3D-like microenvironment platform (127, 211) (Figure 5.1.B). As this

system can support 3D cell culture, it more closely resembles the *in vivo* microenvironment compared to conventional 2D flasks; thus, the CELLine Bioreactor can be utilised as a 3D-like tumour-mimic model for the production of “*in vivo*-like” sEVs.

Despite the many desirable qualities of the CELLine Bioreactors, their use as a 3D-like tissue-mimic model for production of sEVs is still in its infancy, as their impact on cell and EV physiology has not been thoroughly investigated, especially for the culture of engineered cell lines or for long-term culture (127, 211, 214).

It is therefore essential to further characterise the CELLine Bioreactors as they can be potentially elevated from being just “sEV production pipelines” to becoming biologically relevant 3D-like tissue-mimic models, serving as a bridge between 2D and 3D studies.

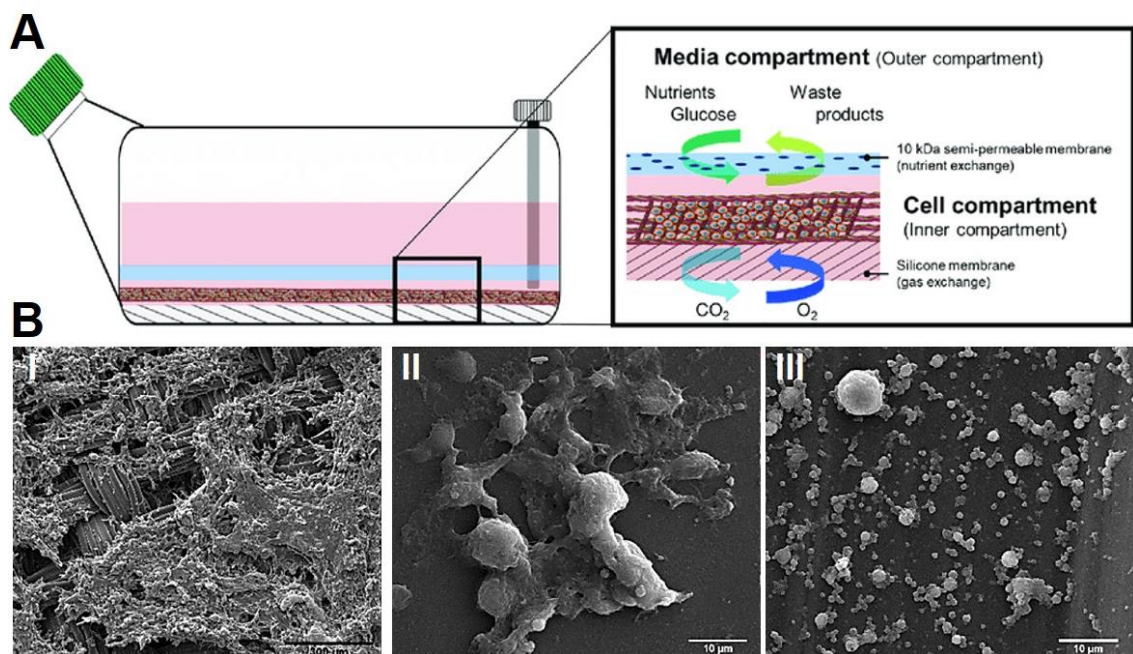


Figure 5.1. Schematic illustration and Scanning Electron Microscopy of the CELLine Bioreactor Flask.

A. The CELLine Bioreactor Flask is a two-compartment culture system with a 2mm “inner cell compartment” for sustainable cell growth at high densities and an “outer media compartment” for placement of cell culture media. The two compartments are separated by a 10 kDa semi-permeable cellulose acetate membrane which allows optimal and continuous diffusion of nutrients with concurrent removal of waste products. Below the inner cell compartment, a silicone membrane enables direct oxygenation and gas exchange. **B.** SEM (Scanning electron microscopy) images of mouse lung epithelial E10 cells seeded in the CELLine Bioreactor Flask: **I.** 3D- growth of cells in the PolyEthylene Terephthalate (PET) woven mesh membrane of the inner cell compartment. **II.** Cell growth in the interior of the semi-permeable membrane separating the inner and outer compartments and **III.** 3D-growth of cells on the silicone membrane below the inner cell compartment.

Figure adapted from “Efficient extracellular vesicle isolation by combining cell media modifications, ultrafiltration, and size-exclusion chromatography” (Guerreiro et al.,2018).

5.2. Aims and Objectives

In this chapter, we aimed to systematically characterise how overexpressing tetraspanins CD63 or CD81 in DU145 cells, cultured long-term in CELLine Bioreactors, may change the phenotype of parental cells and secreted sEVs. Therefore, to achieve this we aimed to:

- To utilise CELLine Bioreactors for culturing DU145 cell lines overexpressing CD63 or CD81 and WT Parallel controls.
- To utilise CELLine Bioreactors for manufacturing sEVs in large quantities.
- To determine potential cell phenotypic differences in Bioreactors (cell cycle, cell growth and fluorescence signal), induced by overexpression of CD63 compared to CD81 in DU145 cells.
- To determine potential phenotypic differences in Bioreactors (expression of sEV-associated markers, fluorescence, size and morphology) induced by overexpression of CD63 compared to CD81 in sEVs.

5.3. Results

5.3.1. Establishing the Bioreactor Characterisation procedure

The CELLLine Bioreactor flasks were seeded with the DU145 cell lines (GFP-CD63, CD81-Tdtomato and their respective WT Parallel controls) and were assessed periodically and long-term (11 weeks) in order to determine the effects of that system on the phenotype of cells and isolated sEVs. The CELLLine characterisation procedure is described in detail in [Figure 5.2](#) and [Section 2.18](#).

5.3.2. Phenotypic Characteristics of Cells in Bioreactors

5.3.2.1. Cell Growth and Adhesion in Bioreactor Flasks

To begin with, we assessed the growth, adhesion and adaptation of the four DU145 cell lines in the Bioreactor Flasks over time, and then investigated the potential effects of tetraspanin overexpression (CD63 or CD81). As detailed in [Figure 5.2](#), we characterised 3 fractions for every cell line, representing different states of adhesion (Adherent, Semi-Adherent and Suspension).

The overall growth of cells in the Bioreactors over time (Weeks 4-11) was measured and showed that the average number of cells recovered from all fractions after 4 weeks of culture (Week 4) was lower than the initial seeding density of 2.5×10^7 cells. Specifically, $\sim 1 \times 10^7$ cells were recovered on average by the Adherent fractions, 2.5×10^6 cells from the Semi-Adherent fractions and $\sim 1 \times 10^7$ cells from the Suspension fractions i.e., a total growth of $\sim 2.2 \times 10^7$ cells after 4 weeks of culture. However, when a lower cell number was returned to the Bioreactors (3.9×10^6 cells) by Weeks 8 and 11 the total cells recovered were significantly higher ($\sim 7-9 \times 10^7$ cells for all fractions and cell lines). This suggested that the original seeding density was important to the establishment of the Bioreactor flask. [Supplementary Figure 13](#) shows the raw cell numbers for each cell line and each fraction over time, as well as the total cell numbers.

Focusing on each fraction separately, we observed changes in the adhesion properties of cells, with an increasing number of cells recovered from the Semi-Adherent and Suspension fractions over time; by Week 11 a 4-fold and 2.5-fold increase in cells from these fractions were recovered compared to Week 4, respectively ([Figure 5.3.A.ii,iii](#)). In addition, a highly significant increase in Adherent cells was observed by Week 8 (7-fold increase), but then decreased by Week 11 ([Figure 5.3.A.i](#)). Despite that,

by the end of the experimental timeline the majority of cells in the Bioreactor Flasks were still Adherent, and the least in the Semi-Adherent state ([Figure 5.3.A](#)). Our observations suggested that a lower seeding cell density in the Bioreactor Flasks resulted in improved cell growth and led to the majority of cells remaining adherent over time. Despite this, the observed increase of Suspension and Semi-Adherent cells could be attributed to issues with cell viability, differences in cell cycle, or may suggest a potential adaptation of cells to a non-adherent state in the Bioreactor Flasks.

Next, we investigated the potential effects of tetraspanin overexpression (CD63 or CD81) on cell growth and adhesion in the Bioreactor Flasks. We observed that consistently lower numbers of overexpressing cells (GFP-CD63 and CD81-Tdtomato) were recovered compared to their WT control cells (GFP-Parallel and Tom-Parallel). This was reflected to the cells of every fraction ([Figure 5.3.A](#) and [Supplementary Figure 13](#)). In an attempt to quantify these differences, the cell numbers of all cell lines were normalised to the seeding density corresponding to each time-point (Week 4-11). This normalisation further confirmed the reduced growth of overexpressing cells compared to their WT control counterparts, for all fractions over time ([Figure 5.3.B](#)). For example, at Week 8, the total number of GFP-CD63 and CD81-Tdtomato cells recovered from the Bioreactors were 20-fold higher than the seeding density, whereas the GFP-Parallel and Tom-Parallel cells were 25-fold and 35-fold higher (respectively), suggesting reduced growth for cells overexpressing CD63 or CD81 ([Figure 5.3.B](#)).

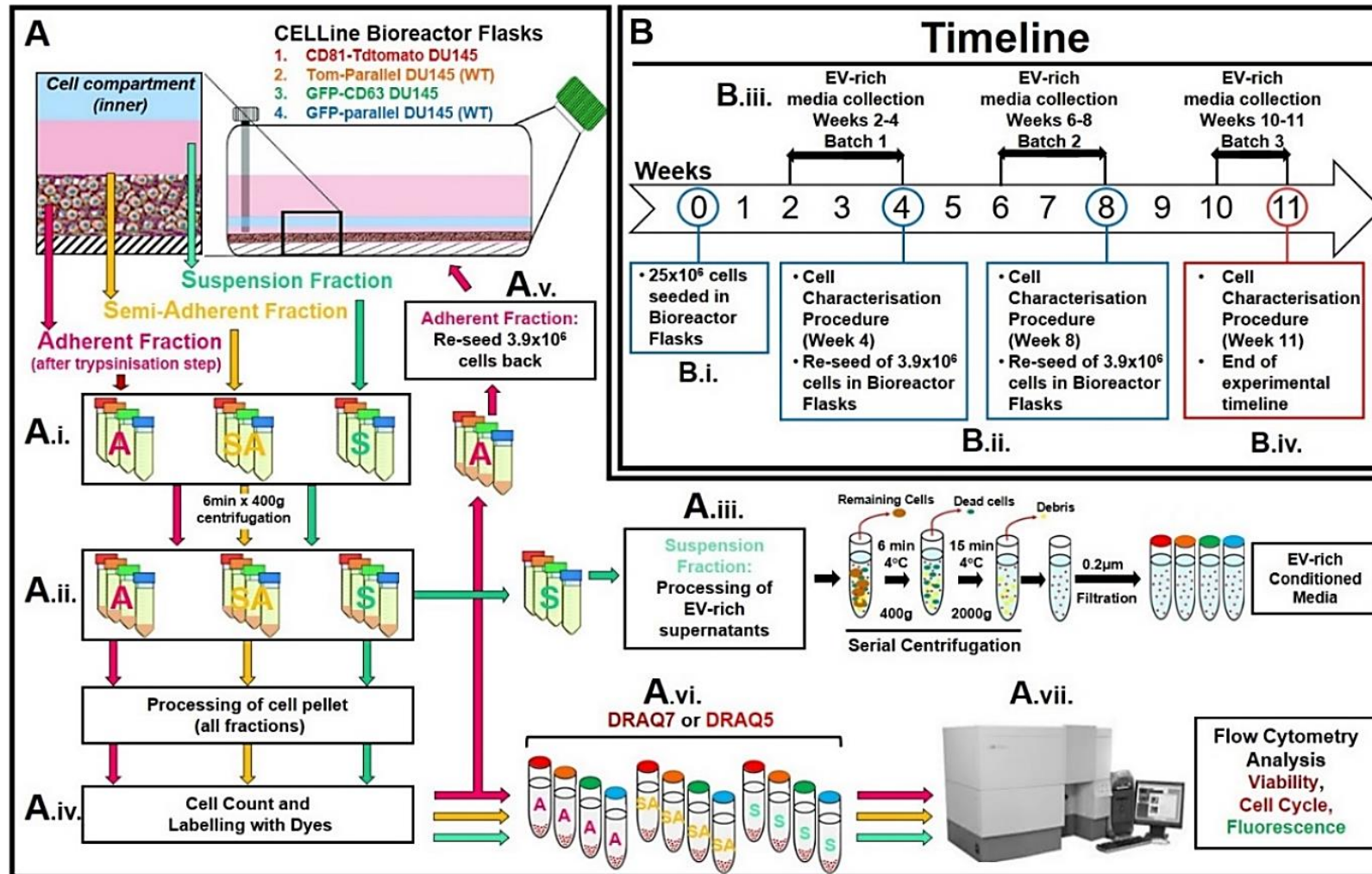


Figure 5.2. Schematic and timeline for Bioreactor Characterisation procedure.

Figure Legend on next page ►

Figure 5.2. Schematic and timeline for Bioreactor Characterisation procedure.

◀ *Figure in previous page*

A. Schematic representation of the steps followed in the CELLine Bioreactor Characterisation procedure. **A(i)** CD81-Tdtomato, GFP-CD63 and WT parallel controls cultured in Bioreactor Flasks, could be isolated from three fractions depending on their adhesion characteristics: Adherent (retrieved after trypsinisation, pink), Semi-Adherent (retrieved after 3x media washes, yellow) and Suspension (retrieved from supernatant, green). **A(ii)** Recovered cells from the three fractions were pelleted after centrifugation (6min x 400g). **A(iii)** The supernatant of the Suspension fraction (EV-rich conditioned media) was further processed with serial centrifugation and filtration to remove dead cells and debris, and then stored at -80°C for EV isolation at a later time. **A(iv-v)** Cell pellets of the three fractions were counted, and a set number of Adherent fraction cells were re-seeded back to the Bioreactors (3.9×10^6 cells). **A(vi-viii)** 5×10^5 cells/ml of every fraction were labelled with either 3µM DRAQ7™ or 20µM DRAQ5™ to assess cell viability and cell cycle (respectively), as well as assess retention of fluorescence signal (GFP, Tdtomato) via flow cytometry. **B.** Timeline followed for Bioreactor Characterisation. **B(i)** Initial seeding density 25×10^6 cells for all cell lines, and at Weeks 4, 8 and 11 post-seeding **B(ii,iv)** the Characterisation procedure was performed as described in **(A)**. **B(iii)** In parallel to cell processing, the EV-rich conditioned media was collected in three Batches: Batch 1: Weeks 2-4, Batch 2: Weeks 6-8 and Batch 3: Weeks 10-11, according to the schematic in **A(iii)**. **B(iv)** Week 11 post-seeding was the endpoint of the experimental procedure with the Bioreactors discarded after characterisation.

5.3.2.2. Cell Viability in Bioreactor Flasks

Cell cycle and cell viability analysis were then performed to investigate why cells overexpressing CD63 or CD81 showed delays in cell growth. Thus, isolated cells from all fractions were labelled with DRAQ7 to assess cell viability via flow cytometry analysis (143, 144); gating strategy for these experiments is shown in [Supplementary Figure 14](#).

Overall, cell viability analysis demonstrated the Adherent cells were consistently the most viable (80-90% viability) for all cell lines, followed by the Semi-Adherent cells (30-60%) and finally the Suspension cells (10-40%) for Weeks 4 to 11 ([Figure 5.4.A](#)). This agreed with a previous study, where the authors cultured BHK (Baby Hamster Kidney) fibroblasts in the CELLLine Bioreactors and reported that the average viability of non-adherent cells was at 40-50% for 6 weeks of culture (215). The viability of Adherent cells marginally decreased at the end of the experimental timeline (lower by 5%), however, this might be attributed to handling, mechanical or trypsinisation stress ([Figure 5.4.A.i](#)). On the other hand, the viability of Semi-Adherent ([Figure 5.4.A.ii](#)) and Suspension cells ([Figure 5.4.A.iii](#)) significantly improved over time compared to Week 4 (increase of 30% cell viability for both fractions).

The potential effects of CD63 or CD81 overexpression on cell viability were assessed by comparing the percentages of viable cells between GFP-CD63 or CD81-Tdtomato cells to their WT Parallel controls ([Figure 5.4.B](#)). We observed no significant differences between the Adherent GFP-CD63 and GFP-Parallel controls in terms of cell viability, however, the Semi-Adherent and Suspension GFP-CD63 were less viable than the controls (~15% less viable for both fractions), as shown in [Figure 5.4.B.i](#). These results suggested that overexpression of CD63 does not have a negative effect on the viability of Adherent cells; however, it might have a negative effect on viability when cells are in the Semi-Adherent or Suspension state.

In contrast to the GFP-CD63 cells, no differences in cell viability were observed between the CD81-Tdtomato and Tom-Parallel cells distributed in any cell fraction ([Figure 5.4.B.ii](#)).

Collectively, our results demonstrated an overall improvement of cell viability over time, suggesting a potential adaptation of the cells of all fractions in the Bioreactor Microenvironment. In addition, these results complemented our previous observations on cell growth; at the first isolation (Week 4) limited growth was noted, which might be partly due to high cell morbidity, even though viability, and concomitantly growth, did improve over time.

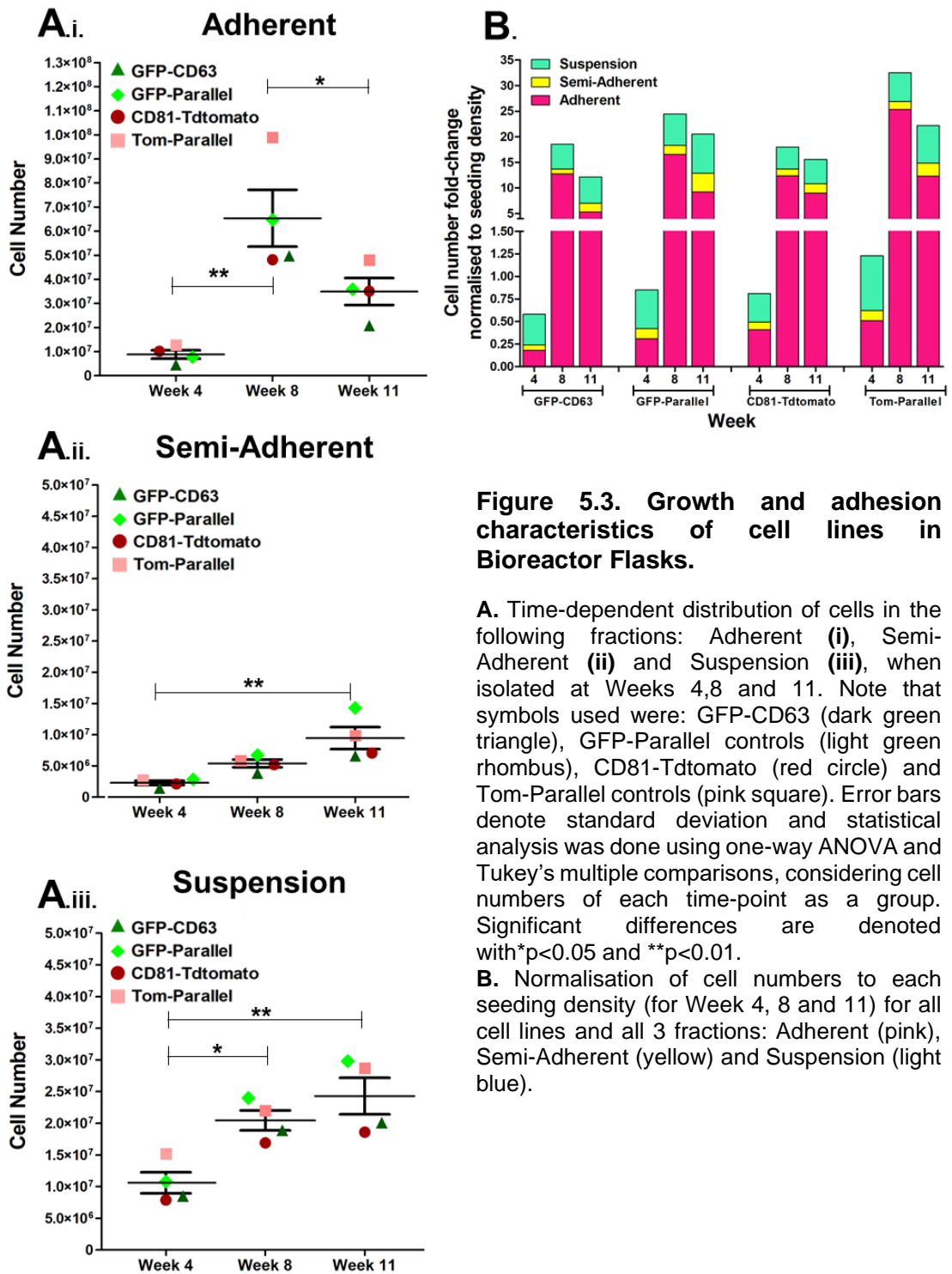


Figure 5.3. Growth and adhesion characteristics of cell lines in Bioreactor Flasks.

A. Time-dependent distribution of cells in the following fractions: Adherent (i), Semi-Adherent (ii) and Suspension (iii), when isolated at Weeks 4,8 and 11. Note that symbols used were: GFP-CD63 (dark green triangle), GFP-Parallel controls (light green rhombus), CD81-Tdtomato (red circle) and Tom-Parallel controls (pink square). Error bars denote standard deviation and statistical analysis was done using one-way ANOVA and Tukey's multiple comparisons, considering cell numbers of each time-point as a group. Significant differences are denoted with * $p < 0.05$ and ** $p < 0.01$.

B. Normalisation of cell numbers to each seeding density (for Week 4, 8 and 11) for all cell lines and all 3 fractions: Adherent (pink), Semi-Adherent (yellow) and Suspension (light blue).

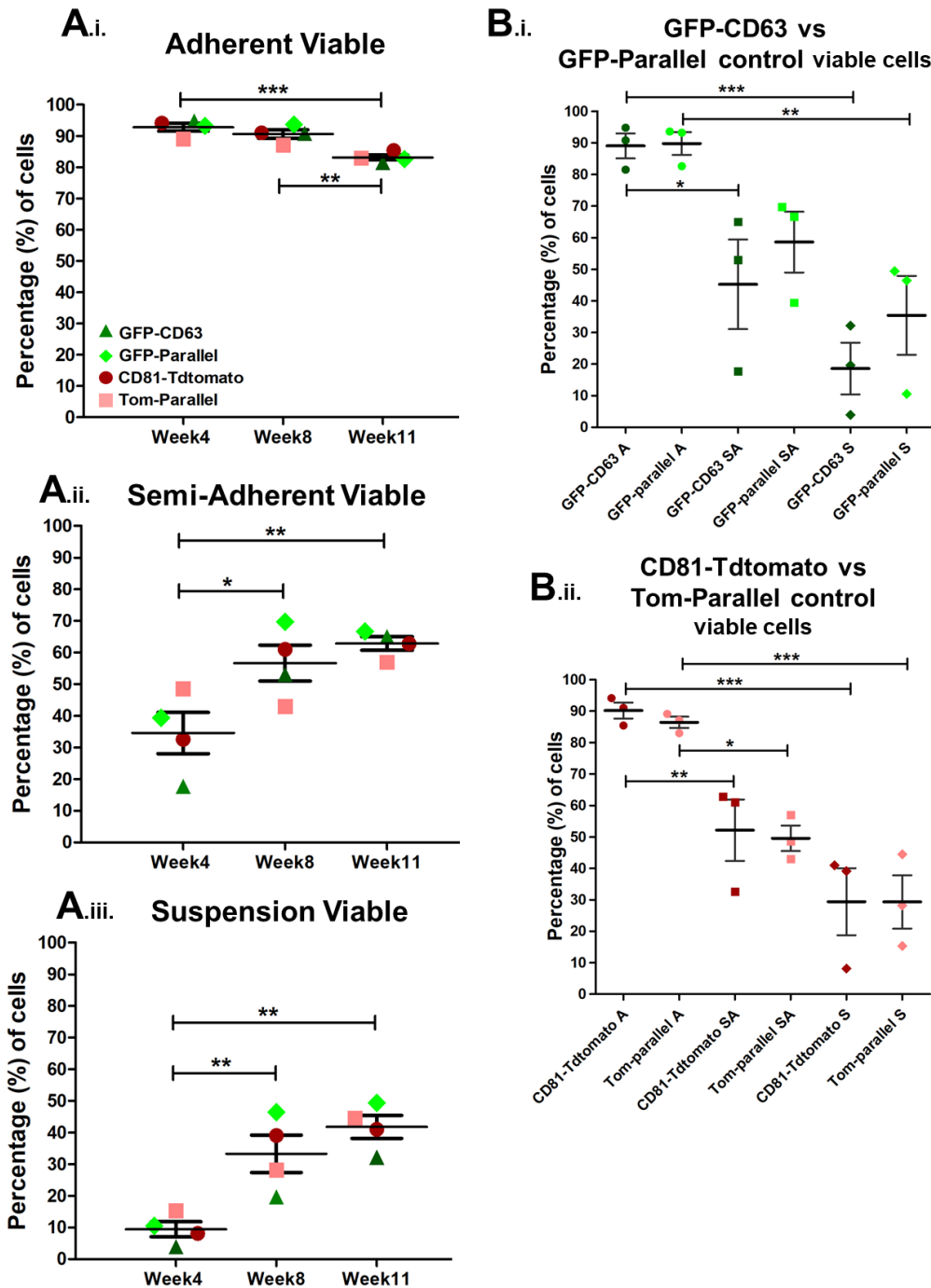


Figure 5.4. Viability of GFP-CD63 and CD81-Tdtomato compared to WT DU145 parallel cell lines in Bioreactor Flasks.

Quantification of DRAQ7 flow cytometry analysis depicting: **A.** The percentage of viable GFP-CD63, GFP-Parallel, CD81-Tdtomato and Tom-Parallel control cells distributed to each fraction, i.e., Adherent (**i**), Semi-Adherent (**ii**) and Suspension (**iii**) fractions for each timepoint. Error bars denote standard deviation and statistical analysis was done using one-way ANOVA and Tukey's multiple comparisons, considering percentage of cells at each timepoint as a single group. **B.** Comparisons of overexpressing cells i.e., (**i**) GFP-CD63 and (**ii**) CD81-Tdtomato, to respective WT Parallel controls showing the percentage of viable cells in each fraction (A=Adherent, SA= Semi-Adherent and S=Suspension). Error bars denote standard deviation and statistical analysis was done using one-way ANOVA and Tukey's multiple comparisons, considering percentage of cells at each fraction as a single group. Significant differences are denoted with * $p < 0.05$, ** $p < 0.01$ and *** $p < 0.0001$.

5.3.2.3. Cell Cycle in Bioreactor Flasks

In a previous chapter (Chapter 3), the cell cycle dynamics of overexpressing cell lines in two-dimensional culture were investigated and showed that the CD81-Tdtomato cells exhibited slower cell cycle progression compared to Tom-Parallel controls, whereas the GFP-CD63 cells had no significant differences to GFP-Parallel control cells. To assess whether this remained unchanged in the Bioreactors over time, cells from all fractions were labelled with DRAQ5 (129) and analysed via flow cytometry (gating strategy shown in [Supplementary Figure 15](#)). Cell cycle changes were assessed by determining the distribution of cells in G₁, S/G₂/M and polyploid cell phase (>2n) over time ([Figure 5.5](#)).

Overall, we observed a significant increase in cycling cells (S/G₂/M phase) for all cell lines over time, notably ~10% increase in GFP-CD63 and GFP-Parallel controls, ~5% in CD81-Tdtomato and ~18% in Tom-Parallel controls ([Figure 5.5.A,B.ii](#)). A decrease in G₁ phase cells was also observed ([Figure 5.5.A,B.i](#)). No notable differences in the population of polyploid cells were observed (>2n cell cycle phase) over time ([Figure 5.5.A.iii](#)), except for Tom-Parallel controls (increase by ~4%) ([Figure 5.5.B.iii](#)).

Next, to determine whether overexpression of CD63 and CD81 altered cell cycle dynamics, we compared the distribution of cells in each cell cycle phase between GFP-CD63, CD81-Tdtomato and their respective controls. Agreeing with our results from Chapter 3, GFP-CD63 and GFP-Parallel cells exhibited similar cell cycle dynamics in the Bioreactor Flasks ([Figure 5.5.A](#)). Conversely, CD81-Tdtomato cells had slower cell cycle progression compared to Tom-Parallel controls, as ~15-20% of CD81-Tdtomato cells were in S/G₂/M phase vs ~15-37% of controls ([Figure 5.5.B.ii](#)). Furthermore, a significantly higher percentage of control cells had progressed to polyploidy (>2n) by Week 11, compared to CD81-Tdtomato cells, as mentioned above ([Figure 5.5.B.iii](#)).

To summarize, in conjunction with previous observations showing increased cell viability and cell growth over time in the Bioreactor Flasks, an increase in cycling cells was also observed (S/G₂/M phase). However, overexpression of CD81 (but not CD63) lead to slower cell cycle progression. The combination of low cell viability, slower cell cycle progression and high numbers of non-adherent cells, might be the result of contact inhibition, perhaps due to the high initial seeding density. A potential caveat of the CELLLine Bioreactors would be cells undergoing contact inhibition due to their high-density growth, which could ultimately induce phenotypical changes to cells and alter secreted sEVs (217). This might explain why seeding a lower number of cells in the Bioreactors resulted in a significant increase in cell growth, as well as improvement in adhesion, cell viability and cell cycle of DU145 cells for the rest of the experimental timeline.

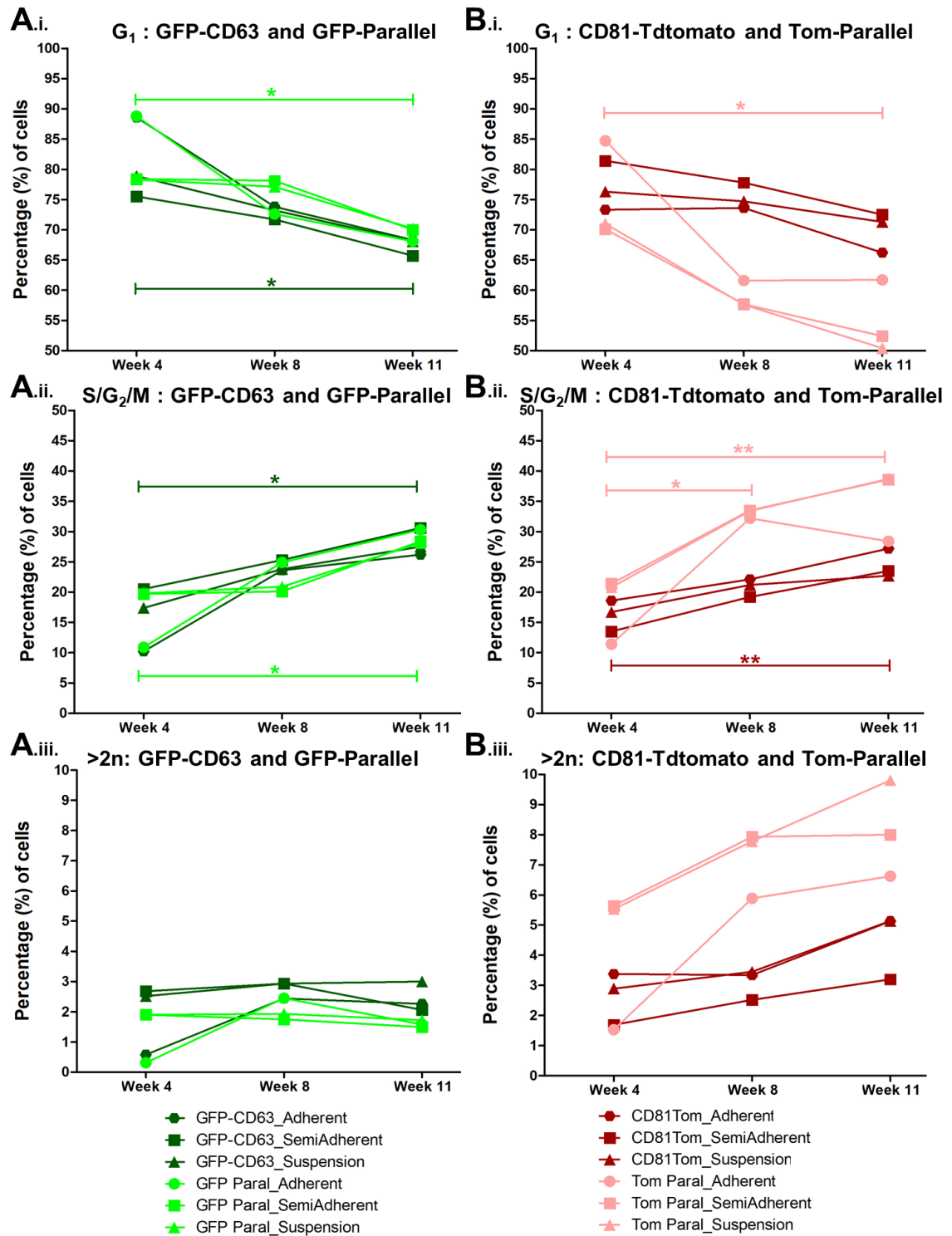


Figure 5.5. Distribution of cells of all fractions in G₁, S/G₂/M and polyloid cell phase over time.

A. Percentage of GFP-CD63 and GFP-Parallel controls in (i) G₁, (ii) S/G₂/M, and (iii) polyplody (>2n) over time (Weeks 4 to 11) for all fractions. **B.** Percentage of CD81-Tdtomato and Tom-Parallel controls in (i) G₁, (ii) S/G₂/M, and (iii) polyplody (>2n) over time (Weeks 4 to 11) for all fractions. Statistical analysis was done using one-way ANOVA and Tukey's multiple comparisons, considering percentage of cells at same time-point as a group. Significant differences are denoted with *p<0.05 and ***p<0.01.

5.3.2.4. Fluorescence Signal Stability in Bioreactor Flasks

Next, it was essential to determine potential changes in the fluorescent signal of the overexpressing cell lines GFP-CD63 and CD81-Tdtomato in the Bioreactor microenvironment over time. This was important to investigate, as the fluorescence of GFP-CD63 and CD81-Tdtomato cells cultured in the Bioreactors, would likely impact the fluorescence of secreted sEVs. To address this issue, the fluorescence signal distributions of GFP-CD63 and CD81-Tdtomato cells were compared with the control cells over time (for all cell fractions) via flow cytometry analysis where measurements were of the viable population only (see [Supplementary Figure 14](#) for gating).

The variance between fluorescence distributions of the samples was compared using the FlowJo™ Chi Squared distribution comparison statistical test (130, 150, 151). This test firstly involved calculation of the baseline variance within the control samples (Chi square value in SD). Specifically, the GFP-Parallel and Tom-Parallel control fluorescence distribution overlays depicted the autofluorescence background of the viable cells in the Bioreactors, and were used to calculate the baseline variance ([Figure 5.6-7.C.ii](#)). This baseline variance was then compared to the Chi Square values of the GFP-CD63 and CD81-Tdtomato fluorescence distributions. Ultimately, the variance between distributions was considered statistically significant when the Chi Square values of the GFP-CD63 or CD81-Tdtomato were higher than the control samples (baseline).

To begin with, our analysis demonstrated that the Adherent GFP-CD63 cells progressively lost their fluorescence signal, with a highly significant shift in their fluorescence distribution of more than 500 Standard Deviations (>500 SD) from Weeks 4 to 11 ([Figure 5.6.A.i,Ci](#)). On the other hand, the Semi-Adherent and Suspension GFP-CD63 cells lost their fluorescence as early as Week 8 ([Figure 5.6.A.ii-iii,Ci](#)).

Conversely, the CD81-Tdtomato Adherent cells retained their fluorescence over this time period, with no statistically significant differences between the fluorescent distributions from Weeks 4 to 11 ([Figure 5.7.A.i](#)). The calculated variance between the CD81-Tdtomato fluorescence distributions was ~30 SD (Weeks 4 to 11), which was lower than the baseline variance of ~70 SD of Tom-Parallel controls, thus it is not considered statistically significant ([Figure 5.7.C.i](#)). The Semi-Adherent and Suspension CD81-Tdtomato cells exhibited an initial decrease of mean fluorescence intensity at Week 8; however, by Week 11 the fluorescence was stabilised ([Figure 5.7.A.ii-iii,Ci](#)). Of note, the GFP-Parallel and Tom-Parallel control auto-fluorescence distributions appeared to differ over time, for example a higher autofluorescence of GFP-Parallel controls was observed in all cell fractions at Week 4 ([Figure 5.6.B](#)), whereas Adherent

Tom-Parallel showed higher autofluorescence at Week 8 ([Figure 5.7.B](#)); this might be attributed to fluctuations in the flow cytometer instrument settings or due to cell handling.

Overall, these results suggested that overexpression of GFP-CD63 in DU145 cells could not be sustained in the Bioreactor Flasks, as the GFP fluorescence diminished to background levels by Week 11. Interestingly, isolation of Adherent GFP-CD63 cells at Week 11 from the Bioreactor Flask and re-seeding in conventional 2D flasks enabled the restoration of GFP fluorescence after 24h (data not shown). This suggested that loss of fluorescence was not due to loss of the GFP-CD63 insert, but rather due to quenching of the GFP fluorophore in the Bioreactor. The nature of this is unknown but could be related to some regions of hypoxia in the high-density bioreactor. This agrees with previous studies showing restoration of GFP fluorescence in varied systems after 4–10h of reoxygenation (218, 219). Fortunately, however, the Tdtomato fluorescence was maintained over time in the CD81-Tdtomato cells from all three fractions, indicating that the Bioreactor system is not detrimental to fluorescently functional expression of Tdtomato in these cells.

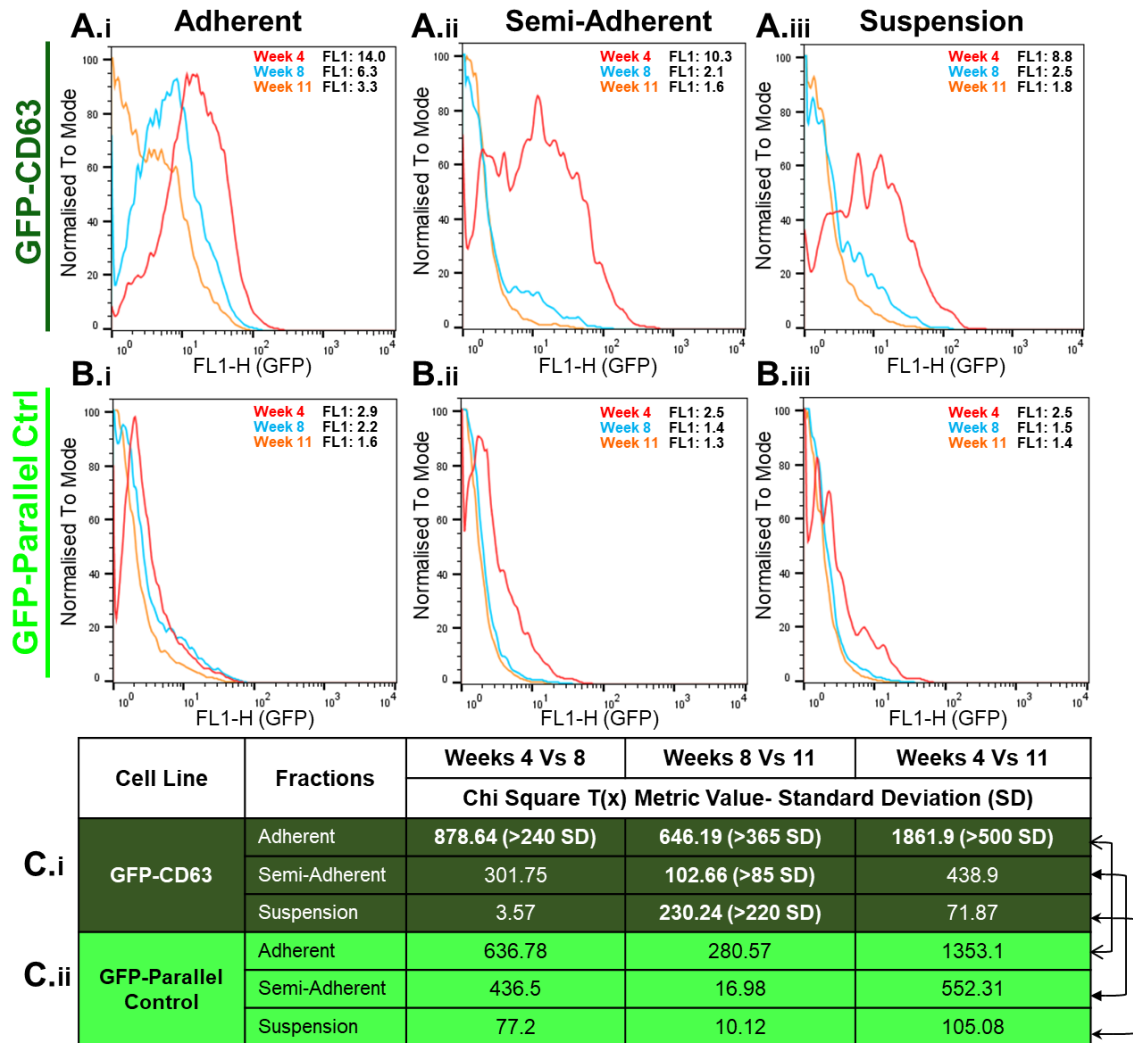
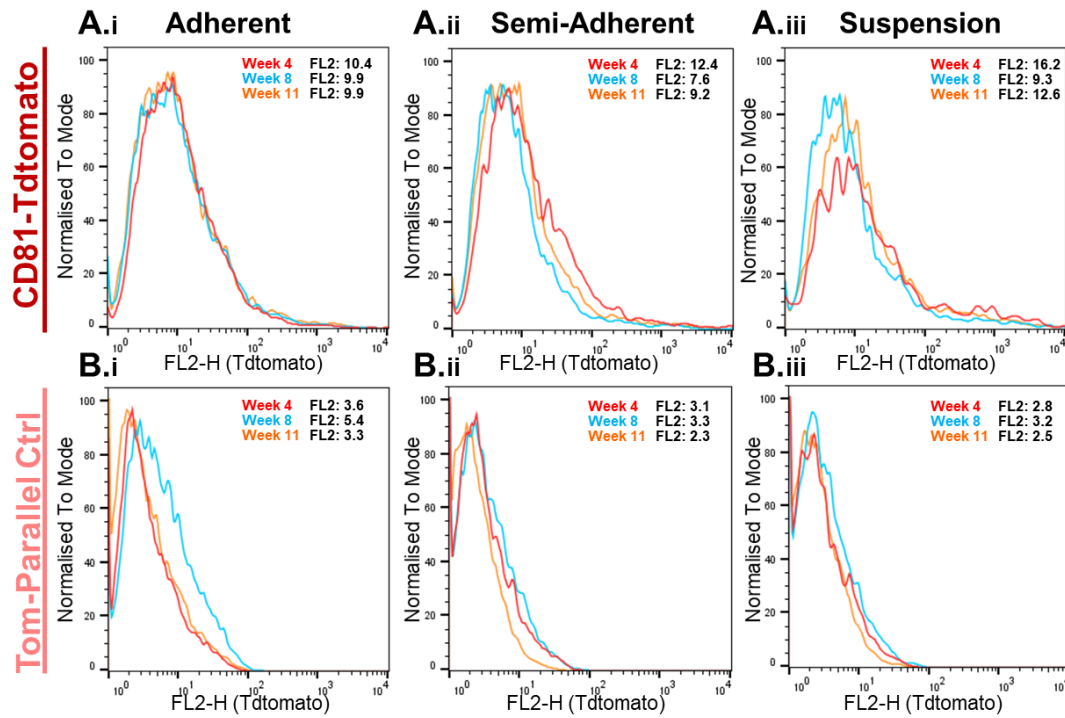


Figure 5.6. Fluorescence signal stability of GFP-CD63 cells in Bioreactor Flasks.

A. GFP-CD63 and **B.** GFP-Parallel histograms representing GFP (FL1) fluorescence distribution overlays of **(i)** Adherent, **(ii)** Semi-Adherent and **(iii)** Suspension viable cells at Week 4 (red), Week 8 (blue) and Week 11 (orange). The geometric mean GFP fluorescence intensity (FL1) of each time-point is noted in the top right corner of histogram overlays. **C.** FlowJo™ Chi Square statistical analysis showing variance of fluorescence between Weeks 4-11 for each cell fraction separately. The analysis was conducted by double comparisons of time-points, i.e., comparisons of Week 4 Vs 8, Week 4 Vs 11 and Week 8 Vs 11, for **(i)** GFP-CD63 and **(ii)** GFP-Parallel cells. The result of each comparison is the calculated Chi Square value, converted into a T(x) metric value which represents the variance between populations in Standard Deviations (SD). The baseline variance of autofluorescence signal is represented by the T(x) values of GFP-Parallel cells**(ii)**. The arrows demonstrate the further comparison of the baseline T(x) values to the fluorescence signal T(x) values (i.e., comparison of GFP-Parallel Vs GFP-CD63 Adherent cells) with variance denoted as statistically significant (bold font) when the latter value is larger than the former. Note that the variance of fluorescence signal above the baseline (in SD) is shown in brackets.



Cell Line	Fractions	Weeks 4 Vs 8	Weeks 8 Vs 11	Weeks 4 Vs 11
		Chi Square T(x) Metric Value- Standard Deviation (SD)		
C.i CD81-TdTomato	Adherent	29.08	0	33.13
	Semi-Adherent	57.54 (>52 SD)	24.28	18.46
	Suspension	8.7 (>8 SD)	34.62 (>7 SD)	0
C.ii Tom-Parallel Control	Adherent	223.72	359.65	69.24
	Semi-Adherent	5.38	107.47	97.84
	Suspension	0	27.25	0.72

Figure 5.7. Fluorescence signal stability of CD81-Tdtomato cells in Bioreactor Flasks.

A. CD81-Tdtomato and **B.** Tom-Parallel histograms representing Tdtomato (FL2) fluorescence distribution overlays of (i) Adherent, (ii) Semi-Adherent and (iii) Suspension viable cells at Week 4 (red), Week 8 (blue) and Week 11 (orange). The geometric mean Tdtomato fluorescence intensity (FL2) of each time-point is noted in the top right corner of histogram overlays. **C.** FlowJo™ Chi Square statistical analysis showing variance of fluorescence between Weeks 4-11 for each cell fraction separately. The analysis was conducted by double comparisons of time-points, i.e., comparisons of Week 4 Vs 8, Week 4 Vs 11 and Week 8 Vs 11, for (i) CD81-Tdtomato and (ii) Tom-Parallel cells. The result of each comparison is the calculated Chi Square value, converted into a T(x) metric value which represents the variance between populations in Standard Deviations (SD). The baseline variance of autofluorescence signal is represented by the T(x) values of Tom-Parallel cells(ii). The arrows demonstrate the further comparison of the baseline T(x) values to the fluorescence signal T(x) values (i.e., comparison of Tom-Parallel Vs CD81-Tdtomato Adherent cells) with variance denoted as statistically significant (bold font) when the latter value is larger than the former. Note that the variance of fluorescence signal above the baseline (in SD) is shown in brackets.

5.3.3. Phenotypic Characteristics of Bioreactor-derived sEVs

Recent studies have utilised the CELLLine Bioreactor Flasks to culture various cell lines and generate sEVs; however, no study to date has used them to culture cell lines overexpressing tetraspanins (CD63 and CD81) conjugated with fluorescent proteins for the purpose of fluorescent sEV isolation (115, 157, 211-214). Based on our previous results demonstrating time-dependent differences in cell viability, cell cycle and fluorescence between the cell lines overexpressing CD63 and CD81 and their WT Parallel counterparts, it was essential to investigate any potential phenotypic changes occurring at the EV level.

Thus, the second part of this chapter focuses on characterisation of EVs isolated from all 4 cell lines cultured in the Bioreactor Flasks, and determination of potential effects of overexpression of CD63 and CD81 on the phenotype of EVs over time. Based on the Bioreactor Characterisation Procedure ([Figure 5.2](#)), the EV-rich conditioned media was isolated every week and batched together (EV Batch 1: Weeks 2-4, Batch 2: Weeks 6-8, Batch 3: Weeks 10-11), so that EVs were isolated at the end of the experimental timeline via the 30% sucrose/D₂O cushion ultracentrifugation method, which results in high purity preparations by isolating small EVs (sEVs $\leq 200\text{nm}$) at a certain density (1.2g/ml) and eliminating the majority of non-vesicular constituents (6, 157). Characterisation of the isolated sEVs included determination of size, expression of sEV-associated markers, fluorescent signal analysis, as well as morphological analysis via Cryogenic Transmission Electron Microscopy (Cryo-TEM).

Of note, the protein and particle concentrations of isolated sEVs were determined using the BCA assay and Nanoparticle Tracking Analysis (NTA), respectively. [Table 2.2](#) shows the protein and particle concentrations for all sEV isolations in detail, for each Batch and every Bioreactor Flask (Bioreactors 1-4, isolations #4-6). Also, [Supplementary Figure 16](#) shows a comparison of sEV protein yield and particle numbers to cells isolated from the Bioreactors. Specifically, the sEV protein yield and particle output were normalised compared to the Adherent and non-Adherent cells (Semi-Adherent and Suspension) isolated from the Bioreactors. We observed that the low numbers of cells at the first isolation (Week 4) were reflected by a low production of sEVs (low protein and particle yield, Week 4). On the other hand, by Weeks 8 and 11 the increased cell growth resulted in concomitant increase of sEV particle numbers and protein yield ([Supplementary Figure 16](#)), as one might anticipate.

5.3.3.1. sEV Cargo Characterisation

Western Blot analysis for sEV-associated markers

Prior to any other characterisation, we conducted Western Blot analysis to determine the purity of our sEV preparations compared to corresponding cell lysates. To preserve sEV sample, minimise the complexity of the experiment, as well as avoid batch-to-batch variability between sEVs, we pooled all EV Batches together at a volume ratio of 1:1:1 (Batch 1: Batch 2: Batch 3). Hence, we generated pooled samples for each sEV type, namely GFP-CD63, CD81-Tdtomato, GFP-Parallel and Tom-Parallel sEVs (Batches 1-3, Weeks 2-11); see [Table 2.2](#) (Batch 1-3 pooled samples) for sEV protein concentration of each of these 4 pooled samples. The compromise of batching sEVs here however, is that information concerning time-dependent changes in sEVs will not be made apparent.

Western Blot analysis (of 10µg protein for sEV and cell lysates) demonstrated the presence of typical endo-lysosomal-associated markers like the ESCRT complex-associated proteins Alix and TSG101, whereas these appeared at relatively very low levels (barely detectable) in corresponding cell lysates. Moreover, we observed the presence of the cell-associated marker GRP94 (endoplasmic reticulum protein) in cell lysates, but it was not readily detectable within the sEV samples. This is a strong indication that the sEV-isolates were not contaminated by cellular contents which are not usually associated with sEVs. GAPDH was also included in the panel, as it is a very reliable antibody that detects a protein that is always found in both sEV and cell lysates, and thus serves as a positive control for the Western Blot transfer, labelling and detection method ([Figure 5.8.A](#)).

Furthermore, expression of the highly sEV-associated tetraspanins CD63 and CD81, was highly enriched in sEVs, and these bands were relatively poor in cell lysates ([Figure 5.8.B,C](#)). Staining for CD63 appeared as a smear or a series of bands, as opposed to a single clear-cut band of a defined molecular weight. This can be due to the extensive glycosylation of CD63 but may also be due to solubility issues of sEVs boiled in the absence of reducing agent. Although difficult to clearly see differences in the CD63 smear, we observed a potential difference in the molecular weight of the major dark zone of the smear for CD63 between GFP-CD63 sEVs and the other EV types. GFP-CD63 sEVs show a higher molecular weight here which is potentially indicative of a combination of CD63 and the fused GFP-CD63 protein expression ([Figure 5.8.B](#)).

Similarly, we observed differential expression of CD81 in CD81-Tdtomato sEVs compared to the other EV types. Besides the endogenous ~20kDa CD81 protein, we detected an array of higher molecular weight bands, which might reflect various CD81-

Tdtomato isoforms; Tdtomato is a tandem dimer and is prone to clustering which might explain these numerous detected bands (220) ([Figure 5.8.C](#)). Furthermore, tetraspanins themselves tend to dimerize/ homo-dimerize so the multiple detected bands might be attributed to the various combinations of endogenous- exogenous CD81 dimers.

Overall Western Blot analysis demonstrated the enrichment of tetraspanins and endo-lysosomal constituents in sEV isolates, and the paucity of cell contents. The data also showed differential expression of CD63 or CD81 on GFP-CD63 and CD81-Tdtomato sEVs, respectively, compared to WT Parallel controls, albeit the CD63 smear remains difficult to fully interpret.

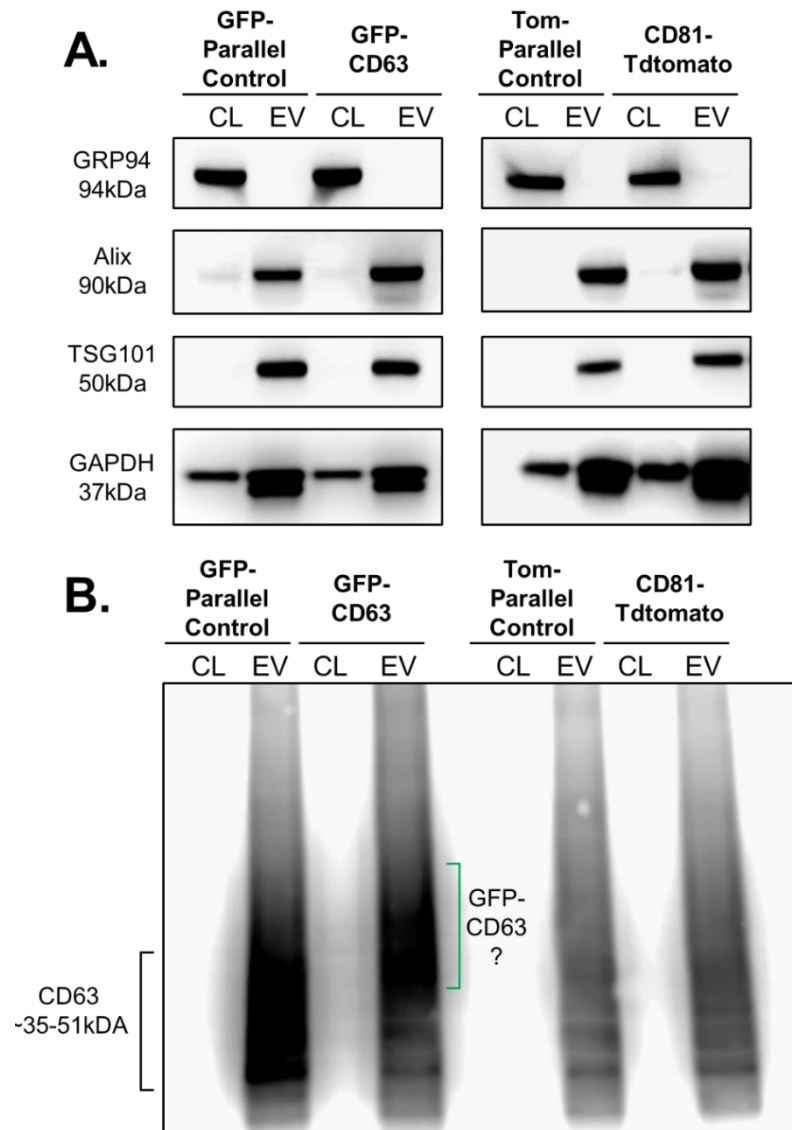
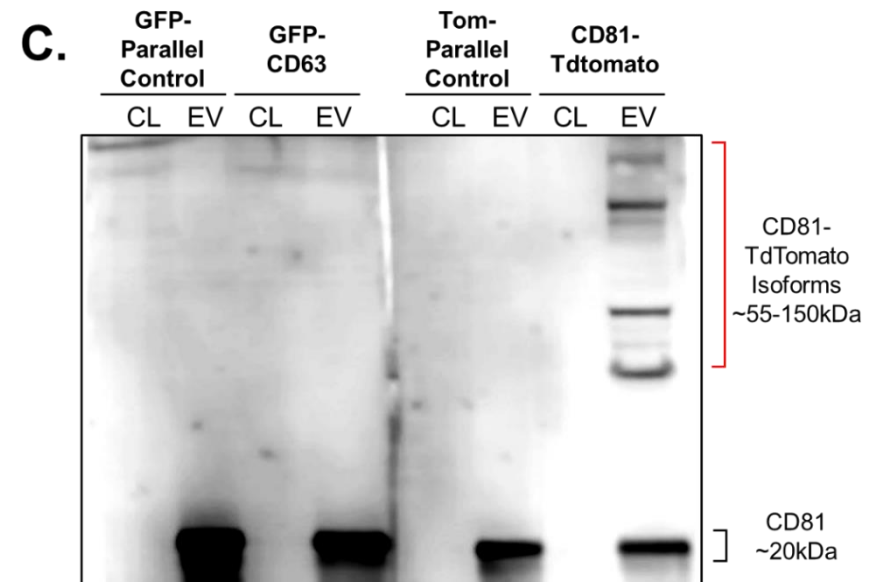


Figure 5.8. Western blot characterisation of Bioreactor-derived sEVs vs corresponding DU145 cells.

Western Blots of GFP-Parallel, GFP-CD63, Tom-Parallel and CD81-TdTomato sEV lysates (Batches 1-3, Weeks 2-11 mix) and corresponding cell lysates (EV and CL, respectively). **A.** Blot for expression of sEV-associated markers Alix and TSG101 and cell-associated endoplasmic reticulum marker GRP94. **B.** Blot for expression of tetraspanin CD63, with indications for potential presence of GFP-CD63 in corresponding sEVs. **C.** Blot for expression of tetraspanin CD81, with indications for presence of CD81-TdTomato isoforms in corresponding sEVs.

Note that 10µg of protein of sEV lysate (EV) or cell lysate (CL) were loaded into parallel lanes followed by SDS-PAGE and Western blotting with primary antibodies as indicated above. GAPDH was used as a loading control.



Immuno-phenotyping assay for sEV-associated markers

Next, to quantify whether overexpression of CD63 and CD81 had any effect on sEV cargo over time in the Bioreactors, the Immuno-Phenotyping ELISA-like assay was performed to determine the levels of various proteins on the surface of sEVs over time (Weeks 2-4, 6-8 and 10-11). For this, sEVs were labelled for the tetraspanins CD9, CD63 and CD81, as well as the sEV-associated MHC Class I receptor (MHC-1).

This analysis showed that all types of Bioreactor-derived sEVs carried CD9, CD63, CD81, and MHC-1, with the highest signal seen for CD9, followed by CD81 and then CD63, whereas MHC-1 was quite variable between EV types ([Figure 5.9-10](#)). These results reflected our previous observations for the levels of sEV-associated markers on sEVs isolated from 2D tissue-culture flasks (Chapter 3). Of note, the relevant isotype controls used (IgG1, IgG2a, IgG2b) demonstrated the low background for the Immuno-Phenotyping ELISA-like assay (more than 100-fold lower) and showed no significant differences between EV types or batches ([Figure 5.9.E-G](#) and [Figure 5.10](#)).

Focusing on each sEV-associated marker separately, we observed that overexpression of CD63 or CD81 had no initial differences on CD9 loading to sEVs (Batch 1, Weeks 2-4), even though by the last Batch (Weeks 10-11) the levels of CD9 decreased slightly compared to their respective parallel control sEVs ([Figure 5.9.A](#)). This was unexpected as we have previously shown (Chapter 3) that overexpression of CD63 (but not CD81) resulted to an increase of CD9 levels in 2D tissue-culture derived sEVs.

Furthermore, we observed as expected, that GFP-CD63 sEVs exhibited higher levels of CD63 compared to respective control sEVs (~1.3 fold-higher), similar to levels in GFP-CD63 sEVs isolated from 2D tissue-culture flasks ([Figure 5.9.B](#)). Conversely, CD81-Tdtomato sEVs exhibited lower CD63 levels than Tom-Parallel controls (especially by Week 11), which differed from previous observations of 2D-derived sEVs, where overexpression of CD81 did not affect the levels of CD63 (Chapter 3) ([Figure 5.9.B](#)).

Interestingly, we observed the opposite for the levels of CD81 on the sEV membrane, with GFP-CD63 sEVs exhibiting lower levels of CD81 compared to GFP-Parallel controls (statistically significant for Weeks 6-11), whereas CD81-Tdtomato sEVs had consistently higher levels of CD81 compared to Tom-Parallel controls (statistically significant for Weeks 2-11) as shown in [Figure 5.9.C](#). These observations differed from our observations from 2D-derived sEVs, which had shown that GFP-CD63 sEVs had higher levels of CD81, and CD81-Tdtomato sEVs had no apparent increase in CD81, thus suggesting a potential shift in the secretion of sEV sub-populations in the 3D-like

Bioreactor microenvironment and a negative relationship between CD81 overexpression and CD63- loading of sEVs and vice versa.

Further supporting this hypothesis, our results demonstrated that Bioreactor-derived CD81-Tdtomato sEVs exhibited consistently lower levels of MHC-1 compared to Tom-Parallel controls (highly statistically significant for Weeks 2-11), suggesting a negative relationship between CD81 overexpression and MHC class-I loading of sEVs. On the other hand, GFP-CD63 sEVs exhibited higher levels of MHC-1 from Weeks 2-8 compared to the respective control sEVs ([Figure 5.9.D](#)), indicating different roles for these tetraspanins in regulating sEV-loading.

Beyond the different repertoire of sEV-associated proteins between GFP-CD63 and CD81-Tdtomato sEV populations, we also observed a time-dependent decrease of the levels of tetraspanins (CD9, CD63 and CD81) in all EV types in the Bioreactors ([Figure 5.10](#)). On the other hand, the levels of MHC-1 increased over time for GFP-Parallel, CD81-Tdtomato and Tom-Parallel control sEVs ([Figure 5.10.B-D](#)), whereas for GFP-CD63 sEVs remained stable over ([Figure 5.10.A](#)). These results were surprising, and the reason behind these time-dependent changes in the Bioreactors is currently unknown, for example this might suggest an increase of secretion of other vesicular populations (e.g., larger EVs) with lower tetraspanin and higher MHC-1 levels or can even suggest the presence of artefacts from the aging Bioreactors (e.g., increased release of protein aggregates interfering with the assay).

Overall, the Immuno-Phenotyping ELISA-like assay demonstrated changes in the composition of sEVs derived from the Bioreactors, as overexpression of CD81 or CD63 lead to differential alterations in the levels of tetraspanins and MHC-1. Furthermore, it revealed a time-dependent change on the levels of these sEV-associated proteins, even though further investigation is necessary to validate this.

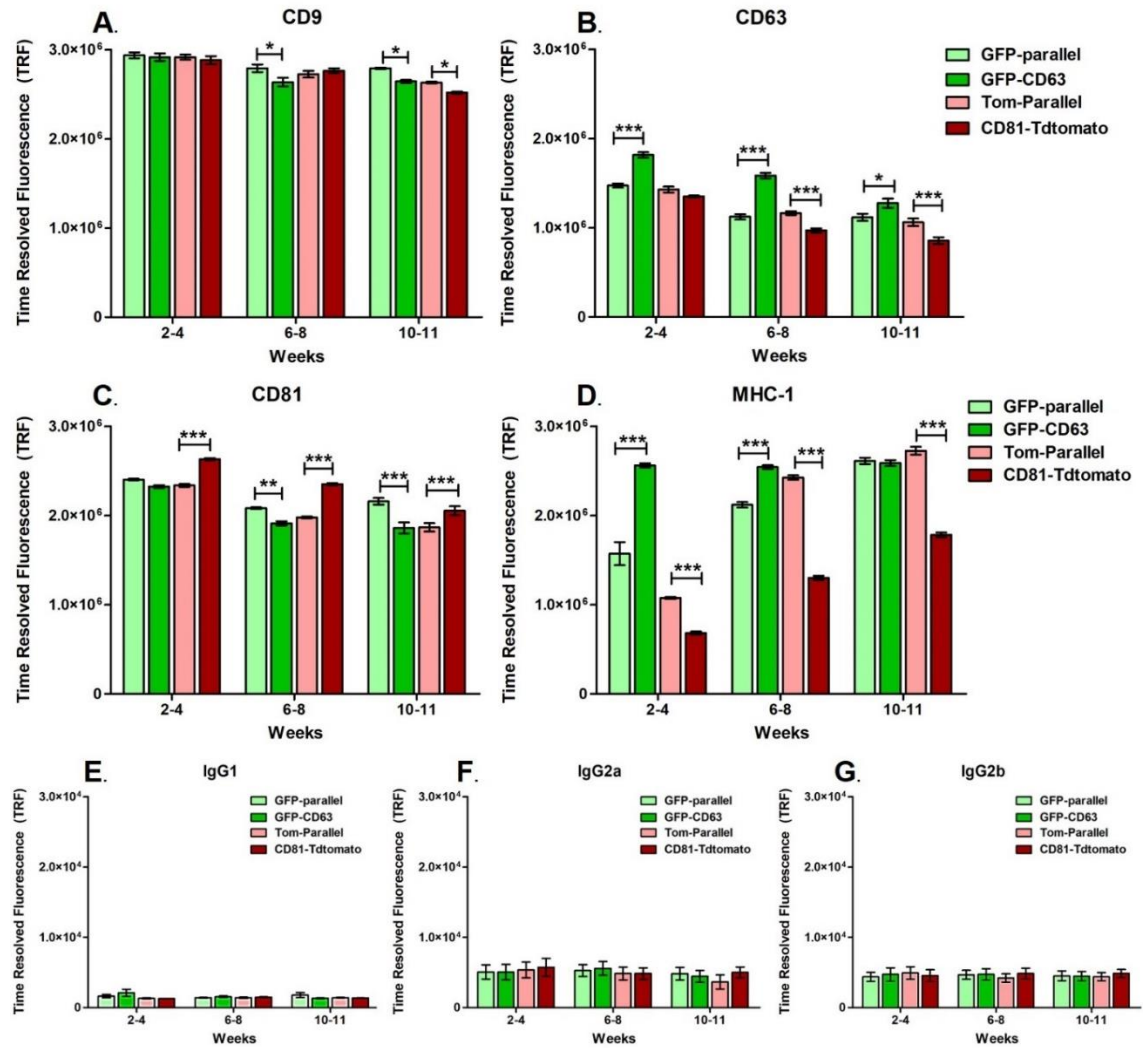


Figure 5.9. Effects of CD63 or CD81 overexpression on Bioreactor-derived sEV cargo.

Bar graphs depict time-dependent batch comparisons of GFP-CD63 vs GFP-Parallel sEVs, as well as CD81-Tdtomato vs Tom-Parallel sEVs regarding sEV cargo proteins : **(A)** CD9, **(B)** CD63, **(C)** CD81 and **(D)** MHC Class I receptor (MHC-1). The relevant isotype controls were also used to determine the assay background; **(E)** IgG1: isotype control for CD63 and CD81, **(F)** IgG2a: isotype control for MHC-1 and **(G)** IgG2b: isotype control for CD9 . This experiment was conducted twice (N=2) with three technical replicates per experiment; error bars denote standard error and statistical analysis was done using two-way ANOVA with Bonferroni post-test multiple comparisons. Only significant differences are denoted in the graphs with * $p < 0.05$, ** $p < 0.01$ and *** $p < 0.0001$. Note: GFP-Parallel (light green), GFP-CD63 (dark green), Tom-Parallel (pink) and CD81-Tdtomato (red).

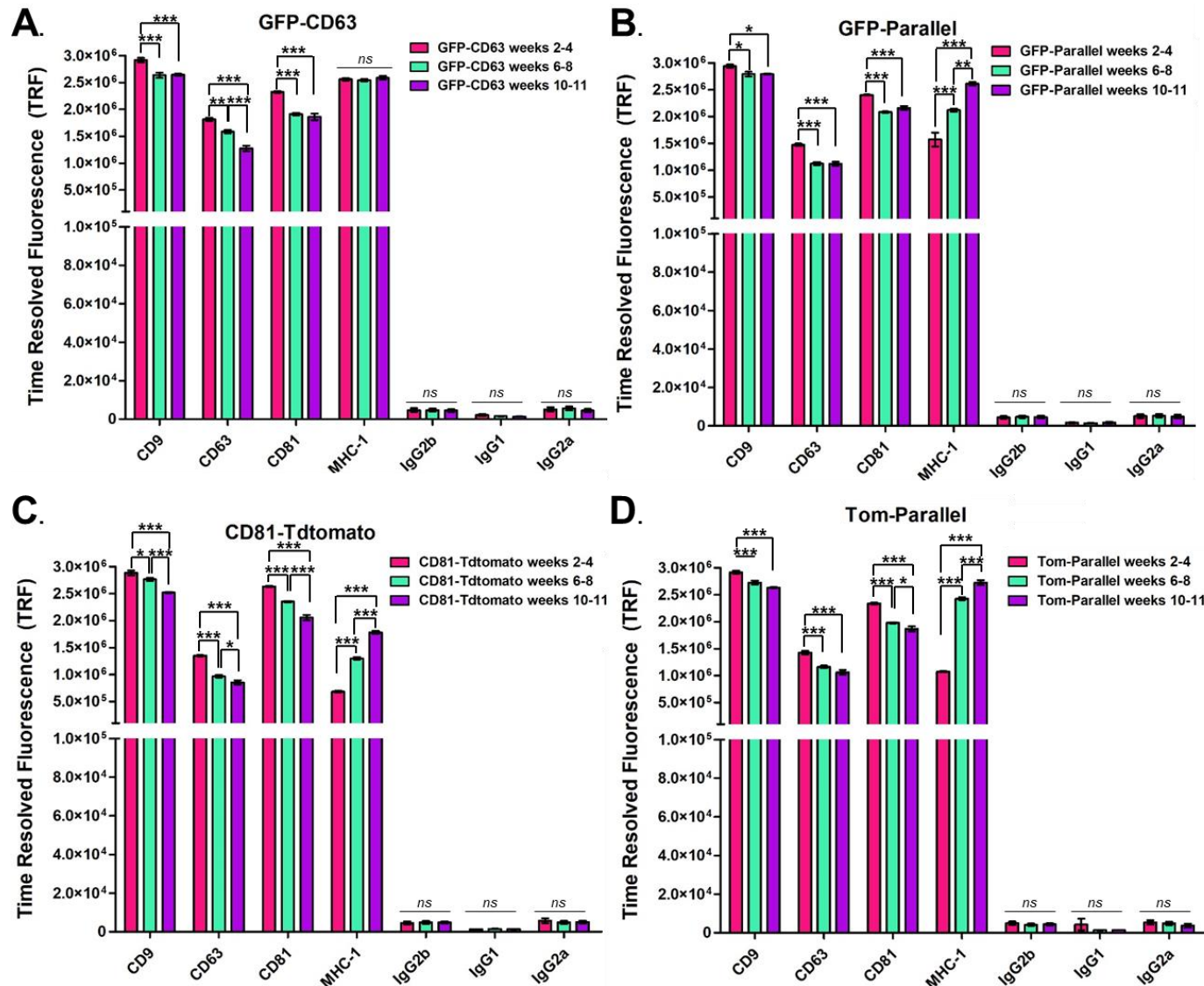


Figure 5.10. Time-dependent effects of Bioreactors on sEV-associated protein markers.

Bar graphs depict the levels of tetraspanins (CD9, CD63, CD81) and MHC Class I receptor (MHC-1) on the membrane of GFP-CD63 (A), GFP-Parallel (B), CD81-Tdtomato (C) and Tom-Parallel (D) sEVs isolated from Bioreactor flasks at Weeks 2-4 (pink), Weeks 6-8 (light green) and Weeks 10-11 (purple). The relevant isotype controls (IgG2b, IgG1 and IgG2a) are used to determine the assay background; IgG2b: control for CD9, IgG1: control for CD63 and CD81, IgG2a: control for MHC-1.

This experiment was conducted twice (N=2) with three technical replicates per experiment; error bars denote standard error and statistical analysis was done using two-way ANOVA with Bonferroni post-test multiple comparisons. Only significant differences are denoted in the graphs with *p<0.05, ***p<0.01 and ****p<0.0001, while non-significant differences are denoted with n.s.

Evaluation of Fluorescence Signal of sEVs

Previous results showed that GFP-CD63 cells progressively lost GFP fluorescence in the Bioreactor Flasks ([Figure 5.6](#)), whereas the fluorescence of CD81-Tdtomato cells remained stable over time ([Figure 5.7](#)). Hence, we aimed to determine if this would be reflected in the isolated sEVs from the Bioreactor, especially since sEVs will be eventually utilised in imaging studies as fluorescent sEV-reporters.

To address this, we analysed sEVs using Nanoscale Flow Cytometry, via the Apogee A50 Microparticle Flow Cytometry System and utilised CD81-Tdtomato, Tom-Parallel control, GFP-CD63 and GFP-Parallel control sEVs isolated from each of the three timepoints i.e., Batch 1 (Weeks 2-4), Batch 2 (Weeks 6-8) and Batch 3 (Weeks 10-11). Furthermore, polystyrene (PS) microspheres with size relevant to sEVs (100 and 200nm) were also used as reference beads. The gating strategy for this experiment is shown in [Supplementary Figure 17](#) and involved: (i) the calibration of the instrument with a mixture of PS and silica fluorescent and non-fluorescent beads, supplied by the manufacturer (Apogee Beads #1493), (ii) gating of sEVs and reference beads for selection of “single events” and (iii) gating based on Tom-Parallel and GFP-Parallel control sEVs to determine positive fluorescence threshold for CD81-Tdtomato and GFP-CD63 sEVs, respectively. Of note, a serial dilution experiment was also done prior to this experiment, which determined the optimal sEV concentration to avoid detection coincidence and swarm effects ([Supplementary Figure 18](#)).

To begin with, fluorescence analysis was conducted on CD81-Tdtomato compared to Tom-Parallel control sEVs ([Figure 5.11](#)), as well as GFP-CD63 compared to GFP-Parallel control sEVs ([Figure 5.12](#)) for each EV Batch. Furthermore, the PS microspheres were also used as reference beads, both for settings optimisation and qualitative comparison of fluorescence signal. These beads were either the non-fluorescent 100 nm NIST and 200nm NTA (shown in [Figures 5.11-12.D.i](#)) or the fluorescent Tetraspeck™ 100nm or 200 nm (shown in [Figures 5.11-12.D.ii](#)). The Tetraspeck™ microspheres can emit blue, green, orange or dark red fluorescence (depending on their excitation) and were used to compare both to GFP and Tdtomato fluorescence (green and orange respectively); these microspheres were also previously compared to sEVs in Chapter 3 for PSF and fluorescence intensity analysis, so their fluorescent properties are well established.

Our results showed that the CD81-Tdtomato sEV population had detectable orange fluorescence, which seemed to slightly increase over time from Batch 1 to Batch 3 (~7% to ~9% of total events, and gMFI increase from 2815.3 to 3453.3) ([Figure 5.11.A-C.ii](#)).

Furthermore, we observed that the detectable fluorescence of CD81-Tdtomato sEVs in all Batches (TOM+ population), had higher mean fluorescence intensity than the 100nm Tetraspeck™ microspheres (gMFI=2489); this was similarly observed previously when imaging 2D tissue-culture- derived CD81-Tdtomato sEVs and Tetraspeck™ microspheres via confocal fluorescence microscopy (Chapter 3). On the other hand, the CD81-Tdtomato sEV mean fluorescence intensity (gMFI= 2815.3- 3453.3) was lower than the 200nm Tetraspeck™ microspheres (gMFI=52892). Comparison of the CD81-Tdtomato sEVs and Tetraspeck™ microspheres are shown in [Figure 5.11.A-C.iii](#); the red solid lines represent the CD81-Tdtomato sEV fluorescence distributions, and the black or pink solid line represent the orange fluorescence distribution of 100nm or 200nm Tetraspeck™ microspheres (respectively).

Interestingly, we also observed that the fluorescence distribution of Tom-Parallel control sEVs i.e., auto-fluorescent signal overlaid with the 100 nm NIST and 200nm NTA blank PS beads, even though the mean fluorescence intensity of Tom-Parallel control sEVs (gMFI=125.3-135.3), was lower than the PS beads (gMFI=211 or 486, respectively), which is expected due to their lower refractive index ([Figure 5.11A-C.iii](#), orange and black/pink dashed lines)

In contrast to CD81-Tdtomato sEVs, GFP-CD63 sEVs showed no detectable green fluorescence compared to the GFP-Parallel control sEVs ([Figure 5.12.A-C.ii](#)), with the mean fluorescence intensities of both sEV populations being quite comparable (GFP-CD63 gMFI=714.3-728.3 and GFP-Parallel controls gMFI= 705-718.3). Furthermore, comparisons of their fluorescence histogram distributions showed an overlap of GFP-CD63 with GFP-Parallel control sEVs and with the non-fluorescent PS reference beads ([Figure 5.12.A-C.iii](#)).

Finally, our Nanoscale Flow Cytometry results were also validated by widefield fluorescence microscopy, where we detected punctate fluorescent signal for CD81-Tdtomato sEVs but were unable to detect any signal for the GFP-CD63 sEVs ([Supplementary Figure 19](#)).

To summarise, our results demonstrated that at least a sub-population of CD81-Tdtomato sEVs has detectable fluorescence, whereas GFP-CD63 sEVs have no detectable fluorescence which might be due to the progressive loss of fluorescence of GFP-CD63 cells in the Bioreactors.

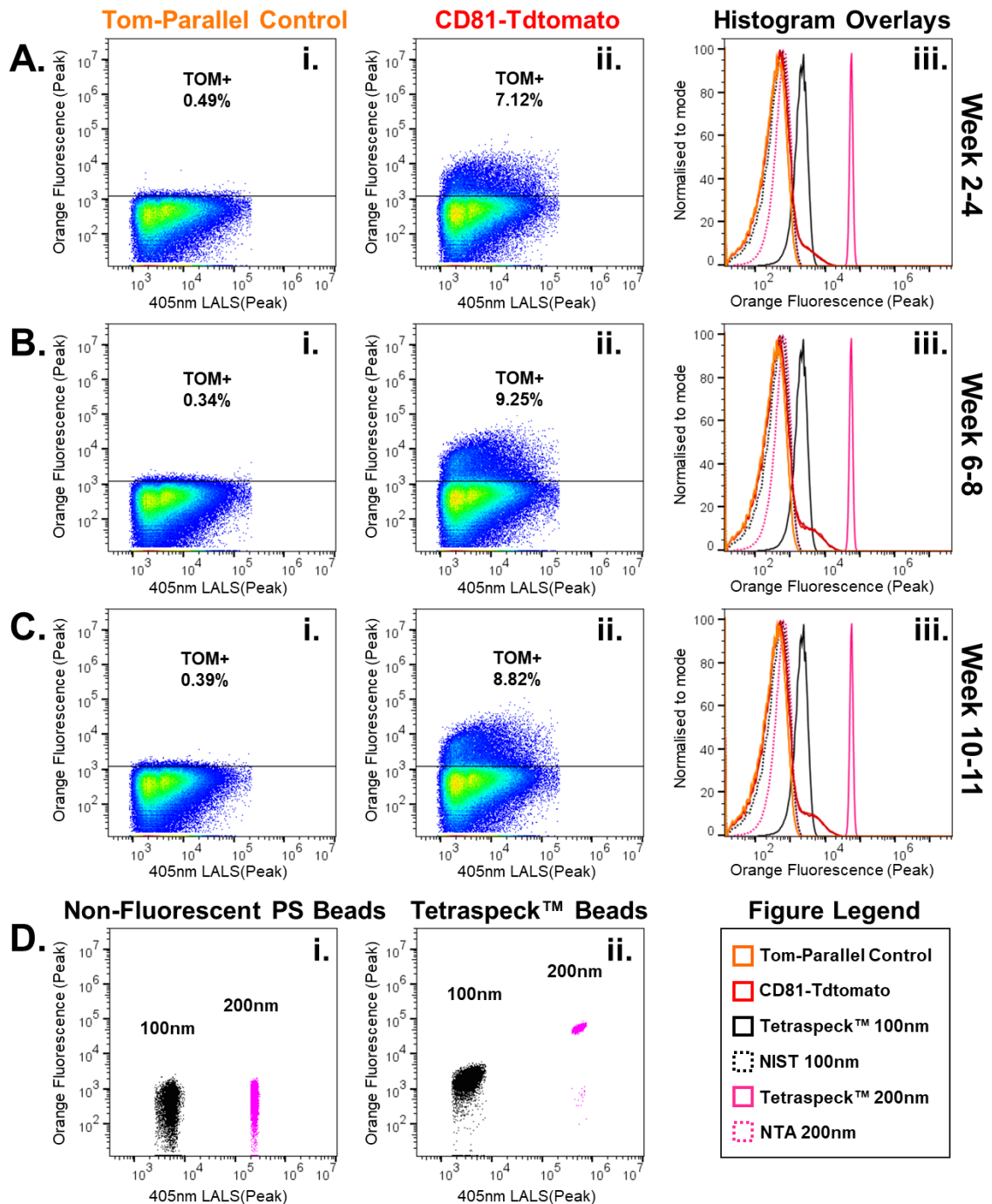


Figure 5.11. Nanoscale Flow Cytometry to detect CD81-Tdtomato sEV fluorescence.

A-C. Nanoscale Flow cytometry plots comparing sEVs at **(A)** Weeks 2-4 (Batch 1), **(B)** Weeks 6-8 (Batch 2) and **(C)** Weeks 10-11 (Batch 3). Figure includes scatter plots of LALS (Large-angle light scatter, indicative of size) Vs Orange Fluorescence (532nm excitation) for **(i)** Tom-Parallel control and **(ii)**, CD81-Tdtomato sEVs of every Batch separately, and **(iii)** Histogram overlays of orange fluorescence signal of sEVs and reference beads. **D.** Scatter plots (LALS Vs Orange Fluorescence) of reference beads: **(i)** non-fluorescent polystyrene (PS) beads (NIST=100nm and NTA=200nm) and **(ii)** Tetraspeck™ fluorescent microspheres (100 and 200nm). Overlays of orange fluorescence of reference beads are shown in **A-C.** for comparison to sEV fluorescence, and Figure Legend of colours/symbols is shown on the bottom right.

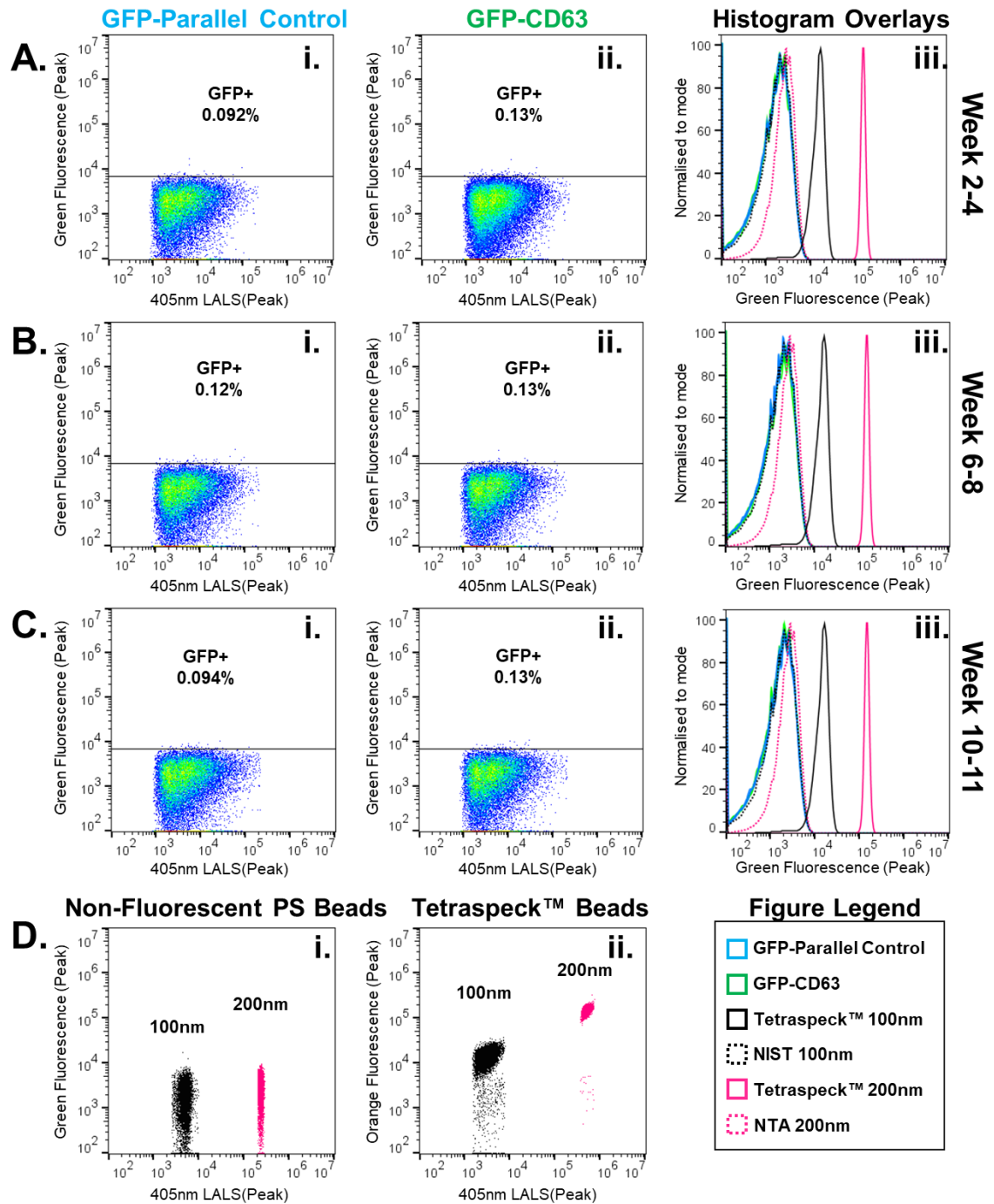


Figure 5.12. Nanoscale Flow Cytometry to detect GFP-CD63 sEV fluorescence.

A-C. Nanoscale Flow cytometry plots comparing sEVs at **(A)** Weeks 2-4 (Batch 1), **(B)** Weeks 6-8 (Batch 2) and **(C)** Weeks 10-11 (Batch 3). Figure includes scatter plots of LALS (Large-angle light scatter, indicative of size) Vs Green Fluorescence (488nm excitation) for **(i)** GFP-Parallel control and **(ii)**, GFP-CD63 sEVs of every Batch separately, and **(iii)** Histogram overlays of green fluorescence signal of sEVs and reference beads. **D.** Scatter plots (LALS Vs Green Fluorescence) of reference beads: **(i)** non-fluorescent polystyrene (PS) beads (NIST=100nm and NTA=200nm) and **(ii)** Tetraspeck™ fluorescent microspheres (100 and 200nm). Overlays of green fluorescence of reference beads are shown in **A-C** for comparison to sEV fluorescence, and Figure Legend of colours/symbols is shown on the bottom right.

Determination of sEV Size Distribution by NTA

As the previous results suggested phenotypic changes of the sEV fluorescence and cargo, another issue that needed to be addressed was whether the overexpression of CD63 and CD81 in the Bioreactor microenvironment had any effect on sEV size. Hence, NTA was performed on isolated sEVs to generate their size distribution profile (shown in [Supplementary Figure 20](#)). Next, the modal and mean sEV sizes were extrapolated from the average NTA size distributions for every sEV type and every EV batch i.e., Batch 1 (Weeks 2-4), Batch 2 (Weeks 6-8) and Batch 3 (Weeks 10-11). This was done to assess potential changes in sEV size after overexpression of CD63 or CD81 in DU145 cells cultured over time in the Bioreactor microenvironment.

To begin with, we observed no significant differences in the modal size of EVs over time (i.e., between batches), with the modal size ranging between 80-150nm, indicative of sEVs ([Figure 5.13.A.i](#)). However, we observed that the mean size of GFP-CD63 sEVs was larger than the GFP-Parallel control sEVs for up to Week 8 in the Bioreactors, even though by the last time-point this was not apparent ([Figure 5.13.A.ii](#)). On the other hand, the mean size of CD81-Tdtomato sEVs was consistently and significantly smaller than Tom-Parallel sEVs over time (~110-140nm for CD81-Tdtomato vs ~160-210nm for Tom-Parallel control sEVs). Interestingly, we also observed that the mean size of sEVs (but not the modal size) appeared to increase over time ([Figure 5.13.A](#)), which might indicate that a small proportion of larger vesicles are being produced in the aging Bioreactors.

To further analyse these changes in sEV size, the FlowJo™ Chi Squared statistical test (130, 150, 151) was used to determine the variance between the size distributions of GFP-CD63 and CD81-Tdtomato sEVs compared with their relevant parallel controls. [Supplementary Figure 21](#) describes processing of the NTA distributions and estimation of the baseline variance for each sEV sample. Through this analysis we confirmed that the size distribution of CD81-Tdtomato sEVs was significantly smaller than control sEVs, which was consistent over time ([Figure 5.13.C](#)). In addition, the CD81-Tdtomato sEV distribution deviated significantly from Tom-Parallel sEVs, varying by more than 68-210 SD ([Figure 5.13.D, bottom row](#)). On the other hand, the size distribution of GFP-CD63 sEVs deviated less from GFP-Parallel sEVs, varying by only 16-19 SD at Weeks 2-4 ([Figure 5.13.B.i,D-left column](#)) and Weeks 6-8 ([Figure 5.13.B.ii,D-mid column](#)).

Collectively, these observations supported that overexpression of CD81 or CD63 resulted in the generation of smaller or larger EV populations respectively. Although, these observed changes in sEV size after overexpression of CD63 were not consistent and not highly significant, in contrast to the changes in sEV size after overexpression of CD81.

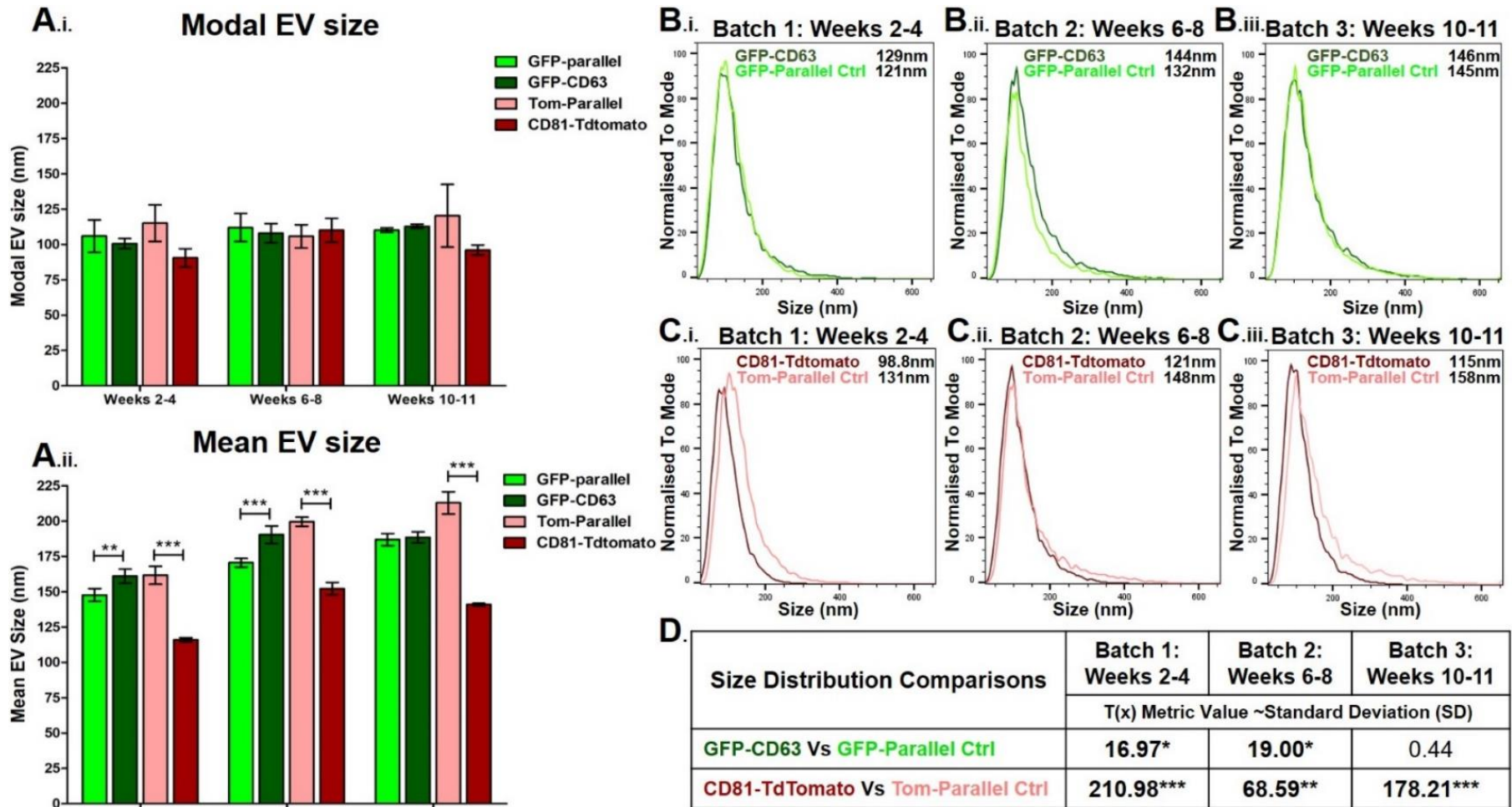


Figure 5.13. Effects of overexpression of CD63 and CD81 on sEV size distribution.

Figure Legend on next page ►

Figure 5.13. Effects of overexpression of CD63 and CD81 on sEV size distribution.

◀ *Figure on previous page*

A. Nanoparticle Tracking Analysis (NTA) was used to calculate the sEV size distributions followed by extrapolation of the **(i)** Modal and **(ii)** Mean size for EV Batches 1 to 3 (Weeks 2-11). Error bars denote standard deviation (sample run in triplicate), and statistical analysis was done using two-way ANOVA with Bonferroni post-test multiple comparisons. Only significant differences are denoted in the graphs with * $p < 0.05$, ** $p < 0.01$ and *** $p < 0.0001$. **B-C.** sEV size distribution overlays **(B)** for GFP-CD63 vs GFP-Parallel control sEVs and **(C)** CD81-Tdtomato vs Tom-Parallel control sEVs comparing **(i)** Batch 1, **(ii)** Batch 2 and **(iii)** Batch 3, with mean sEV size noted in the top right corner of overlays. **D.** FlowJo™ Chi Square statistical analysis table showing size distribution comparisons of the above overlays for Batch 1 (left column), Batch 2 (middle column) and Batch 3 (right column). The result of each comparison is the calculated Chi Square value converted into a T(x) metric value that represents the variance between populations in Standard Deviations (SD). The size variance between sEVs was denoted as statistically significant (bold font) when their Chi Square T(x) values were higher than baseline T(x) values.

5.3.3.2. Cryo-TEM size and morphology analysis of EVs

Cryogenic transmission electron microscopy (Cryo-TEM) was performed to investigate previous results suggesting deviation in size between EV populations. The CD81-Tdtomato and Tom-Parallel control sEVs were selected for this analysis, as they showed the largest differences in size by NTA. To exclude time-dependent changes occurring to EV size, the three EV batches were all pooled together at a 1:1:1 ratio, generating the Tom-Parallel (Weeks 2-11) and CD81-Tdtomato EV (Weeks 2-11) pooled samples.

Cryo-TEM morphological analysis of sEVs

To begin with, exemplary images of CD81-Tdtomato and Tom-Parallel control sEVs ([Figure 5.14](#)) predominantly depicted round vesicular structures with a thick outer boundary, which is indicative of a lipid bilayer and exhibited a diameter typically associated with DU145-derived small EVs ($\leq 100\text{nm}$) (114, 115, 183). Heterogeneity in vesicle size and morphology was also observed. Some EVs presented with more than one lipid bilayer ([Figure 5.14](#), black and grey asterisks), whereas others were spherical enclosing smaller vesicular structures, or were irregularly shaped with some luminal vesicular content or were empty (white asterisks). Large irregular vesicular structures with broken membranes were also observed, albeit as rare events (black dashed oval); these were excluded from analysis unless their membrane was intact. Cryo-TEM also showed non-vesicular amorphous matter surrounding EVs which might indicate protein aggregates or other constituents co-isolated with sEV samples (white dashed line). Small and large electron dense structures were also noted but were disregarded from analysis as they were not considered vesicular (black and white arrows).

To analyse the Cryo-TEM images, the maximum diameter of EVs was measured manually in Fiji™, with 1000 vesicles counted for each EV type, followed by morphology-based analysis ([Figure 5.15](#)). EVs were categorised based on their membrane characteristics i.e., “classic” when having a single membrane, “bi-membrane” or “multi-membrane”, when having two or more membranes respectively, and “irregular sacks”, when having an irregular shape and/or enclosing more structures (examples of these are shown in [Figure 5.14](#)). As expected, the majority of vesicles (>89%) were morphologically considered as “classic EVs” (6). In this category, the CD81-Tdtomato EVs were significantly smaller compared to the controls (77.9nm vs 101.2nm respectively). Smaller percentages of EVs were “bi-membrane” (3.5-5.8%), “irregular sacks” (1.9-3.5%), or “multi-membrane” (1-1.4%), albeit no significant differences in mean EV sizes were observed for these categories.

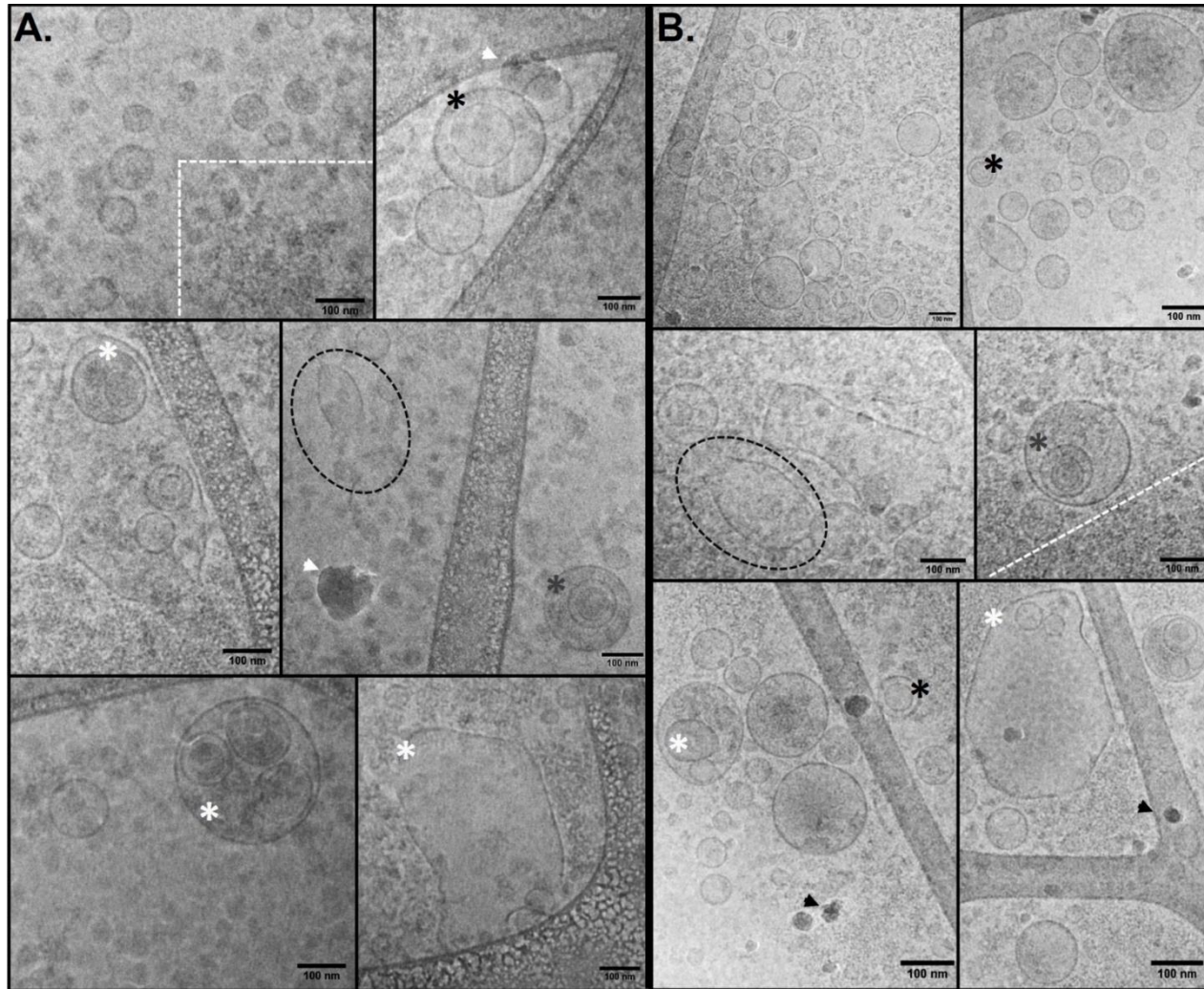


Figure 5.14. Cryo-TEM exemplary images depicting morphology of CD81-Tdtomato and Tom-Parallel EVs.

Images of **(A)** CD81-Tdtomato and **(B)** Tom-Parallel EVs. The majority of EVs appear spherical with thick outer boundary (single lipid bilayer) resembling classic EVs, but other structures are also present including “bi-membrane” (double lipid bilayer, black asterisks), “multi-membrane” (3 or more lipid bilayers, grey asterisks), and “irregular sack” EVs (white asterisks), which are heterogeneous as they can either be spherical and containing smaller EVs inside, or irregular-oblong with or without incorporated EVs. Large irregular vesicular structures with broken membranes were also seldomly observed (black dashed ovals). Non-vesicular diffused contaminants surrounding EVs (possibly protein aggregates) were also present; examples are shown within white dashed lines. Small and large electron dense structures were also present (larger resembling ice crystals); examples are shown with black and white arrows, respectively. Scale bars represent 100nm.

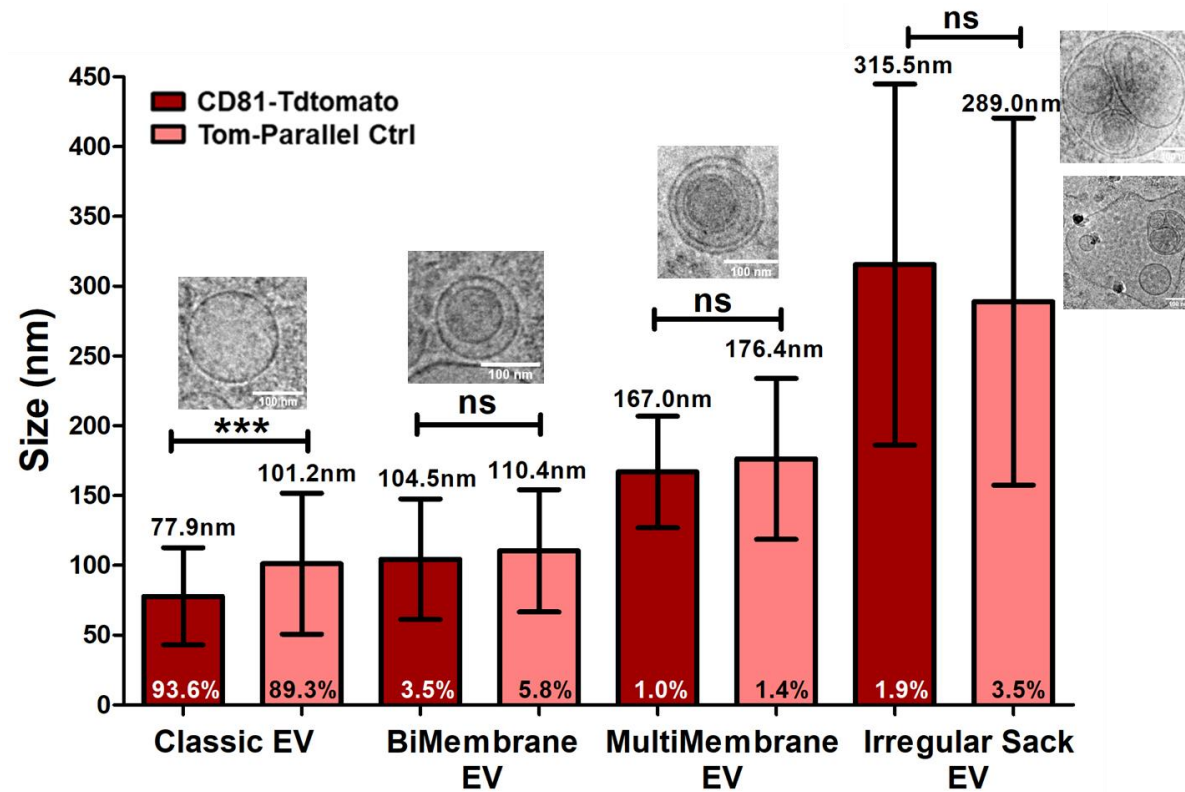


Figure 5.15. Cryo-TEM morphology analysis of EVs.

Graph demonstrating vesicular size based on morphological characteristics of EVs, according to their membrane structure i.e., categorisation into “classic”, bi-membrane”, “multi-membrane” and “irregular sacks” (exemplary images shown above each category with scale bars representing 100nm); mean size is shown above the error bars, and percentage of EVs in every category is shown in the bottom. Note that the size of CD81-Tdtomato (dark red) and Tom-Parallel control (pink) EVs were measured using the Fiji Software (maximum diameter length, 1000 vesicles per EV type). Error bars denote standard deviation and statistical analysis was done using multiple unpaired Student’s T-tests with Welch’s correction with statistical significance denoted with *** $p < 0.01$ or ns where non-significant.

Cryo-TEM size distribution analysis of EVs

Besides morphology, we investigated the size distribution of CD81-Tdtomato EVs compared to respective controls. [Figure 5.16.A](#) shows the range of EV sizes that were manually counted for Tom-Parallel and CD81-Tdtomato EVs (maximum diameter length). Thus, we validated that the CD81-Tdtomato mean EV size (84.3nm) was significantly smaller than Tom-Parallel control EVs (111.7nm). To further quantify the size differences between EVs overexpressing CD81 and controls, EVs were categorised based on their “physical characteristics”, using the nomenclature suggested by the MISEV 2018 guidelines (6) i.e., categorised into “sEVs/ small EVs ” (<200nm) and “IEVs/ large EVs” (>200 nm) ([Figure 5.16.B](#)). Our analysis showed that the CD81-Tdtomato EV population was comprised of a high percentage of sEVs with mean size of 77.26nm; this population was significantly smaller than the Tom-Parallel control sEV population (95.95nm). Conversely, no significant differences were denoted in the size of IEVs between CD81-Tdtomato and Tom-Parallel control EVs ([Figure 5.16.B](#)).

Additionally, we generated the size distributions of CD81-Tdtomato and Tom-Parallel control EVs, (using the FlowJo™ software) and then performed a Chi Square test to statistically compare these EV populations ([Figure 5.16.C](#)). This showed that the size distributions of CD81-Tdtomato and Tom-Parallel control EVs varied significantly by ~20 SD, and their overlay demonstrated the smaller mean size of CD81-Tdtomato EVs ([Figure 5.16.C](#)). Hence, overexpression of CD81-Tdtomato has had a consequence on the repertoire of expelled vesicles, with heightened output of sEVs of “classic” morphology.

Concluding remarks

Overall, Cryo-TEM analysis results validated the previous NTA results and suggested that the mean size of CD81-Tdtomato EVs was smaller than the Tom-Parallel Control EVs, which could be further explained by the presence of a higher percentage of CD81-Tdtomato sEVs (<100nm) in the EV population. Cryo-TEM results also demonstrated morphological differences between CD81-Tdtomato and Tom-Parallel Control EVs, with the majority of the former presenting as “classic EVs”, whereas the latter present with slightly higher percentages of complex EV structures (“bi-membrane”, “multi-membrane”, “irregular sack EVs”). These observations suggest that overexpression of CD81 drove a phenotypic change in EVs which is supported by differences in EV cargo, size, and morphological characteristics.

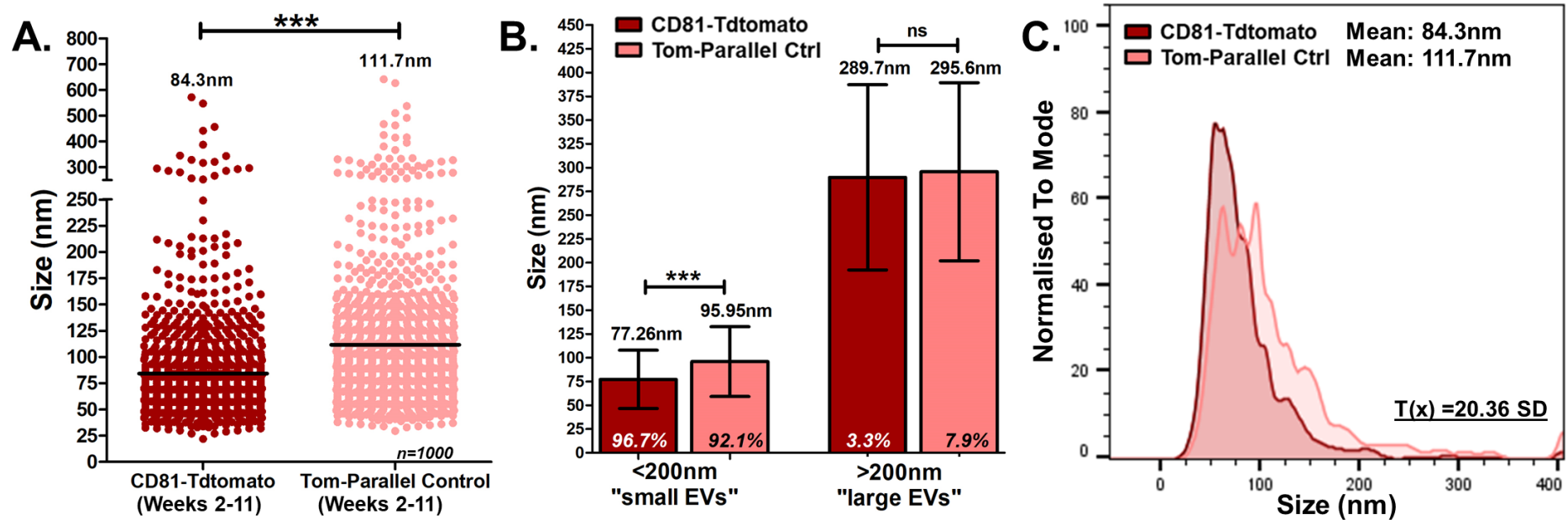


Figure 5.16. Cryo-TEM size distribution analysis of EVs.

A. Plot demonstrating the range of sizes for CD81-Tdtomato and Tom-Parallel control EVs based on manual measurements of maximum diameter length. **B.** Vesicular size based on physical characteristics of CD81-Tdtomato and Tom-Parallel control EVs according to the 2018 MISEV guidelines; categorisation into "sEVs/small EVs" (≤ 200 nm), and "lEVs/large EVs" (> 200 nm). The mean EV size is shown above the error bars, and percentage of EVs in every category is shown in the bottom. Note that the size of CD81-Tdtomato (dark red) and Tom-Parallel control (pink) EVs were measured using the Fiji Software (maximum diameter length, 1000 vesicles per EV type). Error bars denote standard deviation and statistical analysis was done using multiple unpaired Student's T-tests with Welch's correction with statistical significance denoted with *** $p < 0.01$ or ns where non-significant. **C.** Histogram overlays comparing size distributions of CD81-Tdtomato and Tom-Parallel control EVs. The mean EV size and Chi Square T(x) value is shown on each histogram overlay; T(x) represents the variance between the two distributions in Standard Deviations (SD) calculated via the FlowJo™ Chi Square distribution comparisons test.

5.4. Discussion

Currently, many researchers in the field utilise *in vitro* models to generate sEVs (95% of the MISEV2018 guidelines authors (6)). Larger-scale, consistent and reproducible platforms generating highly pure sEVs are now considered to be essential to further EV research (127, 221). Platforms like the CELLLine Bioreactors provide the additional advantage of being a tissue-mimetic platform as they support the 3D-growth of cells, which more closely resembles the tumour microenvironment than a traditional 2D culture (211, 214). Arguably, sEVs generated from a 3D tissue-like microenvironment can more closely reflect *in vivo* sEVs, and can be of more translational and clinical interest for the development of therapeutics or biomarkers, compared to 2D culture-derived sEVs (222).

The major limitation of CELLLine Bioreactors is their unknown impact on the cultured cell and secreted sEV phenotype. Previous studies have indicated phenotypic alterations of cells seeded in other large-scale platforms, like microcarriers in stirred-tank reactors (217). A study investigating human embryonic stem cells in 10 different types of microcarriers, showed that the shape and coating of the microcarriers can drive cells to develop different attachment, growth, viability and pluripotency properties (223). Limited studies have addressed the effects of the CELLLine Bioreactors on growth and viability of cultured cells (127, 210, 215), even though some studies have investigated the phenotype of generated sEVs (127, 211-214).

Hence, it was important to investigate how engineered cell lines overexpressing CD63 or CD81 adapt in the Bioreactors, and what are the potential phenotypic changes in cells and sEVs compared to the WT DU145 controls. This is the first study, to our knowledge, that systematically addresses the long-term effects of the Bioreactor microenvironment on the physiology of WT and genetically modified DU145 cells overexpressing CD63 or CD81, as well on the phenotype of secreted sEVs.

Phenotypic Differences in Cells After Overexpression of CD63 and CD81

Tetraspanins (including CD63 and CD81) are known to interact with a plethora of proteins to regulate cell adhesion and morphology (e.g. via Integrins, Focal Adhesion Kinase, Rho GTPases, β -catenin), as well as cell proliferation (e.g. via c-Met, TGF, EGFR), signalling and protein trafficking (24, 165, 166, 224). Thus, it was essential to investigate the effects of CD63 or CD81 overexpression in DU145 cells cultured in the 3D-like CELLLine Bioreactor, especially since these cell lines serve as the source for generating sEVs.

To begin with, our results suggested that the GFP-CD63 and CD81-Tdtomato cells exhibited reduced growth in the CELLine Bioreactors compared to their WT parallel control counterparts. The slower growth of GFP-CD63 cells was at least partly attributed to the lower viability of the non-adherent fractions (Semi-adherent and Suspension). We can only hypothesise whether the low viability is a result of higher sensitivity of GFP-CD63 cells to anoikis (detachment-induced apoptosis), or a result of increased apoptosis or response to environmental stress or other unknown reasons. A previous study in melanoma supported that CD63 expression is associated with a more epithelial phenotype, as CD63 overexpression inhibits epithelial-to-mesenchymal transition (EMT) *in vitro* (170) which might make these cells more dependent to adhesion. In addition, in Chapter 4, we identified that GFP-CD63 cells exhibited downregulation in Integrin $\alpha 3$; a recent study in kidney epithelial cells demonstrated that knockout of Integrin $\alpha 3$ severely disrupted adhesion (225). Furthermore, GFP-CD63 cells exhibited downregulation of prostaglandin reductase 1 (PTGR1), which was previously shown to suppress PC3 and DU145 PCa cell proliferation by inducing apoptosis (226).

We also observed that GFP-CD63 cells progressively lost their fluorescence, which was reflected also in the generated sEVs. This phenomenon might be attributed to the environmental conditions in the Bioreactor Flask as conditions like acidic pH, low oxygen concentration (hypoxia) and oxidative stress can reduce the fluorescence of GFP (220). Previous studies have indicated that hypoxia is a caveat of static bioreactors, as oxygen distribution is diffusion-dependent and hence limited to distances of 100–200 μm (227, 228). Even though flow perfusion bioreactors were designed to improve the oxygen supply to cultured cells, it was still reported that central oxygen concentrations were low (e.g. 4% (228)), depending on the engineered properties of the bioreactor (227, 228). Hypoxia might be a potential limitation of the CELLine Bioreactors, especially for long-term high-density cell culture, as despite their design allowing for gas transfer, their inner cell compartment is 2mm in depth, which might result in heterogeneous and/or inefficient oxygen dispersion through the compartment. The 3D-like growth of DU145 cells in the Bioreactors might also confer hypoxia, as several studies have shown that low oxygen concentration is a hallmark of PCa (229-231) and is associated with high metabolic waste, acidic pH (“acidosis”) and increase in necrotic cells in the tumour microenvironment (231). Thus, hypoxia or oxidative stress might have conferred the loss of GFP fluorescence and lower viability of the non-adherent GFP-CD63 cells. However further studies are necessary to determine the oxygen concentrations within the CELLine Bioreactors. Despite the issues with cell viability and progressive loss of fluorescence, overexpression of CD63 did not affect cell cycle dynamics, compared to the controls (agreeing with results from 2D culture from Chapter 3).

In contrast to CD63, overexpression of CD81 did not affect the viability of DU145 cells in the Bioreactor, regardless of the adhesion state of the cell. In addition, the fluorescence signal distribution of the viable CD81-Tdtomato cells was similar between adherent and non-adherent fractions and remained stable over time. This might be attributed to the properties of the Tdtomato which is highly photostable, not as sensitive to hypoxia (232, 233) or acidic pH (pKa=4.7 (234)) and has been previously used as a constitutive fluorescent cell-tracking reporter for *in vitro* and *in vivo* studies of hypoxia in PCa models (235, 236).

Overexpression of CD81-Tdtomato did however delay cell cycle progression of adherent and non-adherent cells compared to controls, in agreement with similar observations from Chapter 3. This might be attributed to the potential cytostatic effect (inhibition of cell growth and multiplication) occurring after CD81 overexpression in various cell types including glioma cells, hematopoietic stem cells and astrocytes (167-169).

Phenotypic Differences in sEVs after overexpression of CD63 and CD81

Previous studies investigated the phenotype of secreted sEVs from Bioreactor Flasks (127, 211-214, 216) and some demonstrated that the Bioreactor microenvironment can alter the physiology of sEVs (215,217). EV characterisation focused on defining potential phenotypic changes of the isolated sEVs in terms of size, protein markers, fluorescence, and morphology.

Changes in sEV cargo and fluorescence signal

Firstly, we showed that Bioreactor-derived sEVs had expression of Alix, TSG101, CD63 and CD81, as shown by Western Blot analysis, and membrane expression of CD9, CD63, CD81, as well as the receptor MHC-1, by the immune-phenotyping assay, which are all common markers of sEVs (6).

Interestingly, the levels of CD9, CD63 and CD81 appeared to decrease over time for all sEV types, whereas the levels of MHC-1 increased (except GFP-CD63 EVs, which they remained high and stable). The mechanism behind this is currently unknown, however one can hypothesise that a decrease in tetraspanin levels might potentially reflect “contamination” of the sEV samples with protein/ lipoprotein aggregates or ECM depositions from the aging Bioreactor, especially if we take into consideration the observed increase in sEV protein yield over time (157). On the other hand, the decrease in sEV-associated tetraspanin levels might suggest a shift of secreted EV subpopulations

e.g., towards IEVs, or other tetraspanin-low vesicle populations by the cells aging in the Bioreactor Flasks.

In striking contrast to tetraspanins, the levels of MHC-1 increased over time on Bioreactor-derived sEVs. This perhaps reflects increased secretion of the soluble form of MHC-1, as it has been previously detected in all bodily fluids similarly to sEVs (237). Alternatively, previous studies demonstrated that sEVs expression of disulfide-linked MHC-1 dimers increases when glutathione levels are low (238), which can be attributed to an increase in oxidative stress (239). In addition, a previous study showed that DU145 and PC3 PCa cells secrete MHC-1 under hypoxia crisis (240). These suggest that these changes in EV cargo might reflect environmental stress in the Bioreactor Flasks.

Previous studies from our laboratory showed that cells and sEVs from CELLLine Bioreactors exhibited comparable levels of hsp70, hsp90 and Hsc70 to 2D culture, suggesting that they are not experiencing stress such as hypoxia or starvation (127, 183); however other markers like HIF-1 α (Hypoxia-inducible factor 1-alpha), GLUT1 (Glucose transporter 1) and CAIX (Carbonic anhydrase IX) might be also necessary to accurately determine if cells are under low oxygen concentrations. As we also observed loss of GFP fluorescence in cells and sEVs in these Bioreactors over time, which might be partly due to hypoxic conditions, further investigation on hypoxia and its potential effects on cell and EV phenotype is essential.

Overall, our observations demonstrated that overexpression of CD63 and CD81 led to the generation of different EV subpopulations in the CELLLine Bioreactor, which did not entirely reflect our observations in the 2D conventional tissue culture flasks. Overexpression of CD63 resulted in sEVs with high CD63 and low CD81 loading, whereas overexpression of CD81 resulted to low CD63 and high CD81 loading. Contradictory to our observations, previous studies showed that overexpression of CD63-pHluorin (GFP variant) in HeLa cells (118), and GFP-CD63 in HEK293T cells (122), did not significantly affect the levels of CD81 or other proteins. However, a different study showed that prostate RWPE1 cells with downregulated CD9 or overexpressed CD151, generate sEVs with a different composition of tetraspanins (192). Thus, it seems that overexpression of CD63 or CD81 at the cellular level has altered the levels of tetraspanins and MHC-1 at the EV- level in a different manner, underlining that alterations in the tetraspanin expression can have different implications on cargo loading, composition and potentially secretion of different subtypes of EVs (24). Since CD63 and CD81 exhibit different functions and different protein interactions at the TEMs (Tetraspanin-Enriched Microdomains) (19, 21), our observations indicate that changes in sEVs are specific to the individual tetraspanins concerned, as opposed to a general impact of altering any tetraspanin in the parent cell.

Changes in sEV size- NTA

Further experiments demonstrated that overexpression of CD63 and CD81 led to significant differences in the mean sEV size compared to the WT Parallel controls. Overall, the GFP-CD63 sEVs were slightly larger than GFP-Parallel controls, and CD81-Tdtomato were significantly smaller than the Tom-Parallel control sEVs. These differences in EV size might correlate with the previous results on sEV cargo, as overexpressing different tetraspanins might lead to the biogenesis of different subtypes of EVs which may inadvertently differ in size and protein cargo (19, 156). For example, sEVs isolated from RWPE1 cells with downregulated CD9 or overexpressed CD151, were larger in mean size, suggesting that altering the tetraspanin expression might result in alterations of the physical properties of sEVs (192). Another study also supported our observations, demonstrating changes in morphology, size distribution, sEV-associated surface markers and metabolome of Bioreactor-derived sEVs compared to conventional 2D-derived sEVs (214).

Interestingly, NTA revealed a time-dependent increase in mean size of sEVs. This might be attributed to the increased protein aggregation in the sample, which may have caused clustering of sEVs and lead to the readout of larger vesicles by NTA (241). Protein aggregates can also be tracked by NTA, hence this might have introduced bias and artifacts in the analysis (242). Another possibility is the increasing presence of apoptotic EVs, which can significantly vary in size (243); however, this is unlikely since the cells of all fractions in the CELLline Bioreactors were increasingly more viable and actively dividing over time. The possibility therefore exists that the aging Bioreactor produces sEVs that are different from 2D cultures, with EVs becoming larger in mean size over time (222).

Changes in sEV size- Cryo-TEM

Cryo-TEM analysis validated this deviation in size between CD81-Tdtomato and Tom-Parallel control EV as the mean size of the CD81-Tdtomato was significantly smaller than the controls. Furthermore, this analysis revealed the presence of a population of vesicular structures heterogeneous in size and morphology, even though the majority of were typically associated with “small EVs” (6, 115, 183). Vesicles of larger size were also present, however less prevalently in the CD81-Tdtomato EV population, consistent perhaps with a shift in the type(s) of EVs being produced.

CD81-Tdtomato and Tom-Parallel controls EVs also exhibited morphological heterogeneity, with similar structures previously reported by other Cryo-TEM studies on

a variety of sEV types (244-247). Potential contaminants were seen in both CD81-Tdtomato and control samples; ice crystals (probably due to freezing/thawing), protein aggregates and lipoprotein aggregates. The protein and lipoprotein contaminants could have been co-isolated with sEVs during the various steps of isolation, and they could also be by-products after rupturing sEVs due to manual handling of the sample (244-246). This observation may support the previous hypothesis, that the time-dependent differences observed in sEV cargo (decrease of tetraspanin levels) might reflect protein contamination. This may lead to the increase of soluble proteins which eventually underestimates the sEV particle number used in the Immuno-phenotyping assay. Similarly, the time-dependent changes in sEV size (as observed via NTA) might be attributed to protein aggregation leading to consequent detection of clusters of sEVs, thus overestimating their size.

Taken together, Cryo-TEM analysis of the physical properties and morphological characteristics of both EV types, demonstrate that overexpression of CD81 does not significantly alter the morphological structures of secreted sEVs. However, it results in the potential enrichment of a subpopulation of EVs of smaller size; this might be attributed to the propensity of CD81 to load to small EVs (<100nm) (8, 118) and to be involved in sEV biogenesis potentially by regulating the fission of newly-formed sEVs into MVBs via clustering with other proteins and cholesterol (248). These results may also explain the previous observations of differences in EV cargo (tetraspanins CD9, CD63 and CD81, and receptor MHC-1) in the CD81-Tdtomato sEVs compared to the WT Parallel controls.

5.5. Conclusions

This is the first study, to the best of our knowledge, that systematically characterised the phenotypic effects of long-term culture of stable DU145 cell lines overexpressing the tetraspanins CD63 and CD81 and their secreted sEVs, in the CELLLine Bioreactor system. Our results also underlined that stable cell lines might exhibit different behaviours in the Bioreactor microenvironment, depending on the nature of their genetic modifications. In our study, DU145 cells overexpressing GFP-CD63 exhibited hindered growth (possibly due to lower viability) as well as loss of fluorescence after long-term culture. Conversely, cells overexpressing CD81-Tdtomato exhibited reduced growth due to slower cell cycle progression, however their fluorescence remained stable over time. This was also reflected in the secreted sEVs, as GFP-CD63 sEVs had no detectable fluorescence, whereas CD81-Tdtomato sEVs could still maintain detectable orange fluorescence. This issue suggested that CD81-Tdtomato cells are more suitable for long term culture in the CELLLine Bioreactor and the successful generation of fluorescent sEVs, compared to GFP-CD63 cells. Further characterisation of sEVs demonstrated that overexpression of tetraspanins in DU145 cells cultured in Bioreactors can lead to phenotypic changes in EVs in terms of size, protein markers and morphology. Overexpression of CD63 lead to secretion of sEVs with high CD63/MHC-1 and low CD9/CD81, whereas overexpression of CD81 lead to secretion of sEVs with high CD81 and low CD9/CD63/MHC-1, which might be indicative of enrichment of different subpopulations of sEVs. In addition, overexpression of CD63 lead to the increase in sEV size, whereas overexpression of CD81 lead to the concomitant decrease in sEV size but did not change the morphological properties of sEVs compared to the WT Parallel controls. Taken together, this chapter underlines the importance of characterisation of the CELLLine Bioreactors for long-term culture of cell lines as it unveiled tetraspanin-dependent phenotypic alterations on cells and secreted sEVs; thus, knowledge of these changes is valuable for further mechanistic and functional studies utilising these cells and generated sEVs.

CHAPTER 6:
Nanoparticle and Extracellular
Vesicle Uptake and Retention in
Prostate Cancer and Bone
Marrow- Derived Mesenchymal
Stem Cells

6.1. Introduction

Currently it has been established in the literature that PCa sEVs deliver and exchange cargo as a means of intercellular communication (97), as they can be taken up by other cancer cells (“horizontal transfer”), cells of the tumour microenvironment, like immune cells, fibroblasts and endothelial cells (41, 42, 97), as well as by cells at the bone niche (common PCa metastatic site (57)), like osteoblasts, osteoclasts and bone marrow-derived mesenchymal stem cells (BM-MSCs) (63, 64, 66).

Through this communication-mode, PCa sEVs modulate the microenvironment to promote tumour progression, immune system evasion, stimulate angiogenesis and metastasis, as well as promote the formation of the pre-metastatic bone niche to support metastatic PCa establishment (41, 42). The promotion of pre-metastatic bone niche formation has not been greatly explored yet, even though a few studies have shown that PCa sEVs promote the differentiation of BM-MSCs towards osteoblasts at the bone by transferring pyruvate kinase M2 (PKM2) (64) and non-coding RNA hsa-miR-940 miRNA (66), thus indirectly supporting the formation of the favourable osteoblastic bone metastatic niche (63).

Recent studies have also shed some light into how sEVs exert their cell-to-cell communication functions, by exploring their routes of uptake and fate in recipient cells. Studies demonstrated that sEVs can be internalised in recipient cells via various routes e.g., via clathrin-dependent- (79, 80) or caveolae-dependent- (83, 84) endocytosis (249), phagocytosis (86), micropinocytosis (80), membrane-fusion (77) and receptor-mediated uptake (71, 72). After internalisation, the fate of sEVs in the cell is still not greatly understood, but various mechanisms have been proposed to date; for example, sEVs are believed to be directed to the endo-lysosomal compartment for subsequent release or degradation of their cargo, to be trafficked back to the plasma membrane for re-secretion by MVBs to exhibit “back-fusion” with the MVB membrane, followed by secretion of their cargo into the cytosol, or even become targeted to the nucleoplasmic reticulum (79, 91-94, 109, 111, 177, 250).

Even though many studies have provided valuable insight on the mechanism of sEV entry in cells (69), their main focus was the uptake and internalisation mechanism of sEVs at the single-cell level, whereas the kinetics of sEV uptake (dosing) and distribution in propagating cell populations have not been greatly explored. Further investigation of sEV dosing at the cell population-level is however essential, especially due to the emerging use of sEVs for delivery of therapeutics; this was also emphasized in a recent

ISEV publication, as the better understanding of sEV uptake/retention kinetics could eventually improve the use of sEVs in therapeutic applications (251).

In this Chapter, we aimed to investigate sEV uptake and retention in two-dimensional (2D) dynamic cell systems, by comparing our previously-characterised endogenously fluorescent EV reporters to the standardised Quantum Dot nanoparticles, which are synthetic nanoparticles that have been previously utilised to understand baseline conserved principles of nanoparticle bioprocessing (145, 146, 252, 253).

Quantum Dots (QDs) are inorganic fluorescent nanocrystal semiconductors (10-30nm diameter), usually made of a CdTe/ZnS core-shell (cadmium telluride/zinc sulfide) and functionalised on their outer surface by different molecules that enable cellular entry (254, 255). QDs can be internalised by cells via macropinocytosis as well as clathrin- and caveolae-dependent and -independent endocytosis depending on their functionalisation and the cell type (255, 256).

In this study, we used QD705 fluorescent nanoparticles (emission maximum at ~705nm), which are made from a CdTe/ZnS core conjugated with a custom cell-penetrating peptide (arginine-rich peptide, (257)) that enables cellular entry through the endosomal pathway. QD705 are then delivered into the endosomal compartment as clusters through agglomeration with membrane proteins and surface receptors. The clusters of QD705 within individual vesicles (endosomes/lysosomes) can be seen as discrete fluorescence sources with a bright fluorescence signal (145, 146). This fluorescence remains stable and conserved (i.e., it is not quenched by the intracellular environment) and it is redistributed across cell lineages, such that cellular division can be followed over many generations without being subjected to metabolic degradation (254, 255) and without causing cell toxicity or perturbation of the cell cycle (145, 252, 253). Thus, QD705 nanoparticles are suitable for studying uptake and long-term signal retention via tracking through multiple cell divisions (145, 146, 252, 253), and were selected to characterise the baseline behaviour of our cell systems in nanoparticle bioprocessing.

Furthermore, the PCa-derived CD81-Tdtomato sEVs were also specifically selected for these studies as they could potentially be efficiently detected in recipient cells due to their bright fluorescence and as their phenotype was extensively characterised in previous Chapters e.g., sEV size, protein cargo and fluorescence signal in both 2D and 3D-like microenvironments. Most importantly, the conjugation of the Tdtomato protein to the sEV-specific CD81 protein, enabled the direct detection of fluorescent sEVs *in situ*, without the need for any other dyes (e.g., membrane-specific dyes PKH67, PKH26, DiI, DiR), thus avoiding complications like non-specific staining, structural alterations of EVs

or dye-generated artefacts which sometimes lead to misinterpretation of results (102, 103).

Even though GFP-CD63 sEVs were also generated and characterised like CD81-Tdtomato sEVs, their dim fluorescence prohibited their use for these studies, as their direct detection in recipient cells would not be feasible. As mentioned in Chapter 5, the fluorescence of GFP-CD63 sEVs was not detectable by nanoscale flow cytometry or widefield fluorescence microscopy, due to progressive loss of GFP fluorescence of their parental cells in the Bioreactor Flasks (potentially due to environmental conditions like acidic pH, oxidative stress, or hypoxia).

To summarise, this chapter will characterise and quantify the uptake and retention dynamics of CD81-Tdtomato sEVs compared to the standardised QD705 nanoparticles, in order to elucidate the heterogeneity of dosing, distribution, and retention of nanovesicles vs nanoparticles in the DU145 PCa- and Y201 bone-marrow mesenchymal stem cell- populations, thus reflecting cells in the PCa microenvironment and the pre-metastatic bone niche.

6.2. Aims and Objectives

This Chapter will address sEV uptake and will attempt to quantify sEV retention using CD81-Tdtomato sEVs compared to the established QD705 nanoparticles in two-dimensional propagating cell populations. This benchmarking approach will provide a pragmatic method for comparing the stability, dynamics of uptake as well as retention of the CD81-Tdtomato nanovesicles versus the synthetic QD705 nanoparticles in dynamic cell systems; the DU145 PCa cells (same as the sEV cell of origin) and the Y201 BM-MSCs. Therefore, this chapter aimed:

- To establish a benchmark behaviour of cellular uptake and retention of standardised QD705 nanoparticles in the DU145 PCa cell population.
- To quantify and compare cellular uptake and retention of QD705 nanoparticles in DU145 versus Y201 BM-MSC cell populations.
- To quantify the uptake and retention of CD81-Tdtomato sEVs after their acute delivery in DU145 PCa cells compared to Y201 BM-MSCs.
- To quantify the uptake and retention of CD81-Tdtomato sEVs after their chronic delivery in Y201 BM-MSCs.

6.3. Results

6.3.1. Multi-Platform Quantification of QD705 Uptake in DU145 Cells

6.3.1.1. QD Uptake in DU145 Cells- Flow and Imaging Flow Cytometry

To start the baseline characterisation of nanoparticle dosing, a multi-platform approach was followed (flow-, imaging flow- cytometry and fluorescence microscopy) which enabled the quantification of uptake and retention of QD nanoparticles in DU145 cells.

To begin with, uptake of QDs in DU145 cells was assessed via flow cytometry and imaging flow cytometry. To achieve this, DU145 cells were dosed with 3nM QD705 (QD nanocrystals with Excitation:405-665/ Emission:705nm) for 1h and the fluorescence signal was measured via flow cytometry 24h post-labelling (earliest timepoint where QD705 signal is considered stable (145, 252). The gating strategy to enable analysis for viable cells only is shown in [Supplementary Figure 22](#).

Our results showed that QD705 uptake was heterogeneous in DU145 cells; specifically, the QD705 fluorescence distribution showed 3 distinct and statistically different peaks of fluorescence intensity suggesting High (gMFI= 1850), Intermediate (gMFI= 360) and Low (gMFI= 50) cell uptake of QD705 respectively ([Figure 6.1.A,B](#)). Further data analysis showed that ~50% of DU145 cells exhibited High QD705 uptake, whereas ~30% had Intermediate and ~20% of cells had a Low QD705 uptake ([Figure 6.1.C](#)). Of note, the control samples (no QD705) showed negligible cell auto-fluorescence levels, which were positioned just in range of the flow cytometer.

The heterogeneity in QD705 uptake was reproduced by imaging flow cytometry ([Figure 6.2.A.i](#)); the gating strategy is described in [Supplementary Figure 23](#). Due to the imaging ability of the instrument, cells could be visualised and were further analysed to determine some spatial differences in QD705 fluorescence intensity within the DU145 population. To begin with, the analysis again demonstrated heterogeneous QD705 uptake and distribution of cells in distinct fluorescence intensity peaks with a similar trend to the previous experiment ([Figure 6.2.A.i.ii](#)). Similarly to the flow cytometry experiment, ~55% of DU145 cells exhibited High uptake of QD705, whereas ~25% and ~12% exhibited Intermediate and Low uptake, respectively ([Figure 6.2.A.ii](#)).

However, in this instrument, the QD705 uptake was also designated by a fourth fluorescence intensity peak (Threshold, [Figure 6.2.A](#)). The fourth lower intensity peak

was observed starting on the overlap between the Control and QD705 histograms (Threshold, [Figure 6.2.A](#)); cells within this “threshold” exhibited QD705 fluorescence signal just above background fluorescence i.e., ~ 5% of DU145 cells dosed with QDs ([Figure 6.2.B.iv](#)).

Images from control cells demonstrate this background fluorescence in the “Low” and “Threshold” peaks ([Figure 6.2.C.i,ii](#)), with >95% of untreated control cells exhibiting this threshold fluorescence. The overlap between the control and QD705 histograms arises from the collapse of the dynamic range of the QD705 signal due to the lower sensitivity of the instrument compared to conventional flow cytometers; thus, both the Low and Threshold peaks of this experiment ([Figure 6.2](#)) represent the Low peak of the flow cytometry experiment ([Figure 6.1](#)).

Further analysis of the fluorescent images acquired from this instrument was done to determine the QD705 load per cell, for each of the four fluorescence intensity peaks (High-Intermediate-Low-Threshold) using Spot Count analysis (144) ([Figure 6.2.B.C](#)). It is important to mention that whereas QD705 are nanoparticles, they accumulate upon endocytosis; thus, each spot/cell does not represent a single QD, but rather a cluster of QDs in endosomes. Interestingly the Spot Count analysis showed that cells in the High and Intermediate peaks exhibited a similar distribution of spots per cell e.g., 4-20 spots/cell; however, the High Intensity cells had larger QD705 spots in each cell ([Figure 6.2.B.i](#)) compared to the Intermediate Intensity cells ([Figure 6.2.B.ii](#)). Additionally, as expected, QD705-loaded cells in the Low and Threshold Intensity peaks exhibited mostly 0 to 5 QD705 spots/cell ([Figure 6.2.B.iii,iv](#)); whereas Control cells exhibited only 0 spots/cell in the respective Low and Threshold Intensity peaks ([Figure 6.2.C.i,ii](#)). Overall, these results suggest that the subpopulation of DU145 cells with high QD705 uptake, exhibited significant clustering of QDs compared to the other cells with intermediate and lower QD705 uptake ([Figure 6.2.B](#)).

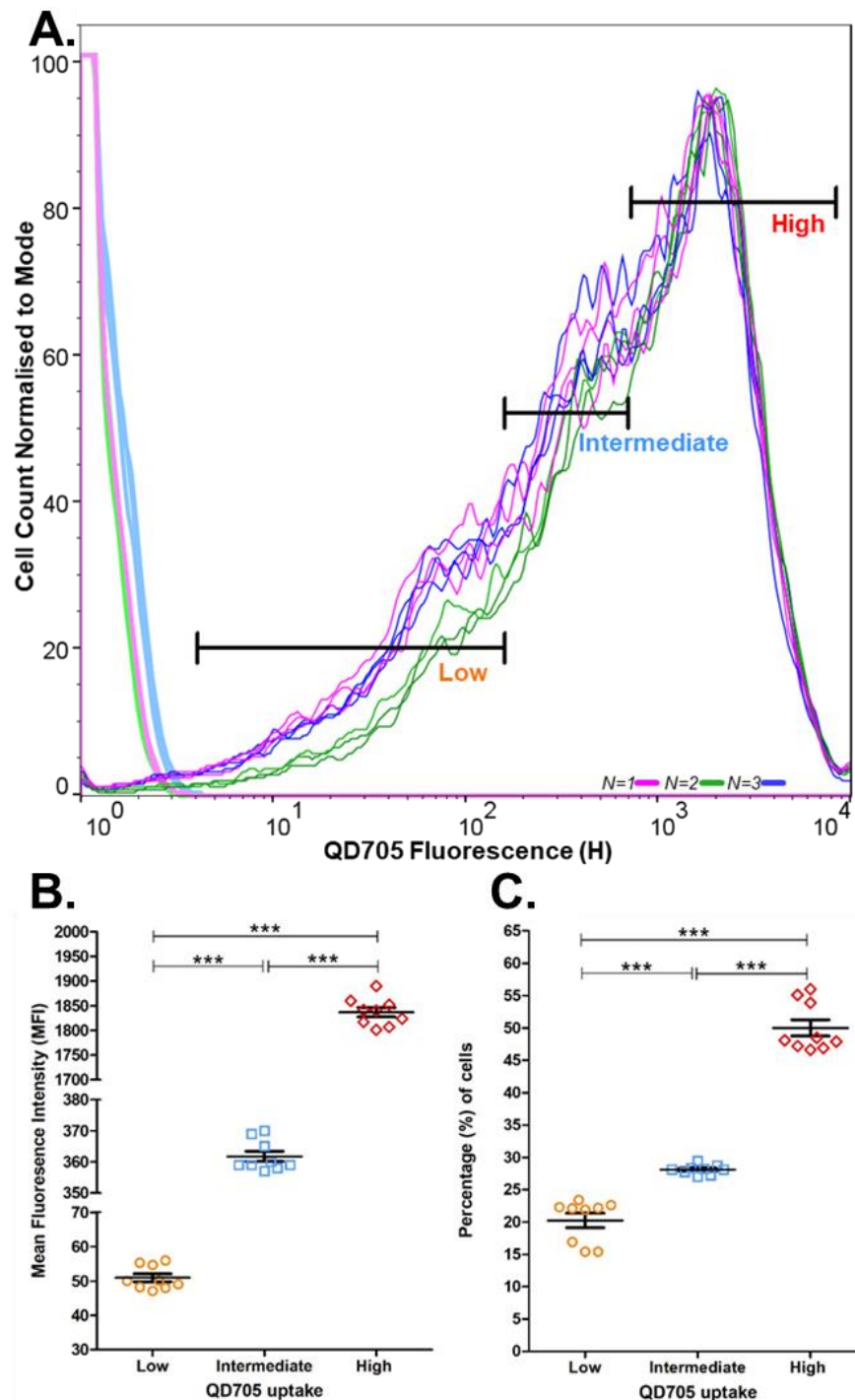


Figure 6.1. Uptake of QD705 nanoparticles in the DU145 cell population.

A. Flow Cytometry QD705 fluorescence intensity histograms 24 hours post labelling of DU145 cells (and control cells) indicating three peaks of QD705 fluorescence intensity; designated by High, Intermediate and Low markings. Intensity histograms represent an overlay of three independent experiments (N=1,2,3 indicated with purple, green and blue lines respectively) and all triplicate conditions (QD705- treated (dark colour) and control samples (light colour)).

B-C. Dot plots of the means of QD705 fluorescence intensity (**B**) and cell percentage (**C**) for all the QD705- treated samples (triplicates) in all three independent experiments (N=1,2,3) divided into the three designated peaks of fluorescence (High-Intermediate-Low). Horizontal lines depict geometric means and error bars denote standard error. Statistical analysis was done using one-way ANOVA and Bonferroni's post-hoc multiple comparisons suggesting highly significant statistical differences (***) ($p < 0.001$).

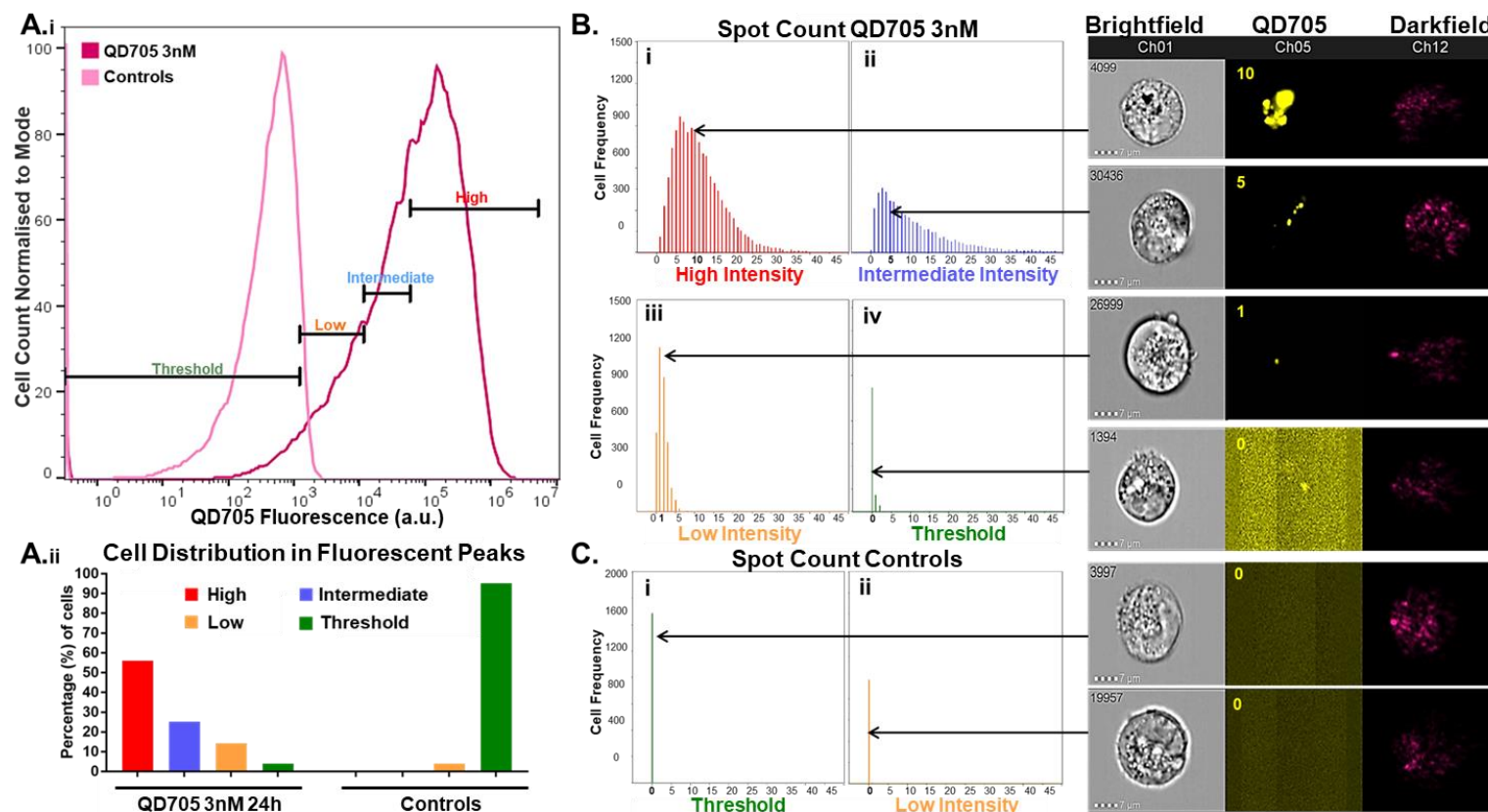


Figure 6.2. Uptake and Spot Count analysis of QD705 nanoparticles in DU145 cells reproduced by imaging flow cytometry.

A.(i) Imaging Flow Cytometry QD705 vs Control fluorescence intensity histograms 24 hours post QD705 labelling of DU145 cells. Four peaks of QD705 fluorescence intensity are designated by the High, Intermediate, Low and Threshold markings. **(ii)** Percentage of QD705-labelled and control cells distributed in each of the four peaks of QD705 fluorescence. **B-C.** Spot count analysis plots depicting the frequency of cells that exhibit numbers of QD705 spots per cell, with relevant exemplary images shown; **(B) QD705-treated cells:** **(i)** High QD705 uptake, **(ii)** Intermediate, **(iii)** Low and **(iv)** Threshold QD705 uptake and **(C) Control cells:** **(i)** Low or **(ii)** Threshold peak with background fluorescence (no QD705 signal). The Spot count analysis algorithm identifies intensity clusters and calculates their number, assuming a discrimination level of intensity at twice the intensity of the background. Ch01: Brightfield Channel, Ch05: QD705 channel (yellow), Ch12: Darkfield/SSC channel (pink), Scale Bars: $7\mu\text{m}$.

6.3.1.2. QD705 Uptake in DU145 Cells- Fluorescence Microscopy

Next QD705 uptake was determined with higher spatial resolution and detection using widefield fluorescence microscopy. This enabled the interrogation of uptake-heterogeneity in DU145 cells, and the influence of cell shape (e.g., area, convexity, roundness, and circularity), without having to remove the cells from the 2D substrate. QD705 uptake was performed as previously described, and 24h post-dosing the cells were fixed and labelled with DAPI and Actin-488 in order to image the nucleus and the cell cytoskeleton, respectively. Analysis showed that uptake of QDs by DU145 cells, resulted in perinuclear (probably endosomal) localisation of QD705, with cells exhibiting heterogeneity in staining ([Figure 6.3.C.i](#)). For single-cell image analysis, a method was devised to extrapolate both cell shape and QD705 fluorescence intensity measurements for every cell. Specifically, analysis involved the subtraction of background fluorescence from cells (using the control untreated cells) to improve the signal-to-noise ratio, then the manual segmentation of each cell to generate cell shape measurements (area, convexity, circularity, roundness), followed by automatic thresholding of QD705 fluorescence to extrapolate QD705 intensity measurements (n=551 cells were analysed); [Figure 2.1](#) shows details for the single-cell analysis method.

As expected, the heterogeneous QD705 uptake by DU145 cells was replicated in this experiment, as evident from the histogram of QD705 fluorescence intensity with three distinct peaks of fluorescence (High-Intermediate-Low) which represents the mean concentration of QD705 per cell ([Figure 6.3.A](#)). To determine if the total QD705 fluorescence of every cell correlated with its shape, a Pearson correlation coefficient was determined for cell area ([Figure 6.3.B.i](#)), circularity ([Figure 6.3.B.ii](#)), roundness ([Figure 6.3.B.iii](#)) and convexity ([Figure 6.3.B.iv](#)). No significant strong correlation between integrated QD705 fluorescence and DU145 cell area, convexity, circularity, or roundness was found ([Figure 6.3.B.i-iv](#)). An exemplary field-of-view image of cells with outlined High, Intermediate and Low QD705 intensity also demonstrated the high clustering of QD705 present in High-loaded cells ([Figure 6.3.C.i](#)), similarly to the previous experiment.

To summarise, this cross-platform analysis demonstrated the high reproducibility of this experiment in all the systems tested, underlining the advantage of using these established nanoparticles to benchmark the behaviour of DU145 cells in taking up QD705. These experiments demonstrated that uptake of QD705 in DU145 cells was heterogeneous, evident from the broad distribution of QD705 fluorescence intensity histograms that depict 3 distinct subpopulations of cells exhibiting high, intermediate, and low uptake (which was not correlated to the shape of these cells).

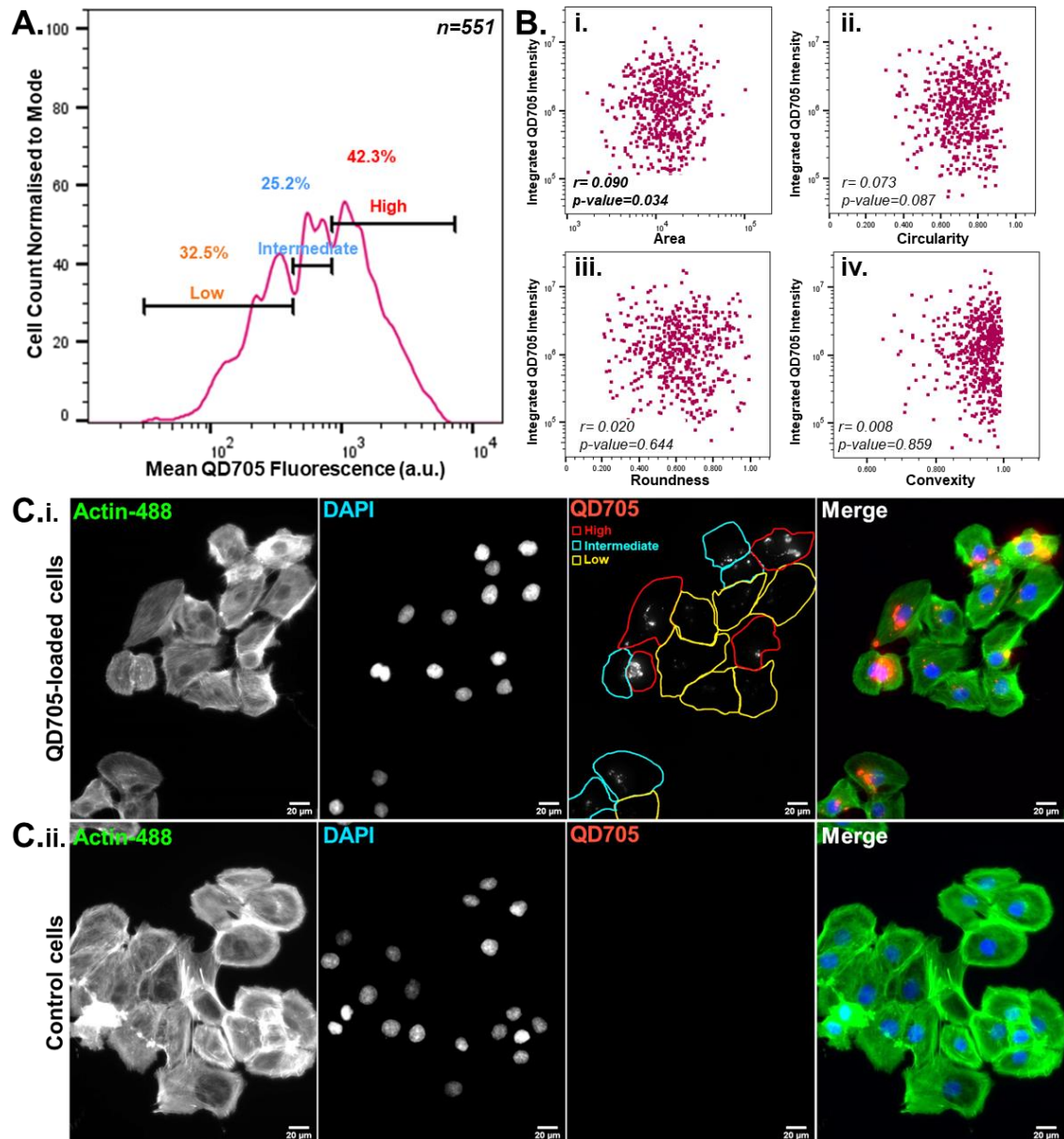


Figure 6.3. Single-cell image analysis QD705- labelled DU145 cells.

A. Histogram representing the distribution of QD705 fluorescence intensity after uptake of QDs by the DU145 cell population (24 hours post-dosing). Three distinct peaks of fluorescence are designated by the High (red), Intermediate (blue) and Low (orange) markings on the histogram. The percentage of QD705-labelled cells distributed in each peak of fluorescence are also shown. **B.** Dot plots representing the relationship of mean QD705 fluorescence to cell characteristics including: **(i)** area, **(ii)** circularity, **(iii)** roundness and **(iv)** convexity. On bottom left corner the Pearson Correlation Coefficient and the p-value for significance is noted (calculated via linear regression analysis) **C.** Exemplary images of **(i)** QD705-loaded cells and **(ii)** control cells showing Actin-488, DAPI, QD705 channel and the 3-channel merged image. Examples of High, Intermediate and Low intensity cells are outlined with red, blue, and orange lines in the QD705 channel (scale bar represents 20 μ m). Note that background fluorescence was subtracted from all QD705 images using the control cells; thus, control cells were omitted from further analysis but shown here for comparison (n=551 QD705-loaded cells were analysed).

6.3.2. Quantification of QD705 Retention in DU145 Cells

As the uptake of QD705 by DU145 cells was previously quantified, it was also important to determine how the QD705 signal would subsequently decay over time across the dividing cell population.

To address this, the fluorescence signal of QD705-treated cells was quantified up to 96h post-dosing via flow cytometry. Specifically, DU145 cells were loaded with QD705, and the signal per cell was measured at 24, 48, 72 and 96h post-labelling, via flow cytometry ([Figure 6.4](#), gating strategy shown in [Supplementary Figure 22](#)). Results showed that as DU145 cells divided, the QD705 fluorescence intensity distributions for the cell progeny decreased (shifted to the left), even though the signal was still detectable even after 96h post-dosing ([Figure 6.4.A](#)). To further support this, the geometric mean of QD705 fluorescence for each experiment (N=1,2,3) was also plotted to demonstrate the loss of fluorescence signal as the assay progressed (gMFI 24h=560, 48h=180, 72h=60 and 96h=20), which is equal to 67.1% loss (from 24 to 48h), 69.4% loss (from 48 to 72h), and 42.5% loss (from 72 to 96h) of QD705 fluorescence signal intensity ([Figure 6.4.B](#)).

In addition, the QD705 fluorescence intensity distributions broadened over time, as shown from the increase of coefficient of variation (CV=112, 140, 181 and 207 at 24-, 48-, 72- and 96-h post-dosing, respectively); shown in detail in [Supplementary Figure 24.A](#). The shifting of QD705 distribution was statistically significant between time-points, as evident by the Chi Square statistical analysis, which showed highly significant variance between the distributions over time ([Supplementary Figure 24.B](#)).

Furthermore, after categorising the cells in the High-Intermediate-Low QD705 uptake subpopulations (gates at 24h-timepoint, [Supplementary Figure 22](#) and [Figures 6.1-3](#)), a gradual shift was observed with the majority of cells being redistributed from the High (~50%) or Intermediate (~30%) peaks to the Lower peak after 96h (>65%) ([Figure 6.4.C](#)); thus underlining the decay of fluorescence signal over time.

These results suggested that the loss of QD705 fluorescence signal was inversely proportional to the increase of cell number (propagation of the DU145 population). Finally, besides the overall decrease of fluorescence over time, the broadening of the distributions also indicated that QD705 were assymmetrically partitioned in daughter cells, as symmetrical partition would entail an overall shift of the distribution and not broadening.

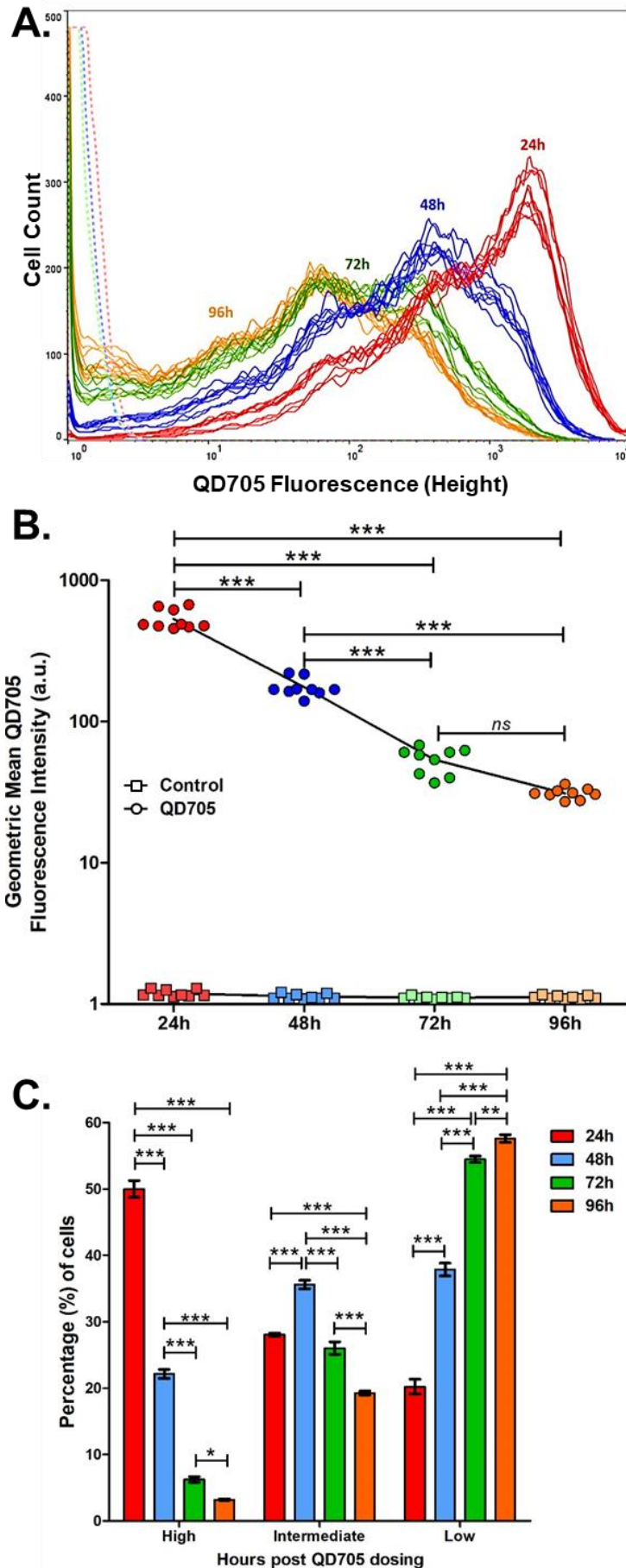


Figure 6.4. QD705 fluorescence signal distribution and decay over time in DU145 cells.

A. QD705 fluorescence intensity histograms representing an overlay of all three independent experiments (N=1,2,3) and all triplicate conditions. QD705-treated sample and control intensity histograms are indicated with solid and dotted lines respectively (24h: red, 48h: blue, 72h: green, 96h: orange).

B. Dot plot showing the geometric mean QD705 fluorescence measured over the progress of the 96-hour assay. **C.** Bar graph representing the percentage of DU145 cells distributed in the three QD705 fluorescence intensity peaks from 24 to 96 hours in 24-hour intervals.

Error bars represent the standard error between all datapoints of N=1,2,3, for each time-point. Statistical analysis was done using two-way ANOVA and Bonferroni's post-multiple comparisons test denoting statistical differences with * $p < 0.05$, ** $p < 0.001$ and *** $p < 0.001$ whereas ns denotes no statistical significance. Comparisons of variance between the QD705 distributions were also conducted using the Chi Square Distributions comparisons test and are shown in [Supplementary Figure 24](#).

6.3.3. Quantification of QD705 Uptake and Retention in Y201 Mesenchymal Stem Cells vs DU145 PCa Cells

Previous experiments investigated the uptake and decay of QD705 in the DU145 population; however, the behaviour of these nanoparticles is not necessarily conserved in other cells. In order to establish the baseline behaviour for dosing of nanoparticles (and then subsequently of sEVs) in a cell line that emulates cells of the pre-metastatic bone niche, the Y201 bone-marrow derived mesenchymal stem cell line (BM-MSCs) was utilised (126). The Y201 BM-MSCs were selected as they exhibit osteoblastic lineage, fibroblastic morphology similar to *in vivo* BM-MSCs, comparable expression of BM-MSC-specific markers and are immortalised, thus allowing for extended investigations (126). As fluorescence microscopy provided both high sensitivity for detection of QDs in DU145 cells, information on cell characteristics and quantification ability, it was selected to investigate dosing of QD705 by Y201 cells, in comparison to DU145 cells.

6.3.3.1. Y201 and DU145 24-Hour Uptake of QD705

DU145 and Y201 cells were labelled with QD705 for 1h (as previous experiments), followed by single-cell images analysis ([Figure 2.1](#)) to assess the fluorescence signal 24h and 72h post-dosing; thus, presenting the signal for uptake and decay respectively. It was observed that the 24-h QD705 fluorescence distribution of Y201 cells was significantly narrower than DU145 cells (CV=56.8 Vs 84.4, respectively), suggesting that Y201 cells exhibited a more uniform uptake of QDs per cell ([Figure 6.5.A.i,ii-24 h](#)). Even though Y201 cell uptake was more uniform than DU145 cells, the reproducible three distinct peaks of QD705 fluorescence could still be defined, with similar distribution of cell percentages in each peak, like DU145 cells i.e., ~55% of Y201 cells exhibited High, ~29% Intermediate and ~16% Low QD705 uptake ([Figure 6.5.C.i,iii](#)). Examples of cells with High, Intermediate and Low QD705 uptake are outlined in the QD705 channel for both DU145 and Y201 cells ([Figure 6.6.A.iii,C.iii respectively](#)).

Interestingly, Y201 cells also exhibited a significantly higher geometric mean QD705 fluorescence per cell (gMFI=1585 vs 955, respectively), thus suggesting higher QD705 uptake (~1.7-fold higher) than DU145 cells ([Figure 6.5.B](#)). Comparisons of Y201 and DU145 24-h uptake distributions supported this, as a statistically significant variance of more than 78 SDs was calculated between the two distributions ([Supplementary Figure 25.C](#)).

Furthermore, single-cell analysis enabled the quantification of different cell characteristics (area, convexity, roundness, circularity) followed by their comparison with

the total QD705 fluorescence to establish any potential correlation. Even though analysis showed that QD705 uptake in DU145 cells was not correlated with cell area ($r=0.04$) ([Figure 6.5.D.iii](#)), for Y201 cells there was a highly significant strong linear correlation between cell area and integrated (total) QD705 fluorescence per cell ($r=0.69$, $p\text{-value}=6.4\times 10^{-127}$) ([Figure 6.5.D.i](#)). On the other hand, no correlation of total QD705 fluorescence intensity with cell shape (convexity, roundness or circularity) was found for either DU145 or Y201 ([Supplementary Figure 26](#)). Of note, by comparing the distributions of cell area between Y201 and DU145 cells, we determined that the mean area of Y201 cells was significantly larger than the area DU145 cells (~3-fold larger mean cell area of Y201 cells, as shown in [Supplementary Figure 25.D](#)).

Besides quantifying the differences in QD705 uptake amplitude and heterogeneity between DU145 and Y201 cells, fluorescence imaging enabled the detection of an apparent difference in QD705 localisation. Specifically, whereas QDs were effectively localised in the perinuclear endosomal compartment in DU145 cells 24h post-dosing ([Figure 6.6.A.iv,v](#)), in the case of Y201 cells, in many instances QDs were found clustered either on the cell membrane or in-between cells on cell protrusions ([Figure 6.6.C.iv,v](#)). This might suggest that in 24h post-dosing QD705 nanoparticles were not completely endocytosed in Y201 cells.

6.3.3.2. Y201 and DU145 72-Hour Retention of QD705

In regards to nanoparticle retention, at 72h post-dosing, the Y201 QD705 fluorescence distribution had decreased (shifted to left) and was broadened, as shown by the increase of CV from 24h to 72h (CV=56.8 to 81.1 respectively, analysis shown in [Supplementary Figure 25.B](#)). This is consistent with the behaviour of DU145 cells, thus underlining that the decay of the QD705 signal is via asymmetrical partitioning of QD705 in the Y201 propagating cell population ([Figure 6.5.A- 72h](#)).

Comparisons of both Y201 and DU145 QD705 distributions at this time-point showed a statistically significant difference between cell lines (>24 SDs), albeit this was less significant than the 24h difference ([Supplementary Figure 25.C](#)). The shifting of the distributions was also evident from the higher percentage of Y201 and DU145 cells in the Low-QD705 fluorescence subpopulations at 72h compared to 24h (66.2% and 50.3% at 72h, respectively) as shown in [Figure 6.5.C.ii,iv](#). Moreover, the geometric mean QD705 fluorescence per cell was significantly lower 72h post-dosing again demonstrating signal decay over time, even though Y201 cells still exhibited higher QD705 signal/cell compared to DU145 cells (gMFI=607 vs 374, respectively, [Figure 6.5.B-72h](#)). This was also indicated from the QD705 fluorescent images, by the lower

signal per field of view and by the higher number of Intermediate- and Low-uptake cells (outlined blue, orange) (Figure 6.6.B.iii,D.iii for DU145 and Y201 respectively). Interestingly, at 72-h post-dosing the strong linear correlation of cell area to total QD705 intensity per cell was still apparent and was highly significant for Y201 cells ($r=0.70$, $p\text{-value}=7.6 \times 10^{-208}$) (Figure 6.5.D.ii), but not for DU145 cells ($r=0.17$, $p\text{-value}= 3.08 \times 10^{-10}$) (Figure 6.5.D.iv).

Finally, in regards to QD705 localisation, it was evident that at 72-h post dosing QD705 staining appeared perinuclear for both DU145 and Y201 cells, suggesting complete endocytosis of the QD705 load and distribution in daughter cells (Figure 6.6.B.iv,v and Figure 6.6.D.iv,v, respectively).

In conclusion, these results provided a baseline characterisation of the different behaviours of DU145 (PCa cell line) and Y201 (mesenchymal stem cell line) in QD705 nanoparticle dosing, with notable differences between cell lines in uptake heterogeneity, uptake magnitude per cell, cellular localisation of QD705 and retention of signal 72h post-dosing.

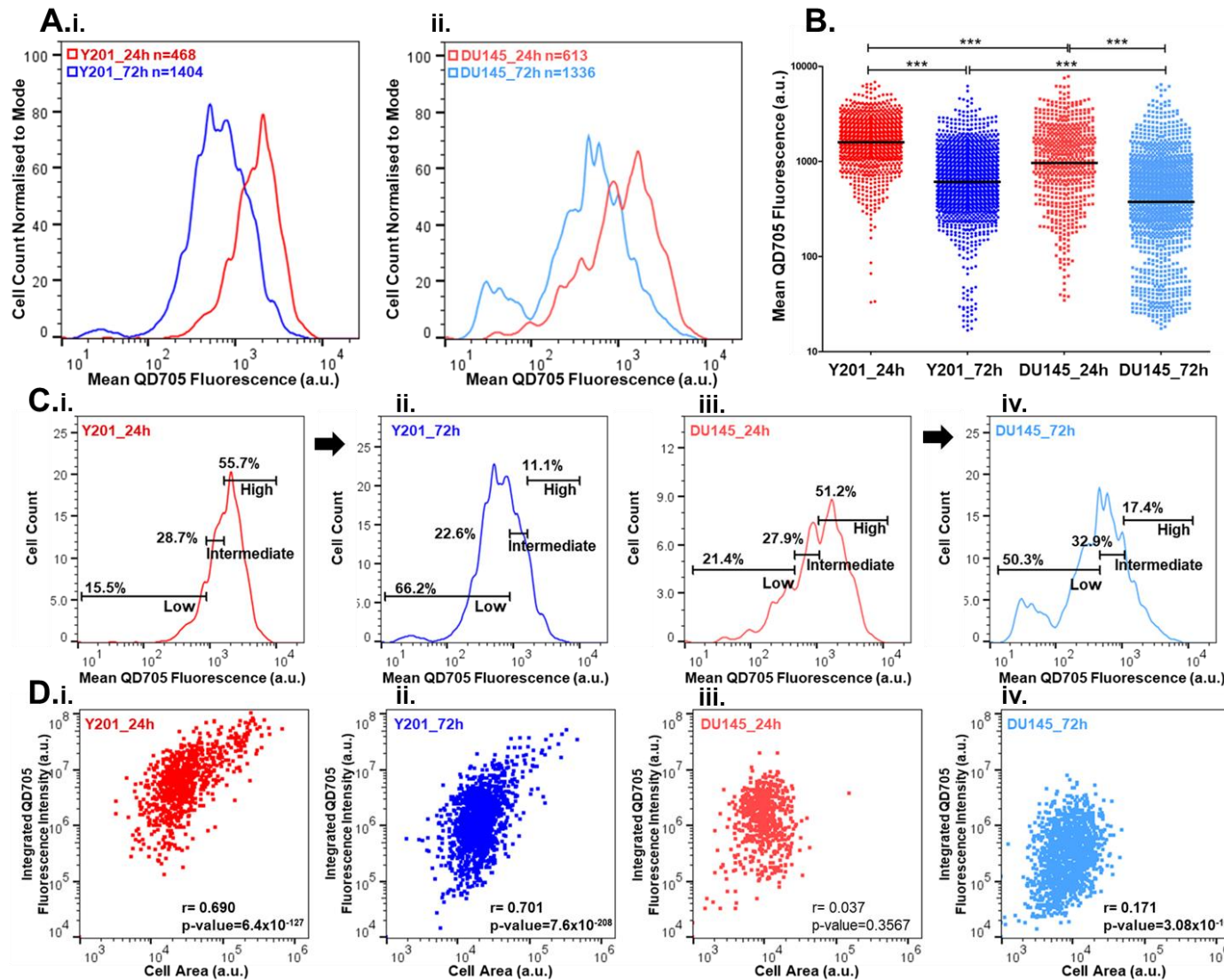


Figure 6.5. QD705 nanoparticle fluorescence signal uptake and retention in DU145 and Y201 cells.

A. Fluorescence intensity histogram overlays for QD705 uptake and retention (24h and 72h post-dosing) for Y201 (**i**) and DU145 (**ii**) cells (number of cells also included, top right). **B.** Dot plot of the mean QD705 fluorescence per cell for every cell line (24-72h). (Black line: Geometric mean). Statistical analysis was done using two-way ANOVA and Bonferroni's post-multiple comparisons (statistical differences, ***p<0.001). **C.** Histograms showing the percentage of cells distributed in each of the 3 QD705 fluorescence intensity peaks (High, Intermediate, Low) for Y201 cells (**i,ii**) and DU145 cells (**iii,iv**). **D.** Dot plots showing the relationship of cell area and total (integrated) QD705 fluorescence for Y201 cells (**i,ii**) and DU145 cells (**iii,iv**). Bottom right: Pearson Correlation Coefficient and p-value for significance (calculated via linear regression analysis).

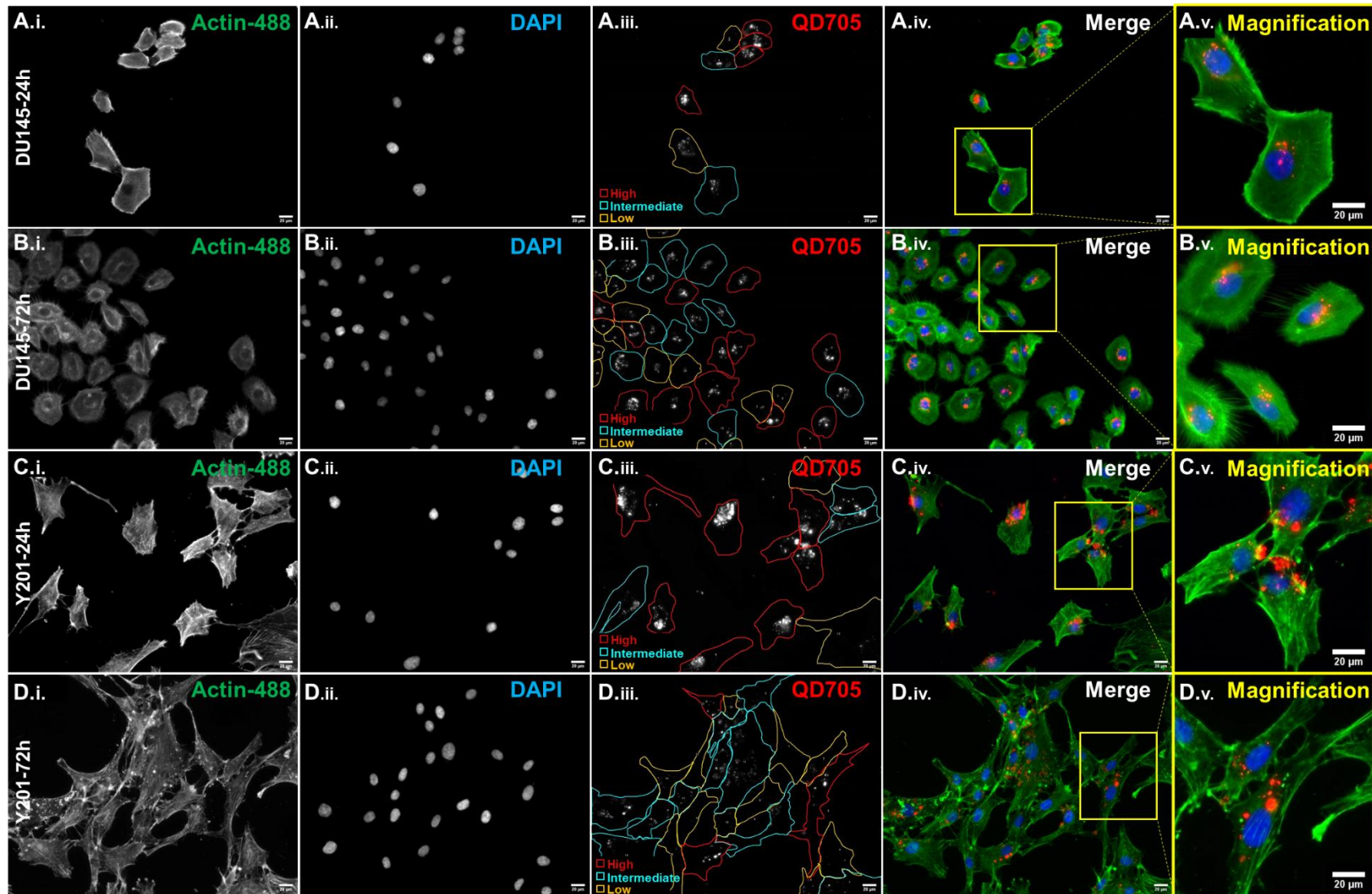


Figure 6.6. QD705 uptake and retention in DU145 and Y201 cells.

Figure and Figure Legend continue in next page ▶

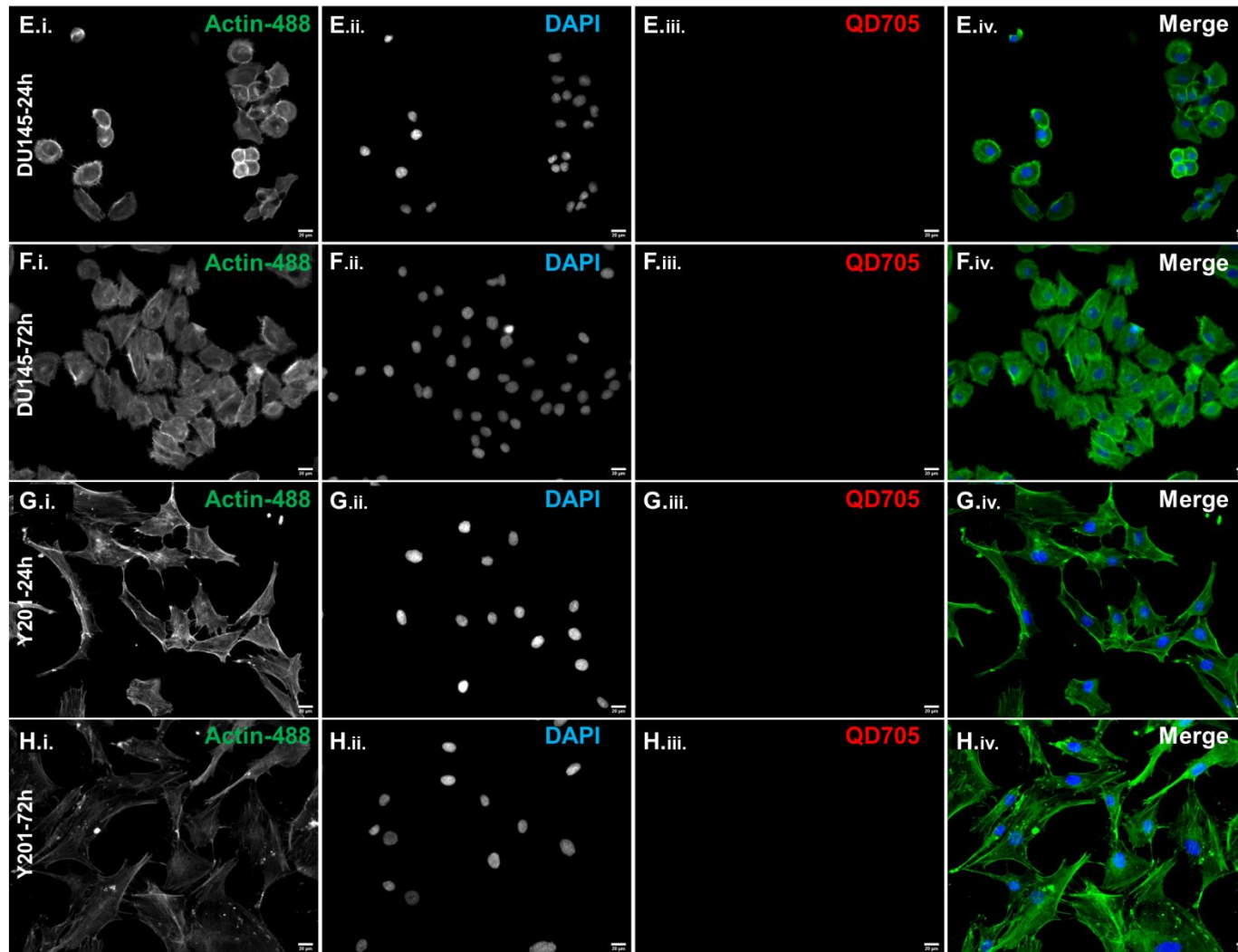


Figure 6.6. QD705 uptake and retention in DU145 and Y201 cells.

► *Figure continued from previous page*

A-D: Images depicting 24-hour uptake and 72-hour retention of QD705 signal in DU145 cells (A, B) and Y201 cells (C, D). Each row shows images of: **(i)** Actin-488 (labelling the cytoskeleton) **(ii)** DAPI (labelling the nucleus), **(iii)** QD705, **(iv)** the 3-channel merged image and **(v)** magnification of an area of interest focusing on the localisation of QD705 in each condition. Examples of High, Intermediate and Low intensity cells are also outlined with red, blue, and orange in the QD705 channel **(iii)**. **E-H:** Images depicting control cells for 24-hour and 72-hour time-points for DU145 cells (E, F) and Y201 cells (G, H). Each row shows images of: **(i)** Actin-488, **(ii)** DAPI, **(iii)** QD705, **(iv)** and the 3-channel merged image. Scale bars represent 20 μ m. Note that background fluorescence was subtracted from all QD705 images using the control cells; thus, control cells were omitted from further analysis but shown here for comparison purposes.

6.3.4. QD705 vs sEV Dosing in DU145 Cells

After benchmarking the uptake and retention of the “synthetic” QD705 nanoparticles where a conserved signal was observed in both cases, it gave context to investigate the dosing of the “biological” extracellular nanovesicles in DU145 and Y201 cells.

Preliminary dosing experiments were done with WT DU145-derived sEVs labelled with the AlexaFluor647-maleimide dye; a method established in the Tissue MicroEnvironment Group where the maleimide functional group of this dye forms a thio-ether linkage with the thiol (-S-H groups) of cysteines on sEV proteins (114, 115). sEVs labelled with this dye (EV-647) were used in an experiment to assess signal intensity and uptake in DU145 cells, in comparison to QD705 prior to using the novel CD81-Tdtomato sEVs. Hence, DU145 cells were labelled for 1h with 3nM QD705 and 50µg/ml EV-647 (concentration previously shown to efficiently label the AG02262 human lung fibroblasts (114, 115)), and the signal was assessed via fluorescence microscopy directly after labelling (0-h timepoint) and after 24h. It was observed that QD705 formed bright-intensity clusters at the cell membrane immediately after the 1-h labelling ([Figure 6.7.A](#)), while 24h later they exhibited bright punctate staining within the perinuclear cell compartment indicating complete cell internalisation ([Figure 6.7.B](#)). On the other hand, EV-647 showed a different spatiotemporal and signal intensity profile with dimmer, punctate staining already localised in the perinuclear cell compartment immediately after the 1-h labelling ([Figure 6.7.D](#)), which almost diminished 24h later ([Figure 6.7.E](#)). To conclude, it was observed that after cell internalisation, both QD705 and EV-647 exhibited punctate signal with perinuclear localisation; however, significant differences in signal intensity and cell delivery dynamics were noted, as shown by the faster internalisation and loss of EV-647 signal. This underlined the need for further investigation on EV-647 uptake (e.g. longer incubation with sEVs) and retention (e.g. shorter timepoints post-labelling, to examine signal decay).

Two preliminary flow cytometry experiments were done to address this. First, sEV uptake dynamics were investigated by dosing DU145 cells with 50µg/ml EV-647 for increasing time-periods (5min, 15min, 30min, 1h, 2h and 3h) followed by quantification of the signal per cell ([Supplementary Figure 27](#)). It was observed that the EV-647 signal was detectable (higher than the negative control samples) even after just 5 minutes of dosing; this signal/cell was shown to positively correlate with the increase of EV-647 incubation time (highest geometric mean EV-647 fluorescence after 3h of labelling) ([Supplementary Figure 27.B](#)). Second, sEV retention was assessed by dosing DU145 cells with 50µg/ml EV-647 for 3h (to achieve the highest signal/cell), followed by quantification of signal decay for up to 18.5h post-labelling (0, 1, 2, 3, 4, 6 and 18.5h

post-dosing). Interestingly, for the first 4h post- sEV dosing, the geometric mean fluorescence seemed to increase (even though sEVs were washed from cells), but eventually started decaying 6h post-dosing, with the lowest signal observed at 18.5h post-EV labelling ([Supplementary Figure 27.C](#)); however, the geometric mean EV-647 signal at this timepoint was still 12-fold higher than the negative controls.

Due to the fact that AlexaFluor647-Maleimide dye binds to cysteines, it might not be absolutely sEV-specific, suggesting that the observed fluorescence signal may not necessarily reflect the EV compartment entirely, as it may occur by “leakage” of the dye to other cysteine-rich cell compartments. These experiments were useful for optimisation, but underline the importance of the endogenously-fluorescent CD81-Tdtomato sEVs. As the Tdtomato fluorescent protein is directly conjugated to an EV transmembrane protein, any observed signal is associated with the presence of EVs and/or EV cargo in the cell; thus, further investigation into EV uptake and retention dynamics was done utilising the endogenously fluorescent CD81-Tdtomato sEVs.

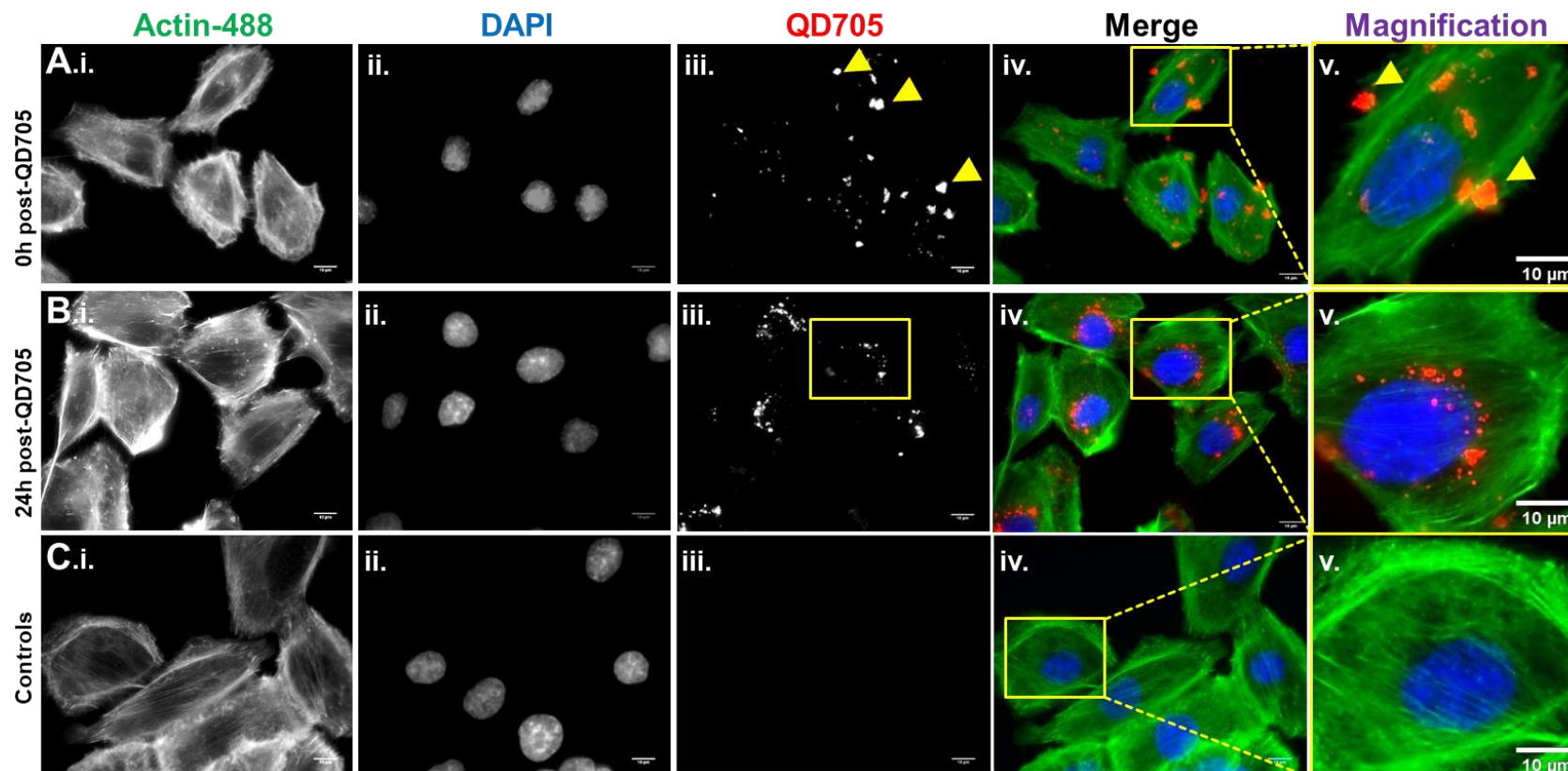


Figure 6.7. QD705 and EV-647 dosing in DU145 cells.

A. DU145 cells labelled with Actin-green (**i**) and DAPI (**ii**) and loaded with QD705 (directly after labelling, 0h post-dosing), showing bright intensity clusters (yellow arrows) (**iii**), localised on the cell membrane (**iv**). Magnified area of interest shows details of QD705 clusters on cell surface (yellow arrows) (**v**). **B.** DU145 cells labelled with Actin-green (**i**) and DAPI (**ii**) and loaded with QD705 (24-hours post-dosing), showing spread punctate, perinuclear localisation (yellow rectangle) (**iii,iv**). Magnified area of interest shows details of QD705 perinuclear staining (**iv**). **C.** Control cells labelled with Actin-green (**i**) and DAPI (**ii**) show no background fluorescence in the QD705 channel (**i-v**). Scale Bars represent 10 μ m. Experiment was repeated 3 times (N=3) and images shown are representative Z-series reconstructed to a 2D image by maximum intensity projection.

Figure and Legend continue on next page ►

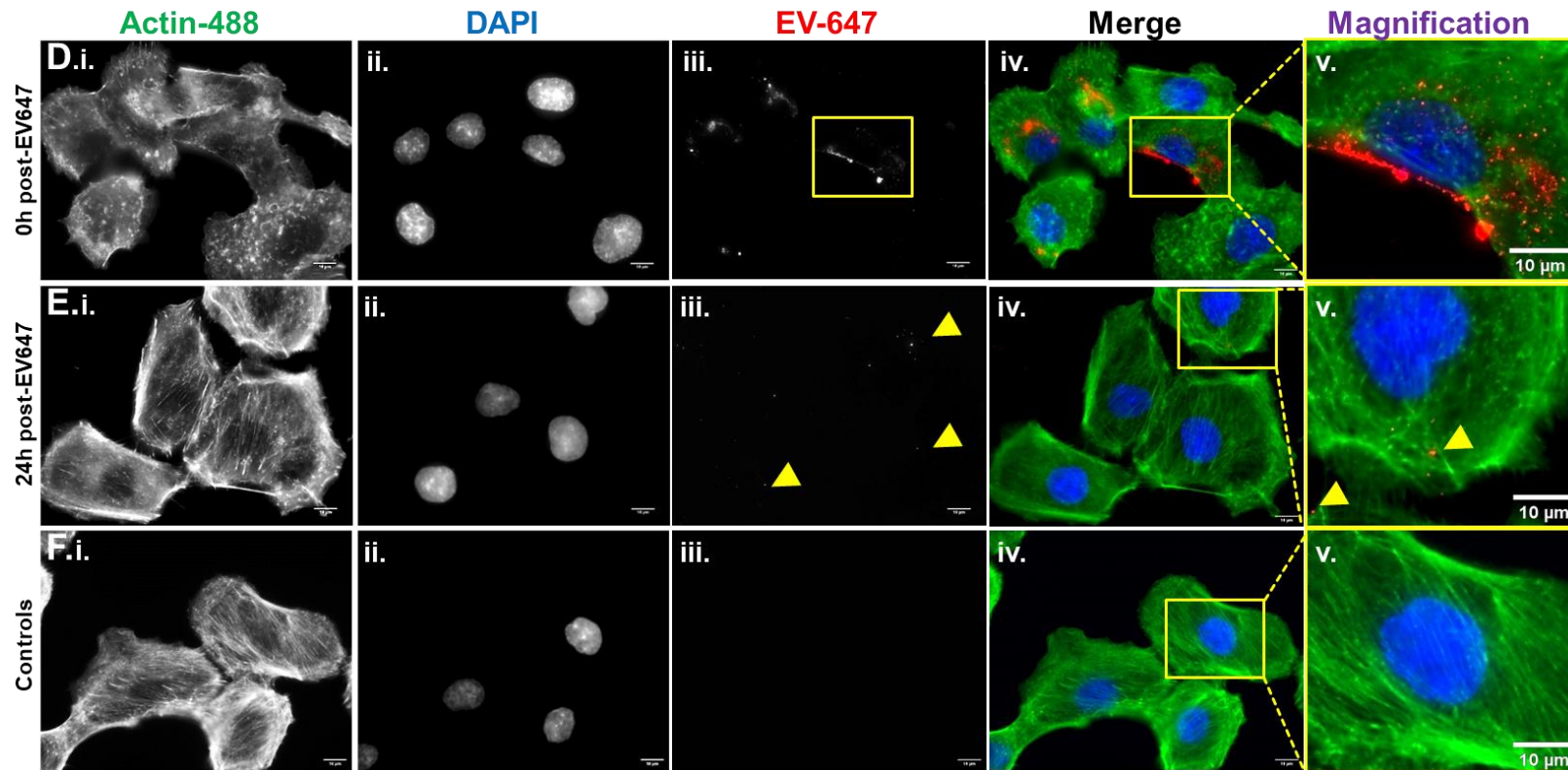


Figure 6.7. QD705 and EV-647 dosing in DU145 cells.

Figure and Legend continued from previous page ►

D. DU145 cells labelled with Actin-green (**i**) and DAPI (**ii**) and loaded with EV-647 (AlexaFluor647-Maleimide labelled sEVs) directly after labelling (0h post-dosing) showing a spread, punctate perinuclear staining of lower intensity than QD705 (yellow rectangle) (**i,ii**). Magnified area of interest shows details of EV-647 perinuclear localisation(**iii**). **E.** DU145 cells labelled with Actin-green (**i**) and DAPI (**ii**) and loaded EV-647 (24-hours post-dosing), show that signal diminished severely (yellow arrows) (**i,ii**). Magnified area of interest shows details of EV-647 signal decay with no specific localisation (**iii**). **F.** Control cells labelled with Actin-green (**i**) and DAPI (**ii**) show no background fluorescence in the EV-647 channel (**i-iii**). Scale Bars represent 10µm. Experiment was repeated 3 times (N=3) and images shown are representative Z-series reconstructed to a 2D image by maximum intensity projection.

6.3.5. Acute CD81-Tdtomato sEV Uptake and Retention in DU145 Cells

Previously, in Results Chapters 3 and 5, the fluorescence signal of DU145-derived CD81-Tdtomato sEVs was characterised via Point-Spread Function analysis, fluorescence microscopy and Apogee nanoscale flow cytometry, and was found significantly brighter than GFP-CD63 sEVs. Especially for Bioreactor-derived EVs, the GFP-CD63 sEV signal was diminished due to loss of fluorescence of the parental cells in the Bioreactors, over time. Thus, CD81-Tdtomato sEVs were used to study sEV uptake and retention dynamics in the parent-cancer cell line of origin, DU145 PCa cells. Furthermore, as seen above with the EV-647 experiments, the sEV-associated fluorescence signal was virtually lost 24h post-dosing; thus, it was firstly essential to address short-term sEV uptake dynamics and determine the time limitations for sEV dosing.

Acute delivery of CD81-Tdtomato sEVs was firstly investigated in the DU145 PCa cells, to determine how these sEVs are taken up and retained by their cells of origin. DU145 cells were dosed with 100µg/ml CD81-Tdtomato sEVs for increasing periods of time (1, 2 and 3h), to assess whether longer exposure to sEVs would result in a greater uptake per cell, determined through the measurement of Tdtomato fluorescence intensity. Following dosing, DU145 cells were imaged live, and single-cell analysis was conducted to quantify the Tdtomato signal per cell and the localisation of sEVs after uptake for each timepoint ([Figure 6.8.A-C](#)). Single-cell image analysis was done by manual segmentation of every cell, removal of background fluorescence using autofluorescence from control cells ([Figure 6.8.D](#)), and then thresholding using Li's Automatic Thresholding Method ([Figure 2.2.A](#) for detailed method). Analysis demonstrated that after just 1h of CD81-Tdtomato sEV dosing, all DU145 cells exhibited internalised sEVs, evident by the intracellular punctate Tdtomato signal which was, in some cases, perinuclear ([Figure 6.8.A.iii](#)). This was also observed when DU145 cells were dosed for 2- and 3h with CD81-Tdtomato sEVs ([Figure 6.8.B,C.iii](#) respectively). Even though the CD81-Tdtomato signal appeared punctate, larger clusters of signal was also present in different areas, demonstrating the potential flocculation of sEVs during dosing ([Figure 6.8.A-C.i](#), blue arrows). Cell internalisation was also demonstrated by the capture of some CD81-Tdtomato sEV signal seemingly in-motion, which was evident from the presence of a "string" signal ([Figure 6.8.A.i-C.i](#), green arrows). This "string" signal was generated by the Z-stack projection of an object moving fast laterally, thus being detected in different spatial coordinates as the Z-stack image was captured.

Interestingly, CD81-Tdtomato sEVs were also present in the extracellular space but seemed immobile and were not completely internalised by cells, even after 3h of incubation ([Figure 6.8.A-C](#), cyan circles).

To investigate whether sEV uptake was associated with the DU145 cell characteristics, correlation analysis was performed using linear regression to determine the Pearson Correlation coefficient and the p-value for significance ([Supplementary Figure 28](#)). Interestingly a significant linear correlation was found between DU145 cell area and total CD81-Tdtomato sEV signal per cell ([Figure 6.8.G](#), [Supplementary Figure 28.Ai,B.i](#)), but no correlation was found for cell circularity, convexity or roundness ([Supplementary Figure 28.A-C.ii-iv](#)). As the cell area associated with the total Tdtomato fluorescence intensity/cell, the total (integrated) intensity was not preferred as a measurement ([Supplementary Figure 28.D](#)). Potential changes in cell shape might occur when cells reach confluency, and this could affect the total intensity per cell. Thus, the mean Tdtomato fluorescence/cell measurement was used to represent the concentration of Tdtomato sEVs per cell ([Figure 6.8.E](#)). Interestingly, single-cell image analysis showed no significant differences in the mean Tdtomato signal per cell between the different dosing times, suggesting that the concentration of CD81-Tdtomato sEVs per cell is stable ([Figure 6.8.E](#)); however total fluorescence intensity (integrated) was seen to increase over the longer incubation ([Supplementary Figure 28.D](#)). In addition, we observed a large deviation of mean Tdtomato signal per cell suggesting uptake heterogeneity for sEVs ([Figure 6.8.E](#)). This observed stability of the mean CD81-Tdtomato sEV concentration was also represented by the similarities in the mean Tdtomato fluorescence distributions between the different dosing times, with the broad fluorescence distributions also representing heterogeneity in sEV uptake ([Figure 6.8.F](#)).

When this experiment was repeated by flow cytometry, we observed a time-dependent increase in the total CD81-Tdtomato fluorescence signal per cell ([Supplementary Figure 29](#)), which was a similar observation to the fluorescence microscopy data when the total CD81-Tdtomato intensity was plotted ([Supplementary Figure 28.D](#)). The flow cytometry experiment also demonstrated a time-dependent increase in the percentage of labelled cells compared to shorter timepoints (68% at 3h compared to 35% at 1h of dosing, [Supplementary Figure 29](#)); however, this was not representative of the live-cell fluorescence imaging experiment where virtually all the cells analysed had taken up sEVs, suggesting that flow cytometry may not be a sensitive enough platform to detect the cells with low levels of CD81-Tdtomato sEVs due to the dim fluorescence signal/cell. Hence, the next CD81-Tdtomato sEV dosing studies were performed using widefield fluorescence microscopy.

Figure 6.8. CD81-Tdtomato sEV dosing in DU145 cells by fluorescence microscopy.

Figure Legend on next page ►

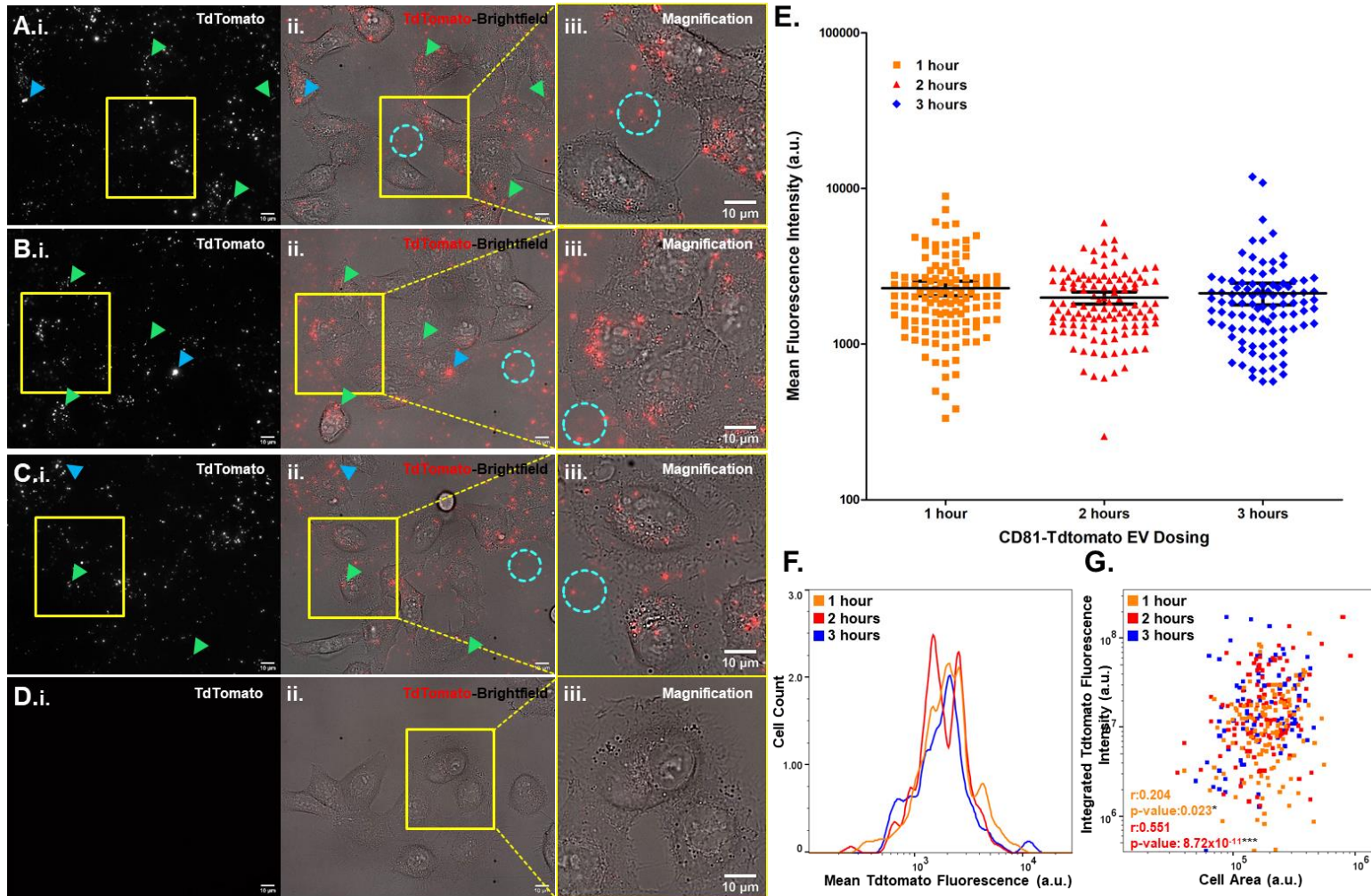


Figure 6.8. CD81-Tdtomato sEV dosing in DU145 cells by fluorescence microscopy.

◀ *Figure on previous page*

A-D. Images depicting the uptake of CD81-Tdtomato sEVs (100µg/ml) in DU145 cells for 1-hour (**A**), 2-hours (**B**) and 3-hours (**C**) of dosing, along with Control cells (**D**), showing:(**i**) Tdtomato, (**ii**) Tdtomato-Brightfield Merged channel and (**iii**) Magnification of area of interest. Green arrows: internalised Tdtomato-sEVs with motion (string signal). Blue arrows: large clusters of Tdtomato-signal. Cyan circles: sEVs in extracellular space. Scale bars represent 10µm. **E.** Dot plot showing the distribution of mean Tdtomato fluorescence intensity per cell for CD81-Tdtomato sEV incubation of 1 hour (n=124), 2 hours (n=119) and 3 hours (n=100). The mean Tdtomato signal per cell represents the concentration of CD81-Tdtomato sEVs per cell. Horizontal black lines represent the mean of means and error bars represent 95% CI, whereas statistical analysis was done using one-way ANOVA and Bonferroni multiple comparisons post-test, however no statistical differences were observed ($p>0.05$). **F.** Mean Tdtomato Fluorescence histogram overlays represent uptake of CD81-Tdtomato sEVs (100µg/ml) in DU145 cells, when dosed for 1-hour (orange), 2-hours (red) and 3-hours (blue). **G.** Scatter plot overlays of DU145 cell area per cell Vs integrated Tdtomato fluorescence for the 1-hour (orange), 2-hours (red) and 3-hours (blue) CD81-Tdtomato dosing. Statistically significant linear correlation of cell area with total (integrated) Tdtomato fluorescence was found for the first 2 hours of sEV-dosing, after linear regression analysis was done showing the Pearson Correlation Coefficients and p-values in bottom left of plot; linear regression analysis was also conducted for integrated Tdtomato fluorescence Vs cell roundness, convexity and circularity and results are shown in [Supplementary Figure 30](#).

6.3.6. Quantification of CD81-Tdtomato sEV Uptake and Retention in DU145 Compared to Y201 Cells.

As previous experiments demonstrated a differential behaviour in uptake and retention of QD705 by Y201 cells, compared to the established behaviour of DU145 cells, it was important to determine whether this deviation would also be apparent in the uptake and retention of CD81-Tdtomato sEVs. Thus, we aimed to determine how Y201 take up and retain EV-signal when they are acutely or chronically exposed to CD81-Tdtomato sEVs. As uptake of sEVs was previously addressed in DU145 cells (CD81-Tdtomato sEVs and EV-647) and as they are the cell line of origin for both sEV types, these cells would be also used for comparison.

6.3.6.1. Acute CD81-Tdtomato sEV Delivery and Retention in Y201 and DU145 Cells

The uptake and retention of CD81-Tdtomato sEVs was assessed after acute delivery in Y201 and DU145 cells. As dosing with CD81-Tdtomato sEVs for 1 to 3h did not significantly alter the concentration of sEVs in DU145 cells ([Figure 6.8](#)), 1-h of sEV dosing was chosen as an acute exposure of Y201 cells (and of DU145 cells for comparison). In addition, as the previous EV-647 experiment addressed how signal was retained in DU145 cells after 24h ([Figure 6.7](#)), assessment of CD81-Tdtomato signal retention was done directly after acute delivery (0h post-dosing) as well as 24- and 48h post-dosing. Furthermore, three different concentrations of CD81-Tdtomato sEVs were used (50, 100 and 200µg/ml), to determine if there is a potential dose-response difference between Y201 and DU145 cells. This experiment was conducted via fluorescence microscopy followed by single-cell image analysis following a similar method as previous experiments ([Figure 2.2](#)).

CD81-Tdtomato sEV Uptake

To begin with, single-cell image analysis of Y201 cells showed a dose-dependent uptake of CD81-Tdtomato sEVs; dosing with 200µg/ml resulted in significantly higher concentration of sEVs per cell (higher mean Tdtomato signal/cell, gMFI=1100) than the lowest concentration (50µg/ml, gMFI=750) and higher than the dosing with 100µg/ml sEVs (gMFI=1000, even though that was not statistically significant) ([Figure 6.9.A.i](#)). Exemplary images demonstrate this dose-dependent uptake for every CD81-Tdtomato sEV concentration tested ([Figure 6.10.B.vi-D.vi](#)). DU145 cells also exhibited a similar

trend ([Figure 6.10.Bi-Di](#)); however, no statistical significance was found after comparing the mean Tdtomato signal/cell between the different sEV concentrations (gMFI=650,700 and 850 for 50, 100 and 200µg/ml) as shown in [Figure 6.9.A.ii](#). In addition, Y201 cells exhibited overall higher uptake of sEVs overall compared to DU145 cells, as evident from the statistically higher mean Tdtomato signal/cell for every concentration (except for the low dose of 50µg/ml which was not significantly different) ([Figure 6.9.B](#)).

Moreover, both cell lines demonstrated heterogeneous uptake of sEVs (for every concentration) as evidenced by their broad Tdtomato fluorescence uptake distributions, albeit DU145 cells exhibited slightly greater heterogeneity due to wider distribution of sEV-signal compared to Y201 cells (range of $CV_{DU145}=21.1-47.7$ and $CV_{Y201}=27.1-32.5$ for all doses tested), as shown in [Figure 6.9.C](#) (0h post-dosing timepoint). This difference in distribution of sEV-signal between DU145 and Y201 cells can be attributed to the higher number of low-dosed DU145 cells that increase the CV of these distributions.

Overall, this heterogeneous uptake of sEVs seemed to be partly attributed to cell heterogeneity; this was evident from the strong linear correlation of Y201 cell area to the total Tdtomato signal/cell, for all concentrations of sEVs tested ([Figure 6.9.D.i](#)). For DU145 cells, the correlation of cell area to total Tdtomato signal/cell was weaker compared to Y201 cells and was not statistically significant ([Figure 6.9.D.ii](#)). On the other hand, the uptake of CD81-Tdtomato sEVs could not be correlated to any other cell characteristic (circularity, roundness, or convexity) for DU145 nor Y201 cells ([Supplementary Figure 30](#)).

Finally, fluorescence images showed that Y201 cells exhibited differential localisation of sEVs compared to DU145 cells ([Figure 6.10.B-D](#)). Specifically, whereas DU145 cells had internalized, punctate and mostly perinuclear Tdtomato signal immediately after the 1h of dosing ([Figure 6.10.B-D.i-iii](#)), in Y201 cells, even though the Tdtomato signal appeared internalized and punctate, its localisation was dispersed through the cytosol with limited perinuclear signal ([Figure 6.10.B-D.iv-vi](#)). Of note, CD81-Tdtomato sEV signal was also present in the extracellular space for both cell lines highlighting the excess availability of sEVs for every dose tested ([Figure 6.10.B-D](#), cyan circles).

CD81-Tdtomato sEV Retention

Assessment of retention of CD81-Tdtomato sEVs 24- and 48h post-dosing showed that Tdtomato signal significantly diminished in DU145 cells. Specifically, single-cell image analysis demonstrated a statistically significant decrease of the mean Tdtomato fluorescence signal per cell ([Figure 6.9.A.ii](#), lowest signal at 48h, gMFI=200-300). In addition, the distribution of Tdtomato fluorescence appeared to shift to lower intensities

and broaden for all the tested doses ([Figure 6.9.C.iv-vi](#)). Exemplary images 24h and 48h post-dosing demonstrate the loss of Tdtomato fluorescence signal, with DU145 cells shown to have processed the majority of sEVs, except for some isolated small clusters of Tdtomato signal with perinuclear localisation ([Figure 6.10.F-H.i-iii](#) and [Figure 6.10.J-L.i-iii](#) for 24h and 48h respectively). Interestingly, some CD81-Tdtomato sEVs were still present in the extracellular space and were not internalized by DU145 cells even at 48h post-dosing ([Figure 6.10.F-H.i-iii](#) and [Figure 6.10.J-L.i-iii](#), cyan circles).

In striking contrast to DU145, Y201 cells exhibited an increase in the mean Tdtomato signal per cell 24h post-dosing. Single-cell image analysis showed a significant increase of the mean Tdtomato fluorescence signal per cell ([Figure 6.9.A.i](#)) and shifting of the Tdtomato fluorescence distributions to higher intensity for all doses tested ([Figure 6.9.C.i-iii](#)). In addition, images demonstrated a dramatic change in Tdtomato signal localisation, from previously cytosolic to now being completely perinuclear ([Figure 6.10.F-H.iv-vi](#)). Furthermore, the majority of CD81-Tdtomato sEVs that were previously seen in the extracellular space disappeared 24h post-dosing ([Figure 6.10.F-H.iv-vi](#)).

Despite this increase of Tdtomato fluorescence signal at 24-h, Y201 cells started exhibiting slight loss of signal 48-h post-dosing, albeit the mean Tdtomato signal per cell was still equal or even exceeded the initial mean fluorescence signal during uptake (0h-post acute sEV delivery) ([Figure 6.9.Ai](#)). This was also apparent from the Tdtomato fluorescence distributions which shifted to lower intensities compared to 24h post-dosing ([Figure 6.9.C.i-iii](#)); however, the CD81-Tdtomato sEV signal still appeared bright, punctate and strongly perinuclear ([Figure 6.10.J-L.iv-vi](#)), similarly to 24h prior.

Comparisons of DU145 and Y201 cells 24- and 48-h post-dosing underlined these prominent differences in CD81-Tdtomato sEV retention dynamics, as evidenced from the highly significant differences in mean Tdtomato fluorescence per cell ([Figure 6.9.B](#)) and difference in localisation of Tdtomato signal between cell lines ([Figure 6.10.F-H,J-L](#)).

To summarize, this experiment demonstrated that both DU145 and Y201 cells exhibited heterogeneous and dose-dependent uptake of sEVs, with Y201 cells overall showing higher concentration of sEVs per cell; however, localisation of signal was predominantly not perinuclear suggesting differential uptake dynamics than DU145 cells. Retention dynamics of CD81-Tdtomato sEVs were also different between DU145 and Y201 cells, with DU145 cells losing the majority of Tdtomato signal 24h post-dosing, while Y201 cells exhibiting an initial increase and then decrease of signal, 24- and 48h after the acute sEV delivery. These results potentially suggest a temporally different uptake and retention of sEVs in Y201 cells, which is also evident from the slower changes in localisation of intracellular CD81-Tdtomato signal and underlined the need for a longer investigation of sEV retention in these cells.

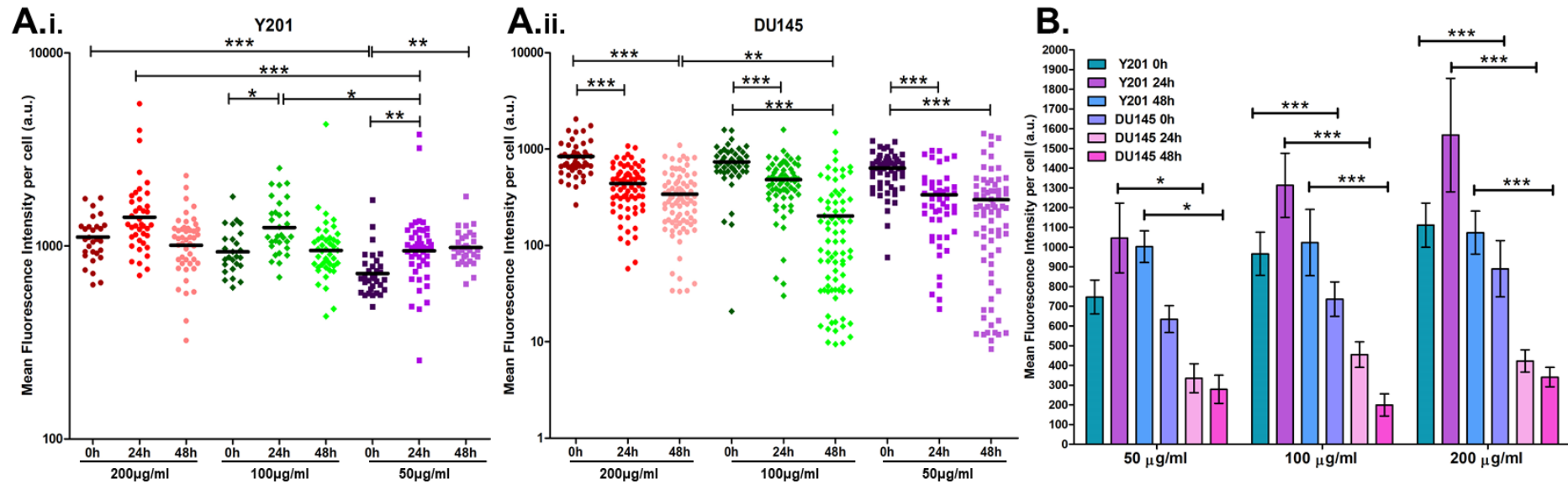


Figure 6.9 CD81-Tdtomato sEV uptake and retention after acute sEV-delivery comparing DU145 and Y201 cells.

A. Dot plots demonstrating the mean Tdtomato fluorescence per cell for **(i)** Y201 and **(ii)** DU145 cells labelled with CD81-Tdtomato sEVs at 0, 24 and 48-hours post-dosing for the 50,100 and 200µg/ml concentrations. **B.** Bar graph showing the differences in uptake/retention between Y201 and DU145 for each sEV dose. Statistical analysis was done using two-way ANOVA and Bonferroni's post-multiple comparisons (statistical differences denoted with * $p < 0.05$, ** $p < 0.01$ and *** $p < 0.001$) and error bars represent the 95% CI (confidence interval).

Figure and Legend continue to next page ►

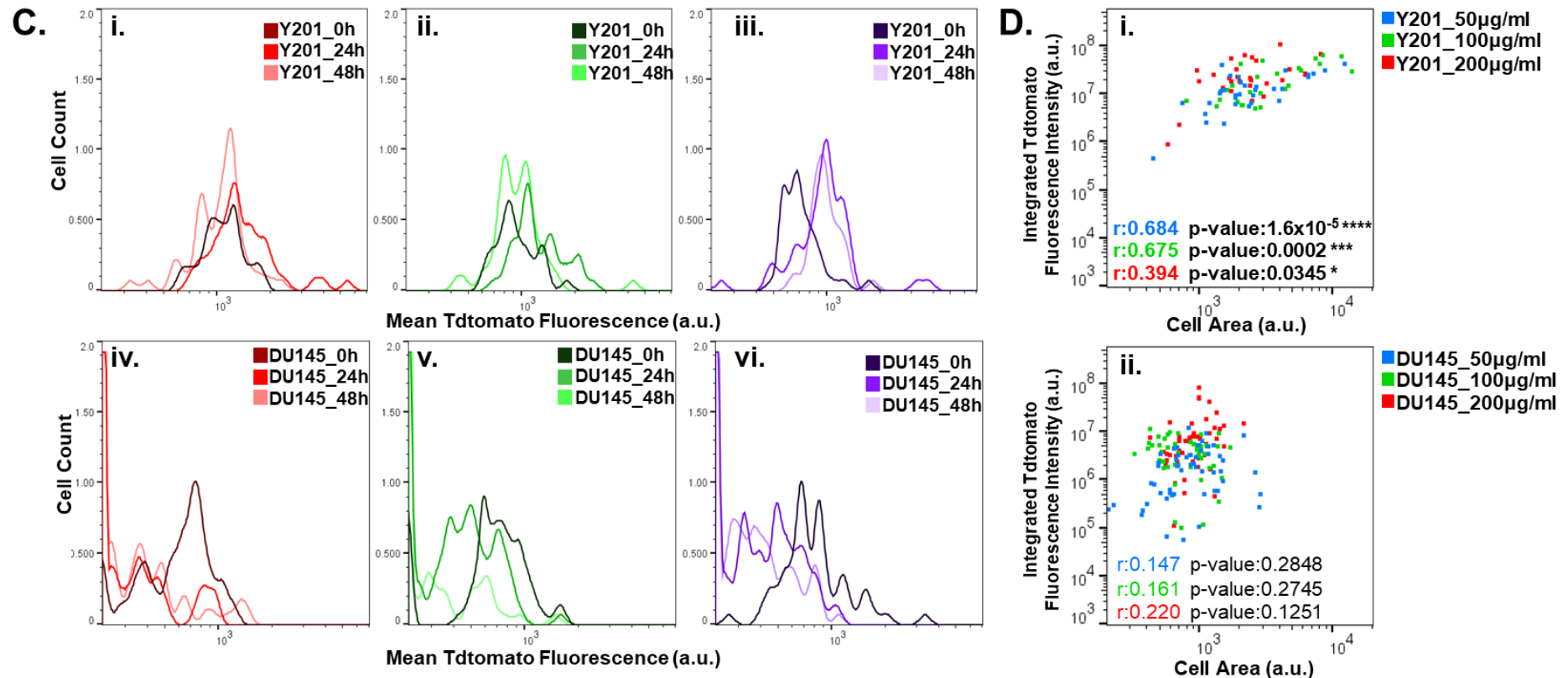


Figure 6.9. CD81-Tdtomato sEV uptake and retention after acute sEV-delivery comparing DU145 and Y201 cells.

◀ *Figure continued from previous page*

C. Histogram overlays showing the distributions of Tdtomato Fluorescence intensity for each timepoint in Y201 cells: **(i)** 200µg/ml, **(ii)** 100µg/ml and **(iii)** 50µg/ml and for DU145 cells: **(iv)** 200µg/ml, **(v)** 100µg/ml and **(vi)** 50µg/ml. **D** Scatter plot overlays for **(i)** Y201 cell- and **(ii)** DU145 cell- Area Vs Total (integrated) Tdtomato fluorescence during sEV uptake (0h-timepoint). Linear regression analysis calculated the Pearson correlation coefficients and p-values which are shown on the plots; statistically significant correlations are designated with bold letters.

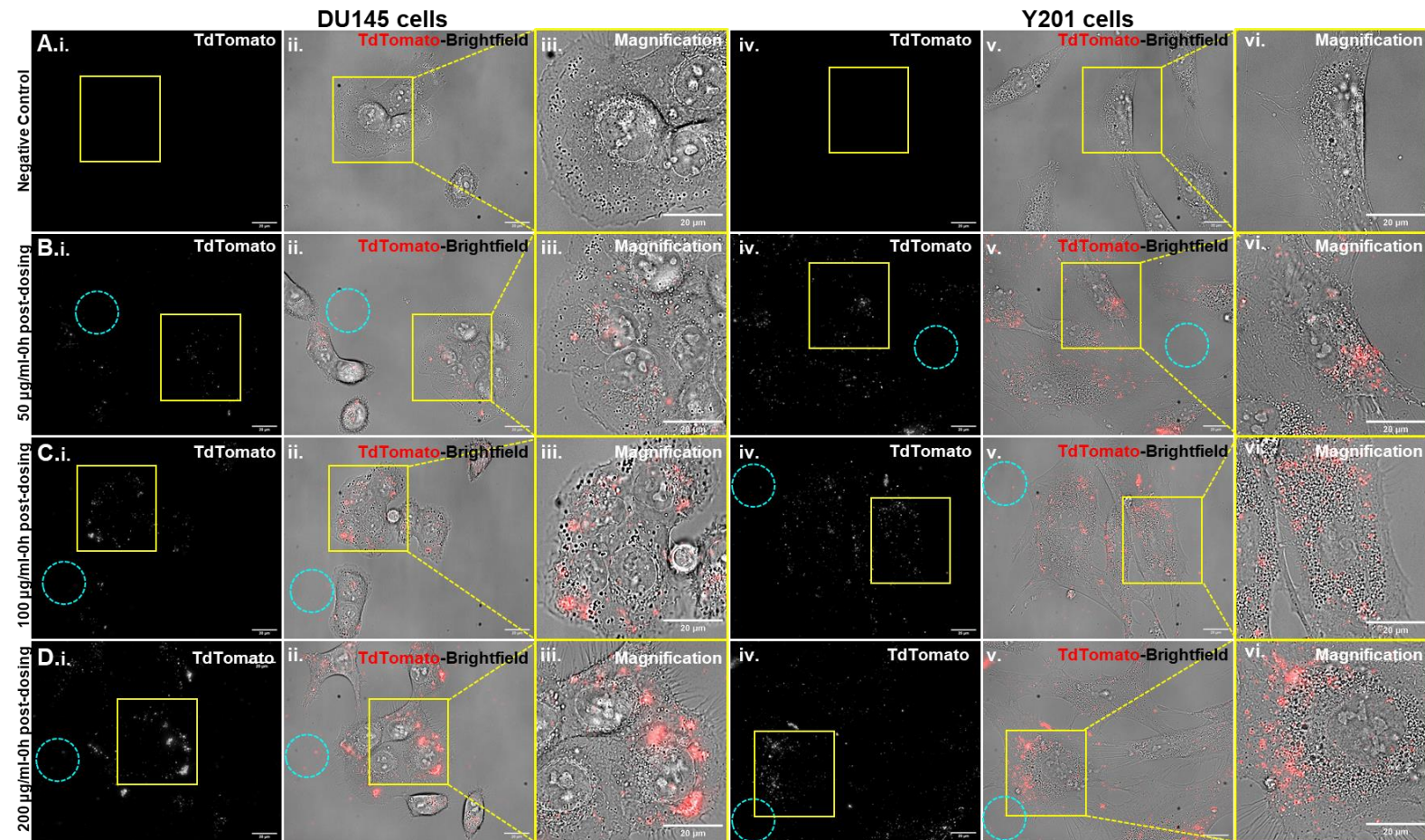


Figure 6.10. Representative images of acute CD81-Tdtomato sEV dosing in DU145 and Y201 cells.

A-D. Uptake of CD81-Tdtomato sEVs directly after 1 hour of incubation (**0h-post dosing**) for the following concentrations: **(A)** 0µg/ml (controls), **(B)** 50µg/ml, **(C)** 100µg/ml and **(D)** 200µg/ml, in DU145 cells (**i-iii**) and Y201 cells (**iv-vi**). Image series include: the Tdtomato channel (**i,iv**), the Tdtomato-Brightfield Merged channel (**ii,v**) and a magnification of area of interest (**iii,vi**) for DU145 and Y201 cells respectively. Cyan circles depict immobilised sEVs in the extracellular space. Scale bars represent 20µm.

Figure continues on next page ►

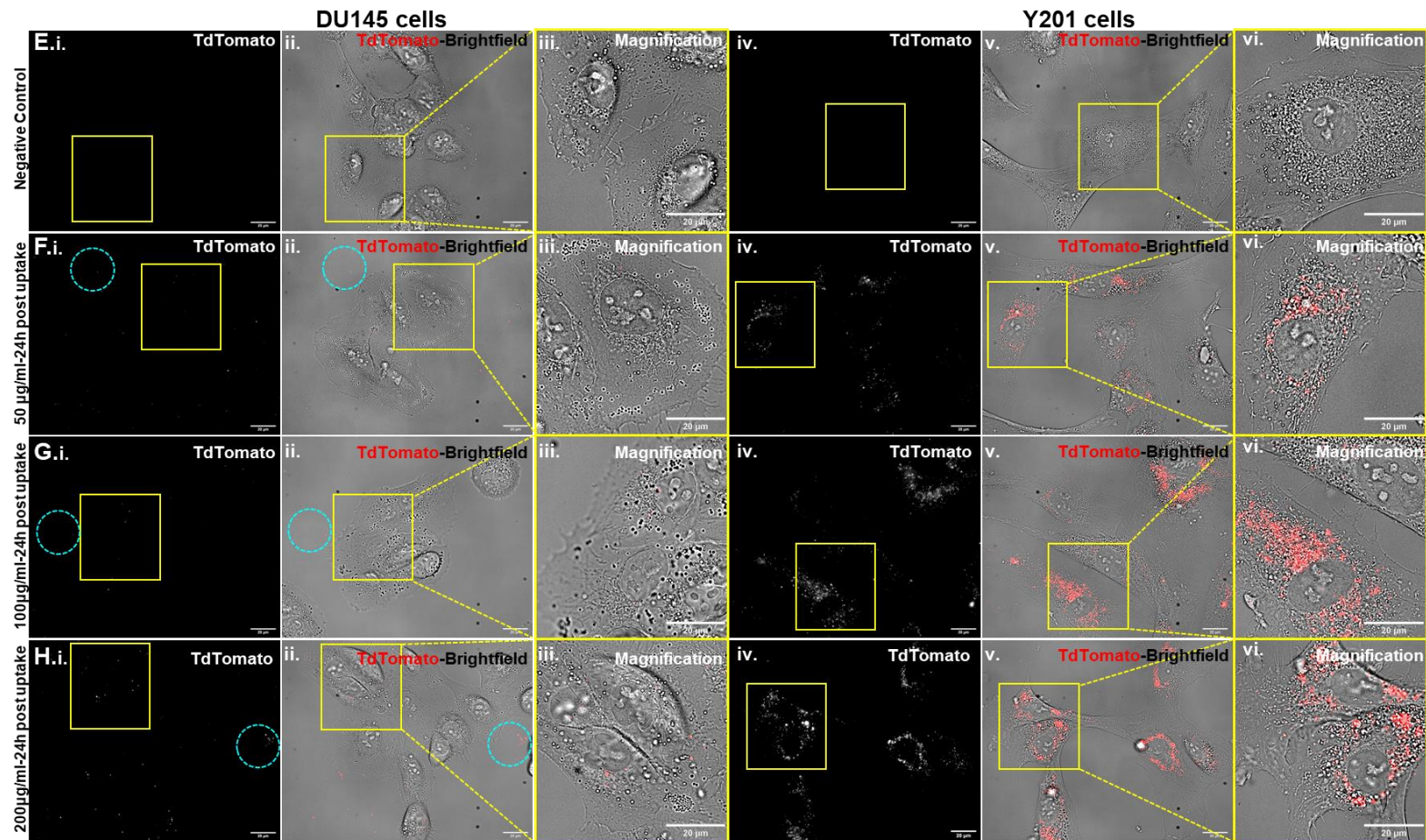


Figure 6.10. Representative images of acute CD81-Tdtomato sEV dosing in DU145 and Y201 cells.

E-H. Retention of CD81-Tdtomato sEVs 24-hours post-dosing for the following concentrations of sEVs: (A) 0µg/ml (controls), (B) 50µg/ml, (C) 100µg/ml and (D) 200µg/ml in DU145 cells (i-iii) and Y201 cells (iv-vi). Image series include: the Tdtomato channel (i,iv), the Tdtomato-Brightfield Merged channel (ii,v) and a magnification of area of interest (iii,vi) for DU145 and Y201 cells respectively. Cyan circles depict immobilised sEVs in the extracellular space. Scale bars represent 20µm.

Figure continues on next page ►

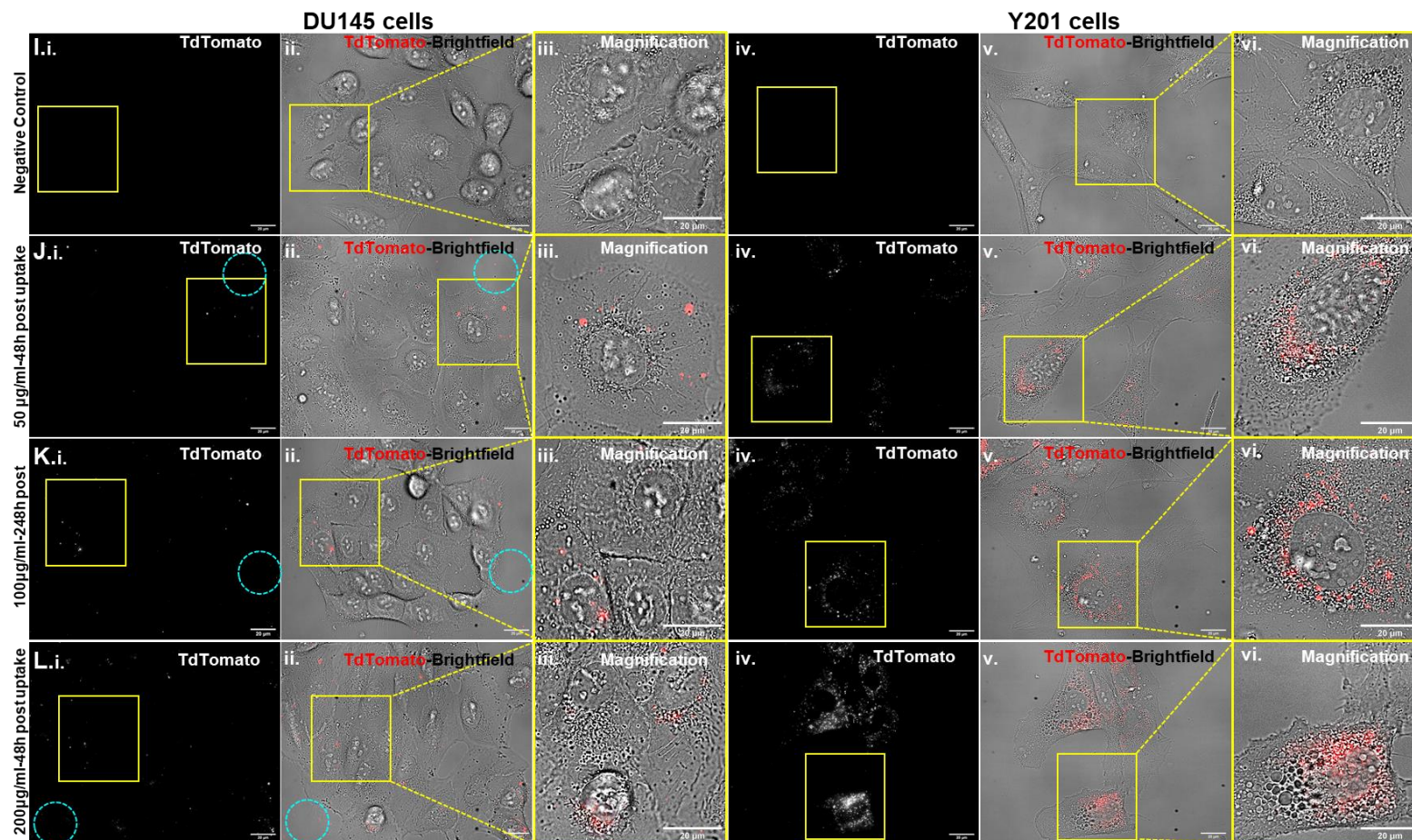


Figure 6.10. Representative images of acute CD81-Tdtomato sEV dosing in DU145 and Y201 cells.

I-L. Retention of CD81-Tdtomato sEVs 48-hours post-dosing for the following concentrations of sEVs: (A) 0µg/ml (controls), (B) 50µg/ml, (C) 100µg/ml and (D) 200µg/ml in DU145 cells (i-iii) and Y201 cells (iv-vi). Image series include: the Tdtomato channel (i,iv), the Tdtomato-Brightfield Merged channel (ii,v) and a magnification of area of interest (iii,vi) for DU145 and Y201 cells respectively. Cyan circles depict immobilised sEVs in the extracellular space. Scale bars represent 20µm. ► *Figure continues from previous page*

6.3.6.2. Chronic CD81-Tdtomato sEV Delivery and Retention in Y201 Cells

The previous experiment demonstrated how the acute or short-term exposure of Y201 mesenchymal stem cells in CD81-Tdtomato sEVs resulted in a heterogeneous and persistent Tdtomato fluorescent signal across the population, even after 48h post-dosing, suggesting that processing of sEVs might be slower than the DU145 parent-cell line. In the context of PCa, BM-MSCs are exposed to cancer derived sEVs (42, 98), and presumably this exposure could be deemed to be more chronic rather than acute in nature.

To determine how a mesenchymal stem cell line can potentially receive and process sEVs after chronic exposure, Y201 cells were dosed with CD81-Tdtomato sEVs for 72h, and Tdtomato signal was assessed directly after dosing (0h) and 24-, 48-, 72- and 96h post-dosing via live-cell fluorescence microscopy. For this experiment, two methods of analysis were used: Field-of-view and Single-cell image analysis ([Figure 2.2](#)). Field-of-view analysis was conducted for all the time-points examined (up to 96h post-dosing), whereas Single-cell analysis could only be conducted up to 48h post-dosing. As this experiment was conducted live, single-cell segmentation after 48h was not possible due to the high cell density. Hence, field-of-view analysis provided an approximate quantification of Tdtomato fluorescence per cell, by normalisation of fluorescence to cell number between time-points i.e., dividing the mean Tdtomato fluorescence to the number of fluorescent cells in each field-of-view.

Field-Of-View Analysis of CD81-Tdtomato Uptake and Retention

To assess the uptake and retention dynamics of Tdtomato signal for each CD81-Tdtomato sEV concentration (200, 100 and 50 μ g/ml), the mean Tdtomato fluorescence per field was calculated for each dose; this appeared to be stable over time (0-96h) for all sEV concentrations ([Figure 6.11.A.i](#)). However, the number of fluorescently labelled cells statistically increased over time, from approx. 10 to 40 cells per field-of view ([Figure 6.11.A.ii](#)). Thus, subsequent normalisation of the field-of-view mean Tdtomato signal to fluorescent cell number, revealed that the mean Tdtomato fluorescence/cell was highest after the 72-h uptake (0h post-dosing), but the signal progressively decayed and significantly decreased over time for all concentrations tested (4-to 7-fold decrease of signal, [Figure 6.11.A.iii](#)).

Next, statistical analysis was conducted to determine potential differences between the CD81-Tdtomato sEV concentrations over time ([Figure 6.11.B](#)). Initially, the Field-of-view analysis showed that dosing with the highest sEV concentration (200µg/ml) resulted to the highest mean Tdtomato signal per field for the first 72h post-dosing, even though at 96h no significant differences between doses was apparent ([Figure 6.11.B.i](#)).

Next, the mean Tdtomato signal per cell was calculated ([Figure 6.11.B.iii](#)), after normalization of the fluorescent signal per field to the number of cells per field ([Figure 6.11.B.ii](#)). Again, the concentration of sEVs positively associated with the uptake per cell, as demonstrated by the highest mean Tdtomato signal when cells were dosed with 200µg/ml, followed by dosing with 100µg/ml and then 50µg/ml CD81-Tdtomato sEVs ([Figure 6.11.B.iii](#)). After the 72-h uptake (0h post-dosing), Y201 cells dosed with 200µg/ml of sEVs were shown to retain significantly more signal than cells dosed with 100µg/ml and 50µg/ml sEVs for up to 48h post-dosing; whereas at 72- and 96h no significant differences in mean Tdtomato signal per cell were apparent between each sEV concentration ([Figure 6.11.B.iii](#)).

Figure 6.11. Field-of-view image analysis of chronic CD81-Tdtomato sEV delivery in Y201 cells.

Figure on next page ►

A. Dose-dependent field-of-view image analysis showing bar graphs for: **(i)** the mean Tdtomato fluorescence per field-of-view, **(ii)** the number of labelled (fluorescent) cells per field-of-view and **(iii)** the calculated Tdtomato fluorescence per cell for each CD81-Tdtomato EV concentration (50, 100 and 200µg/ml) over time (uptake: 0 h post-dosing and retention: 24, 48, 72 and 96h post-dosing). **B.** Time-dependent field-of-view image analysis showing bar graphs for: **(i)** the mean Tdtomato fluorescence per field-of-view, **(ii)** the number of labelled (fluorescent) cells per field-of-view and **(iii)** the calculated Tdtomato fluorescence per cell for each timepoint (uptake: 0 h post-dosing and retention: 24, 48, 72 and 96h post-dosing) for all CD81-Tdtomato EV concentrations (50, 100 and 200µg/ml). The Tdtomato fluorescence/cell was calculated by normalisation of the Tdtomato fluorescence to cell number for every time-point, i.e., by division of Tdtomato fluorescence per field of view to the number of CD81-Tdtomato labelled-cells per field. Error bars represent the mean with 95%CI and statistical analysis was done using two-way ANOVA and Bonferroni's post-multiple comparisons (statistical differences denoted with *p<0.05, **p<0.01 and ***p<0.001).

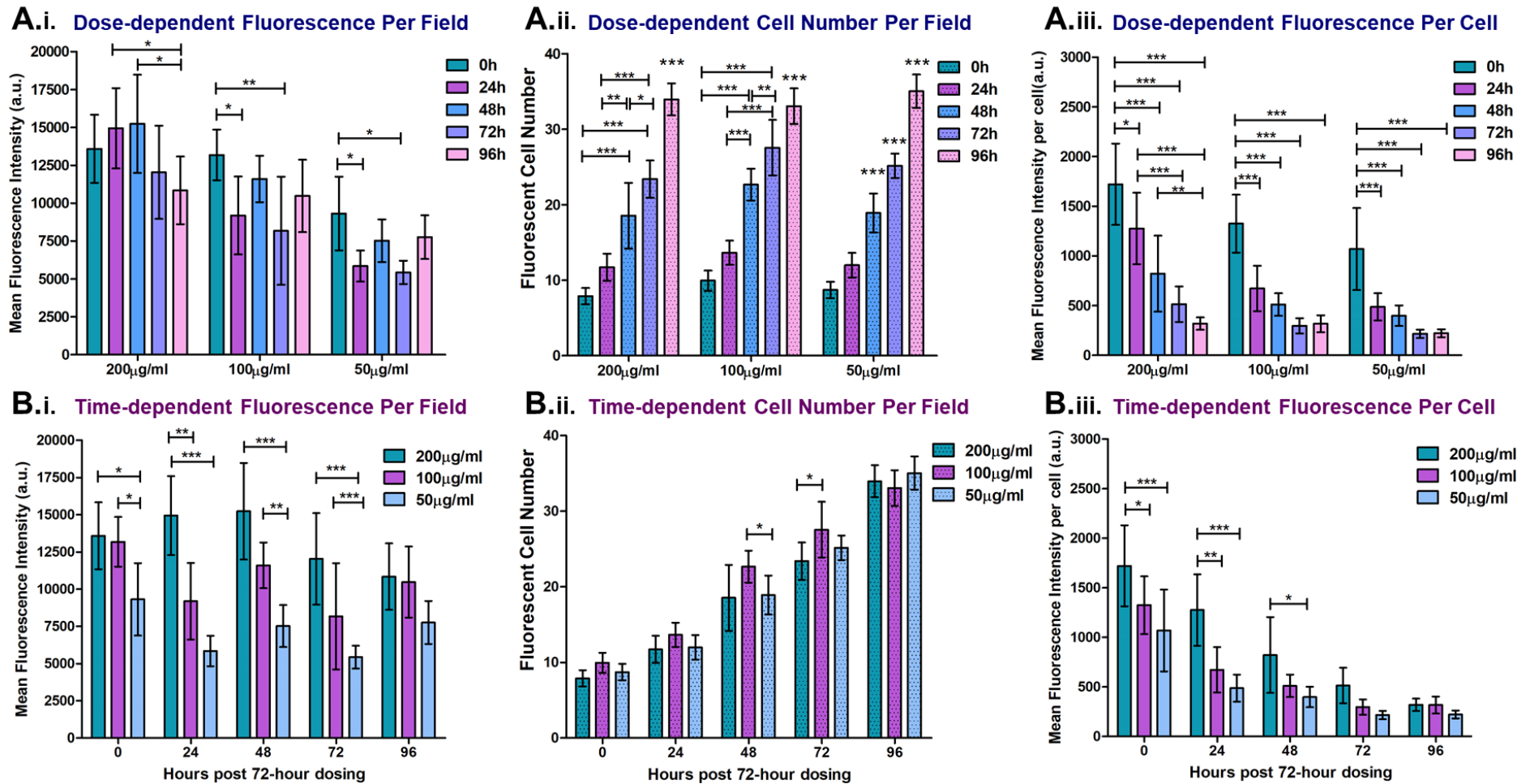


Figure 6.11. Field-of-view image analysis of chronic CD81-Tdtomato sEV delivery in Y201 cells.

◀ Figure Legend on previous page

Single-Cell Analysis of CD81-Tdtomato Uptake and Retention

As mentioned above, the field-of-view analysis provided an estimation of uptake and signal retention of EVs/cell for up to 96h post-dosing; single-cell analysis was also conducted for the first 48h post-dosing to investigate the distributions of CD81-Tdtomato sEV fluorescence intensity between the different doses of sEVs over time ([Figure 2.2.A](#), [Figure 6.12](#)).

In agreement to the previous observations, dosing Y201 cells with 200µg/ml CD81-Tdtomato sEVs resulted to the highest mean Tdtomato signal per cell (highest concentration/cell) indicating higher uptake of sEVs compared to the lower doses (50µg/ml and 100µg/ml), even though the difference to the 100µg/ml sEVs was statistically insignificant ([Figure 6.12.A,C.i](#)). Chi Square Comparisons Analysis of the Tdtomato fluorescence intensity histograms also demonstrated this, as the distribution of cells dosed with 200 µg/ml sEVs was shifted to the right compared to 50µg/ml (4 SD shift, with 33.6% higher events) but was not shifted significantly when compared to 100µg/ml (0 SD shift, but 8.3% higher events) ([Supplementary Figure 31.A](#), with calculation of baseline variance shown in [Supplementary Figure 31.C](#)). In addition, overlay of the Tdtomato histograms demonstrated that the uptake of CD81-Tdtomato sEVs was heterogeneous (at any concentration), as evidenced by the broadness of these distributions ([Figure 6.12.C.i](#)).

Further analysis showed that the Y201 cell area was strongly and significantly correlated with the total CD81-Tdtomato signal/cell, for all the tested sEV concentrations ([Figure 6.12.B](#)). On the other hand, no significant correlation of cell convexity, roundness or circularity to the total Tdtomato signal/cell was found ([Supplementary Figure 32. A,B](#)). Of note, no significant differences were found in cell area, convexity, roundness or circularity between the different EV doses tested, suggesting that cell characteristics were not affected by CD81-Tdtomato sEVs at any dose ([Supplementary Figure 32. C,D](#)).

After the initial sEV uptake (0h post-dosing), the Tdtomato signal decayed over time, as observed from the decrease of mean Tdtomato signal/cell 24- and 48h post dosing. This decrease in mean Tdtomato signal was highly significant for cells dosed with 50 and 100µg/ml sEVs, but not for cells dosed with 200µg/ml sEVs ([Figure 6.12.A](#)). Indeed, the Tdtomato histogram distributions shifted to the left for cells dosed with 100 and 50µg/ml sEVs, specifically 24% and 26% of populations shifted after 48h, respectively (shift of >2 SDs, [Figure 6.12.D.ii,iii](#) and [Supplementary Figure 31.B](#)- Chi square and Overton statistics). However, the distribution of mean Tdtomato signal did not significantly shift for cells dosed with 200µg/ml sEVs, even though 18% of population did decrease to lower intensity (0 SDs shift, [Figure 6.12.D.i](#) and [Supplementary Figure 31.B](#)- Chi square

and Overton statistics). Hence, cells dosed with 200µg/ml CD81-Tdtomato sEVs seemed to retain more signal over time, as shown by the higher mean Tdtomato signal per cell compared to cells dosed with 100 and 50µg/ml sEVs ([Figure 6.12.D.ii,iii](#) and [Supplementary Figure 31.A](#)). The CV was also calculated for each Tdtomato fluorescence histogram, and it appeared to change inconsistently; for example, it increased over time for cells dosed with 200 and 100µg/ml but reduced for cells dosed with 50µg/ml sEVs, suggesting broadening and narrowing of the distributions over time, respectively ([Figure 6.12.D](#)). Thus, the Tdtomato signal might be distributed by asymmetrical partitioning to daughter cells (like the distribution of QDs); however, it is also simultaneously degraded (non-conserved signal).

[Figure 6.13](#) shows representative images for internalised Tdtomato signal during uptake (0h post-dosing) and retention (24- to 96h post-dosing) in Y201 cells for every CD81-Tdtomato sEV concentration tested (200, 100 and 50µg/ml sEVs and control cells). These images show the absence of extracellular Tdtomato signal, suggesting complete internalisation of CD81-Tdtomato sEVs after the initial 72h of continuous incubation with sEVs (uptake, 0h time-point). In addition, they confirm the intracellular perinuclear localisation of the Tdtomato signal, as well as the heterogeneity in Tdtomato signal between Y201 cells which persisted until 96h post-dosing. Finally, these images demonstrate the gradual signal decay over time and the differences in signal between the three CD81-Tdtomato sEV doses ([Figure 6.13](#)).

To summarize, chronic delivery of CD81-Tdtomato sEVs in Y201 cells (72h continuous dosing) resulted in heterogeneous and dose-dependent uptake of sEVs, with the Tdtomato signal appearing as punctate and with perinuclear localisation; this heterogeneity in CD81-Tdtomato sEV dose/cell was found to strongly correlate with Y201 cell area. After uptake, the Tdtomato signal/cell progressively decayed over time for all sEV concentrations tested, even though there was a potential delay in signal processing by cells treated with the highest dose of sEVs (200µg/ml) for the first 48h; whereas at 72- and 96h post-dosing no significant differences were observed between cells treated with any sEV dose. This progressive decrease of Tdtomato signal could be attributed to EV degradation/processing and cell division, which might potentially be done via asymmetrical partitioning of Tdtomato signal to daughter cells.

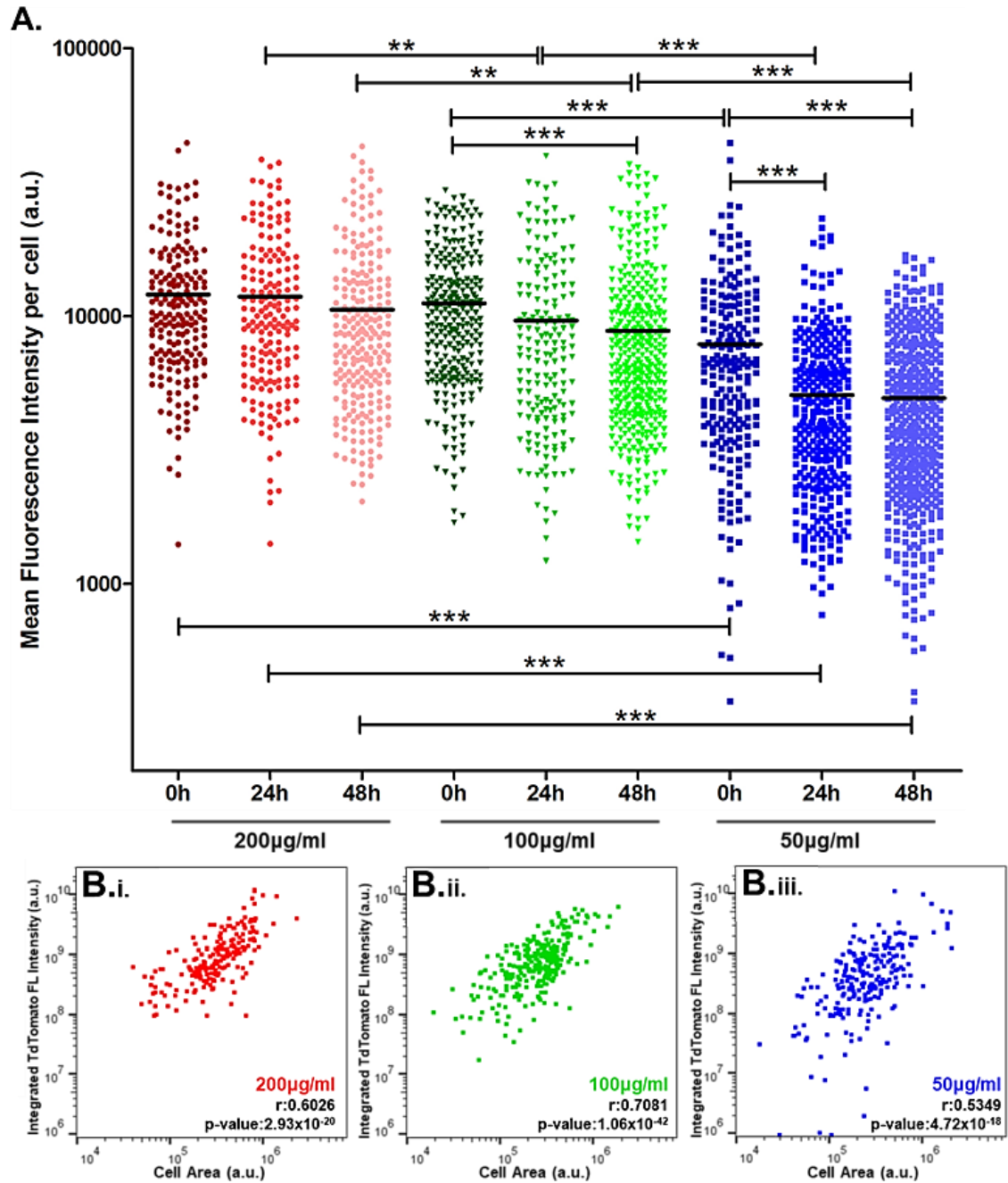


Figure 6.12. Single-cell image analysis of CD81-Tdtomato sEV uptake and retention up to 48 hours post chronic delivery in Y201 cells.

A. Dot plot demonstrating the mean Tdtomato fluorescence per cell for Y201 cells labelled with 200, 100 or 50µg/ml CD81-Tdtomato sEVs at 0, 24 and 48-hours post chronic-dosing. Statistical analysis was done using two-way ANOVA and Bonferroni's post-multiple comparisons (statistical differences denoted with ** $p < 0.01$ and *** $p < 0.001$). **B.** Scatter plots for Y201 cell Area Vs Total (integrated) Tdtomato fluorescence during sEV uptake (0h-timepoint) for **(i)** 200µg/ml, **(ii)** 100µg/ml and **(iii)** 50µg/ml. Linear regression analysis calculated the Pearson correlation coefficients and p-values which are shown on the plots; statistically significant correlations are designated with bold letters.

Figure and Legend continued to next page ►

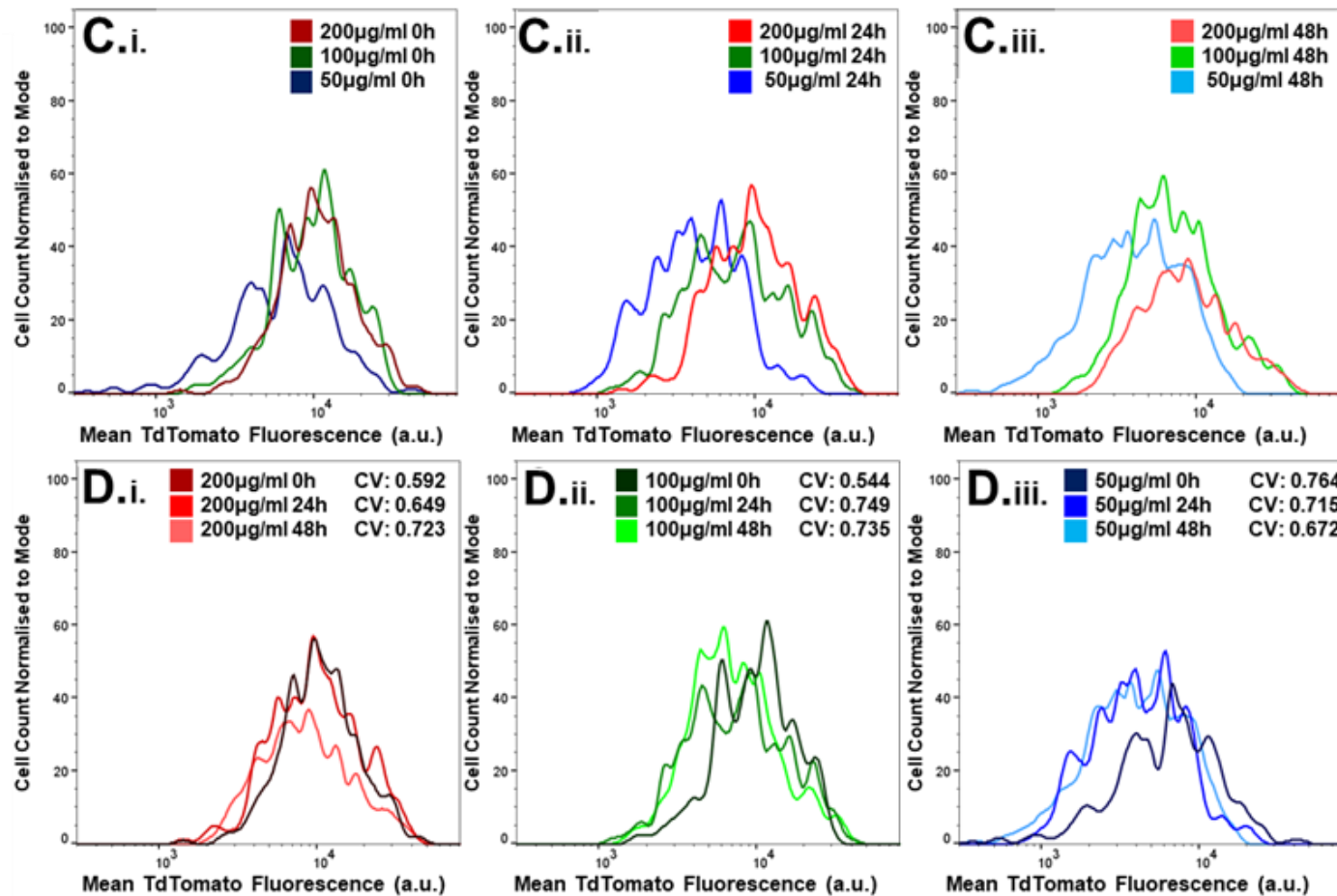


Figure 6.12. Single-cell image analysis of CD81-Tdtomato sEV uptake and retention up to 48 hours post chronic delivery in Y201 cells.

◀ *Figure and Legend continued from previous page*

C. Histogram overlays showing the distributions of Tdtomato Fluorescence intensity for each timepoint in Y201 cells depicting: (i) uptake- 0h post-dosing (ii) retention-24 hours post-dosing and (iii) retention-48 hours post-dosing for each CD81-Tdtomato dose (50, 100 and 200µg/ml). D. Histogram overlays showing the distributions of Tdtomato Fluorescence intensity in Y201 cells for each CD81-Tdtomato EV dose (i) 200µg/ml, (ii) 100µg/ml and (iii) 50µg/ml, over time, with coefficient of variation (CV) shown.

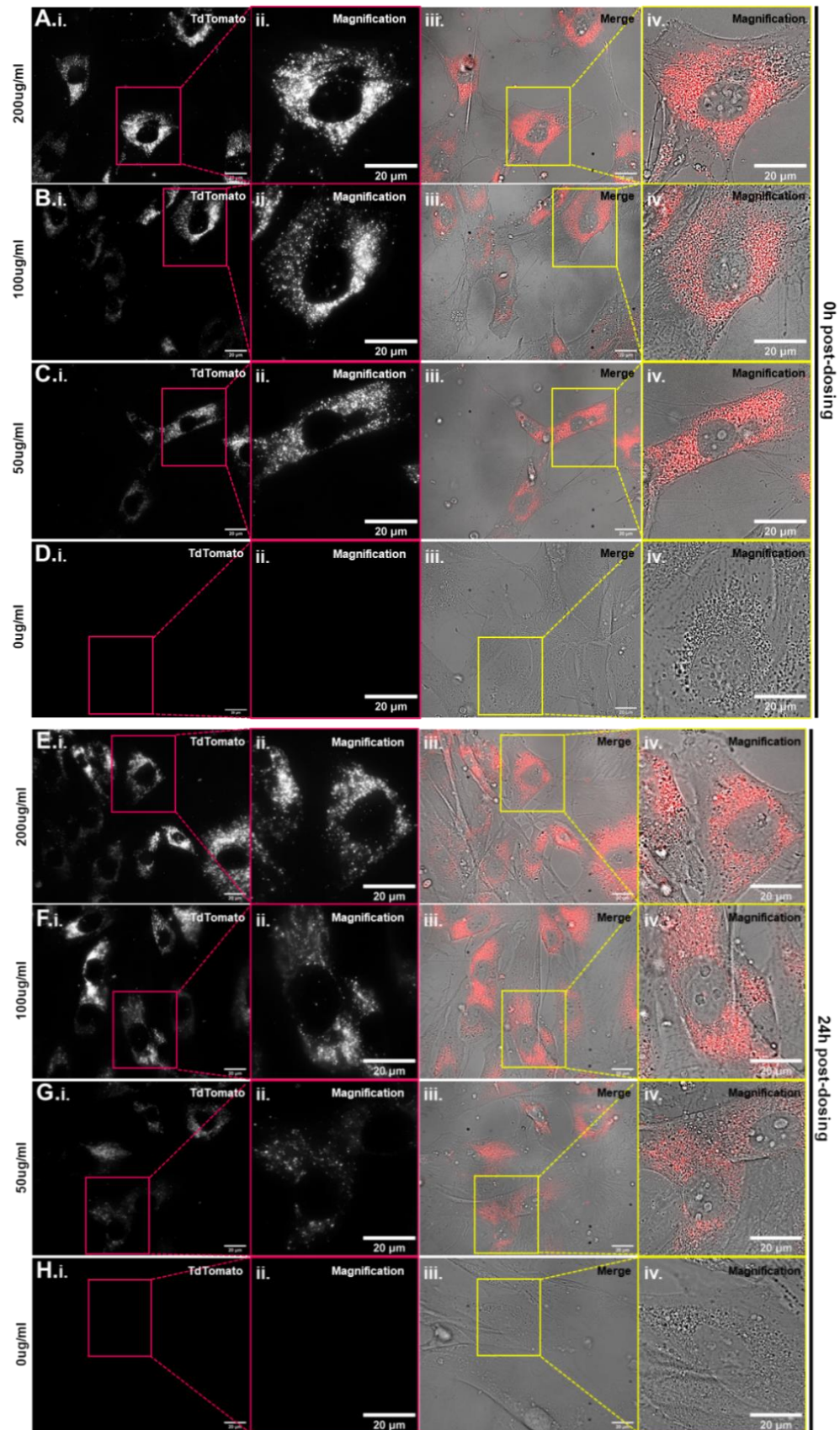


Figure 6.13. Representative images of chronic CD81-Tdtomato sEV dosing in Y201 cells.

Figure continues to next page ►

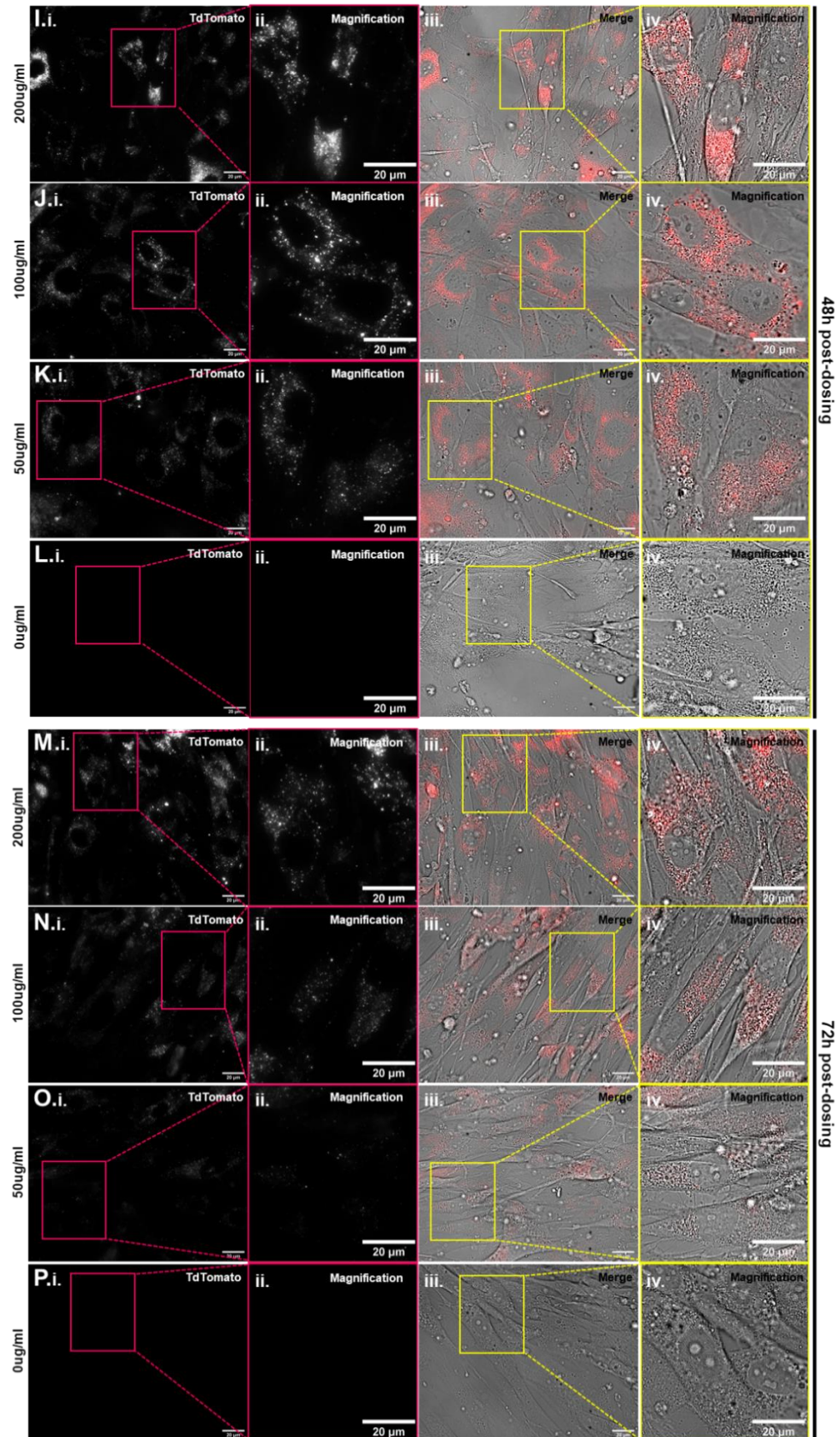


Figure 6.13. Representative images of chronic CD81-Tdtomato sEV dosing in Y201 cells.
Figure continues to next page ▶

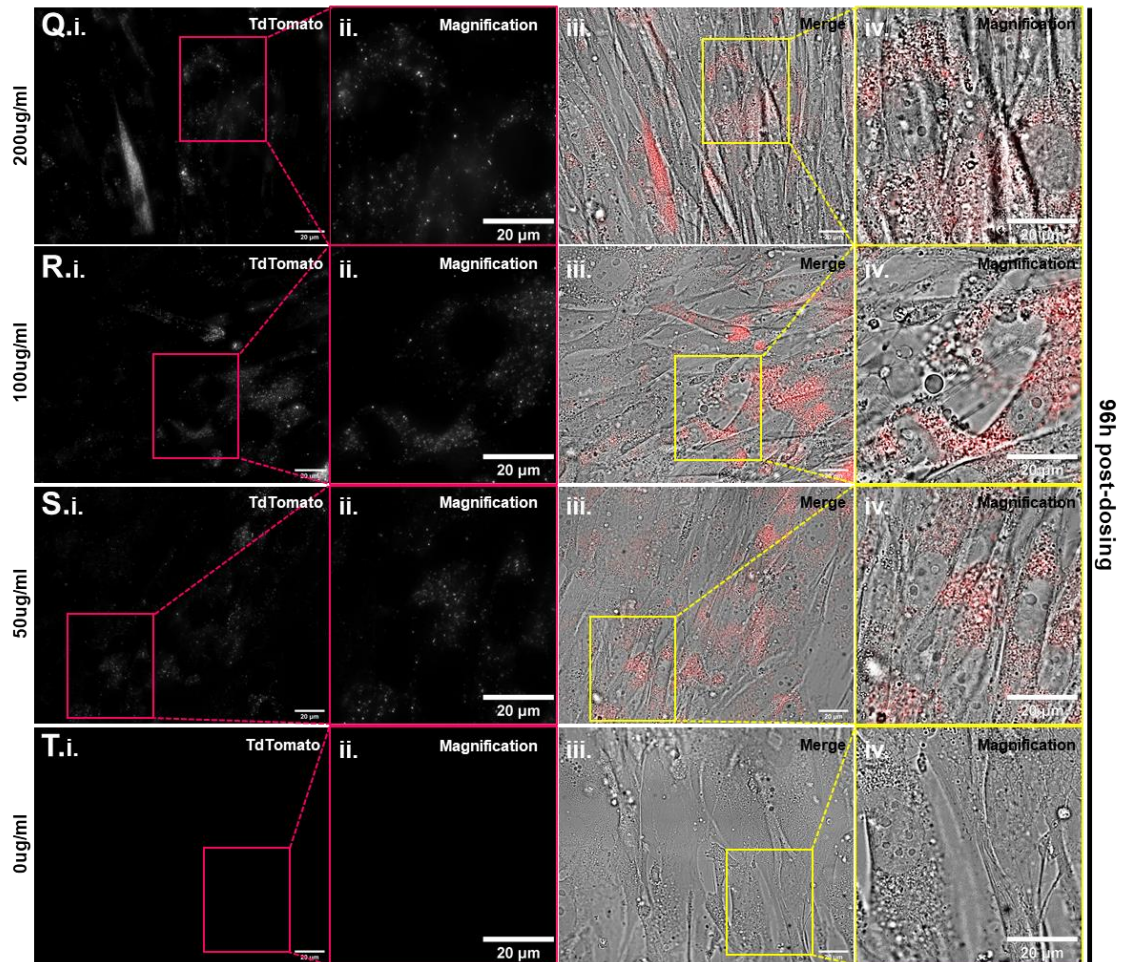


Figure 6.13. Representative images of chronic CD81-Tdtomato sEV dosing in Y201 cells.

► **Figure continued from previous pages**

A-D. Uptake of CD81-Tdtomato EVs directly after 72 hours of exposure (**0h-post dosing**) for the following concentrations: **(A)** 200µg/ml, **(B)** 100µg/ml, **(C)** 50µg/ml and **(D)** 0µg/ml (controls). **E-H.** Retention of CD81-Tdtomato EVs **24h-post dosing** for the following concentrations: **(E)** 200µg/ml, **(F)** 100µg/ml, **(G)** 50µg/ml and **(H)** 0µg/ml (controls). **I-L.** Retention of CD81-Tdtomato EVs **48h-post dosing** for the following concentrations: **(I)** 200µg/ml, **(J)** 100µg/ml, **(K)** 50µg/ml and **(L)** 0µg/ml (controls). **M-P.** Retention of CD81-Tdtomato EVs **72h-post dosing** for the following concentrations: **(M)** 200µg/ml, **(N)** 100µg/ml, **(O)** 50µg/ml and **(P)** 0µg/ml (controls). **Q-T.** Retention of CD81-Tdtomato EVs **96h-post dosing** for the following concentrations: **(Q)** 200µg/ml, **(R)** 100µg/ml, **(S)** 50µg/ml and **(T)** 0µg/ml (controls).

Image series include: the Tdtomato channel **(i)**, the Tdtomato-Brightfield Merged image **(iii)** and magnifications of an area of interest for the Tdtomato Channel (pink) **(ii)** and the Merged image (yellow) **(iv)**. Scale bars represent 20µm.

6.4. Discussion

Distribution of QD Nanoparticles in DU145 and Y201 Cells

This chapter focused on investigating the uptake and retention dynamics of QD705 nanoparticles and CD81-Tdtomato sEVs both in the PCa cells of origin (DU145) and the bone-marrow derived Y201 mesenchymal stem cells, to establish the behaviour of these cell populations in dosing with nanoparticles and nanovesicles.

DU145 and Y201 cells dosed with QD705 exhibited a heterogeneous uptake of QDs, as evidenced by the large variance of the QD705 fluorescence intensity distribution, thus denoting variation in QD load per cell; this agrees with previous dosing studies of QD705 in U2OS (osteosarcoma) cells (145, 146, 252, 253). This heterogeneity in nanoparticle uptake was at least partially attributed to cell area, as a strong positive linear correlation of Y201 cell area to total QD705 load per cell was found; a previous study in human fibroblast cells demonstrated that nanoparticle variation in dosing is mainly due to heterogeneity in cell area (258). This was not apparent for DU145 cells however, perhaps because these cells are relative smaller than Y201 and homogeneous in size; this suggests that other factors may also be driving this variation in QD dose (e.g., the relative distance of a cell to neighbouring cells). However, the possibility that cell area partially drives the uptake of QDs is also supported by the higher uptake of Q705 load in the larger Y201 cells, compared to the smaller DU145 cells which exhibit lower levels of QD705 uptake (lower mean QD705 intensity/cell). Further studies are necessary however to determine if the variability in QD dose/cell is attributed to other factors, like the relationship between neighbouring cells.

Besides the difference of Y201 and DU145 cells in the magnitude of QD load/cell, fluorescence microscopy revealed differences in the localisation of QD705 at this time-point. Whereas the majority of QD705 signal for both cell lines appeared internalised, punctate and with perinuclear localisation, some Y201 cells also exhibited QD705 clusters at the plasma membrane; this aggregation of QD705 is expected when they are endocytosed by cells due to their colloidal nature (255). This suggested that internalisation of QDs by Y201 cells was potentially slower than DU145 cells. Previous studies did show that the QD705 signal appeared diffused and aggregated at the plasma membrane 5h post-incubation for U2OS cells, whereas by 24h QDs were completely internalised as the signal appeared punctate with perinuclear localisation (145, 252). Another study also demonstrated complete internalisation of QD signal in ESC (embryonic stem cells) 24h-post dosing (259).

After the initial uptake of QDs, the observed loss of mean QD705 fluorescence signal over time was expected in both cell lines, as the QD concentration/cell was being redistributed upon cell division, in agreement with previous studies (145, 252, 253). Furthermore, the shifting and broadening of the QD705 fluorescence distributions suggested that as cells divided, nanoparticles were asymmetrically partitioned through the endosomal pathway. If partitioning of the QD705 was symmetric (50% division in every daughter cell), then the distributions would shift to half the x-axis value and the modal cell number would remain the same; thus the small shift and broadening of the distributions indicated asymmetrical partitioning of QDs, as reported previously (145, 252, 253). This asymmetrical partitioning of QDs appeared conserved between DU145 and Y201 cells, even though at the time-point tested (72h post-dosing), Y201 cells exhibited higher mean QD705 concentration/cell, potentially due to the higher initial uptake of QDs (at 24h), or differences in cell cycle dynamics compared to DU145 cells.

In conclusion, these results provided a baseline characterisation of the different behaviours of DU145 (PCa cell line) and Y201 (mesenchymal stem cell line) in QD705 nanoparticle dosing, and revealed similarities in uptake and distribution of nanoparticles, as well as notable differences in uptake magnitude per cell and dynamics for internalisation of QDs. This understanding of synthesised nanoparticle uptake and distribution in the DU145 and Y201 cell populations, has provided a quantifiable benchmark and set a starting point for investigation of the biological nanovesicles (EVs).

Distribution of QDs vs sEVs in DU145 Cells

To elucidate whether sEVs share the same principles as QDs regarding uptake and retention, a preliminary dosing experiment was conducted directly comparing QDs and sEVs (labelled with the AlexaFluor-Maleimide dye-EV-647) and then continuing with the use of CD81-Tdtomato sEVs (as they are endogenously fluorescent).

Firstly, it was observed that EV-647 were taken up faster by DU145 cells compared to QDs, as just 1h post-dosing the EV-associated fluorescence signal appeared internalised. On the other hand, QDs were clustered and bound to the membrane, as expected from previous studies (145, 146, 253). A different study comparing the uptake dynamics of “artificial nanoparticles” (cationic lipid nanoparticles) and HEK-293 sEVs (expressing GFP-CD63) also showed that 80% of sEVs were internalised in Huh7 cells after a 2-h uptake, whereas the cationic nanoparticles were only restricted on the cell membrane, forming large raft-like aggregates (92). Other studies on sEVs also confirmed our observations, as they showed rapid endocytosis of sEVs in cells; for example,

SKOV3 sEVs labelled with CFSE were internalised in SKOV3 cells just after 30min (79), and DU145 sEVs labelled with AlexaFluor-maleimide dye internalised after 30min in lung fibroblasts (114) and HeLa cells (115). In addition B16-F10, PANC-1 and HEK-293 sEVs internalised in PANC-1 cells after 1h of dosing (260), whereas GFP-CD63 HEK-293T sEVs internalised in HEK-293 cells just after 2h (116).

Furthermore, our results showed punctate staining and perinuclear localisation of internalised sEVs, which might indicate targeting to the endosomal/lysosomal compartment; however further investigation is necessary to determine the specific cellular compartment in our cell lines. Previous studies did show the same pattern of perinuclear localisation of sEVs and demonstrated their co-localisation with endosomal/lysosomal markers (79, 91, 92, 111, 114, 115, 177). Specifically, SKOV3 (79), DU145 (114) and PC12 sEVs (91, 111) colocalised with endosomal markers (EEA1, FM4-64) in SKOV3 cells, AG02262 lung fibroblasts and PC12 cells, respectively. In addition, SKBR3 (177), HEK293 (92), PC12 (91, 111) and DU145 sEVs (114, 115) colocalised with lysosomal markers/stains (lysotracker red, LAMP1, dextran) in MRC-5, HEK293, PC12 cells, as well as AG02262 lung fibroblasts and HeLa cells respectively.

After the rapid internalisation of EV-647 observed in our experiment, at 24h post-dosing the majority of fluorescence signal was diminished in DU145 cells, whereas QD signal appeared bright, punctate and with perinuclear localisation (145, 146, 253). This loss of EV-647 signal and loss of perinuclear localisation in DU145 cells might be attributed to “dilution” via cell division and/or processing or lysosomal degradation of sEVs. Previous studies also demonstrated a reduction of signal; specifically PC12 (91) and SW780 (261) sEVs labelled with lipophilic dyes (DiD and PK26 respectively) were continuously incubated with their respective cell of origin and demonstrated reduction of signal after 21- and 14h, respectively, but not a complete loss of signal (91, 261). Interestingly, the first study also observed a gradual translocation of signal from the perinuclear region to the plasma membrane after just 6h, and hypothesised either recycling of the DiD lipophilic dye or exocytosis of sEVs (91). Two other studies showed that dosing of Gli36 glioma cells or HEK293 cells with sEVs endogenously labelled with membrane-bound PalmGFP (108) or GFP-CD63 (116) respectively, resulted in significant reduction of fluorescence after 24h, with the signal in PalmGFP sEV-treated cells plateauing as early as 12h; this phenomenon of signal plateauing (from 12 to 24h) suggested that either some sEVs were not fully processed or some sEV membrane (with the PalmGFP) was recycled in the cells (108). These studies overall hypothesised that decrease of sEV-associated signal might be a result of cell division and recycling/degradation of sEVs, whereas residual signal might be attributed to unprocessed sEVs (91, 108, 116, 261).

However, from the previous studies it became apparent that the different sEV labelling methods might cause misinterpretation of results for the uptake and retention dynamics of sEVs (102, 103) e.g., recycling of the DiD signal back to the membrane (91) and persistence of PalmGFP signal (108) might be attributed to “leakiness” of the dye/reporter to other non-specific membrane components. Similarly, our study initially utilised sEVs labelled with the AlexaFluor-Maleimide dye (EV-647) as they are bright and could be easily used in flow cytometry and fluorescence microscopy experiments; however, due to the nature of the dye to bind cysteine-rich proteins, this posed a risk for “leakiness” to other cell compartments. Indeed, a long-term experiment in a previous study investigating the retention of sEV signal 72h post-dosing in lung fibroblasts, showed that fluorescence appeared diffused in the cell (loss of punctate perinuclear localisation) which raised the concerns of recycling/redistribution of the AlexaFluor-Maleimide dye following decoupling from sEVs (114). Hence, it became apparent that further investigation into sEV uptake and retention dynamics had to be done utilising the endogenously fluorescent CD81-Tdtomato sEVs, as the fluorescent protein is directly conjugated to the sEV cargo; thus, any observed signal is associated with the presence of sEVs and/or sEV cargo in the cell (262).

Distribution of CD81-Tdtomato sEVs in DU145 and Y201 Cells

Acute delivery of CD81-Tdtomato sEVs was firstly investigated in the DU145 PCa cells. Acute dosing with sEVs (1 to 3h) resulted in internalisation, evident by punctate staining, and localisation at the perinuclear region, thus confirming our previous observations and agreeing with the aforementioned studies (79, 91, 92, 111, 114, 115, 177). Some internalised sEVs were captured in-motion, moving from the plasma membrane towards the perinuclear region on string-like membrane structures that resembled the cytoskeleton (115), whereas sEV signal in the extracellular space was completely immobilised on the surface. Some studies have shown that sEVs can move on actin and/or microtubule filaments from the cell periphery to the perinuclear region as use of cytoskeleton inhibitors (e.g., actin inhibitor Cytochalasin D) dramatically reduces sEV internalisation (91, 92, 111); however further studies are necessary to determine if the CD81-Tdtomato sEVs follow this principle. Some larger clusters of CD81-Tdtomato sEVs were also present in the cells; these might occur during isolation via ultracentrifugation or storage in high concentrations in physiological saline solution which naturally promotes flocculation (263, 264).

Single-cell image analysis demonstrated that the uptake of CD81-Tdtomato sEVs was very heterogeneous in the DU145 cell population, as evident by the broad distribution of signal per cell (large SD); this was similar to the uptake of QDs. Interestingly, this uptake heterogeneity was significantly and positively correlated with the area of the cell, suggesting a cell area-dependent uptake of sEVs. To our knowledge this is the first study that reveals a relationship of cell shape with the uptake of sEVs. This correlation of cell area with sEV uptake (as well as uptake heterogeneity) appears to be a conserved principle that sEVs and QDs share (258); this suggests that dosing cells with sEVs is similar, in a nanoparticulate way, to dosing with artificial nanoparticles.

Further analysis showed that the concentration of CD81-Tdtomato sEVs (mean Tdtomato fluorescence) was relatively stable from 1 to 3h of continuous dosing, potentially suggesting that DU145 cells quickly and continuously take up and process sEVs. Observations from previous studies are contradicting, potentially due to cell-line differential characteristics, sEV isolation method and concentration used, or even due to different methods used for quantifying internalised sEV signal. A study on the uptake of B16-F10, PANC-1 and HEK-293 sEVs in PANC-1 cells, demonstrated no significant differences in internalised sEV-associated signal from 1 to 4h of continuous incubation (260). Similarly, an uptake study on HEK293 sEVs showed no increase in internalisation from the first 5min to 4h of constant incubation with HEK293 cells (116). However, other studies, did show a time-dependent increase in internalisation when cells were dosed long-term with sEVs; for example the uptake of DU145 (114), SKOV3 (79) and HEK293 sEVs (108), increased from 0 to 3h in lung fibroblasts, SKOV3 and Gli36 glioma cells, respectively. Other long-term studies showed that the uptake of SW780 and PC12 sEVs in their respective cells of origin only reached signal saturation at 14 h (261) and 21h (91), respectively. It remains to be elucidated if the mean CD81-Tdtomato sEV concentration per cell remained stable from 1 to 3h due to parallel fast sEV degradation by DU145 cells.

The next experiment investigated acute delivery and retention of sEV signal in DU145 and Y201 cells; 1h of sEV incubation (acute dose) was selected as this was the earliest time-point that we confirmed sEV internalisation and perinuclear localisation (as mentioned above). As we previously observed different uptake and retention dynamics of QD705 in Y201 compared to DU145 cells, it was important to determine whether this deviation would be conserved for CD81-Tdtomato sEVs.

Our results suggested that after acute exposure to sEVs, Y201 cells exhibited slower uptake dynamics than DU145 cells; this might be cell-line specific as a previous study showed that DU145 sEV signal was broadly cytosolic in HeLa cells for the first 1h of uptake (115), whereas a different study showed that PC12 sEV- signal was not entirely

accumulated at the perinuclear region of PC12 cells even after 24 h of uptake (91). This was also reflected from the QD experiment, as some Y201 cells exhibited bright clusters of QDs still at the membrane which had not internalised after 24h. A dose-dependent uptake response was also observed in both Y201 and DU145 cells, when 3 increasing concentrations of CD81-Tdtomato sEVs were tested, thus agreeing with previous studies (114, 116, 260, 261).

In addition, this uptake of sEVs was heterogeneous in both cell lines, which was similar to the heterogeneous uptake of QDs, again underlining that QDs and sEVs might share similar nanoparticulate properties. This heterogeneity in sEV uptake was again found to correlate to the area of the cell; in Y201 cells specifically, this linear correlation was strong ($r > 0.5$) and highly significant. Interestingly, Y201 cells seemed to exhibit a higher sEV uptake/cell compared to DU145 cells, as the mean Tdtomato signal/cell was higher for all concentrations and timepoints tested. This was unexpected, as previous studies suggested that sEVs are preferentially taken up by the parent cells, hypothesising that sEV composition is expected to bear the “signature” of the parent cell line and is thus selectively recognised and taken up by the cell line of origin. Specifically, these studies demonstrated a higher uptake of PANC-1 sEVs (than B16-F10 sEVs) in PANC-1 cells (260) and a higher and selective uptake of HEK293T sEVs and human placental MSC-derived sEVs in their respective parent cells, even when cells were co-cultured with other cell lines (116, 265). Another study also showed the preferential uptake of PC3-EVs (higher fluorescence signal/cell) by the metastatic prostate PC3 cells than the benign PNT2 cells, even if a higher percentage of PNT2 cells had taken up sEVs compared to PC3 cells (60% PNT2 Vs 30% PC3 cells) (109). This phenomenon of higher uptake by Y201 cells in our study might be attributed to the larger size of these cells, as we observed a cell area-dependent uptake of sEVs, or by their phenotype (e.g., different internalisation pathways than PCa cells), but further investigation is necessary to validate these hypotheses.

After uptake with CD81-Tdtomato sEVs, DU145 cells exhibited progressive signal decay at 24- and 48-h post-dosing, thus confirming previous observations with loss of EV-647 signal in these cells potentially suggesting sEV degradation (91, 108, 116, 261). Unexpectedly, Y201 cells exhibited an initial increase in Tdtomato signal/cell 24h post-dosing and exclusive localisation of signal to the perinuclear compartment, followed by eventual decrease of signal 48h later. As Y201 cells are highly migratory and have a fibroblastic morphology with prominent filopodia (266), this increase in signal might be due to internalisation of sEVs of the pericellular space while Y201 cells extend and migrate. Indeed previous studies have suggested that cells migrate towards sEV-deposits on the cell surface and can internalise sEVs (119); these captured sEVs can

“surf” on filopodia, followed by moving on the cytoskeleton to eventually reach the endosomal/lysosomal compartment (92, 111). In our study this was further supported by the “disappearance” of sEVs surrounding Y201 cells, whereas they were still present and surrounded the more-stationary epithelial-like DU145 cells for the entirety of the experiment. It remains to be elucidated if that is actually the case for Y201 cells and utilising time-lapse microscopy to track cells and sEVs would be ideal to resolve this.

The final experiment involved chronic delivery of DU145 CD81-Tdtomato sEVs to the Y201 BM-MSCs, in order to mimic the long-term exposure of cells at the pre-metastatic bone niche to cancer-derived sEVs and quantify the uptake and retention of Tdtomato signal in Y201 cells. After a 72-h dosing with CD81-Tdtomato sEVs, the Y201 cells exhibited punctate and perinuclear localisation of Tdtomato signal suggesting internalisation of sEVs (similar observations with previous experiments). Similarly, Y201 cells had heterogeneous uptake of sEVs (which was highly correlated with the area of these cells) and a dose-dependent response; the only exception was the highest sEV concentration tested (200µg/ml) as the distribution of Tdtomato/signal per cell did not significantly differ to the lower dose (100µg/ml), suggesting a potential “biological saturation” of the system. A previous study showed that PANC-1 cells exhibited a dose-dependent uptake of B16-F10, PANC-1 and HEK-293 sEVs, however the uptake of HEK-293 sEVs specifically, reached a plateau after a specific concentration, suggesting that this phenomenon might be cell type- or sEV type- dependent (260).

After uptake, Y201 cells exhibited a time-dependent and dose-dependent decrease of Tdtomato signal, even though residual signal was still present 96h post-dosing. It is unknown if this Tdtomato signal represented intact sEVs or disassociated sEV-cargo; however, this signal was still punctate with perinuclear localisation, potentially in endosomes/lysosomes, so it might represent EVs/EV cargo that has not yet been processed or degraded by these cells. A previous study using AlexaFluor Maleimide-labelled DU145 sEVs, also demonstrated that lung fibroblasts had residual fluorescent signal 72-h post-acute dosing; however this signal was cytosolic and diffused throughout the cells (not punctate or perinuclear) suggesting potential disassociation and recycling of the dye (114). Similarly, another study with PC12 sEVs labelled with the DiD lipophilic dye showed that after a 6-h dosing, some residual signal was localised in the endosomal/lysosomal compartment and some recycled back to the membrane suggesting disassociation of the dye from sEVs (91). Hence, in our study the fate of sEVs after uptake and localisation to the perinuclear compartment still remains to be elucidated; however, various mechanisms have been proposed like targeting of sEVs to the endo-lysosomal compartment for degradation of cargo, trafficking back to the plasma

membrane for re-secretion or, “back-fusion” with the MVB membrane and release of their cargo in the cytosol (79, 91-93, 108, 109, 111, 177, 250).

Interestingly, this experiment also demonstrated that the progressive loss of Tdtomato signal is probably at least partly due to the asymmetrical partitioning of signal to the daughter cells, evident by the decrease of signal and broadening of the Tdtomato fluorescence distributions. It is currently known that endosomes and lysosomes remain intact and separate during mitosis in a stochastic manner, thus resulting in asymmetrical partitioning to daughter cells (267). As the sEV-associated Tdtomato signal is potentially localised to endosomes/lysosomes (79, 91, 92, 111, 114, 115, 177) and it is persistent, then we hypothesise that sEVs are distributed asymmetrically to daughter cells within endosomes. Furthermore, this progressive decrease of mean Tdtomato signal/cell may also be attributed to the simultaneous processing and degradation of sEVs and/or sEV cargo in the Y201 cells. As DU145 cells completely lost their Tdtomato signal shortly after sEV uptake, we hypothesised that the Tdtomato signal could be effectively processed and/ or degraded by at least the parent cells. Further investigation is necessary, however, to determine the distribution of sEVs to daughter cells as the cell population propagates, as well as to investigate the fate and potential function of sEVs and sEV cargo in the cancer cells of origin and the stromal bone-marrow derived MSC's.

6.5. Conclusions

This chapter investigated the uptake and retention dynamics of sEVs in two types of recipient cells (i) DU145 PCa cells (the origin of sEVs) and (ii) Y201 bone marrow-derived mesenchymal stem cells, after establishing the baseline behaviour of these cells in dosing with artificial semiconductor nanoparticles (QDs). Our results demonstrated an interesting difference between cell lines, the slower uptake dynamics of Y201 cells compared to DU145 cells. Despite this, both cell lines exhibited heterogeneous uptake of QDs, which was correlated to the area of these cells; this also justified (at least in part) the higher uptake of QDs observed in the larger-in-size Y201 cells, compared to DU145 cells. Finally, our results showed that both cell lines distributed the QD/signal to daughter cells via asymmetrical partitioning, as the cell populations were propagating. Then investigation progressed to the uptake and retention dynamics of sEVs in these populations, and interestingly many principles observed with QDs were seen to be also conserved for sEVs. Specifically, both cell lines exhibited heterogeneous and dose-dependent uptake of sEVs after acute delivery, which was again reflected by the heterogeneity in cell area, hence possibly explaining the higher uptake of sEVs by the larger Y201 cells. Acute exposure of sEVs also demonstrated the slower uptake dynamics of Y201 cells compared to DU145 cells, thus reflecting similar principles to the uptake of QDs. Similar to acute delivery, the chronic delivery of sEVs to Y201 cells also generated the same observations, and further demonstrated a dose-dependent and time-dependent loss of sEV-associated signal per cell; this progressive loss of signal was potentially attributed to the simultaneous processing/degradation of sEVs and sEV cargo, as well as to their asymmetrical partitioning to daughter cells. Finally, this is the first study to investigate the dosing behaviour of sEVs after establishing the behaviour of QDs in two cell populations, as well as the first study to reveal a correlation between sEV uptake and cell heterogeneity and to demonstrate the potential of asymmetrical partitioning of sEVs to daughter cells.

CHAPTER 7:
Prostate Cancer Derived
Extracellular Vesicle-Induced
Osteogenic Differentiation of
Bone Marrow-Derived
Mesenchymal Stem Cells

7.1. Introduction

As mentioned previously, cancer-derived sEVs exert various roles in the PCa microenvironment, to promote tumour progression and formation of the pre-metastatic niche (41, 42). This multi-faceted biological function of PCa sEVs occurs by their intercellular exchange between cancer cells, cells of the tumour microenvironment (e.g., immune cells, fibroblasts, endothelial cells, etc.) circulating bone-marrow derived mesenchymal stem cells (BM-MSCs), as well as cells of the pre-metastatic niche like osteoblasts, osteoclasts and BM-MSCs, as the bone niche is a common PCa metastatic site (41, 42, 57, 97).

Mesenchymal stem cells (MSCs) have been shown to be directly recruited to the tumour microenvironment, undergo differentiation, and gain the ability to promote tumour progression and metastasis (37, 38, 268). Many studies have shown that uptake of cancer-derived sEVs in MSCs facilitates this differentiation; for example PCa sEVs were shown to induce the differentiation of BM-MSCs to myofibroblasts, thus resulting in gain of pro-angiogenic and pro-invasive functions (48). Similarly, breast- (269), ovarian (270)- and gastric (271)- cancer cell derived sEVs were shown to induce differentiation of adipose or umbilical cord derived MSCs to tumour-supporting myofibroblasts.

Beyond the primary tumour, PCa sEVs have been shown to promote osteoblastic differentiation of BM-MSCs at the pre-metastatic bone niche, even though this is still poorly understood (63, 66). Previous studies have shown that metastatic PCa cells secrete “soluble factors” (63), or sEVs (66) that can be taken up by BM-MSCs resulting to their commitment towards an osteoblastic lineage, which indirectly supports the formation of the favourable osteoblastic bone metastatic niche.

Despite the ongoing interest in the field to understand the mechanisms behind PCa-derived sEV formation of the pre-metastatic niche, the dissemination of sEVs in this secondary site is still not greatly understood. In the previous Chapter, we characterised and quantified the uptake kinetics, retention, and distribution of CD81-Tdtomato PCa EVs after their acute or chronic delivery in the Y201 BM-MSC line, which is an established and well-characterised cell line that can be used to emulate the *in vivo* BM-MSCs at the pre-metastatic bone niche. BM-MSCs demonstrate significant heterogeneity as they contain cells with tripotent differentiation capacity (osteogenic, adipogenic, and chondrogenic), as well as cells with restricted potency (bi-, uni-, and nullipotency) (126). Unfortunately, most *in vitro* studies are hindered by the short lifetime of these cells, as they reach senescence quite fast, thus restricting the extent of these studies. The Genever group addressed these issues by immortalising human BM-MSCs,

thus generating a panel of clonal BM-MSC lines termed Y101, Y201, Y102 and Y202, which maintained exponential cell growth for over 400 days (126). More importantly, global gene expression profile analysis was performed for these 4 clonal cell lines (126) as well as investigation of their migratory and mitotic behaviour (266). The Y201 BM-MSCs selected for our study exhibit osteogenic lineage, fibroblastic morphology (similar to *in vivo* BM-MSCs) and comparable expression of established BM-MSCs candidate markers (positive for CD29, CD44, CD73, CD90, CD105, and CD166 and negative for CD34 and CD45) (126).

Therefore, in this small final Chapter proof-of-principle experiments were conducted to explore whether chronic exposure of Y201 BM-MSCs to DU145 sEVs can commit them to differentiate towards an osteogenic lineage, given the basic principles established from the previous Chapter showing sEV-associated fluorescence signal retention for extensive period of time in the Y20 BM-MSC population after chronic sEV dosing.

7.2. Aims and Objectives

This final Chapter aimed to address whether DU145 PCa-derived sEVs can induce osteogenic differentiation of Y201 BM-MSCs as a proof-of-concept, as well as investigate whether overexpression of CD63 and CD81 in DU145 sEVs can induce differential effects in osteogenic differentiation compared to WT DU145 sEVs. Therefore, the objectives for this Chapter were:

- To assess the late effects of chronic CD81-Tdtomato sEV dosing on osteogenic differentiation of Y201 BM-MSCs by the Alizarin red mineralisation assay.
- To conduct gene expression analysis of early osteogenic differentiation markers RUNX2 (Runt-related) transcription factor and ALP (Alkaline Phosphatase) to assess the effects of GFP-CD63, CD81-Tdtomato or WT DU145 chronic sEV dosing on Y201 BM-MSCs.

7.3. Results

This small final Chapter involved a preliminary exploration to address whether DU145 sEVs could induce osteogenic differentiation of Y201 BM-MSCs; even though the results were preliminary in nature, they established the foundation for future sEV studies in these cells. Previous studies have shown that PCa sEVs can promote differentiation, for example DU145 sEVs induce the differentiation of BM-MSCs to cancer-associated myofibroblasts (48), whereas C4-2B sEVs promote the differentiation of BM-MSCs towards an osteoblastic lineage (66). Thus, as the Y201 BM-MSCs also have osteogenic differentiation potential (126) we hypothesised that DU145 sEVs could promote their osteogenic differentiation. To address this hypothesis, Y201 BM-MSCs were chronically exposed to sEVs (for 72h) to mirror the sEV-dosing experiments of the previous Chapter as the dynamics of uptake and retention of CD81-Tdtomato sEVs have been already established, followed by late and early assessment of osteogenic differentiation.

7.3.1. **Effects of CD81-Tdtomato sEVs on Late Osteogenic Differentiation**

To begin with, Y201 BM-MSCs were dosed with 3 different concentrations of Bioreactor-derived CD81-Tdtomato sEVs: 50, 100 and 200 $\mu\text{g}/\text{ml}$ (μg of sEV protein based on protein concentration assay, shown in [Table 2.2](#), Bioreactors 5-8, isolation #7) in either regular or osteogenic media for 72h (chronic exposure). Of note, the culture of Y201 BM-MSCs in osteogenic media (complete DMEM supplemented with β -glycerophosphate (5mM), dexamethasone (10nM) and 50 $\mu\text{g}/\text{mL}$ ascorbic acid) has been previously shown to promote osteogenic differentiation of Y201 cells after 21 days (126). After the 72-h sEV dosing, the EV-rich media was removed and replenished with regular or osteogenic media respectively (which was also changed every 72h). The end of the assay was 18 days after dosing with sEVs (day 21, late assessment of differentiation), at which point the Alizarin Red S stain was used to visualise and quantify the mineralised calcium depositions that form due to osteoblast mineralisation (148).

Visualisation of the Alizarin Red S stain under the microscope, demonstrated that Y201 cells treated with osteogenic media only had formed distinct punctate red staining with some larger and darker foci (absent in cells treated with regular media only) which are indicative of calcium depositions and osteogenic nodules; these suggested mineralisation due to osteogenic differentiation of the Y201 BM-MSCs ([Figure 7.1.A,B,i](#),

yellow circles). In addition, Y201 cells treated with CD81-Tdtomato sEVs in osteogenic media, showed similar red staining but with a potential dose-dependent increase in the number and size of osteogenic nodules (dark red foci) compared to cells not treated with sEVs (in the same osteogenic media); this suggested a potential positive effect of sEVs in Y201 osteogenic differentiation and mineralisation ([Figure 7.1.A.ii-iv](#), yellow circles). Surprisingly, Y201 cells treated with CD81-Tdtomato sEVs in regular media also showed dark red puncta (potentially osteogenic calcium nodules), which were albeit rare and observed only for cells dosed with 50µg/ml and 100µg/ml sEVs, suggesting that potentially CD81-Tdtomato sEVs alone may be able to drive osteogenic differentiation ([Figure 7.1.B.ii,iii](#), yellow circles).

Next, colorimetric quantification of the Alizarin Red S stain was conducted by dissociation of the dye from the slide, followed by measurement of dye absorbance at 562nm (148). Interestingly, this quantification of the Alizarin Red S stain showed that only cells dosed with the highest CD81-Tdtomato sEV concentration in osteogenic media (200µg/ml) had significantly high levels of osteogenic mineralisation differentiation compared to other sEV doses (~1.4-fold higher, [Figure 7.1.C](#)). Even more surprising was that statistical analysis demonstrated that Y201 cells treated in osteogenic media only (not dosed with sEVs), had significantly higher osteogenic mineralisation than cells dosed with 50µg/ml and 100µg/ml sEVs ([Figure 7.1.C](#)). Clearly, there seem to be discrepancies between microscopic visualisation and colorimetric quantification of the Alizarin Red S dye. For example, even though microscopy images depicted clear dark red osteogenic calcium nodules for the lower sEV concentrations, the colorimetric quantification method (using absorbance of dye at 562nm) was perhaps not sensitive enough to measure them. Alternatively, the Alizarin Red dye perhaps did not thoroughly disassociate from these wells, thus leading to erroneous colorimetric measurements. For future investigation, it is imperative that the Alizarin Red S mineralisation assay is well optimised to ensure high sensitivity colorimetric quantification.

7.3.2. Gene Expression Analysis of the Effects of sEVs on Early Osteogenic Differentiation

As the previous experiment showed that a 72-h exposure of Y201 cells to CD81-Tdtomato sEVs promoted their differentiation down an osteogenic lineage after 21 days (late assessment), we investigated whether sEVs could potentially induce early changes in expression of genes that may be involved in osteogenic differentiation. For gene expression analysis the RUNX2 (Runt-related) transcription factor was firstly selected, as it is considered the “master osteoblast differentiation gene” and its expression increases on the first step of MSC-differentiation towards an osteoblastic lineage (272). As these differentiated osteoprogenitor cells further proliferate and commit towards the osteogenic lineage, the activity of ALP (Alkaline Phosphatase) increases, which is also regulated by RUNX2 (272-275), thus ALP was also selected for qPCR analysis alongside RUNX2, whereas GAPDH was selected as a reference gene.

Gene expression analysis (RUNX2 and ALP) was conducted with Y201 cells treated with WT DU145 PCa sEVs, as well as with sEVs overexpressing CD81-Tdtomato and GFP-CD63, in order to investigate if the different phenotype of these sEVs (evident from proteomics analysis in Chapter 4) would exert different effects in osteogenic-related gene expression. Of note, this experiment required large quantities of sEVs and due to low sEV yield, some necessary compromises had to be made; firstly, GFP-CD63 sEVs could only be dosed at concentration of 0, 50 and 100µg/ml, and secondly, the overall dosing step with sEVs could not be performed in multiple wells (no replicates), even though enough isolated RNA was sufficient for triplicate samples in qPCR analysis. The protein and particle concentrations of isolated Bioreactor-derived GFP-CD63, CD81-Tdtomato and WT-DU145 parallel control sEVs used in this experiment are also shown in [Table 2.2](#) (Bioreactors 5-10, isolations #7-9). It is also important to note that part of this experiment (RNA extraction, cDNA synthesis and qPCR analysis) was conducted in collaboration with Dr Rachel Howard-Jones, a postdoctoral research associate at the Tissue Microenvironment Group.

Collectively, this experiment aimed to determine whether chronic exposure of Y201 BM-MSCs to sEVs (72-h) induced early changes in osteogenic gene expression (RUNX2 and ALP) and whether the phenotypic differences of GFP-CD63, CD81-Tdtomato and WT sEVs would induce different effects on osteogenic gene expression.

To begin with, Y201 BM-MSCs were dosed with 0, 50, 100 and 200µg/ml WT DU145 sEVs and CD81-Tdtomato sEVs and 0, 50 and 100µg/ml GFP-CD63 sEVs both in osteogenic and regular media. Gene expression analysis for GAPDH (selected reference

gene), ALP and RUNX2 genes was done for several time-points: (A) 24h of sEV dosing, (B) 72h of sEV dosing, (C) 24h post-sEV dosing (i.e., 96h of assay) and (D) 72h post-sEV dosing (i.e., 144h of assay), and are shown in [Figure 7.2](#).

Firstly, at 24h of sEV dosing we observed an overall increase in expression of RUNX2 for all sEV concentrations and all sEV types, compared to the negative control samples (0µg/ml sEVs) ([Figure 7.2.A](#)). Interestingly, RUNX2 expression was higher for Y201 cells treated with CD81-Tdtomato sEVs (in all concentrations, 16- to 32-fold higher than control), followed by WT DU145 sEVs and then the GFP-CD63 sEVs ([Figure 7.2.A](#)). Furthermore, comparing cells treated with CD81-Tdtomato sEVs in osteogenic versus regular media demonstrated higher levels of RUNX2 for sEVs in osteogenic media ([Figure 7.2.A.i,ii](#) dark red vs red), except for the highest dose of sEVs in which levels of RUNX2 were similar ([Figure 7.2.A.iii](#), dark red vs red). On the other hand, similar levels of RUNX2 were observed for cells treated with GFP-CD63 sEVs in either medium and any concentration ([Figure 7.2.A](#), dark green and green). Conversely, treating Y201 cells with WT DU145 sEVs in regular media was shown to consistently induce higher RUNX2 expression compared to osteogenic media, especially at the highest sEV dose ([Figure 7.2.A](#), blue and light blue). Regarding expression of ALP, at 24h of dosing with sEVs, levels of ALP were relatively similar between sEVs (in either medium), albeit slightly elevated compared to control levels ([Figure 7.2.A](#)).

At the second time-point (72h of continuous sEV dosing), we observed a decrease in the expression of RUNX2, regardless of sEV type and concentration, with no consistent differences between sEVs in osteogenic or regular media ([Figure 7.2.B](#)). Conversely, we observed an increase in the expression of ALP (except for the lowest sEV dose 50µg/ml [Figure 7.2.B.i](#)), even though similar levels of expression were observed regardless of sEV type or concentration (~6-fold increase, [Figure 7.2.B.ii,iii](#)); similarly to the expression of RUNX2, no consistent differences between cells treated with sEVs in osteogenic or regular media were apparent ([Figure 7.2.B.ii,iii](#)).

Finally, at 24- and 72-h post-sEV dosing, i.e., 96- and 144-h of the assay, we observed further progressive decrease of RUNX2, as well as reduction of ALP, of cells treated with sEVs in osteogenic/regular media, as well as for cells treated only with osteogenic media (without sEVs) ([Figure 7.2.C-D](#)). Specifically, at 144h after starting the assay, the expression of ALP and RUNX2 appeared significantly downregulated for all samples, especially for cells treated with CD81-Tdtomato and WT sEVs (at any concentration) regardless of culture media ([Figure 7.2.D](#)).

To conclude, this gene expression analysis was done as a proof-of-concept and demonstrated that dosing of Y201 cells with DU145 sEVs, sequentially increased the expression of RUNX2 (24h), and then ALP (72h), followed by their mutual

downregulation after 144h, indicative of BM-MSc differentiation towards an osteogenic lineage (272). Dosing of Y201 cells with CD81-Tdtomato sEVs seemed to cause an initial higher increase of RUNX2 than GFP-CD63 and WT DU145 sEVs, even though that was not further reflected in the expression of ALP which was similar between all sEVs. Unexpectedly, these alterations in gene expression were observed for cells treated with sEVs in both osteogenic and regular media, which were also different to cells treated with osteogenic media only; these potentially suggested that DU145 sEVs could solely drive Y201 cells towards osteogenic differentiation. However, as this experiment is preliminary, further investigation of the influence of sEVs in osteogenic differentiation is essential, as well as examination of a larger number of osteogenic genes to determine potential differences in gene regulation between WT DU145 sEVs, and sEVs overexpressing tetraspanins.

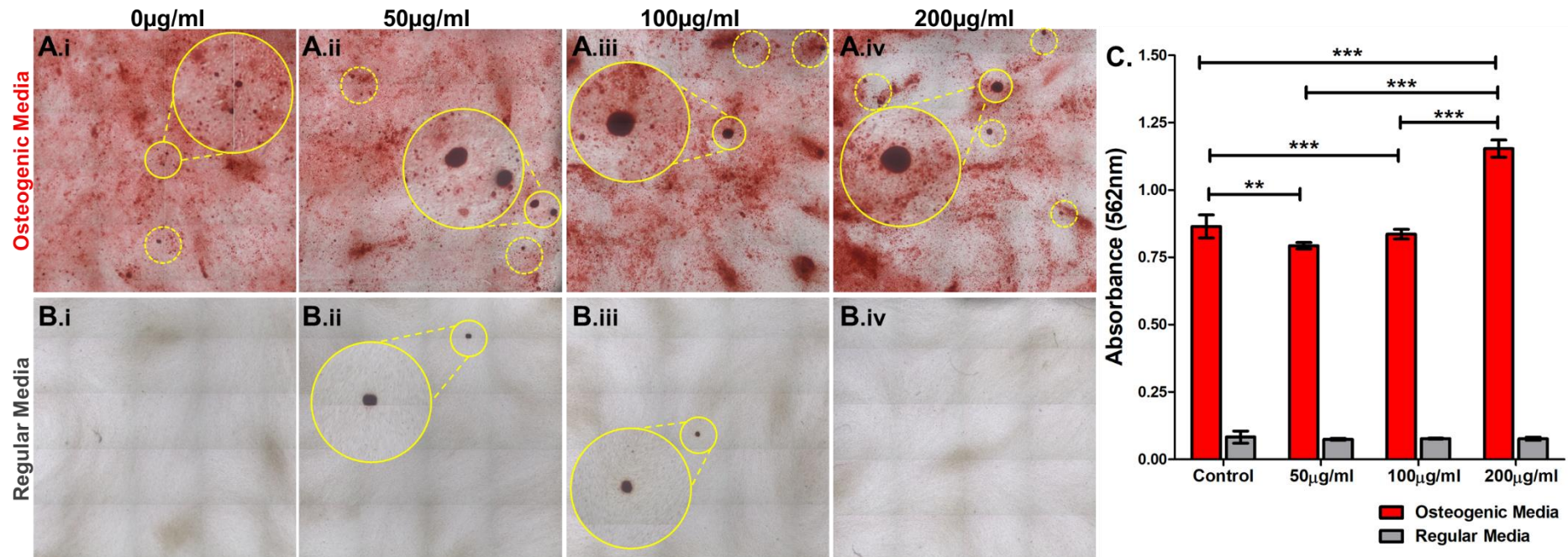


Figure 7.1. Visualisation and quantification of Alizarin Red S Staining in differentiating Y201 cells dosed with CD81-Tdtomato sEVs in osteogenic and regular media.

Microscopy images of Alizarin Red S staining at day 21 for Y201 cells dosed CD81-Tdtomato sEVs (72-hour dosing) in **(A)** osteogenic media and **(B)** regular media for increasing concentrations of sEVs: **(i)** 0 µg/ml, **(ii)** 50 µg/ml **(iii)** 100 µg/ml and **(iv)** 200 µg/ml; yellow circles demonstrate magnification of large dark red foci that represent potential osteogenic calcified nodules. **C.** Colorimetric quantification of Alizarin Red S staining based on absorbance at 562nm. Error bars denote standard deviation. Statistical analysis was done using two-way ANOVA and Bonferroni's post-hoc multiple comparisons suggesting highly significant statistical differences with **p<0.01 and ***p<0.001.

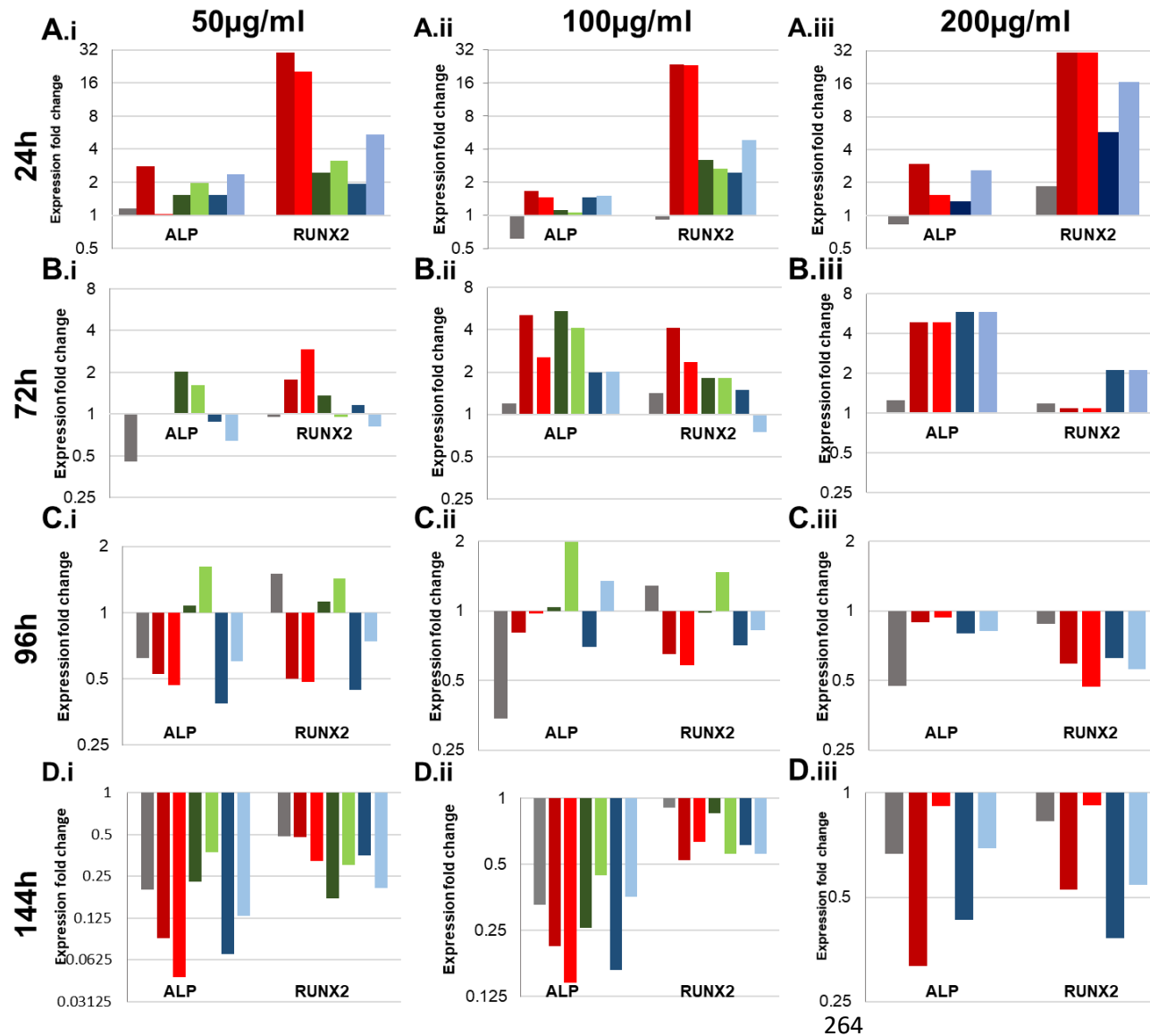


Figure 7.2. Gene expression analysis of osteogenic differentiation genes in Y201 cells dosed with increasing concentrations of sEVs in osteogenic or regular media.

Gene expression analysis for ALP and RUNX2 in Y201 cells at: (A) 24h of sEV dosing, (B) 72h of sEV dosing, (C) 96h (24h post sEV-dosing) and (D) 144h (72h post sEV-dosing). Y201 cells were treated with (i) 50µg/ml, (ii) 100µg/ml and (iii) 200µg/ml DU145 sEVs at either osteogenic (O) or regular (R) media. sEVs used for dosing were: CD81-Tdtomato (red bars), GFPCD63 (green bars) and WT DU145 (blue bars). Untreated negative controls in osteogenic (O) media are shown by gray bars (Ctrl).

Note that graphs show expression fold change of genes compared to untreated negative control samples in regular (R) media.

7.4. Discussion

Recent studies support that BM-MSCs can be effectively recruited by prostate tumours to become part of the tumour-supportive microenvironment stroma (37, 38, 268), or can be differentiated by prostate tumour -derived secreted sEVs towards an osteogenic lineage at the bone, thus supporting the formation of the pre-metastatic niche for PCa metastasis (63, 66), even though the latter has been vastly unexplored.

Hence this small Chapter explored whether DU145 PCa sEVs could differentiate the well-characterised Y201 BM-MSCs (126, 266) towards an osteogenic lineage, and whether the different DU145 sEVs generated and characterised in previous Chapters (CD81-Tdtomato and GFP-CD63 sEVs) could differentially affect the differentiation of Y201 cells. This Chapter represents the proof-of-principle work for determining the early effects of cancer-derived sEVs on BM-MSC differentiation.

The first experiment assessed the late osteogenic differentiation of Y201 cells by Alizarin Red S staining. Alizarin Red reacts with calcium, which is formed after mineralisation by osteoblasts, thus forming a red precipitate (148); this can be visualised and quantified to measure the levels of deposited calcium, and thus, the levels of mineralisation by differentiated cells. CD81-Tdtomato sEVs were used to perturb BM-MSC differentiation, as the dosing, uptake and retention of these sEVs in Y201 cells was already characterised in the Chapter 6 (sEVs and/or sEV-cargo were shown to persist in Y201 cells for at least 168h).

Our preliminary experiment demonstrated that a 72-h exposure of Y201 cells to CD81-Tdtomato sEVs (in osteogenic media) promoted osteogenic differentiation of these cells, as Alizarin Red S staining (at day 21 of the assay) showed enhanced mineralisation with concentrated calcium deposits that increase in abundance (and size) in an sEV dose-dependent manner. The Genever group that generated these Y201 cells, also demonstrated their differentiation towards an osteogenic lineage after 21 days in osteogenic media, by Alizarin Red S staining (126).

Interestingly, in our preliminary experiment, exposure of Y201 cells to CD81-Tdtomato sEVs in regular media also induced a few concentrated calcium foci, which might suggest that sEVs alone could drive osteoblastic differentiation; however, this was not obvious after quantification of the dye. This might be due to the lower sensitivity of the colorimetric detection or accidental detachment of parts of the cell monolayer due to multiple washing steps; a previous study acknowledged this and normalised Alizarin Red S signal to Crystal Violet signal for each well (276). The same study also demonstrated that PCa PC3 sEVs can induce the differentiation of 7F2 osteoblasts towards

mineralization, only when treated with sEVs in osteogenic media (shown by Alizarin Red S staining), and only when dosed with the highest concentration of sEVs (200µg/ml) (276).

A different study demonstrated that EV-rich conditioned media (not sEVs directly) from PCa PC-3 cells can increase the expression of pro-osteoblastic commitment factors in human BM-MSCs (e.g., α_5/β_1 integrins, fibronectin, and osteoprotegerin) and promote their osteoblastic differentiation with concomitant increase in the osteoblastic markers osteocalcin, ALP, and core-binding factor alpha 1 (RUNX2 alias), as assessed after 21 days using the Alizarin Red S mineralisation assay (63). Surprisingly, a different study using A549 lung cancer-derived sEVs showed inhibition of osteogenic differentiation of MSCs, even with the highest concentration of sEVs tested (200µg/ml), as decreased mineral deposition was detected by Alizarin Red S staining; this difference suggests that differentiation of BM-MSCs might be cancer sEV-type specific (277).

To investigate whether different sEV phenotypes affect differentiation of BM-MSCs, and further explore the effects of sEVs on early differentiation of Y201 cells, we performed gene expression analysis for two osteogenic genes, RUNX2 and ALP for cells dosed with 0,50,100 and 200µg/ml WT DU145 sEVs, CD81-Tdtomato sEVs and 0,50 and 100µg/ml GFP-CD63 sEVs both in osteogenic and regular media. These preliminary results showed that dosing of Y201 cells with DU145 sEVs in osteogenic and regular media increased the expression of RUNX2 at 24h of continuous sEV dosing. This observation potentially agrees with the regulation of this marker, as expression of RUNX2 increases early, being one of the earliest transcription factors that promote osteoblastic differentiation of MSCs, which mature into osteoblasts, and eventually osteocytes (273, 274). A previous study also demonstrated upregulation of RUNX2 and osteoblastic differentiation in Y201 cells cultured in osteogenic media only, even though that was observed at day 7 of the assay (126). A different study however showed that transducing MSCs with RUNX2 induced their osteoblastic differentiation and the maximal upregulation of RUNX2, just 24h after transduction (275).

Moreover, we observed that treating cells with CD81-Tdtomato sEVs (in either regular or osteogenic media) induced a dramatic increase in RUNX2 expression compared to GFP-CD63 and WT DU145 sEVs at the first timepoint. This might be due to the differential phenotype of CD81-Tdtomato sEVs. For example, our proteomics analysis from Chapter 4 revealed that the CD81-Tdtomato sEVs express higher levels of Integrin α_2 , which has been shown to promote PCa metastasis and growth at the bone niche (278). Another hypothesis is that these effects might be driven by sEV size; a previous study showed that uptake of smaller EVs is highly efficient compared to larger EVs(106), and our observations from NTA and Cryo-TEM clearly demonstrated the

smaller size of CD81-Tdtomato sEVs compared to the other sEV types, suggesting that potentially these sEVs can be more efficiently internalised by the Y201 BM-MSCs.

Interestingly, at 72h of continuous sEV dosing, we observed a decrease of RUNX2 expression and a concomitant increase in ALP expression; similar levels of ALP expression were observed for Y201 cells treated with all three DU145 sEV types, even if CD81-Tdtomato sEVs caused an initial higher increase of RUNX2 compared to GFP-CD63 and WT DU145 sEVs. A recent publication exhibiting similarities to our study, demonstrated that the delivery of C4-2B PCa sEVs overexpressing GFP-CD63 in the immortalized human BM-MSCs lead to the transfer of the hsa-miR-940 miRNA which resulted to the downregulation of ARHGAP1 and FAM134A and to the eventual increase of ALP expression after a 48-h incubation with sEVs; thus denoting the onset of osteoblastic differentiation of BM-MSCs (66).

It is currently established that after initial upregulation of RUNX2, ALP is directly activated by RUNX2, thus ALP expression is expected to increase as cells differentiate more towards an osteoblastic lineage (272-275). Furthermore, whereas RUNX2 expression is predominantly high during the early stages of differentiation, it gradually declines when cells progress with differentiation (272-275); thus, our observations in differentiating Y201 cells potentially reflect this dynamic between RUNX2-ALP at the first 72h of our assay. Another study also demonstrated the elevation of RUNX2, and then ALP activity in Y201 cells, after their continuous culture in osteogenic media (126).

Unexpectedly, these alterations in RUNX2 and ALP gene expression were observed for Y201 cells treated with sEVs in both osteogenic and regular media, suggesting that DU145 sEVs could potentially drive osteoblastic differentiation even in the absence of osteogenic factors. This result is surprising, as CD81-Tdtomato sEVs in regular media mostly failed to induce significant mineralization of Y201 cells, except some rare occurrences of small potentially calcium foci deposits. However, as the Alizarin Red S staining provides a late assessment of osteogenic differentiation after 21 days, this suggests that perhaps a longer or continuous exposure of Y201 BM-MSCs to CD81-Tdtomato sEVs might be necessary to reflect these early changes in RUNX2 and ALP expression (first 72 hours) in the long-term. A previous study reflected our observations as PCa PC3 sEVs (200µg/ml) induced osteoblastic differentiation, shown by increased expression of 3 osteogenic genes (MMP3, ACVR1, COL1A1) or decreased expression of one gene (DLX5) in 7F2 cells treated with sEVs in both osteogenic and regular media, even though treatment of these cells with PC3 sEVs in regular media only, failed to induce mineralisation, as shown by Alizarin Red S staining (276).

7.5. Conclusions

In conclusion, this proof-of-concept investigation indicated that DU145 PCa sEVs can induce the osteogenic differentiation of Y201 BM-MSCs and showed that overexpression of CD81 or CD63 on EVs can differentially affect the expression of the early osteogenic differentiation markers RUNX2 and ALP. Most surprising was the finding that DU145 sEVs alone could promote the osteogenic differentiation of Y201 BM-MSCs, even in the absence of osteogenic factors. As the findings of this Chapter are preliminary in nature, it is essential to further assess the direct influence of sEVs on osteogenic differentiation, as well as elucidate potential differences in gene regulation between WT DU145 sEVs, and sEVs overexpressing CD63 or CD81 for a larger number of genes that reflect different stages of differentiation.

Chapter 8:

General Discussion

8.1. Summarising Discussion

Cancer-derived sEVs deliver and exchange their cargo mediating cell-to-cell communication, which results in modulation of the tumour microenvironment for promotion of tumour growth, immune system evasion, and stimulation of angiogenesis and metastasis (41, 42). Cancer-derived sEVs also promote the formation of the pre-metastatic niche, due to their ability to disseminate through tissue microenvironments (41, 42). Even if recent advances have been made regarding the various interactions of sEVs with cells, as well as their internalisation and fate pathways with a recipient cell, the mechanisms underlying sEV uptake kinetics, retention and distribution in cell populations and tissues still remain poorly understood.

To address this, high-resolution microscopy is essential to image sEVs *in situ*, thus requiring fluorescence labelling to enable for their detection. Genetic encoding of fluorescent proteins fused with vesicular-associated proteins like the tetraspanins CD63 and CD81, provide a specific method of sEV visualisation, which has been currently adopted by various *in vitro* and *in vivo* studies (116-123). One of the major limitations of this method, is the unknown consequences on the cell and sEV phenotype after tetraspanin overexpression (19). However, many previous studies using these fluorescent tetraspanin reporter systems, have assumed that overexpression of tetraspanins does not alter their cell systems and have not thoroughly characterised them (116, 117, 119, 121, 123).

We hypothesised that overexpressing tetraspanins like CD63 or CD81 would alter the phenotype of sEVs, especially due to their central role in sEV biogenesis, cargo sorting and secretion (22, 24); thus, it was essential to determine any potential phenotypic changes in engineered cells and sEVs. This is particularly important since these engineered cell lines can be used directly *in vitro*, to produce sEVs, which can then in turn be used exogenously in other cell systems.

Acknowledging this current limitation of fluorescent sEV reporters, we generated two DU145 PCa cell lines expressing the fluorescent proteins GFP or Tdtomato fused to CD63 or CD81 respectively, and revealed phenotypic and proteomic differences in cells, as well as their secreted sEVs. To our knowledge, this is the first study that: (i) engineered these GFP-CD63 and CD81-Tdtomato fusion proteins in DU145 PCa cells, (ii) extensively characterised their phenotype and proteome revealing alterations after tetraspanin overexpression, and (iii) utilised them as sEV reporters to study sEV uptake kinetics, retention, and distribution in dynamic cell systems.

Phenotypic Changes in DU145 Cells Overexpressing CD63 or CD81

Our results demonstrated that overexpression of CD63 or CD81 led to phenotypic and proteomic changes in DU145 PCa cells, thus supporting our hypothesis. Overexpression of CD81 altered cell morphology, and slowed cell cycle progression in DU145 cells, without affecting the expression of other EV-associated proteins at the cell membrane. On the other hand, overexpression of CD63 led to opposing morphological changes in DU145 cells, without altering cell cycle dynamics, but exhibited substantial changes in expression of other tetraspanins and sEV-associated proteins at the cell membrane. Proteomic analysis revealed changes after overexpression of CD63 or CD81, with some identified dysregulated proteins involved in metabolism, membrane trafficking, cell growth, and survival, as well as associated with the cytoskeleton, cell adhesion and migration. For example, downregulation of RCC2 expression (Regulator of Chromosome Condensation 2, protein with major role progression through mitosis), as well as downregulation of α -actinin-4 (cross-linking protein anchoring actin cytoskeleton with various intracellular structures) in CD81-Tdtomato cells, might support the observed delay in cell cycle progression or altered morphology, respectively, in these cells (279, 280). Other examples are upregulation of TAP1- antigen peptide transporter 1 (mediates translocation of peptide antigens from cytosol to endoplasmic reticulum for loading onto MHC-1 molecules) and β -2-microglobulin (component of MHC-1) in GFP-CD63 cells, which support the significant overexpression of MHC-1 observed at their cell membrane (281). Overall, our results demonstrated that overexpression of CD63 or CD81 led to different phenotypic changes in DU145 cells, which are probably attributed to their distinct functions (20, 22, 24).

After establishing the phenotypic and proteomic changes of DU145 cells overexpressing tetraspanins in conventional 2D culture, we then transferred them to the 3D-like microenvironment of CELLline Bioreactor Flasks. Currently, Bioreactors have been commonly used by researchers to support large-scale cell growth in order to generate high-yield and high-purity sEV preparations (115, 127, 157, 211-214); however, their long-term effects on the phenotype of cultured cells and sEVs have not been thoroughly investigated.

We hypothesised that this 3D-like microenvironment will have an effect on the phenotype of cells and sEVs and we investigated how engineered stable DU145 cell lines adapt in the Bioreactor Flasks depending on their overexpression of CD63 or CD81, and what are the long-term effects of the Bioreactor on the physiology of cells and the phenotype of secreted sEVs. This is the first study, to our knowledge, that utilised Bioreactor Flasks for culturing fluorescently-conjugated tetraspanin reporter cell lines

and conducted long-term characterisation of these cells and secreted sEVs in this microenvironment.

Interestingly, some phenotypic changes observed in 2D culture were reflected in the 3D-like microenvironment of the Bioreactor Flasks. For example, CD81-Tdtomato cells maintained their fluorescence long-term and exhibited similar cell cycle dynamics as in 2D culture, whereas GFP-CD63 cells exhibited slower growth due to lower cell viability and progressively lost their fluorescence signal. The exact mechanisms behind these phenotypic changes need to be further elucidated, however proteomics analysis can provide some insight. For example we showed downregulation of integrin α_3 expression in GFP-CD63 cells, and a recent study in kidney epithelial cells demonstrated that knockout of integrin α_3 severely disrupts adhesion (225); if this is also the case for PCa, it might indicate that GFP-CD63 cells are not well-adherent and might be more sensitive to anoikis. Furthermore, these cells exhibited downregulation of prostaglandin reductase 1 (PTGR1), which was shown to suppress PC3 prostate cancer cell proliferation by inducing apoptosis (226). In addition, potential Bioreactor microenvironmental factors like acidic pH, oxidative stress or hypoxia, can also affect cells and sEVs grown in these platforms, and might confer to the reduction of GFP fluorescence (220). In fact, oxidative stress or hypoxia might be the major stressor for GFP-CD63 cells in the Bioreactors, as a previous study showed that cells secrete MHC-1 under hypoxia crisis (240), or form MHC-1 dimers when exposed to oxidative stress resulting in apoptosis (239). We indeed observed an increase in membrane expression of MHC-1 via flow cytometry and upregulation of various MHC-1- associated proteins via proteomics analysis (as mentioned above).

Overall, our investigation showed that overexpression of tetraspanins conjugated with fluorescent proteins did not result in an inert change in cells, rather it caused various alterations to their physiology and proteome. Furthermore, phenotypic alterations might also occur due to uncontrolled microenvironmental factors of the platform used to culture these engineered cell lines, which can have detrimental effects into the cells and also potentially affect secreted sEVs. Thus, investigation of the cell phenotype, in conjunction with the careful consideration and characterisation of the cell culture platform is essential when using fluorescently-conjugated tetraspanin reporter cell lines.

Phenotypic Changes in sEVs after Overexpression of CD63 or CD81

As expected, the changes in cell phenotype after overexpression of CD63 or CD81, also led to changes in the phenotype and proteome of secreted sEVs, thus supporting our

initial hypothesis and highlighting the importance of characterising these fluorescent sEVs, as they can be used in various models for the study of sEV uptake and fate, or for functional studies.

Initial characterisation demonstrated that secreted sEVs (isolated from 2D culture of stable cell lines) mostly reflected their cells of origin and exhibited altered expression of tetraspanins and EV-associated proteins (CD9, CD63, CD81, MHC-1) (192). Contradictory to our observations, previous studies claimed that overexpression of CD63-pHluorin (GFP variant) in HeLa cells (118), and GFP-CD63 in HEK293T cells (122), does not significantly alter the levels of CD81 or even CD63 on sEVs.

However, in our study, thorough investigation of the sEV proteome by SWATH-MS proteomics analysis identified various dysregulated proteins in CD81-Tdtomato and GFP-CD63 sEVs compared to WT parallel controls. Highlighting the essential roles of tetraspanins in sEV biogenesis and interactions with other proteins at the TEMs, a plethora of detected dysregulated proteins were associated with sEV biogenesis, membrane trafficking, endosomal/MVB pathways and the ubiquitin-dependent ESCRT complexes. Other dysregulated proteins were found to be involved in adhesion, cytoskeleton, migration, metabolism, growth, survival, and the MHC-1 immune response for GFP-CD63 sEVs in accordance with the parental cells (e.g., upregulation of β 2-microglobulin). The majority of detected dysregulated proteins were not common between CD81-Tdtomato and GFP-CD63 sEVs, and even some of the common proteins exhibited differential expression (e.g., integrin α_2 , VPS4A/B, β -catenin, EPCAM etc.), further highlighting that overexpression of CD63/CD81 drives different sEV phenotypes.

These observations demonstrated that overexpression of CD63 or CD81 in DU145 cells lead to significant and differential changes in the released vesicle composition with potential consequences for their biological functions (12, 156, 192). For example, some interesting proteomic hits like EGFR (upregulated in GFP-CD63 sEVs), β -catenin (upregulated in GFP-CD63, downregulated in CD81-Tdtomato sEVs) and integrin α_2 (upregulated in CD81-Tdtomato sEVs), have been shown to mediate various functions when delivered by sEVs to recipient cells. EV-mediated transfer of EGFR was shown to exert a pro-metastatic effect for gastric cancer cells metastasising to the liver, delivery of β -catenin by sEVs can activate or antagonise Wnt signalling pathway in recipient cells, and integrin α_2 was shown to promote migration and invasion of PCa cells by inducing EMT (282-284). Due to the magnitude of dysregulated proteins that were detected in CD81-Tdtomato and GFP-CD63 sEVs, it would be currently quite challenging to predict their specific impact in recipient cells, thus extensive validation needs to be performed, followed by functional studies for targets of biological interest.

When we extended our phenotypic characterisation to Bioreactor Flask-derived sEVs, we observed that sEVs generated in this 3D-like emulated microenvironment exhibited some alterations compared to sEVs isolated from 2D conventional culture; similarly observed for the parental cells. As expected, we saw loss of fluorescence signal in GFP-CD63 but not in CD81-Tdtomato sEVs, thus reflecting the fluorescence status of their parental cells. Moreover, we observed a change in the levels of EV-associated markers loaded on sEVs compared to 2D culture; for example, we observed a negative relationship between CD81 overexpression and CD63- loading of sEVs and a negative relationship between CD63 overexpression and CD81-loading of sEVs. We also observed significantly high levels of MHC-1 expression in all sEVs, suggesting potential response to hypoxia or oxidative stress in the Bioreactors (238, 240); for GFP-CD63 sEVs this MHC-1 response was also supported by proteomics analysis (as mentioned above). Further investigation is necessary to confirm whether hypoxia or oxidative stress are actually stressors in these Bioreactors, and what are their effects on sEV production, composition and eventually sEV function.

Beyond the fact that altering tetraspanins can result to sEV populations with different cargos (192), these differences between 2D and 3D environments suggest further alterations in the balance of sEV subpopulations in the Bioreactors e.g., more enrichment of CD81+ or CD63+ vesicles, even though the exact mechanisms behind this are unclear. This is also supported by the observed changes in sEV size distributions in the Bioreactors (not observed in 2D), as sEVs overexpressing CD63 or CD81 were slightly larger or significantly smaller than control sEVs, respectively. Supporting our observations, a previous study showed changes in the morphology, size distribution and EV-associated surface markers of Bioreactor-derived sEVs compared to conventional 2D-derived sEVs, as well as significant metabolomic changes (214). Cryo-TEM analysis comparing CD81-Tdtomato with control sEVs verified these size differences, without however significant changes in morphology, but showed an enriched population of vesicles in CD81-Tdtomato sEVs (<100nm in diameter), that was significantly smaller than control sEVs. Even though the exact reasons behind this are not clear, our proteomics analysis revealed dysregulated proteins involved in sEV biogenesis and vesicle fission, like VPS4B and CHMP1B (285, 286), which might play part in generating diverse sEV subpopulations.

To conclude, we showed that these fluorescently-conjugated tetraspanin reporter systems caused significant changes in the cell and sEV phenotype and thus careful consideration is required for: (i) the characterisation of cell lines to establish their phenotype/proteome after tetraspanin overexpression, (ii) the phenotypic characterisation of secreted sEVs to gain some insight into their composition, and (iii)

the characterisation of the cell culture platforms and their potential microenvironmental impact on the phenotype of these cells and sEVs.

Distribution and Functional Effects of sEVs in Dynamic Cell Systems

Despite many studies providing valuable insight on the mechanism of sEV entry in cells, the kinetics of sEV uptake and distribution in dynamic cell systems have not been greatly explored; however, due to the emerging use of sEVs for delivery of therapeutics in tissues, investigation of sEV uptake/retention kinetics is essential, as supported by the 2019 ISEV position paper (251). In our study, after phenotypic and proteomic characterisation of sEVs, the fluorescent CD81-Tdtomato sEVs were used to study sEV uptake kinetics (dosing), retention and distribution in propagating cell populations (DU145 PCa cells and Y201 BM-MSCs representing cells of the tumour microenvironment and the pre-metastatic niche, respectively).

Firstly, we established the baseline behaviour of our cell systems for taking up and distributing the QD705 established nanoparticles (145, 146, 252, 253), and then compared them to CD81-Tdtomato sEVs. To our knowledge, this is the first study that compared Quantum Dots to sEVs to reveal conserved principles but different dynamics in their uptake and distribution in cell populations. We demonstrated that the DU145 PCa and Y201 BM-MS cell populations exhibited heterogeneous uptake of QD705 and CD81-Tdtomato sEVs, which was at least partly positively correlated to the area of the cell (258). This might be of particular importance for the uptake of sEVs delivering therapeutics, as it could at least partly depend on the physical characteristics of the recipient cell/tissue.

Despite this preserved principle of uptake heterogeneity, the QD705 and CD81-Tdtomato sEV uptake dynamics differed significantly between the two cell systems, with the DU145 PCa cells internalising and distributing QDs and CD81-Tdtomato sEVs faster than the Y201 BM-MSCs. The exact reasons behind this are not clear, and still controversial in the literature, with some studies showing preferential uptake of sEVs by their cells of origin, others supporting non-specificity for sEV uptake, and others suggesting that dependence of uptake on highly metabolically active recipient cells (84, 116, 265). As QD705 are functionalised with a non-specific cell-targeting peptide (arginine-rich peptide (257)), and were also internalised and distributed faster in DU145 than Y201 cells (albeit slower than sEVs) this phenomenon might be partly attributed to the physical characteristics of recipient cells. In any case, the identification of target cells that are potentially more receptive to sEVs, or that can internalise and process sEVs

faster or more selective, would be beneficial for therapeutic purposes e.g., for the development of novel specific vectors targeting specific cell populations/tissues.

Finally, we demonstrated that after dosing with QDs the QD705 signal was distributed via asymmetrical partitioning to daughter cells (145, 252, 253). We hypothesise that this is at least partly conserved for CD81-Tdtomato sEVs but with also simultaneous sEV degradation or processing or re-secretion. Internalised sEVs are mostly sequestered to endosomes/lysosomes, and may be asymmetrically partitioned to daughter cells with the asymmetrical partition of endosomes(267); however sEVs can also be rapidly degraded in lysosomes or re-secreted (3, 4).

After characterising the uptake kinetics, retention, and distribution of CD81-Tdtomato PCa sEVs in the Y201 BM-MSC population, we conducted some preliminary experiments which indicated that chronic exposure of these cells to sEVs induced their osteogenic differentiation towards osteoblasts; this was also suggested by previous studies where sEVs differentiate BM-MSCs towards an osteoblastic lineage at the pre-metastatic bone niche (63, 64, 66). Furthermore, we observed differences in the transcription regulation of early osteogenic markers RUNX2 and ALP (273, 274) between the delivery of CD81-Tdtomato, GFP-CD63 and WT DU145 sEVs, however further investigation is necessary to validate these preliminary results and determine whether these translate to differences at the late stages of differentiation, as well as the sEV cargo responsible for these differences. For example, our proteomics analysis revealed that CD81-Tdtomato sEVs have higher levels of integrin α_2 , which has been shown to promote PCa metastasis and growth at the bone niche (278), so integrin α_2 might be a good target for future investigation. A previous study conducting functional studies on RWPE1 prostate sEVs with modified tetraspanins (CD9 downregulation/ CD151 upregulation) showed that delivery of these sEVs can have different functional effects on the migratory and invasive potential of recipient cells, due to differences in the sEV proteome (192). Hence it is possible that different sEV proteomes can drive different functional effects in recipient cells, however further functional studies are necessary to validate this hypothesis.

Overall, our study outlined the principles of sEV uptake kinetics, retention, and distribution in 2D-dynamic cell systems that reflected both parental tumour cells and BM-MSCs which can be found in the tumour microenvironment and pre-metastatic bone niche. Utilising these principles, we conducted preliminary analysis and revealed the ability of sEVs to enhance osteogenic differentiation of BM-MSCs. These studies can be the basis for further investigations in 3D tissue-mimic models encompassing the tumour microenvironment and the pre-metastatic bone niche, which would allow the study of

sEV dissemination in physiological environments and functional assessment of their delivery in surrounding cells.

8.2. Future Directions

In this study we have generated and characterised tetraspanin-conjugated fluorescent sEV reporters, from which CD81-Tdtomato sEVs were then used to establish basic principles of EV uptake kinetics, retention, and distribution in 2-dimensional propagating cell populations. Furthermore, we explored the function of these sEVs in enhancing the osteogenic potential of BM-MSCs, a known role of PCa sEVs in promoting the formation of the pre-metastatic bone niche (53, 54, 56). A more extensive study is necessary however, to establish BM-MSC osteogenic differentiation and the potential induction differences between EV types; for example, additional pro-osteoblastic markers should be investigated such as the upregulation of integrins α_5/β_1 , fibronectin, and osteoprotegerin or downregulation of ARHGAP1 and FAM134A which were shown to commit BM-MSCs towards the osteoblastic lineage (63, 66).

In addition to validation of the functional effects of PCa sEVs on 2D culture systems, we propose that future work focuses on moving towards more physiologically-relevant 3D tissue mimic-models which will better emulate the PCa microenvironment and the pre-metastatic bone niche, and importantly the interplay between them (287, 288). Notably, as PCa is a disease that involves the complex abnormal interactions between PCa cells, stroma cells of the surrounding microenvironment and the ECM, 2D cell culture models still lack important 3D structures and the ECM components necessary for PCa development (30, 31). Thus, 3D biomimetic *in vitro* models, microfluidic models, as well as organ-on-a-chip models are now considered more clinically and physiologically relevant for PCa and can be adapted for sEV studies (287, 288). As we established the basic principles of sEV uptake and distribution in 2D cell systems in our study, and we were also able to detect and optically characterise fluorescent sEVs in 3D hydrogels (Cygel™), more complex 3D cell models can be developed building on those principles.

To achieve this however, a high yield of sEVs is necessary to fully enable for analyses and use in tissue-mimic models. As we mentioned previously, the microenvironment conditions of the fixed-bed CELLLine Bioreactors (210) might need further characterisation as they were not ideal for the GFP-CD63 DU145 cell line, perhaps due to the sensitivity of GFP to potentially acidic pH, oxidative stress or hypoxia of that environment (220, 228). Thus, we propose to use a different system, the FiberCell hollow-fiber bioreactor, as a potential clinically-relevant system for scaled-up sEV manufacture (112, 289, 290). Hollow-fiber bioreactors enable high cell growth, high sEV

yield and high purity of sEV preparations and their 3D-culture perfusion system enables the exchange of nutrients, waste, and gasses, thus improving issues of fixed-bed Bioreactors like hypoxia (112, 289, 290).

Some examples of 3D biomimetic PCa *in vitro* models include cells embedded in hydrogel, collagen or other relevant ECM components which can be utilised to study sEV delivery, uptake and dispersion in 3D space (287, 288). It has been previously suggested that the secretion and phenotype of sEVs in 3D culture is different to 2D conventional culture (222, 291), however the exact kinetics of 3D-secretion or uptake of sEVs have not been further explored. Thus, we propose that 3D tissue-mimic *in vitro* models are developed, to enable the incorporation of various cell types like tumour cells, stromal cells (e.g., fibroblasts, endothelial cells), immune cells or BM-MSCs, as well as ECM components thus giving the ability to recapitulate the primary tumour microenvironment and/or the pre-metastatic niche. For these models, fluorescent sEVs can be exogenously added or pre-embedded to track their delivery, dispersion uptake and distribution by recipient cells. Besides exogenous sEV delivery, these 3D biomimetic models can also incorporate the fluorescently-conjugated tetraspanin stable cell lines directly, to track endogenous sEVs between them and/or with other target cells like BM-MSCs, thus investigating cell-to-cell communication between tumour and pre-metastatic niche.

Beyond these *in vitro* 3D tissue-mimic models, microfluidic (292). and organ-on-a-chip (293) models can also be developed for the study of sEV dispersion in PCa microenvironments and the pre-metastatic bone niche. Microfluidic models consist of a microfluidic device with microchannels, that are connected to a perfusion system to allow for fluid and gas exchange, among other functions. These models have the advantage of parameter control (e.g., pH, temperature, and oxygen concentration), and of incorporation of multiple cell types to emulate the tumour microenvironment and metastatic bone-niche (288, 292). Thus, they can be adapted accordingly for sEV studies either by adding exogenous fluorescent sEVs or incorporating the parental fluorescent tetraspanin cell lines directly to the model. Finally, organ-on-a-chip models can be developed by culturing organ explants (e.g., from prostate tumours or bone metastasis), as they most faithfully recapitulate the *in vivo* microenvironment and can be utilised to exogenously deliver fluorescent sEVs for the study of dispersion and cell-to-cell communication (288, 293).

To summarise, this study has revealed the basic principles of sEV uptake kinetics, retention, and distribution in 2D cell populations, and future work should focus on translating these studies to 3D tissue-mimic models that better represent the *in vivo* microenvironments, in order to investigate crucial unanswered questions regarding sEV dissemination through tumours and the pre-metastatic niche.

Concluding Remark

In the current study, we showed evidence of phenotypical and proteomic alterations of fluorescent sEV reporters after overexpression of tetraspanins CD63 or CD81, both at the cellular and vesicular level. We also revealed the effects of CELLLine Bioreactors on the phenotype of cells and sEVs and emphasised the need for characterisation of the cell culture platforms utilised for fluorescent sEV reporters. Using one of these fluorescent sEV reporters, we investigated and quantified sEV behaviour in dynamic cell systems and revealed conserved principles in sEV uptake kinetics, retention, and distribution. Deciphering these fundamental principles will provide the basis for understanding the physiological dispersion of sEVs in tissue microenvironments, thus underlining the great potential for diverse clinical applications, including the use of sEVs as drug delivery vectors.

REFERENCES

1. Deatherage BL, Cookson BT. Membrane vesicle release in bacteria, eukaryotes, and archaea: a conserved yet underappreciated aspect of microbial life. *Infect Immun*. 2012;80(6):1948-57.
2. Cocucci E, Meldolesi J. Ectosomes and exosomes: shedding the confusion between extracellular vesicles. *Trends Cell Biol*. 2015;25(6):364-72.
3. Gurung S, Perocheau D, Touramanidou L, Baruteau J. The exosome journey: from biogenesis to uptake and intracellular signalling. *Cell Commun Signal*. 2021;19(1):47.
4. van Niel G, D'Angelo G, Raposo G. Shedding light on the cell biology of extracellular vesicles. *Nat Rev Mol Cell Biol*. 2018;19(4):213-28.
5. Battistelli M, Falcieri E. Apoptotic Bodies: Particular Extracellular Vesicles Involved in Intercellular Communication. *Biology (Basel)*. 2020;9(1).
6. Théry C, Witwer KW, Aikawa E, Alcaraz MJ, Anderson JD, Andriantsitohaina R, et al. Minimal information for studies of extracellular vesicles 2018 (MISEV2018): a position statement of the International Society for Extracellular Vesicles and update of the MISEV2014 guidelines. *J Extracell Vesicles*. 2018;7(1):1535750.
7. Willms E, Johansson HJ, Mäger I, Lee Y, Blomberg KE, Sadik M, et al. Cells release subpopulations of exosomes with distinct molecular and biological properties. *Sci Rep*. 2016;6:22519.
8. Théry C, Boussac M, Véron P, Ricciardi-Castagnoli P, Raposo G, Garin J, et al. Proteomic analysis of dendritic cell-derived exosomes: a secreted subcellular compartment distinct from apoptotic vesicles. *J Immunol*. 2001;166(12):7309-18.
9. Hurley JH. ESCRT complexes and the biogenesis of multivesicular bodies. *Curr Opin Cell Biol*. 2008;20(1):4-11.
10. Schmidt O, Teis D. The ESCRT machinery. *Curr Biol*. 2012;22(4):R116-20.
11. Doyle LM, Wang MZ. Overview of Extracellular Vesicles, Their Origin, Composition, Purpose, and Methods for Exosome Isolation and Analysis. *Cells*. 2019;8(7).
12. Stuffers S, Sem Wegner C, Stenmark H, Brech A. Multivesicular endosome biogenesis in the absence of ESCRTs. *Traffic*. 2009;10(7):925-37.
13. Mathieu M, Martin-Jaular L, Lavieu G, Théry C. Specificities of secretion and uptake of exosomes and other extracellular vesicles for cell-to-cell communication. *Nat Cell Biol*. 2019;21(1):9-17.
14. Baietti MF, Zhang Z, Mortier E, Melchior A, Degeest G, Geeraerts A, et al. Syndecan-syntenin-ALIX regulates the biogenesis of exosomes. *Nat Cell Biol*. 2012;14(7):677-85.
15. Trajkovic K, Hsu C, Chiantia S, Rajendran L, Wenzel D, Wieland F, et al. Ceramide triggers budding of exosome vesicles into multivesicular endosomes. *Science*. 2008;319(5867):1244-7.
16. Bonifacino JS, Glick BS. The mechanisms of vesicle budding and fusion. *Cell*. 2004;116(2):153-66.
17. Ostrowski M, Carmo NB, Krumeich S, Fanget I, Raposo G, Savina A, et al. Rab27a and Rab27b control different steps of the exosome secretion pathway. *Nat Cell Biol*. 2010;12(1):19-30; sup pp 1-13.
18. Valadi H, Ekström K, Bossios A, Sjöstrand M, Lee JJ, Lötvall JO. Exosome-mediated transfer of mRNAs and microRNAs is a novel mechanism of genetic exchange between cells. *Nat Cell Biol*. 2007;9(6):654-9.
19. Andreu Z, Yáñez-Mó M. Tetraspanins in extracellular vesicle formation and function. *Front Immunol*. 2014;5:442.
20. Yáñez-Mó M, Barreiro O, Gordon-Alonso M, Sala-Valdés M, Sánchez-Madrid F. Tetraspanin-enriched microdomains: a functional unit in cell plasma membranes. *Trends Cell Biol*. 2009;19(9):434-46.
21. Pols MS, Klumperman J. Trafficking and function of the tetraspanin CD63. *Exp Cell Res*. 2009;315(9):1584-92.

22. Perez-Hernandez D, Gutiérrez-Vázquez C, Jorge I, López-Martín S, Ursa A, Sánchez-Madrid F, et al. The intracellular interactome of tetraspanin-enriched microdomains reveals their function as sorting machineries toward exosomes. *J Biol Chem*. 2013;288(17):11649-61.
23. Zimmerman B, Kelly B, McMillan BJ, Seegar TCM, Dror RO, Kruse AC, et al. Crystal Structure of a Full-Length Human Tetraspanin Reveals a Cholesterol-Binding Pocket. *Cell*. 2016;167(4):1041-51.e11.
24. Termini CM, Gillette JM. Tetraspanins Function as Regulators of Cellular Signaling. *Front Cell Dev Biol*. 2017;5:34.
25. van Niel G, Charrin S, Simoes S, Romao M, Rochin L, Saftig P, et al. The tetraspanin CD63 regulates ESCRT-independent and -dependent endosomal sorting during melanogenesis. *Dev Cell*. 2011;21(4):708-21.
26. Jeppesen DK, Fenix AM, Franklin JL, Higginbotham JN, Zhang Q, Zimmerman LJ, et al. Reassessment of Exosome Composition. *Cell*. 2019;177(2):428-45.e18.
27. Johnstone RM, Adam M, Hammond JR, Orr L, Turbide C. Vesicle formation during reticulocyte maturation. Association of plasma membrane activities with released vesicles (exosomes). *J Biol Chem*. 1987;262(19):9412-20.
28. Pan BT, Teng K, Wu C, Adam M, Johnstone RM. Electron microscopic evidence for externalization of the transferrin receptor in vesicular form in sheep reticulocytes. *J Cell Biol*. 1985;101(3):942-8.
29. Raposo G, Nijman HW, Stoorvogel W, Liejendekker R, Harding CV, Melief CJ, et al. B lymphocytes secrete antigen-presenting vesicles. *J Exp Med*. 1996;183(3):1161-72.
30. Bahmad HF, Jalloul M, Azar J, Moubarak MM, Samad TA, Mukherji D, et al. Tumor Microenvironment in Prostate Cancer: Toward Identification of Novel Molecular Biomarkers for Diagnosis, Prognosis, and Therapy Development. *Front Genet*. 2021;12:652747.
31. Chiarugi P, Paoli P, Cirri P. Tumor microenvironment and metabolism in prostate cancer. *Semin Oncol*. 2014;41(2):267-80.
32. Hägglöf C, Bergh A. The stroma-a key regulator in prostate function and malignancy. *Cancers (Basel)*. 2012;4(2):531-48.
33. Levesque C, Nelson PS. Cellular Constituents of the Prostate Stroma: Key Contributors to Prostate Cancer Progression and Therapy Resistance. *Cold Spring Harb Perspect Med*. 2018;8(8).
34. Sahai E, Atsaturov I, Cukierman E, DeNardo DG, Egeblad M, Evans RM, et al. A framework for advancing our understanding of cancer-associated fibroblasts. *Nat Rev Cancer*. 2020;20(3):174-86.
35. Bergers G, Benjamin LE. Tumorigenesis and the angiogenic switch. *Nat Rev Cancer*. 2003;3(6):401-10.
36. Shiao SL, Chu GC, Chung LW. Regulation of prostate cancer progression by the tumor microenvironment. *Cancer Lett*. 2016;380(1):340-8.
37. Brennen WN, Chen S, Denmeade SR, Isaacs JT. Quantification of Mesenchymal Stem Cells (MSCs) at sites of human prostate cancer. *Oncotarget*. 2013;4(1):106-17.
38. Jung Y, Kim JK, Shiozawa Y, Wang J, Mishra A, Joseph J, et al. Recruitment of mesenchymal stem cells into prostate tumours promotes metastasis. *Nat Commun*. 2013;4:1795.
39. Ridge SM, Sullivan FJ, Glynn SA. Mesenchymal stem cells: key players in cancer progression. *Mol Cancer*. 2017;16(1):31.
40. Zhang X, Yuan X, Shi H, Wu L, Qian H, Xu W. Exosomes in cancer: small particle, big player. *J Hematol Oncol*. 2015;8:83.
41. Shephard AP, Yeung V, Clayton A, Webber JP. Prostate cancer exosomes as modulators of the tumor microenvironment. *Journal of Cancer Metastasis and Treatment*. 2017;3(12):288-301.
42. Webber J, Yeung V, Clayton A. Extracellular vesicles as modulators of the cancer microenvironment. *Semin Cell Dev Biol*. 2015;40:27-34.

43. Lorenc T, Klimczyk K, Michalczywska I, Słomka M, Kubiak-Tomaszewska G, Olejarz W. Exosomes in Prostate Cancer Diagnosis, Prognosis and Therapy. *Int J Mol Sci.* 2020;21(6).
44. Lundholm M, Schröder M, Nagaeva O, Baranov V, Widmark A, Mincheva-Nilsson L, et al. Prostate tumor-derived exosomes down-regulate NKG2D expression on natural killer cells and CD8+ T cells: mechanism of immune evasion. *PLoS One.* 2014;9(9):e108925.
45. Ichim TE, Zhong Z, Kaushal S, Zheng X, Ren X, Hao X, et al. Exosomes as a tumor immune escape mechanism: possible therapeutic implications. *J Transl Med.* 2008;6:37.
46. Webber J, Steadman R, Mason MD, Tabi Z, Clayton A. Cancer exosomes trigger fibroblast to myofibroblast differentiation. *Cancer Res.* 2010;70(23):9621-30.
47. Webber JP, Spary LK, Sanders AJ, Chowdhury R, Jiang WG, Steadman R, et al. Differentiation of tumour-promoting stromal myofibroblasts by cancer exosomes. *Oncogene.* 2015;34(3):290-302.
48. Chowdhury R, Webber JP, Gurney M, Mason MD, Tabi Z, Clayton A. Cancer exosomes trigger mesenchymal stem cell differentiation into pro-angiogenic and pro-invasive myofibroblasts. *Oncotarget.* 2015;6(2):715-31.
49. Wang Z, Tan Y, Yu W, Zheng S, Zhang S, Sun L, et al. Small role with big impact: miRNAs as communicators in the cross-talk between cancer-associated fibroblasts and cancer cells. *Int J Biol Sci.* 2017;13(3):339-48.
50. Vlaeminck-Guillem V. Extracellular Vesicles in Prostate Cancer Carcinogenesis, Diagnosis, and Management. *Front Oncol.* 2018;8:222.
51. Corcoran C, Rani S, O'Brien K, O'Neill A, Prencipe M, Sheikh R, et al. Docetaxel-resistance in prostate cancer: evaluating associated phenotypic changes and potential for resistance transfer via exosomes. *PLoS One.* 2012;7(12):e50999.
52. Souza AG, B Silva IB, Campos-Fernández E, Marangoni K, F Bastos VA, Alves PT, et al. Extracellular vesicles as drivers of epithelial-mesenchymal transition and carcinogenic characteristics in normal prostate cells. *Mol Carcinog.* 2018;57(4):503-11.
53. Akoto T, Saini S. Role of Exosomes in Prostate Cancer Metastasis. *Int J Mol Sci.* 2021;22(7).
54. Furesi G, Rauner M, Hofbauer LC. Emerging Players in Prostate Cancer-Bone Niche Communication. *Trends Cancer.* 2021;7(2):112-21.
55. Li FX, Liu JJ, Xu F, Lin X, Zhong JY, Wu F, et al. Role of tumor-derived exosomes in bone metastasis. *Oncol Lett.* 2019;18(4):3935-45.
56. Thobe MN, Clark RJ, Bainer RO, Prasad SM, Rinker-Schaeffer CW. From prostate to bone: key players in prostate cancer bone metastasis. *Cancers (Basel).* 2011;3(1):478-93.
57. Bubendorf L, Schöpfer A, Wagner U, Sauter G, Moch H, Willi N, et al. Metastatic patterns of prostate cancer: an autopsy study of 1,589 patients. *Hum Pathol.* 2000;31(5):578-83.
58. Probert C, Dottorini T, Speakman A, Hunt S, Nafee T, Fazeli A, et al. Communication of prostate cancer cells with bone cells via extracellular vesicle RNA; a potential mechanism of metastasis. *Oncogene.* 2019;38(10):1751-63.
59. Ye Y, Li SL, Ma YY, Diao YJ, Yang L, Su MQ, et al. Exosomal miR-141-3p regulates osteoblast activity to promote the osteoblastic metastasis of prostate cancer. *Oncotarget.* 2017;8(55):94834-49.
60. Karlsson T, Lundholm M, Widmark A, Persson E. Tumor Cell-Derived Exosomes from the Prostate Cancer Cell Line TRAMP-C1 Impair Osteoclast Formation and Differentiation. *PLoS One.* 2016;11(11):e0166284.
61. Inder KL, Ruelcke JE, Petelin L, Moon H, Choi E, Rae J, et al. Cavin-1/PTRF alters prostate cancer cell-derived extracellular vesicle content and internalization to attenuate extracellular vesicle-mediated osteoclastogenesis and osteoblast proliferation. *J Extracell Vesicles.* 2014;3.

62. Ma Q, Liang M, Wu Y, Dou C, Xu J, Dong S, et al. Small extracellular vesicles deliver osteolytic effectors and mediate cancer-induced osteolysis in bone metastatic niche. *J Extracell Vesicles*. 2021;10(4):e12068.
63. Fritz V, Brondello JM, Gordeladze JO, Reseland JE, Bony C, Yssel H, et al. Bone-metastatic prostate carcinoma favors mesenchymal stem cell differentiation toward osteoblasts and reduces their osteoclastogenic potential. *J Cell Biochem*. 2011;112(11):3234-45.
64. Dai J, Escara-Wilke J, Keller JM, Jung Y, Taichman RS, Pienta KJ, et al. Primary prostate cancer educates bone stroma through exosomal pyruvate kinase M2 to promote bone metastasis. *J Exp Med*. 2019;216(12):2883-99.
65. Chen Q, Shou P, Zheng C, Jiang M, Cao G, Yang Q, et al. Fate decision of mesenchymal stem cells: adipocytes or osteoblasts? *Cell Death Differ*. 2016;23(7):1128-39.
66. Hashimoto K, Ochi H, Sunamura S, Kosaka N, Mabuchi Y, Fukuda T, et al. Cancer-secreted hsa-miR-940 induces an osteoblastic phenotype in the bone metastatic microenvironment via targeting ARHGAP1 and FAM134A. *Proc Natl Acad Sci U S A*. 2018;115(9):2204-9.
67. Soung YH, Ford S, Zhang V, Chung J. Exosomes in Cancer Diagnostics. *Cancers (Basel)*. 2017;9(1).
68. Pang B, Zhu Y, Ni J, Thompson J, Malouf D, Bucci J, et al. Extracellular vesicles: the next generation of biomarkers for liquid biopsy-based prostate cancer diagnosis. *Theranostics*. 2020;10(5):2309-26.
69. Mulcahy LA, Pink RC, Carter DR. Routes and mechanisms of extracellular vesicle uptake. *J Extracell Vesicles*. 2014;3.
70. McKelvey KJ, Powell KL, Ashton AW, Morris JM, McCracken SA. Exosomes: Mechanisms of Uptake. *J Circ Biomark*. 2015;4:7.
71. Rana S, Claas C, Kretz CC, Nazarenko I, Zoeller M. Activation-induced internalization differs for the tetraspanins CD9 and Tspan8: Impact on tumor cell motility. *Int J Biochem Cell Biol*. 2011;43(1):106-19.
72. Rana S, Yue S, Stadel D, Zöller M. Toward tailored exosomes: the exosomal tetraspanin web contributes to target cell selection. *Int J Biochem Cell Biol*. 2012;44(9):1574-84.
73. Sung BH, Ketova T, Hoshino D, Zijlstra A, Weaver AM. Directional cell movement through tissues is controlled by exosome secretion. *Nat Commun*. 2015;6:7164.
74. Hoshino A, Costa-Silva B, Shen TL, Rodrigues G, Hashimoto A, Tesic Mark M, et al. Tumour exosome integrins determine organotropic metastasis. *Nature*. 2015;527(7578):329-35.
75. Grigoryeva ES, Savelieva OE, Popova NO, Cherdyntseva NV, Perelmuter VM. Do tumor exosome integrins alone determine organotropic metastasis? *Mol Biol Rep*. 2020;47(10):8145-57.
76. Al-Nedawi K, Meehan B, Micallef J, Lhotak V, May L, Guha A, et al. Intercellular transfer of the oncogenic receptor EGFRvIII by microvesicles derived from tumour cells. *Nat Cell Biol*. 2008;10(5):619-24.
77. Parolini I, Federici C, Raggi C, Lugini L, Palleschi S, De Milito A, et al. Microenvironmental pH is a key factor for exosome traffic in tumor cells. *J Biol Chem*. 2009;284(49):34211-22.
78. Kaksonen M, Roux A. Mechanisms of clathrin-mediated endocytosis. *Nat Rev Mol Cell Biol*. 2018;19(5):313-26.
79. Escrevente C, Keller S, Altevogt P, Costa J. Interaction and uptake of exosomes by ovarian cancer cells. *BMC Cancer*. 2011;11:108.
80. Tian T, Zhu YL, Zhou YY, Liang GF, Wang YY, Hu FH, et al. Exosome uptake through clathrin-mediated endocytosis and macropinocytosis and mediating miR-21 delivery. *J Biol Chem*. 2014;289(32):22258-67.
81. Kiss AL. Caveolae and the regulation of endocytosis. *Adv Exp Med Biol*. 2012;729:14-28.

82. Hayer A, Stoeber M, Ritz D, Engel S, Meyer HH, Helenius A. Caveolin-1 is ubiquitinated and targeted to intraluminal vesicles in endolysosomes for degradation. *J Cell Biol.* 2010;191(3):615-29.
83. Nanbo A, Kawanishi E, Yoshida R, Yoshiyama H. Exosomes derived from Epstein-Barr virus-infected cells are internalized via caveola-dependent endocytosis and promote phenotypic modulation in target cells. *J Virol.* 2013;87(18):10334-47.
84. Svensson KJ, Christianson HC, Wittrup A, Bourseau-Guilmain E, Lindqvist E, Svensson LM, et al. Exosome uptake depends on ERK1/2-heat shock protein 27 signaling and lipid Raft-mediated endocytosis negatively regulated by caveolin-1. *J Biol Chem.* 2013;288(24):17713-24.
85. Gordon S. Phagocytosis: An Immunobiologic Process. *Immunity.* 2016;44(3):463-75.
86. Feng D, Zhao WL, Ye YY, Bai XC, Liu RQ, Chang LF, et al. Cellular internalization of exosomes occurs through phagocytosis. *Traffic.* 2010;11(5):675-87.
87. Lin XP, Mintern JD, Gleeson PA. Macropinocytosis in Different Cell Types: Similarities and Differences. *Membranes (Basel).* 2020;10(8).
88. Fitzner D, Schnaars M, van Rossum D, Krishnamoorthy G, Dibaj P, Bakhti M, et al. Selective transfer of exosomes from oligodendrocytes to microglia by macropinocytosis. *J Cell Sci.* 2011;124(Pt 3):447-58.
89. Lajoie P, Nabi IR. Regulation of raft-dependent endocytosis. *J Cell Mol Med.* 2007;11(4):644-53.
90. Delenclos M, Trendafilova T, Mahesh D, Baine AM, Moussaud S, Yan IK, et al. Investigation of Endocytic Pathways for the Internalization of Exosome-Associated Oligomeric Alpha-Synuclein. *Front Neurosci.* 2017;11:172.
91. Tian T, Wang Y, Wang H, Zhu Z, Xiao Z. Visualizing of the cellular uptake and intracellular trafficking of exosomes by live-cell microscopy. *J Cell Biochem.* 2010;111(2):488-96.
92. Heusermann W, Hean J, Trojer D, Steib E, von Bueren S, Graff-Meyer A, et al. Exosomes surf on filopodia to enter cells at endocytic hot spots, traffic within endosomes, and are targeted to the ER. *J Cell Biol.* 2016;213(2):173-84.
93. Bissig C, Gruenberg J. ALIX and the multivesicular endosome: ALIX in Wonderland. *Trends Cell Biol.* 2014;24(1):19-25.
94. Corbeil D, Santos MF, Karbanová J, Kurth T, Rappa G, Lorico A. Uptake and Fate of Extracellular Membrane Vesicles: Nucleoplasmic Reticulum-Associated Late Endosomes as a New Gate to Intercellular Communication. *Cells.* 2020;9(9).
95. Clemmens H, Lambert DW. Extracellular vesicles: translational challenges and opportunities. *Biochem Soc Trans.* 2018;46(5):1073-82.
96. Aheget H, Mazini L, Martin F, Belqat B, Marchal JA, Benabdellah K. Exosomes: Their Role in Pathogenesis, Diagnosis and Treatment of Diseases. *Cancers (Basel).* 2020;13(1).
97. Soekmadji C, Russell PJ, Nelson CC. Exosomes in prostate cancer: putting together the pieces of a puzzle. *Cancers (Basel).* 2013;5(4):1522-44.
98. Skog J, Würdinger T, van Rijn S, Meijer DH, Gainche L, Sena-Esteves M, et al. Glioblastoma microvesicles transport RNA and proteins that promote tumour growth and provide diagnostic biomarkers. *Nat Cell Biol.* 2008;10(12):1470-6.
99. Øverbye A, Skotland T, Koehler CJ, Thiede B, Seierstad T, Berge V, et al. Identification of prostate cancer biomarkers in urinary exosomes. *Oncotarget.* 2015;6(30):30357-76.
100. Shen L-M, Quan L, Liu J. Tracking Exosomes in Vitro and in Vivo To Elucidate Their Physiological Functions: Implications for Diagnostic and Therapeutic Nanocarriers. *ACS Applied Nano Materials.* 2018;1(6):2438-48.
101. Pužar Dominkuš P, Stenovc M, Sitar S, Lasič E, Zorec R, Plemenitaš A, et al. PKH26 labeling of extracellular vesicles: Characterization and cellular internalization of contaminating PKH26 nanoparticles. *Biochim Biophys Acta Biomembr.* 2018;1860(6):1350-61.

102. Takov K, Yellon DM, Davidson SM. Confounding factors in vesicle uptake studies using fluorescent lipophilic membrane dyes. *J Extracell Vesicles*. 2017;6(1):1388731.
103. Simonsen JB. Pitfalls associated with lipophilic fluorophore staining of extracellular vesicles for uptake studies. *J Extracell Vesicles*. 2019;8(1):1582237.
104. Dehghani M, Gulvin SM, Flax J, Gaborski TR. Systematic Evaluation of PKH Labelling on Extracellular Vesicle Size by Nanoparticle Tracking Analysis. *Sci Rep*. 2020;10(1):9533.
105. Grange C, Tapparo M, Bruno S, Chatterjee D, Quesenberry PJ, Tetta C, et al. Biodistribution of mesenchymal stem cell-derived extracellular vesicles in a model of acute kidney injury monitored by optical imaging. *Int J Mol Med*. 2014;33(5):1055-63.
106. Caponnetto F, Manini I, Skrap M, Palmari-Pallag T, Di Loreto C, Beltrami AP, et al. Size-dependent cellular uptake of exosomes. *Nanomedicine*. 2017;13(3):1011-20.
107. Morales-Kastresana A, Telford B, Musich TA, McKinnon K, Clayborne C, Braig Z, et al. Labeling Extracellular Vesicles for Nanoscale Flow Cytometry. *Sci Rep*. 2017;7(1):1878.
108. Lai CP, Kim EY, Badr CE, Weissleder R, Mempel TR, Tannous BA, et al. Visualization and tracking of tumour extracellular vesicle delivery and RNA translation using multiplexed reporters. 2015;6:7029.
109. Lázaro-Ibáñez E, Neuvonen M, Takatalo M, Thanigai Arasu U, Capasso C, Cerullo V, et al. Metastatic state of parent cells influences the uptake and functionality of prostate cancer cell-derived extracellular vesicles. *J Extracell Vesicles*. 2017;6(1):1354645.
110. Gray WD, Mitchell AJ, Searles CD. An accurate, precise method for general labeling of extracellular vesicles. 2015;2:360-7.
111. Tian T, Zhu YL, Hu FH, Wang YY, Huang NP, Xiao ZD. Dynamics of exosome internalization and trafficking. *J Cell Physiol*. 2013;228(7):1487-95.
112. Watson DC, Bayik D, Srivatsan A, Bergamaschi C, Valentin A, Niu G, et al. Efficient production and enhanced tumor delivery of engineered extracellular vesicles. *Biomaterials*. 2016;105:195-205.
113. Brown M, Johnson LA, Leone DA, Majek P, Vaahtomeri K, Senfter D, et al. Lymphatic exosomes promote dendritic cell migration along guidance cues. *J Cell Biol*. 2018;217(6):2205-21.
114. Cocks A. Fibroblast Uptake of Prostate Cancer Vesicles. <http://orca.cf.ac.uk/id/eprint/123376> Cardiff University; 2019.
115. Roberts-Dalton HD, Cocks A, Falcon-Perez JM, Sayers EJ, Webber JP, Watson P, et al. Fluorescence labelling of extracellular vesicles using a novel thiol-based strategy for quantitative analysis of cellular delivery and intracellular traffic. *Nanoscale*. 2017;9(36):13693-706.
116. Jurgielewicz BJ, Yao Y, Stice SL. Kinetics and Specificity of HEK293T Extracellular Vesicle Uptake using Imaging Flow Cytometry. *Nanoscale Res Lett*. 2020;15(1):170.
117. Sadovska L, Zandberga E, Sagini K, Jēkabsons K, Riekstiņa U, Kalniņa Z, et al. A novel 3D heterotypic spheroid model for studying extracellular vesicle-mediated tumour and immune cell communication. *Biochem Biophys Res Commun*. 2018;495(2):1930-5.
118. Verweij FJ, Bebelman MP, Jimenez CR, Garcia-Vallejo JJ, Janssen H, Neeffjes J, et al. Quantifying exosome secretion from single cells reveals a modulatory role for GPCR signaling. *J Cell Biol*. 2018;217(3):1129-42.
119. Sung BH, von Lersner A, Guerrero J, Krystofiak ES, Inman D, Pelletier R, et al. A live cell reporter of exosome secretion and uptake reveals pathfinding behavior of migrating cells. *Nat Commun*. 2020;11(1):2092.
120. Verweij FJ, Revenu C, Arras G, Dingli F, Loew D, Pegtel DM, et al. Live Tracking of Inter-organ Communication by Endogenous Exosomes In Vivo. *Dev Cell*. 2019;48(4):573-89.e4.

121. Stickney Z, Losacco J, McDevitt S, Zhang Z, Lu B. Development of exosome surface display technology in living human cells. *Biochem Biophys Res Commun.* 2016;472(1):53-9.
122. Corso G, Heusermann W, Trojer D, Görgens A, Steib E, Voshol J, et al. Systematic characterization of extracellular vesicle sorting domains and quantification at the single molecule - single vesicle level by fluorescence correlation spectroscopy and single particle imaging. *J Extracell Vesicles.* 2019;8(1):1663043.
123. Yoshimura A, Kawamata M, Yoshioka Y, Katsuda T, Kikuchi H, Nagai Y, et al. Generation of a novel transgenic rat model for tracing extracellular vesicles in body fluids. *Sci Rep.* 2016;6:31172.
124. Miesenböck G, De Angelis DA, Rothman JE. Visualizing secretion and synaptic transmission with pH-sensitive green fluorescent proteins. *Nature.* 1998;394(6689):192-5.
125. Zomer A, Steenbeek SC, Maynard C, van Rheenen J. Studying extracellular vesicle transfer by a Cre-loxP method. *Nat Protoc.* 2016;11(1):87-101.
126. James S, Fox J, Afsari F, Lee J, Clough S, Knight C, et al. Multiparameter Analysis of Human Bone Marrow Stromal Cells Identifies Distinct Immunomodulatory and Differentiation-Competent Subtypes. *Stem Cell Reports.* 2015;4(6):1004-15.
127. Mitchell JP, Court J, Mason MD, Tabi Z, Clayton A. Increased exosome production from tumour cell cultures using the Integra CELLine Culture System. *J Immunol Methods.* 2008;335(1-2):98-105.
128. Rieder CL, Palazzo RE. Colcemid and the mitotic cycle. *J Cell Sci.* 1992;102 (Pt 3):387-92.
129. Smith PJ, Wiltshire M, Errington RJ. DRAQ5 labeling of nuclear DNA in live and fixed cells. *Curr Protoc Cytom.* 2004;Chapter 7:Unit 7.25.
130. FlowJo™ Software for Windows. v10.6.2 ed. Becton, Dickinson and Company 2019.
131. Carpenter AE, Jones TR, Lamprecht MR, Clarke C, Kang IH, Friman O, et al. CellProfiler: image analysis software for identifying and quantifying cell phenotypes. *Genome Biol.* 2006;7(10):R100.
132. Lamparski HG, Metha-Damani A, Yao JY, Patel S, Hsu DH, Ruegg C, et al. Production and characterization of clinical grade exosomes derived from dendritic cells. *J Immunol Methods.* 2002;270(2):211-26.
133. Schindelin J, Arganda-Carreras I, Frise E, Kaynig V, Longair M, Pietzsch T, et al. Fiji: an open-source platform for biological-image analysis. *Nat Methods.* 2012;9(7):676-82.
134. Cole RW, Jinadasa T, Brown CM. Measuring and interpreting point spread functions to determine confocal microscope resolution and ensure quality control. *Nat Protoc.* 2011;6(12):1929-41.
135. Arya S, Wiatrek-Moumoulidis D, Synowsky SA, Shirran SL, Botting CH, Powis SJ, et al. Quantitative proteomic changes in LPS-activated monocyte-derived dendritic cells: A SWATH-MS study. *Sci Rep.* 2019;9(1):4343.
136. MacLean B, Tomazela DM, Shulman N, Chambers M, Finney GL, Frewen B, et al. Skyline: an open source document editor for creating and analyzing targeted proteomics experiments. *Bioinformatics.* 2010;26(7):966-8.
137. Tyanova S, Temu T, Sinitcyn P, Carlson A, Hein MY, Geiger T, et al. The Perseus computational platform for comprehensive analysis of (prote)omics data. *Nat Methods.* 2016;13(9):731-40.
138. Pathan M, Keerthikumar S, Ang CS, Gangoda L, Quek CY, Williamson NA, et al. FunRich: An open access standalone functional enrichment and interaction network analysis tool. *Proteomics.* 2015;15(15):2597-601.
139. Benito-Martin A, Peinado H. FunRich proteomics software analysis, let the fun begin! *Proteomics.* 2015;15(15):2555-6.

140. Pathan M, Fonseka P, Chitti SV, Kang T, Sanwlani R, Van Deun J, et al. Vesiclepedia 2019: a compendium of RNA, proteins, lipids and metabolites in extracellular vesicles. *Nucleic Acids Res.* 2019;47(D1):D516-D9.
141. Szklarczyk D, Gable AL, Nastou KC, Lyon D, Kirsch R, Pyysalo S, et al. The STRING database in 2021: customizable protein-protein networks, and functional characterization of user-uploaded gene/measurement sets. *Nucleic Acids Res.* 2021;49(D1):D605-D12.
142. Brohée S, van Helden J. Evaluation of clustering algorithms for protein-protein interaction networks. *BMC Bioinformatics.* 2006;7:488.
143. Akagi J, Kordon M, Zhao H, Matuszek A, Dobrucki J, Errington R, et al. Real-time cell viability assays using a new anthracycline derivative DRAQ7®. *Cytometry A.* 2013;83(2):227-34.
144. Wlodkowic D, Akagi J, Dobrucki J, Errington R, Smith PJ, Takeda K, et al. Kinetic viability assays using DRAQ7 probe. *Curr Protoc Cytom.* 2013;Chapter 9:Unit 9.41.
145. Errington RJ, Brown MR, Silvestre OF, Njoh KL, Chappell SC, Khan IA, et al. Single cell nanoparticle tracking to model cell cycle dynamics and compartmental inheritance. *Cell Cycle.* 2010;9(1):121-30.
146. Summers HD, Rees P, Holton MD, Brown MR, Chappell SC, Smith PJ, et al. Statistical analysis of nanoparticle dosing in a dynamic cellular system. *Nat Nanotechnol.* 2011;6(3):170-4.
147. C.H. L. An iterative algorithm for minimum cross entropy thresholding. 1998;19(18):771-6.
148. Gregory CA, Gunn WG, Peister A, Prockop DJ. An Alizarin red-based assay of mineralization by adherent cells in culture: comparison with cetylpyridinium chloride extraction. *Anal Biochem.* 2004;329(1):77-84.
149. Livak KJ, Schmittgen TD. Analysis of relative gene expression data using real-time quantitative PCR and the 2⁻(Delta Delta C(T)) Method. *Methods.* 2001;25(4):402-8.
150. Roederer M, Hardy RR. Frequency difference gating: a multivariate method for identifying subsets that differ between samples. *Cytometry.* 2001;45(1):56-64.
151. Roederer M, Moore W, Treister A, Hardy RR, Herzenberg LA. Probability binning comparison: a metric for quantitating multivariate distribution differences. *Cytometry.* 2001;45(1):47-55.
152. Overton WR. Modified histogram subtraction technique for analysis of flow cytometry data. *Cytometry.* 1988;9(6):619-26.
153. Duijvesz D, Luider T, Bangma CH, Jenster G. Exosomes as biomarker treasure chests for prostate cancer. *Eur Urol.* 2011;59(5):823-31.
154. Fais S, O'Driscoll L, Borrás FE, Buzas E, Camussi G, Cappello F, et al. Evidence-Based Clinical Use of Nanoscale Extracellular Vesicles in Nanomedicine. *ACS Nano.* 2016;10(4):3886-99.
155. Reiner AT, Witwer KW, van Balkom BWM, de Beer J, Brodie C, Corteling RL, et al. Concise Review: Developing Best-Practice Models for the Therapeutic Use of Extracellular Vesicles. *Stem Cells Transl Med.* 2017;6(8):1730-9.
156. Charrin S, Jouannet S, Boucheix C, Rubinstein E. Tetraspanins at a glance. *J Cell Sci.* 2014;127(Pt 17):3641-8.
157. Webber J, Clayton A. How pure are your vesicles? *J Extracell Vesicles.* 2013;2.
158. Dragovic RA, Gardiner C, Brooks AS, Tannetta DS, Ferguson DJ, Hole P, et al. Sizing and phenotyping of cellular vesicles using Nanoparticle Tracking Analysis. *Nanomedicine.* 2011;7(6):780-8.
159. Llorente A, de Marco MC, Alonso MA. Caveolin-1 and MAL are located on prostasomes secreted by the prostate cancer PC-3 cell line. *J Cell Sci.* 2004;117(Pt 22):5343-51.
160. Jansen FH, Krijgsveld J, van Rijswijk A, van den Bemd GJ, van den Berg MS, van Weerden WM, et al. Exosomal secretion of cytoplasmic prostate cancer xenograft-derived proteins. *Mol Cell Proteomics.* 2009;8(6):1192-205.
161. Wilhelm S, Gröbler B, Gluch M, Heinz H. *Carl Zeiss Principles.* 1997.

162. Zucker RM, Price OT. Practical confocal microscopy and the evaluation of system performance. *Methods*. 1999;18(4):447-58.
163. Kastelowitz N, Yin H. Exosomes and microvesicles: identification and targeting by particle size and lipid chemical probes. *Chembiochem*. 2014;15(7):923-8.
164. Verweij FJ, Bebelman MP, Jimenez CR, Garcia-Vallejo JJ, Janssen H, Neefjes J, et al. Correction: Quantifying exosome secretion from single cells reveals a modulatory role for GPCR signaling. *J Cell Biol*. 2018;217(3):1157.
165. Hemler ME. Specific tetraspanin functions. *J Cell Biol*. 2001;155(7):1103-7.
166. Hemler ME. Targeting of tetraspanin proteins--potential benefits and strategies. *Nat Rev Drug Discov*. 2008;7(9):747-58.
167. Gensert JM, Baranova OV, Weinstein DE, Ratan RR. CD81, a cell cycle regulator, is a novel target for histone deacetylase inhibition in glioma cells. *Neurobiol Dis*. 2007;26(3):671-80.
168. Kelić S, Levy S, Suarez C, Weinstein DE. CD81 regulates neuron-induced astrocyte cell-cycle exit. *Mol Cell Neurosci*. 2001;17(3):551-60.
169. Lin KK, Rossi L, Goodell MA. CD81 Is Essential for HSC Self-Renewal through Suppressing Proliferation. *Blood*. 2008;112(11):76.
170. Lupia A, Peppicelli S, Witort E, Bianchini F, Carloni V, Pimpinelli N, et al. CD63 tetraspanin is a negative driver of epithelial-to-mesenchymal transition in human melanoma cells. *J Invest Dermatol*. 2014;134(12):2947-56.
171. Seubert B, Cui H, Simonavicius N, Honert K, Schäfer S, Reuning U, et al. Tetraspanin CD63 acts as a pro-metastatic factor via β -catenin stabilization. *Int J Cancer*. 2015;136(10):2304-15.
172. Hong IK, Byun HJ, Lee J, Jin YJ, Wang SJ, Jeoung DI, et al. The tetraspanin CD81 protein increases melanoma cell motility by up-regulating metalloproteinase MT1-MMP expression through the pro-oncogenic Akt-dependent Sp1 activation signaling pathways. *J Biol Chem*. 2014;289(22):15691-704.
173. Zhang N, Zuo L, Zheng H, Li G, Hu X. Increased Expression of CD81 in Breast Cancer Tissue is Associated with Reduced Patient Prognosis and Increased Cell Migration and Proliferation in MDA-MB-231 and MDA-MB-435S Human Breast Cancer Cell Lines In Vitro. *Med Sci Monit*. 2018;24:5739-47.
174. Zhang Y, Qian H, Xu A, Yang G. Increased expression of CD81 is associated with poor prognosis of prostate cancer and increases the progression of prostate cancer cells *in vitro*. *Exp Ther Med*. 2020;19(1):755-61.
175. Willms E, Cabañas C, Mäger I, Wood MJA, Vader P. Extracellular Vesicle Heterogeneity: Subpopulations, Isolation Techniques, and Diverse Functions in Cancer Progression. *Front Immunol*. 2018;9:738.
176. Gardiner C, Shaw M, Hole P, Smith J, Tannetta D, Redman CW, et al. Measurement of refractive index by nanoparticle tracking analysis reveals heterogeneity in extracellular vesicles. *J Extracell Vesicles*. 2014;3:25361.
177. Chen C, Zong S, Wang Z, Lu J, Zhu D, Zhang Y, et al. Imaging and Intracellular Tracking of Cancer-Derived Exosomes Using Single-Molecule Localization-Based Super-Resolution Microscope. *ACS Appl Mater Interfaces*. 2016;8(39):25825-33.
178. Suetsugu A, Honma K, Saji S, Moriwaki H, Ochiya T, Hoffman RM. Imaging exosome transfer from breast cancer cells to stroma at metastatic sites in orthotopic nude-mouse models. *Adv Drug Deliv Rev*. 2013;65(3):383-90.
179. Duijvesz D, Burnum-Johnson KE, Gritsenko MA, Hoogland AM, Vredenburg-van den Berg MS, Willemsen R, et al. Proteomic profiling of exosomes leads to the identification of novel biomarkers for prostate cancer. *PLoS One*. 2013;8(12):e82589.
180. Duijvesz D, Rodriguez-Blanco G, Hoogland AM, Verhoef EI, Dekker LJ, Roobol MJ, et al. Differential tissue expression of extracellular vesicle-derived proteins in prostate cancer. *The Prostate*. 2019;79(9):1032-42.
181. Principe S, Jones EE, Kim Y, Sinha A, Nyalwidhe JO, Brooks J, et al. In-depth proteomic analyses of exosomes isolated from expressed prostatic secretions in urine. *Proteomics*. 2013;13(10-11):1667-71.

182. Yang C, Guo WB, Zhang WS, Bian J, Yang JK, Zhou QZ, et al. Comprehensive proteomics analysis of exosomes derived from human seminal plasma. *Andrology*. 2017;5(5):1007-15.
183. Welton JL, Khanna S, Giles PJ, Brennan P, Brewis IA, Staffurth J, et al. Proteomics analysis of bladder cancer exosomes. *Mol Cell Proteomics*. 2010;9(6):1324-38.
184. Ji H, Greening DW, Barnes TW, Lim JW, Tauro BJ, Rai A, et al. Proteome profiling of exosomes derived from human primary and metastatic colorectal cancer cells reveal differential expression of key metastatic factors and signal transduction components. *Proteomics*. 2013;13(10-11):1672-86.
185. Zhang W, Ou X, Wu X. Proteomics profiling of plasma exosomes in epithelial ovarian cancer: A potential role in the coagulation cascade, diagnosis and prognosis. *Int J Oncol*. 2019;54(5):1719-33.
186. Hurwitz SN, Rider MA, Bundy JL, Liu X, Singh RK, Meckes DG. Proteomic profiling of NCI-60 extracellular vesicles uncovers common protein cargo and cancer type-specific biomarkers. *Oncotarget*. 2016;7(52):86999-7015.
187. Kharaziha P, Chioureas D, Rutishauser D, Baltatzis G, Lennartsson L, Fonseca P, et al. Molecular profiling of prostate cancer derived exosomes may reveal a predictive signature for response to docetaxel. *Oncotarget*. 2015;6(25):21740-54.
188. Soekmadji C, Riches JD, Russell PJ, Ruelcke JE, McPherson S, Wang C, et al. Modulation of paracrine signaling by CD9 positive small extracellular vesicles mediates cellular growth of androgen deprived prostate cancer. *Oncotarget*. 2017;8(32):52237-55.
189. Ramteke A, Ting H, Agarwal C, Mateen S, Somasagara R, Hussain A, et al. Exosomes secreted under hypoxia enhance invasiveness and stemness of prostate cancer cells by targeting adherens junction molecules. *Mol Carcinog*. 2015;54(7):554-65.
190. Deep G, Jain A, Kumar A, Agarwal C, Kim S, Leevy WM, et al. Exosomes secreted by prostate cancer cells under hypoxia promote matrix metalloproteinases activity at pre-metastatic niches. *Mol Carcinog*. 2020;59(3):323-32.
191. Kucharzewska P, Christianson HC, Welch JE, Svensson KJ, Fredlund E, Ringnér M, et al. Exosomes reflect the hypoxic status of glioma cells and mediate hypoxia-dependent activation of vascular cells during tumor development. *Proc Natl Acad Sci U S A*. 2013;110(18):7312-7.
192. Brzozowski JS, Bond DR, Jankowski H, Goldie BJ, Burchell R, Naudin C, et al. Extracellular vesicles with altered tetraspanin CD9 and CD151 levels confer increased prostate cell motility and invasion. *Sci Rep*. 2018;8(1):8822.
193. Gillet LC, Navarro P, Tate S, Röst H, Selevsek N, Reiter L, et al. Targeted data extraction of the MS/MS spectra generated by data-independent acquisition: a new concept for consistent and accurate proteome analysis. *Mol Cell Proteomics*. 2012;11(6):O111.016717.
194. Krasny L, Huang PH. Data-independent acquisition mass spectrometry (DIA-MS) for proteomic applications in oncology. *Mol Omics*. 2021;17(1):29-42.
195. Hu A, Noble WS, Wolf-Yadlin A. Technical advances in proteomics: new developments in data-independent acquisition. *F1000Res*. 2016;5.
196. Hallal S, Azimi A, Wei H, Ho N, Lee MYT, Sim HW, et al. A Comprehensive Proteomic SWATH-MS Workflow for Profiling Blood Extracellular Vesicles: A New Avenue for Glioma Tumour Surveillance. *Int J Mol Sci*. 2020;21(13).
197. Chutipongtanate S, Greis KD. Multiplex Biomarker Screening Assay for Urinary Extracellular Vesicles Study: A Targeted Label-Free Proteomic Approach. *Sci Rep*. 2018;8(1):15039.
198. Zhang Y, Liu Y, Liu H, Tang WH. Exosomes: biogenesis, biologic function and clinical potential. *Cell Biosci*. 2019;9:19.
199. Ludwig C, Gillet L, Rosenberger G, Amon S, Collins BC, Aebersold R. Data-independent acquisition-based SWATH-MS for quantitative proteomics: a tutorial. *Mol Syst Biol*. 2018;14(8):e8126.

200. Katsogiannou M, Boyer JB, Valdeolivas A, Remy E, Calzone L, Audebert S, et al. Integrative proteomic and phosphoproteomic profiling of prostate cell lines. *PLoS One*. 2019;14(11):e0224148.
201. Kalra H, Simpson RJ, Ji H, Aikawa E, Altevogt P, Askenase P, et al. Vesiclepedia: a compendium for extracellular vesicles with continuous community annotation. *PLoS Biol*. 2012;10(12):e1001450.
202. Rontogianni S, Synadaki E, Li B, Liefwaard MC, Lips EH, Wesseling J, et al. Proteomic profiling of extracellular vesicles allows for human breast cancer subtyping. *Commun Biol*. 2019;2:325.
203. Bandu R, Oh JW, Kim KP. Mass spectrometry-based proteome profiling of extracellular vesicles and their roles in cancer biology. *Exp Mol Med*. 2019;51(3):1-10.
204. Jackson CE, Scruggs BS, Schaffer JE, Hanson PI. Effects of Inhibiting VPS4 Support a General Role for ESCRTs in Extracellular Vesicle Biogenesis. *Biophys J*. 2017;113(6):1342-52.
205. Griffiths SG, Cormier MT, Clayton A, Doucette AA. Differential Proteome Analysis of Extracellular Vesicles from Breast Cancer Cell Lines by Chaperone Affinity Enrichment. *Proteomes*. 2017;5(4).
206. Sala-Valdés M, Ursa A, Charrin S, Rubinstein E, Hemler ME, Sánchez-Madrid F, et al. EWI-2 and EWI-F link the tetraspanin web to the actin cytoskeleton through their direct association with ezrin-radixin-moesin proteins. *J Biol Chem*. 2006;281(28):19665-75.
207. Abramowicz A, Widlak P, Pietrowska M. Proteomic analysis of exosomal cargo: the challenge of high purity vesicle isolation. *Mol Biosyst*. 2016;12(5):1407-19.
208. Zanetti-Domingues LC, Bonner SE, Iyer RS, Martin-Fernandez ML, Huber V. Cooperation and Interplay between EGFR Signalling and Extracellular Vesicle Biogenesis in Cancer. *Cells*. 2020;9(12).
209. Babic A, Wolpin BM. Circulating Exosomes in Pancreatic Cancer: Will They Succeed on the Long, Littered Road to Early Detection Marker? *Clin Chem*. 2016;62(2):307-9.
210. Trebak M, Chong JM, Herlyn D, Speicher DW. Efficient laboratory-scale production of monoclonal antibodies using membrane-based high-density cell culture technology. *J Immunol Methods*. 1999;230(1-2):59-70.
211. Guerreiro EM, Vestad B, Steffensen LA, Aass HCD, Saeed M, Øvstebø R, et al. Efficient extracellular vesicle isolation by combining cell media modifications, ultrafiltration, and size-exclusion chromatography. *PLoS One*. 2018;13(9):e0204276.
212. Wierz M, Pierson S, Gargiulo E, Guerin C, Moussay E, Paggetti J. Purification of Leukemia-Derived Exosomes to Study Microenvironment Modulation. *Methods Mol Biol*. 2019;1884:231-45.
213. Chen M, Xu R, Rai A, Suwakulsiri W, Izumikawa K, Ishikawa H, et al. Distinct shed microvesicle and exosome microRNA signatures reveal diagnostic markers for colorectal cancer. *PLoS One*. 2019;14(1):e0210003.
214. Palviainen M, Saari H, Kärkkäinen O, Pekkinen J, Auriola S, Yliperttula M, et al. Metabolic signature of extracellular vesicles depends on the cell culture conditions. *J Extracell Vesicles*. 2019;8(1):1596669.
215. Mittermaier J, M.O Z-G. Long - Term High Level Protein Expression in Adherent, Protein - free Growing BHK Cells Using Integra CELLline Adhere ® Bioreactor Flasks. 2004;24:42-3.
216. Jeppesen DK, Nawrocki A, Jensen SG, Thorsen K, Whitehead B, Howard KA, et al. Quantitative proteomics of fractionated membrane and lumen exosome proteins from isogenic metastatic and nonmetastatic bladder cancer cells reveal differential expression of EMT factors. *Proteomics*. 2014;14(6):699-712.
217. Colao IL, Corteling R, Bracewell D, Wall I. Manufacturing Exosomes: A Promising Therapeutic Platform. *Trends Mol Med*. 2018;24(3):242-56.

218. Coralli C, Cemazar M, Kanthou C, Tozer GM, Dachs GU. Limitations of the reporter green fluorescent protein under simulated tumor conditions. *Cancer Res.* 2001;61(12):4784-90.
219. Vordermark D, Shibata T, Brown JM. Green fluorescent protein is a suitable reporter of tumor hypoxia despite an oxygen requirement for chromophore formation. *Neoplasia.* 2001;3(6):527-34.
220. Shaner NC, Steinbach PA, Tsien RY. A guide to choosing fluorescent proteins. *Nat Methods.* 2005;2(12):905-9.
221. Whitford W, Guterstam P. Exosome manufacturing status. *Future Med Chem.* 2019;11(10):1225-36.
222. Thippabhotla S, Zhong C, He M. 3D cell culture stimulates the secretion of in vivo like extracellular vesicles. *Sci Rep.* 2019;9(1):13012.
223. Chen AK, Chen X, Choo AB, Reuveny S, Oh SK. Critical microcarrier properties affecting the expansion of undifferentiated human embryonic stem cells. *Stem Cell Res.* 2011;7(2):97-111.
224. Jiang X, Zhang J, Huang Y. Tetraspanins in cell migration. *Cell Adh Migr.* 2015;9(5):406-15.
225. Yazlovitskaya EM, Viquez OM, Tu T, De Arcangelis A, Georges-Labouesse E, Sonnenberg A, et al. The laminin binding $\alpha 3$ and $\alpha 6$ integrins cooperate to promote epithelial cell adhesion and growth. *Matrix Biol.* 2019;77:101-16.
226. Xue L, Zhu Z, Wang Z, Li H, Zhang P, Chen Q, et al. Knockdown of prostaglandin reductase 1 (PTGR1) suppresses prostate cancer cell proliferation by inducing cell cycle arrest and apoptosis. *Biosci Trends.* 2016;10(2):133-9.
227. Volkmer E, Drosse I, Otto S, Stangelmayer A, Stengele M, Kallukalam BC, et al. Hypoxia in static and dynamic 3D culture systems for tissue engineering of bone. *Tissue Eng Part A.* 2008;14(8):1331-40.
228. Schmid J, Schwarz S, Meier-Staude R, Sudhop S, Clausen-Schaumann H, Schieker M, et al. A Perfusion Bioreactor System for Cell Seeding and Oxygen-Controlled Cultivation of Three-Dimensional Cell Cultures. *Tissue Engineering Part C: Methods.* 2018;24(10):585-95.
229. Fraga A, Ribeiro R, Príncipe P, Lopes C, Medeiros R. Hypoxia and Prostate Cancer Aggressiveness: A Tale With Many Endings. *Clin Genitourin Cancer.* 2015;13(4):295-301.
230. Deep G, Panigrahi GK. Hypoxia-Induced Signaling Promotes Prostate Cancer Progression: Exosomes Role as Messenger of Hypoxic Response in Tumor Microenvironment. *Critical reviews in oncogenesis.* 2015;20(5-6):419-34.
231. Chiche J, Brahimi-Horn MC, Pouyssegur J. Tumour hypoxia induces a metabolic shift causing acidosis: a common feature in cancer. *J Cell Mol Med.* 2010;14(4):771-94.
232. Shaner NC, Campbell RE, Steinbach PA, Giepmans BN, Palmer AE, Tsien RY. Improved monomeric red, orange and yellow fluorescent proteins derived from *Discosoma* sp. red fluorescent protein. *Nat Biotechnol.* 2004;22(12):1567-72.
233. Piatkevich KD, Verkhusha VV. Guide to red fluorescent proteins and biosensors for flow cytometry. *Methods Cell Biol.* 2011;102:431-61.
234. Shaner NC, Patterson GH, Davidson MW. Advances in fluorescent protein technology. *J Cell Sci.* 2007;120(Pt 24):4247-60.
235. Danhier P, Krishnamachary B, Bharti S, Kakkad S, Mironchik Y, Bhujwala ZM. Combining Optical Reporter Proteins with Different Half-lives to Detect Temporal Evolution of Hypoxia and Reoxygenation in Tumors. *Neoplasia.* 2015;17(12):871-81.
236. Bharti SK, Kakkad S, Danhier P, Wildes F, Penet MF, Krishnamachary B, et al. Hypoxia Patterns in Primary and Metastatic Prostate Cancer Environments. *Neoplasia.* 2019;21(2):239-46.
237. Bakela K, Athanassakis I. Soluble major histocompatibility complex molecules in immune regulation: highlighting class II antigens. *Immunology.* 2018;153(3):315-24.
238. Lynch S, Santos SG, Campbell EC, Nimmo AM, Botting C, Prescott A, et al. Novel MHC class I structures on exosomes. *J Immunol.* 2009;183(3):1884-91.

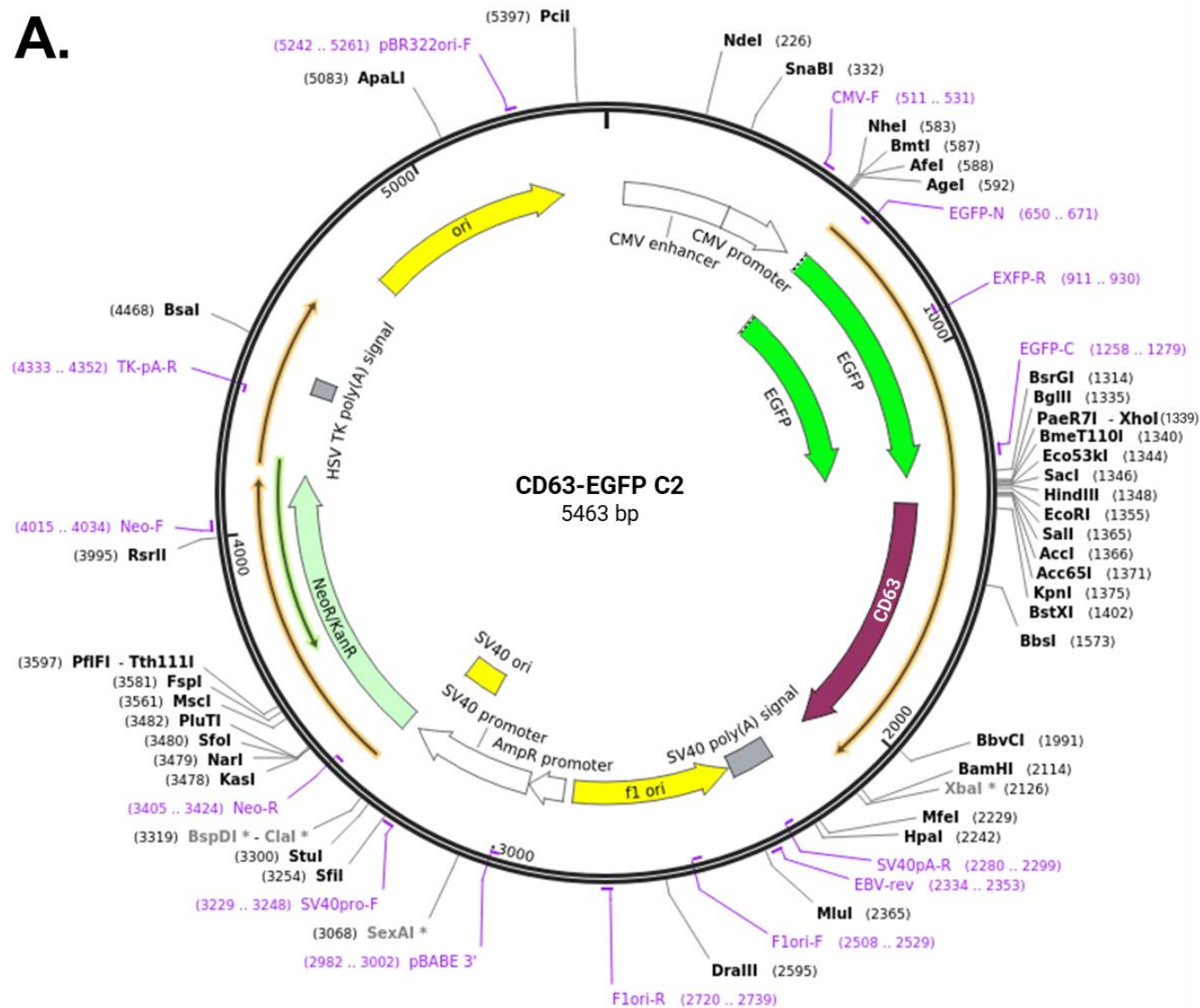
239. Makhadiyeva D, Lam L, Moatari M, Vallance J, Zheng Y, Campbell EC, et al. MHC class I dimer formation by alteration of the cellular redox environment and induction of apoptosis. *Immunology*. 2012;135(2):133-9.
240. Siemens DR, Hu N, Sheikhi AK, Chung E, Frederiksen LJ, Pross H, et al. Hypoxia increases tumor cell shedding of MHC class I chain-related molecule: role of nitric oxide. *Cancer Res*. 2008;68(12):4746-53.
241. Filipe V, Hawe A, Jiskoot W. Critical evaluation of Nanoparticle Tracking Analysis (NTA) by NanoSight for the measurement of nanoparticles and protein aggregates. *Pharmaceutical research*. 2010;27(5):796-810.
242. Gudbergsson JM, Johnsen KB, Skov MN, Duroux M. Systematic review of factors influencing extracellular vesicle yield from cell cultures. *Cytotechnology*. 2016;68(4):579-92.
243. Kakarla R, Hur J, Kim YJ, Kim J, Chwae YJ. Apoptotic cell-derived exosomes: messages from dying cells. *Exp Mol Med*. 2020;52(1):1-6.
244. Emelyanov A, Shtam T, Kamyshinsky R, Garaeva L, Verlov N, Miliukhina I, et al. Cryo-electron microscopy of extracellular vesicles from cerebrospinal fluid. *PLOS ONE*. 2020;15(1):e0227949.
245. Issman L, Brenner B, Talmon Y, Aharon A. Cryogenic transmission electron microscopy nanostructural study of shed microparticles. *PLoS One*. 2013;8(12):e83680.
246. Poliakov A, Spilman M, Dokland T, Amling CL, Mobley JA. Structural heterogeneity and protein composition of exosome-like vesicles (prostasomes) in human semen. *The Prostate*. 2009;69(2):159-67.
247. Zabeo D, Cvjetkovic A, Lässer C, Schorb M, Lötvall J, Höög JL. Exosomes purified from a single cell type have diverse morphology. *Journal of extracellular vesicles*. 2017;6(1):1329476-.
248. Hantak MP, Qing E, Earnest JT, Gallagher T. Tetraspanins: Architects of Viral Entry and Exit Platforms. *J Virol*. 2019;93(6).
249. Morelli AE, Larregina AT, Shufesky WJ, Sullivan ML, Stolz DB, Papworth GD, et al. Endocytosis, intracellular sorting, and processing of exosomes by dendritic cells. *Blood*. 2004;104(10):3257-66.
250. Joshi BS, de Beer MA, Giepmans BNG, Zuhorn IS. Endocytosis of Extracellular Vesicles and Release of Their Cargo from Endosomes. *ACS Nano*. 2020;14(4):4444-55.
251. Russell AE, Sneider A, Witwer KW, Bergese P, Bhattacharyya SN, Cocks A, et al. Biological membranes in EV biogenesis, stability, uptake, and cargo transfer: an ISEV position paper arising from the ISEV membranes and EVs workshop. *J Extracell Vesicles*. 2019;8(1):1684862.
252. Brown MR, Rees P, Wilks S, Summers HD, Errington RJ, Njoh KL, et al., editors. *Computational Simulation of Optical Tracking of Cell Populations Using Quantum Dot Fluorophores* 2007; Berlin, Heidelberg: Springer Berlin Heidelberg.
253. Summers HD, Brown MR, Holton MD, Tonkin JA, Hondow N, Brown AP, et al. Quantification of nanoparticle dose and vesicular inheritance in proliferating cells. *ACS Nano*. 2013;7(7):6129-37.
254. Jaiswal JK, Simon SM. Potentials and pitfalls of fluorescent quantum dots for biological imaging. *Trends Cell Biol*. 2004;14(9):497-504.
255. Martynenko IV, Litvin AP, Purcell-Milton F, Baranov AV, Fedorov AV, Gun'ko YK. Application of semiconductor quantum dots in bioimaging and biosensing. *J Mater Chem B*. 2017;5(33):6701-27.
256. Behzadi S, Serpooshan V, Tao W, Hamaly MA, Alkawareek MY, Dreaden EC, et al. Cellular uptake of nanoparticles: journey inside the cell. *Chem Soc Rev*. 2017;46(14):4218-44.
257. Vivès E, Richard JP, Rispal C, Lebleu B. TAT peptide internalization: seeking the mechanism of entry. *Curr Protein Pept Sci*. 2003;4(2):125-32.
258. Ware MJ, Godin B, Singh N, Majithia R, Shamsudeen S, Serda RE, et al. Analysis of the influence of cell heterogeneity on nanoparticle dose response. *ACS Nano*. 2014;8(7):6693-700.

259. Lin S, Xie X, Patel MR, Yang YH, Li Z, Cao F, et al. Quantum dot imaging for embryonic stem cells. *BMC Biotechnol.* 2007;7:67.
260. Xu L, Faruqu FN, Liam-Or R, Abu Abed O, Li D, Venner K, et al. Design of experiment (DoE)-driven *in vitro* and *in vivo* uptake studies of exosomes for pancreatic cancer delivery enabled by copper-free click chemistry-based labelling. *J Extracell Vesicles.* 2020;9(1):1779458.
261. Franzen CA, Simms PE, Van Huis AF, Foreman KE, Kuo PC, Gupta GN. Characterization of uptake and internalization of exosomes by bladder cancer cells. *Biomed Res Int.* 2014;2014:619829.
262. Chuo ST, Chien JC, Lai CP. Imaging extracellular vesicles: current and emerging methods. *J Biomed Sci.* 2018;25(1):91.
263. Linares R, Tan S, Gounou C, Arraud N, Brisson AR. High-speed centrifugation induces aggregation of extracellular vesicles. *J Extracell Vesicles.* 2015;4:29509.
264. Bosch S, de Beaupaire L, Allard M, Mosser M, Heichette C, Chrétien D, et al. Trehalose prevents aggregation of exosomes and cryodamage. *Sci Rep.* 2016;6:36162.
265. Sancho-Albero M, Navascués N, Mendoza G, Sebastián V, Arruebo M, Martín-Duque P, et al. Exosome origin determines cell targeting and the transfer of therapeutic nanoparticles towards target cells. *J Nanobiotechnology.* 2019;17(1):16.
266. Barnes A.L. OFJ, Carstairs A., Quick S., Stone A.P., Kasprowicz, R. SR, Genever P.G. Exploring the social life of mesenchymal stromal cells by label-free tracking of individual and collective cell behaviour. *Osteoarthritis and Cartilage.* 2018. p. S149.
267. Bergeland T, Widerberg J, Bakke O, Nordeng TW. Mitotic partitioning of endosomes and lysosomes. *Curr Biol.* 2001;11(9):644-51.
268. Barcellos-de-Souza P, Comito G, Pons-Segura C, Taddei ML, Gori V, Becherucci V, et al. Mesenchymal Stem Cells are Recruited and Activated into Carcinoma-Associated Fibroblasts by Prostate Cancer Microenvironment-Derived TGF- β 1. *Stem Cells.* 2016;34(10):2536-47.
269. Cho JA, Park H, Lim EH, Lee KW. Exosomes from breast cancer cells can convert adipose tissue-derived mesenchymal stem cells into myofibroblast-like cells. *Int J Oncol.* 2012;40(1):130-8.
270. Cho JA, Park H, Lim EH, Kim KH, Choi JS, Lee JH, et al. Exosomes from ovarian cancer cells induce adipose tissue-derived mesenchymal stem cells to acquire the physical and functional characteristics of tumor-supporting myofibroblasts. *Gynecol Oncol.* 2011;123(2):379-86.
271. Gu J, Qian H, Shen L, Zhang X, Zhu W, Huang L, et al. Gastric cancer exosomes trigger differentiation of umbilical cord derived mesenchymal stem cells to carcinoma-associated fibroblasts through TGF- β /Smad pathway. *PLoS One.* 2012;7(12):e52465.
272. Capulli M, Paone R, Rucci N. Osteoblast and osteocyte: games without frontiers. *Arch Biochem Biophys.* 2014;561:3-12.
273. Weng JJ, Su Y. Nuclear matrix-targeting of the osteogenic factor Runx2 is essential for its recognition and activation of the alkaline phosphatase gene. *Biochim Biophys Acta.* 2013;1830(3):2839-52.
274. Gomathi K, Akshaya N, Srinaath N, Moorthi A, Selvamurugan N. Regulation of Runx2 by post-translational modifications in osteoblast differentiation. *Life Sci.* 2020;245:117389.
275. Zhao Z, Zhao M, Xiao G, Franceschi RT. Gene transfer of the Runx2 transcription factor enhances osteogenic activity of bone marrow stromal cells *in vitro* and *in vivo*. *Mol Ther.* 2005;12(2):247-53.
276. Lanning B. The role of prostate cancer small extracellular vesicles on the bone environment. <http://orca-mwe.cf.ac.uk/id/eprint/121242>: Cardiff University; 2019.
277. Wang S, Li X, Zhu R, Han Q, Zhao RC. Lung cancer exosomes initiate global long non-coding RNA changes in mesenchymal stem cells. *Int J Oncol.* 2016;48(2):681-9.
278. Adorno-Cruz V, Liu H. Regulation and functions of integrin α 2 in cell adhesion and disease. *Genes Dis.* 2019;6(1):16-24.

279. Shao H, Wang JH, Pollak MR, Wells A. α -actinin-4 is essential for maintaining the spreading, motility and contractility of fibroblasts. *PLoS One*. 2010;5(11):e13921.
280. Guo K, Zhao C, Lang B, Wang H, Zheng H, Zhang F. Regulator of Chromosome Condensation 2 Modulates Cell Cycle Progression, Tumorigenesis, and Therapeutic Resistance. *Front Mol Biosci*. 2020;7:620973.
281. Ortmann B, Androlewicz MJ, Cresswell P. MHC class I/ β 2-microglobulin complexes associate with TAP transporters before peptide binding. *Nature*. 1994;368(6474):864-7.
282. Zhang H, Deng T, Liu R, Bai M, Zhou L, Wang X, et al. Exosome-delivered EGFR regulates liver microenvironment to promote gastric cancer liver metastasis. *Nat Commun*. 2017;8:15016.
283. Dovrat S, Caspi M, Zilberberg A, Lahav L, Firsow A, Gur H, et al. 14-3-3 and β -catenin are secreted on extracellular vesicles to activate the oncogenic Wnt pathway. *Mol Oncol*. 2014;8(5):894-911.
284. Gaballa R, Ali HEA, Mahmoud MO, Rhim JS, Ali HI, Salem HF, et al. Exosomes-Mediated Transfer of Itga2 Promotes Migration and Invasion of Prostate Cancer Cells by Inducing Epithelial-Mesenchymal Transition. *Cancers (Basel)*. 2020;12(8).
285. Colombo M, Moita C, van Niel G, Kowal J, Vigneron J, Benaroch P, et al. Analysis of ESCRT functions in exosome biogenesis, composition and secretion highlights the heterogeneity of extracellular vesicles. *J Cell Sci*. 2013;126(Pt 24):5553-65.
286. Nguyen HC, Talledge N, McCullough J, Sharma A, Moss FR, Iwasa JH, et al. Membrane constriction and thinning by sequential ESCRT-III polymerization. *Nat Struct Mol Biol*. 2020;27(4):392-9.
287. Ellem SJ, De-Juan-Pardo EM, Risbridger GP. In vitro modeling of the prostate cancer microenvironment. *Adv Drug Deliv Rev*. 2014;79-80:214-21.
288. Dondossola E, Paindelli C. In vitro three-dimensional modeling for prostate cancer. *Biomaterials for 3D Tumor Modeling*: Elsevier; 2020. p. 251-86.
289. Yan IK, Shukla N, Borrelli DA, Patel T. Use of a Hollow Fiber Bioreactor to Collect Extracellular Vesicles from Cells in Culture. *Methods Mol Biol*. 2018;1740:35-41.
290. Yan L, Wu X. Exosomes produced from 3D cultures of umbilical cord mesenchymal stem cells in a hollow-fiber bioreactor show improved osteochondral regeneration activity. *Cell Biol Toxicol*. 2019.
291. Rocha S, Carvalho J, Oliveira P, Voglstaetter M, Schvartz D, Thomsen AR, et al. 3D Cellular Architecture Affects MicroRNA and Protein Cargo of Extracellular Vesicles. *Adv Sci (Weinh)*. 2019;6(4):1800948.
292. Reátegui E, van der Vos KE, Lai CP, Zeinali M, Atai NA, Aldikacti B, et al. Engineered nanointerfaces for microfluidic isolation and molecular profiling of tumor-specific extracellular vesicles. *Nat Commun*. 2018;9(1):175.
293. Wu Q, Liu J, Wang X, Feng L, Wu J, Zhu X, et al. Organ-on-a-chip: recent breakthroughs and future prospects. *Biomed Eng Online*. 2020;19(1):9.

APPENDIX I

A.

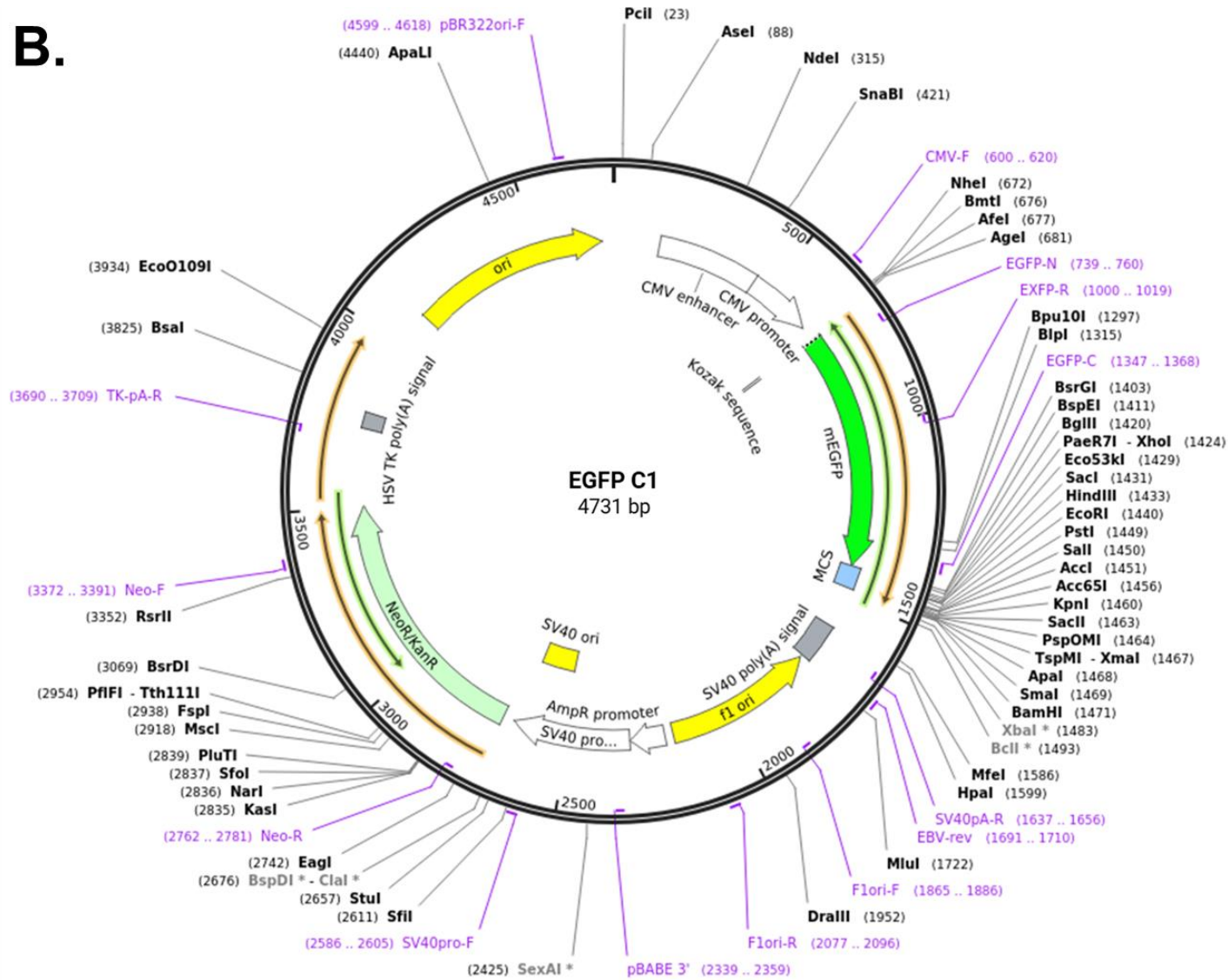


Supplementary Figure 1. Detailed plasmid maps for each DNA construct.

A. Plasmid map of CD63-EGFP C2 (“GFP-CD63”), which was generated by Dr. Paul Luzio and was purchased from Addgene (plasmid #62964). This map was generated in SnapGene Viewer and demonstrates the fusion of the EGFP gene (shown in green colour) to the N-terminus of the CD63 gene (shown in purple colour) in the C2 plasmid.

Figure and Legend continued to next pages ▶

B.



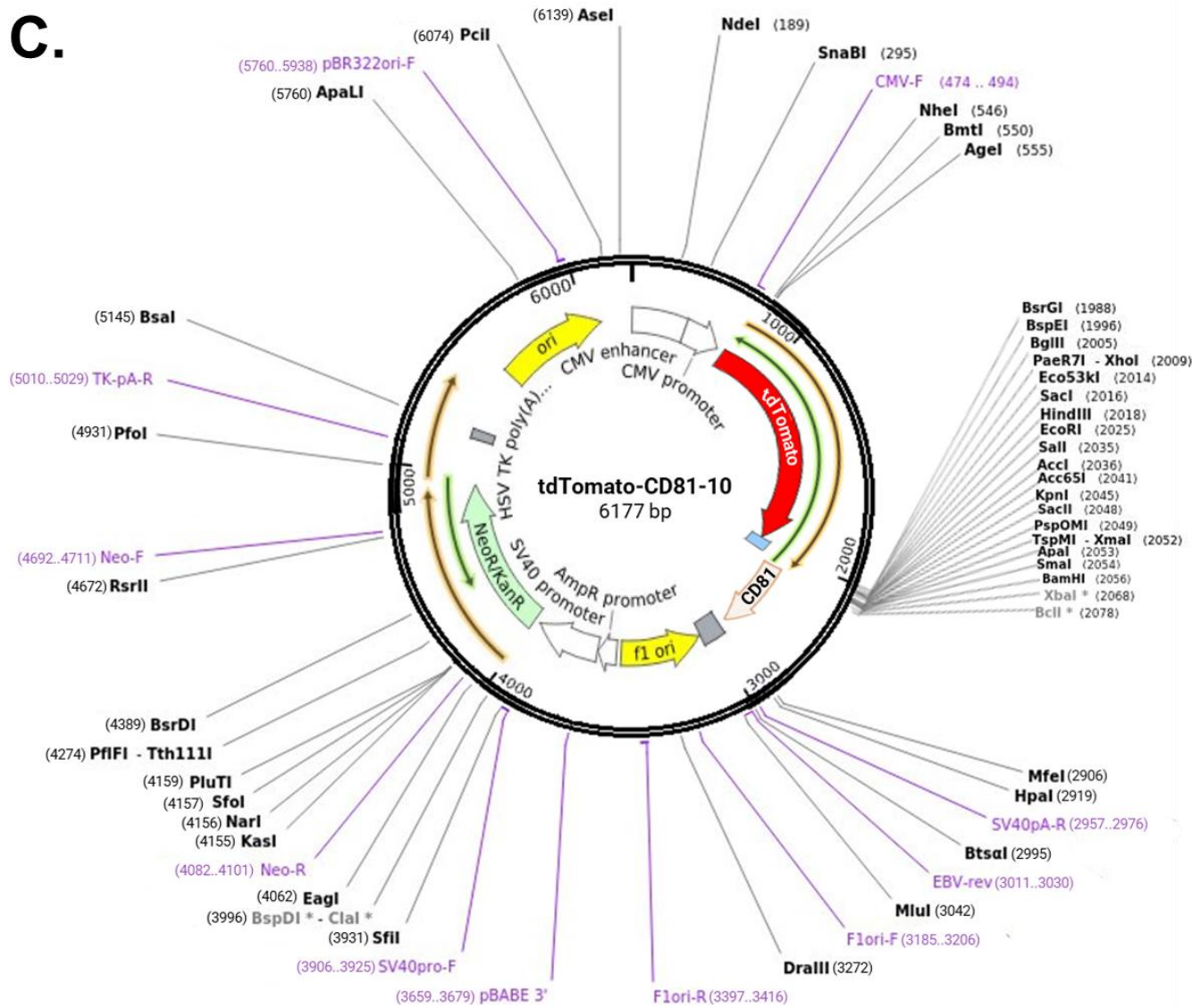
Supplementary Figure 1. Detailed plasmid maps for each DNA construct.

Figure and Legend continued from previous pages ►

B. Plasmid map of EGFP-C1 (“GFP”), which was generated by Dr. Michael Davidson and was purchased from Addgene (plasmid #54759). This map was generated in SnapGene Viewer and shows the EGFP gene in green colour in the C1 plasmid.

Figure and Legend continued to next pages ►

C.

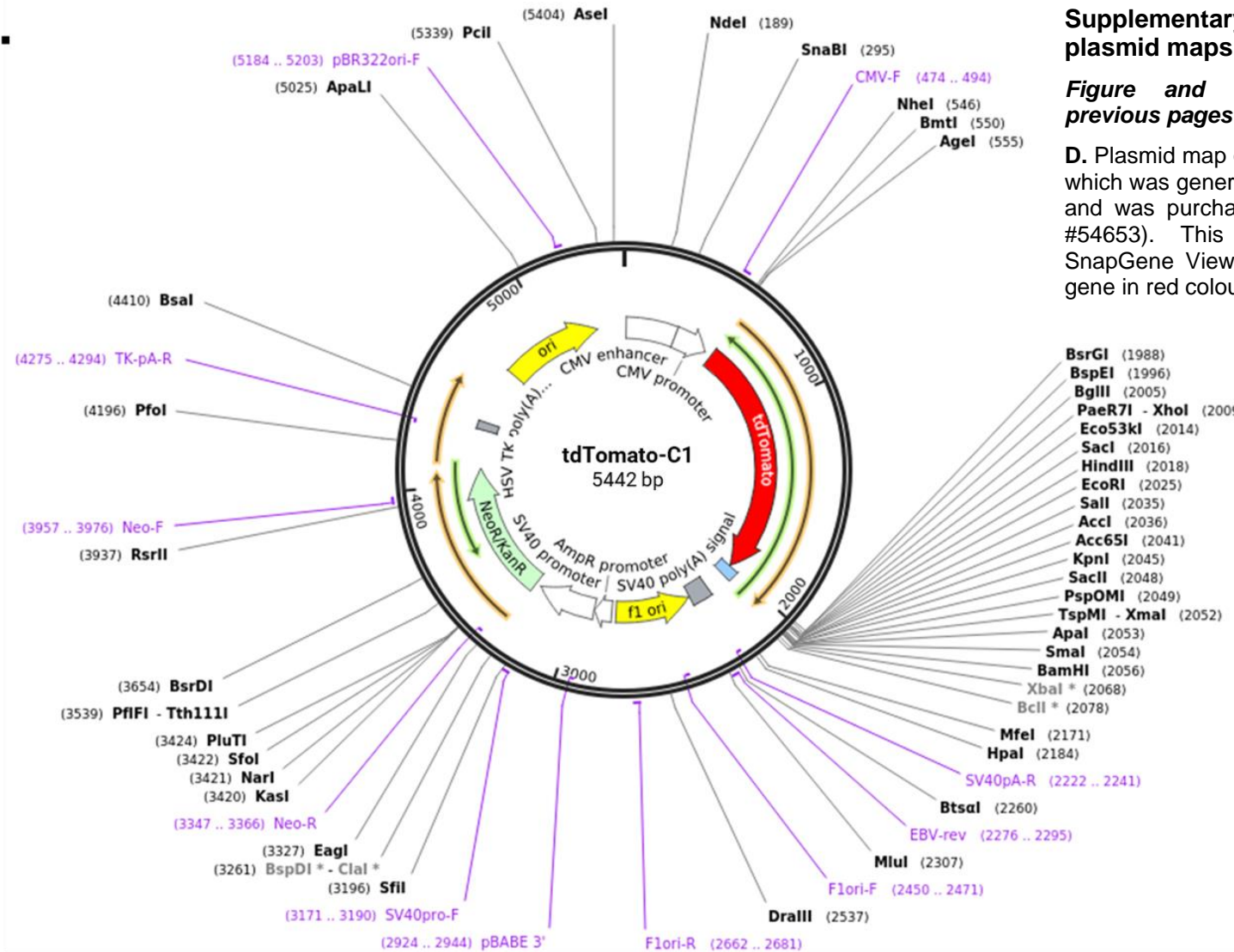


Supplementary Figure 1. Detailed plasmid maps for each DNA construct.

C. Plasmid map of tdTomato-CD81-10 (“CD81-Tdtomato”), which was generated by Dr. Michael Davidson and was purchased from Addgene (plasmid #58078). This map was generated in SnapGene Viewer and demonstrates the fusion of the tdTomato gene (shown in red colour) to the N-terminus of the CD81 gene (shown in orange colour) in the C1 plasmid.

Figure and Legend continued to next pages ►

D.



Supplementary Figure 1. Detailed plasmid maps for each DNA construct.

Figure and Legend continued from previous pages ►

D. Plasmid map of tdTomato-C1 (“Tdtomato”), which was generated by Dr. Michael Davidson and was purchased from Addgene (plasmid #54653). This map was generated in SnapGene Viewer and shows the tdTomato gene in red colour in the C1 plasmid.

A. Maximum Intensity Projection of Z-stack Fluorescent Images

```

1 input = getDirectory("Choose a Directory")           //Selection of folder with saved images
2 processFolder(input);
3
4 function processFolder(input)                       // Function to scan folder
5 {   list = getFileList(input);                       // Function to get number of images in folder and save it to "list" variable
6     for (j = 0; j < list.length; j++)             // Loop created to process each image of the folder sequentially
7
8         {   open (input+list [j]);                 // Open image[A] in folder
9             Name=File.nameWithoutExtension;        // Save image name in "Name" variable without the suffix of the image i.e. without .tiff
10            selectWindow(list [j]);                // Select image[A]
11            run("Duplicate...", "duplicate channels=2"); // Duplicate channel 2 (fluorescence channel of image[A]) to create new image[B]
12            run("Z Project...", "projection=[Max Intensity]"); // Perform maximum intensity Z-projection on image[B] to create new image[C]
13            saveAs("Tiff",input+Name+"_MAX");       // Save image[C] in current folder and name it as image[A]_MAX and suffix .tiff
14            close();                               // Close windows and image[A] and proceed to next image on the folder list to repeat process
15            close(list [j]);
16
17        }
18 }

```

Supplementary Figure 2. Fiji macro code used for image analysis.

Figure and Legend continue to next page ►

B. Fluorescence Background Subtraction

```

1 macro "Batch calculate images [1]"                 //Custom macro code to batch process images
2 {
3     LocationOfFiles = getDirectory("Select Folder"); //Selection of folder with images
4     LocationOfSave = getDirectory("Select Save Location"); //Selection of destination folder to save processed images
5     waitForUser("Open and Select Background Image then click ok."); //Selection of background fluorescent image (negative control sample)
6     BackgroundImage = getTitle();                 //"BackgroundImage" variable created to save title of background image
7     setBatchMode(true);
8     FileList = getFileList(LocationOfFiles);       //Function to get list of images in folder and save it to "FileList" variable
9     NumberOfFiles = FileList.length;              //Calculate number of images in folder and save it to "NumberofFiles" variable
10    for (i=0; i<NumberOfFiles; i+=1)               //Loop created to process each image of the folder sequentially
11    {
12        FileName = FileList[i];                    //"FileName" variable created to assign image[A] name
13        pathtofile = LocationOfFiles+FileName;     //"pathtofile" variable created to save location of image[A] in folder
14        open(pathtofile);                          //open image[A] in specific location
15        name = getTitle();                          //"name" variable created to save image[A] name without suffix
16        run("Calculator Plus", "i1="+name+" i2="+BackgroundImage+" operation=[Subtract: i2 = (i1-i2) x k1 + k2] k1=2.5 k2=-2.5 create"); //Run CalculatorPlus plugin to subtract background image from image[A] in folder
17
18        selectWindow("Result");
19        SaveName = replace(name, ".tif", "_minus_background.tif"); //Rename resulting image[B] as image[A]_minus background and suffix .tiff
20        saveAs("TIFF", LocationOfSave+SaveName);   //Save image[B] at pre-selected destination folder
21        selectWindow(BackgroundImage);             //Reselect Background image to restart loop for next image
22    }
23 }

```

C. Generation of Single-cell Images and Cell Shape Measurements

```

1 macro "Batch calculate images [1]" //Custom macro code to batch process images
2 {
3   input = getDirectory("Choose a Directory") //Selection of folder with whole field-of-view images (with subtracted kd background)
4   waitForUser("Open and Select Fluorescent Image then click ok."); //Manual selection of image [A] in folder and open it
5   FLImage = getTitle(); // "FLImage" variable created to save title of image [A]
6   setBatchMode(true);
7   selectWindow(FLImage); //Selection of opened image [A]
8   for (i = 0; i < 100; i++) //Loop created to process each ROI (manually made previously) which corresponds to the outline of each cell
9   {
10      Name=File.nameWithoutExtension; // "Name" variable created to save image [A] name without suffix
11      roiManager("Select",i); //Selection of cell singlet ROI [a] and overlay on image [A]
12      run("Duplicate...", "duplicate"); //Duplicate only ROI of image [A] hence creating a new image of a single cell[Aa]
13      saveAs("Tiff",input+Name+"_Singlet_"+i+1); //Save new single cell image [Aa] as image[A]_Singlet_[a] with suffix .tiff
14      run("Measure"); //Run measure macro on new single-cell image including cell area, perimeter, shape
15      close();
16      selectWindow(FLImage); //Reselect image [A] to restart loop and proceed with next ROI [b]
17   }
18 }

```

Supplementary Figure 2. Fiji macro code for image analysis. Figure and Legend continue to next page ►

D. Single-cell Automatic Thresholding and Fluorescence Intensity Measurements

```

1 input = getDirectory("Choose a Directory") //Selection of folder with single-cell images (with subtracted background)
2
3 processFolder(input);
4 function processFolder(input) //Function to scan folder
5 {
6   list = getFileList(input); //Function to get number of single-cell fluorescent images in folder and save it to "list" variable
7   for (j = 0; j < list.length; j++) //Loop created to process each single-cell image of the folder sequentially
8   {
9     open (input+list [j]); //Open single-cell fluorescent image[a] in folder
10    selectWindow(list [j]); //Select open single-cell image[a]
11    run("Duplicate...", " "); //Duplicate single-cel image[a]
12    run("Enhance Contrast...", "saturated=0.2 normalize"); //Enhance contrast on duplicate image[a]
13    setOption("ScaleConversions", true); //Convert duplicate image[a] to 8-bit
14    run("8-bit");
15    run("Auto Threshold", "method=Li ignore_black white"); //Use 8-bit duplicate image[a] to apply Li's autothresholding method
16    run("Clear Outside");
17    run("Invert"); //Clear outside thresholded image boundary and invert image
18    run("Create Selection"); //Create selection of inverted image to generate single-cell mask[a*]
19    roiManager("Add"); //Use single-cell image mask[a*] to create ROI
20    close();
21    selectWindow(list [j]); //Select original single-cell fluorescent image[a]
22    roiManager("Select", 0); //Apply mask[a*] ROI to original single-cell fluorescent image[a]
23    roiManager("Measure"); //Run measure macro on single-cell fluorescent image[a] with mask[a*] i.e. mean and total fluorescence intensity etc.
24    close();
25    roiManager("Deselect");
26    roiManager("Delete"); //Delete mask[a*] ROI to allow for next mask[b*]ROI to be generated in next loop (for next single-cell image[b])
27  }
28 }
29 close("");

```

E. Field-of-view Automatic Thresholding and Fluorescence Intensity Measurements

```

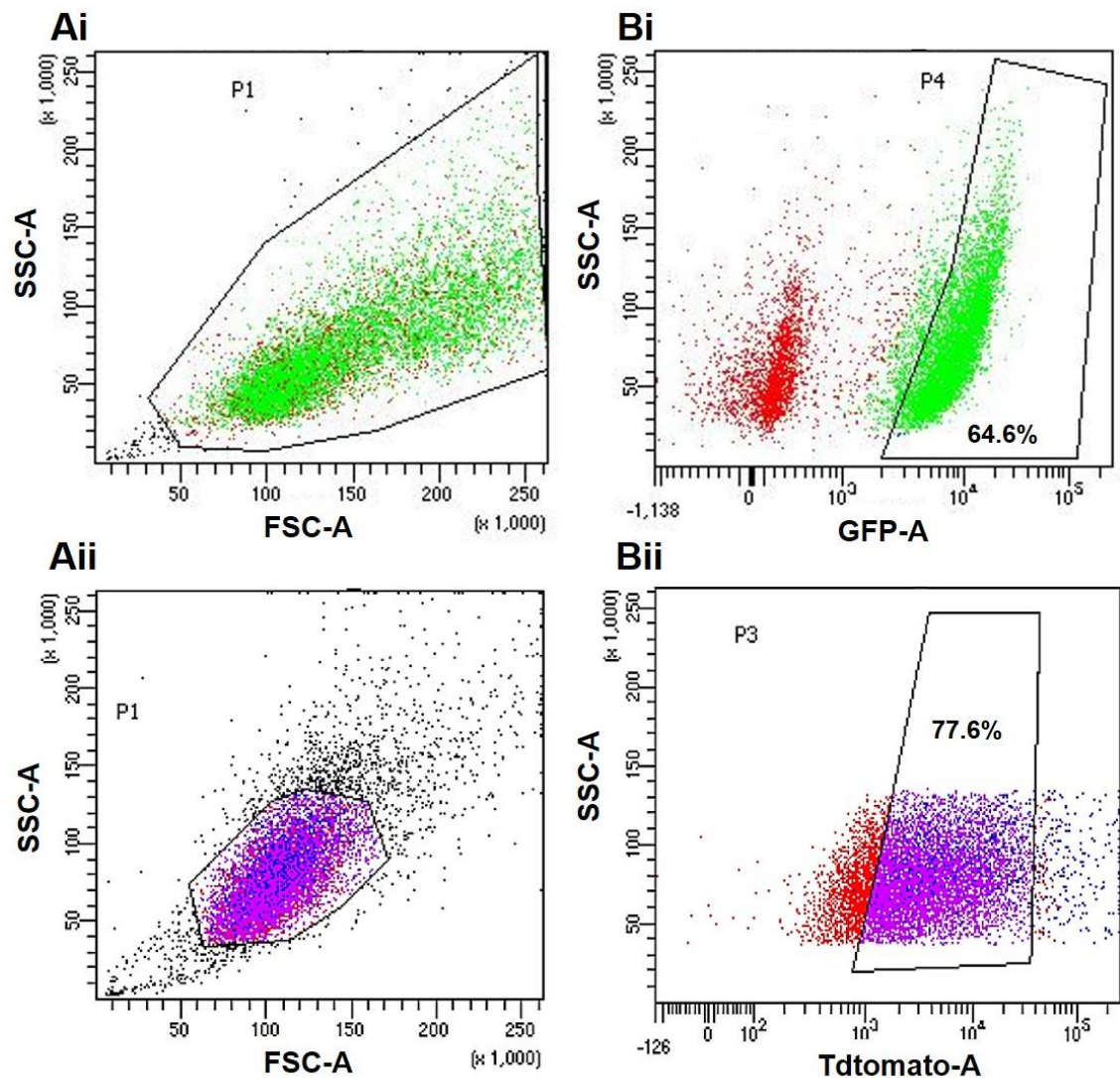
1 input = getDirectory("Choose a Directory") //Selection of folder with whole field-of-view images (with subtracted background)
2 processFolder(input);
3
4 function processFolder(input) //Function to scan folder
5 { list = getFileList(input); //Function to get number of field-of-view fluorescent images in folder and save it to "list" variable
6   for (j = 0; j < list.length; j++) //Loop created to process each field-of-view image of the folder sequentially
7   {
8     open (input+list [j]); //Open field-of-view fluorescent image[a] in folder
9     selectWindow(list [j]); //Select image[a]
10    run("Duplicate...", " "); //Duplicate image[a]
11    run("Enhance Contrast...", "saturated=0.2 normalize"); //Enhance contrast on duplicate image[a]
12    setOption("ScaleConversions", true); //Convert duplicate image[a] to 8-bit
13    run("8-bit");
14    run("Auto Threshold", "method=Li ignore_black white"); //Use 8-bit duplicate image[a] to apply Li's autothresholding method
15    run("Create Selection"); //Create selection of thresholded image to generate field-of-view mask[a*]
16    roiManager("Add"); //Use field-of-view image mask[a*] to create ROI
17    close();
18    selectWindow(list [j]); //Select original field-of-view fluorescent image[a]
19    roiManager("Select", 0); //Apply mask[a*] ROI to original field-of-view fluorescent image[a]
20    roiManager("Measure"); //Run measure macro on field-of-view fluorescent image[a] with mask[a*] i.e. mean and total fluorescence intensity etc.
21    close();
22    roiManager("Deselect");
23    roiManager("Delete"); //Delete mask[a*] ROI to allow for next mask[b*] ROI to be generated in next loop (for next field-of-view image[b])
24  }
25 }
26
27
28 close("*");

```

Supplementary Figure 2. Fiji macro code for image analysis.

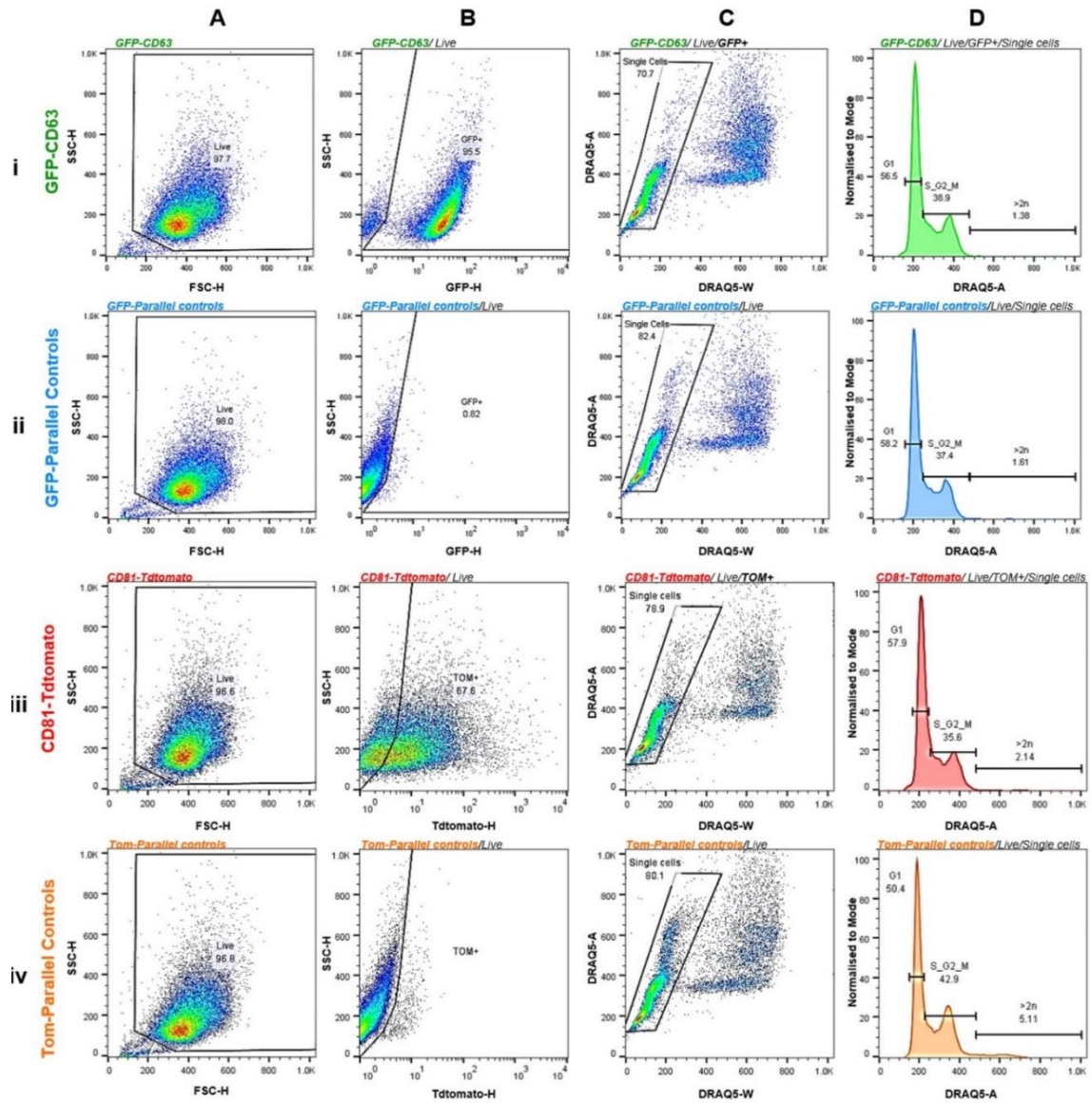
Figure and Legend continued from previous pages ►

The Fiji (v1.52c) macro code used for QD705 and CD81-Tdtomato sEV dosing image analysis including the script for: **A.** Maximum intensity projection of Z-stack fluorescent images to generate 2D images, **B.** Fluorescence background subtraction using the fluorescence channel of negative controls (untreated samples), **C.** Generation of single-cell images (after manual segmentation of each cell boundary) and automated cell shape measurements, **D.** Single-cell automatic thresholding using Li's algorithm and subsequent fluorescence intensity measurements, and **E.** Field-of-view automatic thresholding using Li's algorithm and subsequent fluorescence intensity measurements. Note that macro code is shown with black, blue, pink and yellow lettering (left), whereas annotated comments explaining the algorithm steps are shown in green lettering (right).



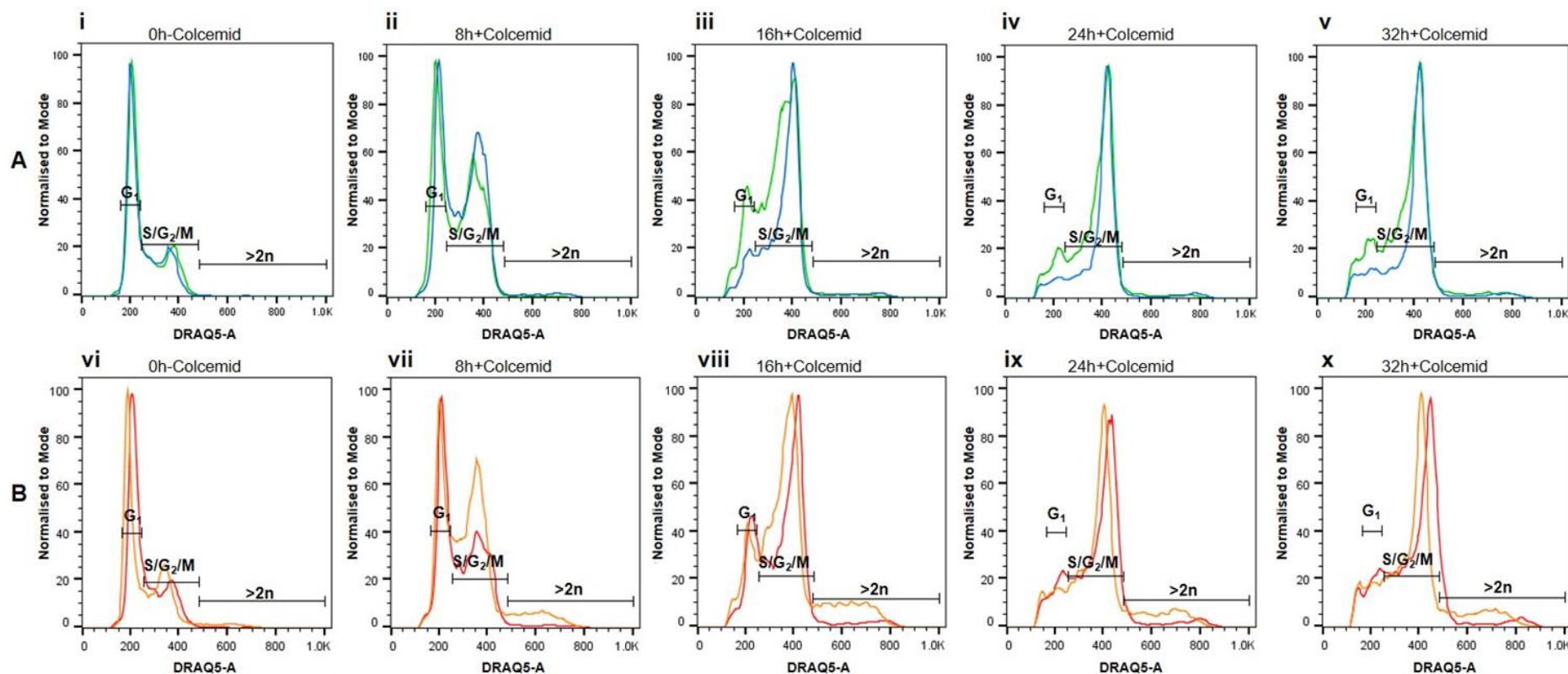
Supplementary Figure 3. Gating strategy for Fluorescence-Activated Cell Sorting (FACS) of GFP-CD63 and CD81-Tdtomato DU145 cells.

A. Forward scatter FSC-A(rea) Vs Side scatter SSC-A(rea) plot to demonstrate the gates used to sort viable **(i)** GFP-CD63 and **(ii)** CD81-Tdtomato DU145 cells (gate P1). **B.** Scatter plots for Fluorescence Intensity A(rea) for **(i)** GFP-A or **(ii)** Tdtomato-A Vs SSC-A(rea) demonstrating the gates used to sort GFP-CD63 and CD81-Tdtomato cells (gates P4 and P3 respectively).



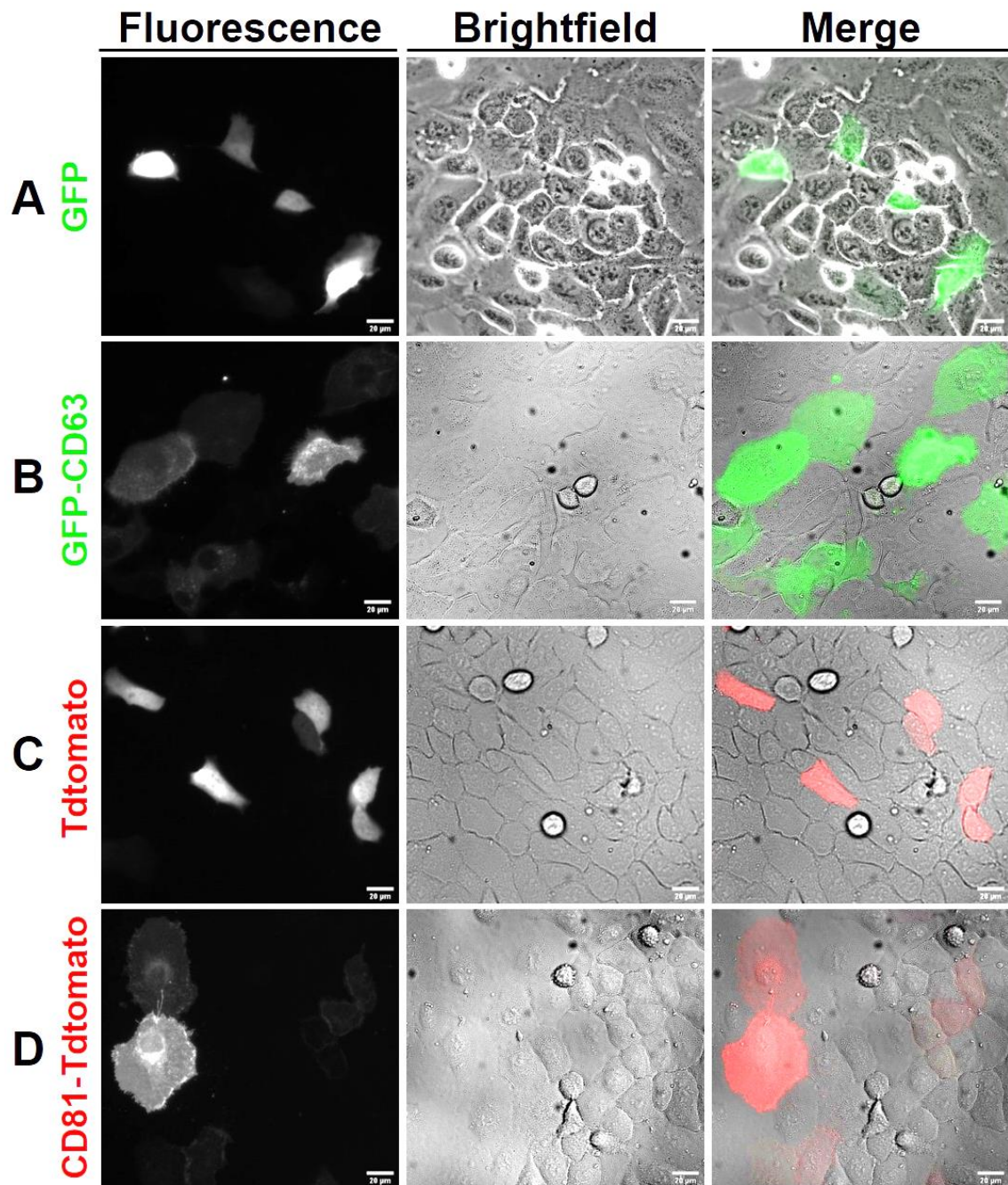
Supplementary Figure 4. Gating strategy for cell cycle analysis of GFP-CD63, CD81-Tdtomato and WT DU145 parallel control counterparts.

A. Example of a Forward scatter (FSC-H) Vs Side scatter (SSC-H) plot demonstrating the standard gate used for cell viability (“Live”) for **(i)** GFP-CD63, **(ii)** GFP-Parallel control, **(iii)** CD81-Tdtomato and **(iv)** Tom-Parallel control cells. **B.** Fluorescence Intensity vs SSC-H plots for **(i)** GFP-CD63 and **(ii)** GFP-Parallel control viable cells (GFP-H vs SSC-H), or for **(iii)** CD81-Tdtomato and **(iv)** Tom-Parallel control viable cells (Tdtomato-H vs SSC-H). Selection gates for fluorescently-positive cells were applied to GFP-CD63 and CD81-Tdtomato cells only (“GFP+” and “TOM+” regions, (i) and (iii) respectively). **C.** DRAQ5-Width(W) vs DRAQ5-Area (A) plots showing doublet discrimination of viable fluorescent cells: **(i)** GFP-CD63 and **(ii)** CD81-Tdtomato, and viable control cells: **(ii)** GFP-Parallel controls and **(iv)** Tom-Parallel controls; the “Single cells” region was selected for further analysis. **D.** DRAQ5-A histogram of **(i)** GFP-CD63, **(ii)** GFP-Parallel controls, **(iii)** CD81-Tdtomato and **(iv)** Tom-Parallel controls; histogram is depicting the cell cycle distribution with gates for G₁, S/G₂/M and Polyploid (>2n) cell cycle phases, used for data analysis.



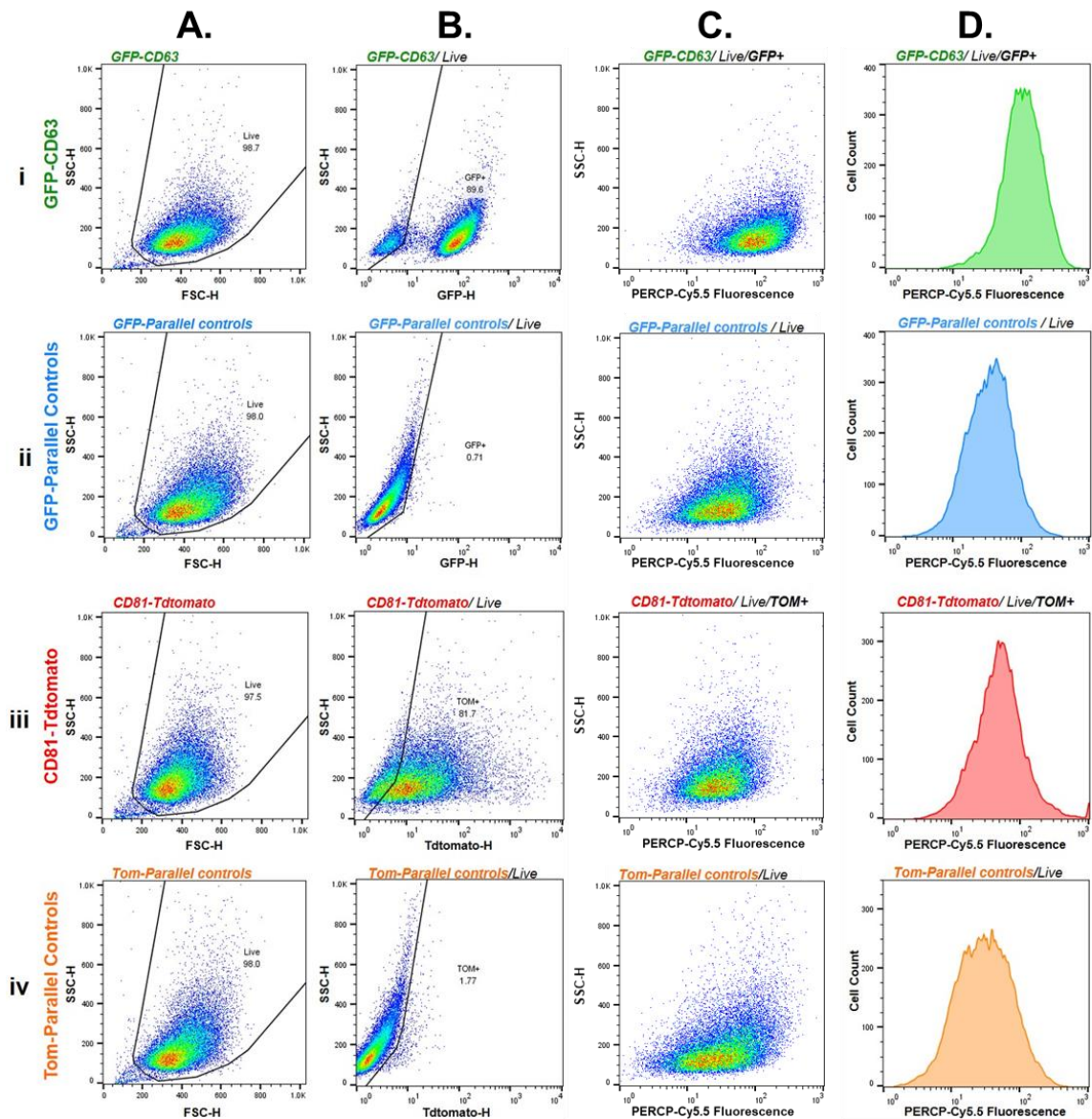
Supplementary Figure 5. Exemplary cell cycle histogram overlays of GFP-CD63, CD81-Tdtomato and WT parallel controls.

A. DRAQ5-Area (A) cell cycle histogram overlays of viable, fluorescent, single GFP-CD63 cells (green) and viable, single GFP-Parallel control cells (blue) treated with Colcemid for: **(i)** 0h (untreated), **(ii)** 8h, **(iii)** 16h, **(iv)** 24h and **(v)** 32h; each histogram overlay is depicting the percentage of cells distributed in each of G₁, S/G₂/M and Polyploid (>2n) cell cycle phase. **B.** DRAQ5-A cell cycle histogram overlays of viable, fluorescent, single CD81-Tdtomato cells (red) and viable, single Tom-Parallel control cells (orange) treated with Colcemid for: **(vi)** 0h (untreated), **(vii)** 8h, **(viii)** 16h, **(ix)** 24h and **(x)** 32h; each histogram overlay is depicting the percentage of cells distributed in each of G₁, S/G₂/M and Polyploid (>2n) cell cycle phase. Note that the exemplary histogram overlays derive from the same independent experiment (N=3) after applying the gating strategy described in [Supplementary Figure 4](#).



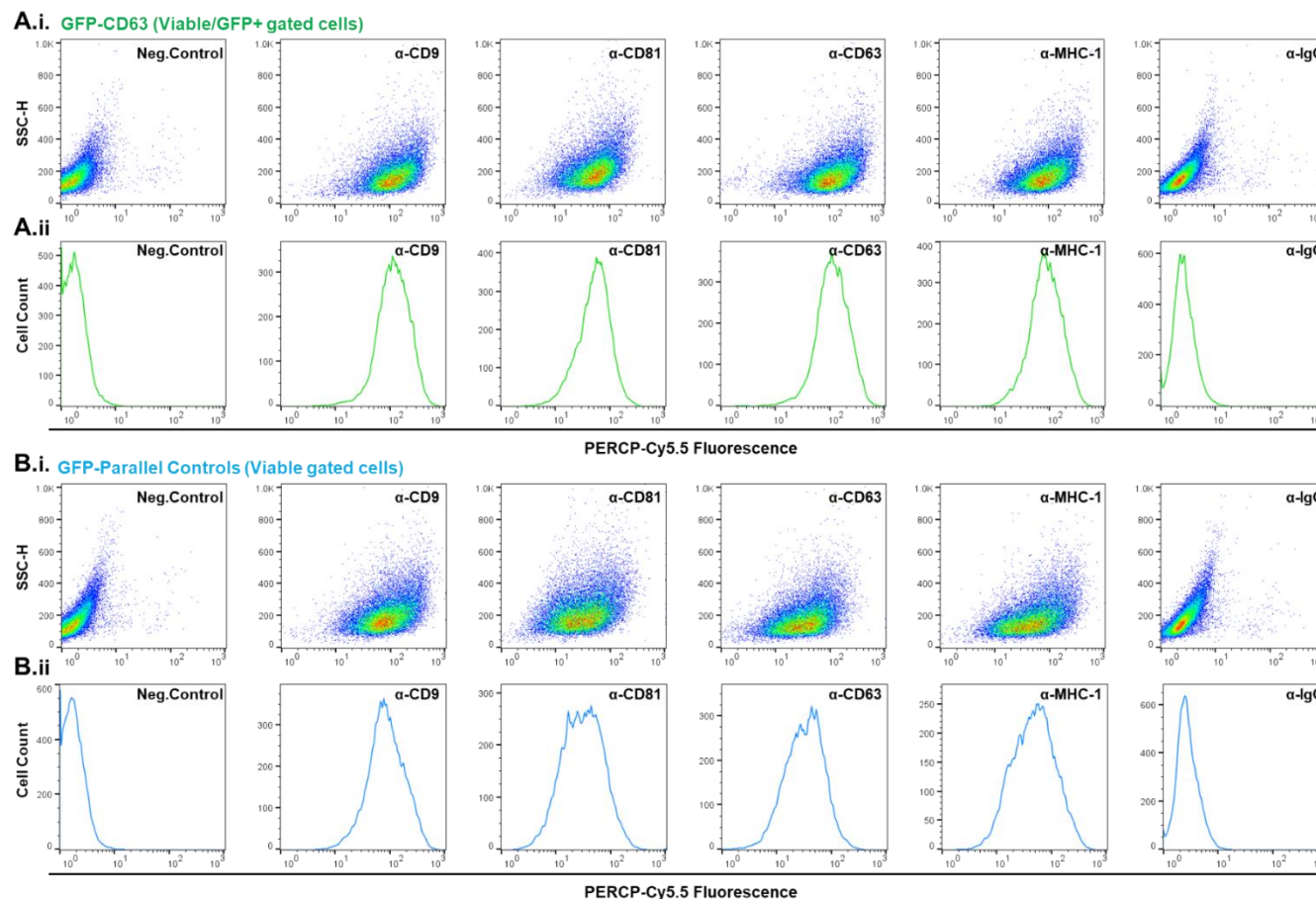
Supplementary Figure 6. Live-cell localisation of GFP, Tdtomato, GFP-CD63 and CD81-Tdtomato in DU145 cells.

Live-cell imaging of transiently transfected DU145 cells with **(A)** untagged GFP or **(C)** untagged Tdtomato, shows cells with diffused cytosolic signal. Transient transfection of **(B)** GFP-CD63 or **(D)** CD81-Tdtomato presented with punctate perinuclear localisation, but predominantly strong expression at cell membrane and protrusions. Left column depicts the fluorescence channel for all DNA constructs, middle column depicts the brightfield channel and right column consists of the merged channel images. Scale bars represent 20 μ m (20x magnification, widefield fluorescence microscope).



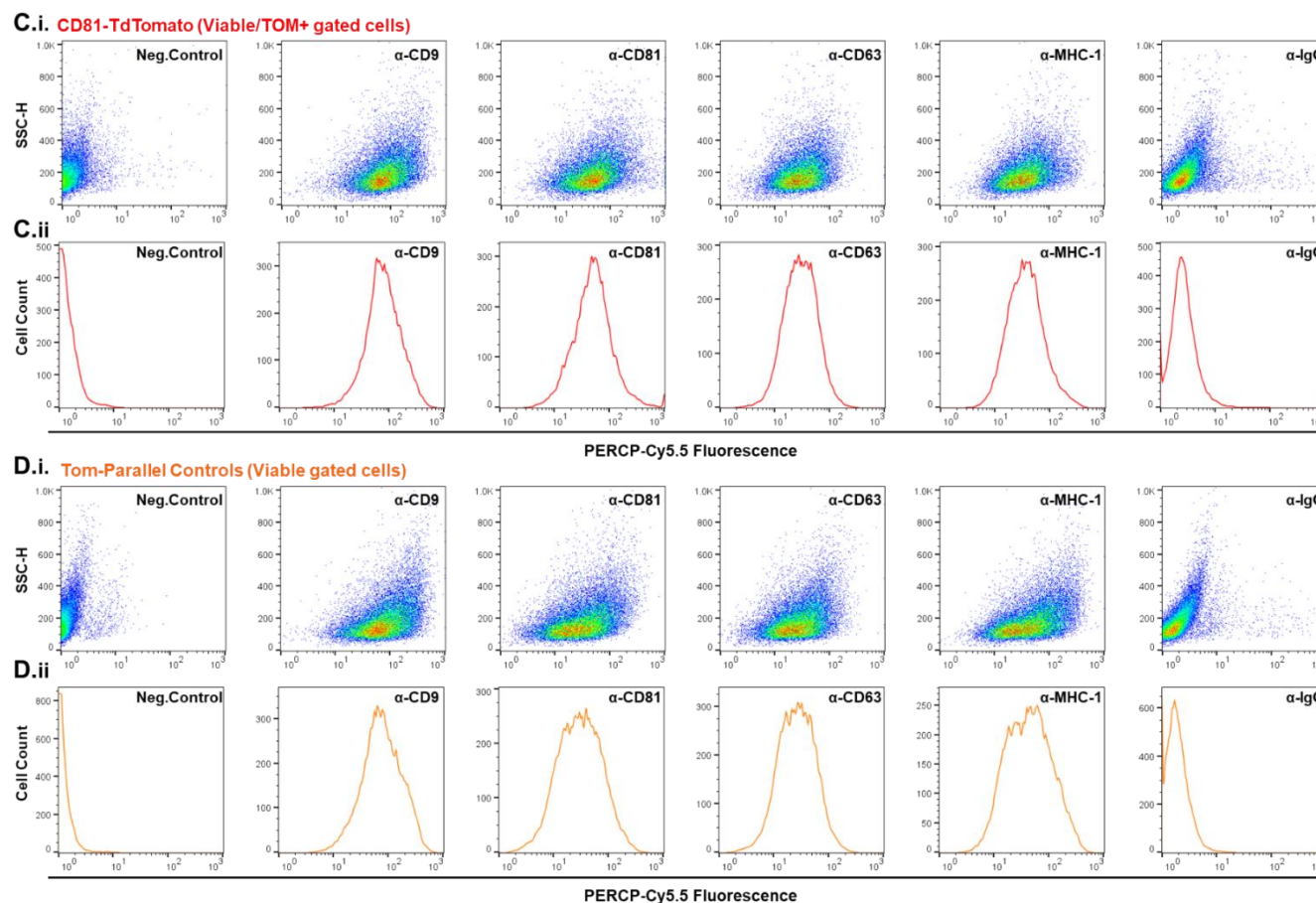
Supplementary Figure 7. Gating strategy for flow cytometry analysis of cellular membrane expression of EV-associated protein markers.

A. Forward scatter (FSC-H) Vs Side scatter (SSC-H) plot demonstrating the standard gate used for cell viability (“Live”) for **(i)** GFP-CD63, **(ii)** GFP-Parallel, **(iii)** CD81-Tdtomato and **(iv)** Tom-Parallel control cells. **B.** Fluorescence Intensity vs SSC-H plots for **(i)** GFP-CD63 and **(ii)** GFP-Parallel control viable cells (GFP-H vs SSC-H), or for **(iii)** CD81-Tdtomato and **(iv)** Tom-Parallel control viable cells (Tdtomato-H vs SSC-H). Selection gates for fluorescently positive cells were applied to **(i)** GFP-CD63 and **(iii)** CD81-Tdtomato cells only (“GFP+” and “TOM+” regions). **C.** PERCP/Cy5.5 fluorescence intensity vs SSC-H plots for viable **(i)** GFP-CD63 (“GFP+” only), **(ii)** GFP-Parallel, **(iii)** CD81-Tdtomato (“TOM+” only) and **(iv)** Tom-Parallel control cells. **D.** PERCP/Cy5.5 fluorescence intensity histograms of **(i)** GFP-CD63 and **(ii)** GFP-Parallel controls labelled with anti-CD63-PERCP/Cy5.5 antibody, and **(iii)** CD81-Tdtomato and **(iv)** Tom-Parallel controls labelled with anti-CD81-PERCP/Cy5.5 antibody. Examples of other antibodies are shown in [Supplementary Figure 8](#) and geometric means of fluorescence intensity histograms were used for further analysis.



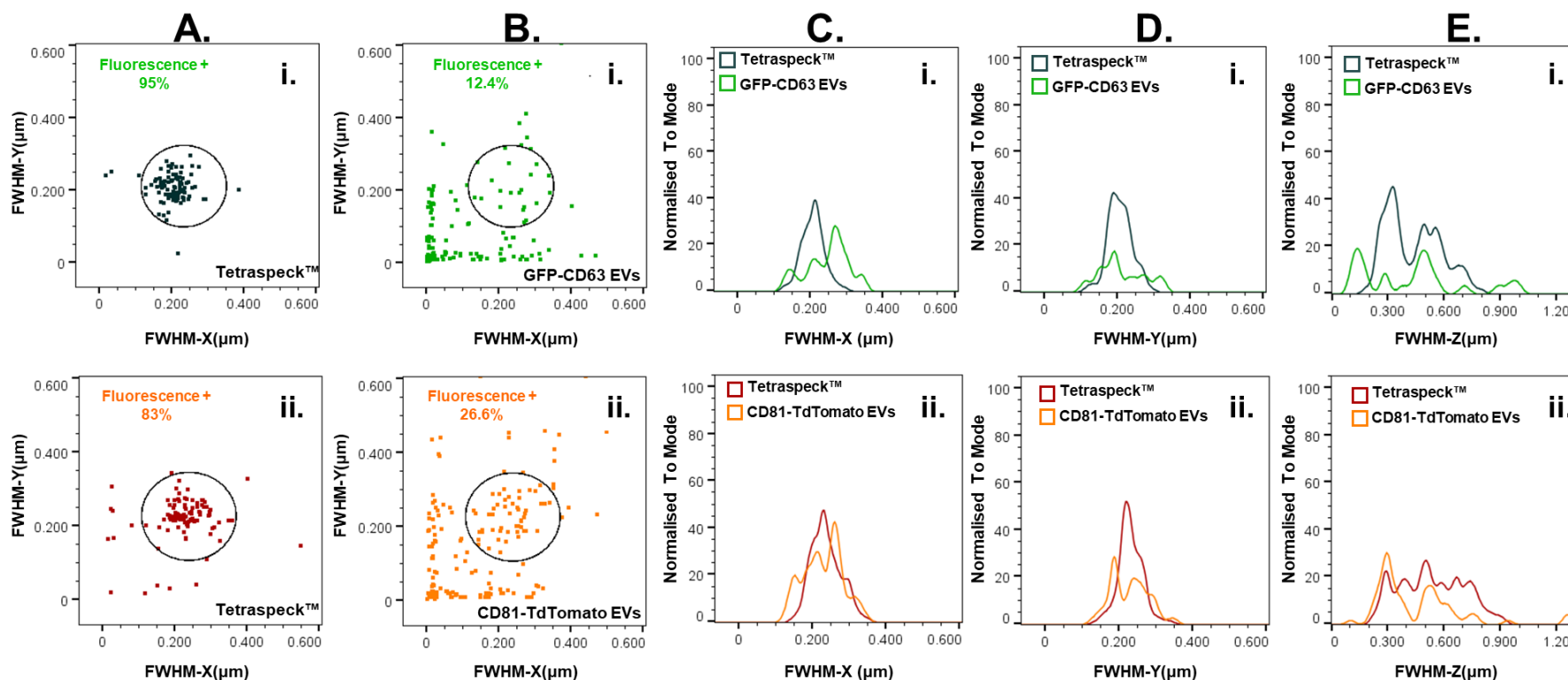
Supplementary Figure 8. Examples of fluorescence scatter plots and histograms for flow cytometry analysis of EV-associated markers in cells.

Examples of (A) GFP-CD63, (B) GFP-Parallel, (C) CD81-Tdtomato and (D) Tom-Parallel cells stained with antibodies against CD9, CD81, CD63, MHC-1 and IgG, as well as unstained controls. Plots show (i) PERCP/Cy5.5 fluorescence intensity vs SSC-H plots for each cell type and condition, as well as (ii) PERCP/Cy5.5 fluorescence intensity histogram for each cell type and condition. **Figure and Legend continue to next page ►**



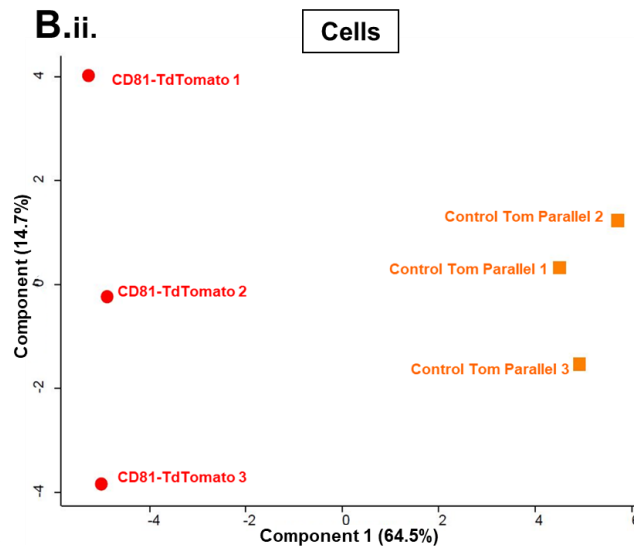
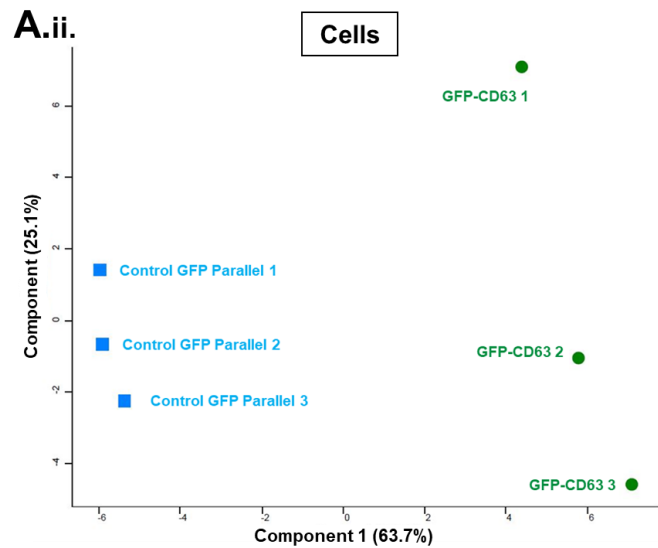
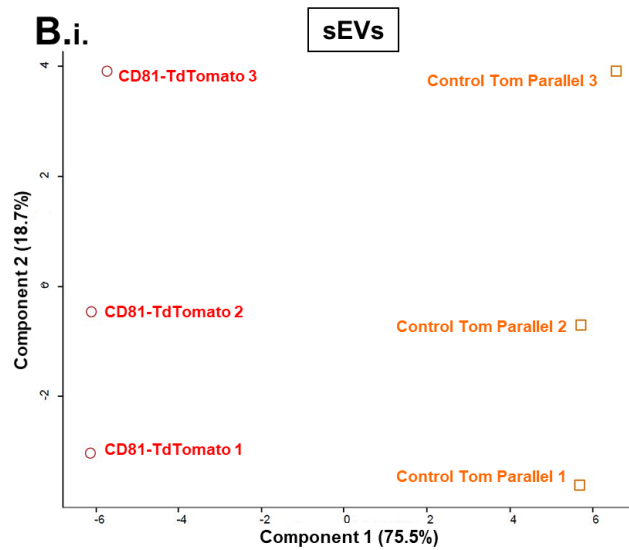
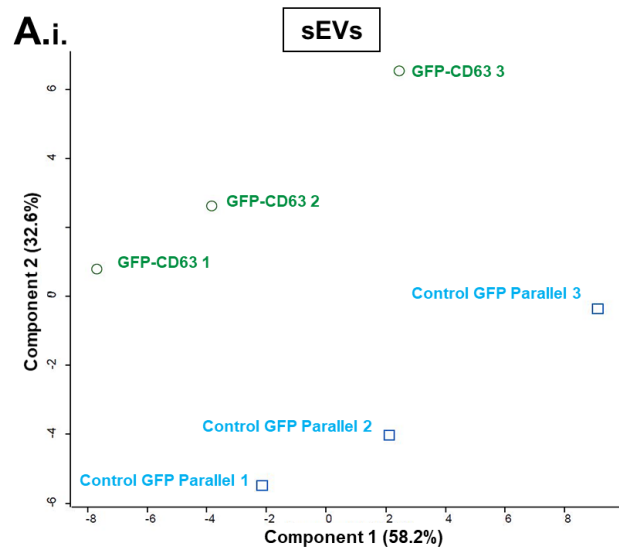
Supplementary Figure 8. Examples of fluorescence scatter plots and histograms for flow cytometry analysis of EV-associated markers in cells.

Figure and Legend continued from previous page ► Note that examples here involve gated cells: Viable and GFP+ or TOM+ for GFP-CD63 and CD81-TdTomato cells, Viable for WT parallel controls. Geometric means of PERCP/Cy5.5 fluorescence intensity for each cell type and condition were then imported into GraphPad Prism for further analysis.



Supplementary Figure 9. FWHM distribution analysis from PSF calculations of GFP-CD63 and CD81-Tdtomato EVs.

Manual selection of particles generated PSFs using the MetroloJ plugin (Fiji Software (v1.52c)) followed by estimation of the lateral and axial FWHM in the green and orange fluorescence channels. These were next imported into FlowJo for gating and FWHM distribution analysis. **A.** Scatter plot of FWHM (X vs Y axis) for gating of particles around 100nm (comparable to EVs), based on Theoretical resolution where FWHM-X is equal to FWHM-Y (black circled gate); this was done using: **(i)** Tetraspект™ (488nm- green fluorescence) and **(ii)** Tetraspект™ (543nm- orange fluorescence) microspheres (100nm diameter). **B.** Scatter plot of FWHM (X vs Y axis) for **(i)** GFP-CD63 EVs (12.4% optically characterised) and **(ii)** CD81-Tdtomato EVs (26.6% optically characterised). **C-E.** Histogram overlays of Tetraspект™ microspheres and EVs FWHM for the: **(C)** X-axis, **(D)** Y-axis and **(E)** Z-axis, showing that Tetraspект™ have more monodispersed distributions of FWH, whereas EVs are more heterogeneous. *Note that number of particles selected for PSF analysis were: Tetraspект™ (n=100), GFP-CD63 EVs (n=176) and CD81-Tdtomato EVs (n=199).*

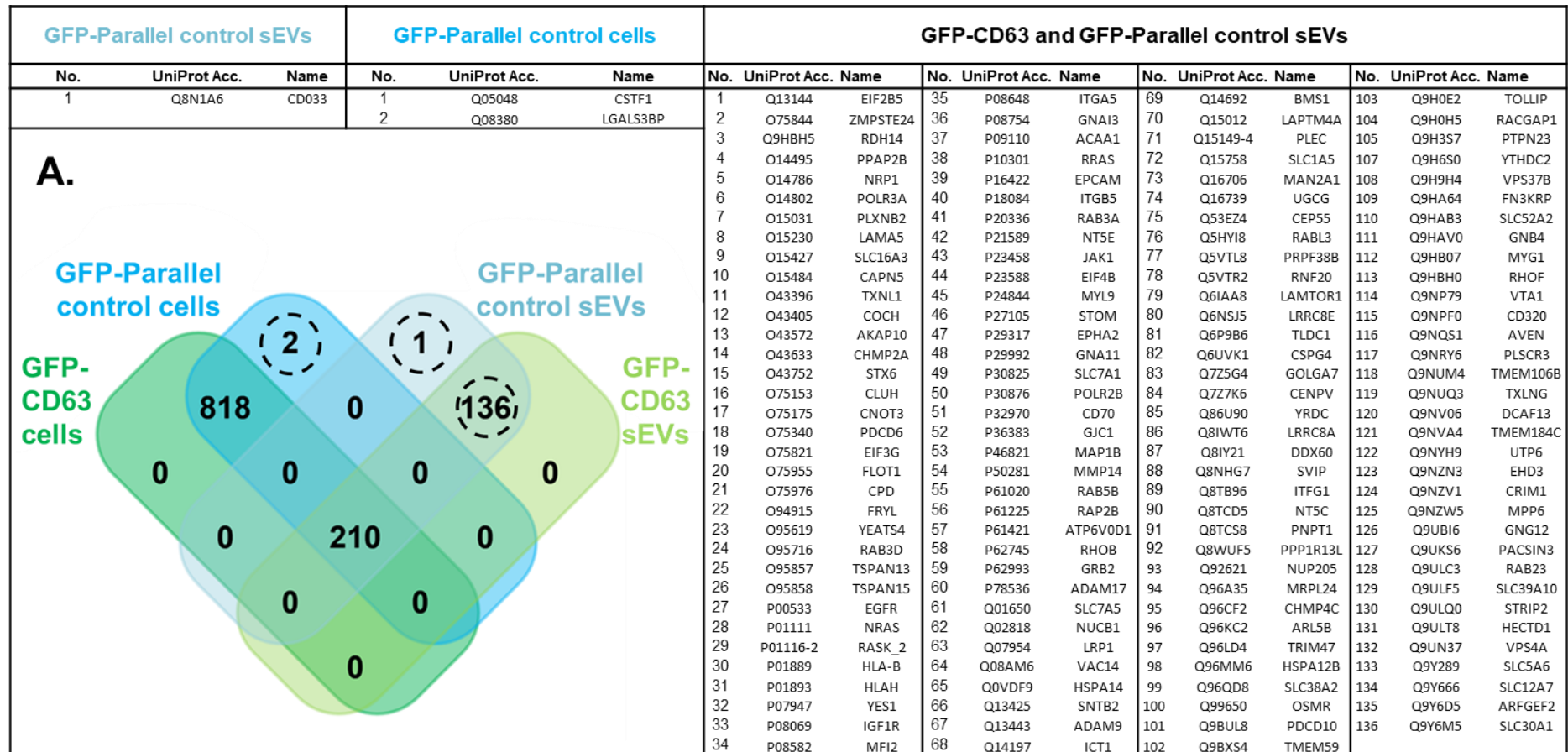


Supplementary Figure 10. Principal Component analysis of cell and sEV samples.

A. Principal component analysis (PCA) of SWATH-MS data from technical replicates of GFP-CD63 versus GFP-Parallel control DU145 sEVs **(i)** and cells **(ii)**.

B. PCA of SWATH-MS data from technical replicates CD81-Tdtomato versus Tom-Parallel control DU145 sEVs **(i)** and cells **(ii)**. The technical replicates are indicated with “1,2,3” at end of sample name. PCA was done in the Perseus Software (MaxQuant) and included all the identified proteins from the SWATH-MS runs (only proteins with a chromatogram peak area variability of less than 50% between two technical replicates, CV<50%).

Symbols: GFP-CD63 (green circles), GFP-Parallel control (blue squares) CD81-Tdtomato (red circles) and Tom-Parallel control (orange square).



Supplementary Figure 11. Venn Diagram unique protein IDs for cells and sEVs.

A. Tables of unique proteins IDs (circled) from Venn Diagram of GFP-CD63 and GFP-Parallel cells and sEVs for: GFP-Parallel control sEVs, GFP-Parallel control cells, and GFP-CD63 and GFP-Parallel control sEVs only, including number, UniProt Accession Number, and Gene name.

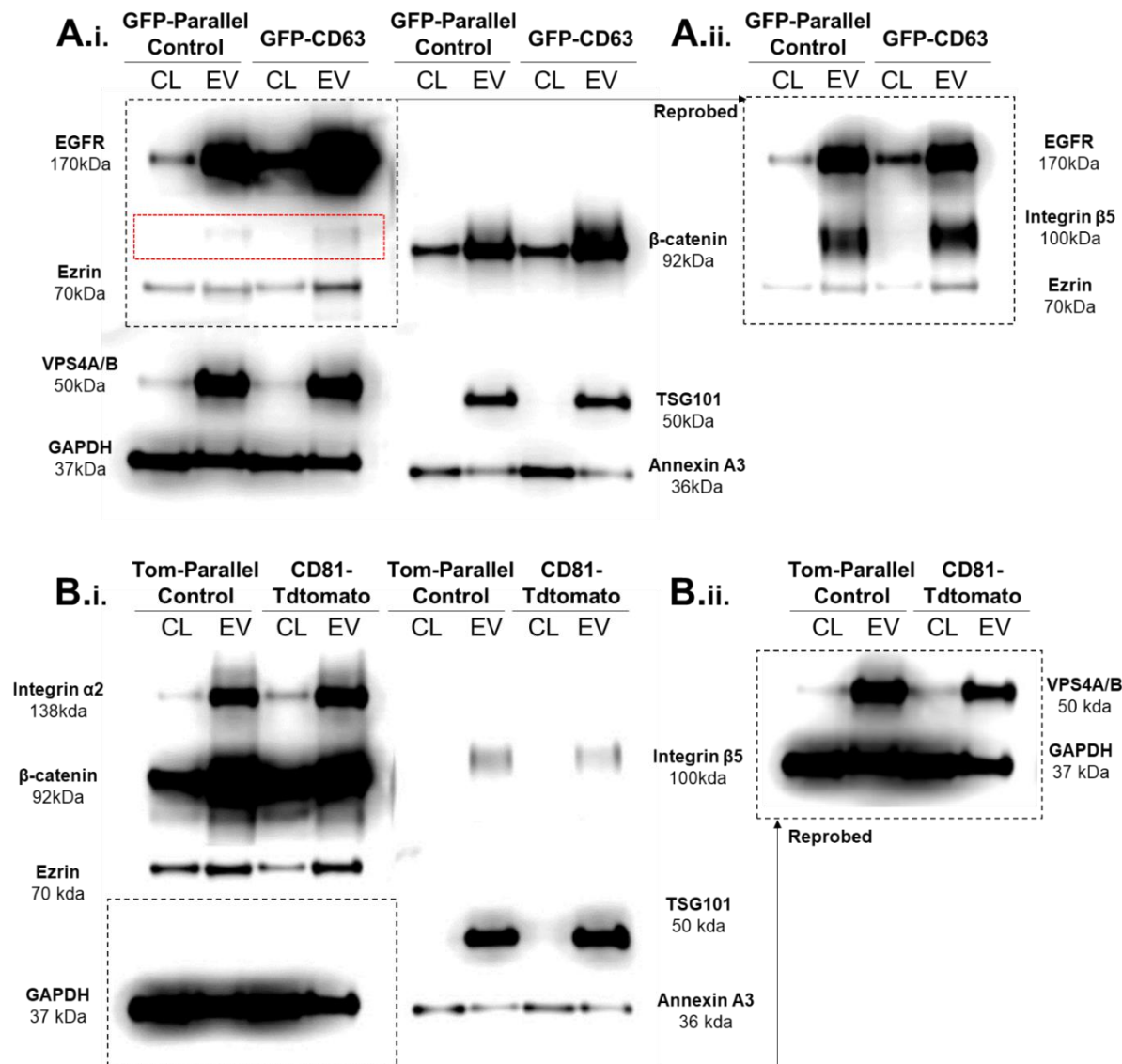
Figure and Figure Legend continues to next page▶

CD81-Tdtomato sEVs			CD81-Tdtomato cells		Tom-Parallel control cells		CD81-Tdtomato and Tom-Parallel control sEVs unique IDs										
No.	UniProt Acc.	Name	No.	UniProt Acc.	Name	No.	UniProt Acc.	Name	No.	UniProt Acc.	Name	No.	UniProt Acc.	Name			
1	P0CG12	CHTF8	1	Q9BQ67	GRWD1	1	Q10570	CPSF1	1	O14802	POLR3A	32	P23458	JAK1			
			2	Q02818	NUCB1				2	Q8TCS8	PNPT1	33	P24844	MYL9			
			3	Q5T160	RARS2				3	A5D8V6	VPS37C	34	P24928	POLR2A			
			4	Q14914	PTGR1				4	O14495	PPAP2B	35	P29317	EPHA2			
<p>B.</p>									5	O14786	NRP1	36	P29992	GNA11	67	Q92621	NUP205
									6	O15031	PLXNB2	37	P30825	SLC7A1	68	Q92930	RAB8B
									7	O15230	LAMA5	38	P30876	POLR2B	69	Q96CT7	CCDC124
									8	O43181	NDUFS4	39	P32970	CD70	70	Q96LD4	TRIM47
									9	O43396	TXNL1	40	P35908	KRT2	71	Q96QD8	SLC38A2
									10	O43405	COCH	41	P36383	GJC1	72	Q99650	OSMR
									11	O43572	AKAP10	42	P41208	CETN2	73	Q9BXS4	TMEM59
									12	O43633	CHMP2A	43	P50281	MMP14	74	Q9H0E2	TOLLIP
									13	O75844	ZMPSTE24	44	P60900	PSMA6	75	Q9H0H5	RACGAP1
									14	O75955	FLOT1	45	P61421	ATP6V0D1	76	Q9H3S7	PTPN23
									15	O75976	CPD	46	P78536	ADAM17	77	Q9H4G4	GLIPR2
									16	O95716	RAB3D	47	P98160	HSPG2	78	Q9H6S0	YTHDC2
									17	O95858	TSPAN15	48	Q07954	LRP1	79	Q9HB07	MYG1
									18	P00533	EGFR	49	Q0VDF9	HSPA14	80	Q9HBH5	RDH14
									19	P01889	HLA-B	50	Q12913	PTPRJ	81	Q9NQS1	AVEN
									20	P02768	ALB	51	Q13443	ADAM9	82	Q9NRY6	PLSCR3
									21	P07942	LAMB1	52	Q15012	LAPTM4A	83	Q9NUQ3	TXLNG
									22	P07947	YES1	53	Q15149-4	SMC1A	84	Q9NZN3	EHD3
									23	P08648	ITGA5	54	Q15758	SLC1A5	85	Q9NZV1	CRIM1
									24	P08754	GNAI3	55	Q16706	MAN2A1	86	Q9P2B2	PTGFRN
									25	P09110	ACAA1	56	Q16739	UGCG	87	Q9ULT8	HECTD1
									26	P10301	RRAS	57	Q53EZ4	CEP55	88	Q9UN37	VPS4A
									27	P11047	LAMC1	58	Q5HYI8	RABL3	89	Q9Y289	SLC5A6
									28	P16422	EPCAM	59	Q5VTL8	PRPF38B	90	Q9Y2I7	PIKFYVE
									29	P18084	ITGB5	60	Q6IAA8	LAMTOR1	91	Q9Y6M5	SLC30A1
									30	P20336	RAB3A	61	Q6UVK1	CSPG4			
									31	P21589	NT5E	62	Q7Z5G4	GOLGA7			

Supplementary Figure 11. Venn Diagram unique protein IDs for cells and sEVs.

► *Figure and Figure Legend continued from previous page*

B. Tables of unique proteins IDs (circled) from Venn Diagram of CD81-Tdtomato and Tom-Parallel cells and sEVs detected in: CD81-Tdtomato sEVs, CD81-Tdtomato cells, Tom-Parallel control cells and CD81-Tdtomato and Tom-Parallel control sEVs only, including number, UniProt Accession Number, and Gene name.

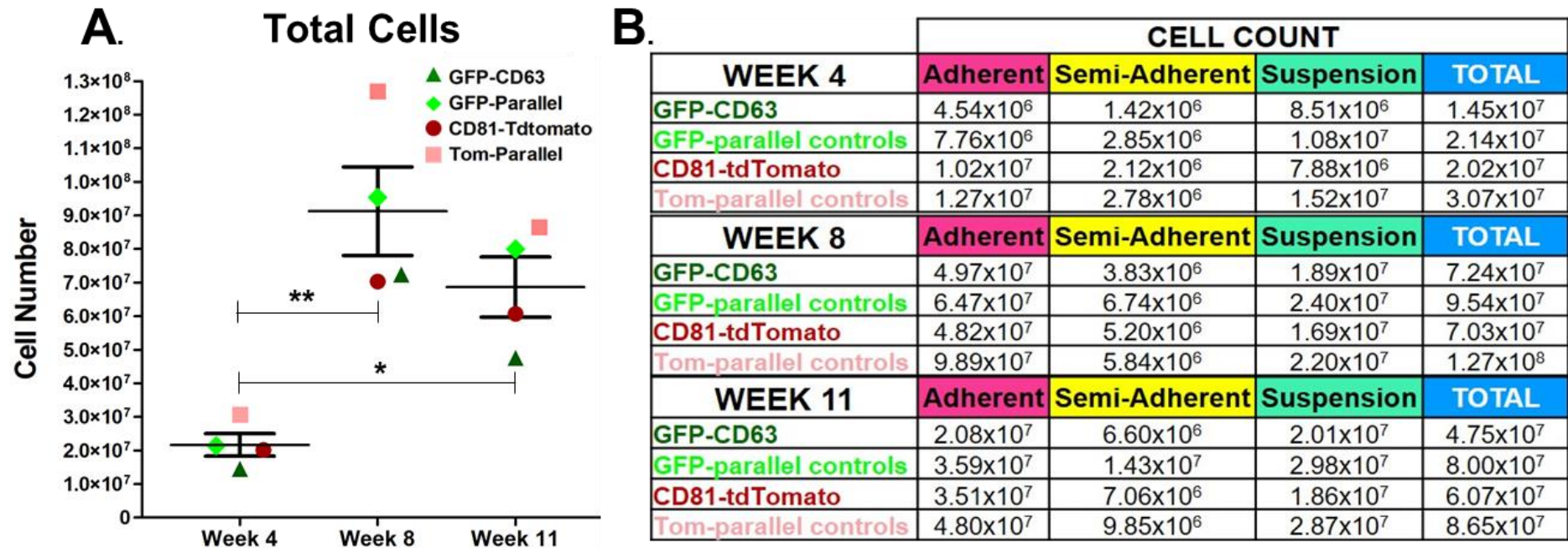


Supplementary Figure 12. Western Blot analysis developed raw membranes.

A.(i) Western Blot membrane after probing with antibodies for GFP-CD63 and GFP-Parallel control cell and sEV lysates. This membrane was separated into segments for probing for EGFR, ezrin, VPS4, GAPDH, β-catenin, TSG101 and annexin A3. **(ii)** The top left segment of the membrane was re-probed separately for Integrin β₅. Note that the red outlined box demonstrates a potential EGFR truncation that might interfere with Integrin β₅ probing, potentially explaining its upregulation, when it was expected to be downregulated.

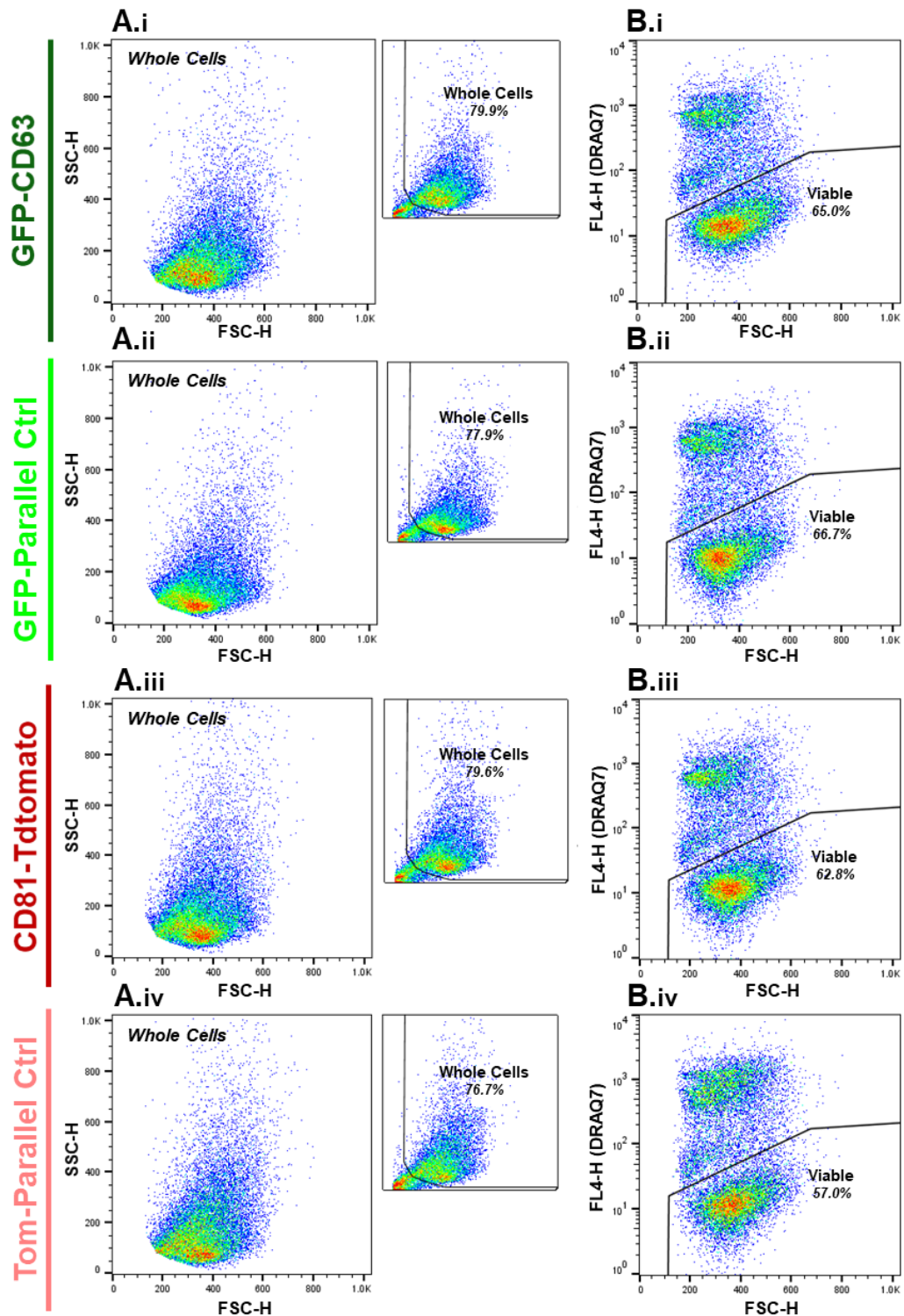
B.(i) Western Blot membrane after probing with antibodies for CD81-Tdtomato and Tom-Parallel control cell and sEV lysates. This membrane was separated into segments for probing of integrin α₂, β-catenin, ezrin, GAPDH, integrin β₅, TSG101 and annexin A3. **(ii)** The bottom left segment of the membrane was re-probed separately for VPS4.

Note that exposure of membranes shown in this figure might be different from Figure 4.11, as this was the final state of membranes after probing and re-probing with all antibodies; selected exposure was used to demonstrate all the detected proteins. CL: cell lysate, EV: sEV lysate.



Supplementary Figure 13. Cell numbers recovered from Bioreactor Flasks.

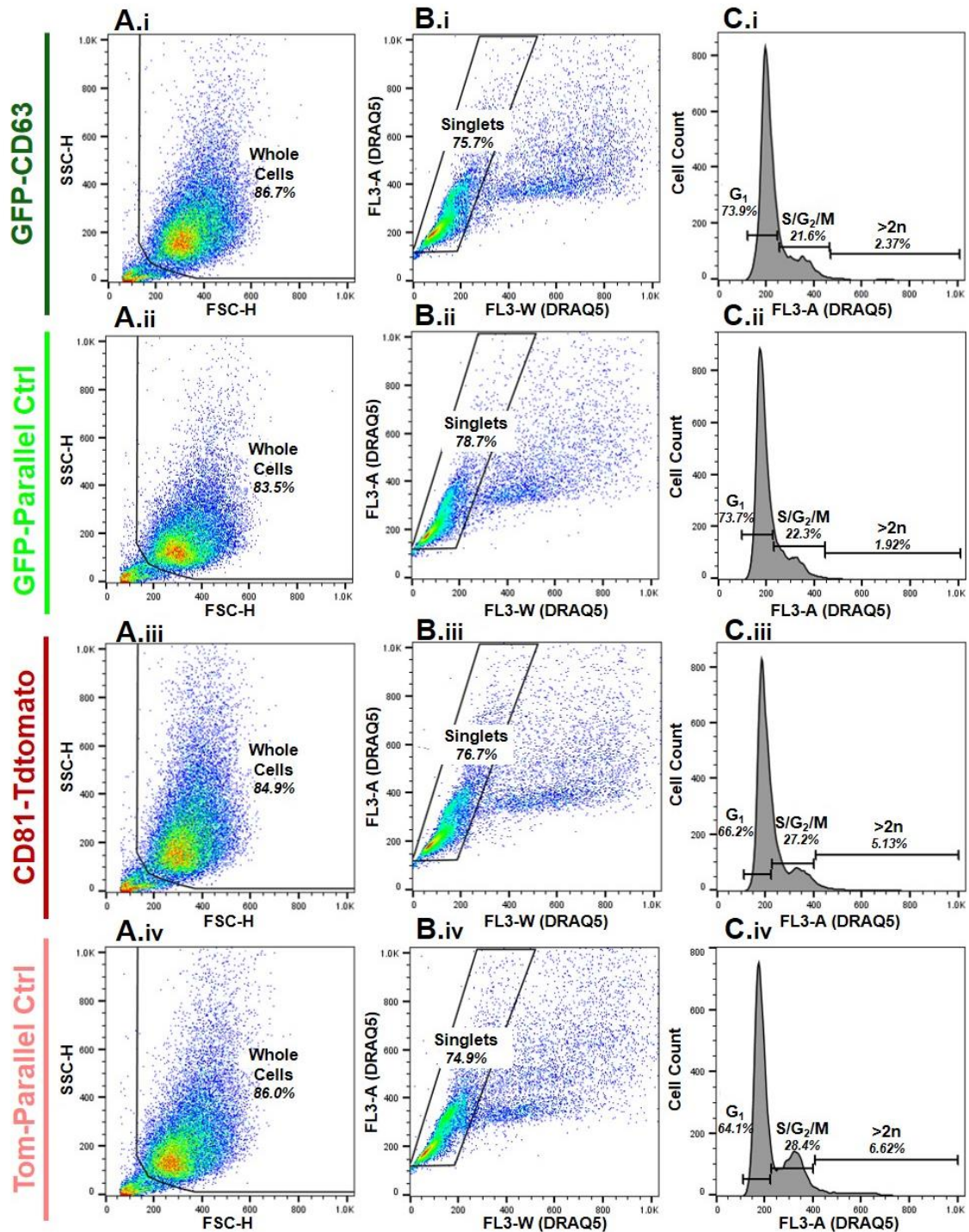
A. Total cell numbers recovered from Bioreactor Flasks (combining all 3 fractions) for GFP-CD63, CD81-Tdtomato and respective WT parallel controls, over the entire Characterisation Procedure (Weeks 4-11). **B.** Table showing raw cell numbers for every fraction separately (Adherent, Semi-Adherent and Suspension) as well as the total, for all 4 cell lines at each timepoint (Week 4,8 and 11).



*Semi-Adherent Fraction Cells (Week 11)

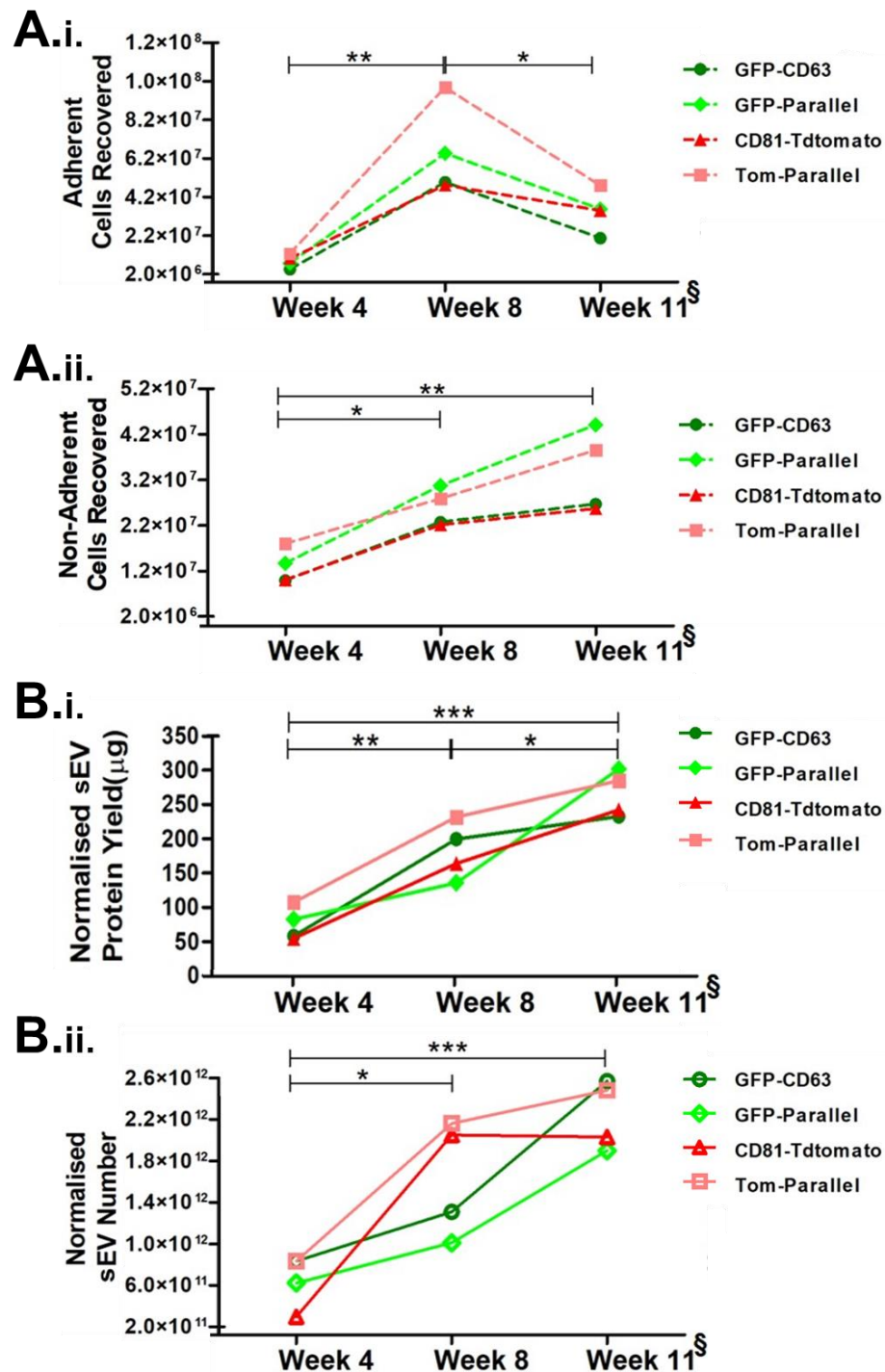
Supplementary Figure 14. Gating strategy for cell viability analysis.

A. Example of a Forward scatter (FSC-H) Vs Side scatter (SSC-H) plot demonstrating the standard gate used for selection of “Whole cells” for: (i) GFP-CD63, (ii) GFP-Parallel control, (iii) CD81-Tdtomato and (iv) Tom-Parallel control cells. Note that the smaller plots on the right depict the gate for “Whole cells” on the ungated cell populations. **B.** Example of a Forward scatter (FSC-H) Vs DRAQ7 fluorescence (FL4-H) plot of “Whole cells” depicting gates for “Viable” cells (low DRAQ7 fluorescence intensity) for: (i) GFP-CD63, (ii) GFP-Parallel control, (iii) CD81-Tdtomato and (iv) Tom-Parallel control cells. Note that the Semi-Adherent cells (at Week 11) have been used to demonstrate the viability gating strategy.



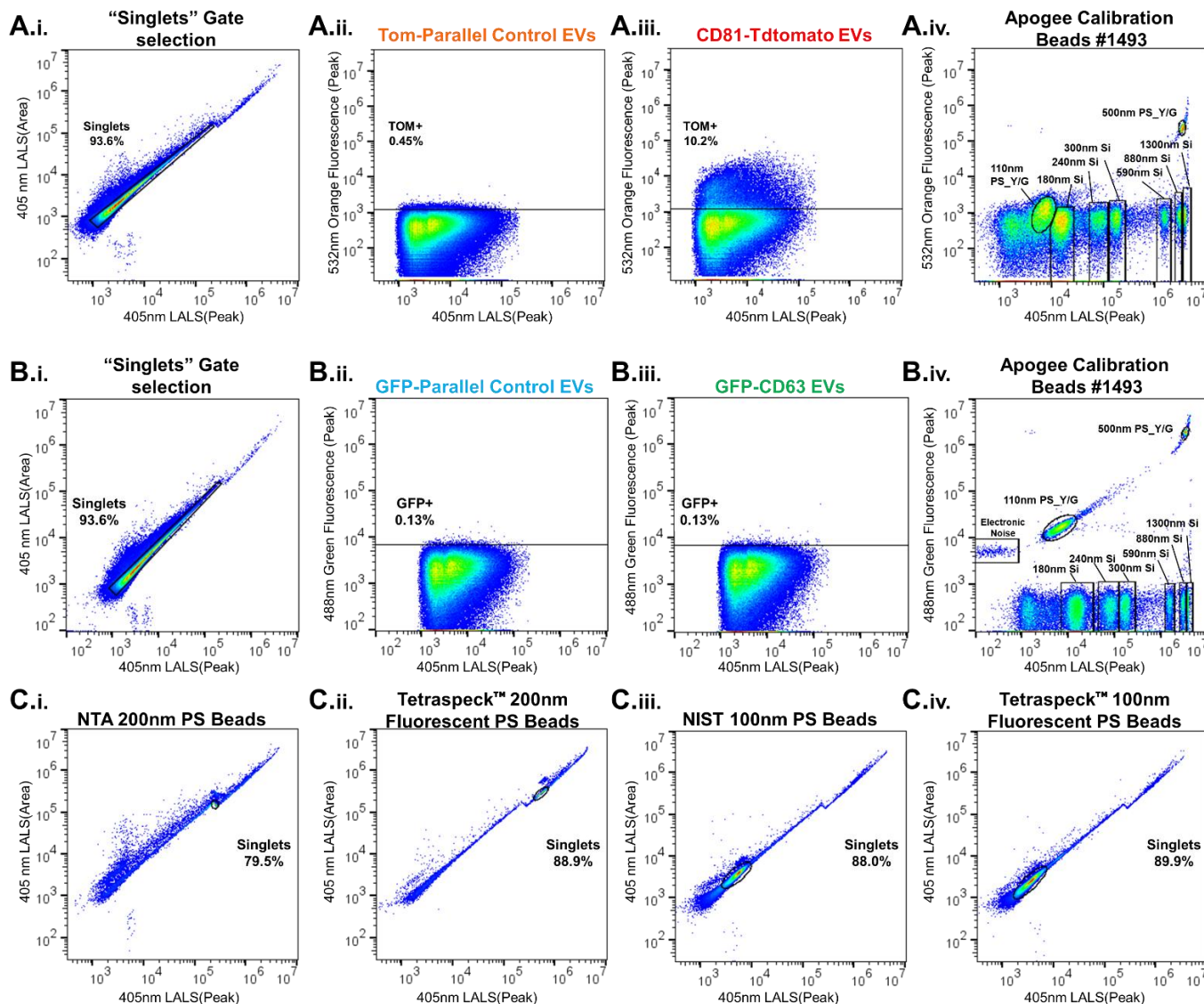
Supplementary Figure 15. Gating strategy for cell cycle analysis.

A. Example of a Forward scatter (FSC-H) Vs Side scatter (SSC-H) plot demonstrating the standard gate used for selection of “Whole cells” for (i) GFP-CD63, (ii) GFP-Parallel control, (iii) CD81-Tdtomato and (iv) Tom-Parallel control cells. **B.** DRAQ5-Width (FL3-W) vs DRAQ5-Area (FL3-A) plots showing doublet discrimination of “Whole cells” for (i) GFP-CD63, (ii) GFP-Parallel control, (iii) CD81-Tdtomato and (iv) Tom-Parallel control cells; the “Singlets” region was selected for further analysis. **C.** DRAQ5-Area (FL3-A) histogram of GFP-CD63 (i), GFP-Parallel controls (ii), CD81-Tdtomato (iii), and Tom-Parallel controls (iv); histogram is depicting the cell cycle distribution with gates for G₁, S/G₂/M and Polyploid (>2n) cell cycle phases, which were used to extrapolate percentage of cells for data analysis. Note that the Adherent cells (at Week 11) have been used to demonstrate the cell cycle gating strategy.



Supplementary Figure 16. Comparison of Bioreactor-derived cell numbers with sEV numbers and protein yield.

A. Number of cells isolated from the CELLine Bioreactors at each time-point (Weeks 4,8 and 11) for: **(i)** Adherent cells and **(ii)** Non-Adherent cells (Semi-Adherent and Suspension cells). **B.** sEVs isolated from the Bioreactor Flasks were normalised per week to account for the different interval between isolations, i.e., 4-week interval for Batches 1 and 2 (Weeks 4 and 8), and 3-week interval for Batch 3 (Week11§): **(i)** sEV protein yield and (BCA assay) and **(ii)** sEV particle number (NTA). Dashed lines represent cell numbers and continuous lines represent corresponding sEVs, with the following colours: GFP-CD63 (dark green), GFP-Parallel (light green), CD81-Tdtomato (red), Tom-Parallel (pink). Statistical analysis was done using one-way ANOVA and Tukey's multiple comparisons, considering samples of same time-point as a group. Significant differences are denoted with * $p < 0.05$ and *** $p < 0.01$.



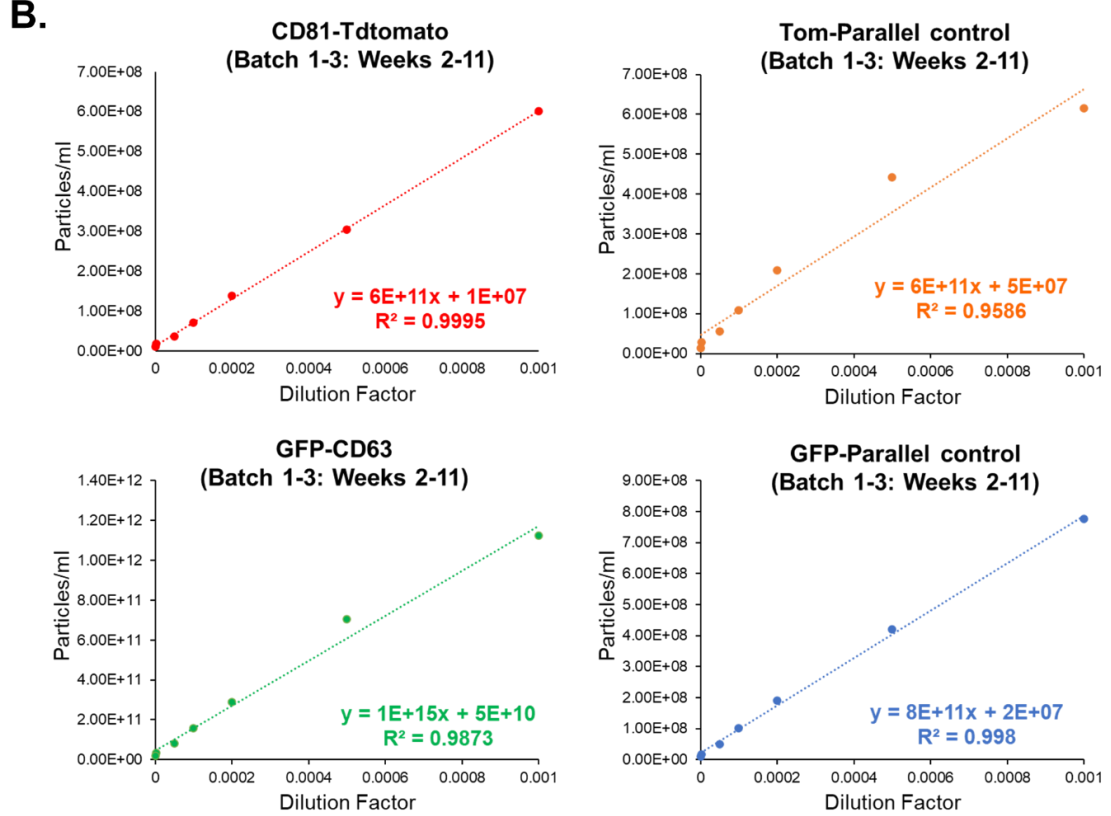
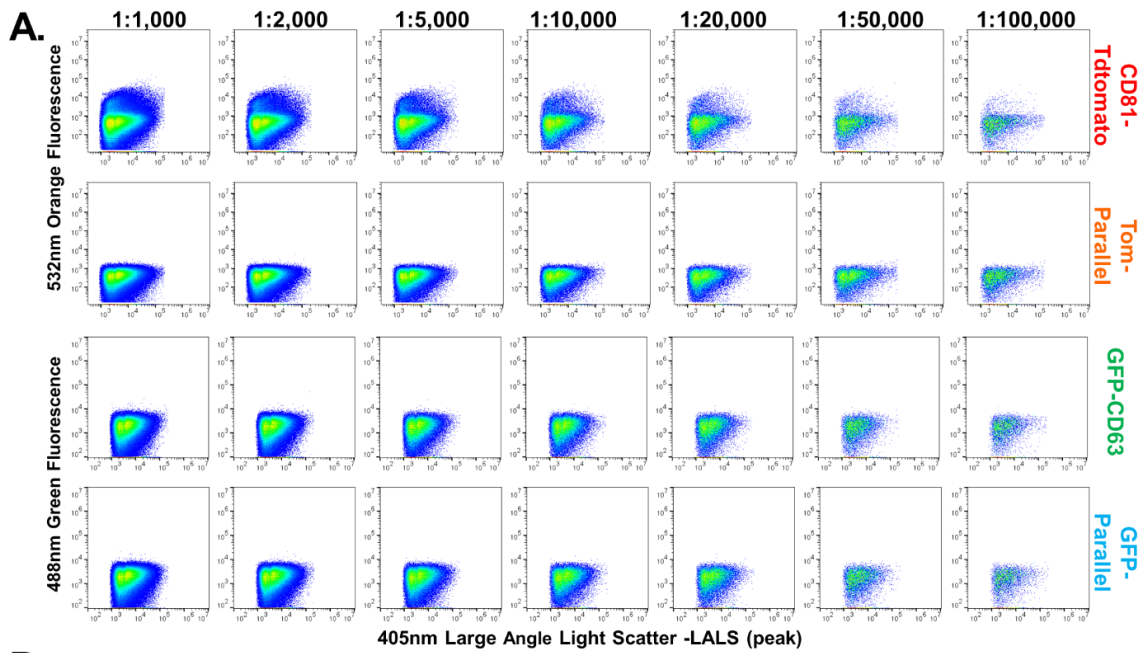
Supplementary Figure 17.
Nanoscale flow cytometry gating strategy for beads and sEVs.

Gating and Calibration for Large-angle light scatter (LALS,405nm) and (A) Orange fluorescence (Excitation: 532nm) or (B) Green Fluorescence (Excitation:488nm).

A(i) Scatter plot (peak vs area) showing “Singlets” gate, denoting removal of particle aggregates. **A(ii-iii)** LALS vs Orange Fluorescence scatter plots of “Singlet” population showing Tdtomato fluorescence (TOM+) gate. **A(iv)** LALS vs Orange Fluorescence scatter plot showing calibration of the Apogee cytometer with manufacturer beads (#1493).

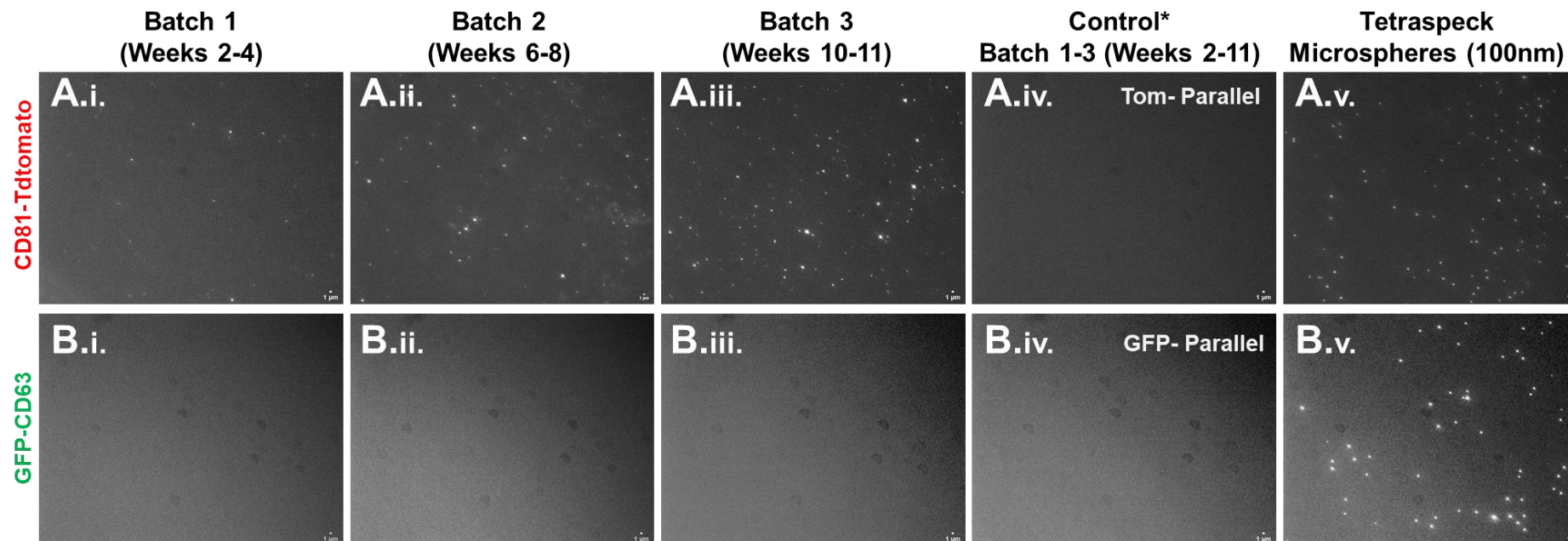
B(i) Scatter plot (peak vs area) showing “Singlets” gate, denoting removal of particle aggregates. **B(ii-iii)** LALS vs Green Fluorescence scatter plots of “Singlet” population showing GFP+ fluorescence gate on (ii)GFP-parallel control and (iii) GFP-CD63 sEVs. **B(iv)** LALS vs Green Fluorescence scatter plot showing calibration of the Apogee cytometer with manufacturer beads (#1493).

C. Gating to remove aggregates (“Singlets” gates) for (i) NTA 200nm, (ii) Tetraspeck 200nm, (iii) NIST 100nm and (iv) Tetraspeck 100nm polystyrene beads.



Supplementary Figure 18. Test for coincidence in Nanoscale flow cytometry.

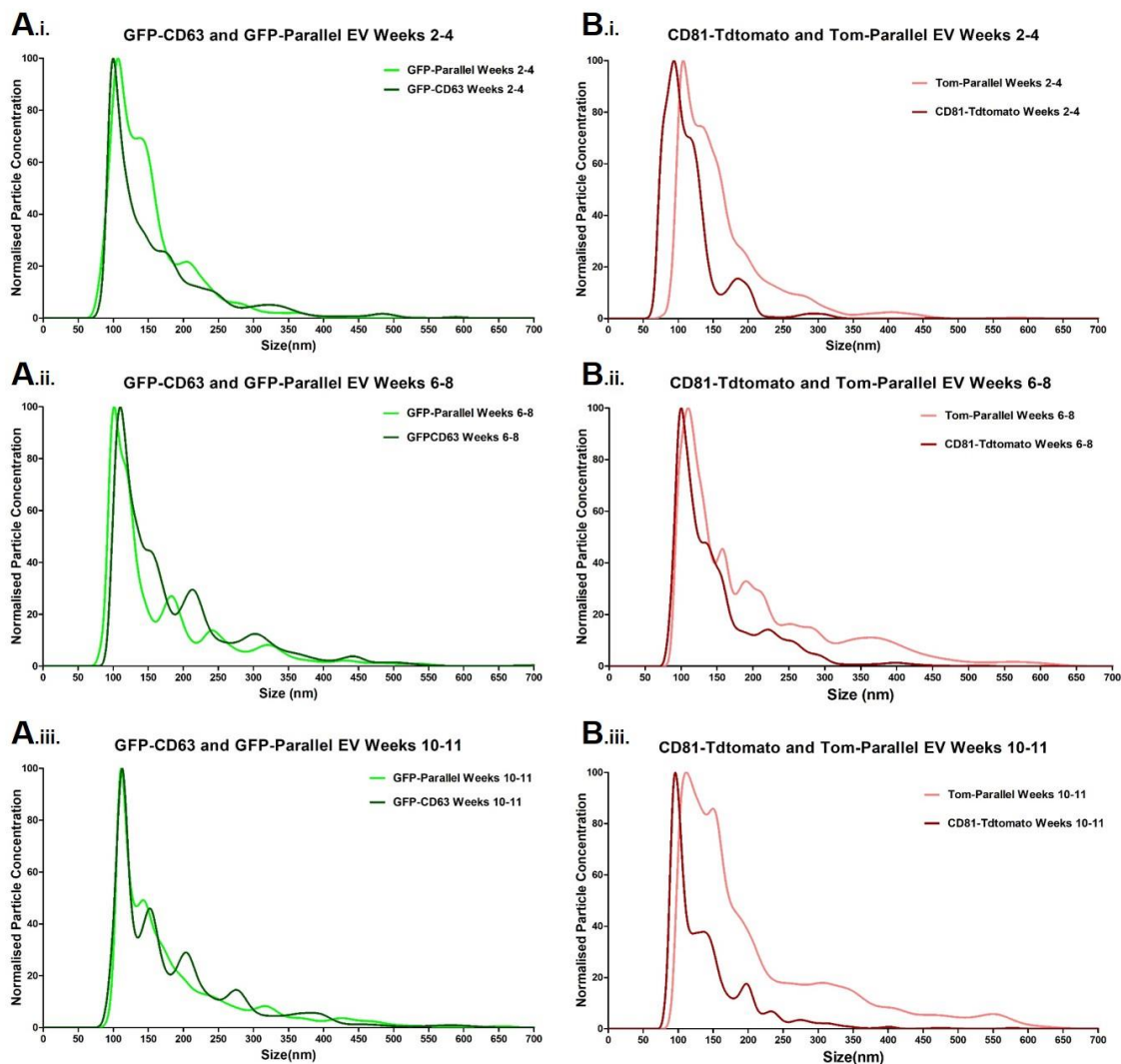
Serial Dilutions of sEVs were made to test for coincidence of detection and potential swarm effects. **A.** Scatter plots of Large-Angle Light Scatter (LALS) vs Fluorescence (Excitation:532nm/Emission: Orange or Excitation:488nm/ Emission: Green) (respectively), showing serial dilution effects on distribution of sEV populations (“Singlets” gate was applied). **B.** Graph of estimated sEV concentration (particle/ml) vs Dilution factor showing proportional drop of all events with increase of dilution factor ($R^2 > 0.95$), and no swarm effects, as determined by linear regression. Note: CD81-Tdtomato (red), Tom-Parallel control (orange), GFP-CD63 (green) and GFP-Parallel control (blue) sEVs from all 3 batches were pooled together to represent the entire sEV population for this analysis (ratio 1:1:1 for each batch) i.e., Batch 1-3: Weeks 2-11.



Supplementary Figure 19. Detection of fluorescence signal of CD81-Tdtomato and GFP-CD63 sEVs by fluorescence microscopy.

A. Detection of red-channel fluorescence signal for: **(i)** Weeks 2-4, **(ii)** Weeks 6-8 and **(iii)** Weeks 10-11 CD81-Tdtomato sEVs, **(iv)** Weeks 2-11 Tom-Parallel control sEVs and **(v)** Tetraspeck 100nm PS microspheres. **B.** Detection of green-channel fluorescence signal for: **(i)** Weeks 2-4, **(ii)** Weeks 6-8 and **(iii)** Weeks 10-11 GFP-CD63 sEVs, **(iv)** Weeks 2-11 GFP-Parallel control sEVs and **(v)** Tetraspeck 100nm PS microspheres. *Scale bars denote 1 μm.*

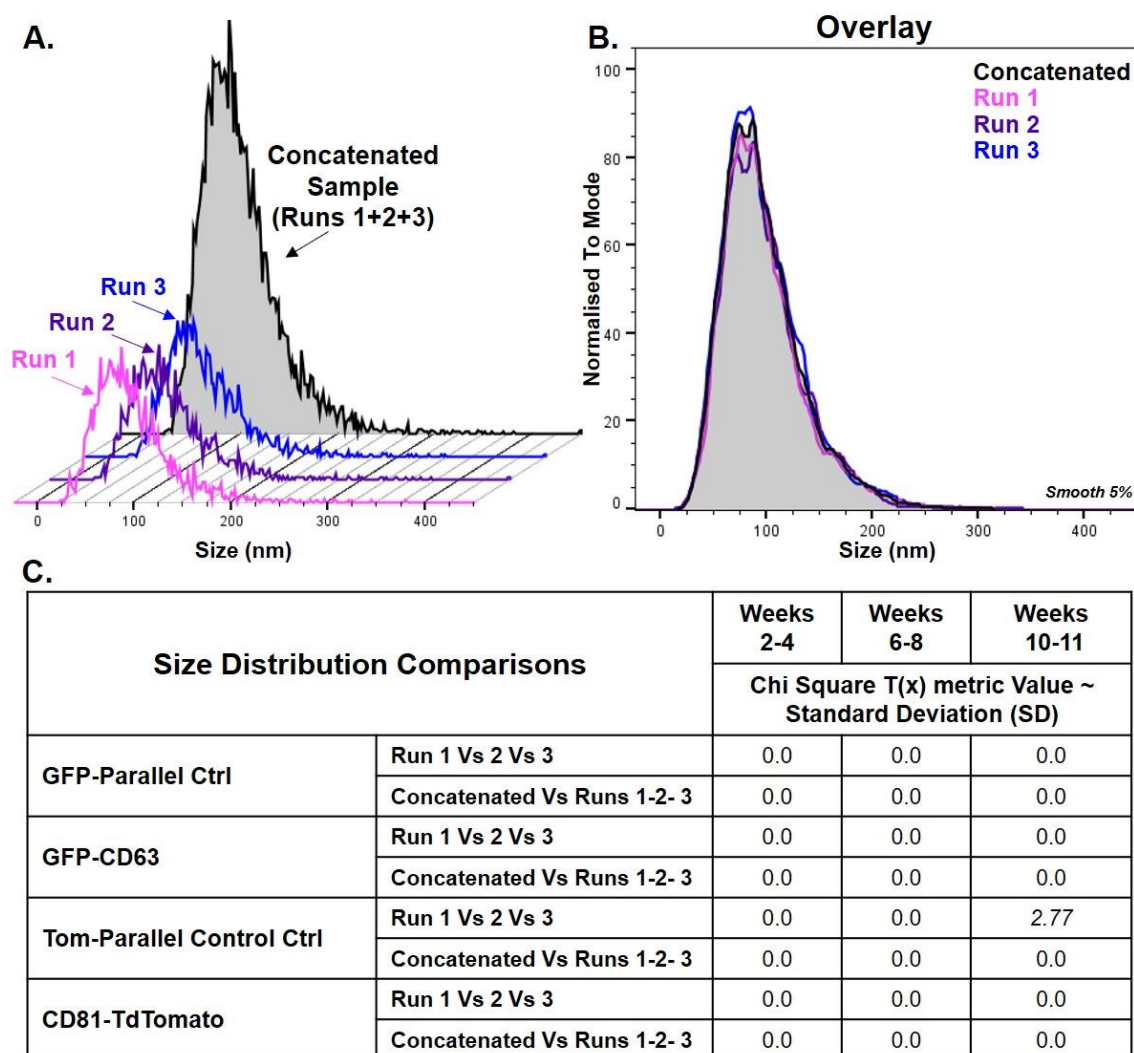
Method: GFP-CD63 and CD81-Tdtomato Bioreactor-derived sEVs Batch 1 (Weeks 2-4), Batch 2 (Weeks 6-8) and Batch 3 (Weeks 10-11) as well as Batch 1-3 mix (volume pooled 1:1:1 for each Batch) of GFP-Parallel and Tom-Parallel control sEVs were prepared for imaging along with the 100nm Tetraspeck™ microspheres (1:1000 dilution). A droplet of each sample was placed in a Nunc™ Lab-Tek™ chambered coverglass and sealed with a glass coverslip. sEVs and microspheres were then imaged using the Zeiss Axiovert 100 widefield fluorescence microscope and the MetaMorph software (Z-step=0.2 μm for 100 slices, x63 magnification, 1.4 NA oil lens). Fluorescence emission filters and exposure times were for GFP: 489/515nm (70% attenuation- 400ms), for Tdtomato: 585/602nm (70% attenuation- for 300ms), followed by maximum intensity projection in the Fiji software (v1.52c).



Supplementary Figure 20. Nanoparticle Tracking Analysis- derived EV size distributions.

A. Nanoparticle Tracking analysis of GFP-CD63 EVs compared to GFP-Parallel control EVs for Weeks 2-4 (Batch 1) (**i**), Weeks 6-8 (Batch 2) (**ii**) and Weeks 10-11 (Batch 3) (**iii**) showing the overlays of EV size distributions (average distributions deriving from a triplicate run of each sample). **B.** Nanoparticle Tracking analysis of CD81-Tdtomato EVs compared to Tom-Parallel control EVs for Weeks 2-4 (Batch 1) (**i**), Weeks 6-8 (Batch 2) (**ii**) and Weeks 10-11 (Batch 3) (**iii**) demonstrating the overlays of EV size distributions (average distributions deriving from a triplicate run of each sample).

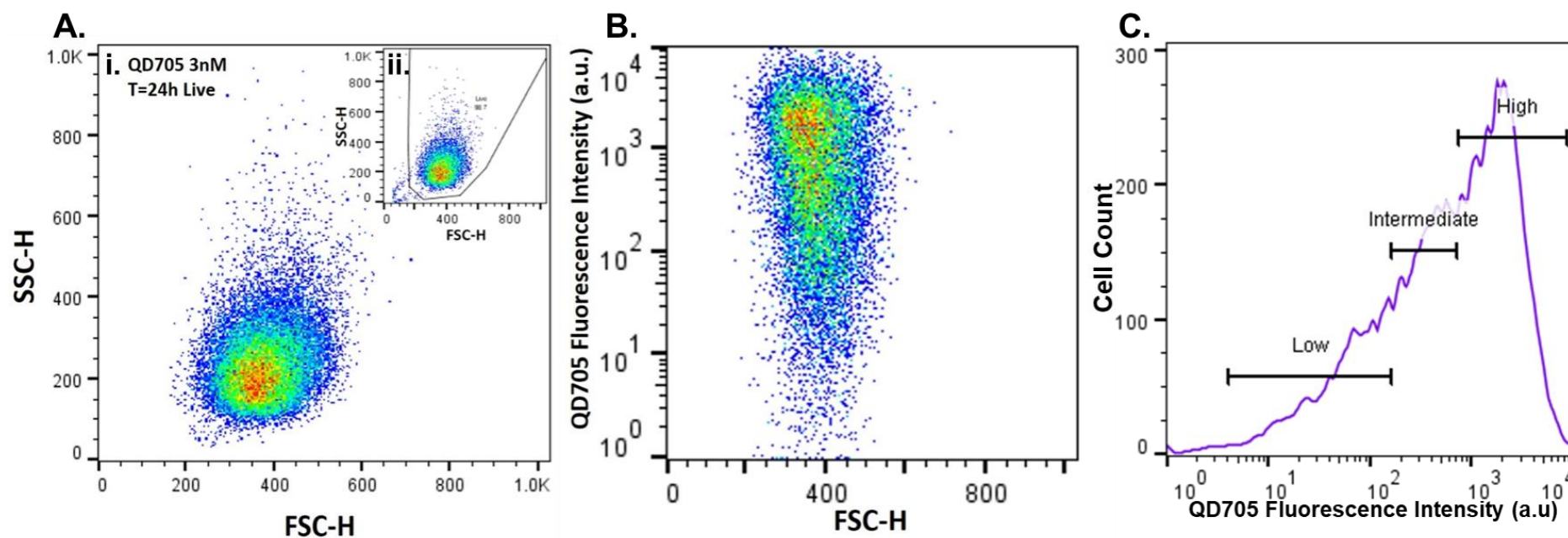
Note: GFP-CD63 (dark green), GFP-Parallel (light green), CD81-Tdtomato (red), Tom-Parallel (pink).



Supplementary Figure 21. sEV size Chi Square distribution comparisons.

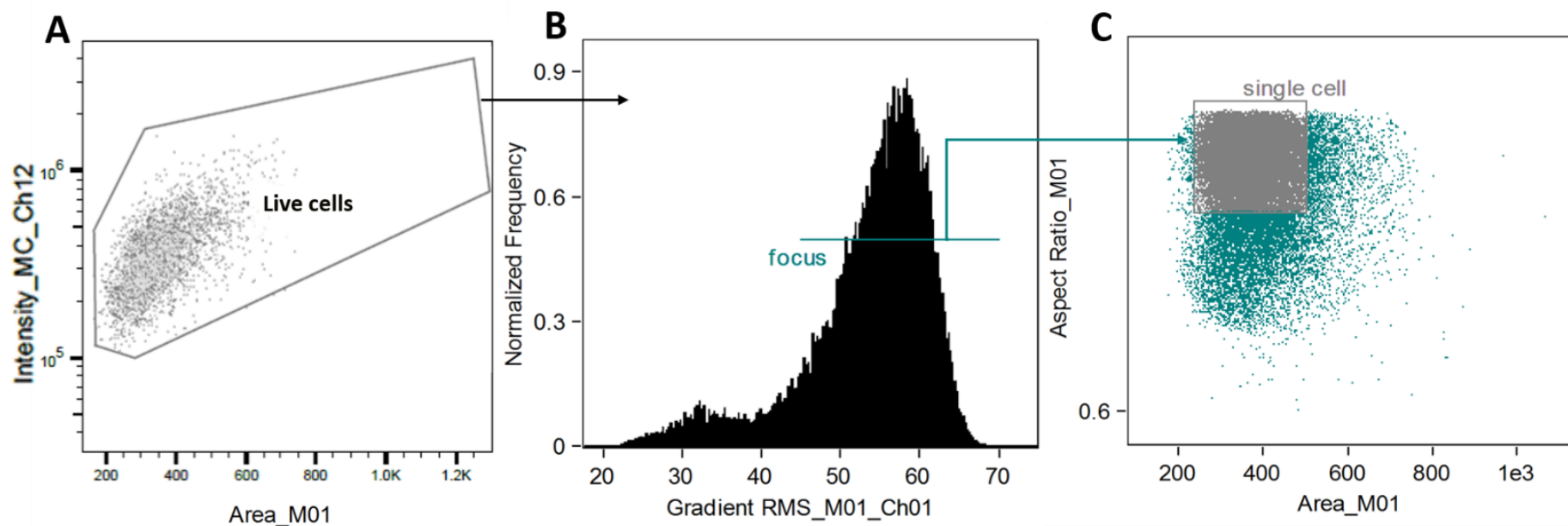
A. NTA size distributions of sEVs deriving from three runs of each EV sample (technical triplicate) i.e., Run 1 (pink), 2 (purple) and 3 (blue) were concatenated (black) to generate the sum of distributions for further statistical analysis. **B.** Overlay of three NTA sEV size distributions (Runs 1, 2, 3) and concatenated distribution, normalised to mode (and smoothing 5%). **C.** FlowJo™ Chi Square statistical analysis table showing baseline variance for each EV sample, which firstly involved triple comparisons of Runs 1 vs 2 vs 3 (for each Batch separately, Batch 1: Weeks 2-4, Batch 2: Weeks 6-8 and Batch 3: Weeks 10-11) to determine deviation of each technical replicate run. Secondly, determination of baseline variance was also conducted between the concatenated sample Vs an average of the Runs 1-2-3 (double comparison). The result of each comparison is the calculated Chi Square T(x) metric value which represents the variance between the three or two size distributions, respectively in Standard Deviations (SD).

Note: Concatenated sEV samples were compared with each other i.e., comparison of different EV types (GFP-CD63, GFP-Parallel, CD81-TdTomato and Tom-Parallel) and comparison of different EV batches (e.g., Weeks 2-4, Weeks 6-8 and Weeks 8-11), in order to calculate their Chi Square T(x) values. When these Chi Square T(x) values were larger than the baseline T(x) values, then their difference in variance (in SD) was considered to be statistically significant.



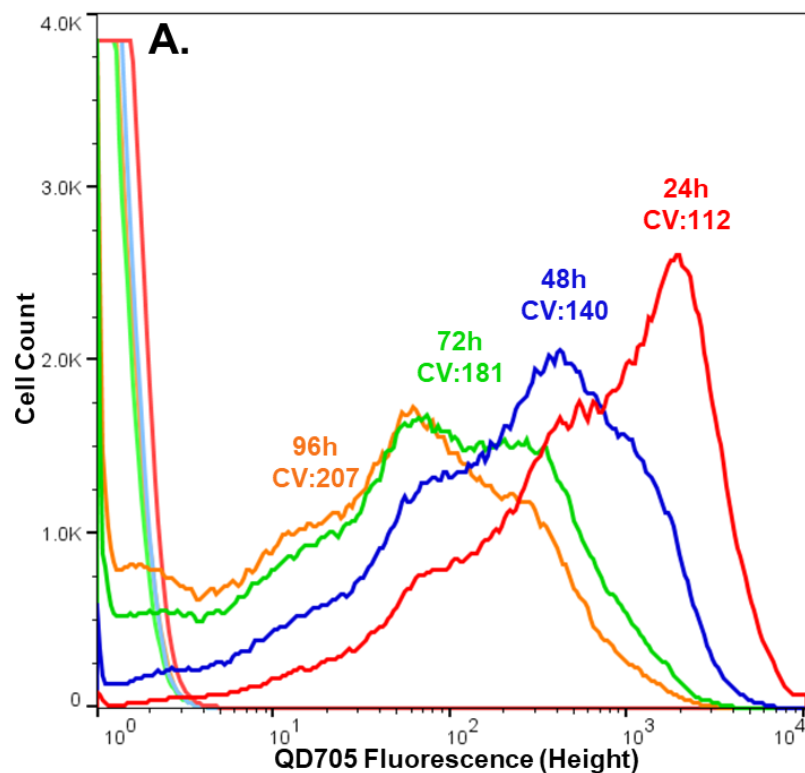
Supplementary Figure 22. Gating strategy for the QD705 uptake and distribution flow cytometry experiment.

A.(i) Example of a Forward scatter (FSC-H) Vs Side scatter (SSC-H) plot (QD705-treated cells 24 hours post-labelling) to demonstrate cell viability after a standard gate was placed **(ii)** to remove dead cells and debris, ensuring analysis of the healthy cell population. The same gate was applied to all QD705-treated samples and controls of all three independent experiments (N=1,2,3). **B.** Example of a FSC-H Vs QD705 Fluorescence Intensity dot plot (same as **A**) to demonstrate the gated viable fluorescent cell population. **C.** Example of a QD705 fluorescence intensity histogram based on the previous gating, which also shows the gates for High, Intermediate and Low fluorescent peaks.



Supplementary Figure 23. Gating strategy for the 24-hour QD705 uptake imaging flow cytometry experiment.

A. The Area_M01 (Cell Area -Brightfield channel) Vs Intensity_MC_Ch12 (Darkfield or SSC channel) plot was used to demonstrate the gate for viable cells which were selected for further gating. **B.** A Gradient RMS (root mean squared)_M01_Ch01 (Brightfield) histogram (line-scan gradient) was used to select viable cells that were focused within the focal plane. **C.** Further gating on the focused cells, in a two-dimensional plot of Area_M01 (Cell Area -Brightfield channel) and Aspect ratio_M01 was done to ensure selection of single cells. The single-cell gate was used for further analysis including QD705 fluorescence intensity histograms and Spot Count analysis of the single-cell fluorescence images.



Concatenated_QD705_24h_N=1-3	GeoMean: 527
Concatenated_QD705_48h_N=1-3	GeoMean: 174
Concatenated_QD705_72h_N=1-3	GeoMean: 52.6
Concatenated_QD705_96h_N=1-3	GeoMean: 31.0
Concatenated_CTRL_24h_N=1-3	GeoMean: 1.19
Concatenated_CTRL_48h_N=1-3	GeoMean: 1.13
Concatenated_CTRL_72h_N=1-3	GeoMean: 1.11
Concatenated_CTRL_96h_N=1-3	GeoMean: 1.12

B.i.

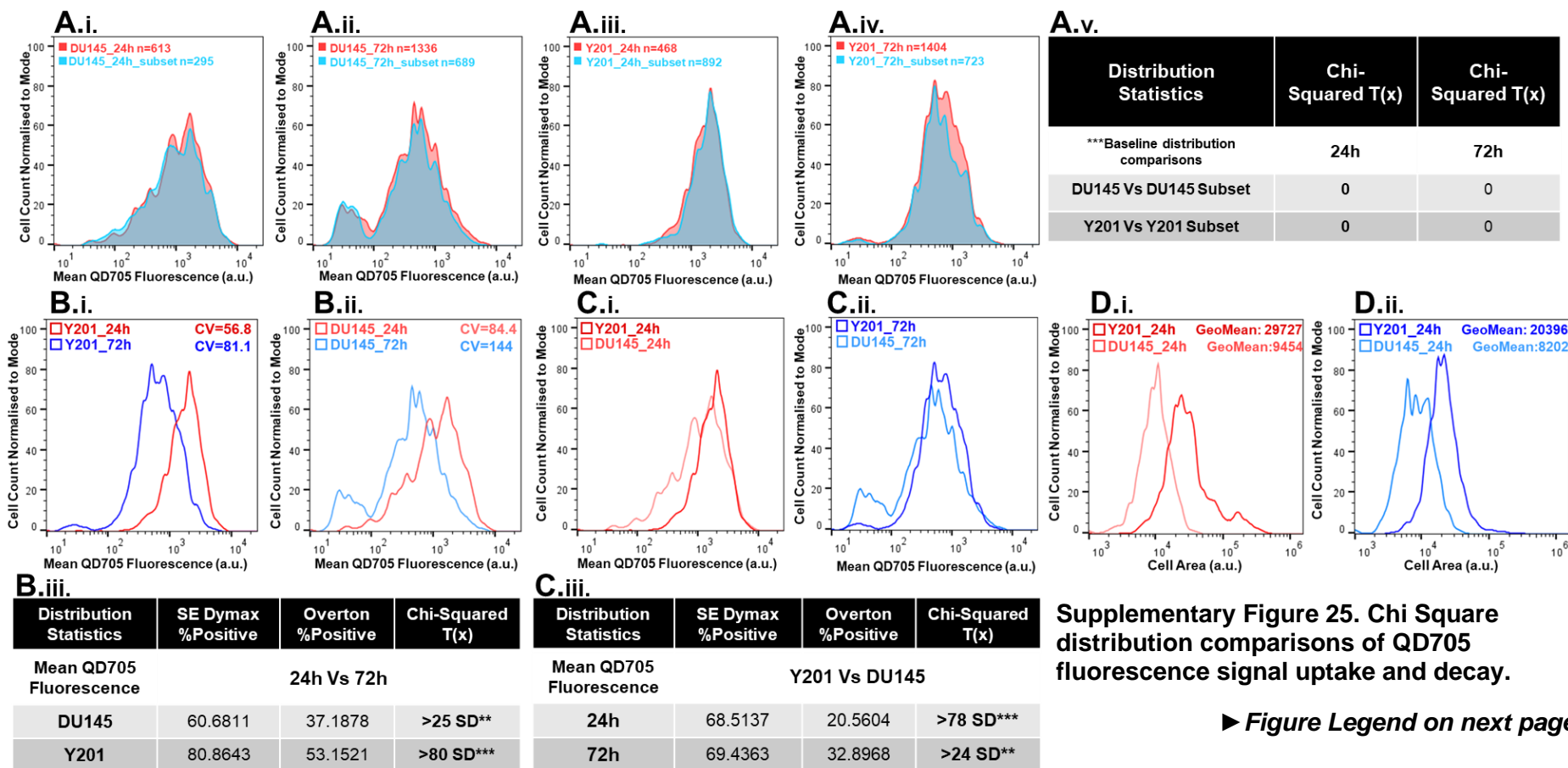
Chi-Squared T(x)						
Comparisons	24h Vs 48h	24h Vs 72h	24h Vs 96h	48h Vs 72h	48h Vs 96h	72h Vs 96h
QD705 Vs QD705	7,613.81	20,431.40	25,821.42	6,448.03	11,631.21	1,216.81
Control Vs Control ***Baseline Variance	996.52	2,383.12	1,732.09	353.43	188.71	62.00

B.ii.

Chi-Squared T(x)				
Comparisons	24h	48h	72h	96h
QD705 Vs Control	60,821.93	58,583.95	51,632.31	46,121.88

Supplementary Figure 24. Chi Square distribution comparisons of QD705 fluorescence signal decay.

A. QD705 fluorescence intensity histograms taken at 24-hour intervals post-labelling with QD705. The QD705 fluorescence intensity histograms were concatenated so that each timepoint includes all the 3 distributions from the three independent experiments (N=1,2,3) for QD705-treated cells and controls. The coefficient of variation (CV) is also shown and the geometric mean of QD705 fluorescence for each timepoint. QD705- treated sample and control intensity histograms are indicated with dark or light colours respectively (24h: red, 48h: blue, 72h: green, 96h: orange). **B.** FlowJo™ Chi Square statistical analysis showing variance of fluorescence between 24-96h for QD705-treated and Control cells. **(i)** Analysis was conducted by double comparisons of time-points (24h Vs 48h, 24h Vs 72h, 24h Vs 96h, 48h Vs 96h and 72h Vs 96h) for QD705-treated cells or Control cells (separately). The result of each comparison is the calculated Chi Square value, converted into a T(x) metric value that represents the variance between populations in Standard Deviations (SD). The baseline variance of autofluorescent signal is represented by the T(x) values of the Control Vs Control comparisons (bottom row). **(ii)** Further Chi Square statistical analysis was conducted by comparing the QD705-treated cells with the control cells for each timepoint (24-96h). Statistical significance is considered when the Chi Square T(x) values are larger than the baseline T(x) and are indicated with bold lettering.



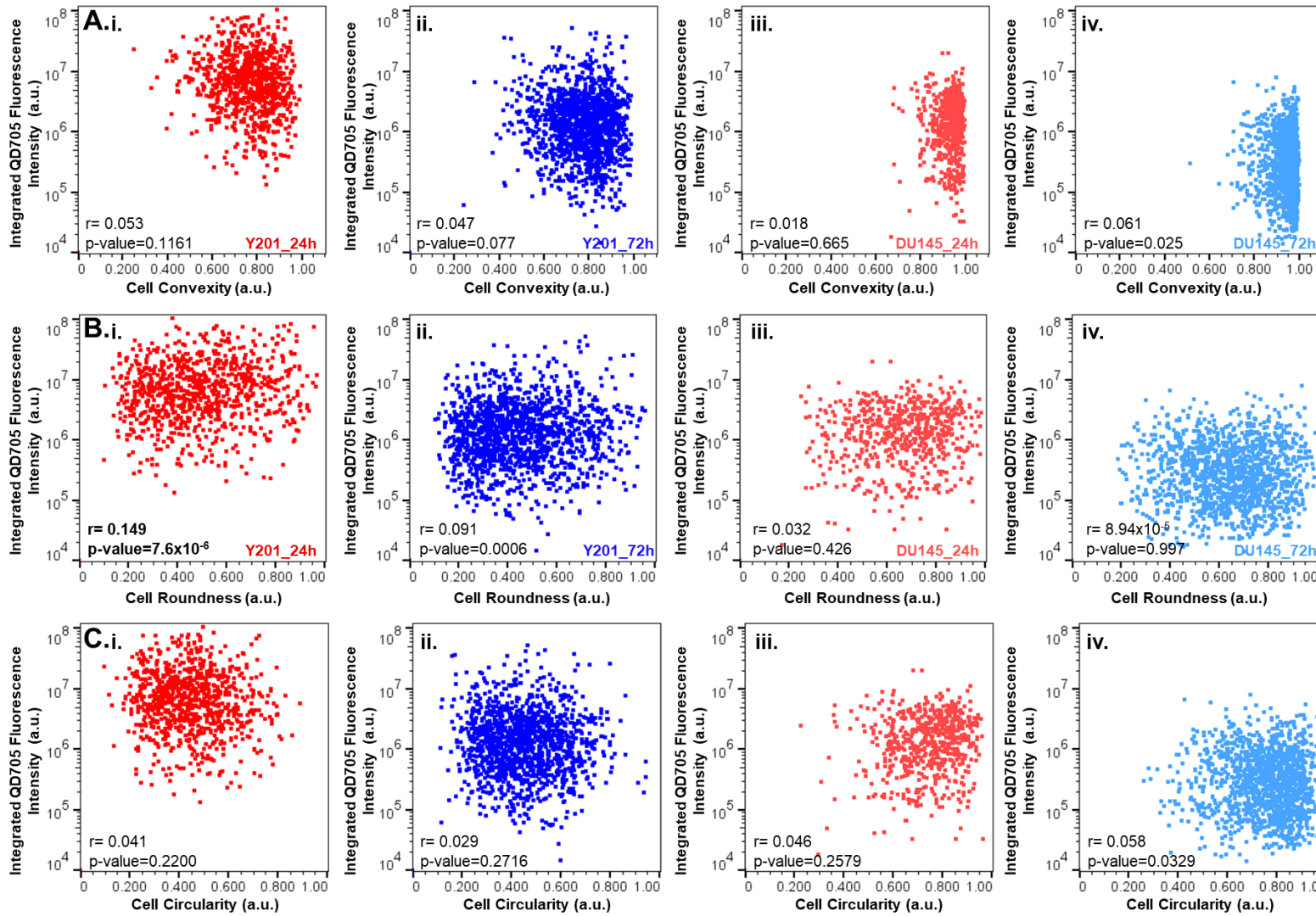
Supplementary Figure 25. Chi Square distribution comparisons of QD705 fluorescence signal uptake and decay.

► Figure Legend on next page

Supplementary Figure 25. Chi Square distribution comparisons of QD705 uptake and decay over time for DU145 Vs Y201 cells.

A. FlowJo™ Chi Square statistical analysis showing calculations of baseline variance between QD705 fluorescence distributions. As the auto-fluorescent signal generated by the Control cells was removed from the QD705-loaded cell images (background subtraction), the baseline variance was not calculated by comparing QD705-loaded and control cells. Alternatively, a random subset of each QD705 fluorescence histogram was generated and was compared to the original distribution for **(i)** DU145 cells 24-hours post-dosing, **(ii)** DU145 cells 72-hours post-dosing, **(iii)** Y201 cells 24-hours post-dosing and **(iv)** Y201 cells 72-hours post-dosing (red: original QD705 fluorescence distribution, blue: subset of original distribution). The number of cells analysed in each distribution (and sub-distribution) are noted on the top left corners of each histogram overlay **(i-iv)**, and the result of each comparison is shown in the table as the Chi Square T(x) metric values which represent the baseline variance between the two populations in SDs **(v)**. *Note that significant differences in variance are shown with bold lettering and ** or ***.* **B.** FlowJo™ Chi Square statistical analysis calculating the variance between the uptake and retention QD705 signal distributions (24- and 72-hours post-dosing respectively) for **(i)** Y201 and **(ii)** DU145 cells, summarising the Chi-square T(x) values (in SDs), along with the SE Dymax %Positive and Overton %Positive percentages which describe the percentage shift of the distributions from 24 to 72 hours (with and without normalisation respectively) **(iii)**. **C.** FlowJo™ Chi Square statistical analysis calculating the variance between the Y201 and DU145 distributions for both uptake **(i)** and retention **(ii)**. The Chi-square T(x) values (in SDs), and the SE Dymax %Positive and Overton %Positive percentages are shown on the table **(iii)**. *Note that significant differences in variance are shown with bold lettering and ** or ***.* **D.** Histogram overlays of Cell Area for Y201 and DU145 cells at **(i)** 24 hours and **(ii)** 72 hours and the geometric Mean Cell Area is shown on the plot.

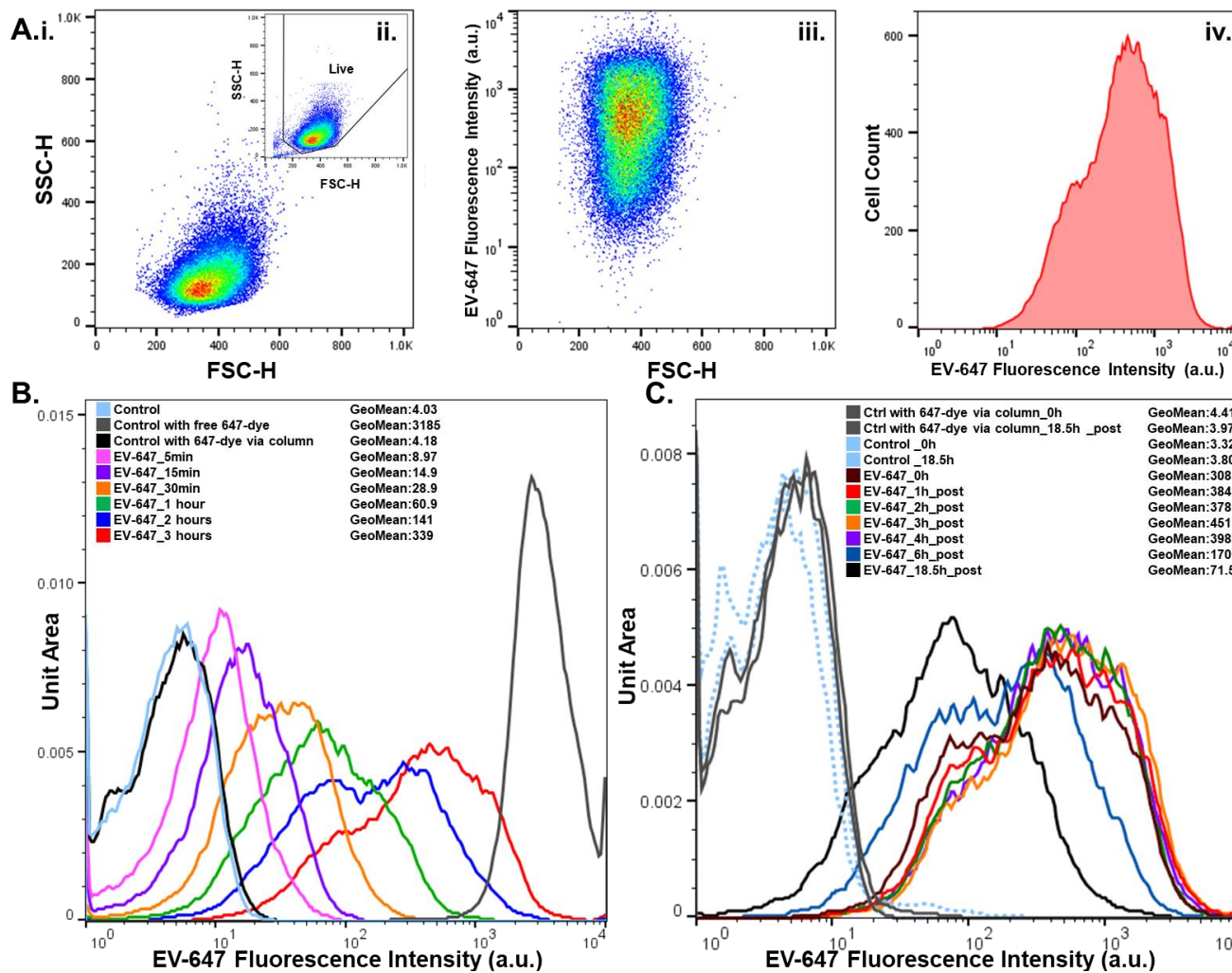
Note: The SE Dymax % Positive algorithm calculates the percentage of events of the latter distribution that are above the former distribution, by normalizing the data to a unit scale to protect against outliers, and by factoring in the distribution of the data. The Overton % Positive algorithm calculates the percentage of events of the latter distribution that are above the former distribution, by subtracting the former distribution.



Supplementary Figure 26.
Relationship of cell characteristics and QD705 fluorescence signal in DU145 and Y201 cells.

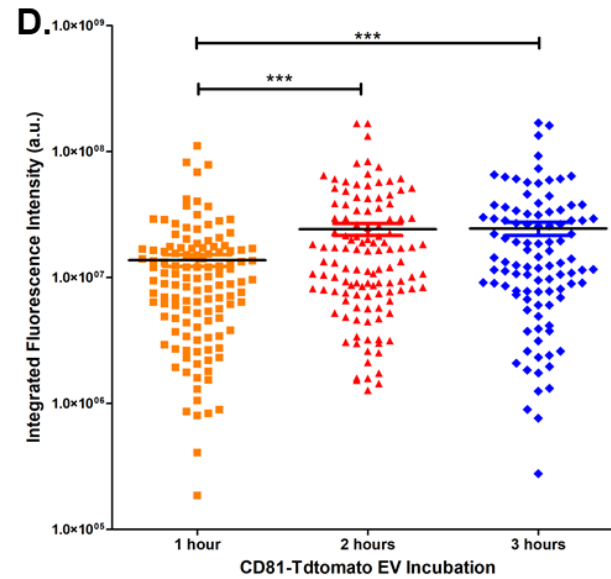
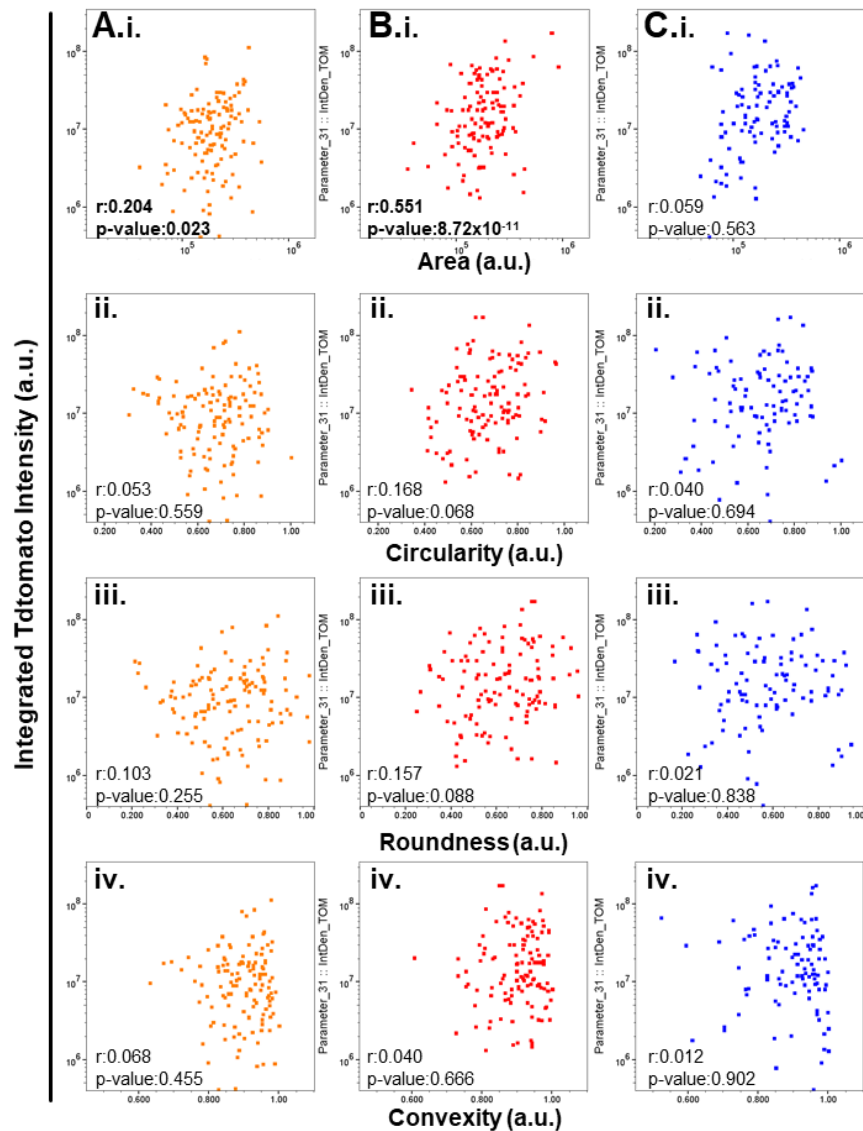
Dot plots depicting the relationship of cell convexity (A), cell roundness (B) and cell circularity (C) with the integrated QD705 fluorescence of Y201 cells (i,ii) and DU145 cells (iii,iv) both 24 hours (i,iii) and 72 hours post-dosing (ii,iv). The Pearson Coefficient and the p-values for significance are also noted (calculated via linear regression analysis)

Note in B.i.: Statistically significant correlation is denoted with bold letter with $r=0.149$ suggesting weak linear correlation



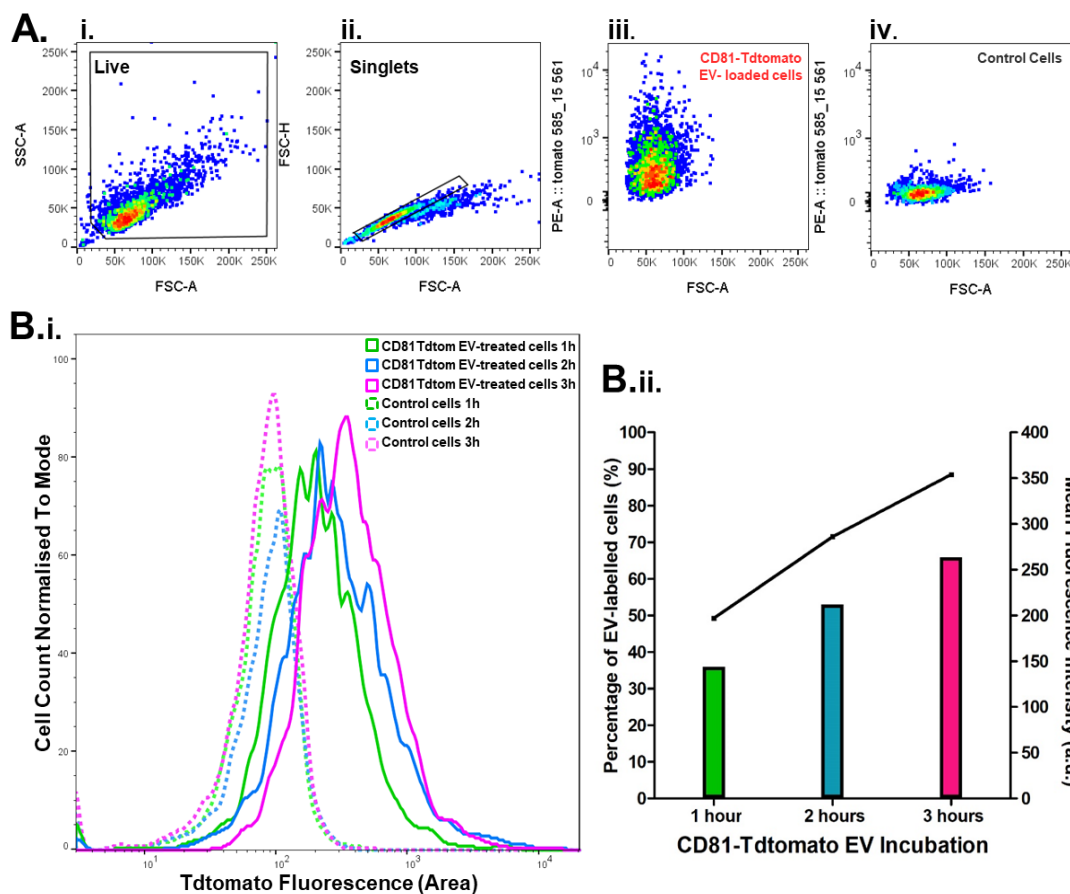
Supplementary Figure 27. EV-647 uptake and retention in DU145 via flow cytometry.

A. FSC-H Vs SSC-H plot to show cell viability after a standard gate was placed (i,ii), FSC-H Vs EV-647 Fluorescence Intensity dot plot to show the gated viable fluorescent cell population (iii) and EV-647 fluorescence intensity histogram based on the previous gating (iv). **B.** Histogram overlays of cells treated with 50µg/ml EV-647 from 5 min to 3 hours, and control cells (untreated, or treated with free dye, or dye that was first passed via spin purification column i.e. treated with the same method as the EV-647 samples). **C.** Histogram overlays of cells treated with EV-647 for 3 hours and then washed to quantify signal retention over time (from 0h to 18.5h post-wash). Control cells are also shown (untreated or treated dye that was first passed via spin column). Geometric Means of fluorescence intensity are also shown (B,C). Method: 50000 DU145 cells were seeded in 24-well plates and labelled with EV-647 as explained in Methods (250µl/well). Negative controls were cells labelled with the Maleimide dye passed via spin column and positive controls were cells treated with free dye for 1h. After labelling, cells were washed with 1XPBS followed resuspension in RPMI media supplemented with 10%exoFBS and 20mM HEPES and analysed via flow cytometry using the BD FACSCalibur flow cytometer (Ex:488nm and Em: 661/16nm BP).



Supplementary Figure 28. CD81-Tdtomato EV uptake and correlation to DU145 cell shape.

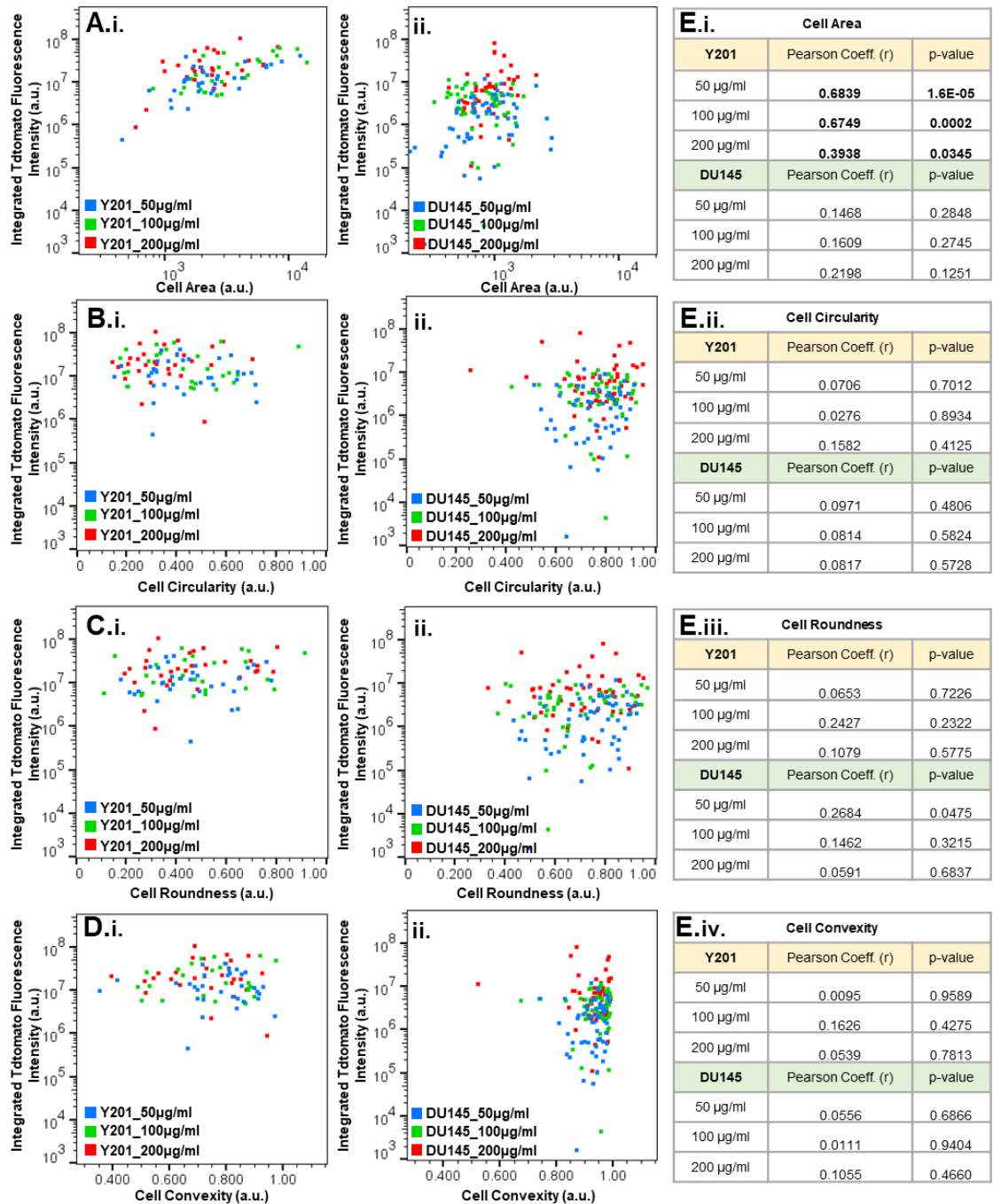
A. Scatter Plots showing the correlation of integrated (total) Tdtomato fluorescence with: **(i)** Cell Area, **(ii)** Circularity, **(ii)** Roundness and **(iv)** Cell Convexity for 1-hour of CD81-Tdtomato EV uptake in DU145 cells. **B-C.** Corresponding plots for the 2-hour (**B**) and 3-hour (**C**) CD81-Tdtomato EV uptake. Linear Regression Analysis showing Pearson Correlation Coefficient (r) and p-value for significance. Significant correlations designated in bold letters and $*p < 0.05$. **D.** Dot plot showing the integrated (total) Tdtomato fluorescence intensity per cell for CD81-Tdtomato EV incubation of 1 hour ($n=124$), 2 hours ($n=119$) and 3 hours ($n=100$). Horizontal black lines represent the mean, error bars represent 95% CI and statistical analysis was done using one-way Anova and Bonferroni multiple comparisons post-test, with significant differences denoted with $***p < 0.001$. This experiment was repeated twice ($N=2$).



Supplementary Figure 29. CD81-Tdtomato EV uptake in DU145 cells by flow cytometry.

A. Gating strategy showing the (i) Forward scatter (FSC-A) Vs Side scatter (SSC-A) plot that demonstrates cell viability after a standard “Live” gate was placed, followed by (ii) a Forward scatter Area Vs Height (FSC-A Vs FSC-H) plot to demonstrate the selection of single cells (“Singlets” gate) thus excluding cell doublets/aggregates from analysis. Examples of FSC-A Vs PE-(A)-Tdtomato Fluorescence Intensity dot plots for CD81-Tdtomato EV-treated cells (iii) and control cells (iv). **B.** Fluorescence intensity histogram overlays demonstrating uptake dynamics of CD81-Tdtomato EVs (100µg/ml) for 1,2 and 3 hours of dosing (i) and combination graph showing the percentage of cells labelled with CD81-Tdtomato EVs (bars-left axis) and the geometric mean fluorescence intensity (line-right axis) of Tdtomato signal for each time-point (ii).

Method: 50000 DU145 cells were seeded in 24-well plates 24 hours prior to dosing in complete RPMI supplemented with 10%exoFBS. The next day, CD81-Tdtomato EVs (Weeks 1-12, generated as explained in Methods) were vortexed for 10sec and after a short spin were diluted in complete RPMI to reach concentration of 100µg/ml. Next, 250µl of EVs was added in every well, as well as complete media in separate wells as negative controls. Then, the plates were manually mixed for 10sec and were placed in a humidifying chamber (100cm dish with 35mm dish filled with 1XPBS to prevent evaporation) in the incubator (37°C, 5% CO₂). Cells were dosed with the EV-rich media for 1-, 2- and 3h, after which the media was removed, followed by washing with 1XPBS, trypsinisation, resuspension in RPMI media supplemented with 10%exoFBS and 20mM HEPES and finally by measuring the Tdtomato fluorescence intensity via flow cytometry using the BD LSR Fortessa flow cytometer (Ex: 561nm, Em: 585/15nm BP).

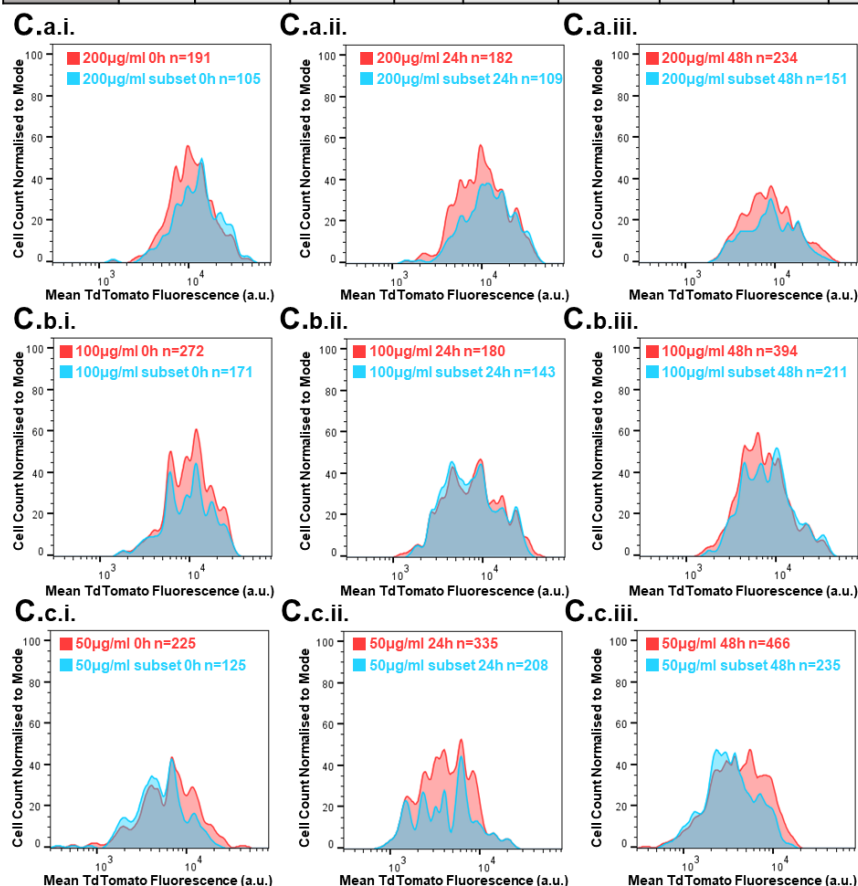


Supplementary Figure 30. Correlation of CD81-Tdtomato EV uptake with DU145 and Y201 cell shape characteristics after acute EV delivery.

Scatter plot overlays of **A.** Cell Area, **B.** Cell Circularity, **C.** Cell Roundness and **D.** Cell Convexity versus the Integrated Tdtomato Fluorescence for each CD81-Tdtomato EV concentration in Y201 cells (**i**) and DU145 cells (**ii**). **E.** Linear Regression Analysis showing Pearson Correlation Coefficient (r) and p-value for significance of correlation for: (**i**) Cell Area, (**ii**) Circularity, (**iii**) Roundness and (**iv**) Convexity. Note that CD81-Tdtomato EV concentrations are designated with: 50µg/ml (blue) ,100µg/ml (green) and 200µg/ml (red).

A.	SE % Pos	Overton % Pos	Chi-Squared T(x)	SE % Pos	Overton % Pos	Chi-Squared T(x)	SE % Pos	Overton % Pos	Chi-Squared T(x)
	50µg/ml Vs 100µg/ml			50µg/ml Vs 200µg/ml			100µg/ml Vs 200µg/ml		
	Distribution Statistics								
0h	60.17	28.65	>3 SD*	71.33	33.61	>4 SD**	37.23	8.30	0 ns
24h	56.83	32.90	>4 SD**	79.43	48.97	>11 SD***	65.18	19.07	0 ns
48h	77.72	32.94	>15 SD***	75.01	40.03	>11 SD***	30.71	13.09	0 ns

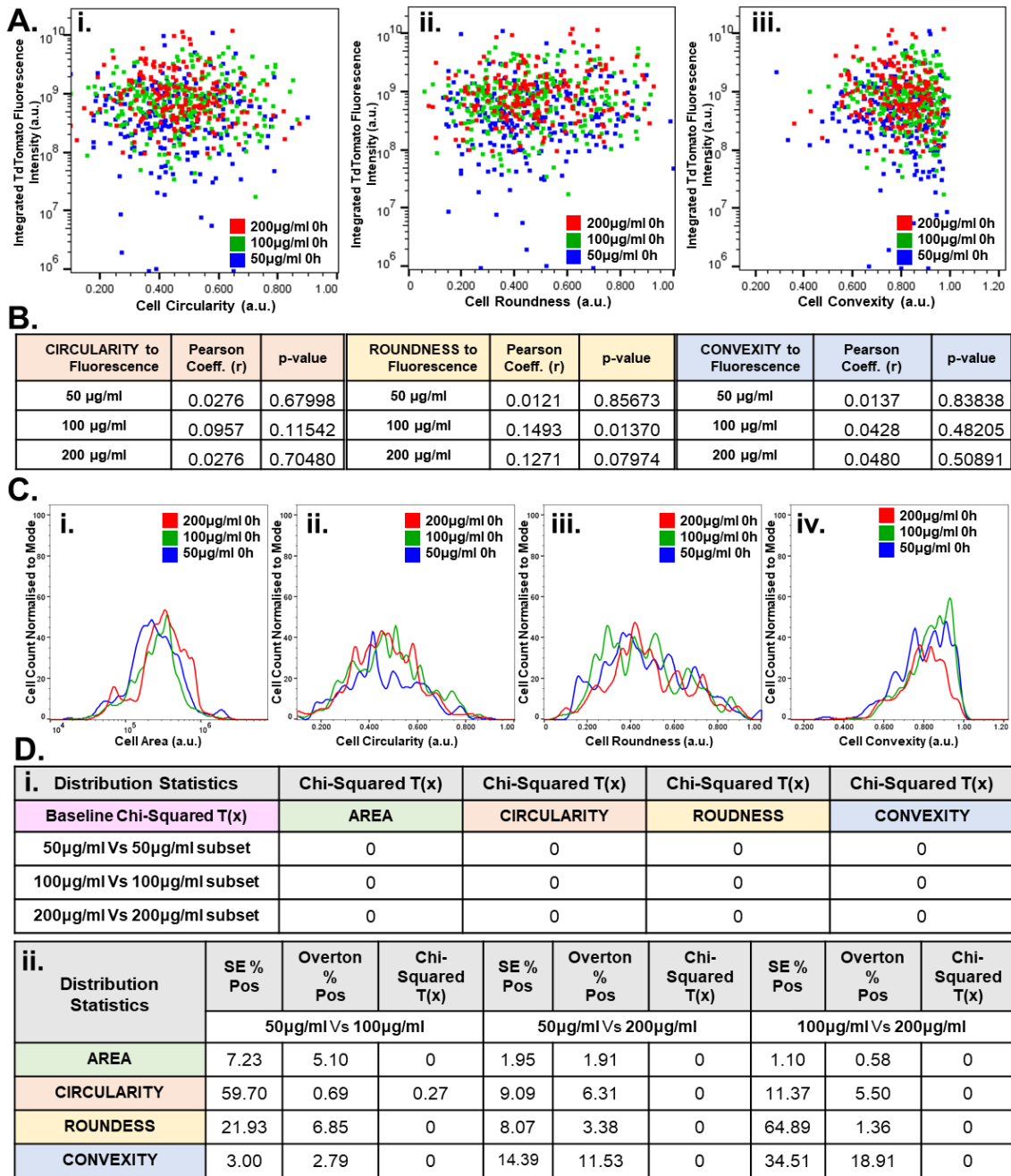
B.	SE % Pos	Overton % Pos	Chi-Squared T(x)	SE % Pos	Overton % Pos	Chi-Squared T(x)	SE % Pos	Overton % Pos	Chi-Squared T(x)
	0h Vs 24h			0h Vs 48h			24h Vs 48h		
	Distribution Statistics								
200µg/ml	45.18	10.07	0 ns	59.63	18.72	0 ns	31.10	13.01	0 ns
100µg/ml	66.10	23.26	<1 SD ns	50.14	23.88	>3 SD*	12.04	8.23	0 ns
50µg/ml	45.48	27.59	>3 SD*	47.01	26.06	>2 SD*	51.72	26.79	>4 SD**



C.d.	Distribution Statistics		Chi-Squared T(x)	Chi-Squared T(x)	Chi-Squared T(x)
	Tdtomato Fluorescence Baseline Chi-Squared T(x)		0h	24h	48h
	50µg/ml Vs 50µg/ml subset		0	0	0
	100µg/ml Vs 100µg/ml subset		0	0	0
	200µg/ml Vs 200µg/ml subset		0	0	0

Supplementary Figure 31. Chi Square distribution comparisons of Tdtomato fluorescence between doses over time in Y201 cells.

A. FlowJo™ Chi Square statistical analysis calculating the variance between each CD81-Tdtomato EV concentration for both uptake (0h) and retention (24h and 48h) with Chi-square T(x) values (in SDs), and the SE Dymax and Overton %Positive percentages shown, which describe the percentage shift of the distributions for each timepoint (with and without normalisation respectively). **B.** Calculations of variance between the uptake and retention Tdtomato signal distributions for each EV concentration, showing the Chi-square T(x) values (in SDs), along with the SE Dymax %Positive and Overton %Positive percentages **C.** Calculations of baseline variance between the Tdtomato fluorescence distributions. As the auto-fluorescent signal generated by the Control cells was removed from the Tdtomato-loaded cell images (background subtraction), the baseline variance was not calculated by comparing Tdtomato-loaded and control cells. Alternatively, a random subset of each Tdtomato fluorescence histogram was generated (blue) and was compared to the original distribution (red): **(a)** 200µg/ml, **(b)** 100µg/ml and **(c)** 50µg/ml and every time-point of each dose: **(i)** 0h, **(ii)** 24h and **(iii)** 48h post-dosing. The number of cells analysed were noted on each histogram overlay and the result of each comparison is shown in Table **C(d)** with the Chi Square T(x) metric values which represent the baseline variance between the two populations in SDs. *Significant differences in variance are shown with bold lettering and *, ** or ***.*



Supplementary Figure 32. Correlations and Chi Square distribution comparisons for cell shape on uptake of CD81-Tdtomato EVs in Y201 cells.

A. Scatter plot overlays of **(i)** Cell Circularity, **(ii)** Roundness and **(iii)** Convexity Vs Integrated (total) Tdtomato Fluorescence for each EV concentration. **B.** Linear Regression Analysis showing Pearson Correlation Coefficient (r) and p-value for significance of correlation for: Cell Circularity, Roundness and Convexity to Tdtomato Fluorescence. **C.** Histogram overlays of **(i)** Cell Area, **(ii)** Circularity, **(iii)** Roundness and **(iv)** Convexity for each EV concentration. **D.** Chi Square Distribution comparisons to determine potential differences in cell shape between each CD81-Tdtomato EV concentration during uptake of EVs (0h post-dosing): **(i)** baseline variance for each concentration by generating a random subset distribution (Supp.Fig.29) and **(ii)** the Chi-square T(x) values (in SDs), along with the SE Dymax %Positive and Overton %Positive percentages for each cell characteristic comparing the different EV concentrations (50µg/ml Vs 100µg/ml, 50µg/ml Vs 200µg/ml and 100µg/ml Vs 200µg/ml). Note that the concentrations on plots are designated by 50µg/ml (blue) , 100µg/ml (green) and 200µg/ml (red).

APPENDIX II

Supplementary Table 1. Proteins significantly up/downregulated in GFP-CD63 vs GFP-Parallel control sEVs

Prot. Acc. Gene Name <i>(continued on next page)</i>	Peptide Count	Raw Chromatogram Area (Log2 Transformed)						Median Norm.Chromatogram Area (Log2 Transformed)						-Log (p-val) >1.3 <i>*p-val<0.05</i>	q-value	Fold Change Difference (log) > 0.5 <i>*FC> 1.4 </i>	T-test Stat
		GFP-CD63			GFP- Ctrl			GFP-CD63			GFP- Ctrl						
sp P01116-2 IRASK	6	16.32	16.02	16.41	15.02	14.85	14.81	18.91	18.60	18.99	17.60	17.43	17.39	3.2683	0.0083	1.3600	10.11
sp P62330 ARF6	6	17.15	17.00	17.05	15.98	15.70	16.06	19.74	19.58	19.63	18.56	18.28	18.65	3.1921	0.0072	1.1546	9.66
sp O43813 LANC1	12	17.08	16.92	16.91	16.27	15.60	15.57	20.67	20.50	20.49	19.86	19.18	19.16	2.0961	0.0142	1.1531	4.91
sp Q96A35 RM24	12	14.98	14.64	14.24	13.63	13.54	13.31	18.56	18.23	17.83	17.22	17.13	16.90	2.0780	0.0152	1.1263	4.85
sp Q0VDF9 HSP7E	6	18.71	18.53	18.38	17.54	17.51	17.32	21.29	21.12	20.97	20.13	20.09	19.90	3.1274	0.0064	1.0866	9.29
sp Q15149-4 PLEC	6	13.32	13.23	13.47	12.31	12.33	12.30	15.91	15.82	16.06	14.90	14.92	14.88	3.8659	0.0000	1.0287	14.37
sp P01893 HLAH	12	18.45	18.29	17.92	17.47	17.20	16.92	22.03	21.87	21.51	21.05	20.78	20.51	2.0102	0.0186	1.0249	4.64
sp P36383 CXG1	6	18.95	18.85	18.58	18.20	17.63	17.67	21.53	21.44	21.16	20.78	20.21	20.26	1.9579	0.0187	0.9582	4.48
sp Q03169 TNAP2	6	17.12	17.02	17.05	16.30	16.01	16.06	19.71	19.60	19.64	18.89	18.59	18.64	3.2218	0.0077	0.9420	9.83
sp O14495 PLPP3	12	18.74	18.74	18.60	18.01	17.71	17.75	21.33	21.32	21.18	20.60	20.29	20.34	2.8970	0.0043	0.8677	8.09
sp P16422 EPCAM	12	19.47	19.25	19.06	18.79	18.38	18.06	22.05	21.83	21.65	21.38	20.96	20.64	1.6112	0.0420	0.8529	3.52
sp O95716 RAB3D	6	17.75	17.79	17.60	17.09	16.88	16.65	20.34	20.37	20.18	19.68	19.47	19.24	2.4110	0.0058	0.8396	6.00
sp P01889 HLAB	12	19.97	19.96	20.01	19.21	19.14	19.10	23.56	23.55	23.60	22.80	22.72	22.69	4.6958	0.0000	0.8321	23.29
sp P15311 EZRI	42	20.45	20.34	20.08	19.79	19.55	19.28	23.29	23.20	22.94	22.55	22.36	22.12	2.1014	0.0125	0.8003	4.92
sp Q96LD4 TRI47	6	18.00	17.94	17.71	17.27	16.99	17.04	20.59	20.52	20.30	19.86	19.57	19.63	2.4964	0.0066	0.7836	6.33
sp P61769 B2MG	12	18.10	17.98	17.96	17.48	17.12	17.13	21.69	21.57	21.55	21.06	20.71	20.72	2.4593	0.0059	0.7705	6.18
sp Q9H0H5 RGAP1	30	20.07	19.87	19.69	19.31	19.09	18.92	22.65	22.46	22.27	21.89	21.68	21.50	2.0900	0.0136	0.7692	4.89
sp P54709 AT1B3	18	18.63	18.54	18.60	17.99	17.81	17.62	21.98	21.92	22.01	21.39	21.20	21.03	2.7074	0.0073	0.7691	7.21
sp P20336 RAB3A	6	17.75	17.79	17.60	17.07	16.96	16.81	20.34	20.37	20.18	19.65	19.54	19.39	2.8793	0.0040	0.7688	8.01
sp Q9BXS4 TMM59	6	17.57	17.20	17.30	16.72	16.38	16.69	20.15	19.79	19.89	19.31	18.96	19.28	2.0946	0.0140	0.7629	4.90
sp P14923 PLAK	72	23.54	23.37	23.24	22.83	22.61	22.45	26.44	26.29	26.16	25.73	25.50	25.38	2.3434	0.0070	0.7599	5.75
sp Q7Z7K6 CENPV	12	21.73	21.50	21.55	21.13	20.78	20.61	25.32	25.09	25.13	24.72	24.36	24.20	1.9579	0.0184	0.7546	4.48
sp P26038 MOES	35	19.93	19.48	19.54	19.07	18.82	18.75	22.97	22.53	22.64	22.10	21.92	21.92	2.1562	0.0095	0.7338	5.10
sp P00533 EGFR	40	21.01	20.77	20.67	20.30	20.08	19.87	23.57	23.33	23.23	22.87	22.64	22.42	1.9584	0.0189	0.7314	4.48
sp O95858 TSN15	6	17.89	17.60	17.84	17.10	17.10	17.01	20.47	20.19	20.43	19.68	19.69	19.59	2.7644	0.0036	0.7079	7.47
sp Q86U90 YRDC	6	19.14	18.97	18.99	18.36	18.38	18.25	21.72	21.55	21.58	20.95	20.97	20.84	3.3482	0.0108	0.6999	10.60
sp Q6P9B6 IMEAK7	12	16.34	16.02	16.05	15.34	15.43	15.54	19.92	19.60	19.63	18.92	19.02	19.13	2.3764	0.0075	0.6982	5.87
sp O43633 CHM2A	6	20.94	20.70	20.65	20.28	20.06	19.90	23.52	23.28	23.23	22.86	22.65	22.49	2.0641	0.0163	0.6785	4.80
sp Q96QD8 S38A2	6	20.41	20.32	20.08	19.82	19.48	19.52	22.99	22.91	22.67	22.41	22.07	22.11	1.9857	0.0181	0.6607	4.56
sp P23526 SAHH	6	16.65	16.65	16.55	16.20	15.93	15.76	19.24	19.23	19.13	18.79	18.51	18.34	2.0912	0.0138	0.6531	4.89
sp Q14126 DSG2	66	22.98	22.96	23.00	22.38	22.34	22.27	25.56	25.54	25.59	24.96	24.93	24.85	4.3041	0.0000	0.6519	18.56
sp Q15365 PCBP1	6	15.84	15.78	15.82	15.21	15.32	14.97	18.43	18.37	18.41	17.80	17.90	17.56	2.4917	0.0064	0.6493	6.31
sp P09382 LEG1	18	19.16	19.08	18.99	18.59	18.38	18.18	22.13	22.03	21.95	21.57	21.43	21.17	2.1230	0.0109	0.6469	4.99
sp Q14197 ICT1	6	14.12	14.20	13.80	13.51	13.09	13.59	16.71	16.78	16.38	16.09	15.68	16.17	1.5113	0.0462	0.6418	3.27
sp P78536 ADA17	6	16.64	16.71	16.40	16.19	15.83	15.82	19.22	19.29	18.98	18.78	18.41	18.41	1.8348	0.0231	0.6349	4.12
sp Q13442 HAP28	6	20.41	20.57	20.43	19.87	19.81	19.82	23.00	23.15	23.01	22.46	22.39	22.41	3.5336	0.0135	0.6331	11.83
sp P62993 GRB2	6	16.09	16.28	15.99	15.72	15.62	15.13	18.68	18.87	18.57	18.31	18.21	17.71	1.4426	0.0501	0.6298	3.10
sp Q53E24 CEP55	6	16.29	16.01	15.97	15.84	15.37	15.20	18.87	18.60	18.56	18.42	17.95	17.78	1.3513	0.0671	0.6229	2.89
sp Q9H9H4 VP37B	6	17.18	16.67	16.62	16.23	16.24	16.18	19.77	19.25	19.21	18.82	18.83	18.76	1.5548	0.0435	0.6063	3.38
sp P12277 KCRB	54	20.84	20.67	20.70	20.06	20.12	20.12	24.31	24.14	24.18	23.54	23.64	23.64	3.3106	0.0090	0.6055	10.36
sp P09972 ALDOC	18	18.19	18.03	17.92	17.59	17.29	17.45	22.36	22.20	22.09	21.76	21.46	21.62	2.1393	0.0092	0.5994	5.05
sp Q9NUM4 IT106B	6	17.12	16.82	16.78	16.13	16.46	16.36	19.70	19.40	18.71	19.04	18.95	1.8201	0.0228	0.5896	4.08	

Appendix II

sp P05362 ICAM1	54	23.51	23.34	23.25	22.99	22.77	22.57	26.24	26.08	26.01	25.73	25.53	25.35	1.9425	0.0193	0.5766	4.43
sp O00299 CLIC1	54	20.21	20.03	20.04	19.53	19.43	19.48	23.18	23.04	23.05	22.59	22.48	22.51	3.3166	0.0098	0.5678	10.40
sp P12429 ANXA3	54	20.78	20.60	20.48	20.18	20.08	19.95	23.67	23.50	23.40	23.09	22.96	22.84	2.1719	0.0080	0.5573	5.15
sp Q15819 UB2V2	6	15.65	15.56	15.36	15.15	14.95	14.80	18.23	18.14	17.95	17.74	17.54	17.38	1.8576	0.0199	0.5556	4.18
sp Q6NSJ5 LRC8E	6	16.74	16.50	16.42	16.27	15.77	15.98	19.33	19.08	19.01	18.85	18.36	18.57	1.4705	0.0473	0.5464	3.17
sp Q8IV08 PLD3	18	20.59	20.42	20.36	20.05	19.92	19.77	23.18	23.01	22.94	22.63	22.51	22.35	2.1473	0.0093	0.5441	5.07
sp P52292 IMA1	6	16.38	16.16	16.21	15.70	15.72	15.69	18.96	18.74	18.79	18.29	18.30	18.28	2.8957	0.0042	0.5418	8.09
sp P55072 TERA	12	16.28	16.09	15.89	15.50	15.72	15.42	19.86	19.67	19.47	19.08	19.30	19.00	1.7020	0.0344	0.5401	3.75
sp P51149 RAB7A	30	21.54	21.47	21.32	20.97	20.91	20.76	24.50	24.42	24.29	23.91	23.91	23.79	2.7593	0.0035	0.5367	7.44
sp O15427 MOT4	6	16.93	16.70	16.74	16.33	16.29	16.15	19.51	19.28	19.33	18.92	18.88	18.73	2.4017	0.0057	0.5333	5.97
sp Q15012 LAP4A	6	16.37	16.45	16.52	15.95	15.89	15.90	18.95	19.03	19.11	18.54	18.48	18.48	3.4056	0.0120	0.5320	10.97
sp P35222 CTNB1	78	21.80	21.61	21.40	21.37	21.14	20.80	25.02	24.83	24.66	24.56	24.33	24.06	1.3608	0.0639	0.5199	2.91
sp Q15758 AAAT	12	21.66	21.46	21.52	21.04	21.01	21.06	24.25	24.05	24.11	23.62	23.60	23.64	2.9812	0.0049	0.5146	8.51
sp Q9UN37 VPS4A	18	19.90	19.86	19.70	19.46	19.29	19.23	22.79	22.74	22.56	22.35	22.16	22.06	2.0061	0.0184	0.5085	4.62
sp Q96C19 EFHD2	12	16.57	16.67	16.79	16.37	16.10	16.05	20.15	20.26	20.38	19.95	19.68	19.63	1.8692	0.0204	0.5063	4.22
sp Q9UQE7 SMC3	6	17.62	17.60	17.35	17.04	16.93	17.07	20.20	20.18	19.93	19.63	19.51	19.66	2.1652	0.0077	0.5050	5.13
sp Q3ZCM7 TBB8	18	16.58	16.41	16.59	17.16	17.09	17.19	20.75	20.58	20.76	21.33	21.26	21.36	3.1667	0.0068	-0.6177	-9.51
sp Q9ULT8 HECD1	6	13.83	14.28	14.09	14.83	14.69	14.61	16.42	16.86	16.68	17.42	17.27	17.20	1.9430	0.0196	-0.6415	-4.43
sp P50454 SERPH	18	20.39	20.39	20.37	21.25	20.82	21.03	24.56	24.56	24.54	25.42	24.99	25.20	2.2076	0.0065	-0.6507	-5.27
sp O75175 CNOT3	6	18.23	17.91	17.97	18.70	18.76	18.62	20.81	20.50	20.55	21.29	21.34	21.21	2.4779	0.0061	-0.6581	-6.26
sp Q14204 DYHC1	24	17.34	16.97	16.70	18.04	17.66	17.26	20.45	20.11	19.96	21.12	20.77	20.61	1.4672	0.0469	-0.6584	-3.16
sp P30876 RPB2	6	19.40	19.39	19.23	20.15	20.07	19.79	21.98	21.98	21.81	22.74	22.65	22.38	2.2489	0.0068	-0.6649	-5.41
sp Q9NQC3-2 RTN4	12	17.98	17.89	17.73	18.51	18.54	18.37	#N/A	21.48	21.31	22.09	22.13	21.96	2.2945	0.0069	-0.6668	-7.41
sp P18084 ITB5	6	16.08	15.98	15.67	16.81	16.62	16.44	18.66	18.56	18.26	19.40	19.20	19.03	1.9384	0.0191	-0.7172	-4.42
sp Q5VTL8 PR38B	6	13.85	13.54	13.29	14.54	14.12	14.23	16.44	16.13	15.87	17.13	16.70	16.82	1.6299	0.0391	-0.7355	-3.57
sp Q02818 NUCB1	6	15.95	15.90	15.65	16.60	16.62	16.51	18.53	18.49	18.24	19.18	19.21	19.09	2.7794	0.0037	-0.7398	-7.53
sp P04264 K2C1	30	20.56	20.45	20.36	21.29	21.22	21.08	23.14	23.03	22.94	23.87	23.80	23.66	3.0455	0.0051	-0.7412	-8.85
sp Q9HA64 KT3K	12	21.18	21.39	20.87	21.94	21.91	21.82	24.77	24.97	24.46	25.53	25.50	25.41	2.0764	0.0168	-0.7454	-4.84
sp O76003 GLRX3	12	16.93	16.75	16.76	17.68	17.56	17.44	20.51	20.33	20.35	21.26	21.15	21.03	2.9678	0.0047	-0.7504	-8.44
sp P13645 K1C10	18	18.81	18.75	18.59	19.63	19.48	19.36	21.39	21.33	21.18	22.21	22.07	21.94	2.8085	0.0039	-0.7722	-7.67
sp P18124 RL7	6	17.46	17.47	17.30	18.50	18.15	18.13	20.04	20.05	19.89	21.08	20.74	20.71	2.5261	0.0068	-0.8491	-6.45
sp Q13144 EI2BE	12	15.47	15.35	15.23	16.25	15.97	16.39	#N/A	18.93	18.81	19.84	19.55	19.97	1.9370	0.0186	-0.9145	-5.55
sp Q9UBG0 MRC2	6	15.35	15.16	15.20	16.37	16.27	16.16	17.93	17.75	17.79	18.96	18.85	18.75	3.6138	0.0180	-1.0295	-12.40
sp O75153 CLU	6	16.22	16.25	16.24	17.36	17.19	17.25	18.81	18.83	18.82	19.95	19.77	19.84	4.4189	0.0000	-1.0317	-19.83
sp Q9NV06 DCA13	6	14.77	14.47	14.35	15.64	15.75	15.78	17.35	17.05	16.94	18.23	18.33	18.36	3.1046	0.0057	-1.1936	-9.17
sp P60510 PP4C	6	16.31	16.00	16.28	18.56	18.54	18.53	18.90	18.59	18.86	21.15	21.13	21.11	4.7453	0.0000	-2.3467	-23.97
sp O76003 GLRX3	12	16.93	16.75	16.76	17.68	17.56	17.44	20.51	20.33	20.35	21.26	21.15	21.03	2.9678	0.0047	-0.7504	-8.44
sp P13645 K1C10	18	18.81	18.75	18.59	19.63	19.48	19.36	21.39	21.33	21.18	22.21	22.07	21.94	2.8085	0.0039	-0.7722	-7.67
sp P18124 RL7	6	17.46	17.47	17.30	18.50	18.15	18.13	20.04	20.05	19.89	21.08	20.74	20.71	2.5261	0.0068	-0.8491	-6.45
sp Q13144 EI2BE	12	15.47	15.35	15.23	16.25	15.97	16.39	#N/A	18.93	18.81	19.84	19.55	19.97	1.9370	0.0186	-0.9145	-5.55
sp Q9UBG0 MRC2	6	15.35	15.16	15.20	16.37	16.27	16.16	17.93	17.75	17.79	18.96	18.85	18.75	3.6138	0.0180	-1.0295	-12.40
sp O75153 CLU	6	16.22	16.25	16.24	17.36	17.19	17.25	18.81	18.83	18.82	19.95	19.77	19.84	4.4189	0.0000	-1.0317	-19.83
sp Q9NV06 DCA13	6	14.77	14.47	14.35	15.64	15.75	15.78	17.35	17.05	16.94	18.23	18.33	18.36	3.1046	0.0057	-1.1936	-9.17
sp P60510 PP4C	6	16.31	16.00	16.28	18.56	18.54	18.53	18.90	18.59	18.86	21.15	21.13	21.11	4.7453	0.0000	-2.3467	-23.97

Supplementary Table 2. Proteins significantly up/downregulated in CD81-Tdtomato vs Tom-Parallel control sEVs

Prot. Acc. Gene Name (continued on next page)	Peptide Count	Raw Chromatogram Area (Log2 Transformed)						Median Norm.Chromatogram Area (Log2 Transformed)						-Log (p-val) >1.3 *p-val<0.05	q-value	Fold Change Difference (log ₂) > 0.5 *FC> 1.4	T-test Stat
		CD81- TOM			Tom- Ctrl			CD81- TOM			Tom- Ctrl						
sp P08727 K1C19	12	17.94	17.69	17.54	14.36	14.51	14.41	21.06	20.87	20.87	18.20	18.54	18.57	4.3209	0.0000	2.49848	18.74
sp P08729 K2C7	12	16.93	16.97	16.86	14.13	13.89	13.75	20.06	20.15	20.19	17.97	17.91	17.91	6.0387	0.0000	2.19962	50.57
sp P08670 VIME	41	20.05	19.93	19.44	17.43	16.94	16.42	22.94	22.83	22.43	21.04	20.71	20.15	2.6456	0.0026	2.09855	6.94
sp P62330 ARF6	6	17.10	17.00	17.12	14.95	14.52	14.49	19.22	19.18	19.44	17.79	17.55	17.65	3.9239	0.0000	1.61782	14.87
sp P54709 AT1B3	17	18.82	18.81	18.60	16.51	16.31	16.62	21.65	21.69	21.63	20.07	20.01	20.52	3.0902	0.0023	1.45682	9.09
sp O14786 NRP1	6	17.12	17.23	17.19	14.96	14.87	15.06	19.25	19.40	19.51	17.80	17.89	18.22	3.1672	0.0000	1.41373	9.52
sp Q06830 PRDX1	6	17.32	17.11	17.12	15.48	14.85	14.58	19.44	19.29	19.44	18.32	17.87	17.74	2.8227	0.0016	1.41371	7.74
sp P09382 LEG1	17	19.24	19.15	19.14	17.09	16.81	16.80	21.59	21.51	21.64	20.28	20.22	20.26	5.2018	0.0000	1.32304	31.21
sp P21980 TGM2	28	18.42	18.38	18.43	16.46	16.43	16.31	21.27	21.29	21.47	19.95	20.08	20.13	4.0392	0.0000	1.28992	15.90
sp Q03169 TNAP2	6	16.98	16.93	17.06	15.21	15.04	14.55	19.11	19.10	19.38	18.06	18.07	17.71	2.9551	0.0019	1.25246	8.38
sp Q96FQ6 S10AG	6	15.27	15.35	15.35	13.48	13.11	13.29	17.39	17.52	17.68	16.32	16.14	16.45	3.2688	0.0000	1.22909	10.11
sp O95716 RAB3D	5	17.68	17.52	17.35	15.69	15.55	15.28	19.54	19.43	19.41	18.27	18.31	18.17	4.5203	0.0000	1.20866	21.04
sp P20336 RAB3A	5	17.68	17.52	17.35	15.69	15.55	15.28	19.54	19.43	19.41	18.27	18.31	18.17	4.5203	0.0000	1.20866	21.04
sp O14495 PLPP3	11	18.78	18.78	18.75	16.96	16.73	16.74	20.76	20.82	20.94	19.64	19.60	19.73	4.2474	0.0000	1.1817	17.95
sp P11021 BIP	12	17.50	17.52	17.71	15.60	15.91	15.52	20.62	20.70	21.03	19.44	19.93	19.68	2.3529	0.0022	1.10126	5.78
sp P26038 MOES	16	19.05	19.07	19.03	17.20	16.88	17.21	21.47	21.61	21.72	20.45	20.29	20.83	2.4239	0.0023	1.07587	6.05
sp P55072 TERA	12	16.62	16.59	16.44	14.91	14.56	14.56	19.75	19.77	19.76	18.76	18.58	18.72	4.4712	0.0000	1.07232	20.45
sp P60903 S10AA	11	17.14	17.33	17.20	15.28	15.32	15.46	20.13	20.38	20.40	19.00	19.22	19.49	2.5169	0.0025	1.06882	6.41
sp P09972 ALDOC	11	18.14	18.02	18.21	16.33	16.25	16.28	21.14	21.07	21.41	20.05	20.14	20.31	2.8942	0.0017	1.04132	8.08
sp P05783 K1C18	11	17.36	17.36	16.97	15.63	15.20	15.39	20.36	20.41	20.17	19.35	19.10	19.42	2.9498	0.0019	1.02159	8.35
sp Q5HYI8 RABL3	5	20.30	20.10	19.94	18.71	18.40	17.86	22.16	22.01	22.01	21.29	21.16	20.75	2.3695	0.0022	0.991428	5.85
sp P51153 RAB13	12	18.18	18.07	17.93	16.63	16.23	16.05	21.30	21.24	21.25	20.48	20.26	20.21	3.4564	0.0000	0.952885	11.30
sp Q15181 IPYR	6	16.97	17.05	16.88	15.35	15.18	15.18	19.09	19.22	19.21	18.19	18.20	18.34	3.9142	0.0000	0.930324	14.78
sp O95858 TSN15	6	17.81	17.80	17.81	16.18	16.08	16.14	19.93	19.98	20.14	19.02	19.10	19.30	2.9512	0.0019	0.876031	8.36
sp Q12913 PTPRJ	5	17.07	17.18	17.01	15.48	15.44	15.47	18.93	19.10	19.07	18.06	18.20	18.36	2.9202	0.0017	0.827156	8.21
sp P62249 RS16	6	15.64	15.48	15.58	13.86	13.95	14.06	17.76	17.66	17.91	16.70	16.97	17.21	2.1262	0.0047	0.814355	5.00
sp P17301 ITA2	36	21.39	21.08	20.96	19.63	19.35	19.30	23.75	23.56	23.61	22.84	22.79	22.86	3.7155	0.0000	0.81237	13.16
sp Q9H082 RB33B	12	20.87	20.73	20.56	19.38	19.10	18.98	23.99	23.91	23.88	23.23	23.12	23.14	4.0693	0.0000	0.765172	16.18
sp Q9H3S7 PTN23	12	19.67	19.59	19.48	18.27	17.93	17.95	21.79	21.77	21.81	21.11	20.96	21.11	3.8371	0.0000	0.731498	14.13
sp P04083 ANXA1	46	19.38	19.31	19.26	17.87	17.73	17.81	22.43	22.41	22.51	21.65	21.69	21.91	2.9192	0.0017	0.703981	8.20
sp O00299 CLIC1	23	19.22	19.15	19.09	17.78	17.52	17.75	21.57	21.51	21.69	20.83	20.74	21.10	2.3819	0.0023	0.701701	5.89
sp Q99650 OSMR	6	17.21	17.25	17.30	15.77	15.86	15.72	19.34	19.43	19.63	18.61	18.88	18.88	2.2698	0.0020	0.674562	5.49
sp P23458 JAK1	5	15.94	15.68	15.84	14.52	14.35	14.17	17.80	17.59	17.90	17.10	17.11	17.07	2.7129	0.0028	0.673475	7.23
sp Q96QK1 VPS35	5	18.13	18.12	17.98	16.83	16.62	16.38	19.99	20.04	20.04	19.41	19.38	19.27	4.0061	0.0000	0.671785	15.60
sp P12429 ANXA3	30	19.94	19.95	19.93	18.47	18.39	18.60	22.24	22.29	22.41	21.47	21.58	21.92	1.9555	0.0052	0.653971	4.47
sp Q92930 RAB8B	5	18.51	18.41	18.20	17.07	16.90	16.81	20.38	20.33	20.26	19.65	19.66	19.70	4.1877	0.0000	0.650524	17.34
sp P12277 KCRB	51	20.66	20.66	20.76	19.19	19.13	19.26	23.54	23.60	23.86	22.85	22.99	23.25	1.8435	0.0072	0.634778	4.14
sp Q16658 FSCN1	12	18.17	18.08	17.75	16.89	16.62	16.21	20.29	20.25	20.08	19.74	19.64	19.37	2.0877	0.0046	0.625879	4.88

Appendix II

sp Q15102 PA1B3	6	15.69	15.89	15.81	14.41	14.25	14.46	17.81	18.07	18.14	17.25	17.28	17.62	1.8032	0.0079	0.622665	4.03
sp P13489 RINI	12	16.55	16.44	16.47	15.22	15.06	14.93	19.68	19.62	19.80	19.07	19.09	19.08	3.4846	0.0000	0.616212	11.49
sp Q8NFJ5 RAI3	22	19.36	19.34	19.45	17.86	18.03	18.04	22.36	22.39	22.65	21.58	21.93	22.07	1.6321	0.0109	0.610269	3.57
sp O15427 MOT4	6	16.77	16.78	16.74	15.28	15.49	15.35	18.89	18.96	19.06	18.13	18.51	18.51	1.8940	0.0059	0.587672	4.29
sp P08758 ANXA5	21	20.11	20.10	20.04	18.77	18.69	18.69	23.09	23.14	23.23	22.48	22.58	22.72	2.6353	0.0026	0.559992	6.90
sp P10301 RRAS	11	17.53	17.61	17.51	16.22	16.08	16.29	20.53	20.66	20.71	19.94	19.98	20.32	1.8581	0.0073	0.553262	4.18
sp Q9NRY6 PLS3	5	17.13	17.14	17.17	16.04	15.76	15.59	18.99	19.05	19.23	18.62	18.52	18.49	2.5938	0.0025	0.551905	6.72
sp P14625 ENPL	17	18.86	18.78	18.85	17.68	17.60	17.53	21.38	21.33	21.54	20.78	20.89	20.93	2.6579	0.0027	0.548912	6.99
sp P23528 COF1	12	19.83	19.87	20.03	18.54	18.54	18.63	22.96	23.05	23.36	22.38	22.57	22.79	1.5009	0.0157	0.545613	3.24
sp Q05639 EF1A2	28	18.05	17.98	17.99	16.81	16.45	16.48	21.44	21.40	21.54	21.00	20.81	20.97	2.7349	0.0028	0.536023	7.33
sp O75436 VP26A	6	13.17	12.97	12.99	12.03	11.67	11.45	15.30	15.14	15.32	14.87	14.69	14.61	2.2794	0.0021	0.527637	5.52
sp P15311 EZRI	17	19.83	19.75	19.56	18.58	18.26	18.10	21.95	21.92	21.91	21.46	21.37	21.37	4.0706	0.0000	0.525494	16.20
sp P62304 RUXE	12	16.70	16.65	16.81	15.48	15.21	15.51	19.83	19.82	20.14	19.32	19.23	19.67	1.4311	0.0165	0.521608	3.08
sp Q8IWT6 LRC8A	10	18.86	18.74	18.76	17.66	17.35	17.39	20.72	20.66	20.82	20.25	20.11	20.29	2.6944	0.0027	0.51803	7.15
sp P78536 ADA17	6	16.49	16.34	16.34	15.39	14.88	14.97	18.61	18.51	18.67	18.23	17.91	18.13	2.0500	0.0046	0.505988	4.76
sp P17987 TCPA	18	17.66	17.57	17.62	17.29	17.11	17.09	20.23	20.22	20.46	20.77	20.79	20.89	2.4265	0.0023	-0.517066	-6.06
sp Q9Y217 FYV1	6	18.37	18.36	18.51	18.15	18.15	18.11	20.50	20.53	20.83	21.00	21.17	21.26	1.7773	0.0099	-0.521908	-3.96
sp Q6UVK1 CSPG4	6	16.59	16.48	16.45	16.37	16.14	16.19	18.72	18.65	18.78	19.22	19.16	19.35	2.8563	0.0016	-0.526918	-7.89
sp P30153 2AAA	6	17.24	17.19	17.05	16.94	16.94	16.79	19.36	19.37	19.37	19.79	19.97	19.95	3.1194	0.0023	-0.530678	-9.25
sp P11047 LAMC1	24	18.78	18.76	18.72	18.48	18.49	18.53	20.90	20.94	21.05	21.32	21.51	21.69	2.0372	0.0046	-0.544613	-4.72
sp Q14764 MPV	6	19.62	19.44	19.23	19.33	19.12	19.12	21.75	21.62	21.56	22.17	22.14	22.27	2.9276	0.0018	-0.554375	-8.24
sp Q9Y490 TLN1	263	23.49	23.45	23.38	23.27	23.13	23.13	26.38	26.39	26.46	26.90	26.94	27.08	3.1444	0.0024	-0.560782	-9.39
sp Q9HBH5 RDH14	6	22.43	22.14	22.22	22.27	22.26	21.59	24.56	24.32	24.54	25.12	25.28	24.75	1.5125	0.0152	-0.574258	-3.27
sp P46776 RL27A	5	15.82	15.60	15.65	15.52	15.40	15.50	17.69	17.51	17.72	18.11	18.16	18.40	2.2164	0.0030	-0.580374	-5.30
sp Q9Y6E2 BZW2	5	19.20	19.09	18.88	19.25	18.77	18.53	21.07	21.00	20.95	21.83	21.53	21.42	2.0041	0.0054	-0.586501	-4.62
sp Q9Y289 SC5A6	6	16.79	16.93	17.02	16.69	16.63	16.80	18.91	19.11	19.34	19.54	19.65	19.96	1.5527	0.0140	-0.596372	-3.37
sp Q9H6S0 YTDC2	6	20.35	20.12	19.95	20.16	19.81	19.85	22.47	22.29	22.27	23.01	22.83	23.00	2.6701	0.0027	-0.601624	-7.05
sp P62879 GBB2	11	18.20	18.31	18.24	18.23	17.82	18.11	21.20	21.36	21.44	21.94	21.72	22.14	1.8777	0.0059	-0.601989	-4.24
sp Q9BQE3 TBA1C	10	16.71	16.90	16.99	16.70	16.55	16.78	19.57	19.82	20.05	20.29	20.31	20.68	1.5082	0.0150	-0.608437	-3.26
sp P52907 CAZA1	12	18.02	17.88	17.81	17.70	17.69	17.75	21.15	21.06	21.13	21.55	21.71	21.91	2.3168	0.0021	-0.608733	-5.65
sp P10515 ODP2	16	15.57	15.90	15.97	15.70	15.47	15.70	19.11	19.49	19.71	19.96	19.91	20.27	1.3607	0.0237	-0.609636	-2.91
sp Q6P2Q9 PRP8	6	17.20	17.61	17.52	17.29	17.19	17.33	19.32	19.79	19.85	20.14	20.21	20.48	1.4745	0.0163	-0.625107	-3.18
sp P04264 K2C1	29	21.50	21.44	21.39	21.41	21.24	21.18	23.58	23.58	23.68	24.22	24.24	24.30	3.9862	0.0000	-0.639229	-15.42
sp P06576 ATPB	16	18.53	18.33	18.20	18.23	18.12	18.24	22.07	21.92	21.94	22.49	22.56	22.82	2.3839	0.0023	-0.646507	-5.90
sp P63244 RACK1	11	19.24	19.16	19.25	19.21	19.10	18.64	22.24	22.21	#N/A	22.93	23.00	22.67	1.8199	0.0080	-0.646568	-5.03
sp P22695 QCR2	12	17.98	18.18	18.20	18.01	17.99	17.92	21.11	21.36	21.53	21.85	22.01	22.08	2.0266	0.0045	-0.650497	-4.69
sp P38646 GRP75	12	16.50	16.60	16.61	16.42	16.39	16.51	19.63	19.77	19.94	20.27	20.41	20.67	1.9847	0.0053	-0.66883	-4.56
sp P18124 RL7	5	17.89	17.82	17.75	17.88	17.58	17.61	19.75	19.73	19.81	20.46	20.34	20.50	3.6254	0.0000	-0.671103	-12.48
sp P24844 MYL9	11	21.90	21.84	21.87	21.81	21.71	21.79	24.90	24.90	25.07	25.52	25.61	25.82	2.5946	0.0026	-0.694974	-6.73
sp O15067 PUR4	6	16.50	16.41	16.25	16.42	16.26	16.19	18.62	18.59	18.57	19.27	19.28	19.35	4.7922	0.0000	-0.704259	-24.63
sp P07437 TBB5	35	20.64	20.69	20.48	20.63	20.45	20.68	23.72	23.84	23.78	24.40	24.40	24.78	2.3276	0.0022	-0.748801	-5.69
sp P41252 SYIC	9	23.27	23.20	22.79	23.27	23.01	22.83	25.98	25.96	25.70	26.70	26.62	26.57	2.7956	0.0015	-0.752087	-7.61
sp P09758 TACD2	27	21.43	21.28	21.19	21.39	21.16	21.08	23.62	23.51	23.55	24.34	24.29	24.33	4.5634	0.0000	-0.761398	-21.57
sp Q9C0C2 TB182	6	19.62	19.70	19.72	19.76	19.64	19.54	21.74	21.88	22.04	22.60	22.67	22.70	2.9638	0.0019	-0.769756	-8.42
sp O75351 VPS4B	12	18.04	18.00	17.93	18.09	17.92	17.91	20.16	20.18	20.25	20.93	20.94	21.07	3.9569	0.0000	-0.782	-15.16
sp Q15836 VAMP3	12	18.03	17.96	18.11	17.90	18.11	18.04	21.15	21.14	21.43	21.75	22.14	22.19	2.0118	0.0054	-0.785109	-4.64

sp Q96LD4 TRI47	6	16.81	16.62	16.51	16.73	16.61	16.63	18.94	18.80	18.83	19.58	19.63	19.79	3.3885	0.0000	-0.810813	-10.85
sp O75874 IDHC	12	17.24	17.24	17.31	17.46	17.21	17.21	20.37	20.42	20.64	21.31	21.23	21.37	3.0818	0.0022	-0.827451	-9.04
sp O43405 COCH	4	16.85	16.99	16.69	16.91	16.69	17.02	18.39	18.58	18.43	19.17	19.13	19.59	2.1939	0.0040	-0.829615	-5.23
sp Q8WUF5 IASPP	6	19.40	19.47	19.54	19.49	19.46	19.57	21.53	21.65	21.87	22.33	22.48	22.72	2.2687	0.0020	-0.832737	-5.48
sp Q7Z7K6 CENPV	12	21.63	21.54	21.57	21.71	21.62	21.51	24.76	24.71	24.89	25.56	25.64	25.67	3.7085	0.0000	-0.834646	-13.11
sp P05198 IF2A	11	18.87	19.03	19.10	19.10	19.03	19.06	21.87	22.08	22.30	22.82	22.93	23.09	2.3691	0.0022	-0.861933	-5.84
sp P02786 TFR1	34	22.02	21.99	21.86	22.05	21.93	22.08	24.96	25.00	25.03	25.74	25.81	26.10	2.8570	0.0016	-0.88545	-7.90
sp Q9NQ88 TIGAR	5	19.08	19.12	18.95	19.28	19.11	19.05	20.94	21.03	21.01	21.86	21.87	21.94	4.7582	0.0000	-0.894146	-24.15
sp O76003 GLRX3	7	17.78	17.82	17.78	17.86	17.97	17.84	20.13	20.22	20.33	20.93	21.21	21.22	2.8608	0.0016	-0.89549	-7.92
sp Q96S97 MYADM	11	19.17	19.05	18.96	19.19	19.14	19.15	22.17	22.10	22.16	22.91	23.04	23.18	3.4082	0.0000	-0.900043	-10.98
sp Q9Y6D5 BIG2	4	19.90	19.74	19.73	19.92	19.90	19.86	21.44	21.33	21.47	22.18	22.33	22.43	3.3739	0.0000	-0.901337	-10.76
sp P35222 CTNB1	67	20.69	20.62	20.43	20.92	20.70	20.47	23.33	23.30	23.32	24.26	24.24	24.21	6.1306	0.0000	-0.915851	-53.32
sp Q6IAA8 LTOR1	12	16.13	16.16	16.30	16.31	16.36	16.54	19.25	19.34	19.63	20.16	20.38	20.70	2.1813	0.0048	-1.00524	-5.18
sp Q14204 DYHC1	26	18.12	18.08	18.02	18.31	18.18	18.20	20.62	20.62	20.71	21.61	21.63	21.79	4.0036	0.0000	-1.02893	-15.58
sp P62333 PRS10	5	16.01	16.19	16.15	16.57	16.10	16.39	17.88	18.10	18.21	19.15	18.86	19.28	2.5268	0.0025	-1.03102	-6.45
sp P21399 ACOC	6	17.21	17.16	17.10	17.51	17.31	17.46	19.33	19.34	19.42	20.35	20.34	20.62	3.4324	0.0000	-1.07288	-11.14
sp Q9P258 IRCC2	11	16.31	16.11	16.01	16.71	16.35	16.20	19.31	19.16	19.21	20.43	20.25	20.23	3.7920	0.0000	-1.07891	-13.76
sp Q09666 AHNK	34	20.68	20.44	20.61	20.85	20.79	20.77	23.82	23.65	23.98	24.78	24.91	25.02	3.0798	0.0022	-1.08531	-9.03
sp P11216 PYGB	6	16.04	16.13	16.20	16.45	16.44	16.34	18.17	18.31	18.52	19.30	19.47	19.50	3.0789	0.0021	-1.08975	-9.03
sp P41208 CETN2	5	17.35	17.30	17.43	17.73	17.60	17.63	19.21	19.21	19.50	20.31	20.36	20.53	3.1687	0.0000	-1.09534	-9.53
sp Q9NQC3-2 RTN4	12	18.95	18.54	18.78	18.96	18.81	19.40	22.08	21.72	22.10	22.80	22.84	23.56	1.7846	0.0100	-1.09822	-3.98
sp Q9Y624 JAM1	12	19.96	19.96	19.98	20.22	20.23	20.37	23.09	23.14	23.30	24.07	24.25	24.53	2.7510	0.0015	-1.10644	-7.41
sp P24928 RPB1	5	16.65	16.58	16.35	16.93	16.74	16.84	18.52	18.49	18.42	19.51	19.50	19.73	3.7721	0.0000	-1.10837	-13.60
sp P61970 NTF2	5	15.97	15.99	16.04	16.21	16.23	16.50	17.83	17.91	18.10	18.79	18.99	19.39	2.3232	0.0021	-1.10918	-5.68
sp P98160 PGBM	6	16.71	16.67	16.53	16.96	16.99	17.04	18.84	18.85	18.85	19.81	20.01	20.19	3.3245	0.0000	-1.15635	-10.45
sp P16422 EPCAM	6	17.53	17.32	17.06	18.05	17.63	17.36	19.66	19.49	19.39	20.89	20.65	20.52	3.0220	0.0020	-1.17655	-8.72
sp Q01650 LAT1	6	17.80	17.75	17.68	18.27	18.19	18.07	19.92	19.93	20.01	21.11	21.21	21.23	4.9619	0.0000	-1.23106	-27.17
sp P55268 LAMB2	11	17.54	17.39	16.74	18.03	17.74	17.20	19.52	19.45	19.02	20.74	20.64	20.31	2.4271	0.0024	-1.23277	-6.06
sp O75976 CBPD	10	18.11	18.02	17.93	18.61	18.40	18.51	20.97	20.93	20.99	22.19	22.16	22.40	4.0815	0.0000	-1.28679	-16.30
sp P18084 ITB5	5	15.54	15.71	15.52	16.31	16.16	15.84	17.40	17.62	17.58	18.90	18.92	18.74	3.9326	0.0000	-1.31469	-14.94
sp P09110 THIK	12	14.46	14.54	14.71	15.29	14.99	15.24	17.59	17.72	18.04	19.13	19.01	19.40	2.8738	0.0017	-1.3974	-7.98
sp P50895 BCAM	23	19.02	19.09	18.85	19.60	19.47	19.57	21.54	21.63	21.54	22.89	22.94	23.12	4.3232	0.0000	-1.41268	-18.76
sp P35908 K22E	11	18.08	17.89	17.00	18.69	18.52	17.91	20.17	20.03	19.26	21.44	21.43	20.88	1.8670	0.0073	-1.42569	-4.21
sp Q96PK6 RBM14	12	16.97	17.18	17.28	17.82	17.80	17.75	20.10	20.36	20.60	21.66	21.82	21.91	3.0473	0.0020	-1.44316	-8.86
sp Q14683 SMC1A	6	17.46	17.46	17.51	18.28	18.06	18.15	19.58	19.64	19.84	21.13	21.08	21.30	3.8806	0.0000	-1.48449	-14.50
sp P60228 EIF3E	6	14.49	13.97	13.32	15.04	14.67	14.51	16.62	16.15	15.65	17.89	17.69	17.67	2.2995	0.0021	-1.61301	-5.59
sp P13645 K1C10	10	18.79	18.55	18.42	19.56	19.38	19.35	20.45	20.21	20.18	21.89	21.87	21.94	4.3059	0.0000	-1.61846	-18.57
sp O43181 INDUS4	6	16.87	16.80	16.81	17.82	17.68	17.74	19.00	18.98	19.14	20.67	20.70	20.89	4.4224	0.0000	-1.71576	-19.88
sp P62701 RS4X	15	17.77	17.72	17.72	19.15	19.06	19.18	20.38	20.40	20.54	22.69	22.77	23.04	4.4607	0.0000	-2.39294	-20.32

Supplementary Table 3. Proteins significantly up/downregulated in GFP-CD63 compared to GFP-Parallel control cells

Prot. Acc. Gene Name (continued on next page)	Peptide Count	Raw Chromatogram Area (Log2 Transformed)						Median Norm.Chromatogram Area (Log2 Transformed)						-Log (p-val) >1.3 *p-val<0.05	q-value	Fold Change Difference (log ₂) > 0.5 *FC> 1.4	T-test Stat
		GFP-CD63			GFP- Ctrl			GFP-CD63			GFP- Ctrl						
spIQ9UL42 PNMA2	24	17.99	17.82	17.78	16.50	16.52	16.42	20.67	20.72	20.66	19.31	19.42	19.36	5.5025	0.0000	1.3182	37.12
spIQ43292 GPAA1	6	17.20	16.80	16.88	16.07	15.63	15.45	19.55	19.39	19.46	18.55	18.23	18.10	2.9354	0.0020	1.1754	8.28
spIQ9UNH7 SNX6	6	16.24	16.14	15.93	15.03	14.85	14.88	18.59	18.73	18.51	17.50	17.45	17.52	4.0920	0.0000	1.1186	16.40
spIQ01581 HMCS1	48	19.29	19.07	19.07	18.04	17.91	17.95	22.47	22.50	22.48	21.38	21.35	21.45	5.4582	0.0000	1.0873	36.19
spIQ03426 KIME	6	15.68	15.12	15.43	14.17	14.57	14.05	18.03	17.71	18.01	16.65	17.17	16.69	2.2925	0.0077	1.0773	5.57
spIQ03518 TAP1	12	17.72	17.42	17.36	16.45	16.26	16.40	20.07	20.01	19.94	18.93	18.86	19.05	4.0499	0.0000	1.0591	16.00
spIP68431 H31	30	20.18	19.76	19.76	19.01	18.79	18.60	24.15	23.98	23.95	23.11	23.01	22.84	3.3260	0.0037	1.0362	10.46
spIQ8N1N4 K2C78	6	19.44	19.24	19.28	18.26	18.21	18.26	21.79	21.83	21.86	20.74	20.82	20.90	4.3945	0.0000	1.0075	19.56
spIQ01469 FABP5	30	20.50	20.35	20.43	19.52	19.38	19.43	23.81	23.90	23.95	22.95	22.94	23.03	4.2217	0.0000	0.9120	17.69
spIP84243 H33	18	19.99	19.64	19.70	18.97	18.79	18.65	23.92	23.82	23.86	23.04	22.98	22.88	4.1107	0.0000	0.9019	16.58
spIQ8VVV7 UBCP1	6	15.26	14.83	15.25	14.27	14.14	14.07	17.61	17.42	17.83	16.75	16.74	16.72	2.7642	0.0026	0.8807	7.47
spIP20337 RAB3B	6	16.49	16.58	16.59	15.63	15.66	15.61	18.84	19.17	19.17	18.11	18.26	18.26	2.6381	0.0031	0.8503	6.91
spIQ8NG68 TTL	5	18.61	18.08	18.03	17.82	17.08	17.10	20.70	20.41	20.34	20.04	19.42	19.48	1.6885	0.0205	0.8345	3.72
spIQ9UDY4 DNJB4	12	18.55	18.35	18.50	17.73	17.55	17.45	20.89	20.95	21.08	20.21	20.16	20.10	3.6769	0.0000	0.8184	12.87
spIQ71DI3 H32	30	21.48	21.03	21.15	20.54	20.37	20.10	25.20	24.97	25.10	24.39	24.35	24.12	2.7763	0.0027	0.8056	7.52
spIQ9BYT8 NEUL	6	16.32	15.87	16.09	15.49	15.18	15.04	18.67	18.46	18.66	17.97	17.79	17.68	2.7016	0.0033	0.7862	7.18
spIP56385 ATP5I	6	17.70	17.41	17.29	16.74	16.55	16.64	20.05	20.00	19.87	19.21	19.15	19.28	3.4645	0.0025	0.7594	11.35
spIP30050 RL12	6	19.23	18.93	18.95	18.49	18.23	18.13	21.58	21.53	21.52	20.96	20.83	20.78	3.5338	0.0000	0.6852	11.83
spIP07686 HEXB	18	18.42	18.19	18.41	17.63	17.50	17.43	21.16	21.22	21.40	20.54	20.59	20.60	3.1234	0.0026	0.6807	9.27
spIQ9H8H0 NOL11	6	15.81	15.60	15.36	15.18	14.78	14.97	18.15	18.19	#N/A	17.65	17.38	#N/A	1.3803	0.0393	0.6576	4.74
spIQ15116 LSM1	6	16.74	16.30	16.42	16.16	15.63	15.50	19.09	18.89	19.00	18.64	18.23	18.15	1.8004	0.0157	0.6544	4.02
spIQ58FF6 H90B4	6	18.94	18.87	18.90	18.32	18.10	18.14	21.29	21.46	21.48	20.80	20.70	20.79	3.1837	0.0030	0.6491	9.61
spIP52758 RIDA	12	17.95	17.90	17.90	17.23	17.23	17.19	21.30	21.49	21.48	20.71	20.83	20.84	2.9514	0.0021	0.6286	8.36
spIP00813 ADA	6	15.96	15.86	16.01	15.54	14.89	15.33	18.31	18.46	18.59	18.02	17.49	17.97	1.5422	0.0288	0.6239	3.35
spIQ9H0G5 INSRP1	6	17.19	16.93	17.03	16.44	16.49	16.14	19.54	19.52	19.60	18.92	19.09	18.78	2.6198	0.0031	0.6237	6.83
spIP08134 RHOC	12	19.18	19.17	19.21	18.59	18.50	18.48	22.53	22.76	22.79	22.07	22.10	22.12	2.6975	0.0033	0.5984	7.17
spIP50991 TICPD	12	18.51	18.29	18.48	17.89	17.69	17.71	21.86	21.88	22.05	21.37	21.29	21.35	3.0494	0.0023	0.5929	8.87
spIP14735 IDE	12	18.76	18.67	18.74	18.20	18.00	17.98	22.11	22.26	22.32	21.68	21.60	21.63	3.0610	0.0023	0.5909	8.93
spIQ15785 TOM34	12	16.29	16.25	16.27	15.48	15.58	15.77	19.64	19.84	19.84	18.95	19.18	19.42	1.7821	0.0168	0.5901	3.97
spIP33991 MCM4	60	19.47	19.30	19.28	18.85	18.85	18.42	22.69	22.75	22.61	22.21	22.33	21.75	1.4979	0.0306	0.5879	3.24
spIP61769 B2MG	12	18.41	18.24	18.42	17.73	17.68	17.69	21.76	21.83	21.99	21.21	21.28	21.33	2.7384	0.0034	0.5842	7.35
spIP52292 IMA1	24	18.14	17.78	17.91	17.30	17.48	17.16	21.97	21.86	22.00	21.25	21.58	21.26	2.1220	0.0099	0.5782	4.99
spIP17812 PYRG1	6	17.59	17.37	17.43	16.96	16.75	16.74	19.93	19.96	20.01	19.44	19.35	19.39	4.0482	0.0000	0.5750	15.99
spIQ13630 FCL	6	17.77	17.49	17.29	17.17	16.61	16.85	20.12	20.08	19.87	19.65	19.21	19.50	1.7068	0.0203	0.5685	3.77
spIP23381 SYWC	12	19.20	19.00	19.05	18.61	18.47	18.28	22.55	22.59	22.63	22.09	22.07	21.92	3.1958	0.0031	0.5616	9.68
spIP98179 RBM3	12	17.68	17.61	17.54	17.05	16.95	16.94	21.03	21.20	21.12	20.53	20.55	20.59	3.3352	0.0038	0.5596	10.52
spIQ9H9J2 RM44	6	16.33	16.07	15.88	15.76	15.18	15.47	18.68	18.66	18.46	18.24	17.79	18.12	1.6493	0.0228	0.5525	3.62
spIQ9UIA9 XPO7	6	16.10	15.86	15.75	15.46	15.04	15.36	18.45	18.45	18.32	17.94	17.64	18.00	1.9900	0.0121	0.5491	4.57
spIQ15270 SPTC2	6	14.18	14.23	14.23	13.82	13.39	13.58	16.53	16.82	16.81	16.30	16.00	16.22	1.8366	0.0154	0.5447	4.12
spIP60510 PP4C	12	16.36	16.07	15.97	15.86	15.56	15.15	19.71	19.66	19.55	19.34	19.17	18.80	1.4890	0.0310	0.5387	3.22
spIQ6NZI2 CAVN1	24	20.71	20.55	20.42	20.09	19.89	19.93	24.06	24.14	24.00	23.57	23.49	23.57	3.3711	0.0040	0.5228	10.74
spIP13798 ACPH	30	19.64	19.50	19.48	19.08	18.91	19.01	22.72	22.84	22.81	22.27	22.20	22.36	3.0315	0.0022	0.5140	8.77

sp Q92544 TM9S4	12	16.61	16.02	16.48	16.80	16.70	16.98	19.96	19.61	20.06	20.28	20.30	20.63	1.3905	0.0392	-0.5285	-2.98
sp Q9H4A6 GOLP3	18	16.13	16.04	15.90	16.58	16.34	16.50	19.06	19.16	19.02	19.62	19.54	19.70	2.9851	0.0021	-0.5381	-8.53
sp P62266 RS23	6	18.48	18.47	18.51	19.02	18.92	18.93	20.83	21.06	21.09	21.50	21.52	21.58	2.4522	0.0051	-0.5389	-6.16
sp P22234 PUR6	18	17.69	17.41	17.41	17.96	17.90	17.74	20.66	20.66	20.65	21.20	21.27	21.13	3.7593	0.0000	-0.5416	-13.50
sp P62857 RS28	30	20.00	19.79	19.87	20.30	20.19	20.14	22.63	22.69	22.78	23.24	23.26	23.24	3.6182	0.0000	-0.5442	-12.43
sp P40261 NNMT	30	18.27	17.95	17.95	18.55	18.30	18.36	20.88	20.76	20.68	21.39	21.26	21.31	2.8084	0.0027	-0.5468	-7.67
sp P46063 RECQ1	6	16.70	16.63	16.58	17.17	17.15	17.05	19.05	19.22	19.16	19.65	19.75	19.70	3.1562	0.0028	-0.5562	-9.45
sp P54709 AT1B3	18	18.35	18.14	18.28	18.75	18.67	18.71	21.51	21.51	21.65	22.05	22.12	22.18	3.1429	0.0028	-0.5590	-9.38
sp Q9H7N4 SFR19	6	13.32	13.12	13.29	13.64	13.76	13.88	15.67	15.71	15.86	16.12	16.36	16.53	1.9609	0.0122	-0.5881	-4.49
sp Q8N335 GPD1L	6	15.28	15.12	15.22	15.77	15.64	15.78	17.63	17.72	17.80	18.25	18.24	18.42	2.7747	0.0027	-0.5896	-7.51
sp O14957 QCR10	6	16.19	15.98	16.39	16.56	16.70	16.87	18.54	18.57	18.97	19.04	19.30	19.51	1.4141	0.0377	-0.5914	-3.04
sp O00767 ACOD	6	16.02	15.51	15.51	16.33	16.02	16.26	18.36	18.10	18.09	18.81	18.62	18.90	2.0904	0.0106	-0.5940	-4.89
sp P84085 ARF5	12	15.02	14.84	14.96	15.48	15.56	15.42	18.37	18.43	18.54	18.95	19.16	19.07	2.8437	0.0018	-0.6147	-7.83
sp P60059 SC61G	6	16.23	16.27	16.38	16.89	16.80	16.84	18.57	18.86	18.96	19.37	19.40	19.49	2.1709	0.0094	-0.6194	-5.15
sp Q15436 SC23A	12	16.87	16.73	16.81	17.39	17.27	17.40	20.22	20.32	20.39	20.87	20.87	21.05	2.8577	0.0019	-0.6212	-7.90
sp P63167 DYL1	12	16.42	15.94	16.38	16.87	16.75	16.92	19.77	19.53	19.96	20.35	20.35	20.56	2.0135	0.0119	-0.6647	-4.65
sp O00483 INDUA4	6	16.22	15.97	16.10	16.56	16.80	16.77	18.56	18.57	18.68	19.04	19.40	19.41	2.2120	0.0084	-0.6818	-5.29
sp P30043 BLVRB	30	19.48	19.22	19.18	19.89	19.91	19.96	22.78	22.79	22.75	23.35	23.49	23.59	3.2591	0.0034	-0.7049	-10.05
sp P07602 SAP	12	15.80	15.42	15.59	16.31	16.21	16.26	19.15	19.01	19.17	19.79	19.81	19.91	3.5093	0.0028	-0.7204	-11.66
sp P21266 GSTM3	12	14.93	14.87	14.65	15.76	15.45	15.21	18.28	18.46	18.23	19.24	19.05	18.86	2.2931	0.0073	-0.7252	-5.57
sp P62140 PP1B	12	16.28	16.16	15.94	16.89	16.73	16.73	19.63	19.75	19.52	20.37	20.33	20.37	3.3586	0.0039	-0.7253	-10.66
sp Q92615 LAR4B	6	18.52	17.68	18.04	18.98	18.77	18.56	20.87	20.27	20.62	21.46	21.37	21.21	1.7970	0.0156	-0.7601	-4.01
sp Q9BYZ2 LDH6B	6	18.48	18.27	18.20	19.18	19.09	18.75	20.83	20.86	20.78	21.66	21.69	21.40	2.8520	0.0018	-0.7622	-7.87
sp P60903 S10AA	30	20.75	20.61	20.80	21.44	21.32	21.42	24.19	24.28	24.47	25.04	25.03	25.18	2.9231	0.0019	-0.7688	-8.22
sp Q92522 H1X	12	16.36	16.27	16.33	17.04	17.03	17.06	19.71	19.86	19.91	20.51	20.64	20.71	3.1826	0.0029	-0.7934	-9.61
sp P43490 NAMPT	128	22.03	21.82	21.85	22.69	22.62	22.56	24.78	24.79	24.80	25.56	25.61	25.60	6.0465	0.0000	-0.7956	-50.80
sp O00422 SAP18	12	15.38	15.27	15.25	16.10	16.13	15.86	18.73	18.86	18.83	19.57	19.73	19.51	3.3158	0.0036	-0.8001	-10.40
sp P11166 GTR1	6	17.36	17.30	17.36	18.10	18.06	18.09	19.71	19.89	19.94	20.58	20.66	20.73	3.2228	0.0032	-0.8124	-9.84
sp P68371 TBB4B	24	19.57	19.28	19.30	19.98	20.31	20.10	22.91	22.87	22.88	23.46	23.92	23.75	2.4548	0.0051	-0.8208	-6.17
sp P61353 RL27	18	19.71	19.78	19.68	20.51	20.46	20.46	22.06	22.38	22.26	22.99	23.06	23.11	2.9429	0.0020	-0.8216	-8.32
sp Q8WX92 NELFB	6	14.00	14.02	13.79	14.88	14.62	14.68	16.35	16.61	16.37	17.36	17.22	17.32	3.1078	0.0025	-0.8608	-9.19
sp P13645 K1C10	18	16.93	16.79	16.82	17.33	17.27	17.34	19.81	19.91	19.23	20.52	20.54	20.65	1.8951	0.0139	-0.9190	-4.29
sp Q15369 ELOC	6	15.15	14.50	14.02	15.43	15.39	15.43	17.50	17.09	16.60	17.91	17.99	18.08	1.6131	0.0229	-0.9299	-3.52
sp Q53H82 LACB2	6	16.21	16.22	16.36	17.22	17.09	17.06	18.56	18.81	18.94	19.70	19.69	19.70	2.9499	0.0021	-0.9301	-8.35
sp P61513 RL37A	12	14.54	14.43	14.38	15.62	15.17	15.25	17.89	18.02	17.96	19.10	18.77	18.89	3.1411	0.0027	-0.9651	-9.37
sp Q15102 PA1B3	12	18.41	17.71	17.02	18.75	18.63	18.47	20.76	20.30	19.60	21.23	21.23	21.12	1.3393	0.0440	-0.9714	-2.86
sp P15954 COX7C	6	16.45	16.36	16.17	17.31	17.31	17.33	18.80	18.95	18.75	19.79	19.91	19.97	3.6818	0.0000	-1.0546	-12.90
sp P61313 RL15	18	16.65	16.40	16.42	17.47	17.53	17.43	19.85	19.90	19.93	20.81	21.05	21.00	3.8084	0.0000	-1.0618	-13.90
sp Q9Y3T9 NOC2L	18	16.73	17.28	17.05	18.48	18.40	18.10	19.44	20.11	19.88	21.06	21.10	20.87	2.3326	0.0069	-1.1993	-5.71
sp O75828 CBR3	18	17.62	17.56	17.59	19.31	19.18	19.19	20.85	21.08	21.11	22.19	22.20	22.26	3.8452	0.0000	-1.2022	-14.20
sp O14684 PTGES	6	17.30	16.97	17.22	18.31	18.24	18.34	19.65	19.56	19.80	20.79	20.84	20.99	3.7040	0.0000	-1.2053	-13.07
sp P26006 ITA3	6	16.55	16.60	15.79	17.58	17.56	17.43	18.90	19.19	18.37	20.06	20.16	20.07	2.2024	0.0082	-1.2796	-5.26

Supplementary Table 4. Proteins significantly up/downregulated in CD81-Tdtomato compared to Tom-Parallel control cells

Prot. Acc. Gene Name <i>(continued next page)</i>	Peptide Count	Raw Chromatogram Area (Log2 Transformed)						Median Norm.Chromatogram Area (Log2 Transformed)						-Log (p-val) >1.3 <i>*p-val<0.05</i>	q-value	Fold Change Difference (log2) > 0.5 <i>*FC> 1.4 </i>	T-test Stat
		CD81- TOM			Tom- Ctrl			CD81- TOM			Tom- Ctrl						
sp O94925-3 GLSK	6	15.86	15.90	15.93	14.49	14.27	14.43	18.25	18.39	18.54	17.05	16.88	17.07	3.7682	0.0055	1.3922	13.57
sp P98179 RBM3	12	17.73	17.75	17.64	16.42	16.67	16.46	21.12	21.23	21.24	19.99	20.27	20.09	3.5543	0.0044	1.0806	11.97
sp Q9Y217 MTMR6	6	16.25	16.31	16.50	14.92	15.04	15.25	18.64	18.79	#N/A	17.49	17.64	17.88	2.1533	0.0152	1.0425	6.62
sp Q01581 HMCS1	78	20.37	20.33	20.23	19.20	19.19	19.08	23.87	23.94	23.97	22.91	22.93	22.86	5.0486	0.0000	1.0306	28.56
sp O94925 GLSK	6	17.44	17.59	17.63	16.36	16.49	16.46	19.83	20.07	20.23	18.92	19.09	19.10	2.8322	0.0116	1.0078	7.78
sp P55809 SCOT1	48	20.18	20.12	20.03	18.97	19.08	18.99	23.32	23.38	23.39	22.31	22.46	22.40	4.4243	0.0059	0.9769	19.90
sp Q53H82 LACB2	6	18.08	18.16	18.13	17.09	17.17	17.11	20.46	20.64	20.74	19.65	19.78	19.75	3.2602	0.0059	0.8899	10.06
sp O75368 SH3L1	6	16.19	15.85	15.80	15.28	14.86	14.90	18.57	18.34	18.40	17.85	17.46	17.53	2.3931	0.0136	0.8238	5.93
sp Q16762 THTR	6	16.03	16.11	15.74	14.88	15.16	15.08	18.42	18.59	18.35	17.45	17.76	17.71	2.5923	0.0153	0.8127	6.72
sp P04040 CATA	6	16.74	16.67	16.62	15.79	15.74	15.76	19.13	19.16	19.23	18.36	18.34	18.39	4.7969	0.0000	0.8069	24.69
sp O00483 NDUA4	6	17.13	17.25	17.39	16.30	16.34	16.44	19.52	19.73	19.99	18.87	18.95	19.08	2.1816	0.0150	0.7837	5.19
sp Q13423 NNTM	84	20.94	20.84	20.78	19.96	19.93	19.97	23.79	23.82	23.89	23.02	23.03	23.11	4.3599	0.0054	0.7822	19.17
sp Q9UFN0 NPS3A	6	14.94	14.85	15.07	13.90	14.26	14.10	17.33	17.34	17.68	16.47	16.87	16.74	2.0097	0.0177	0.7569	4.63
sp O00244 ATOX1	12	17.57	17.47	17.49	16.78	16.56	16.67	20.95	20.96	21.09	20.35	20.17	20.30	3.2691	0.0060	0.7280	10.11
sp Q99519 NEUR1	6	14.98	15.12	14.38	14.22	14.16	14.09	17.37	17.60	#N/A	16.79	16.77	16.73	2.3915	0.0135	0.7259	8.01
sp Q13509 TBB3	12	19.35	19.32	19.14	18.45	18.43	18.51	22.74	22.81	22.74	22.02	22.03	22.15	3.9108	0.0068	0.6995	14.75
sp A6NDU8 CE051	30	17.88	17.75	17.62	17.13	16.85	17.00	21.76	21.71	21.69	21.17	20.91	21.08	2.9698	0.0106	0.6639	8.46
sp Q9BYN0 SRXN1	18	17.65	17.41	17.30	16.58	16.83	16.48	20.35	20.25	20.24	19.53	19.83	19.50	2.3783	0.0138	0.6600	5.88
sp P20618 PSB1	24	19.41	19.38	19.29	18.62	18.55	18.64	22.80	22.87	22.90	22.19	22.15	22.28	3.7527	0.0054	0.6505	13.45
sp P17301 ITA2	60	19.20	19.11	19.06	18.36	18.32	18.35	22.35	22.34	22.40	21.71	21.67	21.75	4.6380	0.0000	0.6500	22.52
sp Q81V08 PLD3	6	16.78	16.53	16.39	15.79	15.80	15.84	19.17	19.02	19.00	18.36	18.40	18.48	3.2830	0.0048	0.6488	10.20
sp P08582 TRFM	6	15.22	15.25	14.89	14.42	14.32	14.37	17.61	17.73	17.49	16.99	16.92	17.01	2.9949	0.0099	0.6405	8.58
sp P21291 CSRFP1	48	20.22	20.15	20.08	19.42	19.42	19.37	23.61	23.63	23.68	22.99	23.02	23.01	4.9834	0.0000	0.6396	27.51
sp Q9H4L4 SENP3	6	16.32	16.18	16.30	15.43	15.45	15.68	18.71	18.67	18.91	18.00	18.06	18.31	2.2158	0.0146	0.6389	5.30
sp P53677 AP3M2	6	18.26	18.07	18.04	17.58	17.36	17.17	20.65	20.55	#N/A	20.15	19.96	19.81	1.7394	0.0278	0.6267	4.70
sp Q56VL3 OCAD2	6	16.01	15.93	15.82	15.40	15.04	15.13	18.39	18.42	18.42	17.97	17.65	17.76	2.5439	0.0139	0.6197	6.52
sp P0DP23 CALM1	30	21.48	21.48	21.45	20.79	20.76	20.74	24.80	24.91	25.01	24.27	24.29	24.31	3.2722	0.0047	0.6143	10.13
sp Q8NF37 PCAT1	42	19.66	19.74	19.62	18.99	18.93	18.95	22.99	23.17	23.18	22.50	22.49	22.53	3.2011	0.0074	0.6074	9.71
sp Q8IZ07 AN13A	6	15.62	15.59	15.69	14.97	14.77	15.02	18.01	18.07	18.30	17.54	17.38	17.66	2.1460	0.0155	0.6044	5.07
sp P08134 RHOC	12	18.77	18.89	18.76	18.13	17.98	18.18	22.16	22.38	22.37	21.70	21.59	21.82	2.4401	0.0136	0.6024	6.11
sp Q9UBR2 CATZ	6	17.35	17.15	17.12	16.33	16.57	16.59	19.74	19.64	19.72	18.90	19.18	19.23	2.3037	0.0147	0.5997	5.61
sp Q10471 GALT2	6	16.54	16.64	16.58	15.78	15.93	15.93	18.93	19.13	19.19	18.34	18.54	18.56	2.3320	0.0144	0.5992	5.71
sp Q9UDY4 DNJB4	18	18.25	18.28	18.26	17.64	17.52	17.56	20.63	20.77	20.87	20.21	20.12	20.19	2.8656	0.0114	0.5823	7.94
sp P18031 PTN1	36	20.13	20.07	20.02	19.43	19.32	19.31	23.14	23.19	23.26	22.65	22.59	22.62	3.9071	0.0065	0.5743	14.72
sp P07099 HYEP	30	19.20	19.08	19.00	18.50	18.37	18.43	21.85	21.82	21.85	21.32	21.21	21.34	3.7516	0.0053	0.5479	13.44
sp P35754 GLRX1	6	17.06	16.92	16.66	16.31	16.15	16.24	19.45	19.41	19.26	18.88	18.75	18.87	2.8206	0.0124	0.5382	7.73
sp Q9Y2W2 WBP11	6	15.54	15.67	15.69	15.06	15.03	14.89	17.93	18.16	18.29	17.62	17.64	17.52	2.0596	0.0168	0.5356	4.79
sp P43490 NAMPT	158	23.08	23.00	22.94	22.34	22.34	22.34	25.90	25.93	25.94	25.37	25.39	25.41	5.2669	0.0000	0.5338	32.40
sp P28070 PSB4	42	19.53	19.47	19.35	18.78	18.80	18.83	22.83	22.91	22.91	22.31	22.32	22.41	3.6286	0.0048	0.5328	12.51
sp Q03169 TNAP2	36	18.52	18.47	18.29	17.84	17.77	17.76	21.44	21.47	21.41	20.94	20.87	20.92	4.3502	0.0052	0.5288	19.06
sp Q9H2G4 TSLY2	6	17.06	17.17	17.39	16.62	16.53	16.56	19.45	19.66	19.99	19.18	19.13	19.20	1.5141	0.0415	0.5273	3.28
sp Q8NFJ5 IRAI3	18	16.74	16.62	16.70	16.10	15.88	16.17	20.71	20.69	20.89	20.26	20.07	20.39	2.0266	0.0171	0.5271	4.69

Appendix II

sp P08727 K1C19	129	24.33	23.98	23.83	23.32	23.51	23.38	27.56	27.28	27.21	26.72	26.94	26.81	1.8705	0.0227	0.5251	4.22
sp Q9UK22 FBX2	12	18.06	17.90	17.78	17.47	17.20	17.23	21.45	21.39	21.38	21.04	20.81	20.87	2.6273	0.0129	0.5017	6.86
sp P05556 ITB1	12	18.93	18.86	18.88	18.21	18.33	18.30	22.32	22.34	22.49	21.78	21.93	21.94	2.6188	0.0142	0.5007	6.83
sp P32320 CDD	54	20.19	20.17	20.04	20.61	20.48	20.47	23.69	23.76	23.75	24.29	24.22	24.23	4.1644	0.0046	-0.5111	-17.11
sp Q96C19 EFHD2	132	21.36	21.21	21.10	21.56	21.65	21.59	24.81	24.77	24.72	25.23	25.33	25.29	3.8091	0.0058	-0.5148	-13.90
sp P63279 UBC9	6	15.64	15.57	15.20	16.03	15.90	15.73	18.03	18.05	17.80	18.59	18.51	18.36	2.1408	0.0154	-0.5248	-5.05
sp P36776 LONM	6	13.95	14.23	13.84	14.61	14.36	14.32	16.34	16.72	16.45	17.18	16.96	16.95	1.7693	0.0257	-0.5290	-3.94
sp P49588 SYAC	6	18.36	18.28	18.15	18.71	18.72	18.65	20.74	20.76	20.75	21.27	21.32	21.28	5.3912	0.0000	-0.5379	-34.81
sp O43707 ACTN4	60	21.87	21.81	21.69	22.34	22.22	22.15	25.26	25.30	25.30	25.91	25.82	25.79	3.8407	0.0062	-0.5497	-14.16
sp O43175 SERA	131	22.33	22.23	22.16	22.69	22.65	22.64	25.49	25.48	25.51	26.05	26.03	26.05	5.9936	0.0000	-0.5503	-49.28
sp Q58FF6 H90B4	6	17.81	17.81	17.63	18.23	18.18	18.18	20.20	20.30	20.24	20.80	20.78	20.81	4.2469	0.0048	-0.5515	-17.95
sp Q96C36 P5CR2	18	17.68	17.64	17.21	17.96	18.00	17.90	20.91	20.99	20.64	21.33	21.47	21.40	2.1081	0.0161	-0.5541	-4.94
sp Q5JT29 SYAM	12	15.55	15.55	15.34	16.08	15.98	15.74	18.94	19.03	18.95	19.65	19.58	19.37	2.5228	0.0132	-0.5591	-6.43
sp P78330 SERB	6	16.28	16.23	15.92	16.83	16.50	16.50	18.67	18.72	18.53	19.40	19.10	19.14	2.2120	0.0145	-0.5735	-5.29
sp Q8WXX5 DNJC9	12	16.56	16.70	16.25	17.04	17.06	16.95	19.95	20.19	19.85	20.61	20.67	20.58	2.4080	0.0139	-0.6233	-5.99
sp P54577 SYYC	72	20.00	19.89	19.78	20.43	20.38	20.39	22.79	22.81	22.83	23.44	23.44	23.47	5.6357	0.0000	-0.6366	-40.09
sp Q9P258 RCC2	12	16.89	16.98	17.02	17.58	17.51	17.46	20.28	20.47	20.63	21.15	21.11	21.09	2.5378	0.0137	-0.6570	-6.49
sp Q92841 DDX17	18	18.50	18.43	18.37	19.01	18.99	18.93	21.77	21.80	21.86	22.47	22.49	22.47	4.7239	0.0000	-0.6699	-23.67
sp Q15434 RBMS2	12	16.61	16.28	16.07	16.78	17.02	16.85	19.00	18.76	18.68	19.35	19.63	19.48	2.2418	0.0149	-0.6729	-5.39
sp P84243 H33	18	19.04	18.97	18.62	19.67	19.50	19.35	23.02	23.04	22.81	23.82	23.68	23.57	2.6752	0.0137	-0.7349	-7.07
sp P68431 H31	30	19.22	19.21	18.88	19.96	19.85	19.58	23.25	23.36	23.14	24.18	24.09	23.85	2.5746	0.0146	-0.7865	-6.64
sp P62072 TIM10	12	13.87	14.27	14.51	14.97	15.00	14.83	17.26	17.75	18.11	18.54	18.60	18.46	1.5237	0.0413	-0.8270	-3.30
sp Q9C002 NMES1	18	18.03	17.93	17.93	18.76	18.70	18.68	22.00	22.01	22.12	22.91	22.89	22.90	4.5905	0.0000	-0.8573	-21.91
sp Q96R05 RET7	6	14.97	14.57	14.68	15.47	15.50	15.64	17.36	17.06	17.29	18.04	18.10	18.28	2.8423	0.0110	-0.9041	-7.83
sp Q96MM6 HS12B	6	14.95	14.90	15.12	15.83	15.89	15.77	17.34	17.39	17.73	18.40	18.49	18.40	2.7596	0.0140	-0.9461	-7.44
sp Q9Y617 SERC	18	18.98	19.05	18.89	19.72	19.73	19.81	22.13	22.32	22.26	23.11	23.17	23.28	3.6734	0.0049	-0.9493	-12.84